UNIVERSIDADE FEDERAL FLUMINENSE

INSTITUTO DE GEOCIÊNCIAS

PROGRAMA DE PÓS-GRADUAÇÃO EM DINÂMICA DOS OCEANOS E DA TERRA

ELOÍSE HELENA POLICARPO NEVES

APPLICATION OF SEISMIC ATTRIBUTES TO ENHANCE THE IDENTIFICATION OF BOTTOM SIMULATING REFLECTORS IN THE UMITAKA SPUR GAS HYDRATE PROVINCE, JOETSU BASIN, JAPAN

NITERÓI – RJ, BRAZIL

2020

ELOÍSE HELENA POLICARPO NEVES

APPLICATION OF SEISMIC ATTRIBUTES TO ENHANCE THE IDENTIFICATION OF BOTTOM SIMULATING REFLECTORS IN THE UMITAKA SPUR GAS HYDRATE PROVINCE, JOETSU BASIN, JAPAN

Dissertation submitted to the Programa de Pós-Graduação em Dinâmica dos Oceanos e da Terra at Universidade Federal Fluminense as a partial requirement for obtaining a Master's degree

Concentration area: Marine Geology and Geophysics.

Advisors:

Prof. Dr. Antonio Fernando Menezes Freire

Prof. Dr. Cleverson Guizan Silva

NITERÓI - RJ, BRAZIL

2020

Ficha catalográfica automática - SDC/BIG
Gerada com informações fornecidas pelo autor

N511a Neves, Eloise Helena Policarpo
Application of seismic attributes to enhance the identification of Bottom Simulating Reflectors in the Umitaka Spur gas hydrate province, Joetsu Basin, Japan / Eloise Helena Policarpo Neves ; Antonio Fernando Menezes Freire, orientador ; Cleverson Guizan Silva, coorientador. Niterói, 2020.
322 f. : il.

Dissertação (mestrado)-Universidade Federal Fluminense, Niterói, 2020.

DOI: http://dx.doi.org/10.22409/PPGDOT .2020.m.10737849754

1. Seismic Attributes. 2. Gas Hydrates. 3. BSR. 4. Japan Sea. 5. Produção intelectual. I. Freire, Antonio Fernando Menezes, orientador. II. Silva, Cleverson Guizan, coorientador. III. Universidade Federal Fluminense. Instituto de Geociências. IV. Título.

CDD -

Bibliotecário responsável: Sandra Lopes Coelho - CRB7/3389

ELOÍSE HELENA POLICARPO NEVES

APPLICATION OF SEISMIC ATTRIBUTES TO ENHANCE THE IDENTIFICATION OF BOTTOM SIMULATING REFLECTORS IN THE UMITAKA SPUR GAS HYDRATE PROVINCE, JOETSU BASIN, JAPAN

Dissertation presented to the Programa de Pós-Graduação em Dinâmica dos Oceanos e da Terra at Universidade Federal Fluminense, as a partial requirement for obtaining a Master's degree

Concentration Area: Marine Geology and Geophysics

Approved on October 22, 2020.

EXAMINATION BOARD

_____

Prof. Antonio Fernando Menezes Freire, Dr (Advisor) - Deptº de Geologia/LAGEMAR-UFF

_____

Prof. Cleverson Guizan Silva, Dr. (Advisor) - Deptº de Geologia/LAGEMAR-UFF

_____

Prof. Ryo Matsumoto, Dr. - Meiji University

_____

Prof. José Antonio Cupertino, Dr. - PUCRS

ACKNOWLEDGEMENTS

I thank Professor Ryo Matsumoto, from Meiji University, in addition to the Japan Agency of Marine and Earth Science Technology (JAMSTEC) for releasing the single-channel seismic data from Japan Sea used in this study.

To CAPES for financing this project.

To Schlumberger for the Petrel 2019 license available to Universidade Federal Fluminense (UFF).

To my advisors, Dr. Cleverson Guizan (UFF) and Dr. Fernando Freire (UFF). I am very grateful to you for having further awakened my passion for Geophysics. You were the bright spots of my mind.

To the evaluation board, for having accepted the invitation and for the fundamental role of giving feedback on the work. An assessment helps to evolve, by making the person learn from the mistakes and see the hits.

To Dr. Luiz Alberto Santos (PETROBRAS/UFF), who guided me during my Geophysics graduation. Thank you for all the philosophical lessons transmitted. You inspired me a lot with your wisdom, which ended up being a stimulus in my studies. Thank you for the art of humility to learn.

To the authors of the works used and cited in the references, because without your research, I would be unable to create syllogisms. Thus, this work would be non-existent. Thank you for the indirect collaboration.

To Dr. Marco Cetale (UFF), Dr. Wagner Lupinacci (UFF), and other teachers that I had throughout my life for the shared teachings. Even those who failed me and made me learn from my mistakes and that life is not just about victories.

My dear colleagues from the Hydrate Research Project at GIECAR, Ana Carolina F. Dominguez and Laisa da Fonseca Aguiar, for all their complicity. Working with you was very enjoyable. We are unconventional people.

To the UFF research group, GIECAR, composed of very competent and generous professionals, I am grateful to be part of this team. Among the members of this team, I would like to thank Eberton (Tone) Rodrigues, Flávio Oliver and Leonardo Viana, whose help was essential for this work. To Fernando Vizeu and Mario Martins for their kindness and shared wisdom. To the friendship of my dear friends from class and journey, Carolina Ferreira and Maíra Cordeiro. To Thais Candido for the companionship in geoscientific events. To Igor Lima and Lídia Calônio for the feedback on my Seminar I. To Leonardo Teixeira for the rides and conversations after the Seismic Tomography classes. And also, to Sergio Cirino and Rodrigo Mota for connecting me remotely to UFF during the pandemic and for their willingness to help.

To Alice Vasconcellos, Ammir Karsou, Ana Schanzembach, Clara Porto, Frank Bulhões, Juliana Naveira, Kenji Motoki, Ricardo Pereira, Rodrigo Ferro, Thiago Cuzzatti and Vitor Schuback for their support. To Maristela Moreira and Leonardo Oliveira from the Geology and Geophysics Department, for all the assistance. Thanks to all my friends and colleagues not mentioned, for the moments in communion.

During the pandemic, academic lives were essential. I would like to thank the GISIS group for the lectures, especially those by Dr. Marcílio Matos (IME) and Dr. Rodrigo Portugal (UNICAMP) about seismic attributes. To SBG for the lectures of "junt@sadistância", among them, the lives of Claudemir Santos (PETROBRAS) and Dr. Evelyn Sanchez (UFVJM) about studies on Mars.

To the Brazilian Society of Geophysics (SBGf) for defending the rights of geophysicists. I am happy to have a birthday on the same day of its creation, October 30th.

To my lovely family. Thank you for all your unconditional love, encouragement and investment in education. To my grandparents Bida, Jacy and Geraldo. To my late grandmother Marly, who died a week before I took the Masters exam and is now a dear dust in space. To my parents and siblings, who are the guides of my life.

Lastly, I would like to thank my astronomer aunt Dr. Maria Elizabeth Zucolotto (Museu Nacional/UFRJ), who is my great scientific inspiration in the family for such dedication in meteorite research. Like the Bendegó that resurfaced like a phoenix from the ashes after the fire in 2018, she also rose. Since my childhood I have followed her relentless search for meteorites on

her travels, each time without return, but now she has finally found the meteorites from Santa Filomena - PE, Brazil. Thank you for the example that persistence is worth it.

The willingness to admit ignorance has made modern science more dynamic, supple and inquisitive than any previous tradition of knowledge.

Yuval Noah Harari

RESUMO

Investigar a presença de hidratos de gás em subsuperfície é importante para a prevenção de riscos ambientais, para exploração dessa fonte de energia menos poluente que o óleo e o carvão e, até mesmo, como análogo no estudo de Marte. Dessa forma, o objetivo deste trabalho foi interpretar a *Base of Gas Hydrates Stability Zone* (BGHSZ), em Umitaka Spur, uma província conhecida pela presença de hidratos de gás, da Bacia de Joetsu, Japão. Para isso, foram utilizados os dados sísmicos 2D monocanal adquiridos em 2007 (*NT07-20 Expedition)* e 2008 (*NT08-09 Expedition*) e processados pela *Japan Agency for Marine-Earth Science and Technology* (JAMSTEC). A metodologia consistiu na aplicação de seis atributos sísmicos para realçar os *Bottom Simulating Reflectors* (BSRs), através do software Petrel 2019, da Schlumberger. Esses atributos foram Envelope, Amplitude RMS, Pseudo Relevo, Impedância Acústica Relativa, Decomposição Espectral e Frequência Instantânea. Os dois atributos sísmicos Envelope e Amplitude RMS realçaram as altas energias de amplitude das seções sísmicas. Assim, os atributos geológicos Pseudo Relevo e Impedância Acústica Relativa destacaram as descontinuidades e os altos contrastes de impedância do dado sísmico. Enquanto decomposição espectral e frequência instantânea serviram para destacar as atenuações sísmicas, realçando dessa forma a zona de gás livre abaixo do BSR. Dessa forma, essa metodologia foi fundamental para reduzir as ambiguidades intrínsecas à geofísica, ao realçar os BSRs através da avaliação sísmica de mais de uma propriedade física (amplitude e frequência) e dos atributos geológicos que destacaram as falhas da complexa geologia local.

Palavras-chave: Atributos Sísmicos. Hidratos de Gás. BSR. Mar do Japão.

ABSTRACT

Investigating the presence of gas hydrates in the subsurface is important for the prevention of geohazards, for the exploitation of this cleaner energy source than oil and coal, and even as an analogue in the Mars study. Thus, the goal of this work was to interpret the Base of Gas Hydrates Stability Zone (BGHSZ), in Umitaka Spur, a province known for the presence of gas hydrates, in the Joetsu Basin, Japan. For this, 2D Single Channel Seismic (SCS) data acquired in 2007 (NT07-20 Expedition) and 2008 (NT08-09 Expedition) and processed by the Japan Agency for Marine-Earth Science and Technology (JAMSTEC) were used. The methodology consisted of the application of six seismic attributes to highlight the Bottom Simulating Reflectors (BSRs), using Schlumberger Petrel 2019 software. These attributes were Envelope, RMS Amplitude, Amplitude Volume Technique (AVT), Relative Acoustic Impedance (RAI), Spectral Decomposition and Instantaneous Frequency. The two seismic attributes Envelope and Amplitude RMS highlighted the high amplitude energies of the seismic sections. Thus, the AVT and RAI geological attributes highlighted the discontinuities and the high impedance contrasts of the seismic data. As instantaneous frequency and spectral decomposition, they served to highlight the seismic attenuations, thus enhancing the free gas zone below the BSR. Thus, this methodology was fundamental to reduce ambiguities intrinsic to geophysics, by highlighting BSRs through the seismic assessment of more than one physical property (amplitude and frequency) and the geological attributes that highlighted the faults of this complex geological framework.

Keywords: Seismic Attributes. Gas Hydrates. BSR. Japan Sea.

List of Figures

Table of Contents

Chapter 1 INTRODUCTION

The research of gas hydrates is relevant for paleo environments studies and preventing geological hazards, such as slides and slumps caused by their dissociation and for understanding the impact on the atmosphere caused by a possible release of large amount of their gases, such as methane and ethane, due to widespread decoupling of them on Earth (Kvenvolden, 1993; Sloan, 2003; Chong et al., 2016). Besides that environmental importance, gas hydrates are unconventional petroleum resources with great potential energy, due to the fact that they have a carbon quantify twice more than all fossil fuels combined and are distributed evenly around the world (Chong et al., 2016). Furthermore, studies point the presence of methane clathrates outside the Earth, as on Mars (e.g., Oze and Sharma, 2005; Chastain and Chevrier, 2007; Hu et al., 2016; Webster et al., 2018). Thereby, terrestrial gas clathrates serves as analogues in the study of Mars.

One of the countries that most develops studies about gas hydrates is Japan (Matsumoto et al., 2011b; Chong et al., 2016). The study area of this dissertation is Umitaka Spur, an anticline located in the Joetsu Basin, eastern margin of Japan Sea. It is a province well known for the occurrence of gas hydrates. According to Matsumoto et al. (2011c), studies focusing on the origin and significance of shallow, massive to fracture-filling gas hydrates in this place began since 2004 by a research consortium of universities, national institutes and industries. Thus, miscellaneous studies involving gas hydrates issues in this area have been carried out, such as acoustic and seismic surveys (e.g., Saeki et al., 2009; Ayoama and Matsumoto, 2009; Nakatani et al., 2013), geophysical (e.g., Santos et al., 2009; Santos et al., 2020), geochemical and geological analysis (e.g., Matsumoto et al., 2005, 2009, 2011a,b, 2017 a,b; Freire, 2010; Freire et al., 2009, 2011, 2012; Kakuwa et al., 2013; Nakajima et al., 2014; Hiruta et al., 2016).

Accordingly, for this work, 2D Single-Channel Seismic (SCS) profiles acquired and provided by the Japan Agency for Marine-Earth Science and Technology (JAMSTEC) to Universidade Federal Fluminense (UFF) were used. These data are from two Expeditions, NT07-20 and NT08-09, which occurred in 2007 and 2008, respectively. In order to estimate the Base of Gas Hydrate Stability zone (BGHSZ), the goal of this work is to highlight Bottom Simulating Reflectors (BSRs) of all these seismic profiles, which are seismic features related to the BGHSZ. Due to the complexity of the geological framework, without the aid of a seismic attribute, it becomes very difficult for an interpreter to characterize the real BSRs without making mistakes,

because of the ambiguity intrinsic to this geophysical seismic method. Therefore, in order to highlight the real BSR of each seismic section, six seismic attributes were applied in this work, using the Schlumberger Petrel 2019 license available to UFF. These seismic attributes were Envelope, RMS Amplitude, Amplitude Volume Technique, Relative Acoustic Impedance, Spectral Decomposition and Instantaneous Frequency. Respectively, two attributes that measure amplitude (Envelope and RMS), two of geological assignment (AVT and RAI) and two that measure the frequency of the seismic signal (Spectral Decomposition and Instantaneous frequency) were used. The contribution of this work is the knowledge of the effects of the application of six seismic attributes in the identification of BSRs and free gas zones in seismic profiles from this area, which is also useful for others areas of the world. For instance, show which seismic attribute is useful to reduce the geophysical ambiguity of regions with "double BSRs" (e.g., Posewang and Mienert, 1999; Foucher et al., 2002; Hornbach et al., 2003; Nakajima et al., 2014).

1.1 Dissertation Structure

In the next chapter (Chapter 2) will be approached about gas hydrates and them relevance. Third, the study area in Chapter 3. Then, in the Chapter 4, a literature review about geophysical elements will be talked, such as seismic reflection method and seismic attributes. Chapter 5 will address the methodology used in this study and the results of this work will be discussed in Chapter 6. Finally, the conclusions (Chapter 7) followed by the references used in this dissertation. The extra parts performed in this work are in the Appendix.

Chapter 2 GAS HYDRATES

Gas hydrates or natural gas clathrates are crystalline solid compounds formed by water molecules (H_2O), which trap one or more gases inside them. They have a solid physical appearance similar to solid water ice (Figure 2.1). Its interiors can consist of hydrocarbons, such as methane (CH_4) and ethane (C_2H_6), or non-hydrocarbons, such as carbon dioxide (CO_2), hydrogen sulfide (H_2S), hydrogen (H_2) and nitrogen (N_2) (Sloan, 2003). Due to the fact that methane gas is the most commonly found gas stored, gas hydrates are also known as methane clathrates.

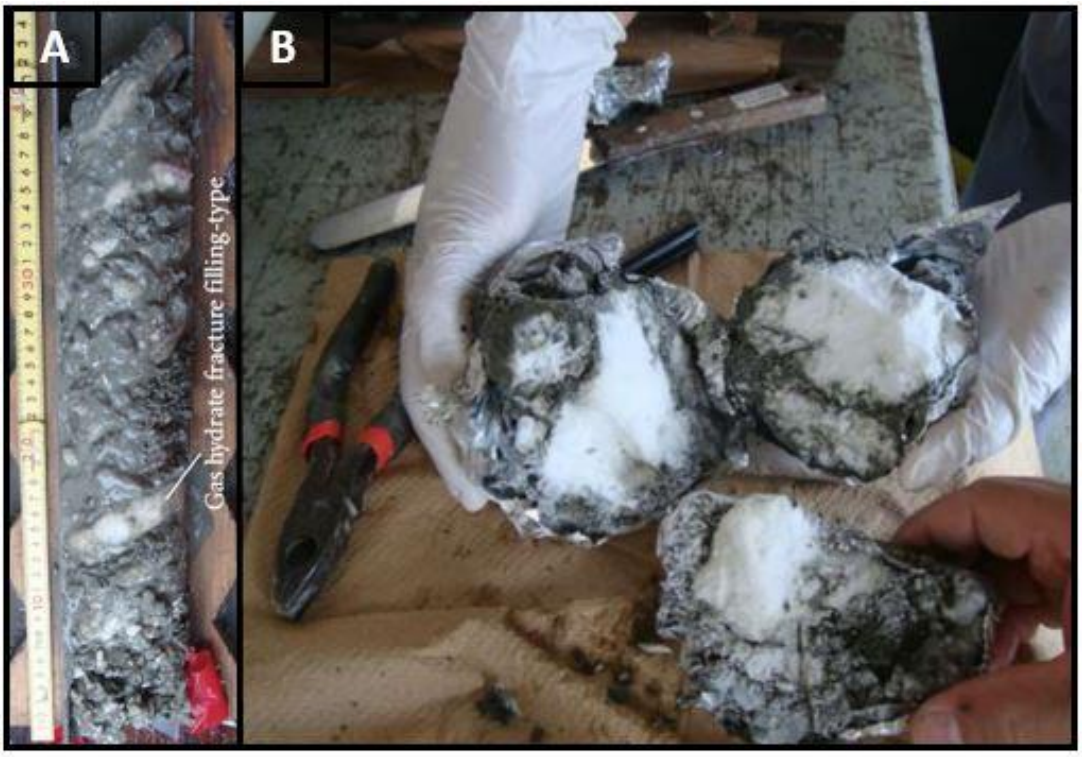

Figure 2.1. Gas hydrates-bearing sediments recovered by piston-core in Joetsu Basin, eastern margin of Japan Sea. (A) Fracture-filling gas hydrate (**Freire et al., 2012**) (B) Blocky-gas hydrates fragments (**Freire, 2010**).

The chemical structures of gas hydrates are distinguished into three categories: Cubic Structure I, Cubic Structure II and Hexagonal Structure H (Figure 2.2). The formation of these three structures will depend on the conditions of temperature and pressure, the amount of water trapped, the size and the chemical nature of the gas molecules (Sloan, 2003; Chong et al., 2016). For instance, thermogenic gases typically generate type II and H structures (Chong et al., 2016).

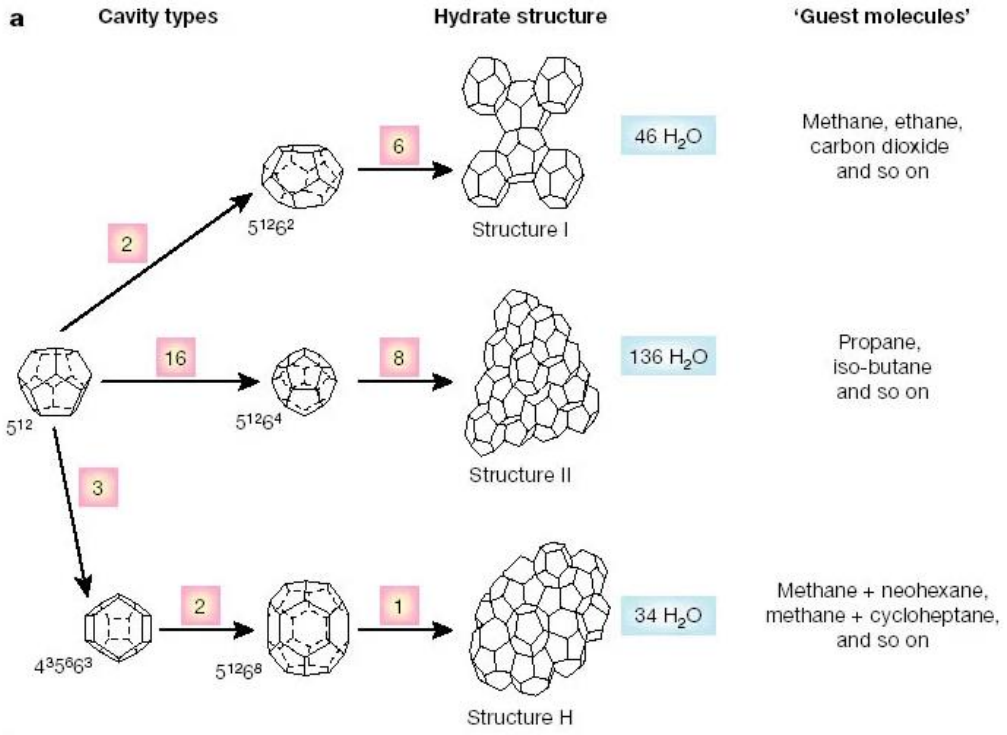

b

Hydrate crystal structure	I		II		H		
Cavity	Small	Large	Small	Large	Small	Medium	Large
Description	5^{12}	$5^{12}6^2$	5^{12}	$5^{12}6^4$	5^{12}	$4^35^66^3$	$5^{12}6^8$
Number of cavities per unit cell	2	6	16	8	3	2	1
Average cavity radius (Å)	3.95	4.33	3.91	4.73	3.91†	4.06†	5.71†
Coordination number*	20	24	20	28	20	20	36
Number of waters per unit cell	46		136		34		

*Number of oxygens at the periphery of each cavity.
†Estimates of structure H cavities from geometric models.

Figure 2.2. The three common hydrate unit crystals structure (**Sloan, 2003**).

2.1 Gas sources

There are three types of hydrate natural gas genesis: biogenic, thermogenic and abiotic (Figure 2.1). The origin of biogenic methane gas is the most commonly found and it occurs through biological processes at low temperatures, derived from the actions of methanogenic bacteria, which consume carbon dioxide (CO_2) and release methane (CH_4) in its metabolism, in shallow zones of the sedimentary package, less than 1000 meters (Paull et al., 1993; Clennell, 2000). Hence, biogenic gases have high methane purity (C1/C2>100), according to Chong et al., 2016.

Otherwise, a thermogenic origin occurs by thermal cracking of organic matter of fossil origin at great depths and high temperatures, inside the sedimentary column of a basin, in deep zones where temperatures can vary between 80-100 ^{0}C (Paull et al., 1993; Clennell, 2000).

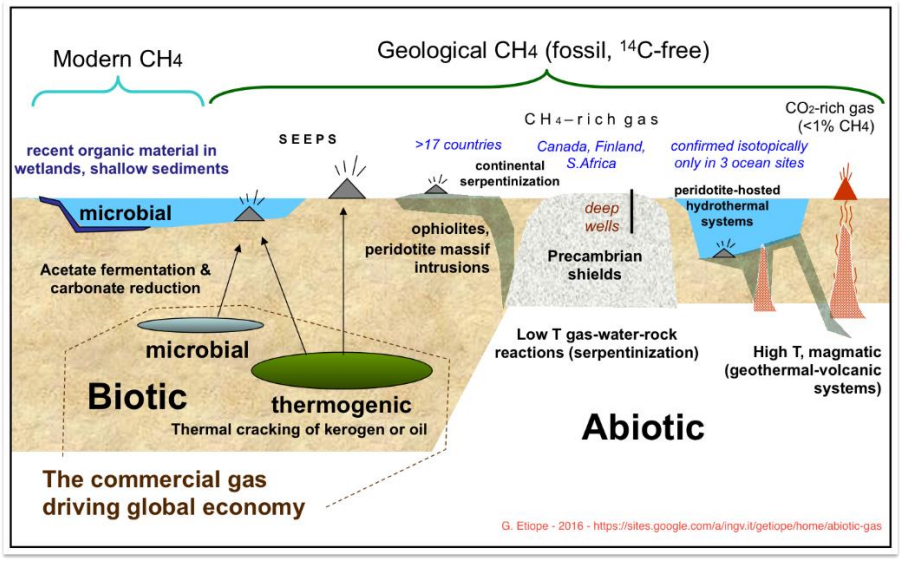

Figure 2.3. Methane origin on Earth. (**Etiope, 2016**)

Unlike biogenic gas, thermogenic gas does not have a high purity of methane gas (C1/C2<100). The distinction between these origins can also be made by geochemical analysis of the stable isotopes of carbon ($^{13}C/^{12}C$) and hydrogen ($^{2}H/^{1}H$) (Schoell, 1980 in Etiope, 2015). For instance, thermogenic gas has an isotopic carbon 13 signature greater than -60‰ while biogenic has a signature less than -60‰ (Bernard et al, 1976 in Kvenvolden, 1993). As can be seen in Figure 2.4, we have the Bernard Diagram from Off-Joetsu area, Japan, where hydrate-bound gas is generally dominated by methane with C1/(C2+C3) ratio of 400 or more while isotopic carbon 13 signature widely ranges from -74‰ to -30‰ VPDB (Matsumoto et al., 2017a).

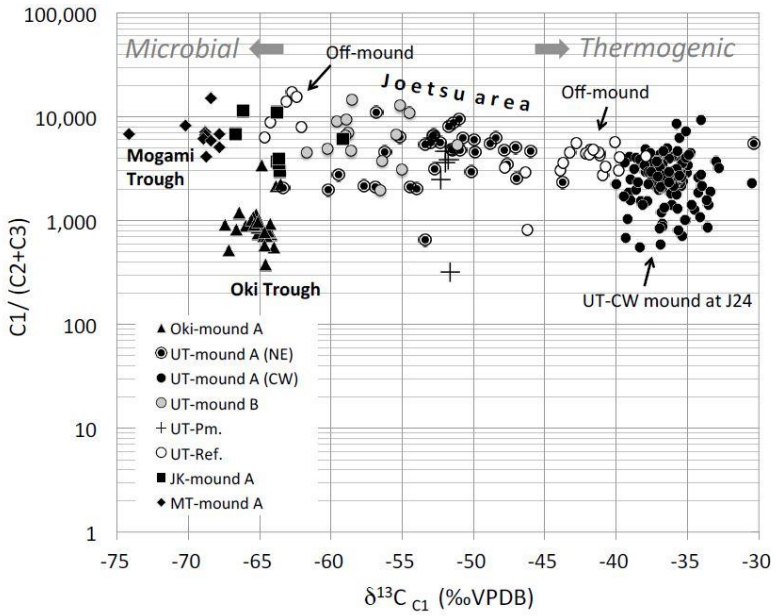

Figure 2.4. Bernard plot of hydrate-bound gas from Oki Trough, Mogami Trough (MT), Joetsu Knoll (JK) and Umitaka (UT), Off-Joetsu area, Japan.

On the other hand, the abiotic origin is the least common and it is neither biogenic nor thermogenic (Figure 2.3). Abiotic hydrocarbons arises from geological processes such as low temperature (<100-150^{o}C) serpentinization in ophiolitic rocks (ultramafic rocks), and from geothermal processes in high temperatures (>150-200^{o}C) in volcanic or hydrothermal settings (Etiope et al., 2011). For instance, serpentinization of olivine and pyroxene (Oze and Sharma, 2005) produces large amounts of hydrogen (H2) which in theory may react with CO2 or CO to form hydrocarbons, also known as Fischer-Tropsch Type (FTT) reactions (Etiope et al., 2011).

2.2 Base of the Gas Hydrates Stability Zone

Gas hydrates are stable only under specific pressure-temperature conditions. They are stable at high pressures (typically above 0.6 MPa) and at low temperatures, generally below 27^{o}C (Sloan, 2003). This maximum stability temperature may vary depending on the gas composition. For example, mixture of gases (such as methane, ethane and propane) are more resistant at higher temperatures and lower pressures than a pure methane hydrate, so they can exist in deeper depths (Chong et al., 2016).

The Base of the Gas Hydrates Stability Zone (BGHSZ) marks the maximum depth and the maximum temperature of gas clathrate stability (Figure 2.5). In the pressure-temperature domain, the position of phase-boundary is determined not only by the composition of the gas mixture, but also by geothermal gradient and in situ properties, such as ionic impurities in the water and pore sediment type and permeability (Kvenvolden, 1993; Chong et al., 2016). For instance, in Figure 2.5, according to Chong et al., 2016, methane mixed are computed via CSM Gem (Sloan and Koh, 2007), with a model natural gas mixture consisting of 93% methane, 5% ethane and 2% propane.

Thereby, the occurrence of gas hydrates is restricted to shallow geosphere. It is distributed (Figure 2.6) in permafrosts of polar continental regions and on continental slopes (marine environments) where water depths exceed about 300 m (Kvenvolden, 1993). According to Makogon et al. (2007), over 220 gas hydrates deposits have been discovered. The yellow balls correspond only to the hydrate deposits indirectly inferred by the seismic reflector called BSR (Figure 2.6), as will be seen in the following subsection (2.3). So, this map (Figure 2.6) is not current, for instance, along Brazil's continental margin nodules of gas hydrates in sediments were recovered by piston cores from Rio Grande Cone, in the Pelotas Basin, western South Atlantic margin (e.g., Miller et al., 2015; Ketzer et al., 2019, 2020), and from Amazon deep-sea fan, in the Foz do Amazonas Basin, in the Equatorial Atlantic margin (e.g., Ketzer et al., 2018).

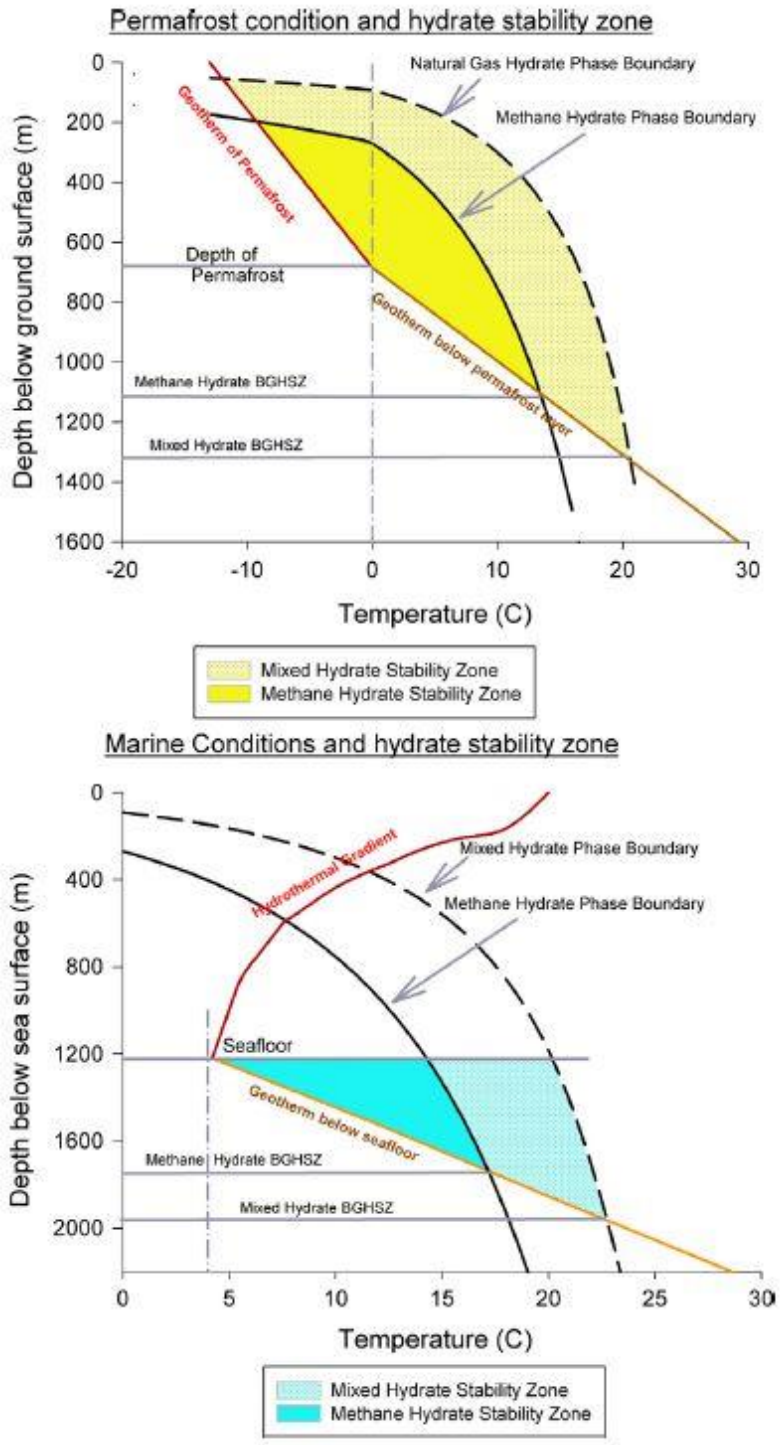

Figure 2.5. Hydrate Stability Zone in Nature. Geothermal gradients applied in permafrost region were 1.9 ^{o}C/100 m and 3.2 ^{o}C/100 m (Holder et al., 1984), whereas hydrothermal and geothermal gradients for marine setting were retrieved from Birchwood et al., 2008 (**Chong et al., 2016**).

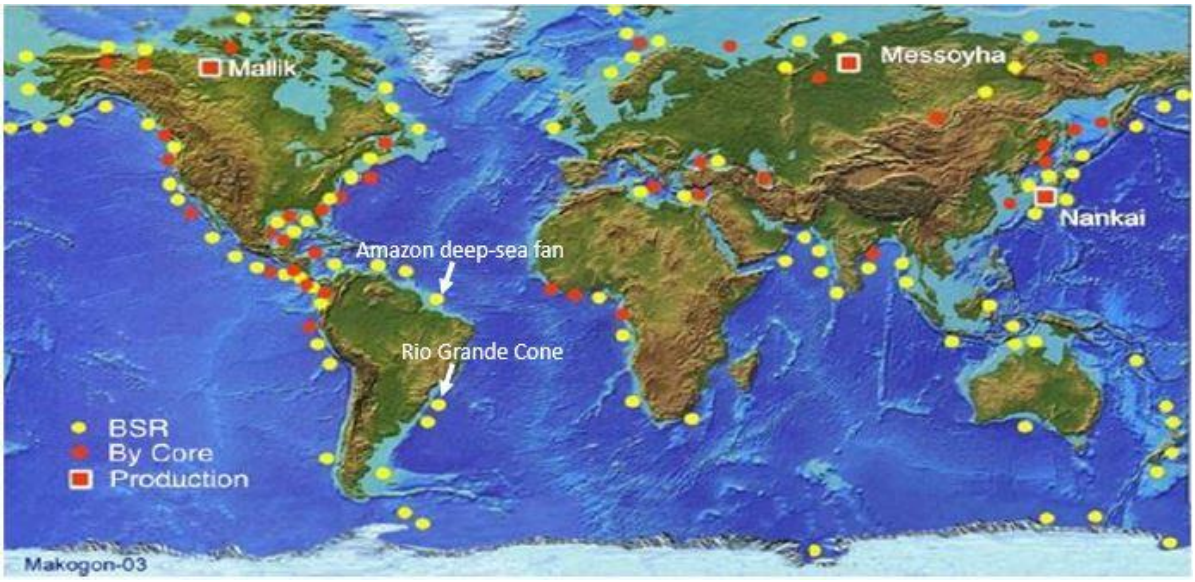

Figure 2.6. Worldwide distribution of gas hydrates deposits. The white arrows were inserted by us to highlight the Brazilian regions where the gas hydrates were recovered by piston cores recently (**Modified from Makogon et al., 2007**).

2.3 Indirect detection of Gas Hydrates

The seismic reflection method is a geophysical method widely applied in the recognition of gas hydrates. In marine seismic profiles, the presence of gas hydrates in sediments is associated with two main seismic features: blanking and Bottom Simulating Reflector (BSR). Blanking is a transparent seismic effect caused by the reduction of amplitude. It is typically observed above the BSR due to the shadow effect of high reflective "hard-ground" near the seafloor (Matsumoto et al., 2017a), and also associated vertically with gas chimneys, such as rising fluids in the BGHSZ (Wood et al., 2002) and free gas bubbles within the fractures (Zuhlsdorff and Spiess, 2004 in Chun et al., 2011).

Bottom Simulating Reflector is a seismic reflector that is parallel and has a reverse polarity in relation to the seafloor reflector (Figure 2.7), besides being an indicator of the BSHGZ (Kvenvolden, 1993; Buffett, 2000). This occurs due to the fact that the BSR has a negative impedance contrast, because it is a coefficient reflection at an interface between the high-velocity of gas hydrate cemented sediments and the underlying low-velocity gas-bearing sediments. The increase in velocity in the overlying layer is assigned to the presence of icy solids in pore volume due to the presence of gas hydrates which can cement and strengthens the sediment matrix (Stoll

et al., 1971; Dvorking et al., 1991 in Buffet, 2000). Whereas lower sediments below BSR are filled with free gas in the pore space that reduce P-wave velocities.

Several studies involving seismic velocity field reveal this. For instance, Tinivella et al., (2009) when generating a smoothed velocity field after a tomographic inversion, obtained a velocity increase from 1800 m/s to about 2500 m/sin the corresponding layer of gas hydrate-bearing sediments whereas in the layer below (free gas layer) about 1400 m/s, in South Shetland Margin, offshore the Antarctic Peninsula. Another example, Posewang and Mienert (1999) reported anomalously high velocities with a maximum of 1850 m/s immediately above the BSR whereas below it extremely low velocities about 1400 m/s.

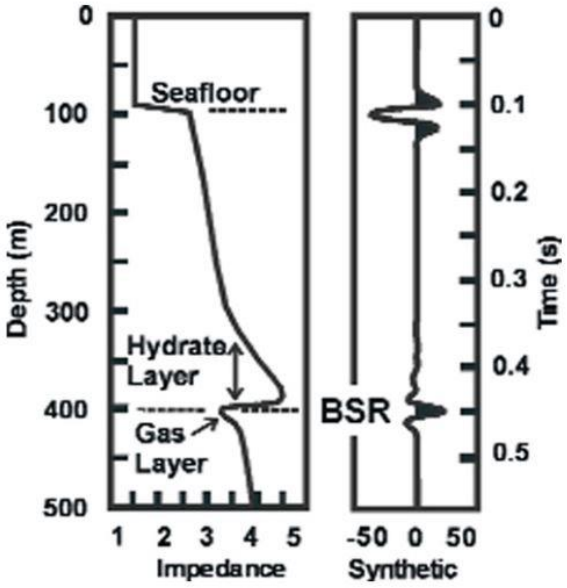

Figure 2.7. Simple synthetic that reproduces the main features of the BSRs (**Dallimore and Hyndman, 2001**)

However, this identification of the true BSR corresponding to BGHSZ is not always trivial, because there may be cases of the occurrence of seismic reflectors similar to BSR. For instance, there are several studies that address the occurrence of more than one BSR (e.g., Posewang and Mienert, 1999; Foucher et al., 2002; Hornbach et al., 2003; Nakajima et al., 2014). For instance, Posewang and Mienert (1999) reported a presence of double BSR in sections of seismic reflection profiles from the Storegga Slide area west of Norway. In addition to Norway,

there are reports of double BSR detected in seismic profiles from Japan too. As is in Nankai Trough, Japanese east coast (e.g., Foucher et al., 2002) and on the eastern flank of Joetsu Knoll, Joetsu Basin, Japanese west coast (e.g., Matsumoto et al., 2009; Nakajima et al., 2014).

For instance, note in Figure 2.8, there is more than one seismic reflector with reverse polarity in relation to the seafloor reflector, being parallel to it. The reasons for the occurrence of this are uncertain. There are many hypotheses about this. First hypothesis, these reflectors can mean changes in the BGHSZ due to sea level change or temperature change of bottom waters between Quaternary glacial-interglacial cycles (Posewang and Mienert, 1999; Matsumoto et al., 2009; Nakajima et al., 2014). Thus, one of these reflectors would be a "current BSR" while the other would be a "Paleo-BSR". For instance, Hornbach et al. (2003) interpreted a "current BSR" and a "Paleo-BSR" in seismic profiles from Blake Ridge, United States.

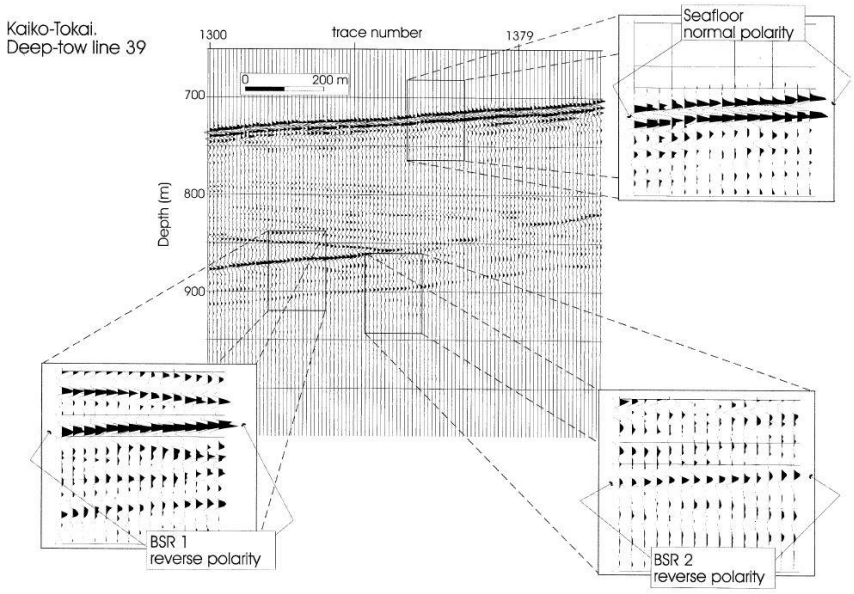

Figure 2.8. Zoomed seismic section from the upper slope of the eastern Nankai margin, Japan (water depth 720-730 m) displaying amplitudes and phase of the two BSRs (**Foucher et al., 2002**).

However, regarding to the Last Glacial Maximum (LGM), around 18 ka B.P., there are questions about the distinct effects on the stability curve of the consequences of the decrease in temperature and the sea level fall. The decrease in temperature would cause a down-shift of the

GHSZ, whereas the sea-level fall would cause a hydrostatic pressure release so, lead to an uplift of the GHSZ (Posewang and Mienert, 1999; Matsumoto et al., 2009). For instance, Foucher et al. (2002) studied the effects that changes in pressure and temperature in sediments cause on the base position of the GHSZ (Figure 2.9).

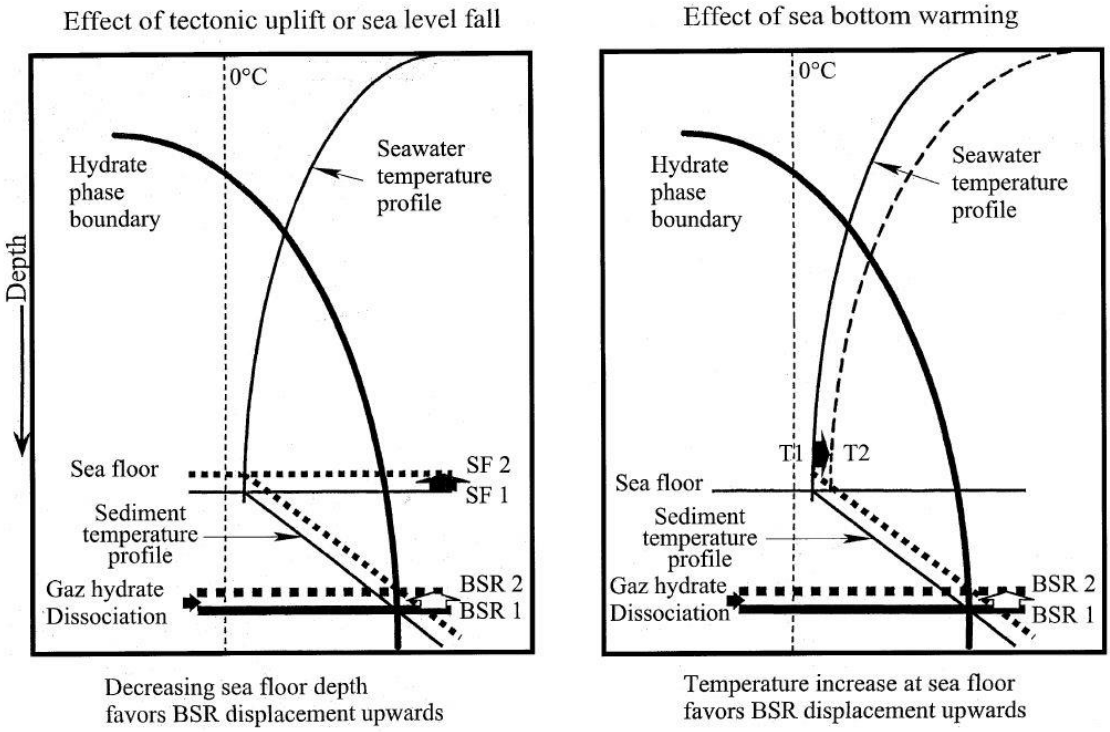

Figure 2.9. Sketch illustrating the displacement of BSR (at base of gas hydrate stability zone) as a consequence of a retracting zone of gas hydrate stability in response to a pressure decrease at the seafloor consecutive to tectonic uplift or sea level fall (left), or a sea bottom warming (right) (**Foucher et al., 2002**).

Beyond these hypotheses, other factors that must be considered. Extra BSR could be a reflector related to a sedimentary heterogeneity inherited from deposition or maybe irreversible sediment alteration in zones of formation or dissociation of hydrates (Foucher et al., 2002). For instance, it could be a carbonate precipitation or a bacterial methane oxidation near hydrate accumulations in the sediment, depending on the study area. For example, Foucher et al. (2002) reported that "near surface precipitation of authigenic carbonates is a common occurrence at seepage sites and outcrops of cemented sediments have been observed at many locations on eastern Nankai margin (Ashi and Tokuyama, 1998; Lallemand et al., 1992; Henry et al., 1999; this issue)".

In the seismic data used in this work from Umitaka Spur, Japan, more than one seismic reflector with reverse polarity in relation to the seafloor reflector, being parallel to it was also found. In my opinion, the "Paleo BSR" hypothesis is the least correct, because BSR is a seismic reflector that represents the impedance contrasts between GHSZ and the free gas zone below it. Thus, when the phenomenon ceases, this impedance contrast would cease. Therefore, this negative reflection coefficient would imply a physical anomaly due to other reasons, such as sedimentary heterogeneity. Thus, this work highlighted the importance of applying seismic attributes to distinguish a true from a false BSR. The discussion of the results and their interpretation are in Chapter 6.

2.4 Direct identification

The presence of gas hydrates can be observed directly near the seafloor through geological features, such as mounds (Figure 2.10) and pockmarks, and through direct sampling by piston and push cores. Mounds and pockmarks are geological features associated with gas hydrates occurrence because the concentration of gas hydrates increases the volume in the pore space arrangement mounds and the dissociation of gas hydrates causes the collapse of the sediments, generating pockmarks.

Figure 2.10. Outcrop of gas hydrates in a mound in the central part of Umitaka Spur. Photograph was taken by JAMSTEC's Hyper Dolphin ROV (**Freire, 2010**).

For instance, in Joetsu Basin (study area of this work), thorough surveys of mounds and pockmarks in this area revealed that the mounds are characterized by actual gas hydrate activities while the pockmarks had been formed as an result of the collapse of mounds caused by large-scale release of methane during the Last Glacial Maximum (LGM), as proposed by Matsumoto et al. (2009).The sea-level fall during the LGM, could have caused the BGHS to become destabilized, causing the dissociation of gas hydrates and thus the upward migration of methane gas and sand (Figure 2.11). Hence, this would cause the collapse of mounds, generating turbidity currents and slumps or slides.

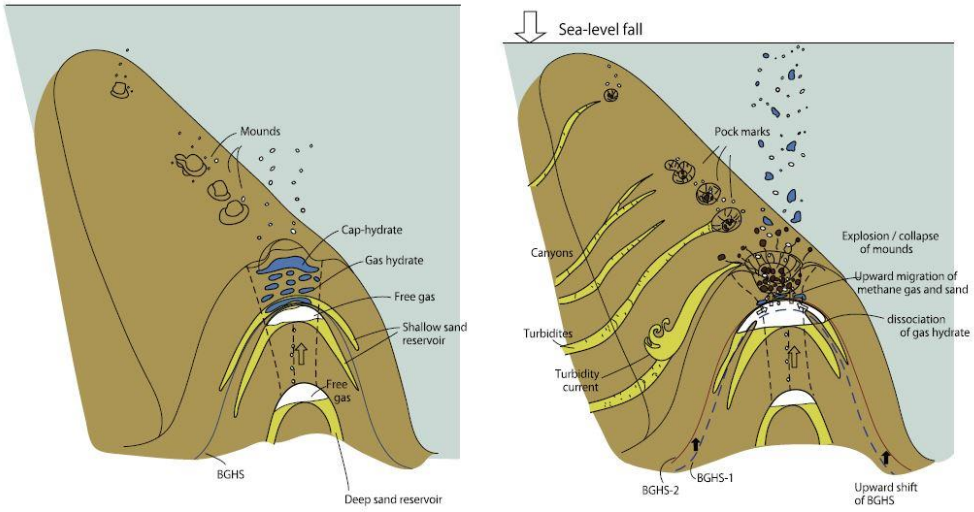

Figure 2.11. Conceptual model exhibiting the formation of pockmarks and submarine canyons on the Joetsu Knoll, in Joetsu Basin, eastern margin of Japan Sea (**Nakajima et al., 2014**).

Besides that, after a drilling well, sedimentary intervals with gas hydrates in a geophysical logging are generally known to have high velocities Vp and Vs, low dielectric constant, high resistivity and thus low thermal conductivity (Goldberg et al., 2000). For instance, note in Figure 2.12b that at about 115 meters below seafloor (mbsf), the J24 LWD values have an extremely low natural gamma-ray (0 API), a high resistivity of 100 to 1000 ohm-meters and a high acoustic velocities (Vp) of 2500 m/s to 3500 m/s (Matsumoto et al., 2017b). Therefore, these values correspond to the sedimentary intervals with gas hydrates.

Furthermore, note in Figure 2.12a, that the BSR in gas chimneys appears at 0.12s to 0.14s two way time (TWT), while in the surrounding sediments, BSR depth ranges from 0.20 to 0.22 second TWT below seafloor. Besides that, observe the blanking zones associated with the gas chimneys. According to Matsumoto et al. (2017b), the sharp pull-ups strongly indicate that high velocity material, perhaps gas hydrate, exists within the gas chimneys.

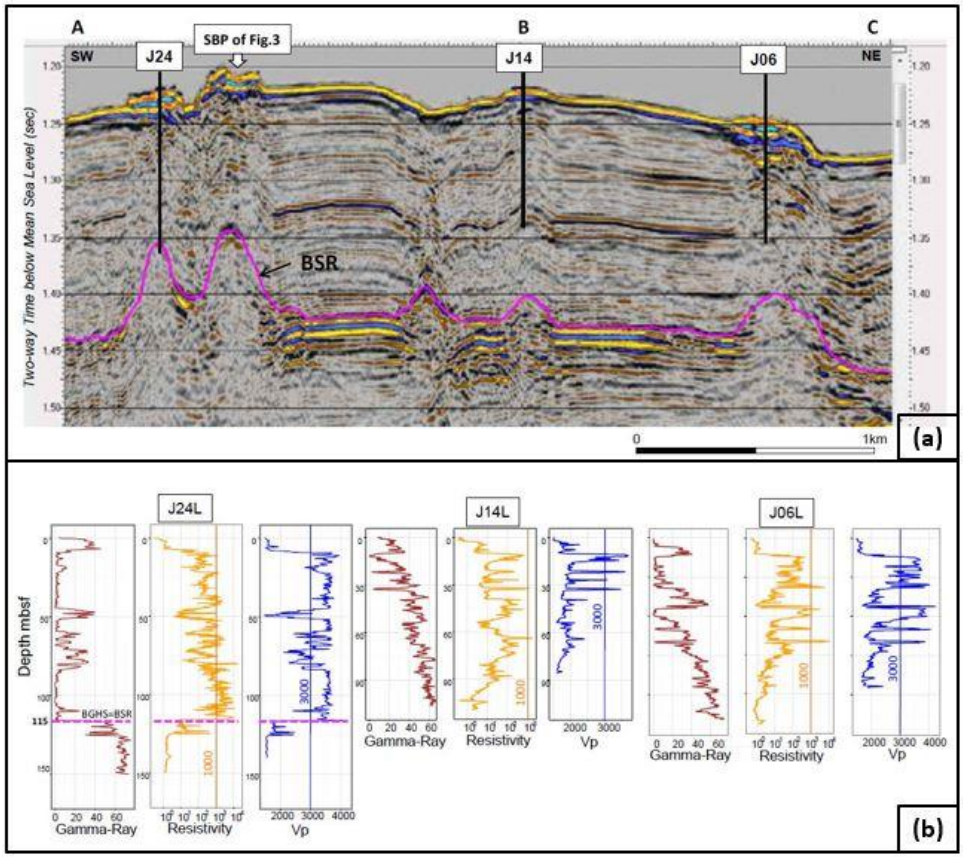

Figure 2.12. Data from the central part of the Joetsu Basin, Japan. (a) high-resolution 3D seismic profile; (b) Logging-while-drilling (LWD) profiles at Sites J24, J14, and J06 on the HR 3D profile (**Matsumoto et al., 2017b**).

2.5 Recovery techniques

Briefly, gas hydrates recovery methods consist of destabilizing the Base of the Gas Hydrate Stability Zone (BGHSZ). The challenges of theses explorations are related to the endothermic tendency of gas hydrates and with the geohazards associated with low sediment

compaction, due to the shallow depth of the BGHSZ, which can generate seafloor mining. Although there is still no exploration of hydrates on a large scale, the main methods proposed are depressurization, thermal stimulation and chemical inhibitor injection (**Figure 2.13**).

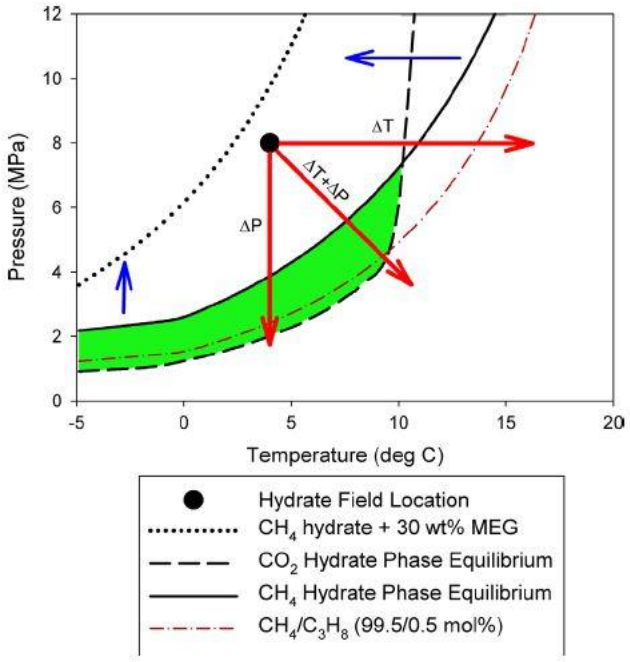

Figure 2.13. Schematic Diagram of commonly proposed gas hydrates recovery techniques. Red arrows indicate depressurization (vertical), thermal stimulation (horizontal) and combination of both methods. Blue arrows indicate inhibitor injection technique. Green zone indicates CH4-CO2 exchange (**Chong et al., 2016**).

The depressurization technique achieves gas production by lowering the pressure, whereas the thermal stimulation increasing the temperature of the hydrate deposit below the hydrate equilibrium at the local pressure-temperature conditions, dissociating into water and gas (Chong et al., 2016). The advantage of depressurization is that it requires less energy as compared to thermal stimulation, but it requires heat transfer and the drilling of many wells to achieve production at adequate levels. Thus, the solution to increase your productivity is to use depressurization technique mutually with the thermal stimulation, such as the huff and puff method (Song et al., 2015; Chong et al., 2016).Whereas chemical inhibitor injection method involves introduction of chemical (thermodynamic and kinematic inhibitors) that can alter the phase

boundary of hydrate system such that the hydrate dissociates at in situ conditions. Ethylene glycol and methanol are thermodynamic inhibitors, for example.

Besides that, the displacement of the phase boundary with the injection of carbon dioxide is an interesting method, because in addition to allowing methane to be recovered from hydrate reservoirs, it sequester CO_2, which could be a future form of cleaner energy (Chong et al., 2016). According to Chong et al. (2016), dioxide carbon injection and CH_4/CO_2 exchange process assists in recovering methane from hydrate reservoir and at the same time be sequestered in the natural formation as CO_2 hydrate (Ohgaki and Inoue, 1995; Ebinuma, 1993). Assuming an ideal scenario where the same amount of, if not more, CO_2 is captured in the formation than natural gas produced, the energy generation process can become carbon neutral (Chong et al., 2016).

Low hydrate dissociation rate is observed when the hydrates dissociates at temperature below freezing temperature ice point (less than 0^oC) yet outside the BGHSZ. This phenomenon is known as "self-preservation" or "anomalous preservation" (Handa et al., 1986; Shimada et al., 2005; Komai et al., 2004 in Chong et al., 2016). The explanation for the phenomenon is that the endothermic heat of the dissociation causes an endothermic reaction of the hydrate, causing the dissociated water to solidify, forming ice, thus preventing further dissociation within the hydrate region. The disadvantage is that it is difficult to have gas production by depressurization and thermal stimulation. The advantage is that the gas hydrate can be used as a means of transport and storage of natural gas in the long term, such as space travel.

2.6 Relevance of the study of gas hydrates

Studying gas hydrates is important both scientifically and economically. Monitoring them is relevant for geologic hazard prevention, paleo environment studies and even, search of origin of life in Mars and potential fuel for space travel. For example, the presence of gas hydrates in subsea pipelines can block flows in oil and gas activities, being an industrial risk (Makogon et al., 2007). Therefore, it is important to study them to inhibit them within these ducts.

2.6.1 Geohazards Prevention

As previously seen in sections (2.3 and 2.4), the study of hydrates is crucial in understanding paleoclimates. There are hypotheses that during the LGM, despite the decrease in temperature being favorable to the increase in the depth of the BGHS, the resulting drop in sea level could have generated the migration of the BGHS upward. So, consequently generate the migration of gas and sand upwards and the collapse of mounds and finally, submarine landslides (Nakajima et al., 2014). Thus, it is important to understand the consequences of the past to prevent those of the future.

For example, in the same way that a possible dissociation of gas hydrates can lead submarine slides and slumps (Kvenvolden, 1993), and thus, local tsunamis, it on a large scale would consequently emit greenhouse gases into the atmosphere, which could generate global warming. According to Sloan (2003), Kennet et al. (2003) thoroughly documents the evidence of late quaternary climate change caused by hydrates, commonly called the "hydrate gun hypothesis", in which hydrate methane caused significant global warming less than 15 ka.

2.6.2 Studies on Mars

Gas hydrates on Earth serves as analogues in studies of the climate system of Mars. According to Webster et al. (2018), since 2004, there have been numerous reports of methane in Mar's atmosphere by Earth-based remote sensing and from Mars orbit. For instance, the Curiosity rover from NASA (National Aeronautics and Space Administration) recently detected strong seasonal variations of methane in the Martian atmosphere (Figure 2.14) and scientists want to understand the reasons for this (Chanstain and Chevrier, 2007; Hu et al., 2016; Webster et al., 2018).

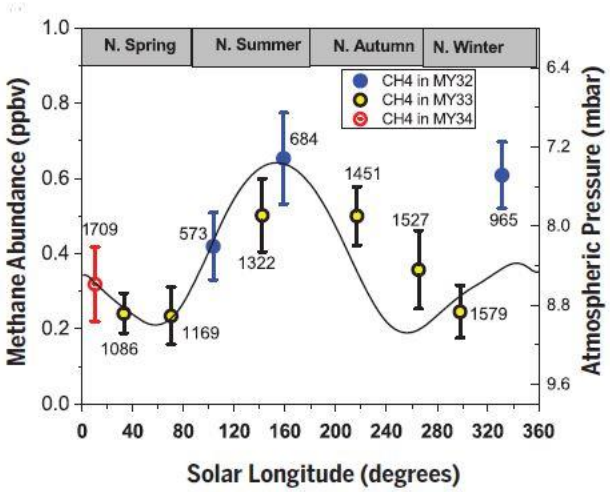

Figure 2.14. Strong seasonal variation of methane in the Martian atmosphere (**Webster et al., 2018**).

Then, a lot of questions have arisen regarding the origin of this methane gas in the atmosphere of Mars. One of the hypotheses pointed out would be the emission from gas hydrates dissociation (Figure 2.15). In addition, as gas hydrates on Earth have three different types of sources (biogenic, thermogenic and abiotic), this has also led to other debates. For example, if the biogenic origin of a gas clathrate on Mars were proven, this would be a tracer of life outside Earth (Oze and Sharma, 2005).

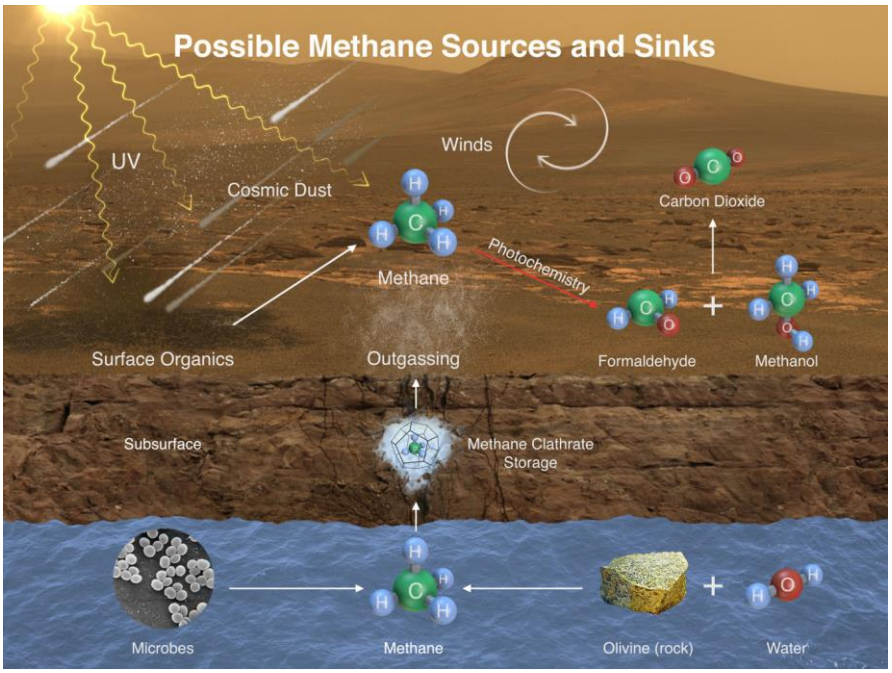

Figure 2.15. Possible Methane Sources and Sinks on Mars. (**NASA/JPL-Caltech/SAM-GSFC/Univ. of Michigan, 2014**).

However, it is believed that the origin of Martian hydrates is abiotic, due to geological processes at low temperature from serpentinization in ultramafic rocks, such as olivine. Thereby, there are many questions to be resolved about Mars and gas hydrates play a key role in these searches.

2.6.3 Energy Matrix

Beyond these scientific factors, gas hydrates have a prominent energetic potential. For instance, according to Kvenvolden (1993), 1 m^3 of methane hydrate can contain up 164 m^3 of methane gas and 0.8 m3 of water at standard temperature and pressure conditions. Besides that, gas hydrates are the largest source of hydrocarbon in the world (Buffet, 2000), that have a carbon quantity twice more than all fossil fuels combined (Chong et al. 2016).

For instance, according to Kvenvolden (1998), the Potential Gas Committee (1981) estimated ranges of methane carbon values from a low of 1.4 x $10^{13} m^3$ of methane gas in Arctic permafrost regions to a high 7.6x 10^{18} m ^{3} of methane gas in oceanic sediment. Besides that, in

unconventional reservoirs the gas hydrates serve as trap in the free gas zone, acting as a seal for rising gas (Posewang and Mienert, 1999). Despite exploratory recovery difficulties, it is a good future energy resource, because this energy is cleaner than oil and coal, even exist the method which sequester CO_2 and catch the methane from gas clathrates reservoirs (Ledley et al., 1999 in Tinivella et al., 2009; Chong et al., 2016).

Therefore, studying gas hydrates is very relevant, because this study is important both on Earth and outside. Based on these chief issues covered throughout this introductory chapter, this work aims to apply geophysical methods that highlight the BSRs and blanking, which are seismic features associated with the BGHSZ, in seismic profiles. These seismic profiles were acquired in a known province of shallow gas hydrates occurrence, as will be seen in the next chapter.

Chapter 3 STUDY AREA

3.1 Localization

The Joetsu Basin is located on the eastern margin of Japan Sea (Figure 3.1). In Joetsu Basin there are two anticlines, Umitaka Spur and Joetsu Knoll. Since 2004, studies related to gas hydrates origin and significance in this area have been carried out by a research consortium of universities, national institutes and industries (Matsumoto et al., 2011c). The focus of this work is the gas hydrates seismic features of the anticline Umitaka Spur.

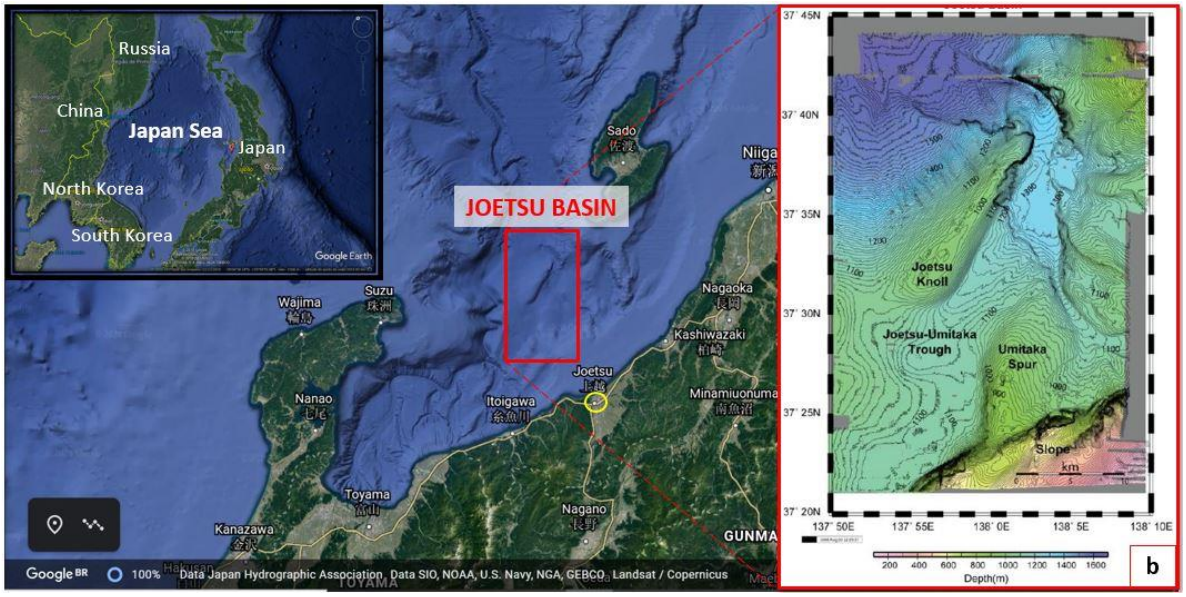

Figure 3.1. Schematic Map of the Study Area taken from Google Earth. (b) Joetsu Basin (**Freire, 2010**).

The Umitaka Spur is an asymmetric anticline with a nearly N-S trend and has been formed since the Middle Pliocene, when the tectonic style changed from extensional to compressive (Takeuchi, 1996 in Freire et al., 2011). The spur is located approximately 30 km offshore Joetsu city (Figure 3.1) and encompasses an area of 43 km^2. The crest is at a water depth around 900 m and the base of the spur is around 1100 m of water depth. This anticline has a gentle slope to the eastern side and a steep slope in the west side (Freire et al., 2011).

North of Umitaka Spur is the anticline Joetsu Knoll. Joetsu Knoll is also an asymmetric anticline, with a 22 km long and 7 km wide NE-SW trending, but it began forming more recently, since the Pleistocene (<1.3Ma), during Quaternary (Muramoto et al., 2007 in Nakajima et al., 2014). The southern part of Umitaka Spur is connected to the continental slope, which plays an important role in the contribution of sediments as debris-flows (Freire et al., 2011).

3.2 Geology Setting

Japan Sea is a composite back-arc basin formed behind the Japanese island-arc system initiated by the rifting of the eastern margin (Figure 3.2) of the Eurasian Continent (Suzuki, 1979 in Okui et al., 2008), accompanied respectively by clockwise and counter-clockwise of southwestern and northeastern Japan, during the Early Miocene (Otofuji et al., 1985 in Nakajima et al., 2014). The Joetsu Basin was also formed in the Miocene. During the Middle Miocene, due to initial rifting, there was a marine transgression, thus, the Joetsu Basin was filled chiefly by deep-marine siliceous shale with minor sandstone (Okui et al., 2008). During this epoch, a high production of organic matter under anoxic conditions favored the development of good source rocks from the Nanatani (16-12.5 Ma) and Lower Teradomari (12.5-8 Ma) formations (Hirai et al., 1995 in Okui et al., 2008).

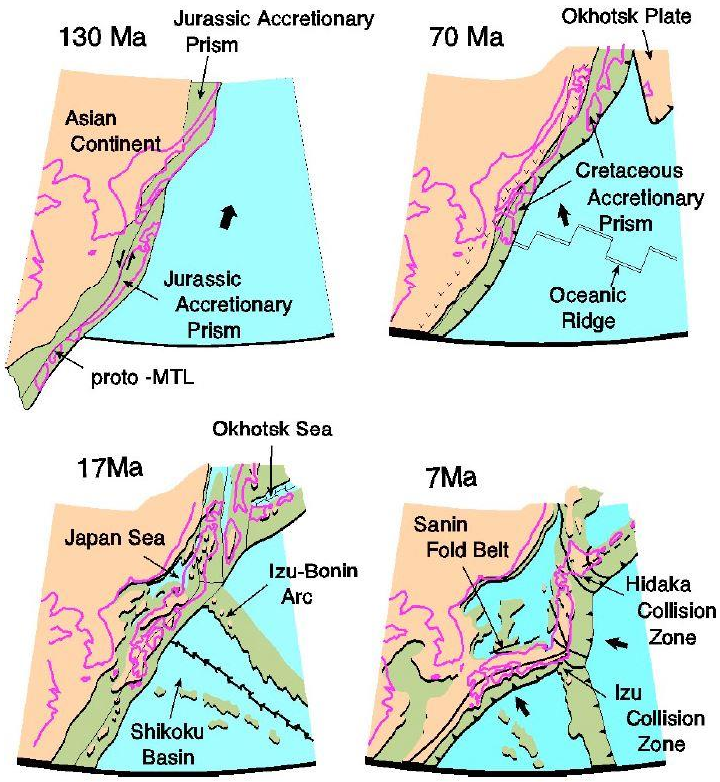

Figure 3.2. Tectonic Evolution of the Japan Sea (**Taira, 2001**).

Still in the Miocene, from around 10 Ma to 7 Ma, the Japan Sea was tectonically stable (Freire et al., 2011). Thus, from the Late Miocene to the Pliocene, coarse-grained sediments (tuffaceous sandstone and siltstone) were transported to the Joetsu Basin and deposited as turbidites fans, which became primary reservoirs in the Lower Teradomari (12.5-8 Ma), the Upper Teradomari (8-5.5 Ma) and the Shiiya (5.5-3.5 Ma) formations (Sato et al., 1987 in Okui et al., 2008).

During the Pliocene, the eastern margin of the Japan Sea changed into an E-W compression, accompanied by basin inversion (Okamura et al., 1995 in Nakajima et al., 2014). Hence, engendered kitchen areas with matured source rocks and a series of northeastern-trending to southwestern-trending anticline-syncline have been created (Okui et al., 2008). Thus, several potential petroleum traps were formed during this period (Imamura, 2000 in Okui et al., 2008).

Overlapping the Shiiya formation, the Nishiyama (3.5-1.3 Ma) formation is composed mainly of fine mudstones with sandstones, including also volcanic rocks, such as dacites and

andasites (Freire et al., 2011). The most recent formation is Haizume, it has been deposited since the Late Pliocene and it is dominated chiefly by clayey sediments (Son et al., 2001 in Freire et al., 2011). Currently, an incipient subduction occurs between the Amur and Okhotsk plates (Figure 3.3).

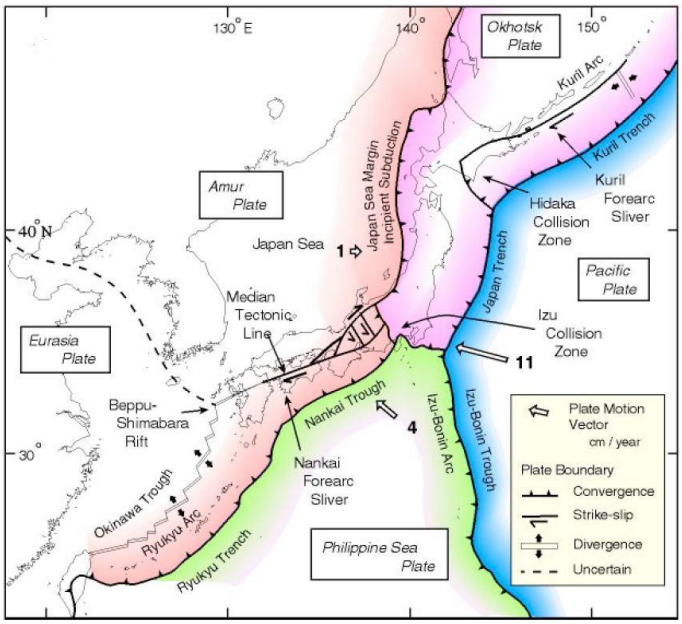

Figure 3.3. Actual Plate Boundaries of the Japanese Arc System. Note the incipient subduction of the Amur Plate (**Taira, 2001**).

3.3 Petroleum System

In Joetsu Basin, a total of three explorations wells were drilled (Figure 3.4), two in Umitaka Spur in 2004 (METI Sado Nansei Oki-Shallow and Deep; Okui et al., 2008) and one in Joetsu Knoll in 2013 (Joetsu Kaikuy; Okawa et al., 2016; Nguyen et al., 2016) by the Ministry of Economy Trade and Industry of Japan (METI). Some of the lithological information from previous section (3.2) was taken from integrated studies of these two wells, METI Sado Nansei Oki-Shallow (water depth 971 m) and Deep (water depth 885 m).These wells were drilled after an acquisition of a 3D seismic survey in 2001. This survey had a prominent role, because through it important information and samples were collected, such as methane hydrates (Okui et al, 2008). During this

survey gas bubbles were observed escaping from the seafloor near the top of the Umitaka Spur structure and small amounts of oil were recovered from soil samples.

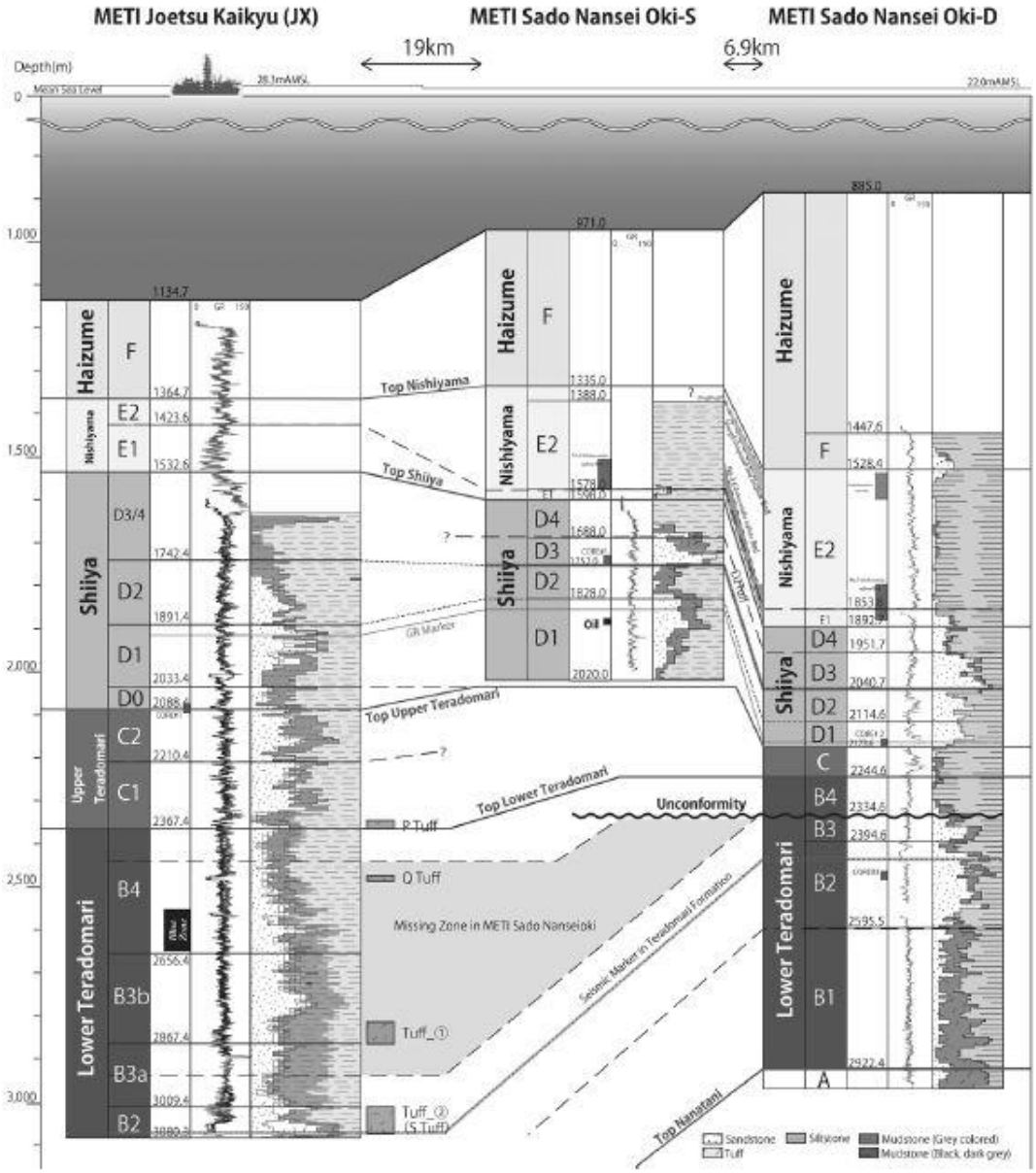

Figure 3.4. Well correlation (**Okawa et al., 2016**).

Part of the history of the active petroleum system was told in the previous section (3.2). Despite the maturation of the source rock has occurred only since the Pliocene, oil and gas

generated and migrated very quickly (Okui et al., 2008). First, they migrated horizontally along sandstones networks from Teradomari and Shiya Formations (Figure 3.5). Then, vertically through faults reaching the Nishiyama Formation. However, this trap has leaked and some gas pass through the Haizume Formation, reaching the seafloor.

The occurrence of seeps and plumes escaping from the seafloor indicates the lack of trapped gas (Matsumoto et al., 2005; Aoyama and Matsumoto, 2009 in Freire, 2010). Although the weak efficiency of both seal and trap for conventional oil and gas production, this scenario is perfect for gas hydrates reservoirs due to the gas supply (Freire, 2010). The existence of source rock, the thermal history of the Joetsu Basin and the vertical fault system of the Umitaka Spur, associated with the temperature and pressure conditions (low temperature and high pressure) provide the necessary circumstances for the precipitation of methanogenic gas hydrates (Freire, 2010).

3.4 Previous studies about gas hydrate

Besides that acquisition of a 3D seismic survey in 2001 reported by Okui et al. (2008), an analogue observation of a number that large depressions Joetsu Basin, that looked similar to gas venting pockmarks of the Atlantic and Pacific margin of North America were recognized in 2003, during a reconnaissance and geotechnical survey for the deep exploration well targeted conventional oil and gas (Matsumoto et al., 2011c). In addition, gas-chimney-like structures have also been identified by deep-tow acoustic surveys and after research expeditions, a number of gigantic methane plumes were observed and massive gas hydrates were recovered from mound-like topography nearby the pockmarks.

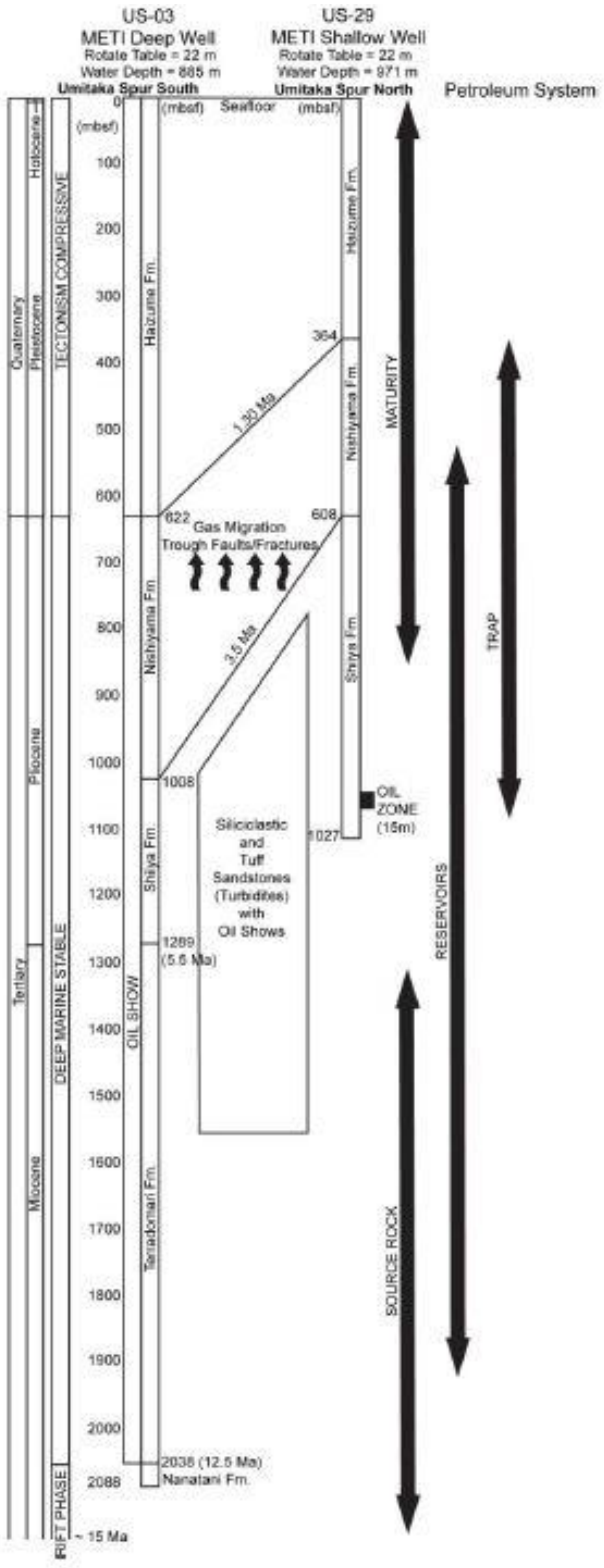

Figure 3.5. Petroleum System Diagram of Umitaka Spur based on information from the two wells (METI Sado Nansei Oki-Deep and -Shallow) in Okui et al. (2008) (**Freire, 2010**).

Thereby, since 2004, a research consortium of universities, national institutes and industries, have conducted a series of sea expeditions with the target to observe, to describe and to understand the origin and significance of shallow, massive to fracture-filling Joetsu gas hydrates (Matsumoto et al., 2011b). Thus, miscellaneous studies involving gas hydrates issues in this area have been carried out, such as acoustic and seismic surveys (e.g., Saeki et al., 2009; Ayoama and Matsumoto, 2009; Nakatani et al., 2013), geophysical (e.g., Santos et al., 2009; Santos et al., 2020), geochemical and geological analysis (e.g., Matsumoto et al., 2005, 2009, 2011a,b, 2017a,b; Freire, 2010; Freire et al., 2009, 2011, 2012; Kakuwa et al., 2013; Nakajima et al., 2014).

According to Matsumoto et al. (2011a), these pockmarks and mounds have about 50 to 500 m in diameter and 10 to 50 m deep and high, respectively. They are mainly observed on the crestal zone of Joetsu Knoll and Umitaka Spur (Figure 3.6).

Around and on mounds of Umitaka Spur and Joetsu Knoll, a number of gigantic methane plumes (600-700 high) and numerous gas venting sites have been observed (Figure 3.7). These sites are close associated with bacterial mats and carbonate crusts and concretions (Matsumoto et al., 2011a). Through the geochemical analysis of the carbon isotope ratio, the origins of these methane were identified (Okui et al., 2008; Freire, 2010; Matsumoto et al., 2011b, 2017a). Thus, thermogenic and biogenic methane generation occur in Joetsu Basin. Most of these gases are thermogenic, this was confirmed by the carbon isotope ratio values heavier than -50‰. Whereas carbon isotope ratio of ascending mixed gas is increasingly depleted in ^{13}C (Freire, 2010; Matsumoto et al., 2011b). Deep-seated gas migrates through the host sediments, in which microbial methane generation is taking place (Matsumoto et al., 2011a). For instance, in Figure 2.4 was shown the Bernard Diagram from Off-Joetsu area. Note the mound values from the central-west of the Umitaka Spur ("UT-CW mound at J24" in Figure 2.4), they are from typical thermogenic source, with isotopic carbon 13 signature values of -40‰ to -30‰ VPDB (Matsumoto et al., 2017a).

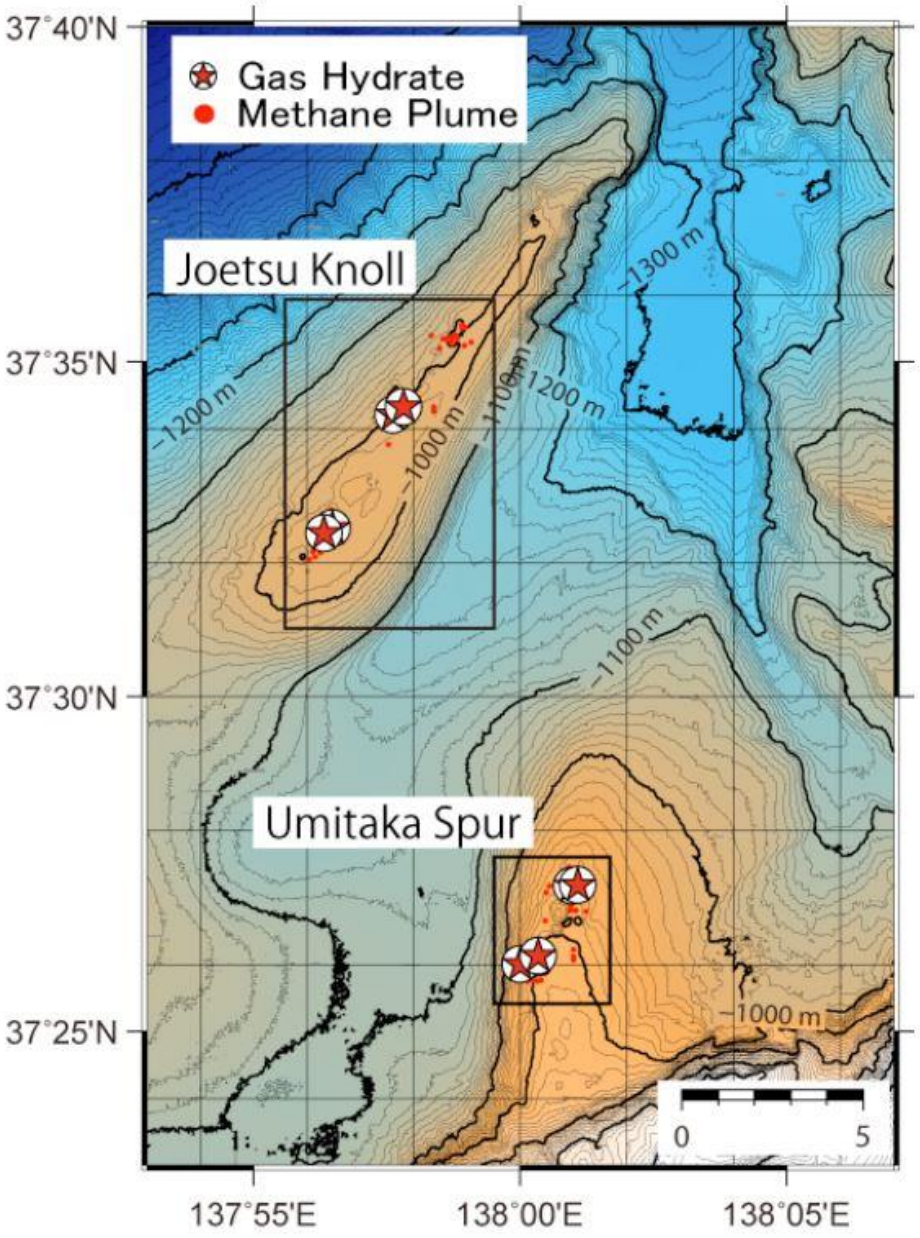

Figure 3.6. Location of the occurrence of gas hydrates outcrops detected by ROVs dives and methane plumes observed by echo sounder in Joetsu Basin (**Matsumoto et al., 2011a**).

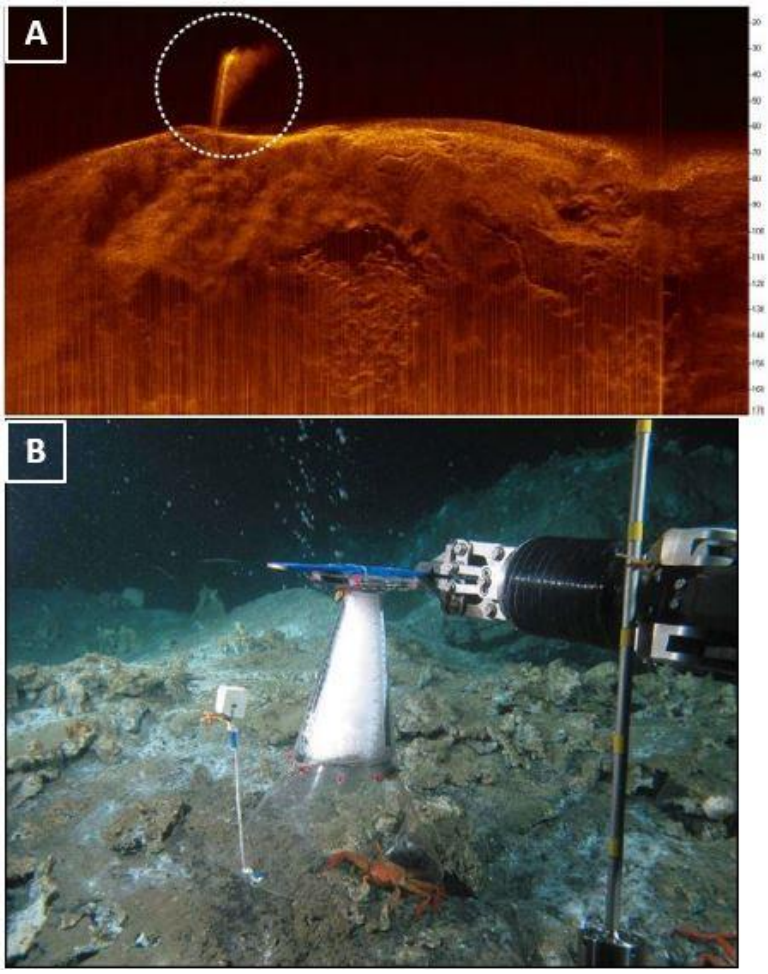

Figure 3.7. Methane plumes occurrence in Umitaka Spur. (A) A methane plume capture in row data of the Side Scan Sonar (400 kHz) from UROV (**Nakatani et al., 2013**). (B) Image taken from **ROV Hyper Dolphin (2007)**.

Moreover, through previous studies of seismic surveys, such as 3D and 2D, BSRs and blanking zones have been identified (e.g., Saeki et al. 2009; Matsumoto et al., 2009, 2011a,b, 2017a,b; Freire et al. 2011; Nakajima et al., 2014). These seismic surveys play a prime role in understanding gas hydrates occurrence. For instance, through the methane hydrate stability equation in seawater proposed by Dieckens and Quinby-Hunt (1994), Matsumoto et al. (2009) infer a depth of 115 mbsf to the Base of the Gas Hydrate Stability in Umitaka Spur (Figure 3.8), where the bottom water temperature and thermal gradient are 0.3 ^{0}C and 10 ^{0}C/100 m, respectively (Matsumoto et al., 2011b).

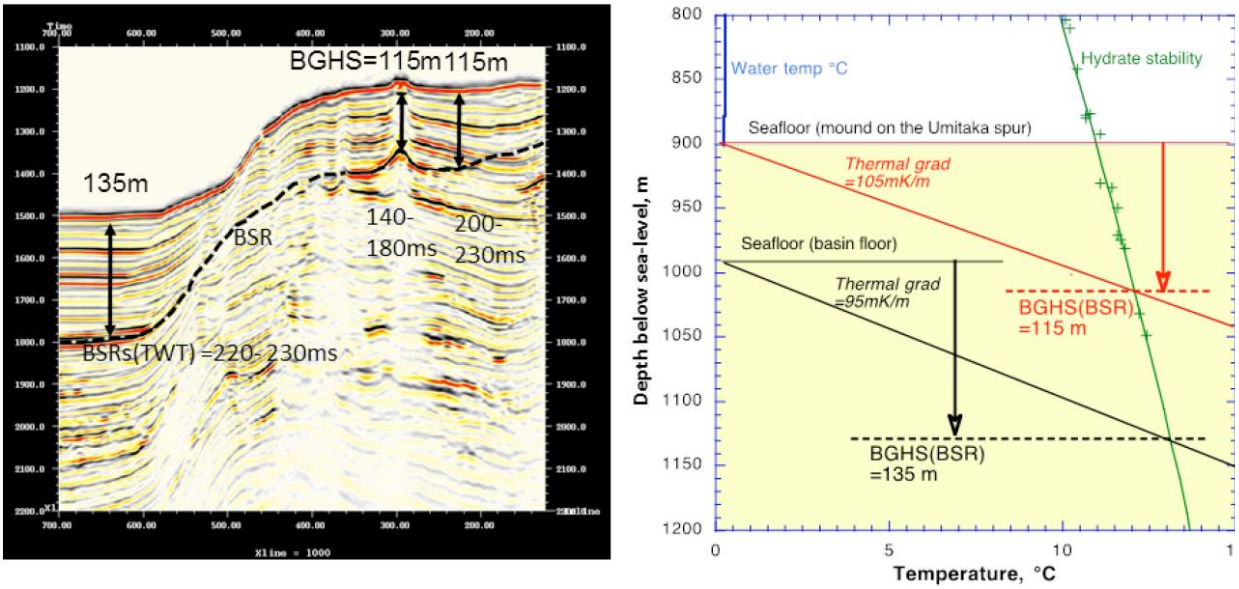

Figure 3.8. Estimation of the depth of BGHS on Umitaka Spur (~900 mbsf) and basin floor (~1000 mbsf) (**Matsumoto et al. 2011a**).

Furthermore, according to Matsumoto et al. (2011a), these seismic profiles served to show that the gas chimney capped by mounds are not "mud volcanoes", because reflections of parallel layers around gas chimneys are traceable into the chimney. Thus, these indicate that the sediments in chimneys are effective conduits of fluid-flow conveying deep-seated gas and gas-containing waters. Besides that, several BSRs are observed in two ways, outside and within gas chimneys. The BSRs outside the gas chimneys widely occur nearly horizontally, though weak and discontinuous, in parallel to bedding on and around Umitaka Spur, at 0.20-0.23s two way travel (TWT) below seafloor. Whereas BSRs within gas chimneys are strong, uneven and occur at 0.14-0.18s TWT, revealing a velocity pull-up structure (Matsumoto et al. 2011a,b).

These lower TWT and high velocity anomaly "indicate massive accumulation of gas hydrates in the shallow part of gas chimneys above BSR, because heat flow over gas chimneys is observed to be nearly identical to the other area", as reported by Matsumoto et al. (2011b). Whereas, in the BSRs outside gas chimneys, low velocity anomaly is observed. For instance, Saeki et al. (2009) through a velocity analysis of 3D seismic survey data reported anomalously low velocities (1200-1300 m/s) above the BSR horizon, possible affected by the presence of free-gas bubbles (Matsumoto et al., 2009, 2011b; Freire, 2010).

Beyond that, based on drilling data from METI Sado Nansei Oki-Deep and –Shallow on the Umitaka Spur (Figure 3.4 and Figure 3.5) and the information of previous studies, such as the recognition of the top of Nishiyama formation in SCS profiles (e. g., Okui et al., 2008; Saeki et al. 2009), Freire et al. (2011) inferred the depths (mbsf) of each of the reflectors, using the top of Nishiyama Fm. as a reference(Table 1). The only two horizons that were previously described in the two wells were the bottom of the sea and the top of the Fm. Nishiyama, the horizons H1 to H6 of Haizume formation were proposed by Freire (2010). Besides that, Freire et al. (2011) estimated an average interval velocity on the sediments (Table 1) of the northern and southern part of Umitaka Spur from 2D SCS surveys carried by the R/V Natsushima from the JAMSTEC (Freire, 2010). These 2D seismic profiles provided by JAMSTEC also are the object of study of this dissertation (Chapter 5) and all these previous interpretations are fundamental to this work. For instance, the Figure 5.2 shows these seismic profiles and the signatures of the carbon isotopes ratio of samples taken from Umitaka Spur. More recently, after a high-resolution 3D seismic acquisition, Logging-while-drilling (LWD) profiles at Sites J24, J14, and J06 were done in Umitaka Spur (Figure 2.12) and more accurate physical data were collected.

Table 1
Time, depth and velocity of Haizume Fm. Seismic events inferred from the depth of Nishiyama Fm. Observed on both METI Deep and Shallow wells (**Freire et al, 2011**).

Depth and velocity of Haizume Fm. seismic events inferred from the depth of Nishiyama Fm. observed on both METI Deep and Shallow wells.

Epoch	Stratigraphy	Seismo Facies	TWT(ms)	OWT(ms)	OWT(msbsf)	Depth(mbsf)	Velocity(m/s)
Data from US-03 (METI Deep Well)							
Holocene	Haizume Fm.	Seafloor	1200	600			
Pleistocene		H1	1280	640	40	66	1659
		H2	1390	695	95	158	
		H3	1480	740	140	232	
		H4	1550	775	175	290	
		H5	1620	810	210	348	
		H6	1750	875	275	456	
Pliocene	Nishiyama Fm.	Nishiyama	1950	975	375	622	
Data from US-29 (METI Shallow Well)							
Holocene	Haizume Fm.	Seafloor	1300	650			
Pleistocene		H1	1370	685	35	57	1618
		H2	1400	700	50	81	
		H3	1480	740	90	146	
		H4	1530	765	115	186	
		H5	1600	800	150	243	
		H6	1700	850	200	324	
Pliocene	Nishiyama Fm.	Nishiyama	1750	875	225	364	

TWT=two way travel; OWT=one way travel; msbsf=milliseconds below the seafloor; mbsf=meters below the seafloor.

According to Matsumoto et al. (2011a), the mechanism and timing of shallow accumulation of gas hydrates have not been well understood due to the difficulty to penetrate down

the mounds by piston and box core. Therefore, due to the difficulty of using direct method, the indirect method remains the easiest way to understand gas hydrate accumulations. Thus, aiming at these questions, this work seeks to collaborate with the understanding of the best tools of geophysical analysis for the identification of seismic reflectors associated with the presence of gas hydrates (BSRs), through 2D single-channel seismic data provided by JAMSTEC. For instance, seismic attributes that aim to highlight the weak BSRs and blanking zone associated with gas chimneys will be addressed in this work.

Chapter 4 LITERATURE REVIEW

4.1 Seismic Reflection Method

The seismic reflection method plays a prominent role in the search for hydrocarbons. Since the 1930s, it has been the most widely used geophysical technique (Reynolds, 2011) due to high accuracy, high resolution and great penetration (Telford, 1990). Seismic exploration methods are an offspring of earthquake seismology and involve basically the same type of measurements as it. However, despite having similar measurement parameters, the energy sources are different. Earthquake seismology uses natural seismic waves to estimate the physical nature of rocks, whereas exploration seismic uses artificial elastic waves generated by a controlled and mobile source (Sheriff, 1995).The arrival times and dips of these artificial seismic events, such as P-waves, were received by receptors (Figure 4.1) and recorded by seismographs. In marine acquisition these detectors are hydrophones, whereas in terrestrial environment are geophones. Then, the information obtained, such as physical properties and geometry of subsurface structures, are used in geological structure estimation (Taner, 2001; Reynolds, 2011).

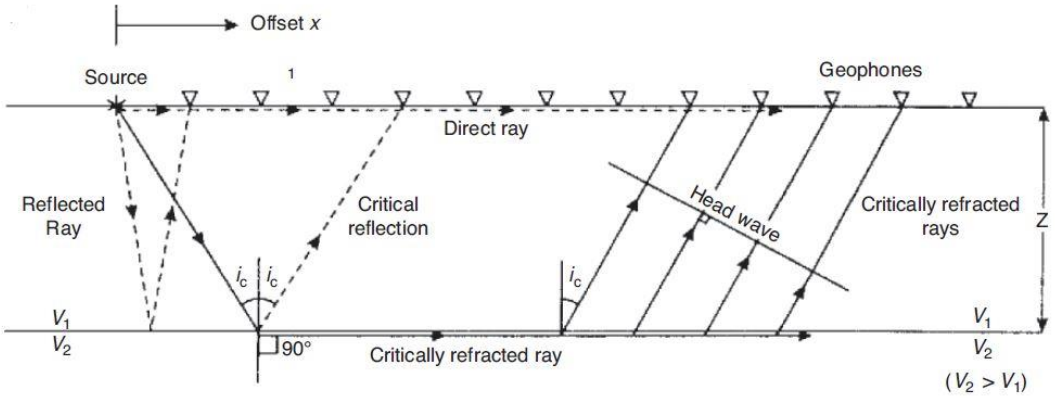

Figure 4.1. Raypath diagram showing the respectives paths for direct, reflected and refracted rays (**Reynolds, 2011**).

In the seismic reflection survey, the relative proportions of transmitted and reflected energy are calculated by the contrast in acoustic impedance across the interface, which is the reflection coefficient. The reflection coefficient is determined by the Zoeppritz's equations

(Equation 1; Zoeppritz, 1919), which measure the ratio of the amplitude and reduce to a very simple form for normal incidence (Sheriff, 1995). The acoustic impedance of a rock is the product of its P-wave velocity (v) and its density (ρ). The propagation of a P-wave will depend on the bulk and shear elastic moduli, as well as the density of the material (Kearey, 2002).

$$R = \frac{A_1}{A_0} = \frac{v_2\rho_2 - v_1\rho_1}{v_2\rho_2 + v_1\rho_1} = \frac{Z_2 - Z_1}{Z_2 + Z_1} \quad (1)$$

Therefore, in the seismic reflection method, the seismic energy pulses reflected by the geological interfaces are recorded by receivers at an angle of incidence close to normal. In this way, the travel times measured at the receivers can be converted into depth estimates of the interfaces (Kearey, 2002).

The Compressional Wave velocity varies with depth, due to the different physical properties of the layers (Equation 2), such as density (ρ), the bulk (k) and shear moduli of dry marine sediments (G), as reported by Helgerud et al. (1999). For example, the trend is for velocity to increase vertically with depth due to sedimentary compaction and may vary horizontally due to lateral lithological changes within the individual layers. In addition, considering a constant wavelength absorption value of a seismic pulse, waves of higher frequencies attenuate faster than lower frequencies, as a function of time or distance (Kearey, 2002). So the tendency is for the seismic pulse to progressively widen over time.

$$V_P = \sqrt{\frac{k + \frac{4}{3}G}{\rho}} \quad (2)$$

Then, based on the Properties of Sediment Constituents material table, conclusions can be drawn about the properties of the gas-hydrate bearing sediment.

Table 2
Properties of Sediment Constituents (**Helgerud et al., 1999**).

Constituent	Volume (%)	K (GPa)	G (GPa)	ρ (g/cm^3)
Clay	60	20.9	6.85	2.58
Calcite	35	76.8	32	2.71
Quartz	5	36.6	45	2.65
Gas Hydrate	Variable	7.9	3.3	0.90
Water	Variable	2.4-2.6	0	1.032
Methane Gas	Variable	0.10-0.12	0	0.23

Thus, although the density of the gas hydrate is greater than that of methane gas, as the Bulk volume of the gas hydrate is approximately 66 times greater than that of methane gas and the shear moduli is also greater, the speed of primary wave of gas hydrate is much larger than that of methane gas.

Therefore, as the BSR is the seismic interface between a layer filled with gas hydrates and below it is the free gas zone, its reflectivity coefficient given by Equation 1 will be negative. This is the physical theory behind the indirect method of identifying gas hydrates seen in subchapter 2.3.

4.2 Seismic Processing

Through the acquired seismic data, a seismic processing must be performed to improve the signal-to-noise ratio and make a better estimate of the velocities of the layers (Yilmaz, 2001). In this way, it will be conceivable to extract the information necessary for the geological interpretation of the processed seismic section.

The seismic processing flow is changeable according to the needs of each appraiser (Yilmaz, 2001). Thus, there are several stages of seismic processing. However, as the focus of this work is the application of seismic attributes, two steps will only be briefly addressed: filtering and migration.

4.2.1 Filtering

There are several types of filtering, including frequency filtering, inverse filtering and velocity filtering. Among these, the two main ones are frequency filtering and inverse filtering. The frequency filtering, such as band pass filter, has the advantage of increasing the signal to noise ratio, but does not generate a good vertical resolution. While the inverse filtering, such as predictive deconvolution, improves the vertical resolution, but has the drawback of not obtaining a good signal-to-noise ratio (Kearey, 2002).

For instance, band pass filter is essential to remove the frequencies above the Nyquist Frequency from the seismic data. The Nyquist frequency is the ratio of one over twice the time sampling interval (Kearey, 2002). If there are frequencies higher than Nyquist in the seismic data, there will be distortion, generating the well-known aliasing. Thus, a filter must be used to remove these unwanted frequencies.

4.2.2 Migration

According to Schulte (2012) “migration is the process which the seismic data is properly placed in the subsurface by moving event to their correct positions”. For instance, in Figure 4.2 d, note the focus point, where the waves come together to form a single reflector. Therefore, the velocity used in the “case d” would be the best migration velocity chosen in a Diffraction Velocity Analysis Migration used by a data processor (Santos et al., 2020).

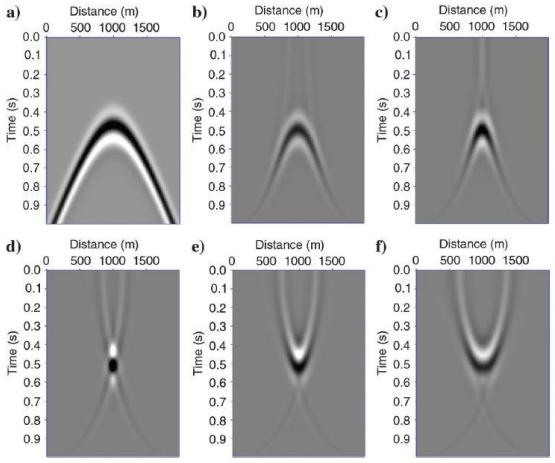

Figure 4.2. (a) Seismogram and (b-f) the migration results of increasing the velocity from 1500 m/s to 2500 m/s at each 250 m/s increment in a zero-offset migration. **(Santos et al., 2020).**

Furthermore, in addition to collapse diffractions from seismic data, the migration step is crucial for increasing spatial resolution. Then, it makes the seismic data more interpretable and coherent (Claerbout, 1971; Yilmaz, 2001; Schulte, 2012; Santos et al., 2020).

4.3 Seismic Attributes

Seismic attributes are the main tools used to predict lithology of the seismic reflection data and to do reservoir characterization, which can act as filters that quantify properties of seismic images (Taner, 2001; Barnes, 2016). Figure 4.3 gives a brief overview of the history of evolution of seismic attributes. According to Chopra and Marfurt (2005), some of the most important seismic attributes emerged long before digital recording, during the time of papers records, such as frequency analysis for optimization of filter settings from magnetic analog recording (Anstey, 2005). Note that (Figure 4.3), after 1970, seismic attributes started to be offered in color commercially (Balch, 1971 in Taner et al., 1979) and complex trace analysis began to be made. In this way, the complex trace allow the unique separation of envelope amplitude and phase information and also the calculation of instantaneous frequency while the color seismic sections assists the interpreter to visualize the spatial changes (Taner et al., 1979). From then on, the seismic attributes and their uses have evolved to nowadays.

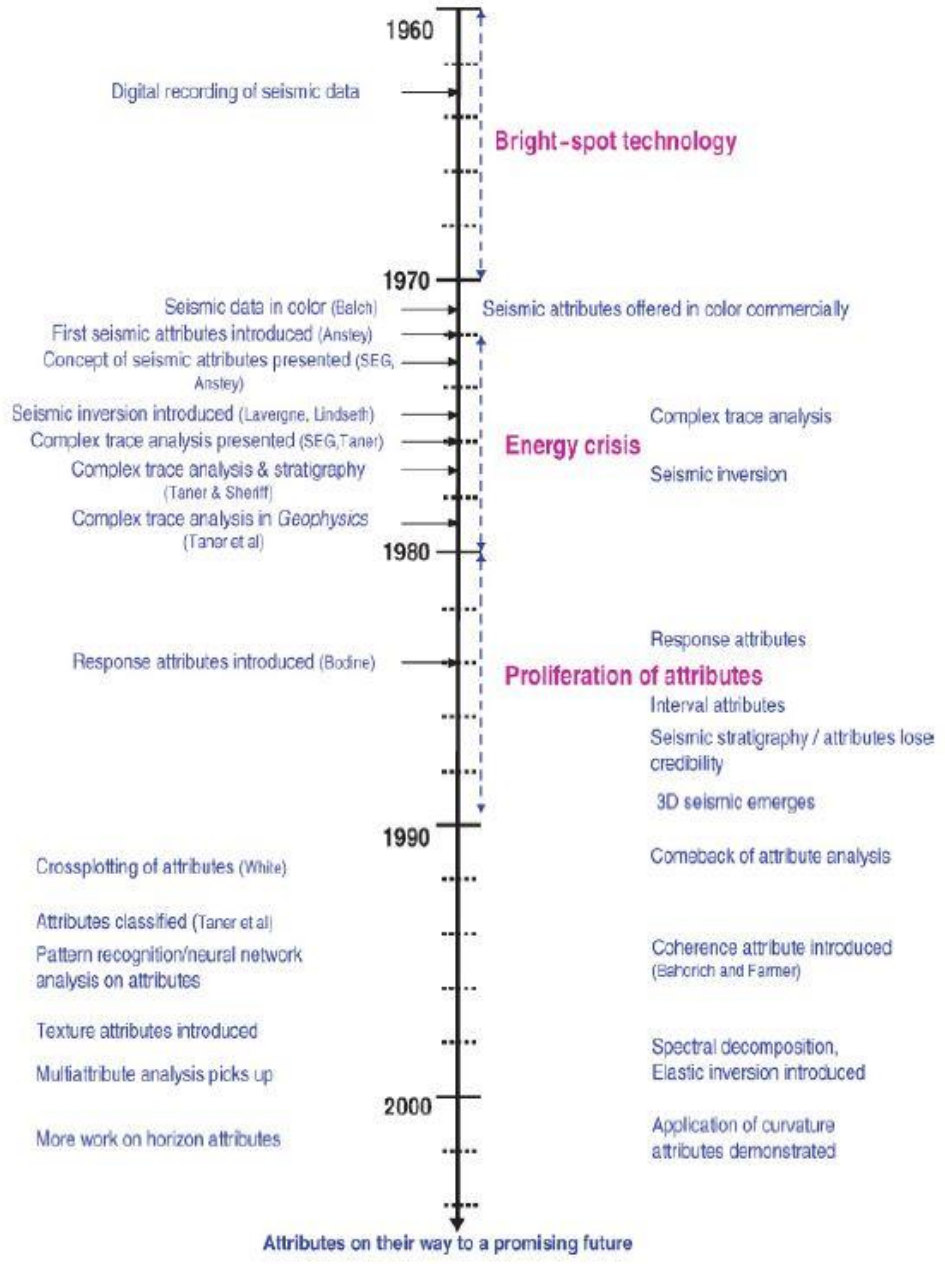

Figure 4.3. A time line of seismic attributes developments (**Modified from Barnes (2001) in Chopra and Marfurt, 2005**).

As cited by Barnes (2016), Chen and Sidney (1997) distinguished seismic attributes by the property measured into three types: geological, geophysical and mathematical (Figure 4.4). Geological attributes record structural (dip, azimuth, curvature and discontinuity), whereas geophysical attributes note properties of seismic waves and wavelets, such as amplitude, phase,

frequency and bandwidth. Mathematical attributes are the least useful and they have lack inherent geological significance. They record statistics of seismic data, such as averages, variances, counts and ratios (Barnes, 2016).

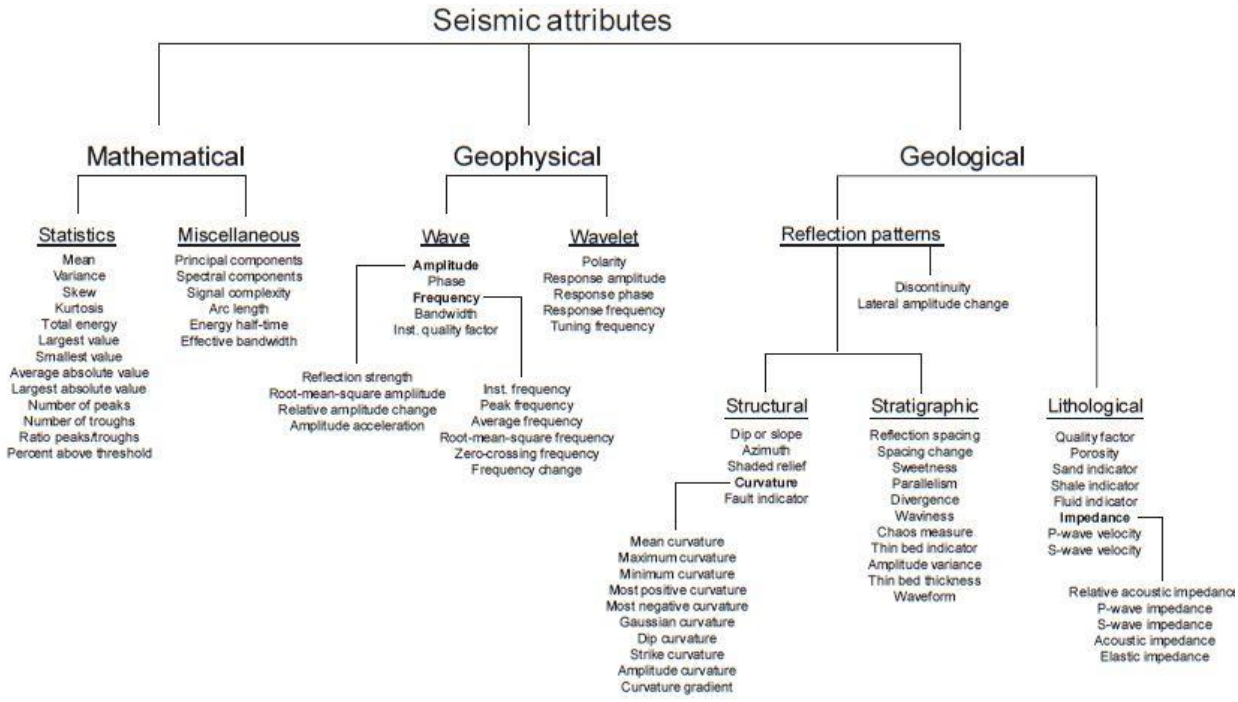

Figure 4.4. Seismic attributes categorized by the property measured (**Barnes, 2016**).

In this work, geophysical attributes were used to measure some physical properties, such as amplitude (e.g., Amplitude Envelope and Root Mean Square Amplitude) and frequency (e.g., Spectral Decomposition and Instantaneous Frequency). Besides that, Amplitude Volume Technique and Relative Acoustic Impedance are considered as a geological attribute for measuring the relative lithological impedance (Figure 4.4), and they are also applied in this work.

Therefore, as the data used in this work are post-stack seismic data, in the following subsections, the six seismic attributes used in the methodology of this study will be addressed. First, the two attributes that measure the amplitude, Amplitude Envelope and Root Mean Square (RMS) Amplitude will be defined. Sequentially, Amplitude Volume Technique and Relative

Acoustic Impedance, whose process involves transforming a cosine wave into a sine wave (phase change of -90º). Then, the seismic attributes that involves the frequency content analysis will be addressed respectively, spectral decomposition and instantaneous frequency.

4.3.1 Amplitude Envelope

Amplitude envelope also called "Reflection Strength", "Instantaneous Amplitude" and "Instantaneous Envelope" is a complex seismic trace attribute (Figure 4.5; Taner et al., 1979) defined by the Equation 3. The real seismic trace is the $f(t)$while $q(t)$ is the quadrature trace.

$$A(t) = (f(t)^2 + q(t)^2)^{\frac{1}{2}} \quad (3)$$

The Envelope seismic attribute measures total instantaneous energy and has a direct relationship to the contrast of acoustic impedance. So, this attribute allows a better emphasis on the contrast of acoustic impedance of the BSRs.

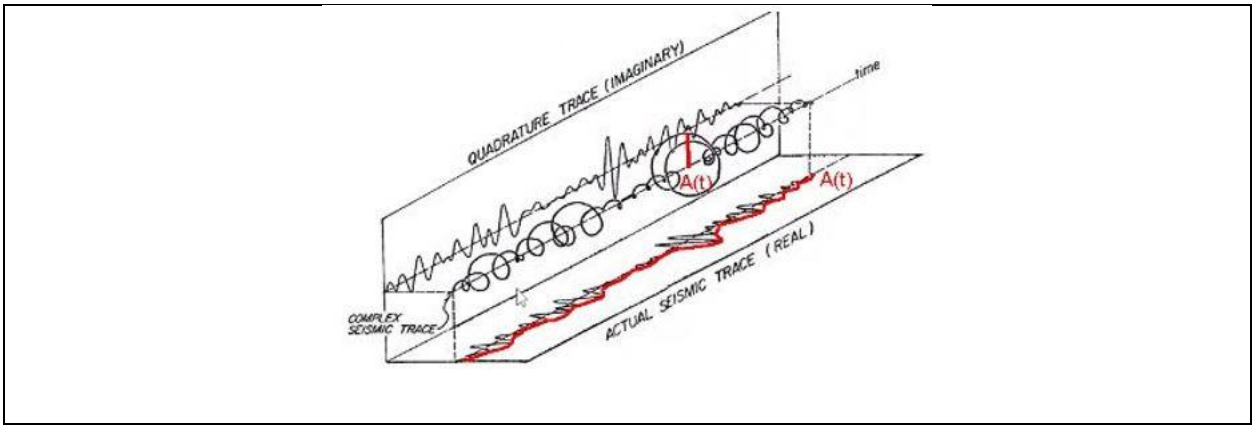

Figure 4.5. Isometric diagram of portion of an actual seismic trace. Instantaneous Envelope highlighted in red. (**Modified from Taner et al., 1979**).

For instance, this seismic attribute was used to identify BSRs in Brazilian regions, as in Pelotas - RS by Barros (2009) and Foz do Amazonas (Aguiar et al., 2019). However, the

drawback of this attribute is that it makes the seismic data loses some vertical resolution (Chen and Sidney, 1997).

4.3.2 Root-Mean-Square (RMS) Amplitude

RMS amplitude is an amplitude attribute. Amplitude refers to the magnitude of the seismic traces values or trace envelope. It measures (Figure 4.6) the variation of the average energy in an interval between horizons or in volume (Barnes, 2016). Hence, it is always positive, as a result, this attribute emphasis both positive and negative maximum amplitudes, and is independent of the polarity or phase of the data.

This single-trace windowed attribute is useful to identify bright spots and dim spots caused by gas, tuning, hard streaks or porosity changes (Barnes, 2016) and track lithologic changes such as deltaic channel and gas sand (Chen and Sidney, 1997). For instance, Okui et al. (2008) applied this seismic attribute to identify the porous sandstone reservoir corresponding to the Shiya Formation, Umitaka Spur, in the study area (Chapter 3).

Thus, due to the fact that the study area of this work involves free gas zones migrating through faults (gas chimneys) and gas hydrates that reduce the porosity of sedimentary layers, it is interesting to apply these attributes. Besides that, for the application of the Amplitude Volume Technique, it is necessary to apply this attribute.

4.3.3 Amplitude Volume Technique

The Amplitude Volume Technique (técnica Volume de Amplitudes – tecVA) was first proposed by Bulhões (1999) and later it was expanded by Bulhões and de Amorim (2005) being possible to be used in seismic volumes both in time and in depth, based on the elementary seismic bed. The elementary seismic bed is the layer of rock of less thickness that the seismic data can solve and its thickness M, which is half of the shortest period (highest frequency),is used as a weighting factor for the calculation of the tecVA seismic data (Bulhões and de Amorim, 2005).

This technique consists of applying an inverse Hilbert Transform in the average Root-Mean-Square or the average of the Absolute Values of the Amplitudes, which also consists of

applying a phase shift of -90º in RMS Amplitude seismic attribute (Figure 4.6). To do this, you first need to choose the window (M) in time or depth to be used in calculating the average RMS (Bulhões and de Amorim, 2005). The choice of this window is a decisive moment, because it will be responsible for the resolution of the seismic data. For example, according to Vernengo and Trinchero (2015), when the mobile window is very long, the result of the RMS calculation will be perceived as a more softened trace with an aspect similar to that an envelope. Whereas when the window is shorter, the aspect is different and the resolution is better (Barnes, 2016; Vernengo and Trinchero, 2015).

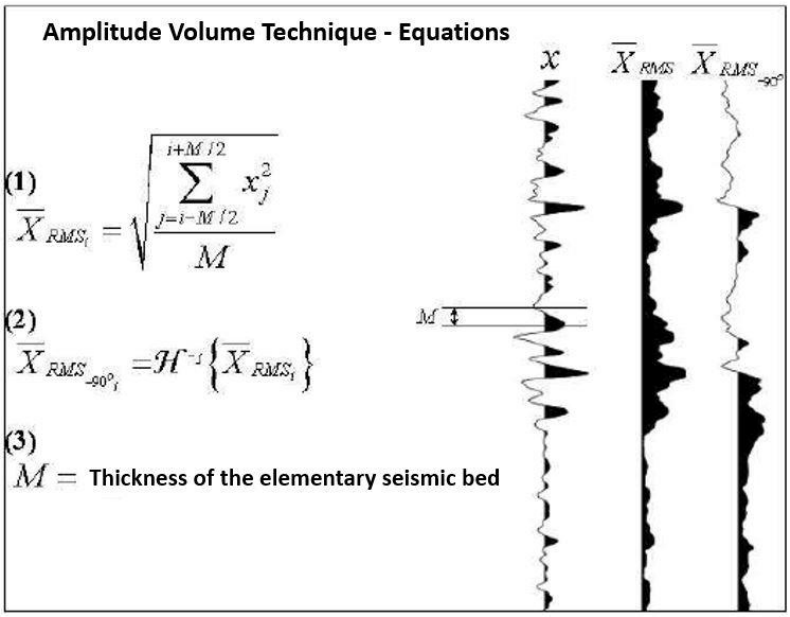

Figure 4.6. Volume Amplitude Technique equations and effects on seismic traces (**Bulhões and de Amorim, 2005**).

Hence, as a result, this pseudo relief attribute comprises, at the same time, amplitude data and the fluctuations of the seismic fundamental frequency (amplitude, frequency and modulate phase). Then, being able to reveal seismic characteristics with small fluctuation, such as faults and channels by trace-by-trace correlation (Bulhões and de Amorim, 2005). Besides that, it is useful to highlight the high impedance contrasts and, consequently, to enhance the geology embedded in the seismic data, highlighting the discontinuities and lateral variations of seismic facies, both horizontally and vertically. Thereby, according to Bulhões and de Amorim (2005),

this attribute can highlight lithologies such as low and high velocities sand, conglomerates, volcanic, intrusive, shale generators and carbonates.

For instance, in Brazil, Oreiro et al. (2008) used this technique to study igneous rocks and dikes at surroundings areas of Santos and Campos Basins, and Costa et al. (2016) also used it to indicate dikes and sills from seismic discontinuites of Serra Geral, Paraná Basin. Furthermore, Ferro (2018) used to analyze the existing salt tectonics and its influence on the type of trapping associated with hydrocarbon reservoirs in the south-central portion of the Espírito Santo Basin.

Another example, outside Brazil, Vernego and Trinchero (2015) obtained good responses in the identification of fault systems and intrusive bodies in seismic data from Golfo San Jorge Basin, Argentina, when applying Amplitude Volume technique. This is a region known for an unconventional reservoir of shale gas.

Therefore, in the context of this work, as the BSRs are seismic features that have a high impedance contrast, this attribute can be useful in highlighting the BSR. In addition, as seen in the previous chapter (Chapter 3), the study area is a tectonically active zone, with several faults, where gases migrate to the subsurface through these. So, this attribute would be ideal to highlight this fault system.

4.3.4 Relative acoustic impedance

Whereas Amplitude Volume Technique transforms a cosine wave into a sine wave by Hilbert Transform (Figure 4.6), Relative Acoustic Impedance (RAI) transforms it by an integration (Equation 4; Taner, 2001).The phase of the seismic wavelet must be zero for RAI (Barnes, 2016).

$$\ln(\rho v) = 2\int_{t=0}^{t=T} f(T)dt \qquad (4)$$

It acts like a recursive inversion, which rotates the phase of the trace by 90 degrees and boosts low frequencies with respect to high frequencies (Barnes, 2016). So, it records

differences in acoustic impedance from a background trend and is employed primarily as a relative measure of porosity (Barnes, 2016) and for extracting meaningful interpretation from seismic data (Chopra et al., 2009).

Thus, this attribute helps in the identification of seismic facies. Therefore, as there are blanking zones in our study area caused by the presence of gas, this attribute would be good for highlighting these off reflectors. For example, Emujakpurue and Enyenihi (2020) used this attribute to identify hydrocarbons from Akos field, Niger Delta, Nigeria. Besides that, de Matos et al. (2014) applied this attribute in 3D seismic data from the Campos Basin, Brazil.

4.3.5 Spectral Decomposition

Spectral Decomposition consists of the transformation of the seismic data in the frequency domain (Partyka et al., 1999). This process can be done through some techniques, such as Short-Window Discrete Fourier Transform (SWDFT), Continuous Wavelet Transform (CWT), Complete Ensemble Empirical Mode Decomposition (CEEMD) and Matching Pursuit (Lin et al., 2013; Honório et al., 2017). For time data, the analysis window will be in seconds, so the spectral components will be measured in cycles / s or Hertz. Whereas analyzing in-depth seismic data, spectral components will be measured in cycles / km. Thus, greater attention will have to be paid when uploading data to commercial software, as SEGY files are stored in a microsecond sample interval (Lin et al., 2013).

This seismic attribute is based on the mathematical concept of the Fourier technique, in which any waveform can be decomposed into a series of sine (or cosine) waves whose frequencies are integer multiples of the basic repetition frequency 1/T (Figure 4.7). A periodic waveform can be expressed in two distinct domains: time domain and frequency domain. The time domain expresses the wave amplitude as a function of time, whereas the frequency domain expresses the amplitude and phase of its constituent sine waves as a function of frequency. Frequency spectra (line spectra) are known for a series of discrete amplitude values and wave phase components for preset frequency values, distributed between 0 Hz and the Nyquist frequency (Kearey, 2002).

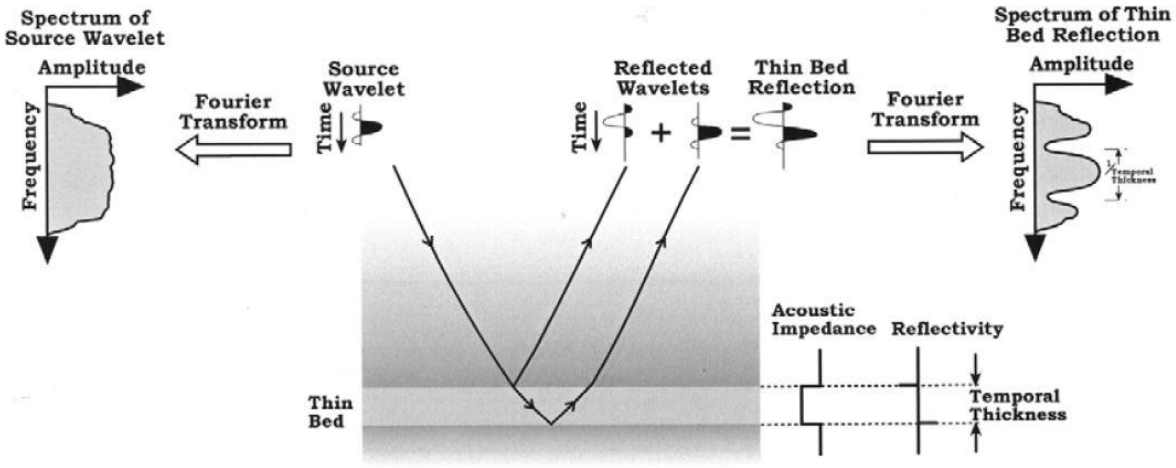

Figure 4.7. Thin-bed spectral imaging (**Partyka et al., 1999**).

This attribute is useful to extract detailed stratigraphic patterns with thickness related to dominant frequencies processed with seismic (Laughling et al., 2002). As seen in Figure 4.8, depending on the chosen frequency for the Spectral Decomposition, you can highlight thinner and thicker reflectors. In this way, this seismic attribute is good for highlighting a specific objective of a seismic interpreter.

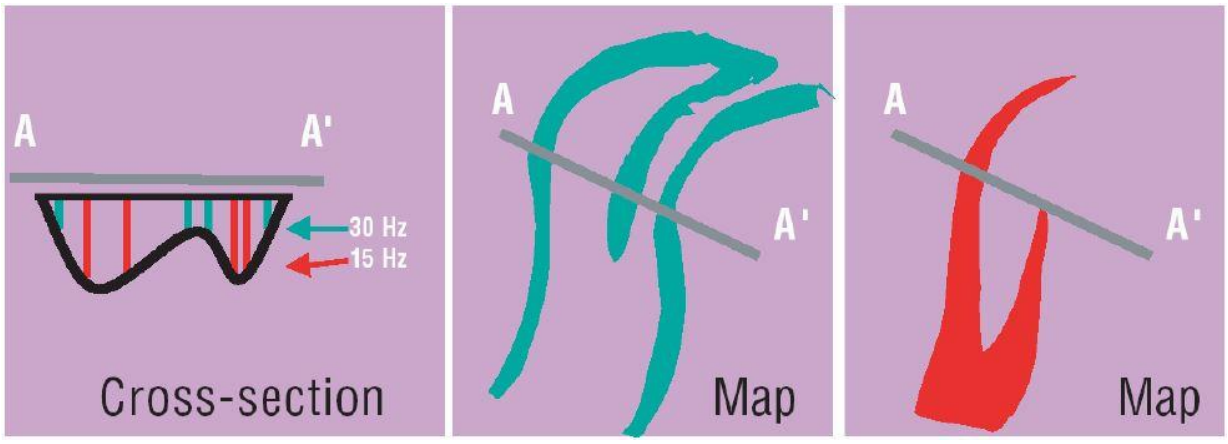

Figure 4.8. Thin-bed interference. On the left, an example of thin reservoir with varying thickness seismic data. On the middle, seismic data with higher dominant frequency, which would highlight the thinner parts of the reservoir on amplitude maps. While on the right, seismic data with a lower dominant frequency that would highlight the thicker parts on an amplitude map **(Laughlin et al., 2002).**

Therefore, this attribute can be used to highlight the contrasts of seismic attenuation in gas hydrates and free gas zone reservoir. There are many studies that have used this seismic

attribute to identify BSRs associated with gas hydrates. For instance, Santos et al. (2009) used spectral decomposition to estimate hydrate bearing sediments at Joetsu Knoll, in Joetsu Basin, Japan. Besides that, in Brazil, de Oliveira (2009) applied this attributes in Pelotas Basin – RS and Aguiar (2020) in Foz do Amazonas –AM both to highlight the BSRs in seismic profiles.

4.3.6 Instantaneous Frequency

This is a complex trace attribute defined (Figure 4.9 d) as the derivative of instantaneous phase ((Figure 4.9 c) at time, $d_y(t)/f(t)$, in degrees/ms or radians/ms (Chen and Sidney, 1997).

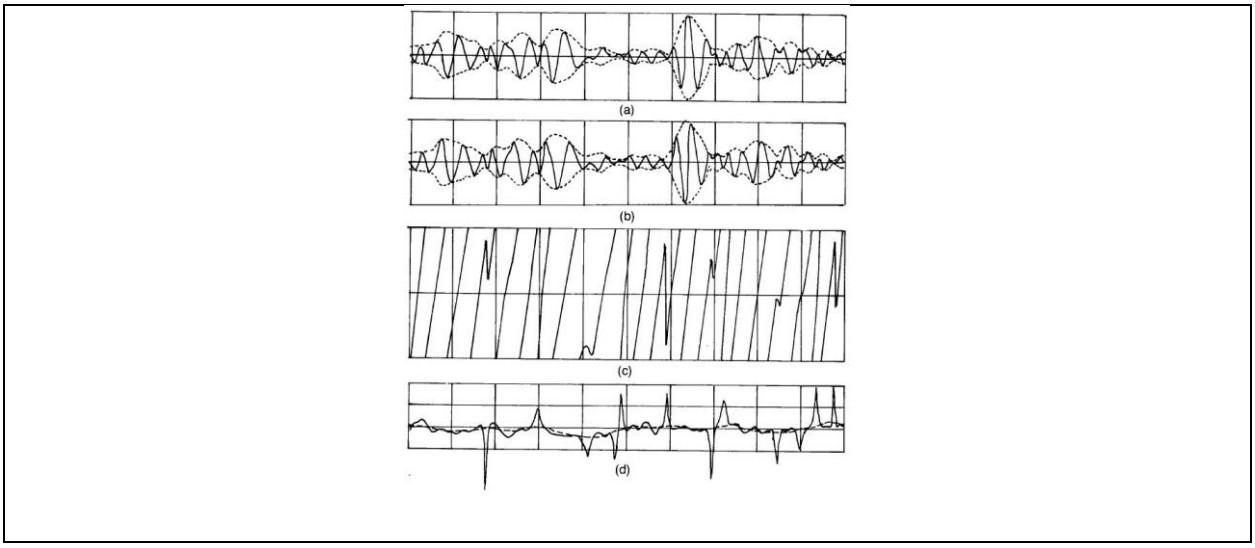

Figure 4.9. (a) Real seismic trace. (b) quadrature. (c) phase. (d) instantaneous frequency, and weighted average frequency (**Taner et al., 1979**).

This attribute is useful for stratigraphy discontinuity, used for estimation of seismic attenuation caused by hydrocarbons (oil and gas) reservoirs that causes drop-off high frequency components (Chen and Sidney, 1997), so identifying abnormal attenuation and thin-bed tuning (Chopra and Marfurt, 2007). Besides that, according to Taner (2001), it is also useful as fracture zone indicator, since fractures may appear as lower frequency zones.

For instance, Okui et al. (2008) also applied this seismic attribute to identify the porous sandstone reservoir corresponding to the Shiya Formation, Umitaka Spur, Joetsu Basin, Japan. Besides that, Barros (2009) applied this to identify the BSR in seismic profiles of Pelotas –RS, Brazil. Thus, it would be interesting to apply this attribute to identify the seismic attenuation of the free gas zone present in Umitaka Spur, Joetsu Basin.

Chapter 5 MATERIALS AND METHODS

The material of this study consists of the 2D marine seismic profiles provided by the Japan Agency for Marine-Earth Science and Technology (JAMSTEC). JAMSTEC made the marine seismic acquisition (subchapter 5.1) over Umitaka Spur (subchapter 5.2) and processed the data (subchapter5.3).

The main goal of this work was to identify the Bottom Simulating Reflectors (BSRs), which correspond seismically to the Base of the Gas Hydrates Stability Zone (BGHSZ) of the Umitaka Spur. However, due to the complex geology of the study area, it was necessary apply six seismic attributes to help with interpretation. For this, was used the Schlumberger Petrel 2019 license available to Universidade Federal Fluminense (UFF). The steps of this methodology are explained in detail in the subchapter 5.4.

5.1 Single Channel Seismic (SCS) acquisition

On September 28 to October 16, 2007 (NT07-20 Expedition) and on April 29 to May 21, 2008 (NT08-09 Expedition), a 2D single channel seismic (SCS) survey was conducted by the R/V Natsushima of the JAMSTEC in the Joetsu Basin. The source of both acquisition systems consisted of two Bolt air guns, with a volume of 40 cubic inches in each and they were operated simultaneously at a pressure of 14 MPa (Freire, 2010). They were deployed at 30 m behind the ship with depths ranging from 1.5 to 7.4 m owing to the sea water wave movement (Freire et al., 2011). The receiver of both acquisitions consisted of a short streamer (SIG type) with 48 hydrophones equally spaced at 1 m. It was also attached to the ship (at a distance of 166.5 m) and at a minimum offset of 136.5 m from the source (Figure 5.1).

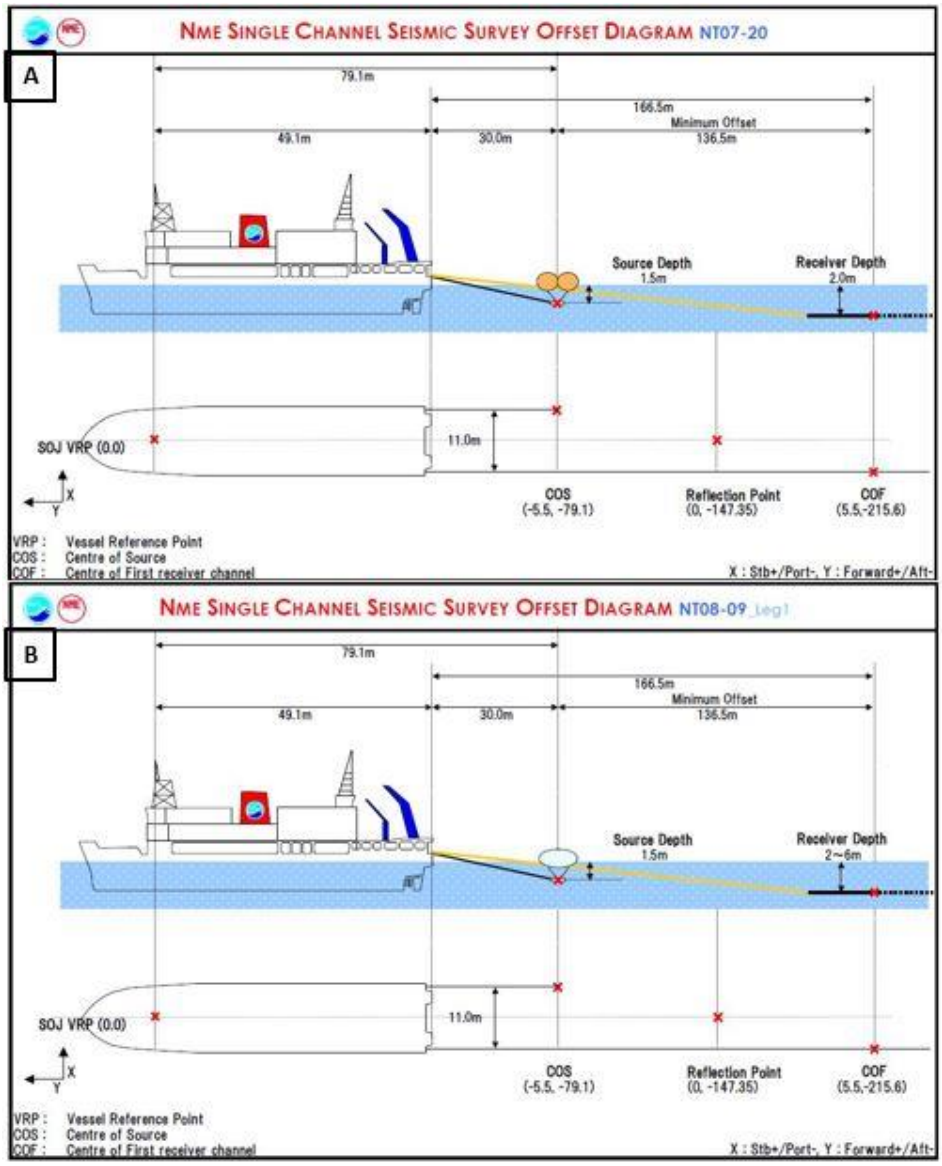

Figure 5.1. 2D Single Channel Seismic (SCS) offset of the (A) NT07-20 Expedition (**JAMSTEC, 2007**). (B) NT08-09 Expedition (**JAMSTEC, 2008**).

The ship was sailing at a speed of 3.1 knots and shots were being fired every 5 s, which corresponds to an average shot spacing of 8.3 m, as reported by Freire et al. (2011). The recording time of seismogram was 4.0 s with 1 ms sampling, according to Freire (2010). Hence, as the sampling rate is 1 ms, the Nyquist frequency is equivalent to 500 Hz. Thus, to avoid an aliasing,

frequencies above 500 Hz must be removed from the seismic data from both Expeditions in the seismic processing step (subchapter 5.3) by the JAMSTEC.

5.2 SCS survey

The SCS survey covered an area of 77 km^2 of the Umitaka Spur and surrounding areas (Freire, 2010; Freire et al., 2011). Twenty five dip profiles were shot across the spur from west to east, about 7 km in length each. For the purpose of studying the stratigraphy and structure of the anticline and to identify accumulations of free gas and gas hydrates, these dip lines were obtained in an average spacing of 0.4 km. Besides that, a total of four strike and semi-strike profiles were made in this survey, approximately 15 km in length each run parallel to the anticline axis of the spur. These strike seismic lines establish relationship between gas chimney structures, seep site mounds and pockmarks. Moreover, they determine the link between the two wells, METI Sado Nansei-oki Shallow and Deep, as reported by Freire (2010) and Freire et al. (2011).

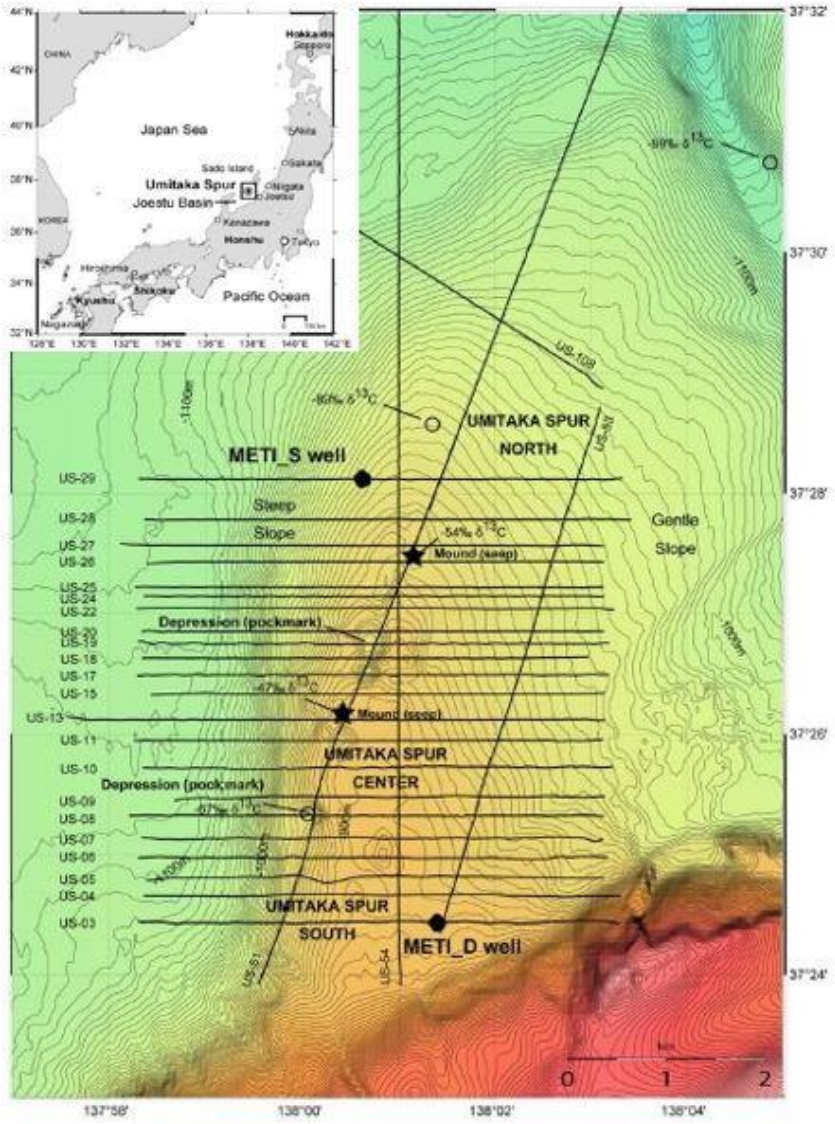

Figure 5.2. 2D SCS location map of the Umitaka Spur. These seismic lines were obtained from both NT07-20 and NT08-09 Expeditions. Stars indicate plume/seep locations. Open circles indicate carbon isotope analyses of sediments (**Freire, 2010**).

5.3 SCS processing by JAMSTEC

These acquired data was processed by the Japan Agency for Marine-Earth Science and Technology (JAMSTEC) in eight main steps (Figure 5.3). The first step consisted of pre-processing, which were done the visualization of seismic raw data and the edition of seismic traces to eliminate damaged traces. Then, a static correction was done to compensate the system delay. In the third step, a band pass filter with frequency limits of 25-30-360-400 Hz was done to eliminate undesired low frequency oscillation and spurious signals greater than the Nyquist frequency of 500 Hz, as reported by Freire et al. (2011).

In the fourth stage, a spherical divergence correction was applied in time domain to the seismic reflection data to eliminate the amplitude reduction resulting from the wavefront expansion. Subsequently, a predictive deconvolution was performed, with a prediction distance of 6 ms and an operator length of 150 ms, which increased trace frequency content (Freire, 2010; Freire et al., 2011).

Finally, in the six and seven steps, a frequency-wave number migration (Stolt Migration) for constant common offset gathers was carried out with a constant velocity of 1500 m/s. Hence, the migration with this velocity increased section quality at shallow depths, but was not appropriate for deeper horizons because they have higher velocities. After migration, with the intention of removing migration artifacts above the seafloor, the section was muted over the sea bottom, as reported by Freire et al. (2011).

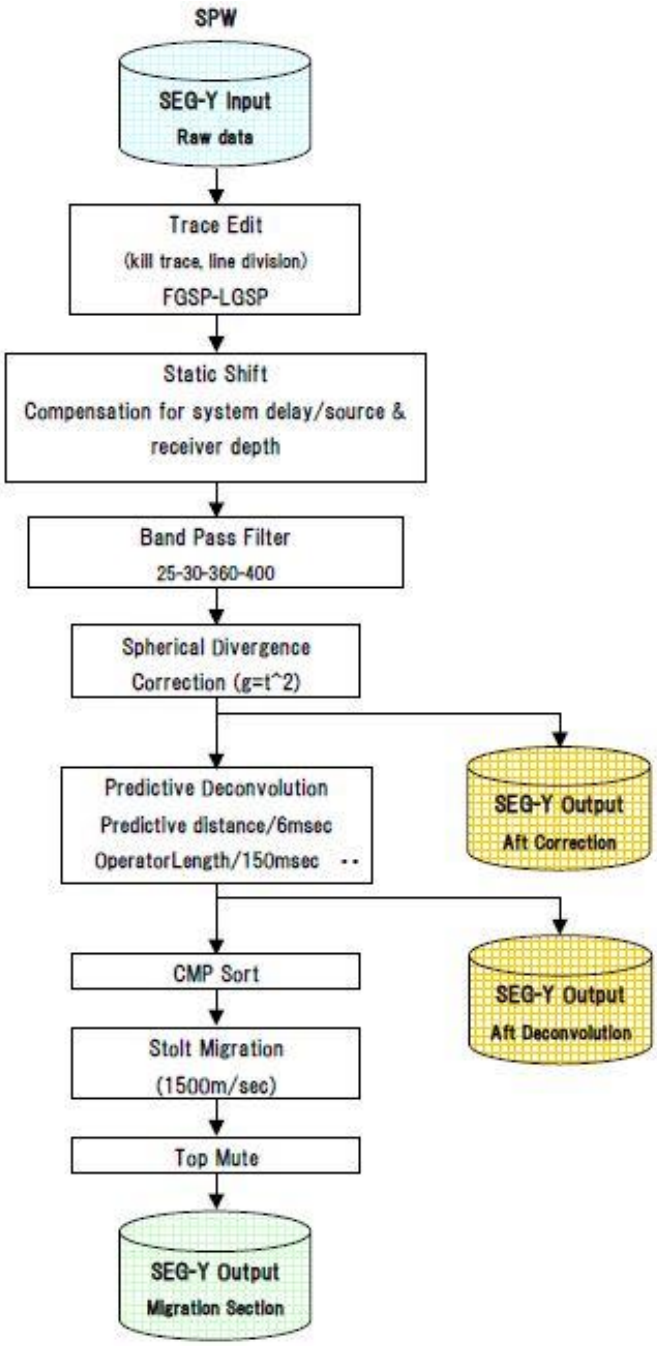

Figure 5.3. Seismic Processing Flowchart used by JAMSTEC **(JAMSTEC, 2007)**.

5.4 Methodology

The main steps of this work are illustrated in Figure 5.4. The work chief objective is to identify the Base of the Gas Hydrates Stability Zone (BGHSZ) of the Umitaka Spur, which is the fifth and final step. For this, it is necessary to identify the true BSRs. However, as the geology of the study area is complex, it was required to apply the seismic attributes to enhance the BSRs, which was the main methodology of this work.

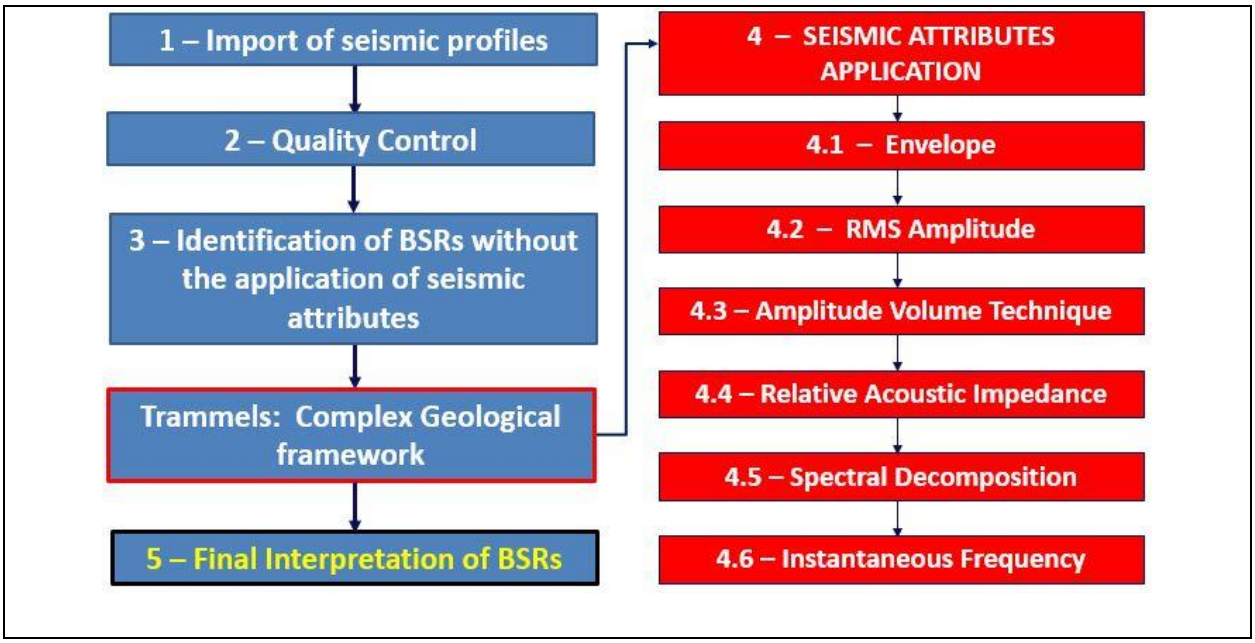

Figure 5.4. Main Work Steps.

First, all of the 2D post-stack seismic lines on time domain (SEG-Y format) provided and already migrated by the JAMSTEC (subchapter 5.3) were loaded into the Petrel 2019 software (Figure 5.5). Then, a quality control of these seismic profiles was carried out, so only a seismic line was discarded because it was well curved, which was SP.2(4_FSP) from the 2007 acquisition (NT07-20 Expedition). Thus the seismic lines used in this work became twenty eight in total and the final number of them corresponds to the final number of the lines in Figure 5.2. For example, the SP.1(ut-4) seismic line from NT08-09 Expedition corresponds to US-04 in Figure 5.2. Therefore, a grid of the seafloor was done through the interpretations of the seafloor horizon of these twenty eight seismic profiles (Figure 5.6).

NT07-20	NT08-09
SP.2(3_FSP)	SP.1(ut-4)
SP.2(4_FSP)	SP.1(ut-5)
SP.2(6_FSP)	SP.1(ut-7)
SP.2(8_FSP)	SP.1(ut-9)
SP.2(11_FSP)	SP.1(ut-10)
SP.2(12_FSP)	SP.1(ut-14)
SP.2(13_FSP)	SP.1(ut-15)
SP.2(17_FSP)	SP.1(ut-18)
SP.2(19_FSP)	SP.1(ut-20)
SP.2(22_FSP)	SP.1(ut-23)
SP.2(24_FSP)	SP.1(ut-26)
SP.2(27_FSP)	SP.1(ut-28)
SP.2(29_FSP)	SP.1(ut-53)
SP.2(51-1_FSP)	SP.1(ut-54)
SP.2(51-2_FSP)	

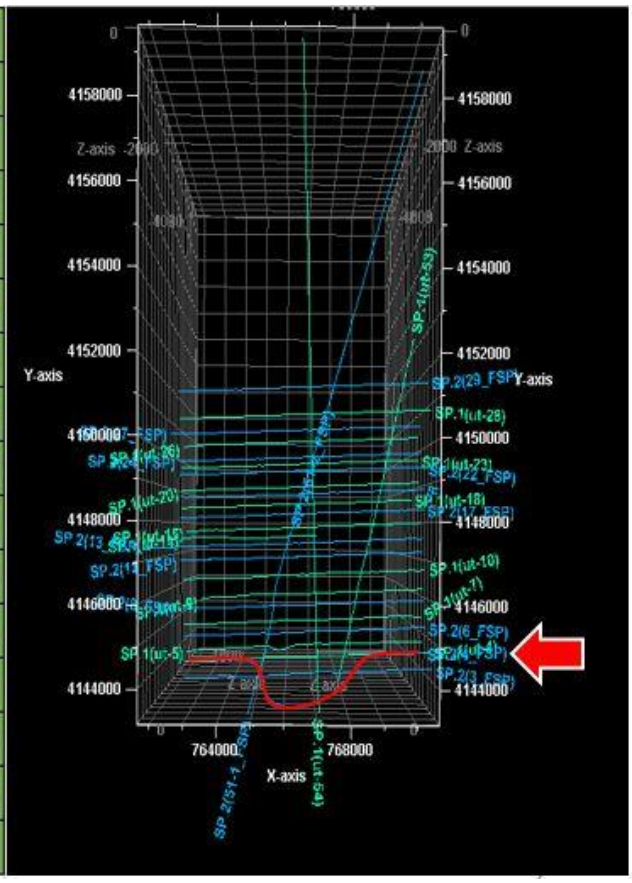

Figure 5.5. On the left, the table with the seismic lines of the NT07-20 and NT08-09 Expeditions. On the right, the seismic lines of the NT07-20 (blue lines) and NT08-09 (green lines) loaded into the Petrel. The seismic line SP.2(4_FSP) removed is highlighted in red.

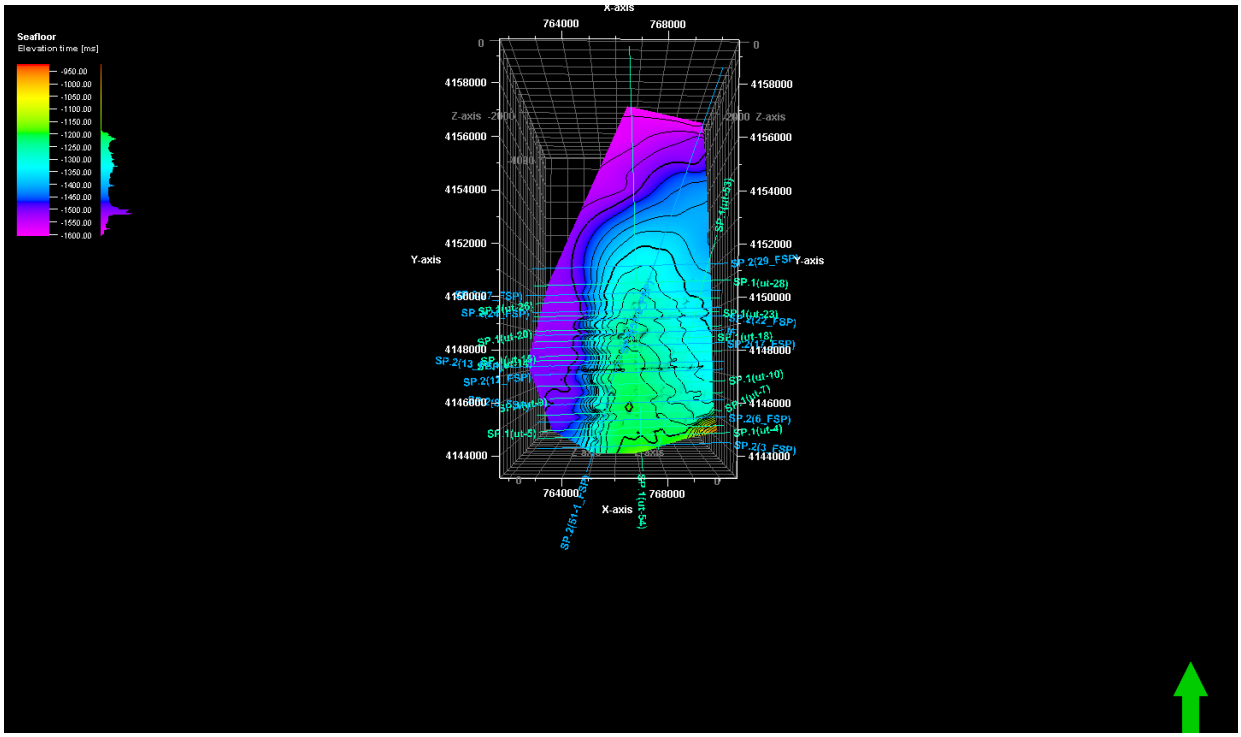

Figure 5.6. 2D SCS profiles and the grid of the seafloor. The color scale refers to the Elevation time (ms) of the seafloor grid. So, the deepest zones (longest times, close to 1600 ms TWT) are in purple while the shallowest zones (shortest times, close to 950 ms TWT) are in warmest colors.

Secondly, the possible Bottom Simulating Reflectors (BSRs) of the seismic profiles were identified near the seafloor without any application of seismic attributes (Figure 5.7). However, as reported by Matsumoto et al. (2011b) the BSRs are generally weak, discontinuous and patchy in this region (Chapter 3), which makes it difficult to interpret those seismic horizons.

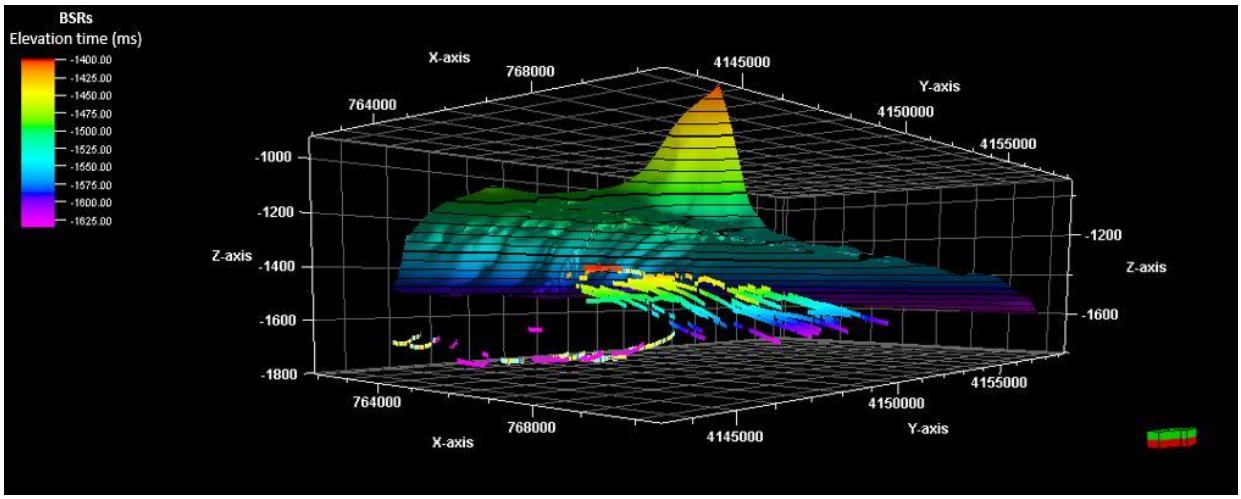

Figure 5.7. The seafloor grid generated in Petrel. Below it are plotted the interpreted BSRs of each seismic line without the aid of the application of seismic attributes. The color scale refers to the Elevation time (ms) of the BSRs. Thus, the longer the time, the greater the depth. Red colors correspond to shallow zones (close to 1400 ms TWT), while purple colors represent deeper zones (close to 1625 ms TWT).

In addition, another factor that hinders the visualization of these reflectors is the complex geological framework of the study area. As seen previously (Chapter 3), this region is tectonically active (Taira, 2001) and is full of geological faults, which intersect these reflectors and whereby the methane gas migrates vertically from deep sources and laterally from carrier beds causing an acoustic transparency (Freire et al., 2011). Furthermore, in some seismic sections there are hyperboles that were not collapsed during the migration step of the seismic processing carried out by JAMSTEC, which are mainly present in these fault regions of the Central part of the Umitaka anticline. For instance, in Figure 5.8 we can see diffractions associated with fault zones and blanking zones in the SP.2(19_FSP) seismic line. So, makes it difficult to see the continuity of the BSR.

Moreover, more than one seismic reflector with reverse polarity in relation to the seafloor reflector, being parallel to it was also found. As seen in the subchapter 2.3, there is a geophysical ambiguity, which can make the interpreter confuse the BSR (BGHSZ) with another negative physical anomaly in the shallower areas, above the BGHSZ. Hence, without the aid of a seismic attribute, it becomes very difficult for an interpreter to characterize the real BSRs without making mistakes.

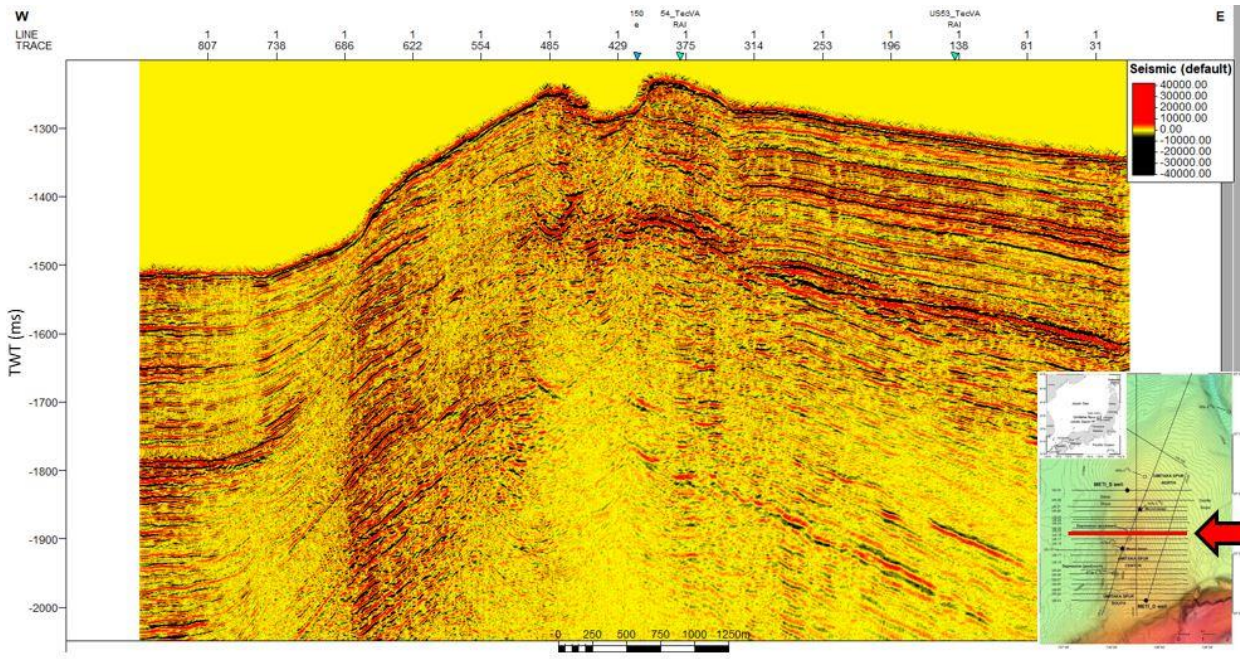

Figure 5.8. 2D Single Channel Seismic Line SP.2(19_FSP) from NT07-20 Expedition.

5.4.1 Seismic Attribute Application

Therefore, in order to highlight the real BSR of each seismic section in this complex framework, the seismic attributes were used. They were applied through the "Volume Attributes" command of the Petrel software in the seismic interpretation tab. Moreover, to make the analysis of amplitude values and frequency spectra, the commands "Extract Value" and "Open Spectral Analysis Tool" were used in the Petrel, respectively.

The Envelope was used to highlight amplitude anomalies. After, the Amplitude RMS, which has a similar function, was used as a part of the generation stage of the Amplitude Volume Technique (AVT).

Then, aimed to highlight the high impedance contrasts and the faults of the seismic data, the AVT was applied. To apply the AVT seismic attribute, the Root Mean Square attribute was first applied to all the seismic sections. The window length was 3 ms, which was the smallest window option. This frequency window was used because the smaller the chosen window, the better resolution (Vernengo and Trinchero, 2015). After, was done a rotation of the zero phase to

-90º in the seismic profile with the RMS amplitude seismic attribute already applied. Thus, the seismic section with the AVT applied was obtained. Thereby, in the Petrel 2019 software, this technique consists of applying two volume attributes: RMS amplitude and a Phase Shift of -90º in the RMS Amplitude.

The Relative Acoustic Impedance (RAI) is driven by geological assumptions and was applied to enhance thin layers below the tuning thickness (Chopra et al., 2009). After the application of these two geological attributes (AVT and RAI), the two frequency attributes were applied to measure seismic attenuation in seismic profiles.

Before applying these attributes, an analysis of the frequency spectrum was made to obtain information on the frequency domain in each seismic profile. Thus, an area of interest was chosen for each seismic profile. Therefore, a spectral analysis was made only of the components of this zone, to find out what is the dominant frequency of this unconventional reservoir system.

In Petrel, the Spectral Decomposition (SD) was done using the volume attribute "Generalized Spectral Decomposition", which is called this way because it has the option of using more than one type of transform according to the parameter selected by the interpreter. As the spectral decomposition in practice comes down to highlighting a certain central frequency of the seismic data through a transform, which in this case was the Continuous Wavelet Transform, for this evaluation six different central frequencies were applied, with a fundamental frequency of 25 Hz. Part of the methodology is explained in more detail in the next chapter (subchapter 6.1.6). For example, the dominant frequency in the SP.2(19_FSP) seismic section data was 100 Hz. Then, with a fundamental frequency of 25 Hz, six distinct spectral decompositions were applied: 25; 50; 75; 100; 125; 150 Hz, respectively. Ultimately, the instantaneous frequency attribute was applied to estimate the free gas zone because it causes drop-off high frequency components below the BSR, due to the seismic attenuation properties of the methane gas.

Chapter 6 RESULTS AND DISCUSSION

In this work, the six seismic attributes were applied to each seismic section, twenty eight seismic profiles in total, and the BSRs of each section were interpreted. Besides that, as it is known from previous studies that BGHSZ occurs at around 115 mbsf (Matsumoto et al., 2009, 2011a,b, 2017a,b), the focus of this work was the seismic quality of the shallower zone, corresponding to the Haizume Formation of the Late Quaternary.

Due to the vast number of seismic lines, only two lines were selected for this discussion, SP.2(19_FSP) and the strike line SP.2(51-1_FSP) from NT07-20 Expedition (Figure 6.1), which correspond with the seismic sections US-19 and US-51 in Figure 5.2, respectively. In this chapter, the results of the application of the six seismic attributes will be addressed, where a discussion will be made according to the collaboration of these previous works, covered in Chapter 3. The other seismic profiles and their respective results of the application of the seismic attributes are found in Appendix.

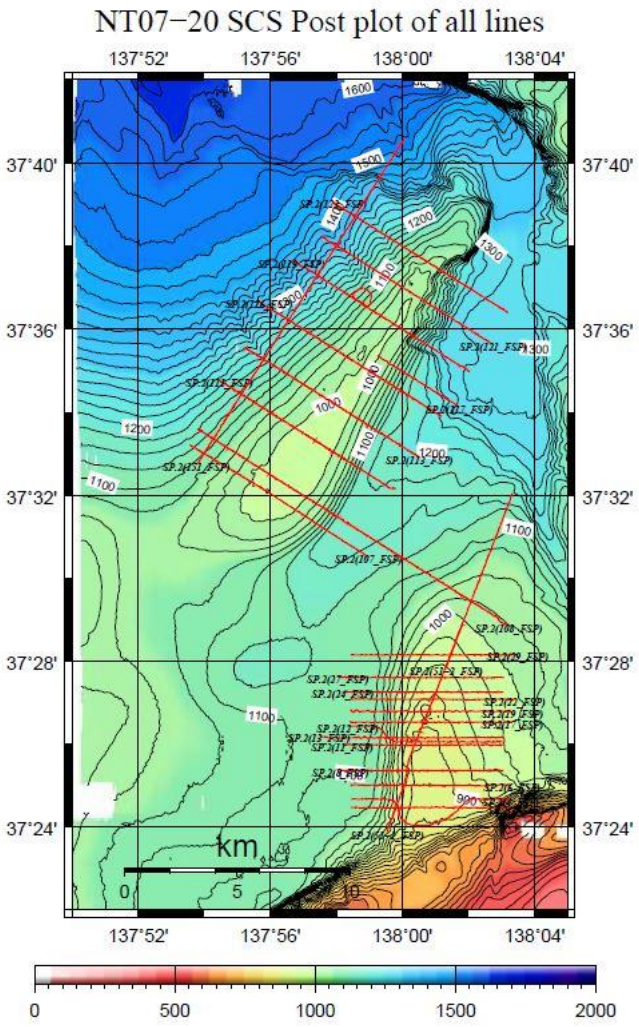

Figure 6.1. The 2D Single Channel Seismic (SCS) survey of NT07-20 Expedition from Joetsu Knoll and Umitaka Spur, Joetsu Basin, Japan (**JAMSTEC, 2007**).

This sorting was carried out according to the most interesting seismic features, such as pockmarks, Bottom Simulating Reflectors (BSRs) and even, flat spot in US-19, based on the work of Freire et al. (2011). For instance, note in that interpretation (**Error! Reference source not found.**) that exists two types of methane gas migration, vertical, where the flow is greater and coming from the depths, whereas laterally through the carrier beds the flow is less intense. However, realize that you cannot infer this just by viewing the SCS US-19 (Figure 6.2a). Therefore, it is important to apply seismic attributes.

Furthermore, according to geochemical analysis of the area, there are two different sources of methane gas area (Matsumoto et al., 2005, 2009; Freire, 2010; Freire et al., 2011). As reported by Bernard et al. (1976 in Kvenvolden, 1993), thermogenic gas has an isotopic carbon 13 signature greater than -60‰ while biogenic has a signature less than -60‰ (subchapter 2.1). Thus, we can see in Figure 6.2 by the seafloor mud gas analysis that the gas hydrate is thermogenic in the central part of the pockmark where there is an intense flow of gas from the depths through the faults, while biogenic at the edges of the anticline.

Besides that, note that in the right corner of US-19, between approximately 1.5 and 1.8 seconds two way travel (TWT), there are two different and important interfaces (BSR and flat spot). Thus, this will be the area of interest for this discussion on the application of seismic attributes in the US-19 seismic line.

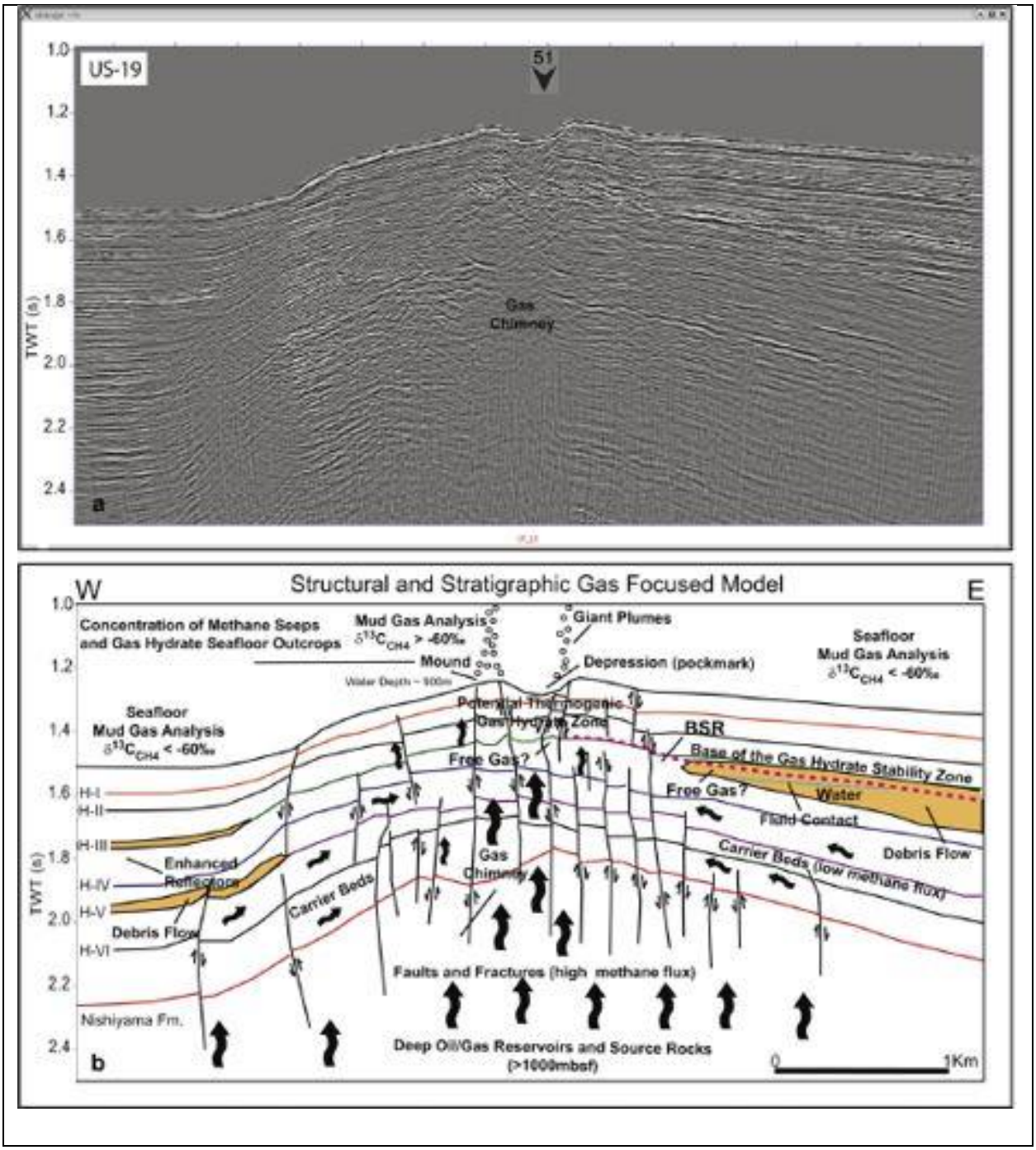

Figure 6.2. (a) US-19 seismic profile (b) Model for gas hydrate occurrence and main features of the Umitaka Spur gas hydrate/free gas system. Number at the top indicates where the US-51 strike SCS line roughly cross the US-19 dip SCS line (**Modified from Freire et al., 2011**).

The US-51 section was also chosen because it intersects through all seismic sections and there are also several pockmarks associated with the gas chimney (Figure 6.3).

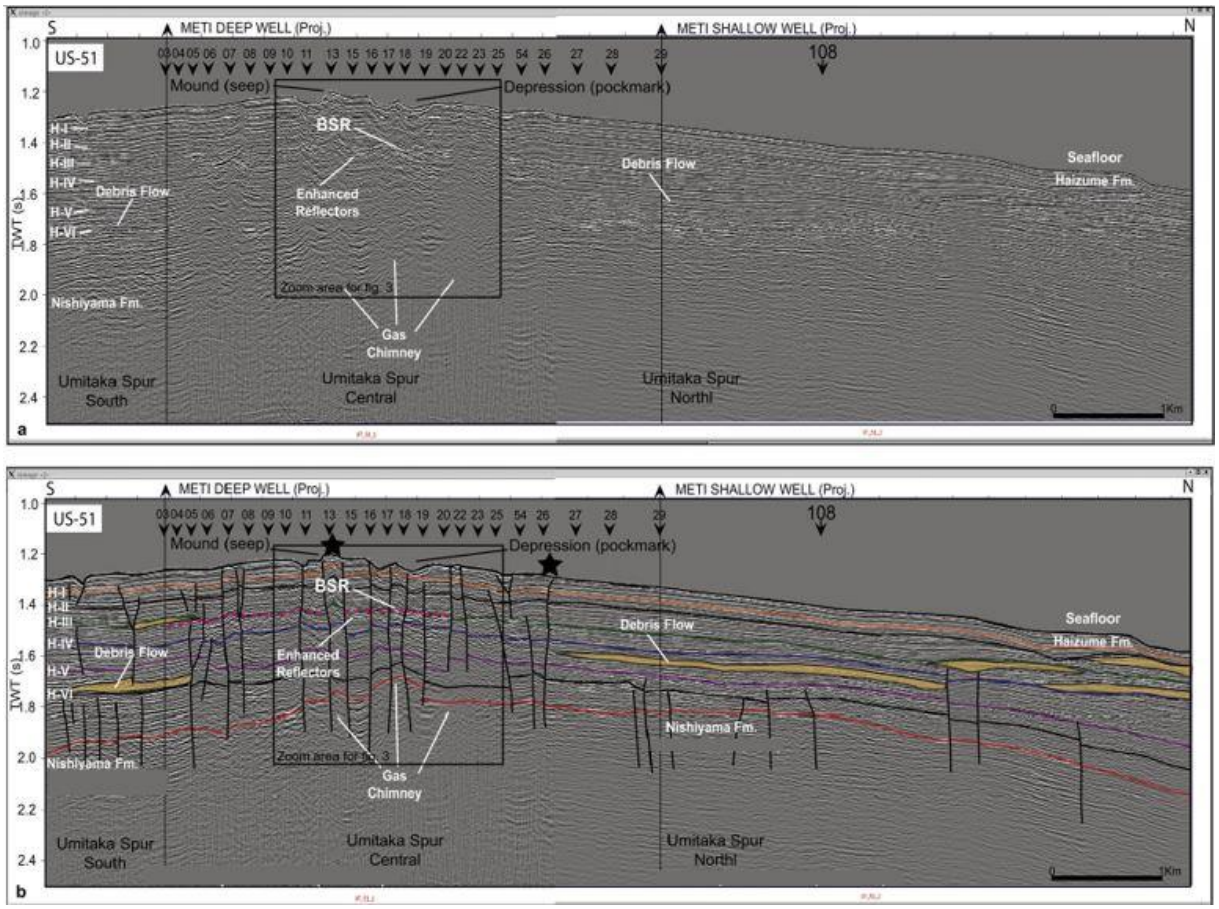

Figure 6.3. (a) non-interpreted and (b) interpreted images of the near-strike SCS section US-51. Note mounds and pockmarks (depressions) at the seafloor in the central part of the spur, where fracturing is greater. Stars indicate plume/seep locations. Numbers at the top show where the dip SCS lines cross the strike SCS line. METI Deep and Shallow wells are project (**Modified from Freire et al., 2011**).

6.1 Seismic Attributes Analysis

As seen in subchapter 2.3, the criterion for identifying a BSR is to recognize a reflector with a reverse polarity parallel to the seafloor reflector, which often crosscut the bedding plane of the host sediments. They are phase reversal reflectors due to the negative impedance-contrast that marks the hydrate/free gas phase boundary, high amplitude seismic event, which mimics the seafloor reflector (Hornbach et al., 2003). Thus, if the seafloor reflector is represented as black (positive) reflector in these seismic profiles, the BSR in this convention will be characterized by a bright spot (strong white reflector), for instance. However, in these seismic profiles they aren't so oblique to bedding planes, they are most often parallel to the layers, and there are more than one

reflector similar to BSR, so the application of seismic attributes is fundamental to highlight the true BSR.

6.1.1 Envelope

The Amplitude Envelope represents total instantaneous energy and because it is sensitive to changes in acoustic impedance, it highlights the high contrasts of acoustic impedance of the seismic signal. It varies approximately between zero and the maximum amplitude value of the trace.

Note in Figure 6.4 that it highlighted the strong impedance contrasts of the interfaces corresponding to the seafloor and BSR of the US-51 strike-line, corresponding to the highest amplitude values (blue colors). Thus, the BGHSZ corresponds to the blue horizon approximately in 1500 ms. This is in line with data from previous studies, where the BSR is this region is approximately 115 mbsf. Besides that, notice the vertical red spots intersecting white areas, they might be the results of the gas migration pathways along faults, fractures and carrier beds.

However, also note that if we don't have the information of the BSR region from previous studies, we couldn't exactly say that BGHSZ is in 115 mbsf due to ambiguity of other reflectors that were also highlighted with the application of the Envelope. For instance, note that when comparing with Figure 6.4, we notice that there is a strong energy on the erosive surface of the Debris Flow between H-VI and H-V, and that the H-II horizon could also be a BSR.

Nevertheless, regarding the H-II horizon being a BSR or "Paleo BSR", in my opinion these hypotheses are discarded. Based on previous studies, we know that BGHSZ is approximately 115 mbsf (Matsumoto et al., 2009; 2011a,b; 2017a,b; Freire, 2010). For instance, Freire et al. (2011) interpreted the BSR close to the H-III horizon in the US-51 seismic section (Figure 6.3). Thus, the BSR is close to the H-III reflector and not to the H-II.

Besides that, I don't believe that the anomaly highlighted in the black rectangle near the H-II horizon is a Paleo BSR (Figure 6.4). As seen in subchapter 2.3, BSR is a seismic reflector that represents the interface between impedance differences (the hydrates and free gas phase boundary, which seismically marks the BGHSZ. Thus, in my opinion, if BGHSZ instability occurs,

this phenomenon will cease and consequently the high impedance contrast will also disappear. I do not believe in former BSRs, sometimes they can remain scars, related to the diagenetic process, but without regional character.

Zooming in on the US-19's area of interest, we can also see that this attribute does not serve to distinguish a BSR from a flat spot and the H-I and H-II horizons (Figure 6.5), because it highlights all the high amplitude anomalies. Hence, it is not good to differentiate a BSR from another reflector with a high amplitude anomaly.

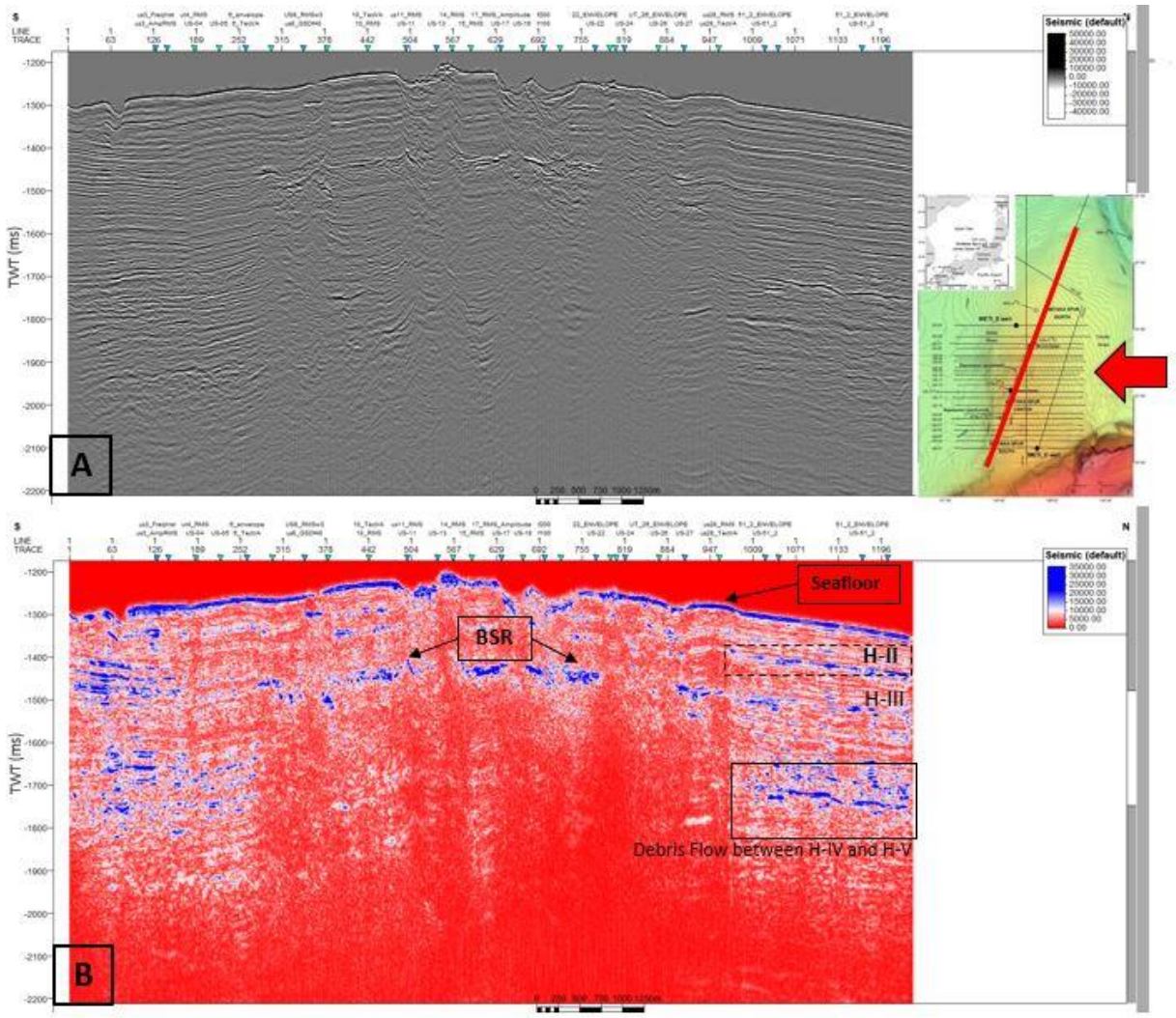

Figure 6.4. US-51 without (A) and with Envelope Amplitude (B).

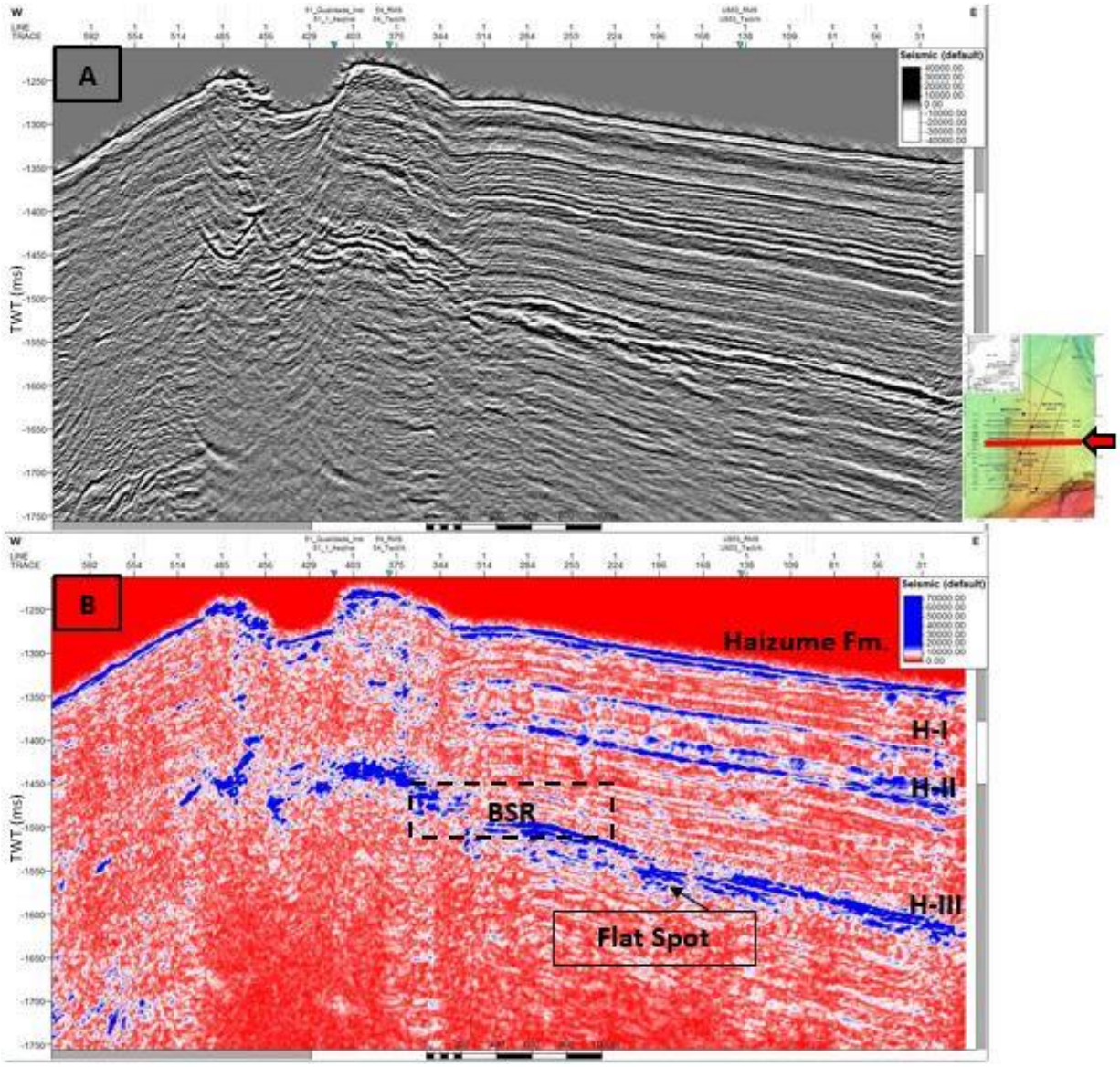

Figure 6.5. US-19 without (A) and with Envelope Amplitude (B).

Furthermore, for example, if we extract the amplitude values with the Petrel "Extract Value" command, we will see that both the H-II horizon and the BSR have high negative amplitudes (Table 3). Thus, the envelope attribute is not so useful in distinguishing a true from a false BSR. Therefore, it is not recommended to use only this attribute to reach a final conclusion.

Table 3
Seismic amplitudes of the seafloor, H-II horizon (Haizume Formation) and BSR from 2D SCS US-19 profile

Trace Number	Seafloor	H-II	BSR
314	14228.88	-10339.99	-22070.32
313	14510.95	-9220.52	-30020.16
312	17056.59	-16435.85	-17994.60
311	16665.69	-25086.44	-23654.47
310	12946.41	-31102.40	-34190.47
309	16597.57	-32079.30	-31590.57
308	18154.07	-27075.16	-21704.91
307	18056.42	-24819.03	-12596.83
306	9822.05	-16012.96	-5092.01
305	3805.52	-14316.16	-7302.52

6.1.2 RMS Amplitude

In addition to this attribute being used to generate the Amplitude Volume Technique attribute, as well as the Envelope, it is useful to highlight extreme amplitude anomalies. Note in Figure 6.6, what was mentioned about the importance of choosing the window length (5.4.1). The smaller the chosen window, the better resolution. Then, the seismic image generated with a 3 ms window length is greater sharpness than with a 9 ms window length.

Thereby, to apply the AVT, only the 3 ms window length was used.

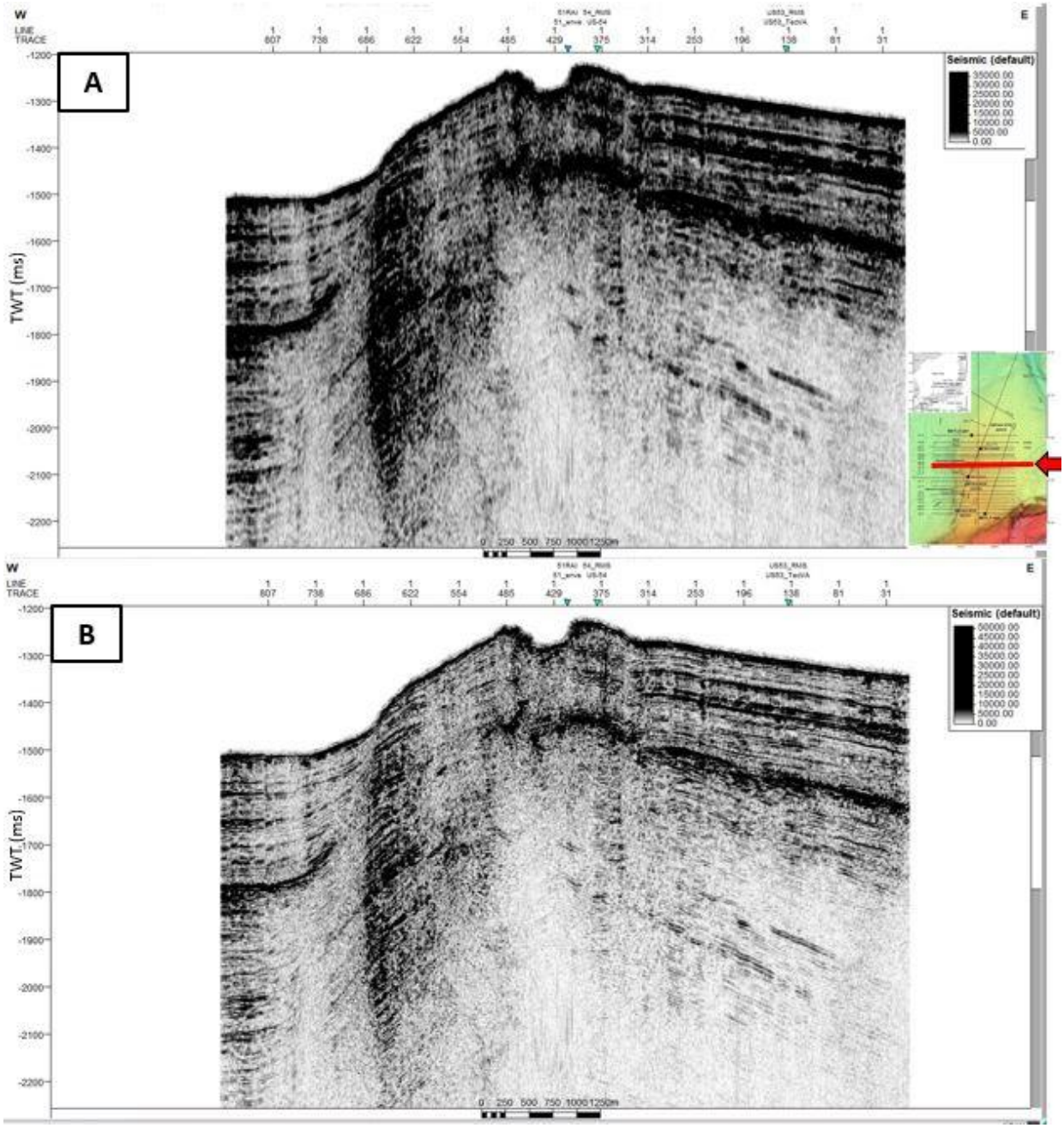

Figure 6.6. US-19 with RMS Amplitude applied. (A) 9 ms window length (B) 3 ms window length.

6.1.3 Amplitude Volume Technique

Then, after applying a phase shift of -90ºin the seismic image with a RMS Amplitude (Figure 6.6 B), we obtained Figure 6.7. Note that this attribute highlighted the structures very well, both the faults and the interface associated with BSR. Then, it is possible to view the stretches of BSRs that were previously weak and to interconnect them.

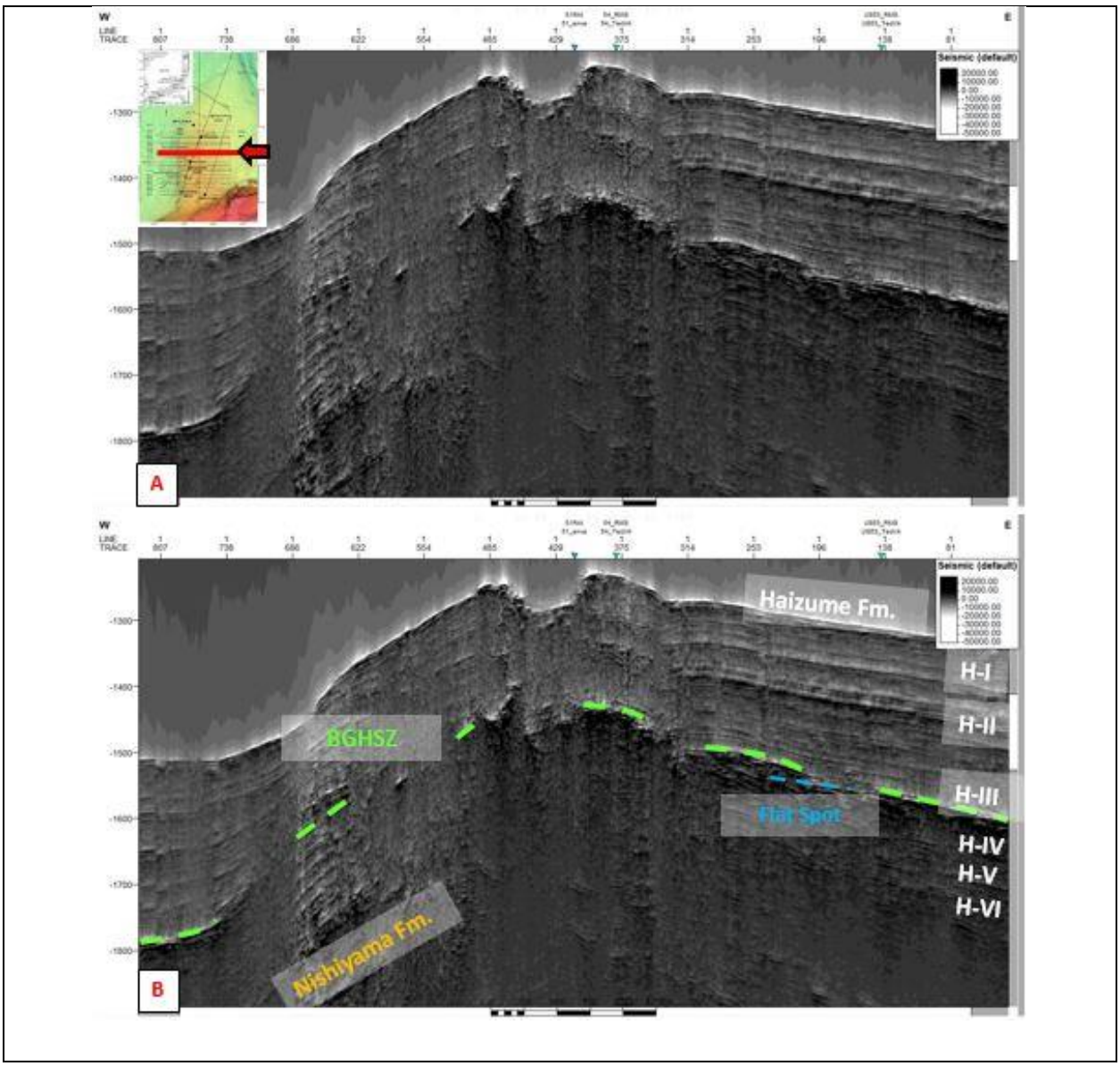

Figure 6.7. (A) non-interpreted (B) interpreted seismic images of the SCS section US-19 with Amplitude Volume Technique.

Moreover, note the pseudo-relief effect of this attribute that gives a sensation of a 3D seismic image, where the gaps are related to the gas chimneys (Figure 6.8). Then, it is great to interpret fault system.

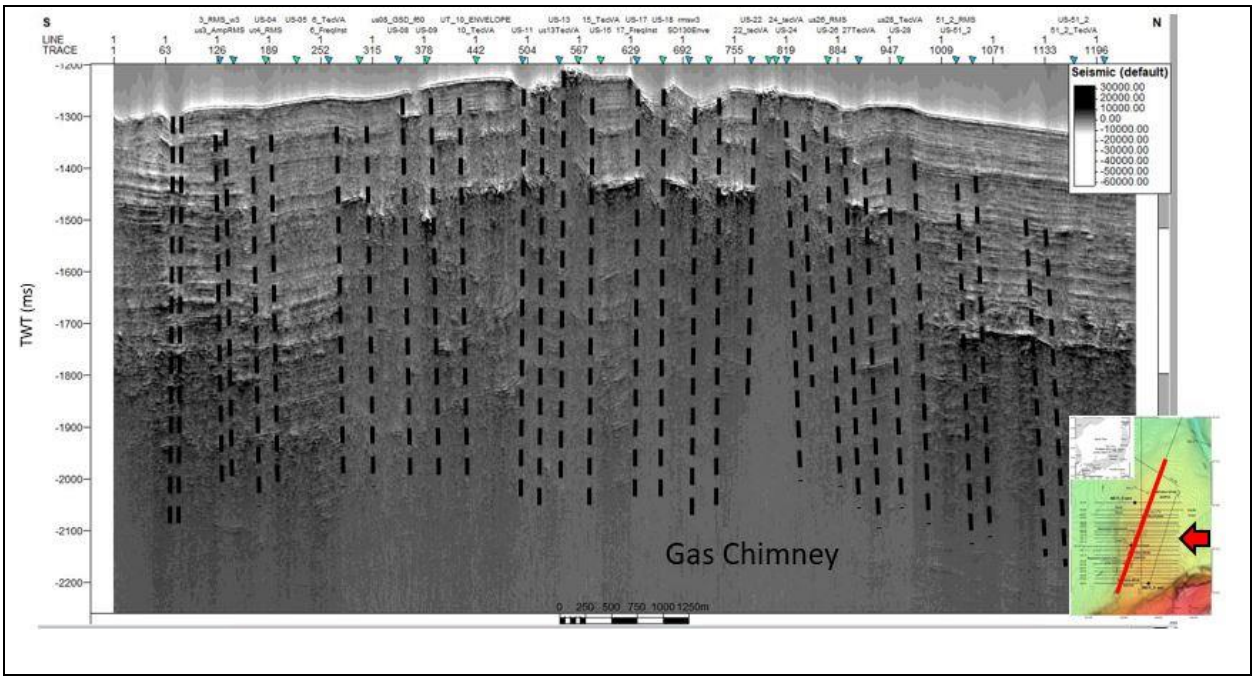

Figure 6.8. US-51 Complex fractures viewed with AVT.

6.1.4 Relative Acoustic Impedance

This attribute made the weak BSRs more striking and it also reduced the acoustic transparency (blanking) of regions where gas is possibly present, such as gas chimneys.

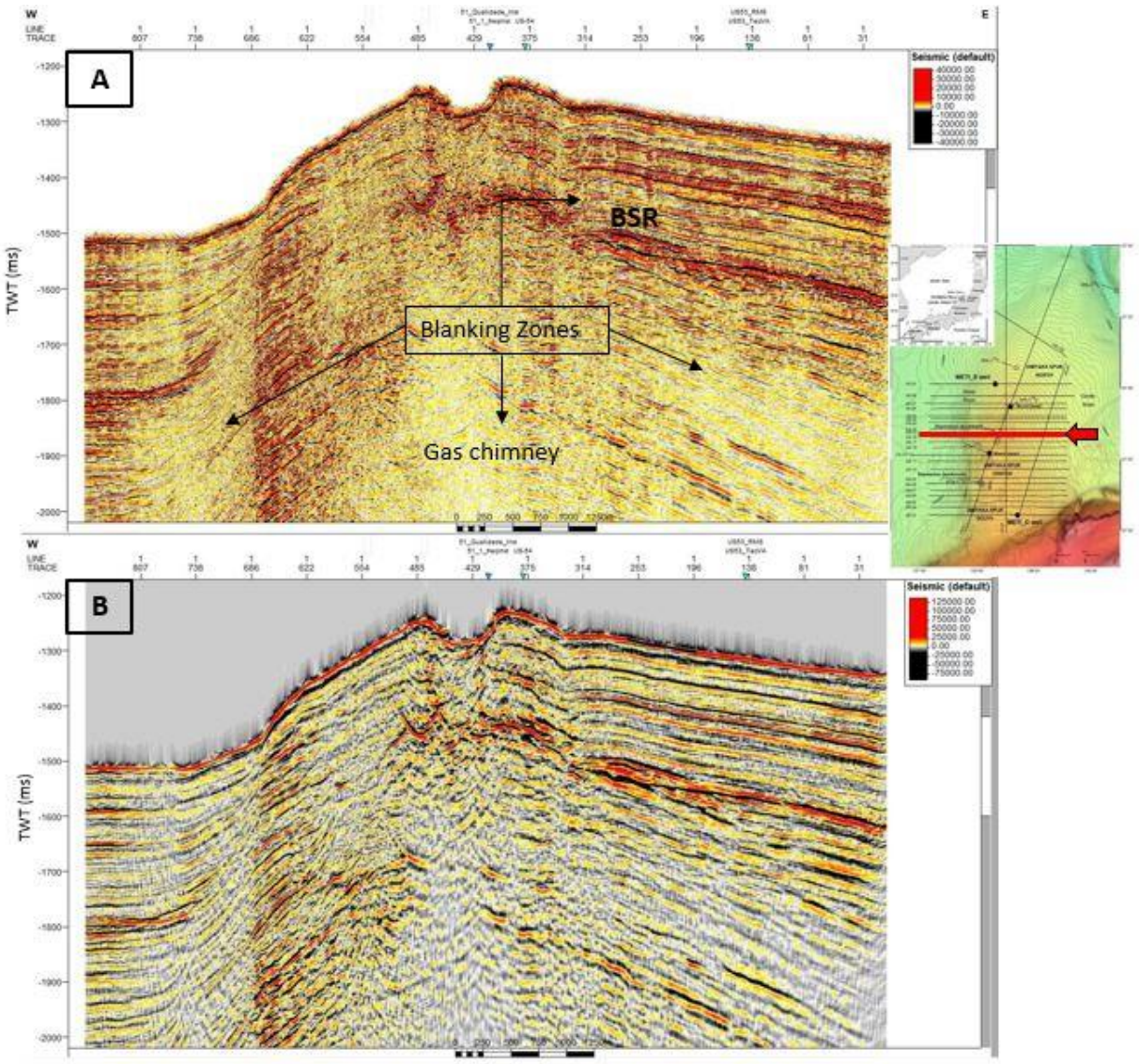

Figure 6.9. US-19 without (A) and with Relative Acoustic Impedance (B). Note that from (A) to (B) there was an enhancement of all reflectors.

Thereby, there was a gain in the image, so the areas that were previously blind due to the blanking effect were more visible with the application of the seismic attribute. In this way, the seismic reflectors became stronger and clearer. However, there is a drawback in this general gain, such as highlighting the noises (Figure 6.10 A). Notice in the purple circle that the diffractions in the fault zones have been highlighted. The zone interpreted in yellow shows the debris flow and the flat spot represents the gas zone with high water saturation.

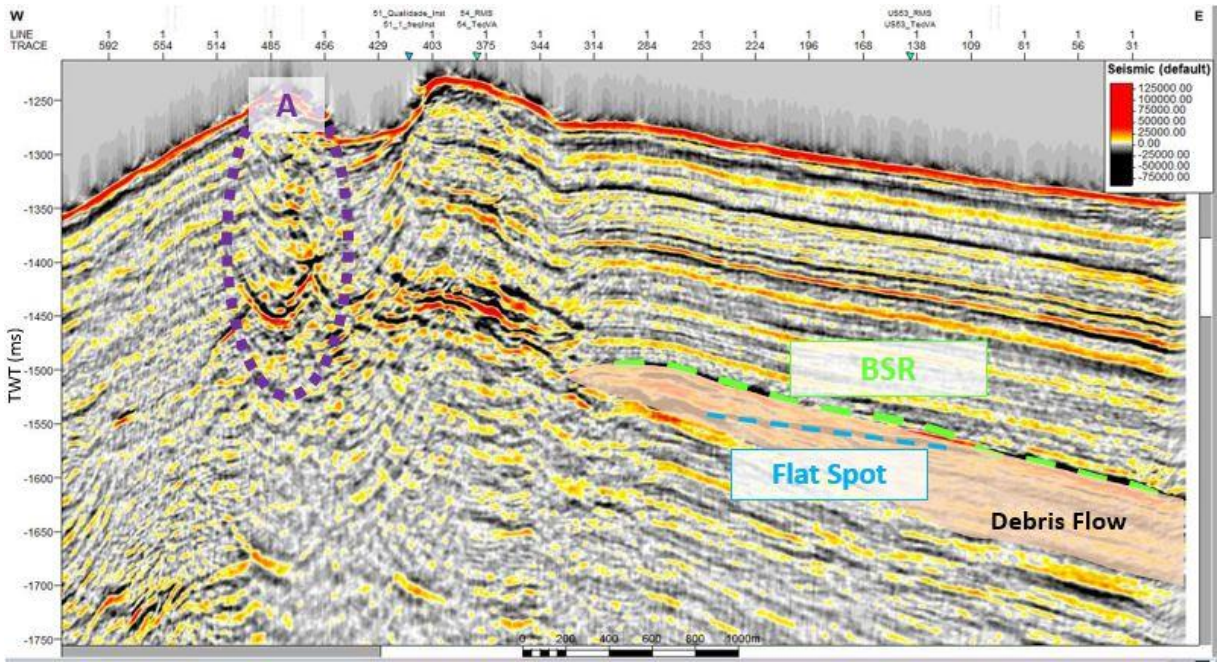

Figure 6.10. US-19 with RAI. (A) diffractions highlighted. BSR plus flat spot in the debris flow.

Besides that, this attribute also did not serve to distinguish the active BSR from the H-II horizon. Therefore, we have to measure the frequency to do this discrimination by analyzing the seismic attenuation.

6.1.5 Spectral Analysis

Before applying the seismic frequency attributes, it is good to check the dominant frequencies of the seismic data for a better understanding of the dynamics involved. Then, first the visualization of the Power (dB) of the Frequencies (Hz) of the entire seismic line US-19 was made (Figure 6.11).

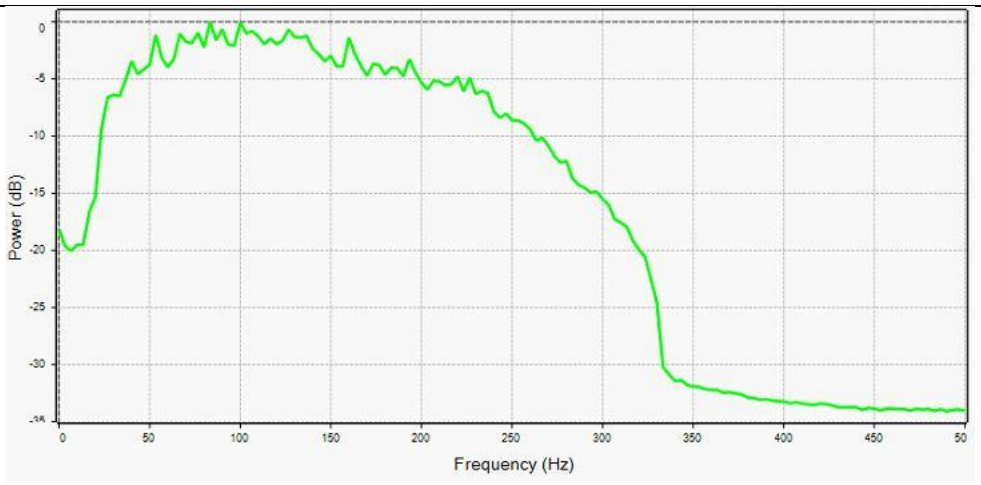

Figure 6.11. Spectral Analysis of the entire SCS section US-19.

Note from graph in Figure 6.11 that the most dominant frequencies of the seismic data are in the peaks between 80 and 100 Hz, which makes sense, as the 2D SCS is a high resolution seismic. Besides that, note that the higher frequencies are less dominant, because as seen in subchapter 5.3, during the seismic processing a band pass filter of 25-30-360-400 Hz was applied. Furthermore, due to physical properties, the tendency is for higher frequencies to be attenuated more quickly than the lower ones. So, the seismic data is correct as expected.

6.1.6 Spectral Decomposition

Before applying Spectral Decomposition, a spectral analysis was also performed (Figure 6.12). However, this analysis was more thorough, it was done only in the chosen area of interest, which corresponds to the area where we have the BSR and the flat spot (Figure 6.10).

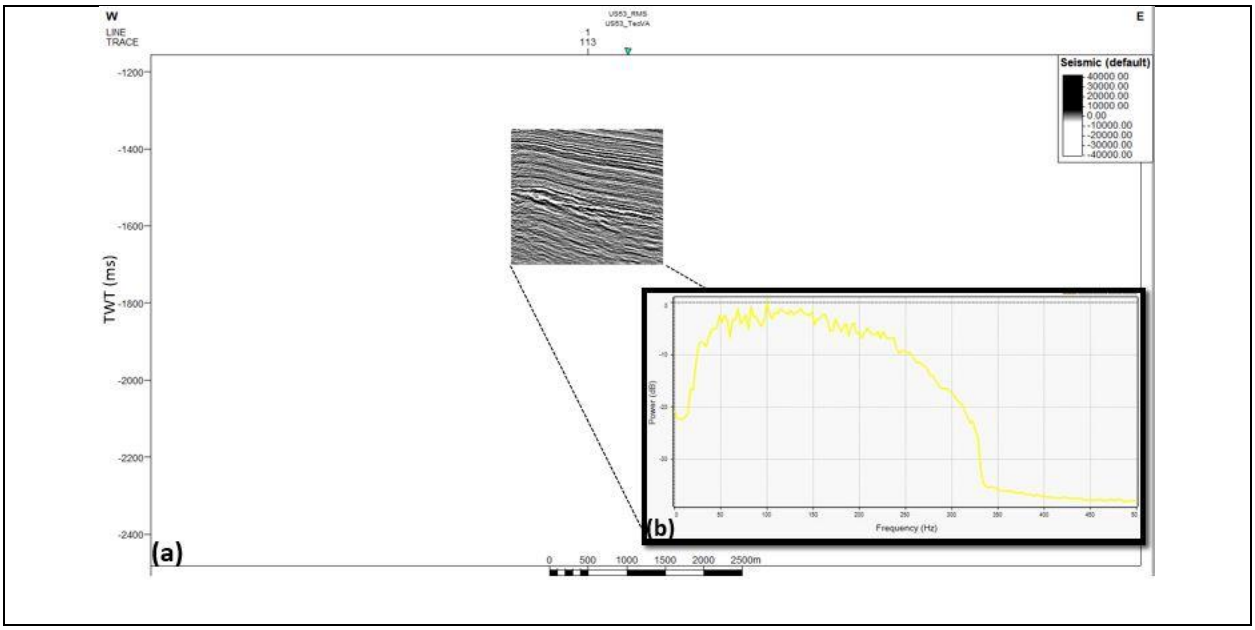

Figure 6.12. US-19 chosen area of interest (a) and its frequency analysis (b).

Thus, in order to know which central frequencies to choose for the application of the spectral decomposition, a zoom was made in the region where there is a greater concentration of peaks in the power versus frequency graph (Figure 6.12b). Then, it is observed that the frequency of 100 Hz is the most dominant of this zone of interest (Figure 6.13).

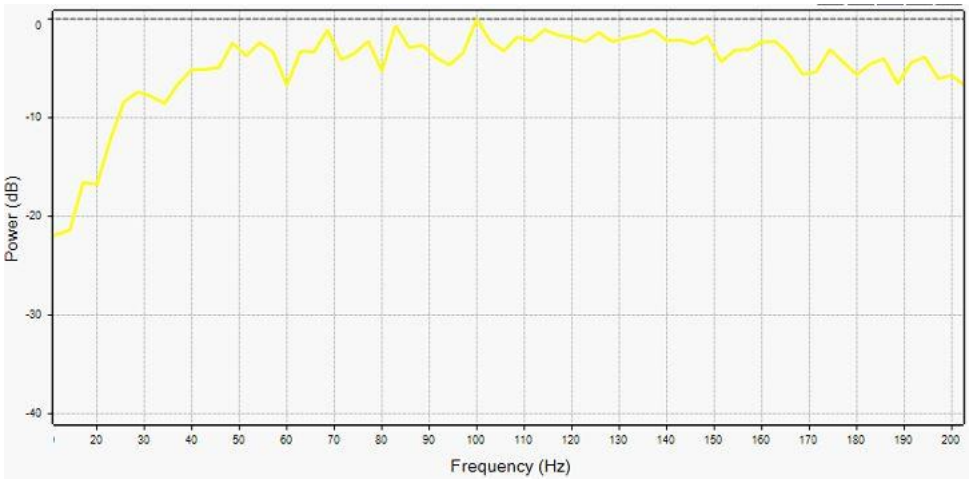

Figure 6.13. Dominant Frequencies in the selected US-19 area.

As seen in subchapter 4.3.5, Spectral Decomposition serves to highlight a certain frequency of the seismic data. Since the higher frequencies are attenuated more quickly than the lower, a zone of free gas would attenuate all of these high frequencies, for instance. That way, the lowest frequencies would remain in the free gas zones.

Therefore, based on this theory, the ideal is to choose a lower frequency to highlight the free gas zone. Whereas to highlight the presence of gas hydrates above the BGHSZ, it would be better to use a higher frequency. As the frequency of 100 Hz is the most dominant in the seismic data, it will probably be the best one to see the seismic reflectors. Thus, from it five other frequencies were chosen to analyze the effects of these different spectral decompositions in the US-19 seismic section with a fundamental frequency of 25 Hz. Then, six spectral decompositions were applied with a central frequency of: 25, 50, 75, 100, 125 and 150 Hz (Figure 6.14).

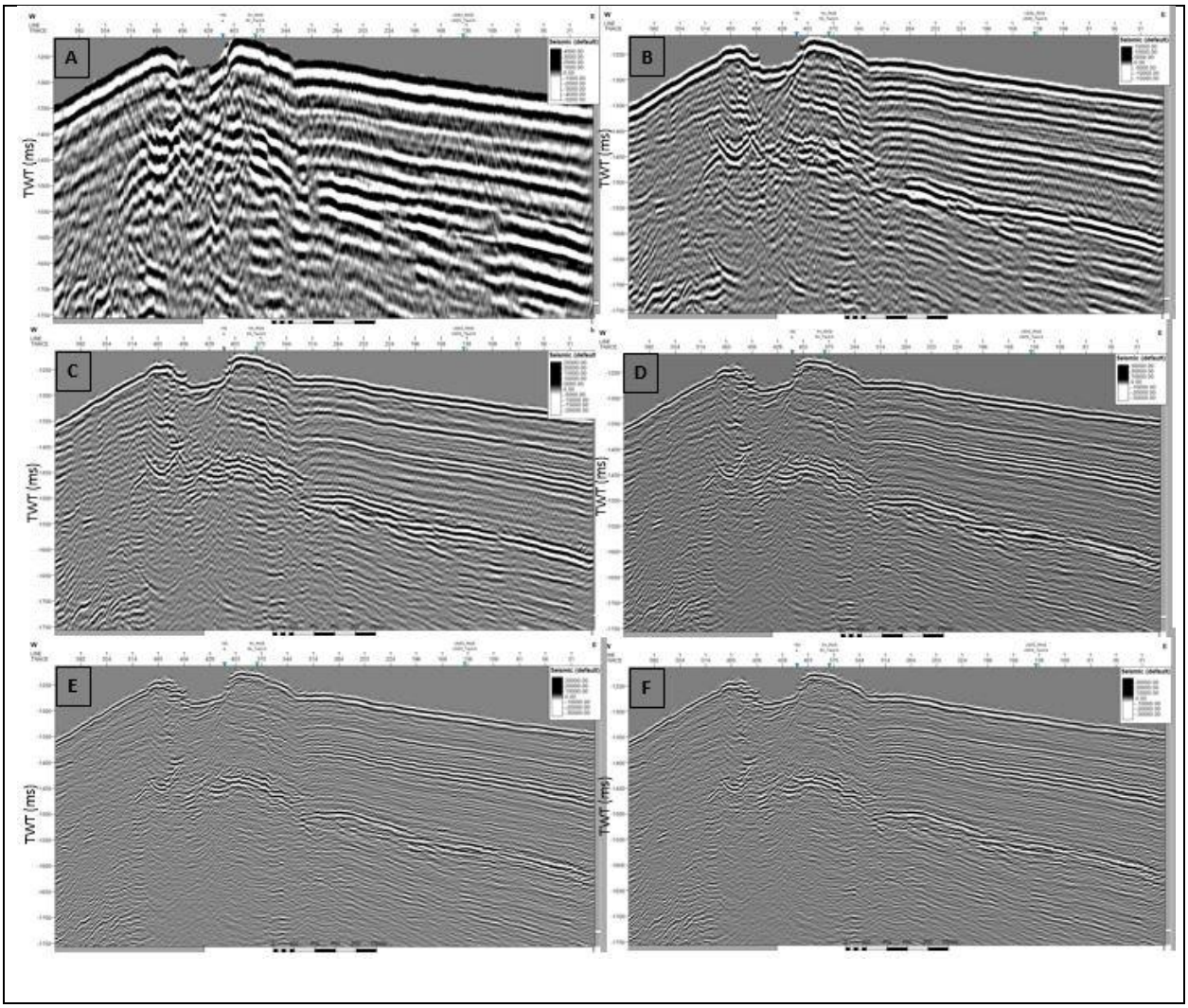

Figure 6.14. Spectral Decomposition of US-19 with (A) 25 Hz (B) 50 Hz (C) 75 Hz (D) 100 Hz (E) 125 Hz (F) 150 Hz.

Incredibly, all images are on the same scale (Figure 6.14, A-F). Apparently, it seems that the image corresponding to the SD with a frequency of 25 Hz is with a greater zoom, because the seismic reflectors are thicker. This is due to thin bed interference. As reported by Laughlin et al. (2002), in thin reservoirs a lower dominant frequency would highlight the thicker parts on an amplitude map and this is what happened when choosing a central frequency of 25 Hz. While seismic data with a higher dominant frequency highlight the thinner parts of the reservoir on amplitude maps, as seen in Figure 6.14 E-F. Thereby, from A to F, we have the illusion that the scale is increasing, while in fact it is the same, what changed was the frequency parameters of the Spectral Decomposition.

Note that the most balanced result obtained for the interpretation of the reflectors, was the frequency of 100 Hz (Figure 6.14). As was the case with the US-51 frequency analysis (Figure 6.15), but it will not be covered in detail here.

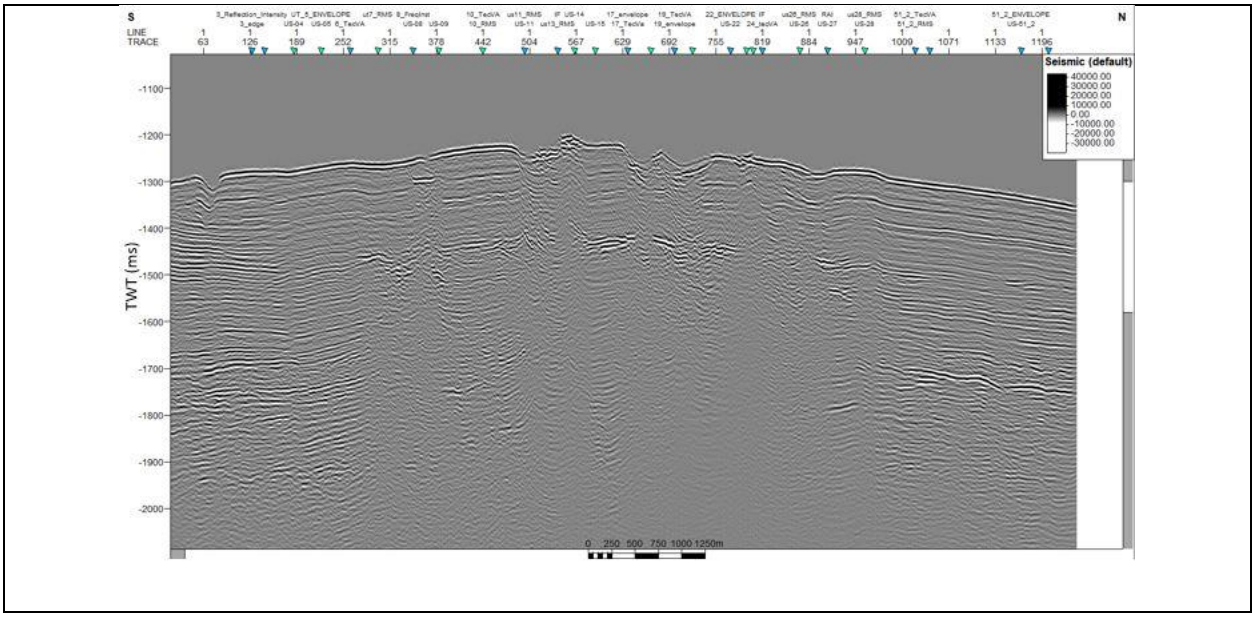

Figure 6.15. SCS US-51 with Spectral Decomposition with a central frequency of 100 Hz.

6.1.7 Spectral Decomposition plus Envelope

Thus, the envelope attribute was applied to highlight the energies after the application of spectral decomposition. So, in this way, highlight the BSR, which is the boundary between the free gas zone and the gas hydrates stability zone (Figure 6.16).

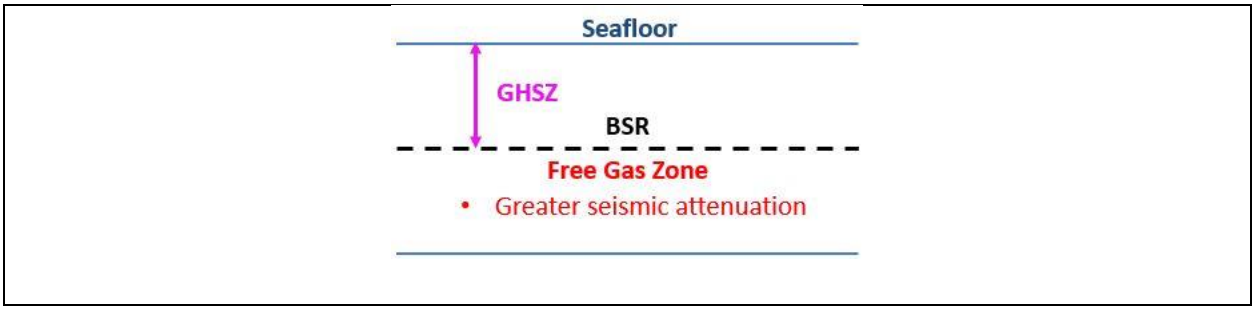

Figure 6.16. Theoretical scheme showing the highest seismic attenuation below the BSR.

Thus, applying the Envelope to the Spectral Decompositions (Figure 6.14) of section US-19, Figure 6.17 was obtained.

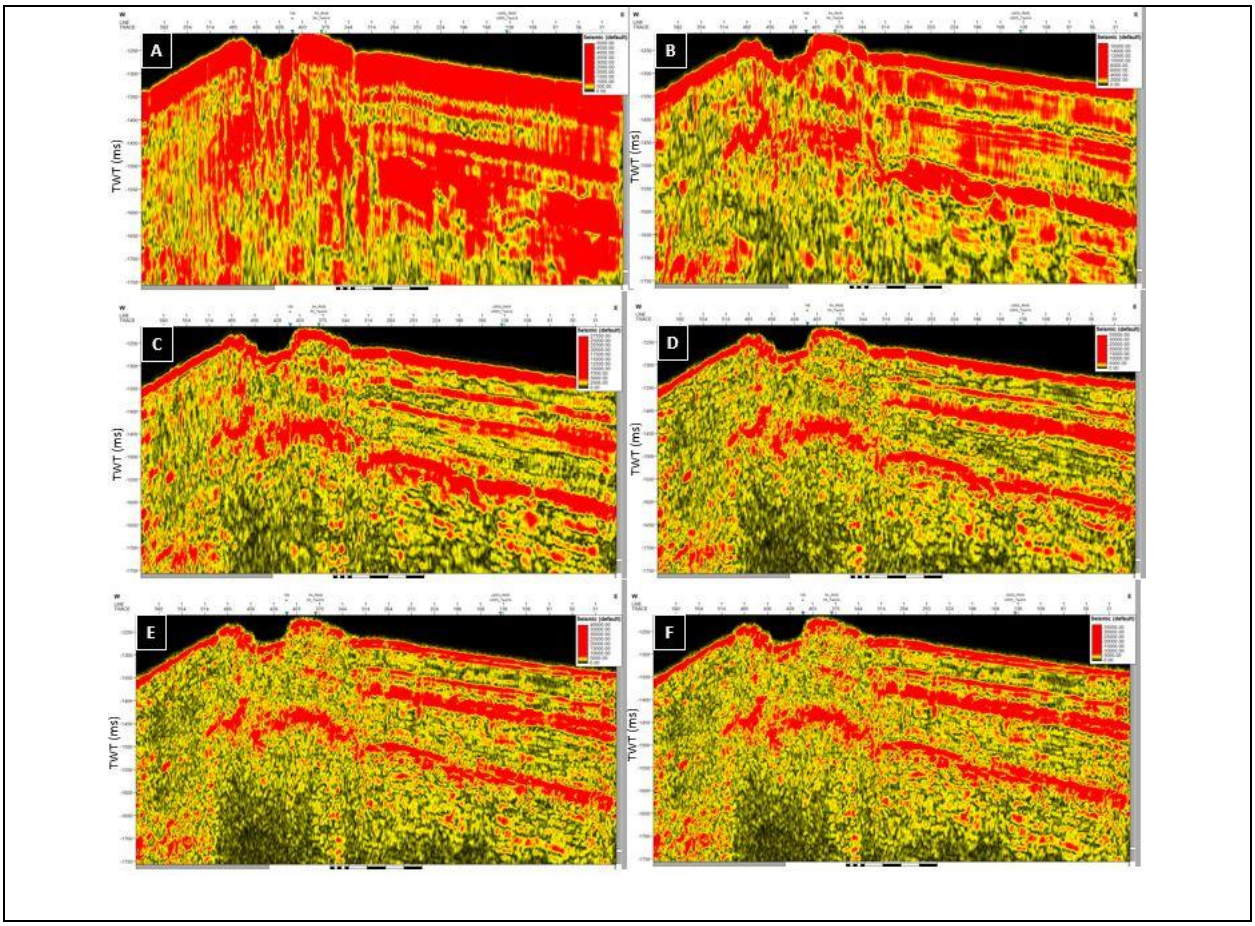

Figure 6.17. Spectral Decomposition plus Envelope of US-19 with (A) 25 Hz (B) 50 Hz (C) 75 Hz (D) 100 Hz (E) 125 Hz (F) 150 Hz.

Note in the figure above (Figure 6.17), that the Spectral Decomposition plus Envelope with the lowest central frequency (25 Hz) highlighted more the regions where there is a greater seismic attenuation, leaving huge red spots below the BSR. While with the higher frequencies, there was a greater thinning of the layers, better highlighting the BSR and the strong horizons above it (H-1 and H-2 of the Haizume Formation). The BSR is clearer in Figure 6.17 D, where it is in the red zone between 1.4 and 1.6 seconds TWT.

Thus, also applying the envelope seismic attribute on the spectral decomposition with a central frequency of 100 Hz, we obtain this result (Figure 6.18) from section US-51.

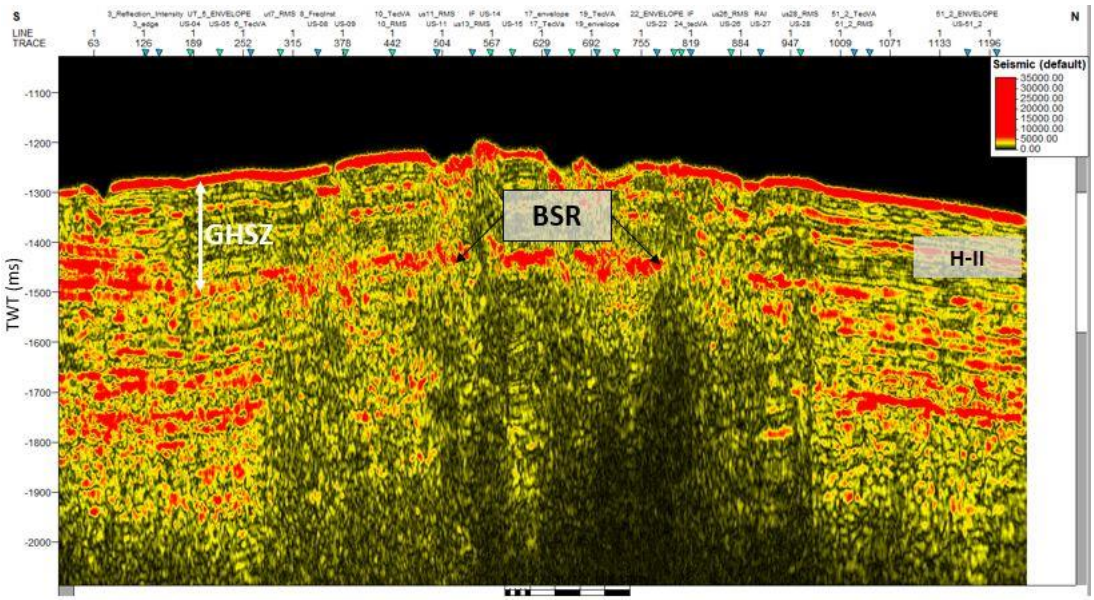

Figure 6.18. SCS section 51 Spectral Decomposition with a central frequency of 100 Hz plus Envelope.

Therefore, note that the combination of these two attributes served to highlight the BSR. However, it is observed that the distinction between the true BSR and the strong anomaly of the H-II horizon can only be made due to the bibliographic references of the region and due to the previous attributes application, such as AVT, which highlighted the BSR from H-III and H-II reflectors. Thus, use only spectral decomposition is not enough to reduce geophysical ambiguity.

6.1.8 Instantaneous Frequency

Ultimately, the Instantaneous Frequency seismic attribute was applied. Note that in the image generated after applying this attribute in the US-51 seismic section, there is a greater dominance of the lower frequencies in the deeper areas (Figure 6.19). In this color scale used, the red spots correspond to 0 Hz. Thus, a greater seismic attenuation is observed in the zones below 1.7 seconds TWT, approximately 0.5 TWT bsf and they should be free gas accumulation from deep sources.

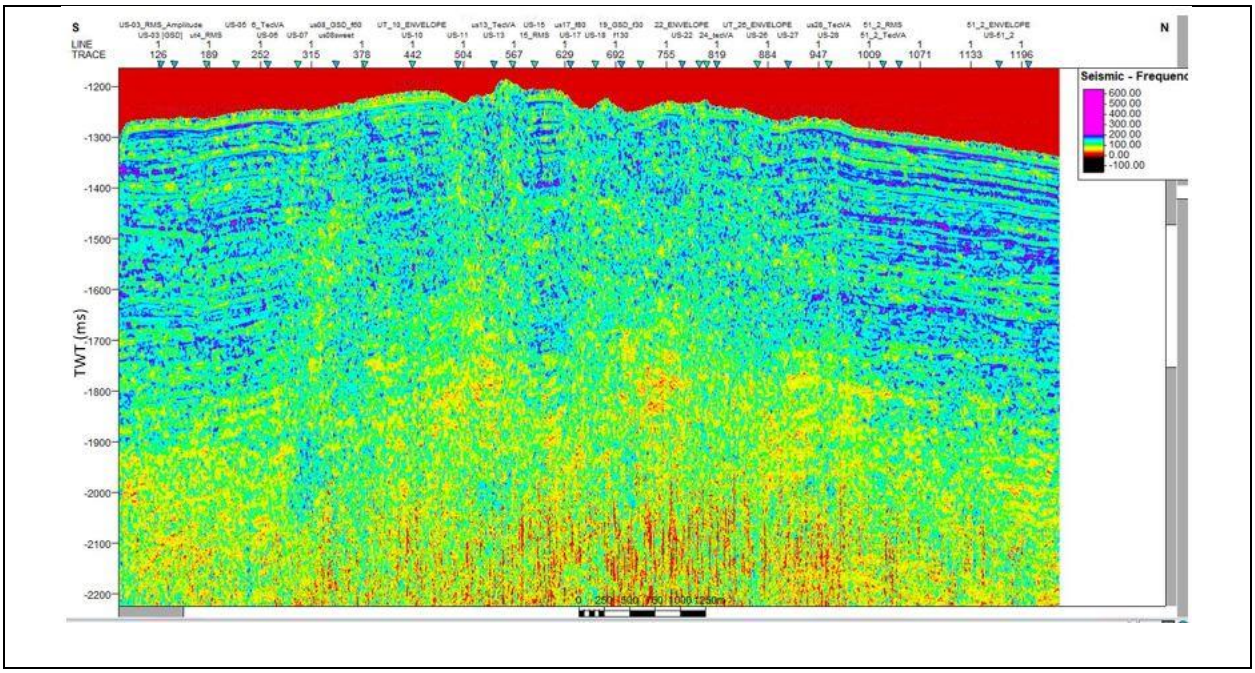

Figure 6.19. SCS section 51 with instantaneous frequency attribute. Red, yellow and green spots represent frequency values close to 0 Hz, 50 Hz and 100 Hz, respectively. While purple spots represent frequency values approximately greater than 200 Hz (higher frequency values).

Besides that, the zones with yellow and green spots are also areas in which there is an anomalous attenuation of the seismic signal. Hence, they represent areas of free gas migration-accumulation. While blue and purple spots represent regions with less seismic attenuation. So, since the gas hydrates only exist in the Gas Hydrate Stability Zone (GHSZ), only the purple and blue spots above the BSR (less than 1.6 s TWT) can mean their presence in the sediments. While the other purple and blue zones below the BSR should represent compacted sediments. Thus, considering these observations and zooming in on the shallow central part, the interpretations of Figure 6.20 can be made. Note that gas hydrates should serve as a seal fort the free gas zone.

In addition, also note the unusual presence of high gas concentration in gas chimney structures above BSR (yellow spots in Figure 6.20). This result matches the abnormally low acoustic velocities observed above BSR in previous work. For instance, as seen in subchapter 3.4, Saeki et al. (2009) through a velocity analysis of 3D seismic survey data reported anomalously low velocities (1200-1300 m/s) above the BSR horizon, possible affected by the presence of free-gas bubbles (Matsumoto et al., 2009, 2011b; Freire, 2010). These low velocities were also observed in the well data (Figure 2.12b) by Matsumoto et al. (2017a,b).

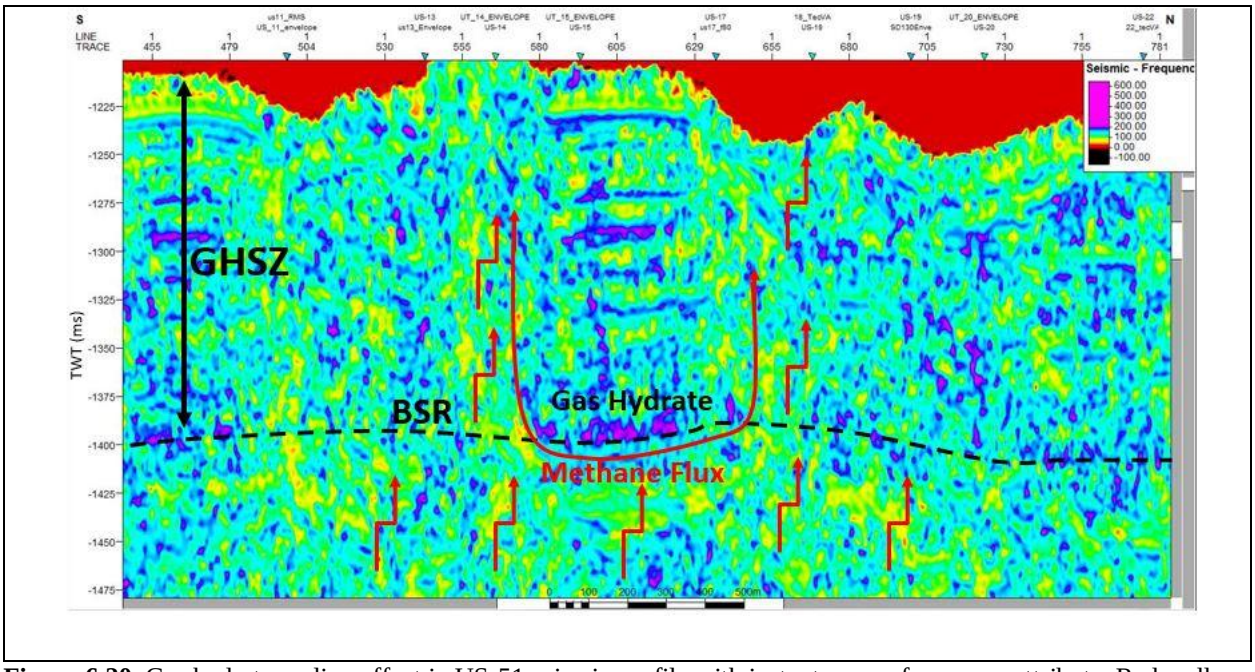

Figure 6.20. Gas hydrate sealing effect in US-51 seismic profile with instantaneous frequency attribute. Red, yellow and green spots represent frequency values close to 0 Hz, 50 Hz and 100 Hz, respectively. While purple spots represent frequency values approximately greater than 200 Hz (higher frequency values).

Besides that, comparing the seismic interpretation of US-19 (Figure 6.2) from Freire et al. (2011) with the result obtained after applying the IF (Figure 6.21) is possible to relate the seismic attenuation with the presence of gas, which migrates vertically through the faults and laterally through the carrier beds (Freire et al, 2011). Note the red spots between 2.0 s and 2.4 s TWT, corresponding to the lowest frequencies values (Figure 6.21). They may occur due to the high flow of methane from deep sources, which migrates vertically through the faults (Figure 6.22). This is probably the source of the thermogenic gas hydrates found on the surface in the pockmark, reported by geochemical studies (e.g., Matsumoto et al., 2005, 2009, 2011a,b, 2017a,b; Freire, 2010; Freire et al., 2011). As seen in Chapter 3, a numerous gas venting sites have been observed in Umitaka Spur (Figure 3.6, Figure **3.7** and Figure **5.2**) and through the geochemical analysis of the carbon isotope ratio, the origin of these methane were identified (Okui et al., 2008; Freire, 2010; Matsumoto et al., 2011b).

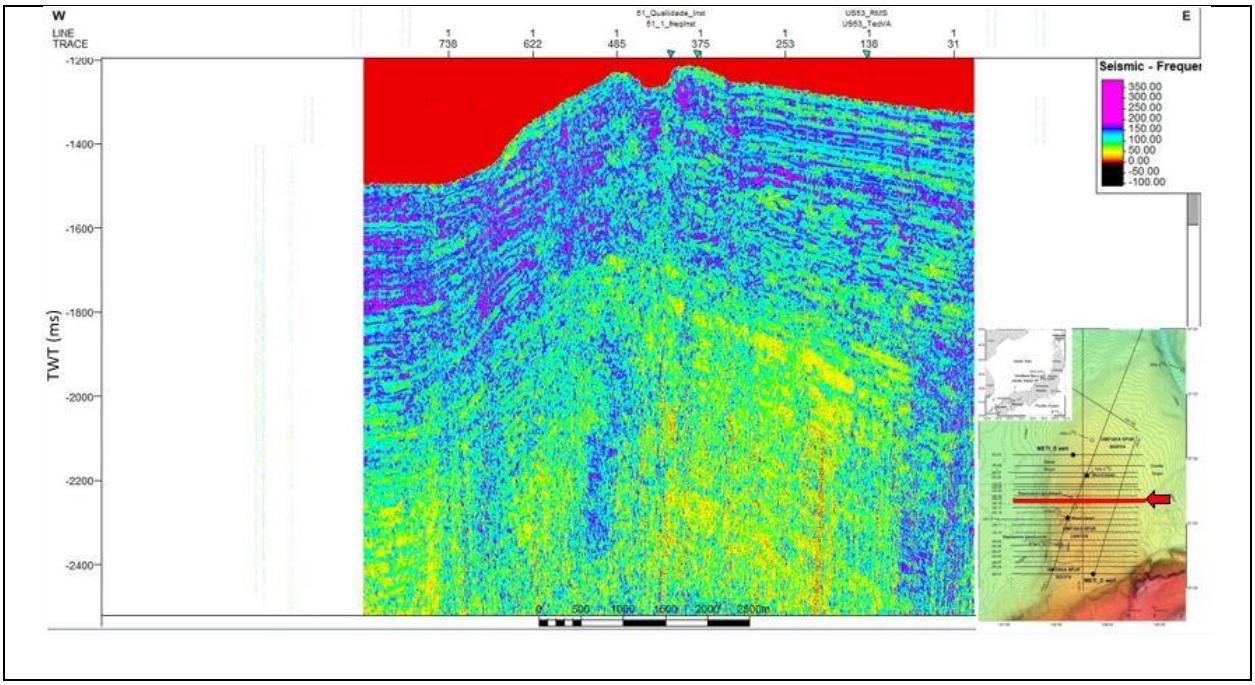

Figure 6.21. SCS section US-19 with instantaneous frequency attribute. Red, yellow and green spots represent frequency values close to 0 Hz, 50 Hz and 100 Hz, respectively. While purple spots represent frequency values approximately greater than 175 Hz (higher frequency values).

In addition, note the relationship between the yellow and green spots regions and the blanking zones observed previously (Figure 6.9 A). So, the origin of blanking in gas chimney is a consequence of the presence of gases that attenuate the signal, generating this acoustic transparency. As reported by Matsumoto et al. (2017a), there is a shadow effect caused by the existence of energy absorptive free gases within gas chimneys in Umitaka Spur.

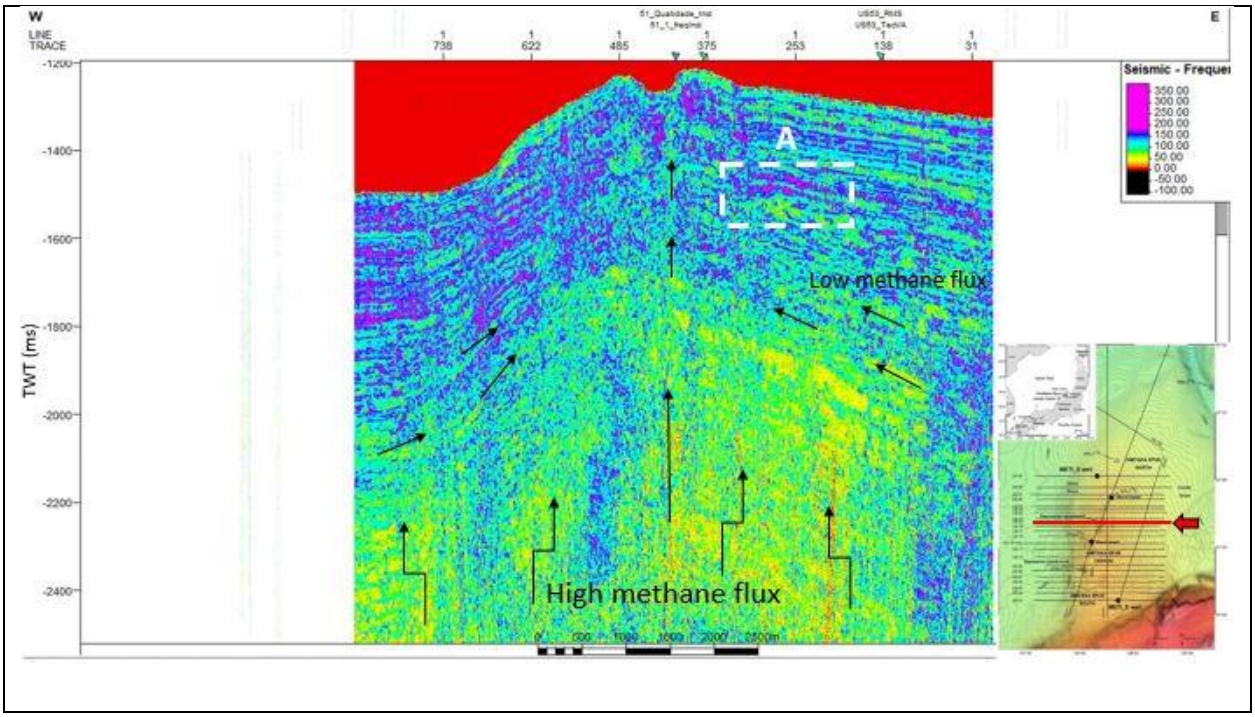

Figure 6.22. SCS section US-19 with instantaneous frequency attribute. The arrows show the flow of methane. Rectangle (A) highlights the contrast of seismic attenuation between purple and yellow spots. Red, yellow and green spots represent frequency values close to 0 Hz, 50 Hz and 100 Hz, respectively. While purple spots represent frequency values approximately greater than 175 Hz.

Besides that, also note that the rectangle A highlights a large contrast of seismic attenuation (Figure 6.22). Note that there is a greater attenuation of the seismic signal (yellow spot) below, while a lesser attenuation just above (purple spot). By zooming in on the zone of interest (Figure 6.23), we can attribute this greater attenuation to the free gas zone (yellow spot), which is just below the BSR corresponding to the BGHSZ. Thus, these purple spots above should be hydrates filled in fractures of sediments sealing the free gas zone.

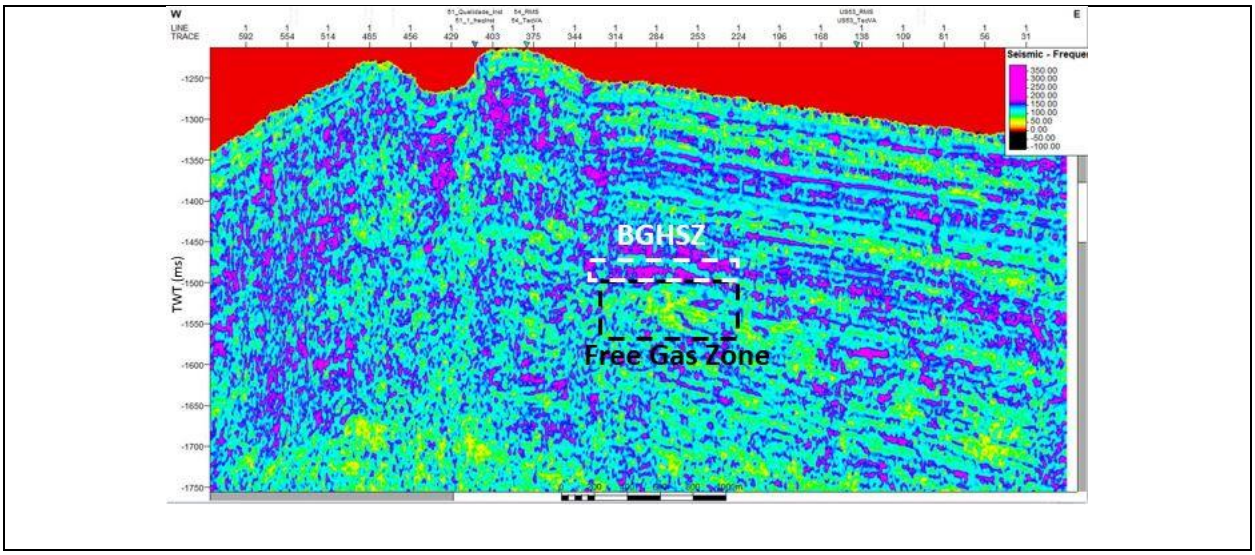

Figure 6.23. SCS section US-19 with instantaneous frequency attribute. Yellow and green spots represent frequency values close to 50 Hz and 100 Hz, respectively. While purple spots represent frequency values approximately greater than 175 Hz. This could possibly mean gas hydrate at the Base of the Gas Hydrate Stability Zona (BGHSZ) serving as a seal for the free gas zone.

Moreover, it is important to highlight the sedimentary heterogeneity involved in the region, which may also explain these different color patches. For instance, coincidence of accumulations zones of hydrate with Methane Derived Authigenic Carbonates (MDACs) were observed in Umitaka. Based on Matsumoto et al. (2017), this coincidence may imply cogenetic relation, so enhanced methane flux caused carbonate precipitation while also leading to hydrate accumulation.

Furthermore, instantaneous frequency attribute served to highlight the possible hydrates blocks below the pockmark (purple spots). This is important for that question about the relationship between Last Glacial Maximum (LGM), sea level fall, massive dissociation of methane hydrates and pockmarks formation (Figure 6.24), that was covered in the subchapters 2.3 (Figure 2.9) and 2.4 (Figure 2.11).

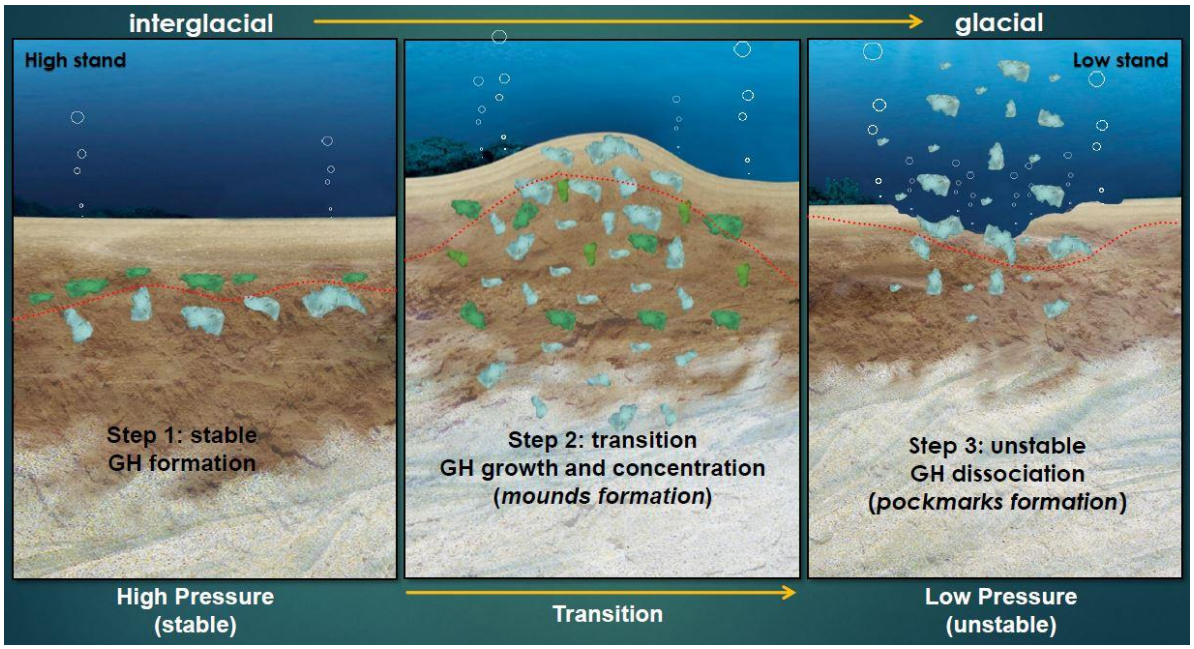

Figure 6.24. Model showing the 3 different contexts. From left to right, formation of gas hydrates and mounds, and collapse of surface-type methane hydrate accumulation. The red dashed line represents the Sulfate Methane Transition (SMT). Green sediments represent carbonates while grayish white sediments near them represent hydrates (**Modified from Matsumoto et al. (2009) in Freire, 2017**).

According to Matsumoto et al. (2009), during the LGM, due to pressure release caused by sea level fall, methane hydrate around the depth of BGHS was dissociated, generating large volumes of methane gas, which in turn migrated upward to the seafloor because there was insufficient free water to form hydrate in clay-silt stones. Hence, a large-scale release of methane would cause a large depression and deposition of black-dark layers (Matsumoto et al., 2009).

This hypothesis was also supported by the geochemical analysis of MDCAs (Watanabe et al., 2008; Sanno, 2008; Suzuki, 2010 in Matsumoto et al. 2017a). Matsumoto et al. (2017a) reported that the age of MDCAs, centered at around 20 ka, seems to indicate that the eustatic sea level fall toward the LGM caused massive dissociation of gas hydrates and consequent methane migration on and around active mounds due to shoal up of BGHS by at least 10 meters; accelerated Anaerobic Oxidation of Methane (AOM) and carbonate precipitation at Sulfate Methane Transition (SMT); formation of gas hydrates in shallow subsurface where the ample free waters are available for hydrate formation. The age of MDCAs was determined by U-Th radioactive disequilibrium methods at National Taiwan University.

Thus, by zooming in on the pockmark, we can see the possible sediments filled with hydrates, in the purple spots (Figure 6.25), where the seismic attenuation is less. Note that the color scale has been modified to highlight only those possible regions. Thereby, according to previous works, this pockmark of the US-19 seismic profile should be the result of the explosion of a mound after a dissociation of the gas hydrates due to the reduction of the pressure of the water layer during the LGM.

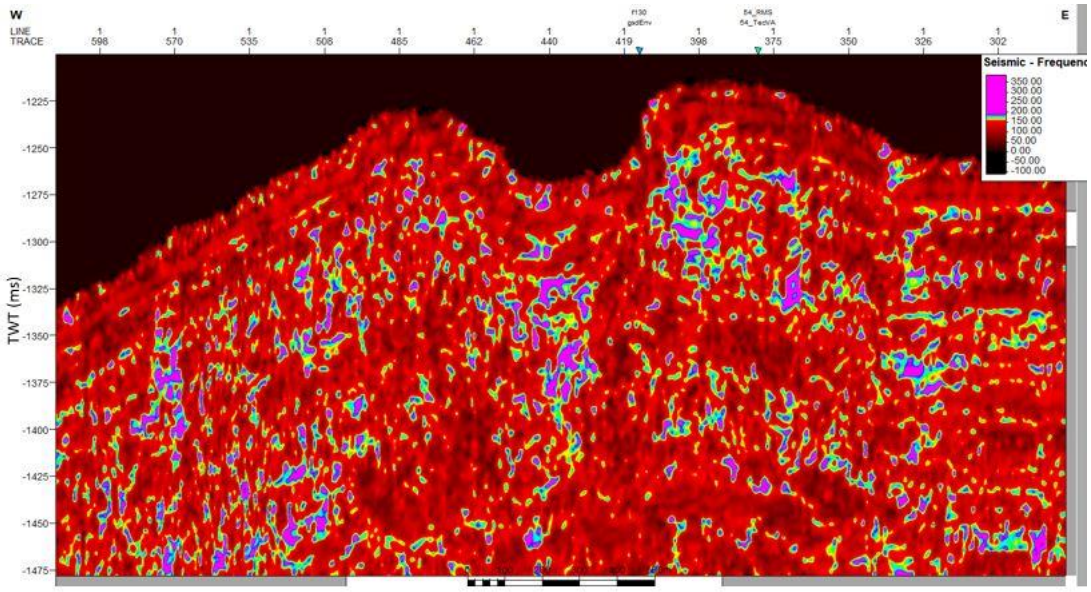

Figure 6.25. Pockmark and Gas hydrates (purple spots) of US-19 seismic profile with instantaneous frequency attribute. The purple spots represent frequency values above 200 Hz. While red spots mean frequency values below 150 Hz.

Therefore, the instantaneous frequency seismic attribute is fundamental to highlight the free gas zone. In this way, it also served to highlight the true BSR, which seismically corresponds to the BGHSZ, due to the fact that below the true BSR there should be a greater seismic attenuation (free gas zone) contrasting with a lower seismic attenuation over it (sediments filled with hydrates). Then, applying the instantaneous frequency attribute was crucial to distinguish the true BSR (close to H-III reflector) from the H-II reflector.

6.2 Final Results

Therefore, each seismic attribute played a fundamental role in identifying the BSR of each seismic section. Thus, the identification of the BSR was made by analyzing each result of the application of the six seismic attributes. Then, making a comparison between the results, for each seismic section, the BSR seismic horizon was interpreted (Figure 6.26). In total, twenty eight horizons interpreted (fourteen from the NT07-20 Expedition seismic sections and fourteen from the NT08-20 Expedition). The results of the application of the six seismic attributes and the respective interpretations of the BSRs are found in the Appendix.

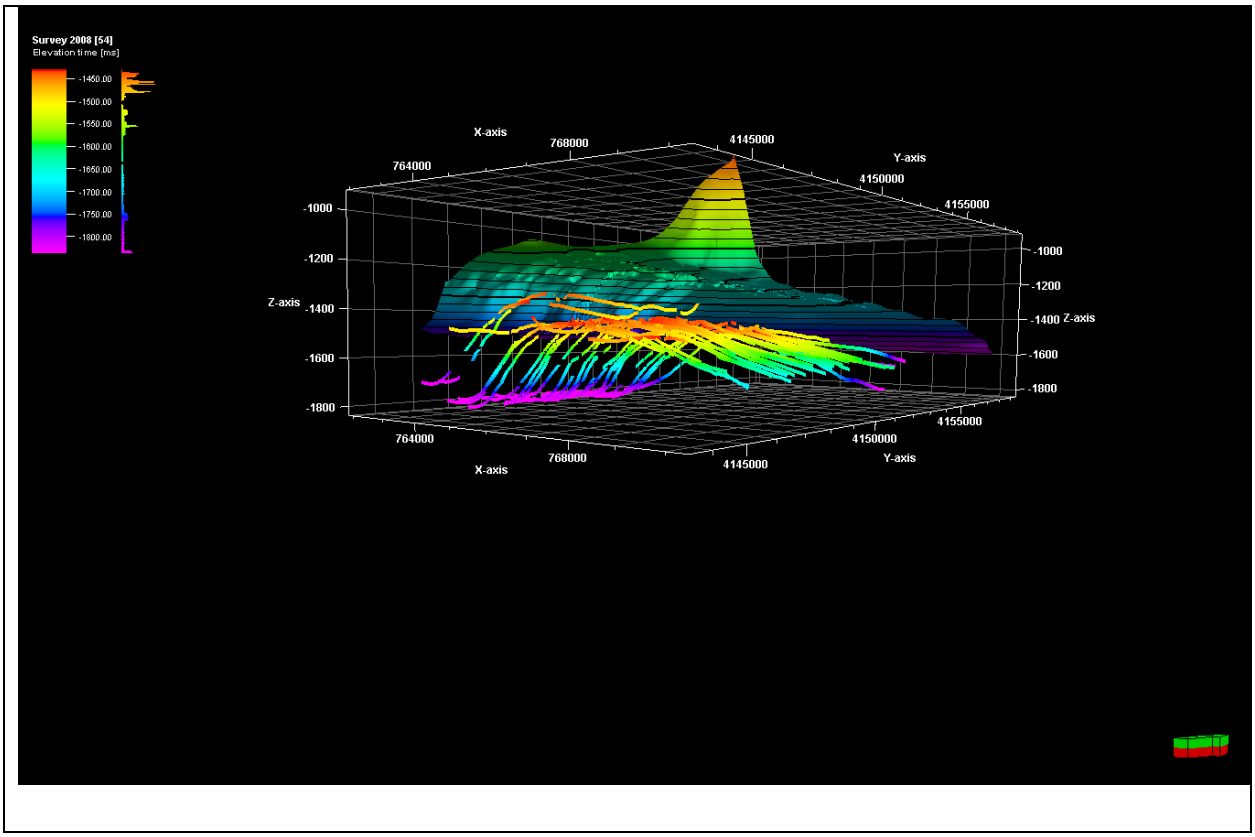

Figure 6.26. Interpreted BSRs for each seismic section below the seafloor grid. The data is in milliseconds. The color scale refers to the Elevation time (ms) of the BSRs. Thus, the longer the time, the greater the depth. Red colors correspond to shallow areas (close to 1.4 s TWT), while purple colors represent deeper zones (1.8 s TWT). "Survey 2008 [54]" to the right of the color scale shows the values of elevation time (ms) of the BSR from US-54 (SP.1(ut-54) from NT08-09 Expedition).

Thus, making a comparison between the initial (Figure 5.7) and final interpretation we have Figure 6.27. Note that the application of seismic attributes was essential for a better

interpretation (Figure 6.27B), because it enhanced the BSR, making them more visibly and continuous. Whereas, in the scenario of the initial interpretation (Figure 6.27A), BSRs in the original seismic section are weak, discontinuous and patchy.

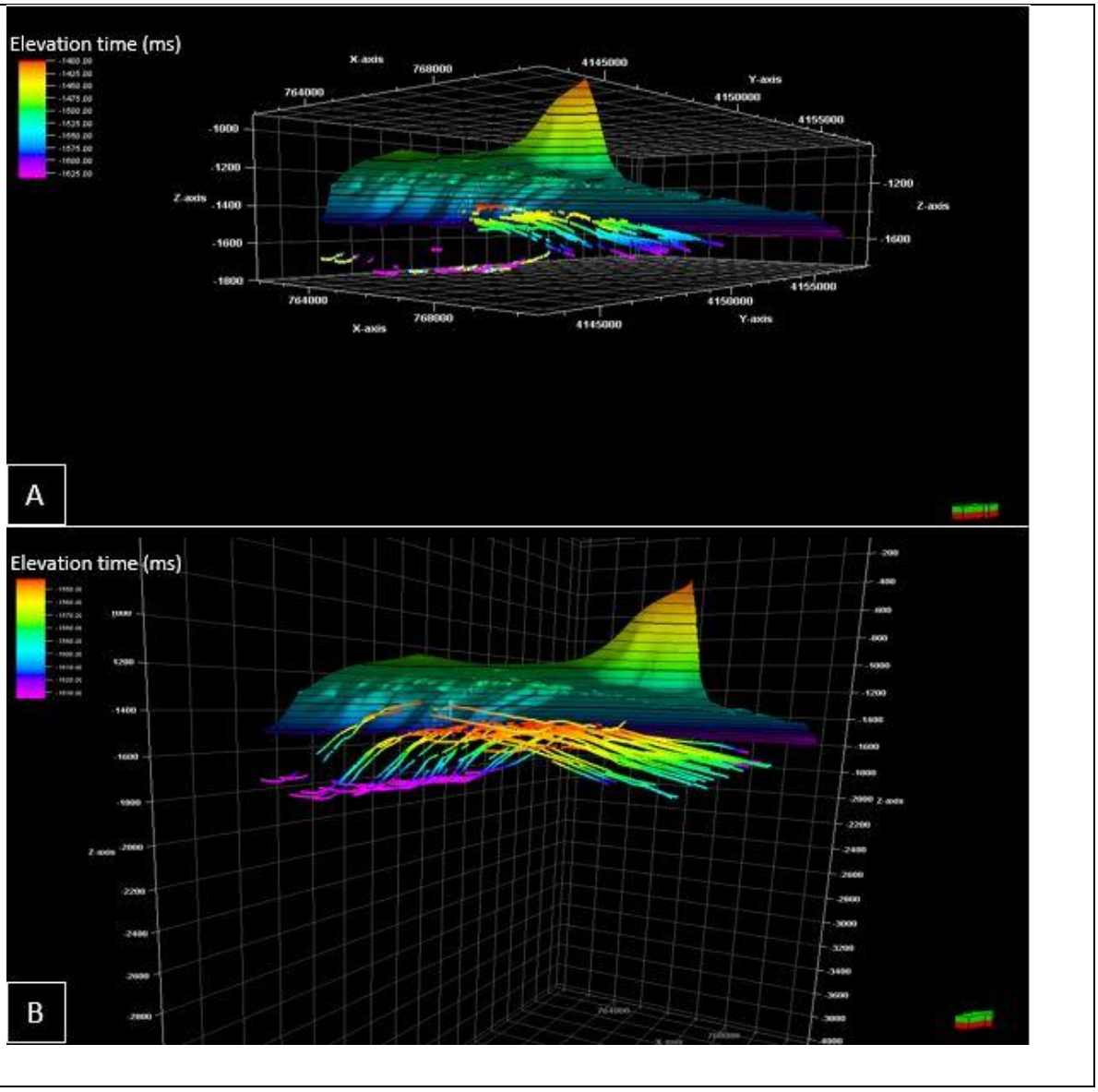

Figure 6.27. Interpreted BSRs for each seismic section below the seafloor grid (A) initial interpretation; (B) final interpretation. Both data are in Two-Way Travel time (ms). The color scale refers to the Elevation time (ms) of the BSRs.

Thus, evaluating the final result obtained (Figure 6.28), the BSRs in gas chimney ranges from 1.4 s to 1.5 s TWT, approximately 0.2 s TWT below seafloor. While in surrounding sediments ranges from 1.6 s to 1.8 s TWT, about 0.4 TWT bsf.

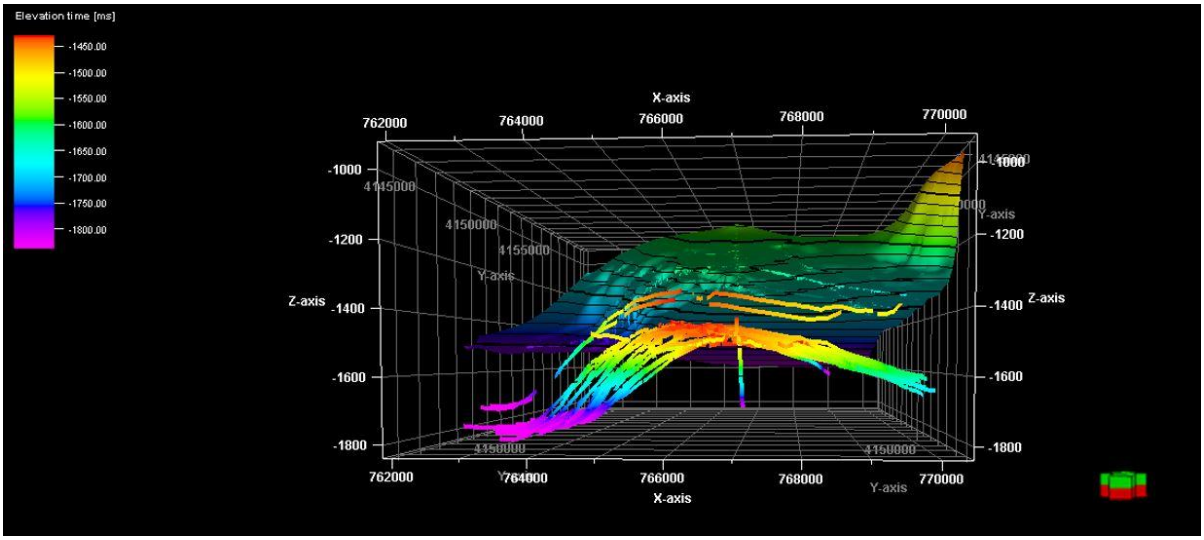

Figure 6.28. Interpreted BSRs for each seismic section below the seafloor grid. The scale color corresponds to the elevation time in Two-Way Travel (milliseconds) of the BSRs.

Furthermore, while identifying BSRs in these seismic profiles, as in previous studies (e.g., Freire et al., 2010; Freire et al., 2011) flat spots were identified in certain seismic profiles below the BSR, which indicates gas with high water saturation. Then, this seismic reflector was also interpreted (Figure 6.29), approximately 1.6 s TWT (about 0.2 s TWT bsf). This from an economic point of view is bad because it reduces the viability of gas production from natural gas hydrates (Walsh et al., 2009). Nevertheless, from a scientific point of view it is good, because the flat spot served as a seismic response that the geophysical method used really works.

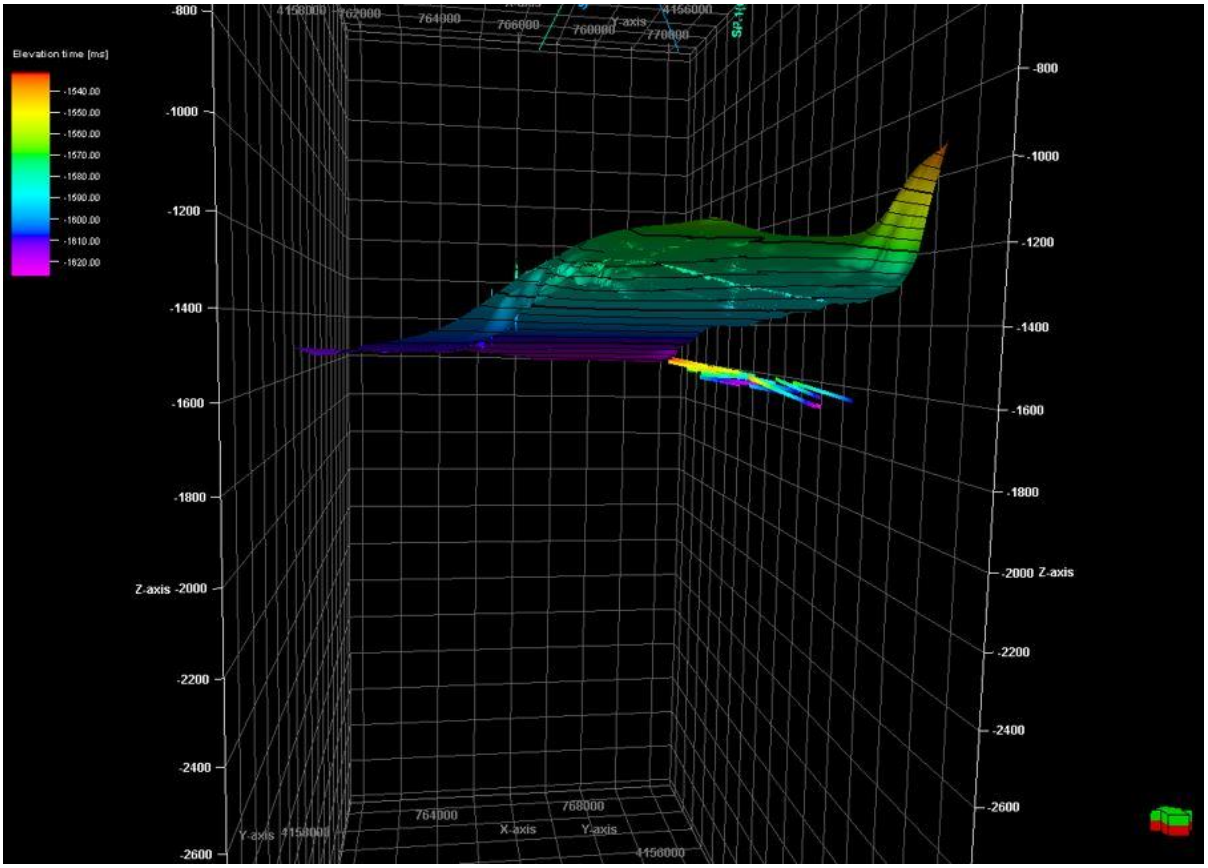

Figure 6.29. Flat Spot horizon interpreted below seabed grid. The data is in milliseconds. The color scale refers to the Elevation time (ms) of the flat spots. Red colors mean shallower zones (shorter time TWT, less than 1540 ms TWT), while purple color mean deeper areas (close to 1620 ms TWT).

However, the focus of this work was the application of seismic attributes to enhance BSRs. Even though the seismic attributes algorithms were created to work with multi-channel data and the data used in this work is single-channel, so its use is impaired by the low multiplicity of the signal, good results were obtained and the objective of this work was achieved. Analyzing the interpreted BSRs, notice the shallow areas in red (Figure 6.28 and Figure 6.30). These zones are associated with gas chimneys, where the upward migration of hydrocarbon gases develops gas hydrates accumulations, and that is also associated with occurrence of mounds and pockmarks, as noted in previous work (e.g., Matsumoto et al. 2009, 2011a, 2017a.b; Freire et al., 2011). In Figure 6.30 this is more visible, note that the central, shallower part (red color of the BSRs, close to 1.4 s TWT) coincides with the zones of occurrence of mound and depression visible in the seafloor grid, in green (close to 1.2 s TWT).

In addition, the frequency attributes showed that this region something unusual occurs, which is the presence of free gas above the BSR. This is evidenced by the anomalously low velocities (1200-1300 m/s) found from velocity analysis of 3D seismic data reported by Saeki et al. (2009 in Matsumoto et al. 2011b) and also reported by the Logging-while-drilling (LWD) profiles from Matsumoto et al. (2017a,b), which imply the existence of free gas in shallow sediments, within the gas hydrate stability zone.

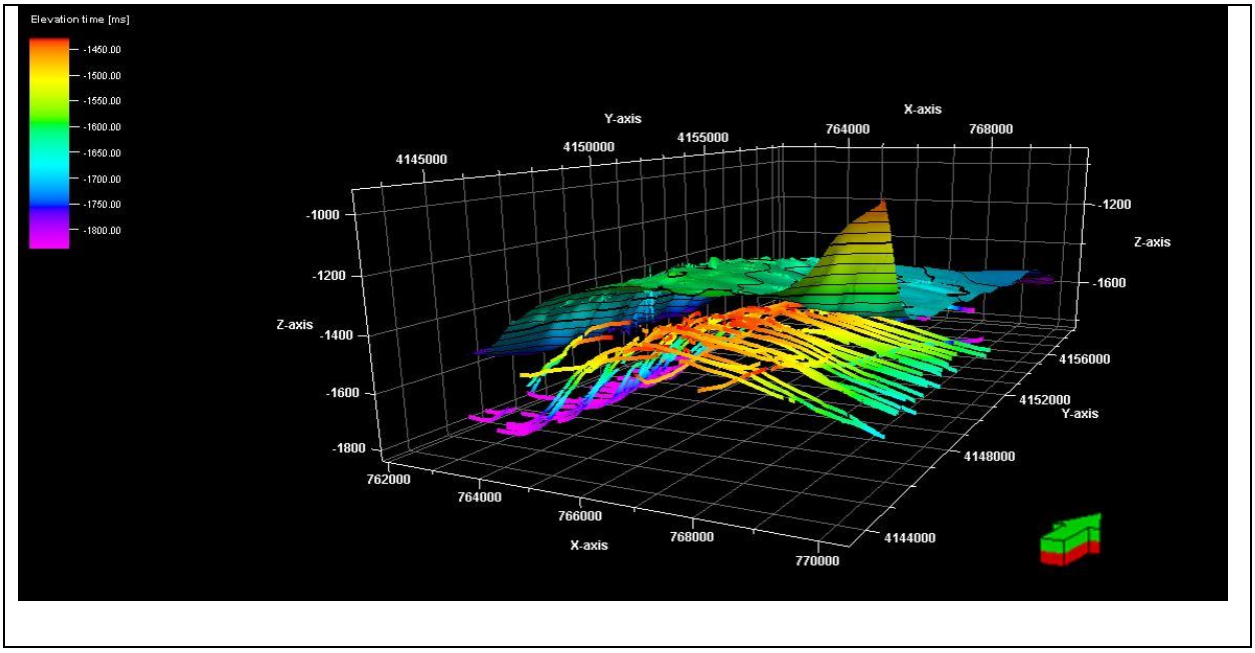

Figure 6.30. All BSRs interpreted below the seabed grid. Data is in TWT milliseconds. The color scale refers to the Elevation time (ms) TWT of the BSRs.

Chapter 7 CONCLUSION

This work developed a methodology for the interpretation of the Base of the Gas Hydrate Stability Zone, in the Umitaka Spur gas hydrate province, Joetsu Basin, Japan, which constituted the application of seismic attributes to enhance Bottom Simulating Reflectors. Due to the local geological complexity, such as gas chimneys that generate acoustic transparency of the signal and discontinuities of the BSRs, in addition to the presence of more than one reflector with reverse polarity that mimics the seafloor reflector in the shallow areas of the Haizume Formation, it is not trivial to make this interpretation without an aid of these seismic attributes. So, there is a need to apply seismic attributes to facilitate the visualization of BSRs and free gas zones associated with these unconventional reservoirs in the seismic profiles.

Thus, in this work, 6 seismic attributes were applied to twenty eight single-channel 2D seismic profiles provided by JAMSTEC, acquired in 2007 (NT07-20 Expedition) and 2008 (NT08-09 Expedition). Respectively, two attributes that measure amplitude (Envelope and RMS), two of geological assignment (AVT and RAI) and two that measure the frequency of the seismic signal (Instantaneous frequency and Spectral Decomposition) were used.

The Envelope seismic attribute served to highlight the regions of greatest amplitude energy. However, it proved ineffective to distinguish a true BSR from another reflector with high impedance contrast.

Amplitude RMS generated a result similar to the application of the envelope, but this attribute was more used in order to be able to apply the Amplitude Volume Technique. Both the AVT seismic attribute and the Relative Acoustic Impedance served to highlight the impedance contrasts of the layers and thus the discontinuities, allowing a better visualization of the sections intercepted by faults. The RAI attribute made reflectors stronger, reducing the effects of acoustic transparency of free gas zones.

Ultimately, the analysis of the frequency domain of the seismic data was made. Thus, the Instantaneous Frequency and Spectral Decomposition seismic attributes were applied to investigate the seismic attenuation of the data. Thus, because the higher frequencies tend to be attenuated more quickly than the low ones, and because the presence of free gas attenuates the seismic signal, these attributes highlighted the free gas zone strongly present in Umitaka Spur,

where the lower frequencies are more dominant in seismic profiles. In this way, both attributes served to highlight the BSR, which comparatively is like a border that separates a zone of greater attenuation (free gas zone below) from a milder seismic attenuation (gas hydrates in sediments above). Thus, these seismic attributes were relevant to reduce the ambiguities of the attributes that measure only amplitude. For instance, applying the instantaneous frequency attribute was crucial to distinguish the true BSR (close to H-III reflector) from H-II reflector, as it showed that the current zone of stability of gas hydrates is close to the horizon H-III, where there is currently a free gas zone just below. In addition, these attributes also reaffirmed something out of the ordinary that occurs in this region, which is the presence of free gas above the BSR.

Therefore, seismic attributes play a fundamental role in the analysis of subsurface layers. They reduce the uncertainties inherent to Geophysics, giving the interpreter greater security. Thus, through the bibliographic references of the region and after the application of these attributes, it can be reaffirmed that the Base of the Gas Hydrates Stability Zone really lies at approximately 115 mbsf and there is an unusual presence of free gas within the gas hydrate stability zone, as previously reported.

REFERENCES

Aguiar, L. da F. (2020). Identification of Bottom Simulating Reflectors in the Foz do Amazonas Basin, Northern Brazil, using seismic amplitudes, seismic attributes and frequency analysis. 61 p. Dissertação (Mestrado em Geologia e Geofísica Marinha) – Programa de Pós-Graduação em Dinâmica dos Oceanos e da Terra, Universidade Federal Fluminense, Niterói.

Aguiar, L., Freire, A., Santos, L., Dominguez, A., Neves, E., Silva, C., & Santos, M. (2019). Analysis of seismic attributes to recognize bottom simulating reflectors in the foz do amazonas basin, Northern Brazil. *Revista Brasileira de Geofisica*, *37*(1). https://doi.org/10.22564/rbgf.v37i1.1988

Anstey, N. (2005). Attributes in color: the early years. *CSEG Recorder*, *30*(3), 12-15.

Aoyama, C., Matsumoto, R. (2009). Acoustic Surveys of Methane Plumes by Quantitative Echo Sounder in Japan Sea and the Estimate of the Seeping Amount of the Methane Hydrate Bubbles. *Chigaku Zasshi (Jounal of Geography)*, *118*(1), 156–174. https://doi.org/10.5026/jgeography.118.156

Ashi, J., Tokuyama, H., (1998). Diffusive cold seepage at the Tokai thrust of the eastern Nankai accretionary prism. *International Symposium on Japan-France KAIKO-Tokai Project*, Tokyo, p. 48.

Balch, A. H. (1971). Color sonagrams: A new dimension in seismic data interpretation. *Geophysics*, *36*(6), 1074-1098.

Barnes, A. E. (2001). Seismic attributes in your facies. *CSEG recorder*, *26*(7), 41-47.

Barnes, A. E. (2016). Handbook of Poststack Seismic Attributes. In *Handbook of Poststack Seismic Attributes*. https://doi.org/10.1190/1.9781560803324

Barros, C. S. (2009). Análise de Atributos Sísmicos Para Caracterização de Hidratos de Gás no Cone do Rio Grande. 62 p. Trabalho de Conclusão de Curso (Bacharelado em Geofísica) – LAGEMAR. Universidade Federal Fluminense – Niterói, RJ.

Bernard, B. B., Brooks, J. M., & Sackett, W. M. (1976). Natural gas seepage in the Gulf of Mexico. *Earth and Planetary Science Letters*, *31*(1), 48-54.

Birchwood, R., Noeth, S., & Jones, E. (2008). Safe drilling in gas hydrate prone sediments: findings from the 2005 drilling campaign of the Gulf of Mexico gas hydrates Joint Industry Project (JIP). *Natural Gas & Oil*, *304*, 285-4541.

Buffett, B. A. (2000). Clathrate hydrates. *Annual Review of Earth and Planetary Sciences*, *28*(1), 477-507.

Bulhões, É. M. (1999, August). Técnica "VOLUME DE AMPLITUDE" para mapeamento de feições estruturais. In *6th International Congress of the Brazilian Geophysical Society* (pp. cp-215). European Association of Geoscientists & Engineers.

Bulhões, É. M., & de Amorim, W. N. (2005, September). Princípio da SismoCamada Elementar e sua aplicação à Técnica Volume de Amplitudes (tecVA). In *9th International Congress of the Brazilian Geophysical Society* (pp. cp-160). European Association of Geoscientists & Engineers.

Chastain, B. K., & Chevrier, V. (2007). Methane clathrate hydrates as a potential source for martian atmospheric methane. *Planetary and Space Science*, *55*(10), 1246-1256.

Chen, Q., & Sidney, S. (1997). Seismic attribute technology for reservoir forecasting and monitoring. *The Leading Edge*, *16*(5), 445-448.

Chong, Z. R., Yang, S. H. B., Babu, P., Linga, P., & Li, X. S. (2016). Review of natural gas hydrates as an energy resource: Prospects and challenges. *Applied energy*, *162*, 1633-1652.

Chopra, S., & Marfurt, K. J. (2005). Seismic attributes—A historical perspective. *Geophysics*, *70*(5), 3SO-28SO.

Chopra, S., & Marfurt, K. J. (2007). *Seismic attributes for prospect identification and reservoir characterization*. Society of Exploration Geophysicists and European Association of Geoscientists and Engineers.

Chopra, S., Castagna, J., & Xu, Y. (2009). Relative acoustic impedance application for thin-bed reflectivity inversion. In *SEG Technical Program Expanded Abstracts 2009* (pp. 3554-3558). Society of Exploration Geophysicists.

Chun, J. H., Ryu, B. J., Son, B. K., Kim, J. H., Lee, J. Y., Bahk, J. J., ... & Nehza, O. (2011). Sediment mounds and other sedimentary features related to hydrate occurrences in a columnar seismic blanking zone of the Ulleung Basin, East Sea, Korea. *Marine and Petroleum Geology*, *28*(10), 1787-1800.

Claerbout, J. F. (1971). Toward a unified theory of reflector mapping. *Geophysics*, *36*(3), 467-481.

Clennell, M. B. (2000). Hidrato de Gás Submarino: Natureza, Ocorrência e Perspectivas Para Exploração na Margem Continental Brasileira. *Revista Brasileira de Geofísica*, *18*(3)

Costa, D. F. B. D., Santos, W. H. D., Bergamaschi, S., & Pereira, E. (2016). Analysis of the geometry of diabase sills of the Serra Geral magmatism, by 2D seismic interpretation, in Guareí region, São Paulo, Paraná basin, Brazil. *Brazilian Journal of Geology*, *46*(4), 605-615.

Dallimore, S. R.; Hyndman, R. D. Natural Gas Hydrate Studies in Canada, 2001. vol. 26, n. 5. Available online at. https://csegrecorder.com/articles/view/natural-gas-hydrate-studies-in-canada. (accessed 07.15.20).

de Matos, M. C., Penna, R., Johann, P., & Marfurt, K. (2014). Relative acoustic impedance from wavelet transform. *Interpretation*, *2*(1), SA107-SA118.

de Oliveira, O. M. V. (2009). Decomposição espectral de dados sísmicos usando a transformada de wavelet: aplicação no estudo das acumulações de hidratos de gás na bacia de Pelotas. 2009. 60 p. Dissertação (Mestrado em Engenharia de Reservatório e de Exploração de Petróleo) – Universidade Estadual do Norte Fluminense, Macaé, RJ.

Dvorkin, J., Mavko, G., & Nur, A. (1991). The effect of cementation on the elastic properties of granular material. *Mechanics of materials*, *12*(3-4), 207-217.

Ebinuma, T. (1993). *U.S. Patent No. 5,261,490*. Washington, DC: U.S. Patent and Trademark Office.

Emujakporue, G. O., & Enyenihi, E. E. (2020). Identification of seismic attributes for hydrocarbon prospecting of Akos field, Niger Delta, Nigeria. *SN Applied Sciences*, *2*, 1-11.

Etiope, G. (2015). Natural gas seepage. *The Earth's Hydrocarbon Degassing, Springer*, *640*.

Etiope, G., Schoell, M., & Hosgörmez, H. (2011). Abiotic methane flux from the Chimaera seep and Tekirova ophiolites (Turkey): understanding gas exhalation from low temperature serpentinization and implications for Mars. *Earth and Planetary Science Letters*, *310*(1-2), 96-104.

Ferro, R.P. (2018). Caracterização geofísica para identificação de oportunidades exploratórias na porção centro-sul da bacia do Espírito Santo, Sudeste do Brasil. 150 p. Dissertação (Mestrado em Geologia e Geofísica Marinha) – Programa de Pós-Graduação em Dinâmica dos Oceanos e da Terra, Universidade Federal Fluminense, Niterói.

Foucher, J. P., Nouzé, H., & Henry, P. (2002). Observation and tentative interpretation of a double BSR on the Nankai slope. *Marine Geology*, *187*(1-2), 161-175.

Freire, A. (2017). Gas hydrates and the Gas Seeps Phenomenon. In *ALAGO WORKSHOP*.

Freire, A. F. M. (2010). An integrated study on the gas hydrate area of Joetsu Basin, eastern margin of Japan Sea, using geophysical, geological and geochemical data. *The University of Tokyo, Graduate School of Frontier Sciences*.

Freire, A. F. M., Matsumoto, R., & Akiba, F. (2012). Geochemical analysis as a complementary tool to estimate the uplift of sediments caused by shallow gas hydrates in mounds at the seafloor of Joetsu Basin, eastern margin of the Japan Sea. *Journal of Geological Research*, *2012*.

Freire, A. F. M., Matsumoto, R., & Santos, L. A. (2011). Structural-stratigraphic control on the Umitaka Spur gas hydrates of Joetsu Basin in the eastern margin of Japan Sea. *Marine and Petroleum Geology*, *28*(10), 1967-1978.

Freire, A. F. M., Sugai, T., & Matsumoto, R. (2009). O uso de cinzas vulcânicas para correlações estratigráficas na margem leste do Mar do Japão. *Boletim de Geociências da Petrobras*, *18*(1), 97-121.

Freire, A. F. M., Sugai, T., & Matsumoto, R. (2009). O uso de cinzas vulcânicas para correlações estratigráficas na margem leste do Mar do Japão. *Boletim de Geociências da Petrobras*, *18*(1), 97-121.

G. Etiope Home Page, 2016. Abiotic Gas. Available online at. https://sites.google.com/a/ingv.it/getiope/home/abiotic-gas (accessed 07.28.20.).

Goldberg, D. S., Collett, T. S., & Hyndman, R. D. (2000). Ground truth: in-situ properties of hydrate. In *Natural Gas Hydrate* (pp. 295-310). Springer, Dordrecht.

Handa, Y. P. (1986). Calorimetric determinations of the compositions, enthalpies of dissociation, and heat capacities in the range 85 to 270 K for clathrate hydrates of xenon and krypton. *The Journal of Chemical Thermodynamics*, *18*(9), 891-902.

Helgerud, M. B., Dvorkin, J., Nur, A., Sakai, A., & Collett, T. (1999). Elastic-wave velocity in marine sediments with gas hydrates: Effective medium modeling. *Geophysical Research Letters*, *26*(13), 2021-2024.

Henry, P., Thomas, M., & Clennell, M. B. (1999). Formation of natural gas hydrates in marine sediments: 2. Thermodynamic calculations of stability conditions in porous sediments. *Journal of Geophysical Research: Solid Earth*, *104*(B10), 23005-23022.

Hirai, A., Okada, S., Wakamatsuya, S., Miyamoto, Y., & Hachinohe, K. (1995). Organic geochemical relationship between pooled oils and distribution of their source rocks in the Niigata basin, Japan. *Sekiyu Gijutsu Kyokaishi*, *60*(1), 87-97.

Hiruta, A., Klügel, A., & Matsumoto, R. (2016). Increase in methane flux and dissociation of iron and manganese oxides recorded in a methane-derived carbonate nodule in the eastern margin of the Sea of Japan. *GeoResJ*, *9*, 104-116.

Holder, G. D., Kamath, V. A., & Godbole, S. P. (1984). The potential of natural gas hydrates as an energy resource. *Annual Review of Energy*, *9*(1), 427-445.

Honório, B. C. Z., de Matos, M. C., & Vidal, A. C. (2017). Progress on empirical mode decomposition-based techniques and its impacts on seismic attribute analysis. *Interpretation*, *5*(1), SC17-SC28.

Hornbach, M. J., Holbrook, W. S., Gorman, A. R., Hackwith, K. L., Lizarralde, D., & Pecher, I. (2003). Direct seismic detection of methane hydrate on the Blake Ridge. *Geophysics*, *68*(1), 92-100.

Hu, R., Bloom, A. A., Gao, P., Miller, C. E., & Yung, Y. L. (2016). Hypotheses for near-surface exchange of methane on Mars. *Astrobiology*, *16*(7), 539-550.

Imamura, T. (2000). Interpretation and assessment of thrust structures: Prediction using information from mechanical properties of rocks, stress distributions and kinematic picture:(Based on the interpretation of the Niigata basin, Japan). *Sekiyu Gijutsu Kyokaishi*, *65*(1), 28-39.

JAMSTEC. < http://www.jamstec.go.jp/jir/infolib/meta_pub/id_NT07-20_leg1-2_all> (accessed 02.13.2019).

JAMSTEC. <http://www.godac.jamstec.go.jp/catalog/data/doc_catalog/media/NT08-09_leg1-2_all.pdf> (accessed 02.13.2019).

Kakuwa, Y., Nakajima, T., Kumon, F., Matsumoto, R., Nakamura, Y., Ohi, T., & Machiyama, H. (2013). Description of sediments recovered during the cruise of MD179 in the Japan Sea, Umitaka Spur and its surrounding area, off Joetsu. *Journal of the Japanese Association of Petroleum Technology*, *78*, 97-103.

Kearey, P., Brooks, M., & Hill, I. (2002). An Introduction to Geophysical Exploration. –Blackwell.

Kennett, J. P., Cannariato, K. G., Hendy, I. L., & Behl, R. J. (2003). Methane hydrates in quaternary climate change: the clathrate gun hypothesi. *Methane Hydrates in Quaternary Climate Change: The Clathrate Gun Hypothesis*, *54*, 1-9.

Ketzer, J. M., Augustin, A., Rodrigues, L. F., Oliveira, R., Praeg, D., Pivel, M. Reis, A., Silva, C., & Leonel, B. (2018). Gas seeps and gas hydrates in the Amazon deep-sea fan. *Geo-Marine Letters*, *38*(5), 429-438.

Ketzer, M., Praeg, D., Pivel, M. A., Augustin, A. H., Rodrigues, L. F., Viana, A. R., & Cupertino, J. A. (2019). Gas seeps at the edge of the gas hydrate stability zone on Brazil's continental margin. *Geosciences*, *9*(5), 193.

Ketzer, M., Praeg, D., Rodrigues, L. F., Augustin, A., Pivel, M. A., Rahmati-Abkenar, M., ... & Cupertino, J. A. (2020). Gas hydrate dissociation linked to contemporary ocean warming in the southern hemisphere. *Nature communications*, *11*(1), 1-9.

Komai, T., Kang, S. P., Yoon, J. H., Yamamoto, Y., Kawamura, T., & Ohtake, M. (2004). In situ Raman spectroscopy investigation of the dissociation of methane hydrate at temperatures just below the ice point. *The Journal of Physical Chemistry B*, *108*(23), 8062-8068.

Kvenvolden, K. A. (1993). Gas hydrates—geological perspective and global change. *Reviews of geophysics*, *31*(2), 173-187.

Kvenvolden, K. A. (1998). A primer on the geological occurrence of gas hydrate. *Geological Society, London, Special Publications*, *137*(1), 9-30.

Lallemand, S. E., Glaçon, G., Lauriat-Rage, A., Fiala-Médioni, A., Cadet, J. P., Beck, C., Sibuet, M. Iiyama, J.T., Sakai, H., & Taira, A. (1992). Seafloor manifestations of fluid seepage at the top of a 2000-metre-deep ridge in the eastern Nankai accretionary wedge: Long-lived venting and tectonic implications. *Earth and planetary science letters*, *109*(3-4), 333-346.

Laughlin, K., Garossino, P., & Partyka, G. (2002). Spectral Decomposition applied to 3D. *AAPG Explorer*, *23*(5), 28-31.

Ledley, T. S., Sundquist, E. T., Schwartz, S. E., Hall, D. K., Fellows, J. D., & Killeen, T. L. (1999). Climate change and greenhouse gases. *Eos, Transactions American Geophysical Union*, *80*(39), 453-458.

Lin, T., Zhang, B., Guo, S., Marfurt, K., Wan, Z., & Guo, Y. (2013). Spectral decomposition of time-versus depth-migrated data. In *SEG Technical Program Expanded Abstracts 2013* (pp. 1384-1388). Society of Exploration Geophysicists.

Makogon, Y. F., Holditch, S. A., & Makogon, T. Y. (2007). Natural gas-hydrates—A potential energy source for the 21st Century. *Journal of petroleum science and engineering*, *56*(1-3), 14-31.

Matsumoto R., Okuda, Y., Hiruta, A. and others (2009), "Formation and collapse of gas hydrate deposits in high methane flux area of the Joetsu basin, eastern margin of Japan Sea", Journal of Geography (in Japanese)

Matsumoto, R., Hiromatsu, M., & Sato, M. (2011, July). Fluid flow and Evolution of gas hydrate mounds of Joetsu Basin, Eastern Margin of Japan Sea: Constraints from high-resolution

geophysical survey by AUV. In *Proceedings of the 7th International conference on gas hydrate. Edinburgh, July* (pp. 17-21).

Matsumoto, R., Kakuwa, Y., Snyder, G., Tanahashi, M., Hiruta, A., Oi, T.,Ohkawa, S., Tomaru, H., Numanami, H., Chen, C.,& Morita, S.(2017). Occurrence and Origin of thick deposits of massive gas hydrates, eastern margin of the Sea of Japan Sea". *Proceedings of the 9th ICGH*, Denver, United States of America, 2017

Matsumoto, R., Okuda, Y., & Aoyama, C. (2005, June). Methane plumes over a marine gas hydrate system in the eastern margin of Japan Sea: A possible mechanism for the transportation of subsurface methane to shallow waters. In *Proceedings of the 5th International Conference on Gas Hydrates, Trondheim, Norway* (Vol. 3, pp. 749-754).

Matsumoto, R., Ryu, B. J., Lee, S. R., Lin, S., Wu, S., Sain, K., Pecher, I., & Riedel, M. (2011). Occurrence and exploration of gas hydrate in the marginal seas and continental margin of the Asia and Oceania region. *Marine and Petroleum Geology*, *28*(10), 1751–1767. https://doi.org/10.1016/j.marpetgeo.2011.09.009

Matsumoto, R., Tanahashi, M., Kakuwa, Y., Snyder, G., Ohkawa, S., Tomaru, H., & Morita, S. (2017). Recovery of thick deposits of massive gas hydrates from gas chimney structures, eastern margin of Japan Sea: Japan Sea Shallow Gas Hydrate Project. *Fire in the Ice*, *17*(1), 1-6.

Miller, D. J., Ketzer, J. M., Viana, A. R., Kowsmann, R. O., Freire, A. F. M., Oreiro, S. G., Augustin. A., H. and others, (2015). Natural gas hydrates in the Rio Grande Cone (Brazil): A new province in the western South Atlantic. *Marine and Petroleum Geology*, *67*, 187-196.

Muramoto, K. (2007). A petroleum system in the deep water of the Sado Nanseioki area in the Japan Sea based on the results of the MITI" Sadooki Nanai" Seismic Survey and the METI" Sado Nanseioki" Wells. *J. Jpn. Assoc. Petroleum Technol.*, *72*, 618-627.

Nakajima, T., Kakuwa, Y., Yasudomi, Y., Itaki, T., Motoyama, I., Tomiyama, T., & Tanahashi, M. (2014). Formation of pockmarks and submarine canyons associated with dissociation of gas hydrates on the Joetsu Knoll, eastern margin of the Sea of Japan. *Journal of Asian Earth Sciences*, *90*, 228-242.

Nakatani, T., Yoshida, H., Hyakudome, T., Ishibashi, S., Sugesawa, M., Ota, Y., & Machiyama, H. (2013, September). Dives of cruising-AUV "JINBEI" to methane hydrate area on Joetsu knoll and Umitaka Spur. In *2013 OCEANS-San Diego* (pp. 1-5). IEEE.

NASA/JPL-Caltech/SAM-GSFC/Univ. of Michigan, 2014. Possible Methane Sources and Sinks. Available online at. https://www.jpl.nasa.gov/spaceimages/details.php?id=pia19088 (accessed 07.29.20).

Nguyen, B. T. T., Kido, M., Okawa, N., Fu, H., Kakizaki, S., & Imahori, S. (2016). Compaction of smectite-rich mudstone and its influence on pore pressure in the deepwater Joetsu Basin, Sea of Japan. *Marine and Petroleum Geology*, *78*, 848-869.

Ohgaki, K., & Inoue, Y. (1995). A proposal for gas storage on the bottom of the ocean, using gas hydrates. *Oceanographic Literature Review*, *6*(42), 515.

Okamura, Y., Watanabe, M., Morijiri, R., & Satoh, M. (1995). Rifting and basin inversion in the eastern margin of the Japan Sea. *Island Arc*, *4*(3), 166-181.

Okawa, N., Imahori, S., Kakizaki, S., Kido, M., Yamashina, O. and others (2016) Geological summary of "METI Joetsu Kaikyu (JX*)". Journal of the Japanese Association for Petroleum Technology, 81*(3), p. 243-255.

Okui, A., Kaneko, M., Nakanishi, S., Monzawa, N., & Yamamoto, H. (2008). An integrated approach to understanding the petroleum system of a frontier deep-water area, offshore Japan. *Petroleum Geoscience*, *14*(3), 223-233.

Oreiro, S. G., Cupertino, J. A., Szatmari, P., & Thomaz Filho, A. (2008). Influence of pre-salt alignments in post-Aptian magmatism in the Cabo Frio High and its surroundings, Santos and Campos basins, SE Brazil: an example of non-plume-related magmatism. *Journal of South American Earth Sciences*, *25*(1), 116-131.

Otofuji, Y. I., Matsuda, T., & Nohda, S. (1985). Paleomagnetic evidence for the Miocene counter-clockwise rotation of Northeast Japan—rifting process of the Japan Arc. *Earth and Planetary Science Letters*, *75*(2-3), 265-277.

Oze, C., & Sharma, M. (2005). Have olivine, will gas: serpentinization and the abiogenic production of methane on Mars. *Geophysical research letters*, *32*(10).

Partyka, G., Gridley, J., & Lopez, J. (1999). Interpretational applications of spectral decomposition in reservoir characterization. *The leading edge*, *18*(3), 353-360.

Paull, C. K., Ussler III, W., & Borowski, W. S. (1993). *Sources of biogenic methane to form marine gas hydrates: In situ production or upward migration?* (No. DOE/ER/61010-T12). North Carolina Univ., Chapel Hill, NC (United States).

Reynolds, J. M. (2011). *An introduction to applied and environmental geophysics*. John Wiley & Sons.

Saeki, T., Hayashi, M., Furukawa, T., Inamori, T., & Asakawa, E. (2009). 3D seismic velocity structure below mounds and pockmarks in the deep water southwest of the Sado Island. *AGUFM*, *2009*, OS43C-02.

Sanno, R. (2009). Origin and the U–Th ages of carbonate concretions of gas hydrate field, Joetsu basin, eastern margin of Japan Sea. Master Thesis, Department of Earth & Planetary Science, The University of Tokyo.

Santos, L. A., Freire, A. F. M., & Matsumoto, R. (2009, August). Q estimation in hydrate bearing sediments at Joetsu Knoll-Japan Sea. In *11th International Congress of the Brazilian Geophysical Society* (pp. cp-195). European Association of Geoscientists & Engineers.

Santos, L. A., Neves, E. H. P., Freire, A. F. M., Santos, M. A. C., Matsumoto, R., & Ajus, C. M. (2020). Diffraction velocity analysis in a single-channel seismic survey in the Joetsu Basin. *Geophysics*, *85*(2), U47-U53.

Sato, O., Funayama, M. & Annaka, H. (1987). Sedimentary facies and porosity properties for sandstone reservoirs in the Kakizaki Oki Structure, Niigata Prefecture, Japan. *Journal of the Japanese Association for Petroleum Technology*, *52*, 58–69 [in Japanese with English abstract].

Schoell, M. (1980). The hydrogen and carbon isotopic composition of methane from natural gases of various origins. *Geochimica et Cosmochimica Acta*, *44*(5), 649-661.

Schulte, B. (2012). Overview on the Fundamentals of Imaging. *CSEG Recorder*, *37*, 40.

Sheriff, R. E., & Geldart, L. P. (1995). *Exploration seismology*. Cambridge university press.

Shimada, W., Takeya, S., Kamata, Y., Uchida, T., Nagao, J., Ebinuma, T., & Narita, H. (2005). Texture change of ice on anomalously preserved methane clathrate hydrate. *The Journal of Physical Chemistry B*, *109*(12), 5802-5807.

Sloan Jr, E. D., & Koh, C. A. (2007). *Clathrate hydrates of natural gases*. CRC press.

Sloan, E. D. (2003). Fundamental principles and applications of natural gas hydrates. *Nature*, *426*(6964), 353-359.

Song, Y., Cheng, C., Zhao, J., Zhu, Z., Liu, W., Yang, M., & Xue, K. (2015). Evaluation of gas production from methane hydrates using depressurization, thermal stimulation and combined methods. *Applied Energy*, *145*, 265-277.

Stoll, R. D., Ewing, J., & Bryan, G. M. (1971). Anomalous wave velocities in sediments containing gas hydrates. *Journal of Geophysical Research*, *76*(8), 2090-2094.

Suzuki, M. (2010). Reconstruction of the environment of Japan Sea for the last 33,000 years based on foraminifereal assemblage and isotopic ratio : Consideration on anomalies of benthic environment", Master Thesis, Department of Earth & Planetary Science, The University of Tokyo.

Suzuki, U. (1979). Petroleum geology of the Sea of Japan, Northern Honshu. *Journal of Japanese Association of Petroleum Technologists*, *44*, 291-307.

Taira, A. (2001). Tectonic evolution of the Japanese island arc system. *Annual Review of Earth and Planetary Sciences*, *29*(1), 109-134.

Takeuchi, A. (1996). Recent crustal movements and strains along the eastern margin of Japan Sea floor. *Geology and Geophysics of the Japan Sea*, *1*, 385-398.

Taner MT (2001) Seismic attributes: Canadian Society of Exploration Geophysicists Recorder 26(9):48–56

Taner, M. T., Koehler, F., & Sheriff, R. E. (1979). Complex seismic trace analysis. *Geophysics*, *44*(6), 1041-1063.

Telford, W. M., Telford, W. M., Geldart, L. P., Sheriff, R. E., & Sheriff, R. E. (1990). *Applied geophysics*. Cambridge university press.

Tinivella, U., Loreto, M. F., & Accaino, F. (2009). Regional versus detailed velocity analysis to quantify hydrate and free gas in marine sediments: the South Shetland Margin case study. *Geological Society, London, Special Publications*, *319*(1), 103-119.

Vernengo, L., & Trinchero, E. (2015). Application of amplitude volume technique attributes, their variations, and impact. *The Leading Edge*, *34*(10), 1246-1253.

Walsh, M. R., Hancock, S. H., Wilson, S. J., Patil, S. L., Moridis, G. J., Boswell, R., ... & Sloan, E. D. (2009). Preliminary report on the commercial viability of gas production from natural gas hydrates. *Energy Economics*, *31*(5), 815-823.

Watanabe, Y., Nakai, S. I., Hiruta, A., Matsumoto, R., & Yoshida, K. (2008). U–Th dating of carbonate nodules from methane seeps off Joetsu, Eastern Margin of Japan Sea. *Earth and Planetary Science Letters*, *272*(1-2), 89-96.

Webster, C. R., Mahaffy, P. R., Atreya, S. K., Moores, J. E., Flesch, G. J., Malespin, C., ... & Gomez-Elvira, J. (2018). Background levels of methane in Mars' atmosphere show strong seasonal variations. *Science*, *360*(6393), 1093-1096.

Wood, W. T., Gettrust, J. F., Chapman, N. R., Spence, G. D., & Hyndman, R. D. (2002). Decreased stability of methane hydrates in marine sediments owing to phase-boundary roughness. *Nature*, *420*(6916), 656-660.

Yilmaz, Ö. (2001). *Seismic data analysis: Processing, inversion, and interpretation of seismic data*. Society of exploration geophysicists.

Zoeppritz, K. (1919) Uber reflexion und durchgang seismischer wellen durch Unstetigkerlsflaschen. *Berlin, Uber Erdbebenwellen VII B, Nachrichten der Koniglichen Gesellschaft der Wissenschaften zu Gottingen, math-phys. K1*, (57), 84.

Zuhlsdorff, L., & Spieß, V. (2004). Three-dimensional seismic characterization of a venting site reveals compelling indications of natural hydraulic fracturing. *Geology*, *32*(2), 101-104.

APPENDIX A–2D SCS PROFILES WITH SEISMIC ATTRIBUTES

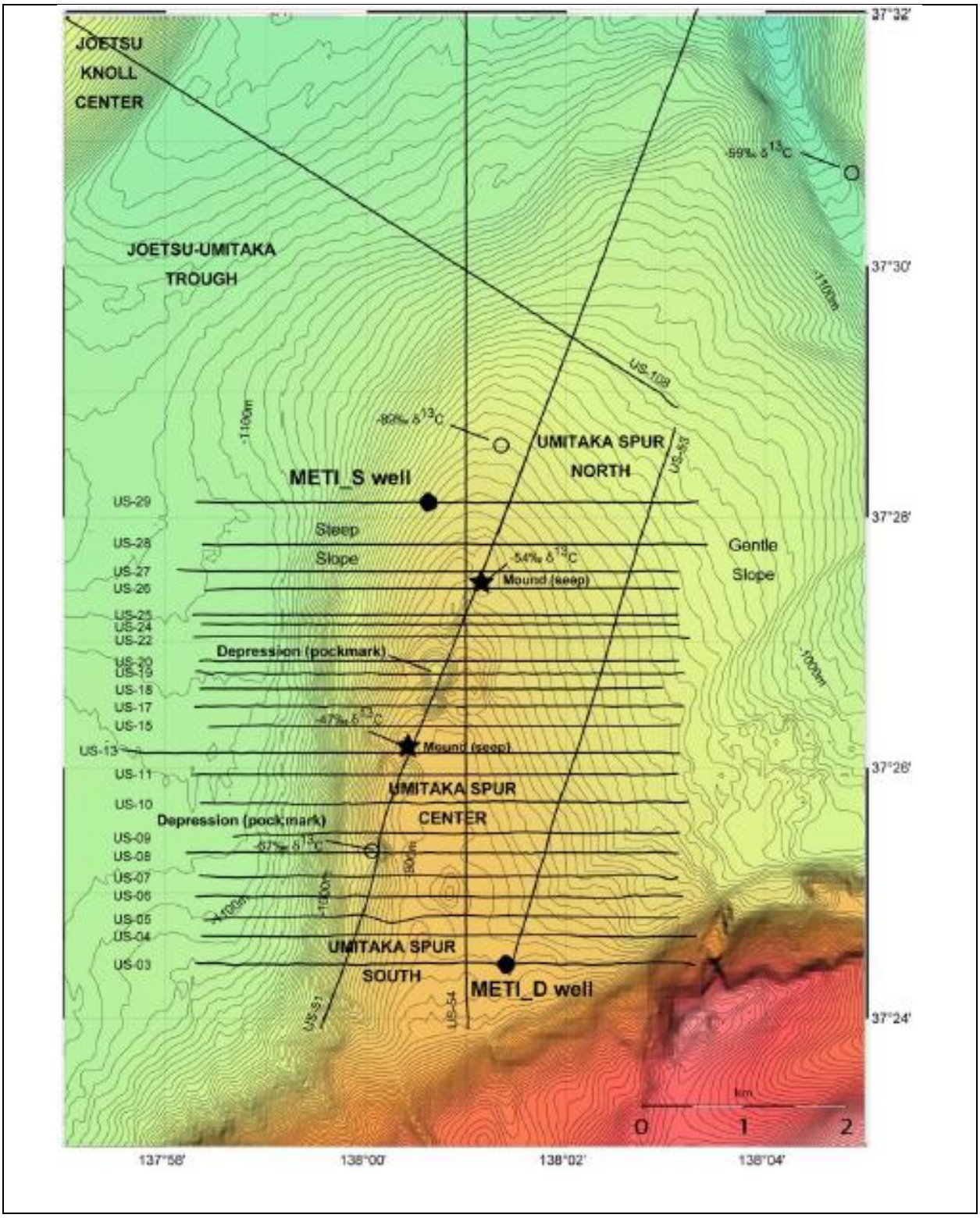

2D SCS seismic profiles location map (Freire, 2010).

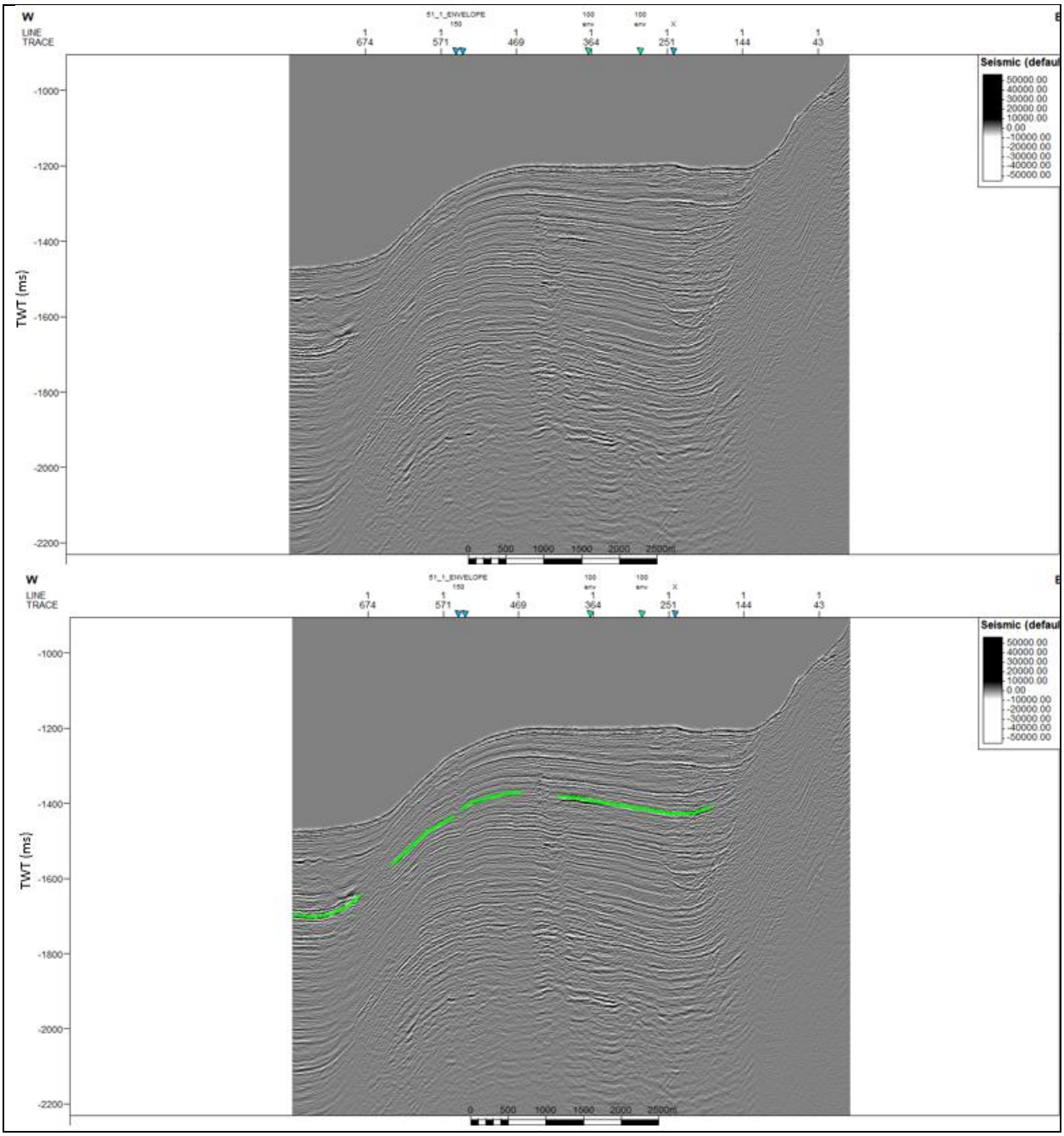

SCS profile US-03 without application of seismic attribute. Green line indicates the BSR.

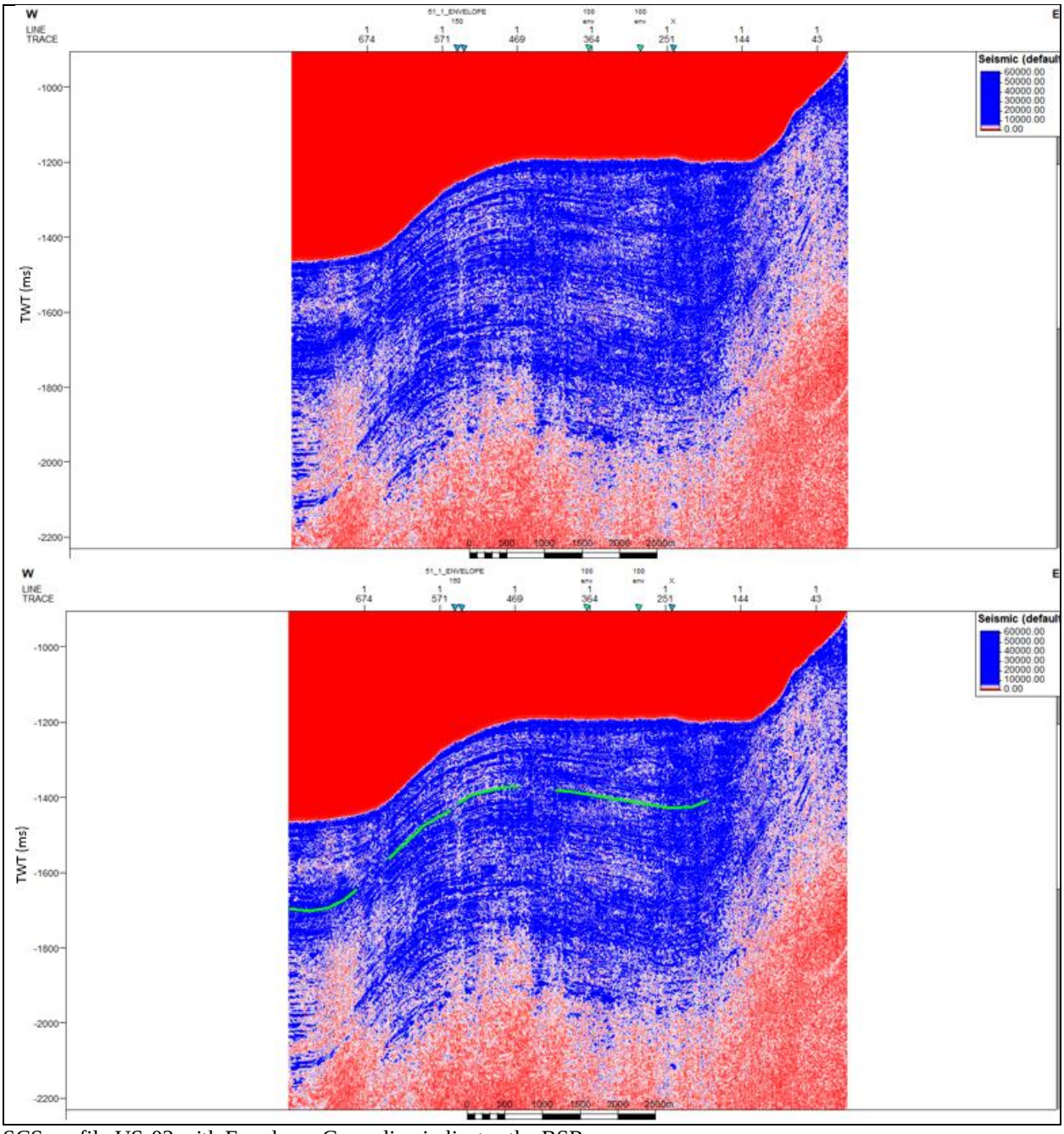

SCS profile US-03 with Envelope. Green line indicates the BSR.

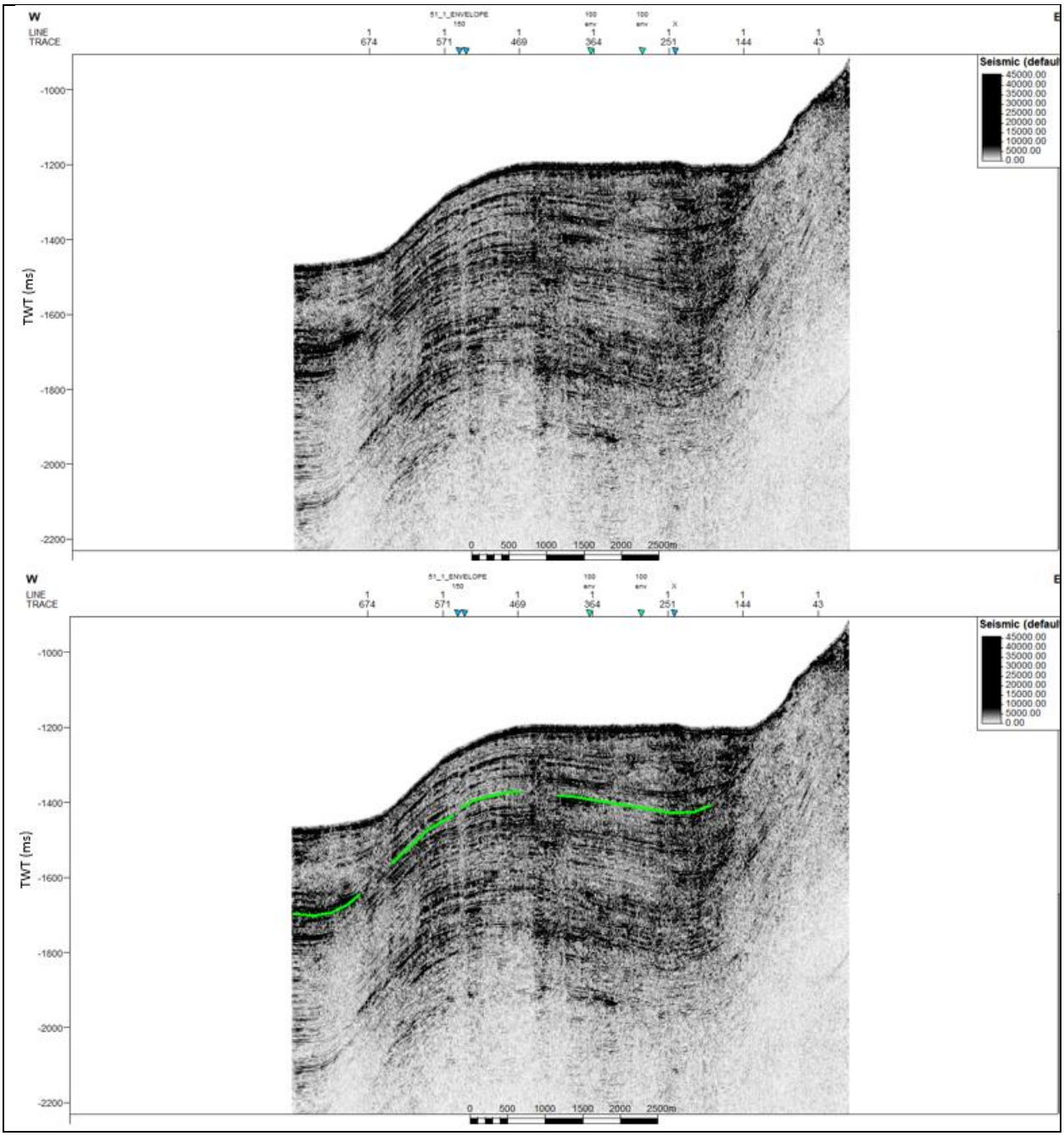

SCS profile US-03 with RMS Amplitude. Green line indicates the BSR.

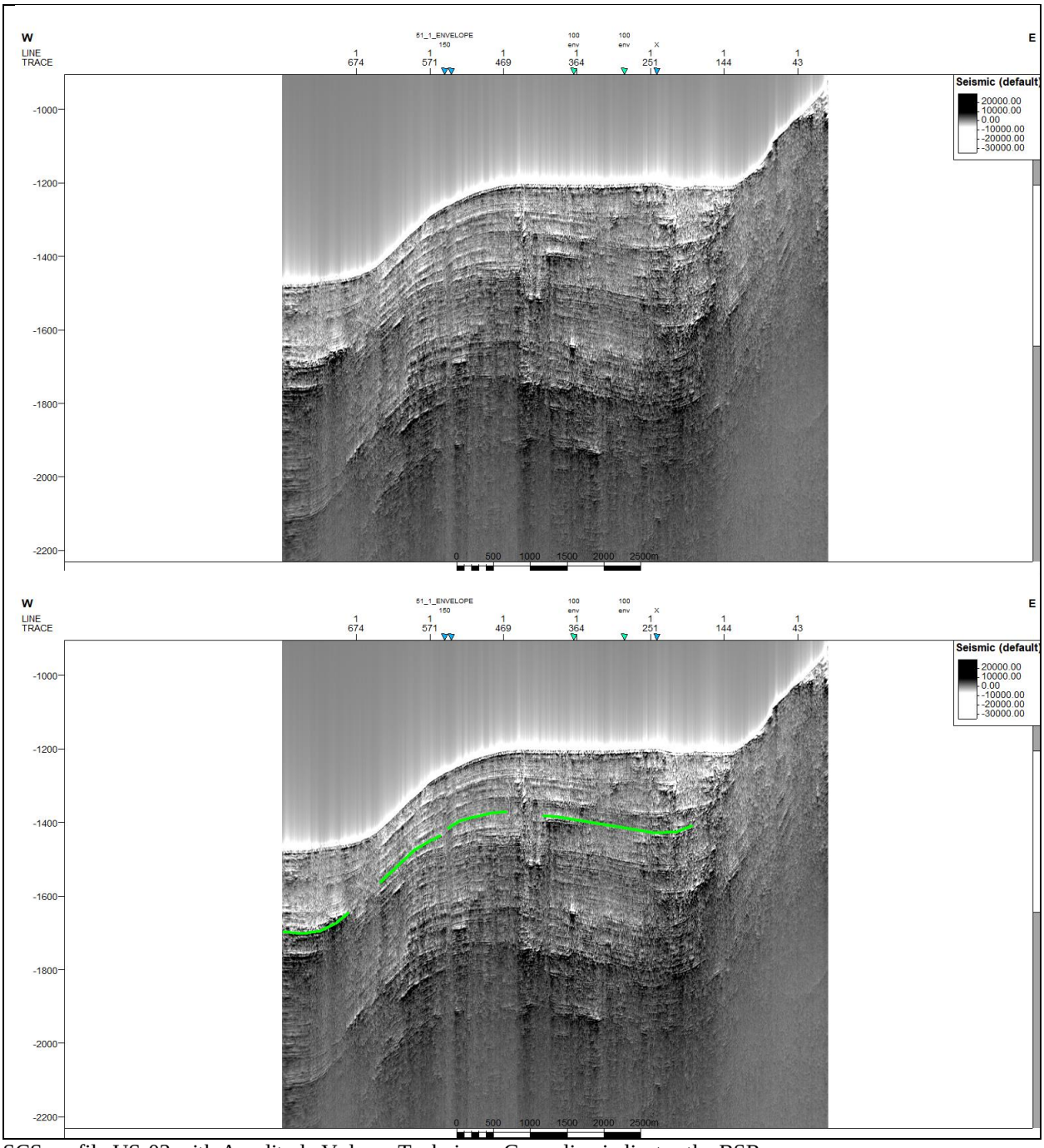

SCS profile US-03 with Amplitude Volume Technique. Green line indicates the BSR.

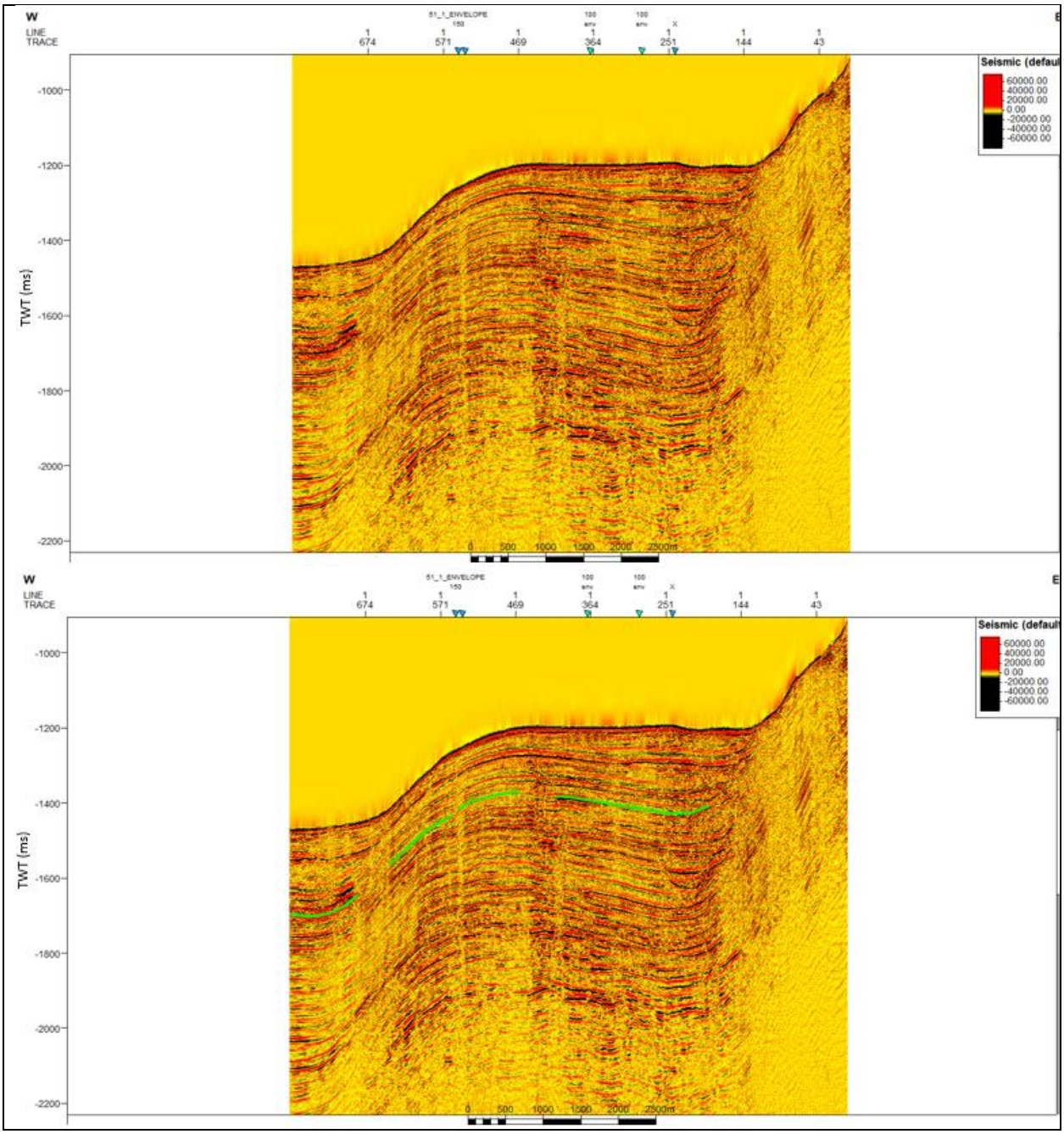

SCS profile US-03 with Relative Acoustic Impedance. Green line indicates the BSR.

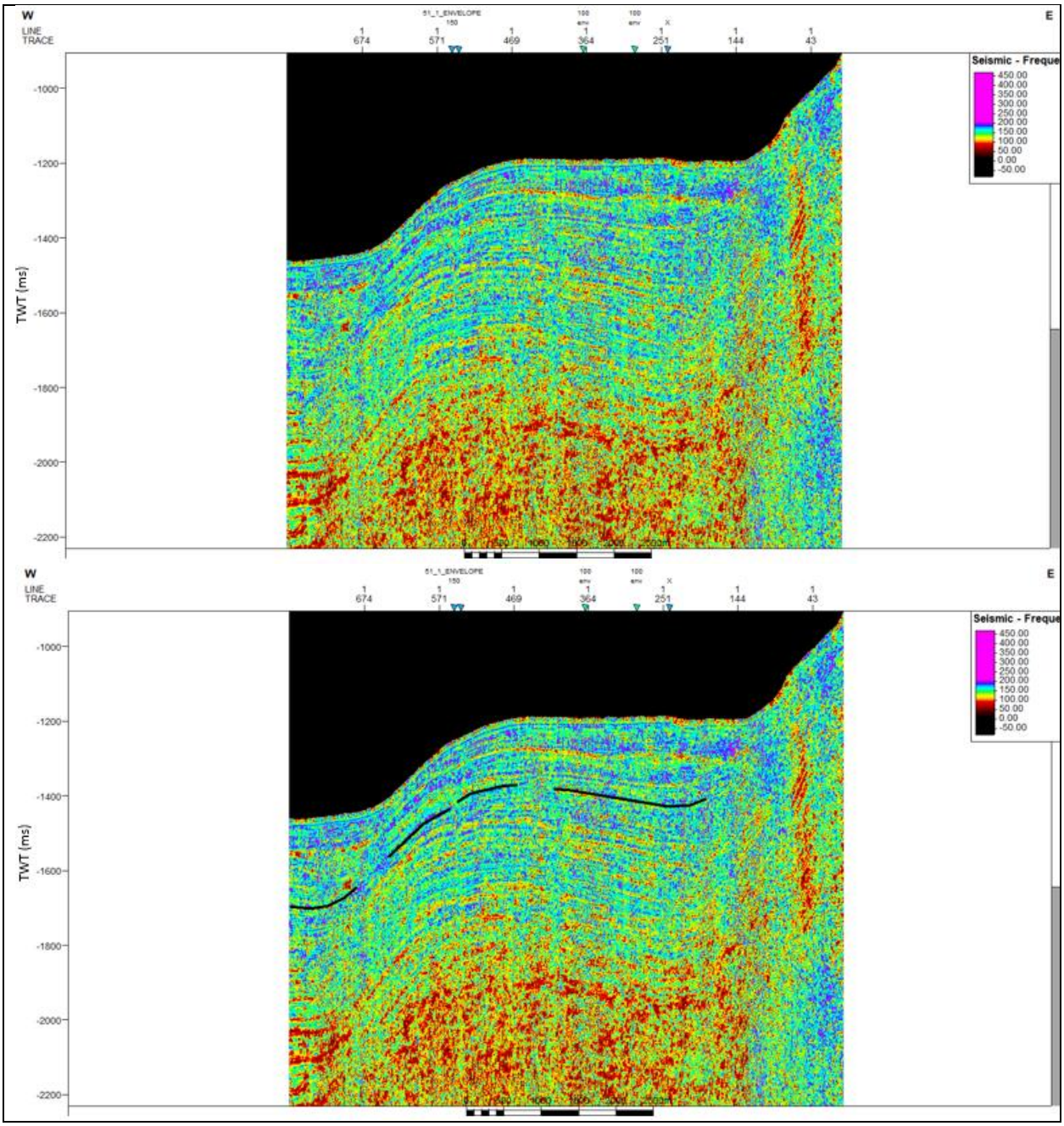

SCS profile US-03 with Instantaneous Frequency. Black line indicates the BSR.

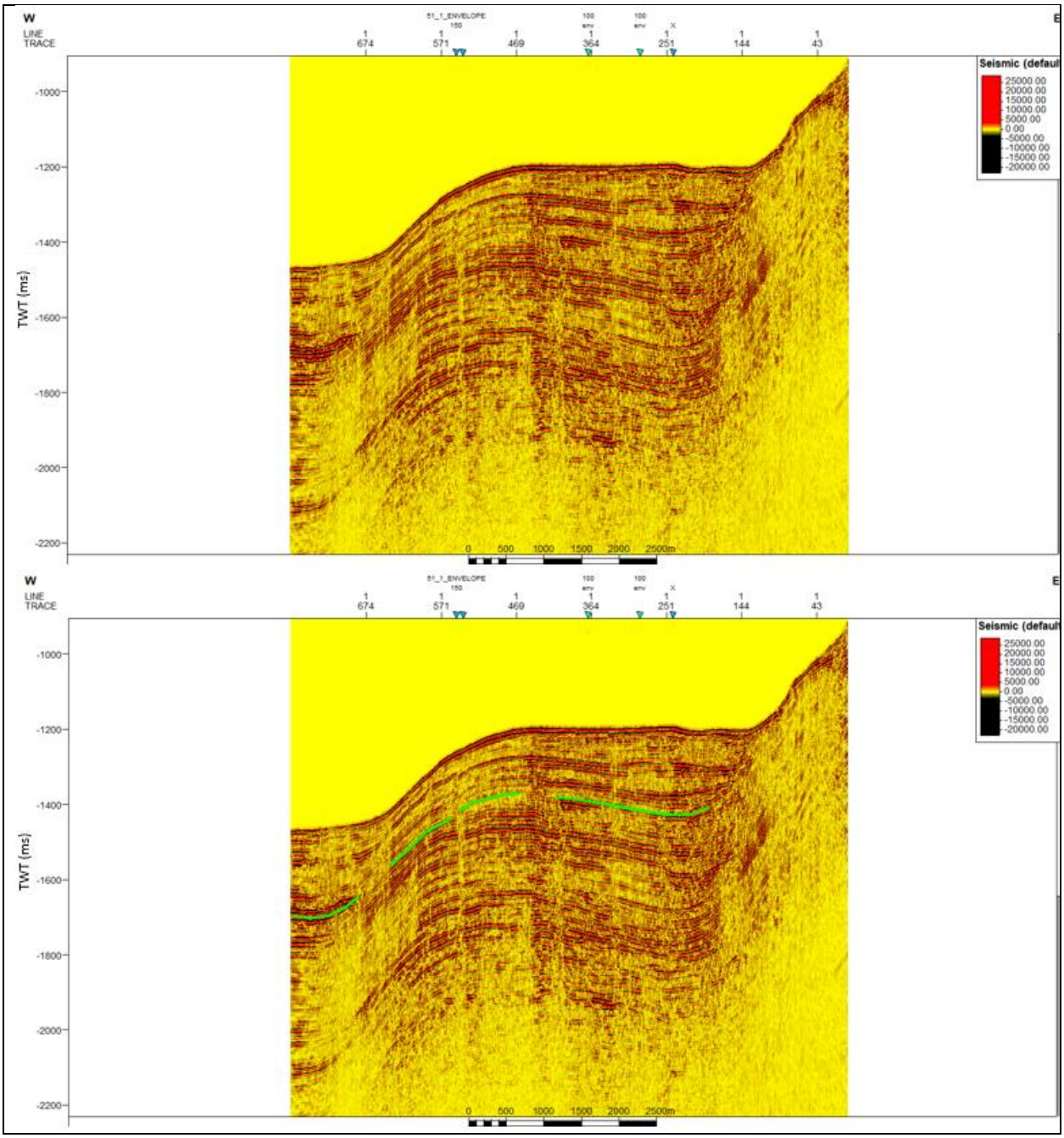

SCS profile US-03 with Spectral Decomposition of 100 Hz. Green line indicates the BSR.

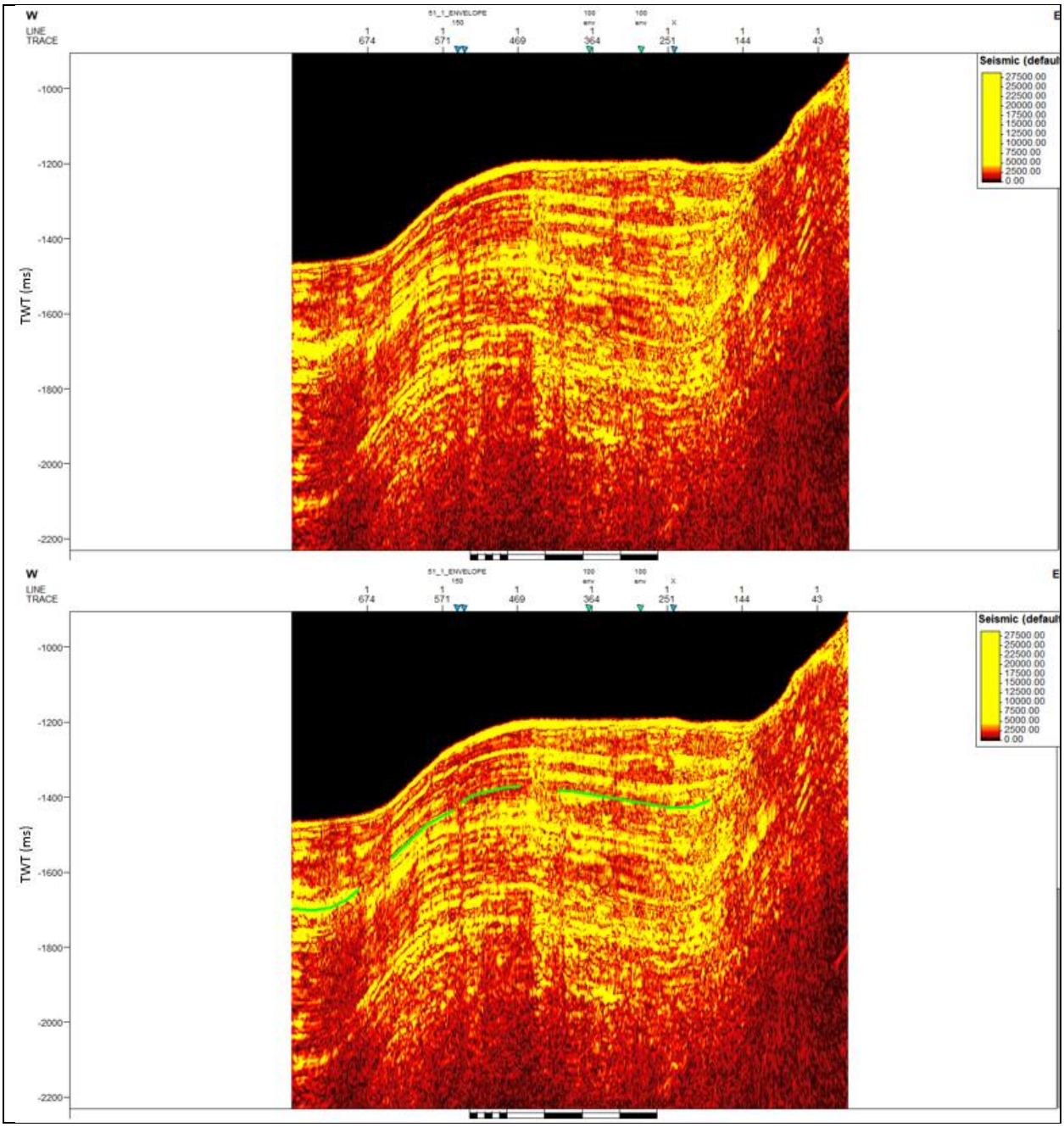

SCS profile US-03 with Spectral Decomposition of 100 Hz plus Envelope. Green line indicates the BSR.

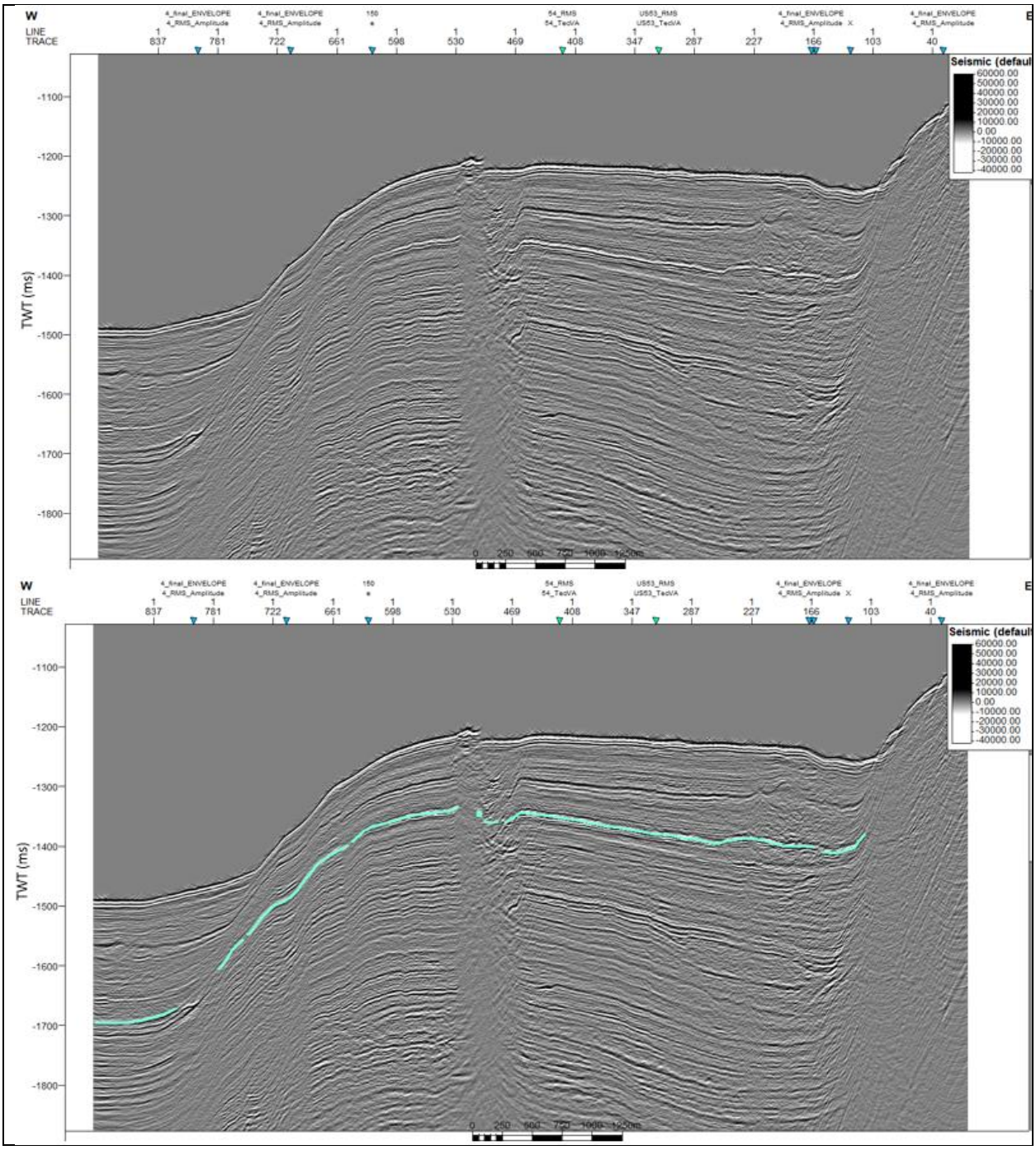

SCS profile US-04 without application of seismic attribute. Blue line indicates the BSR.

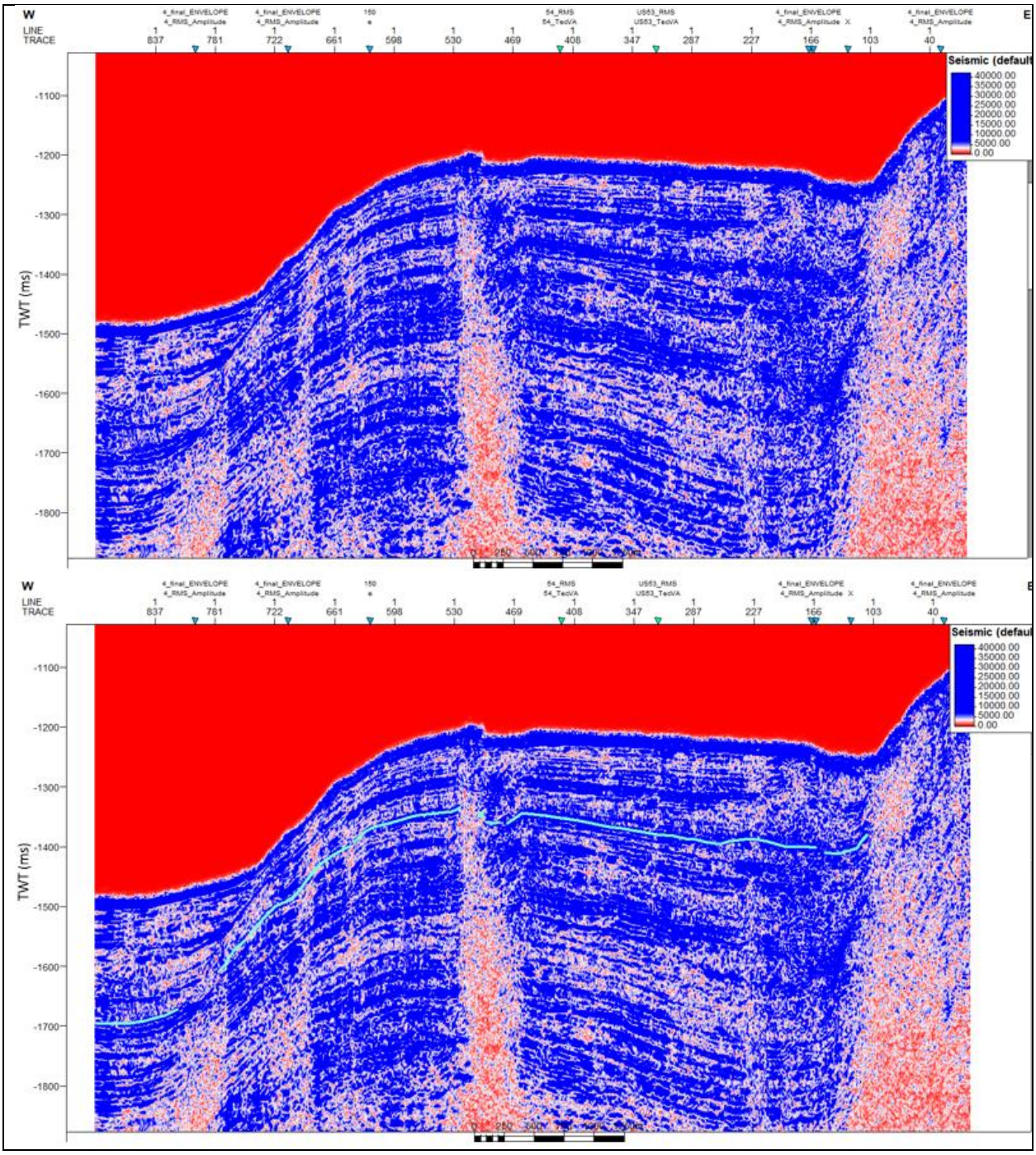

SCS profile US-04 with Envelope. Blue line indicates the BSR.

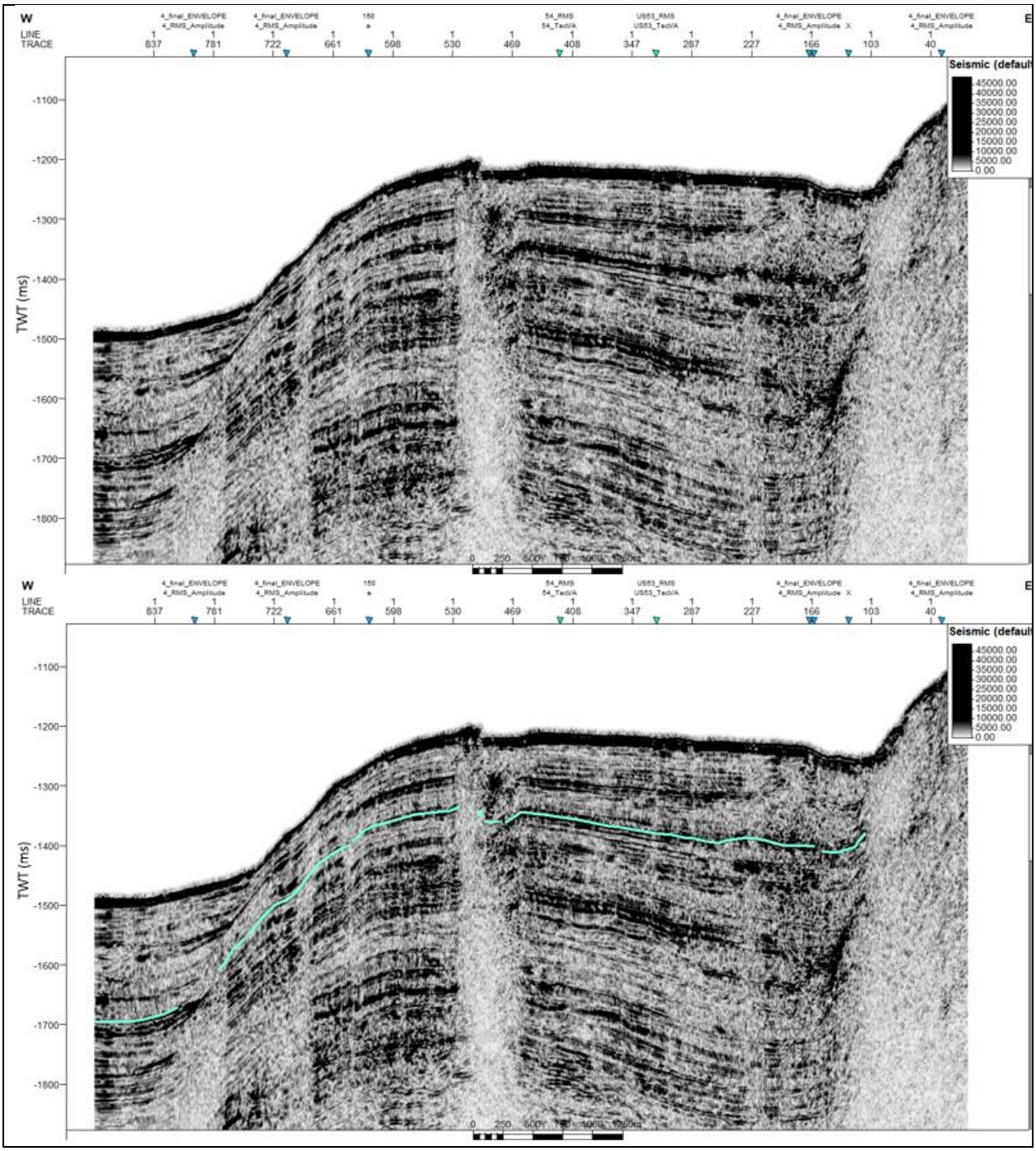

SCS profile US-04 with RMS Amplitude. Blue line indicates the BSR.

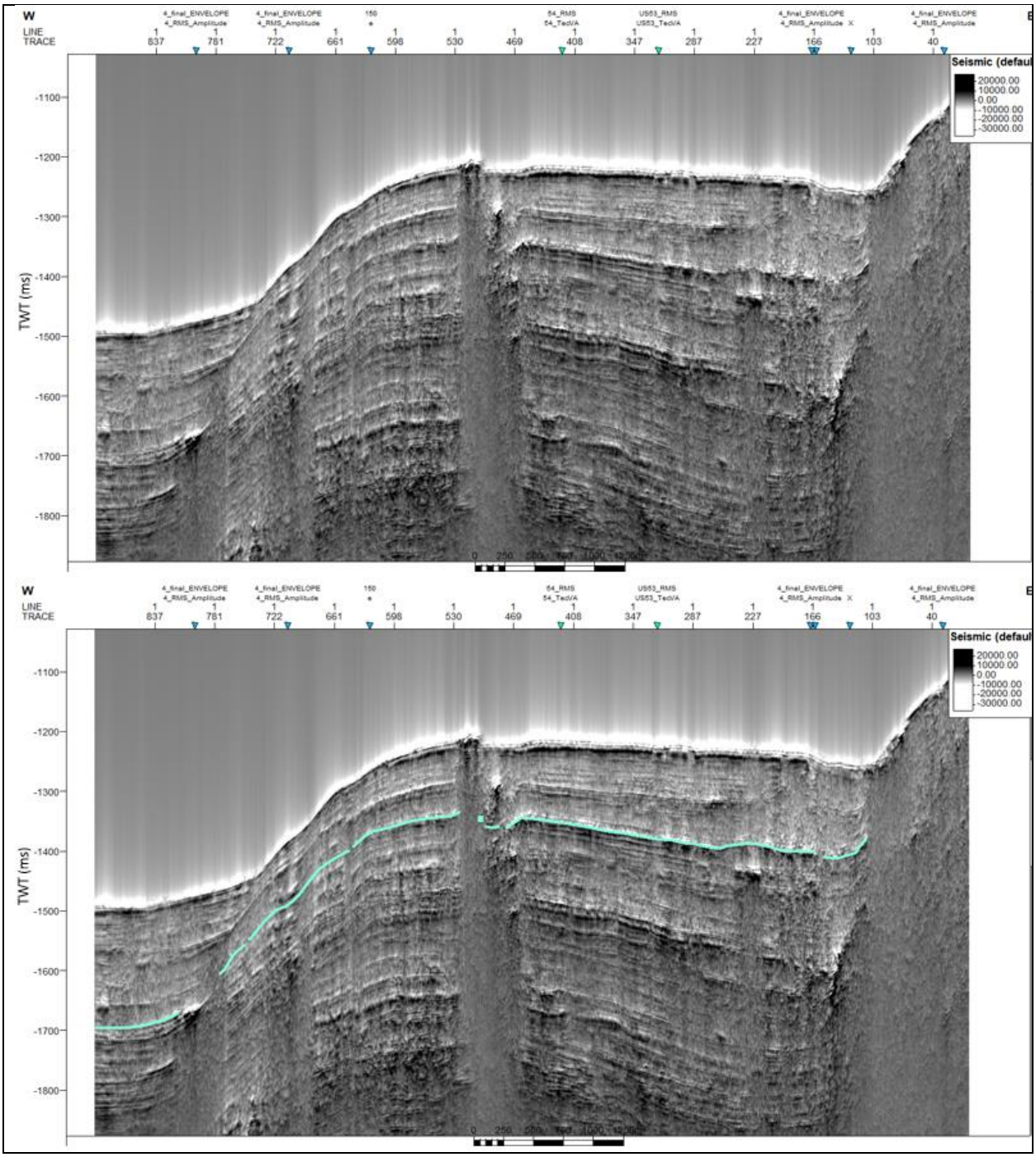

SCS profile US-04 with Amplitude Volume Technique. Blue line indicates the BSR.

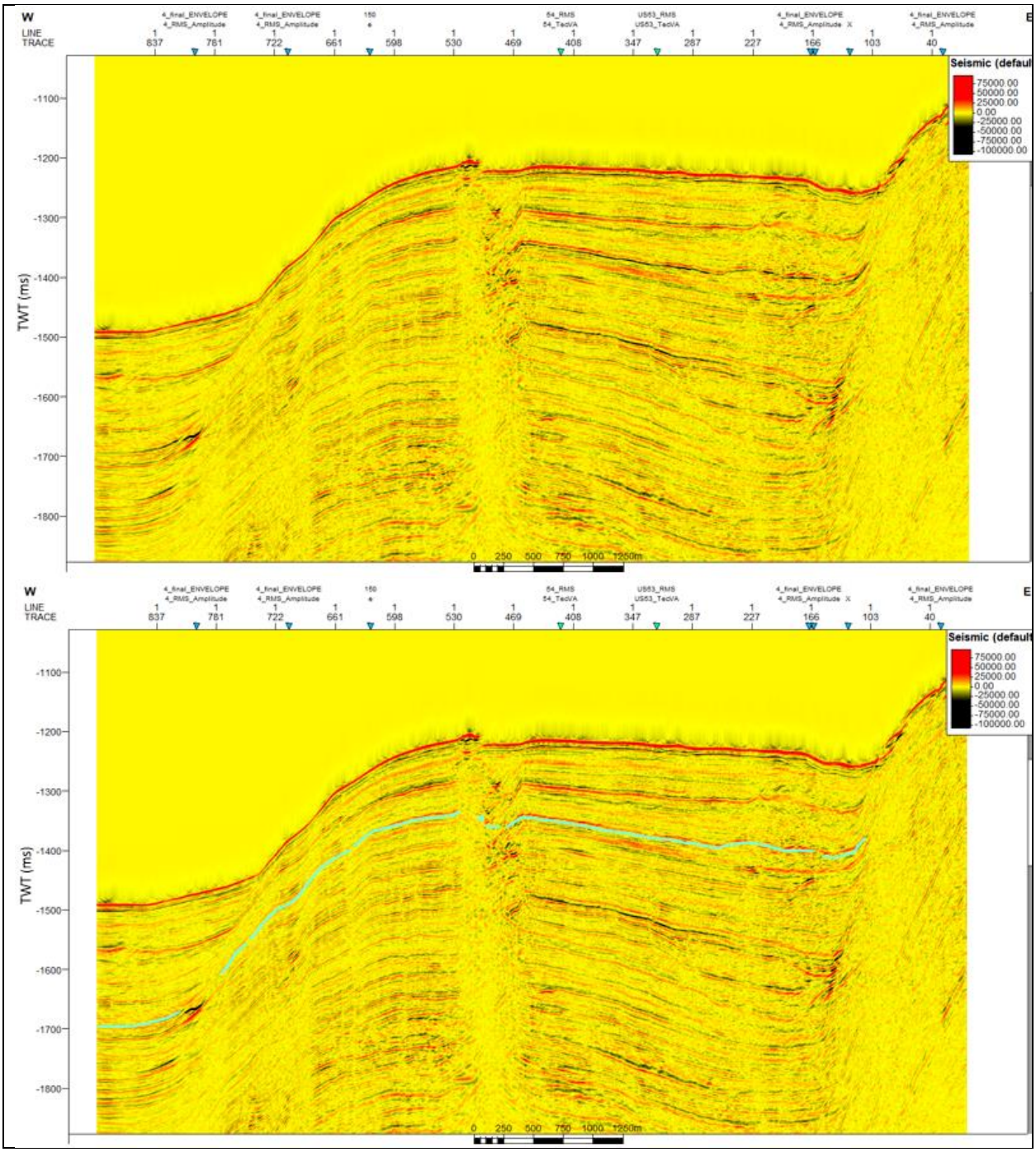

SCS profile US-04 with Relative Acoustic Impedance. Blue line indicates the BSR.

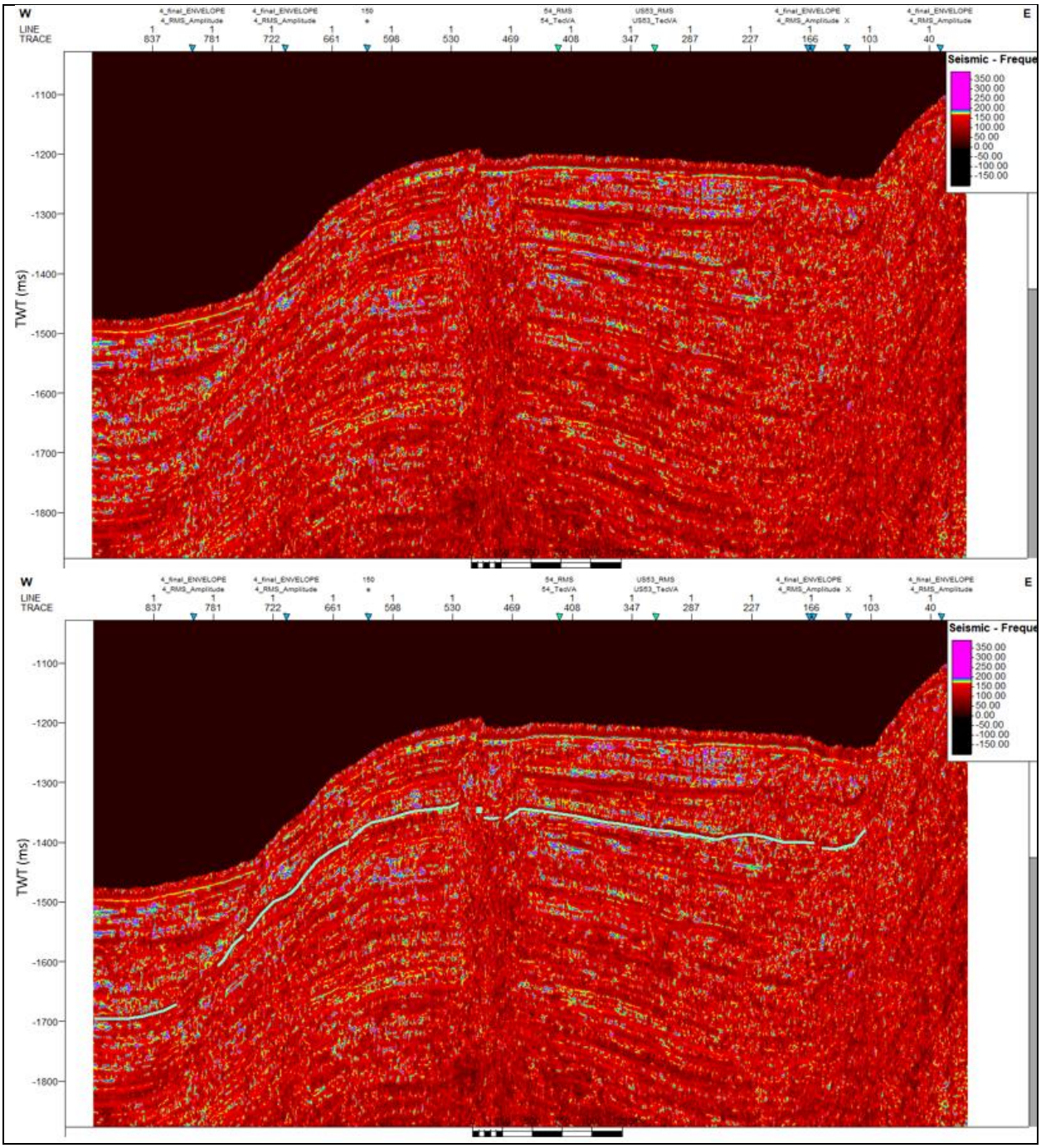

SCS profile US-04 with Instantaneous Frequency. Blue line indicates the BSR.

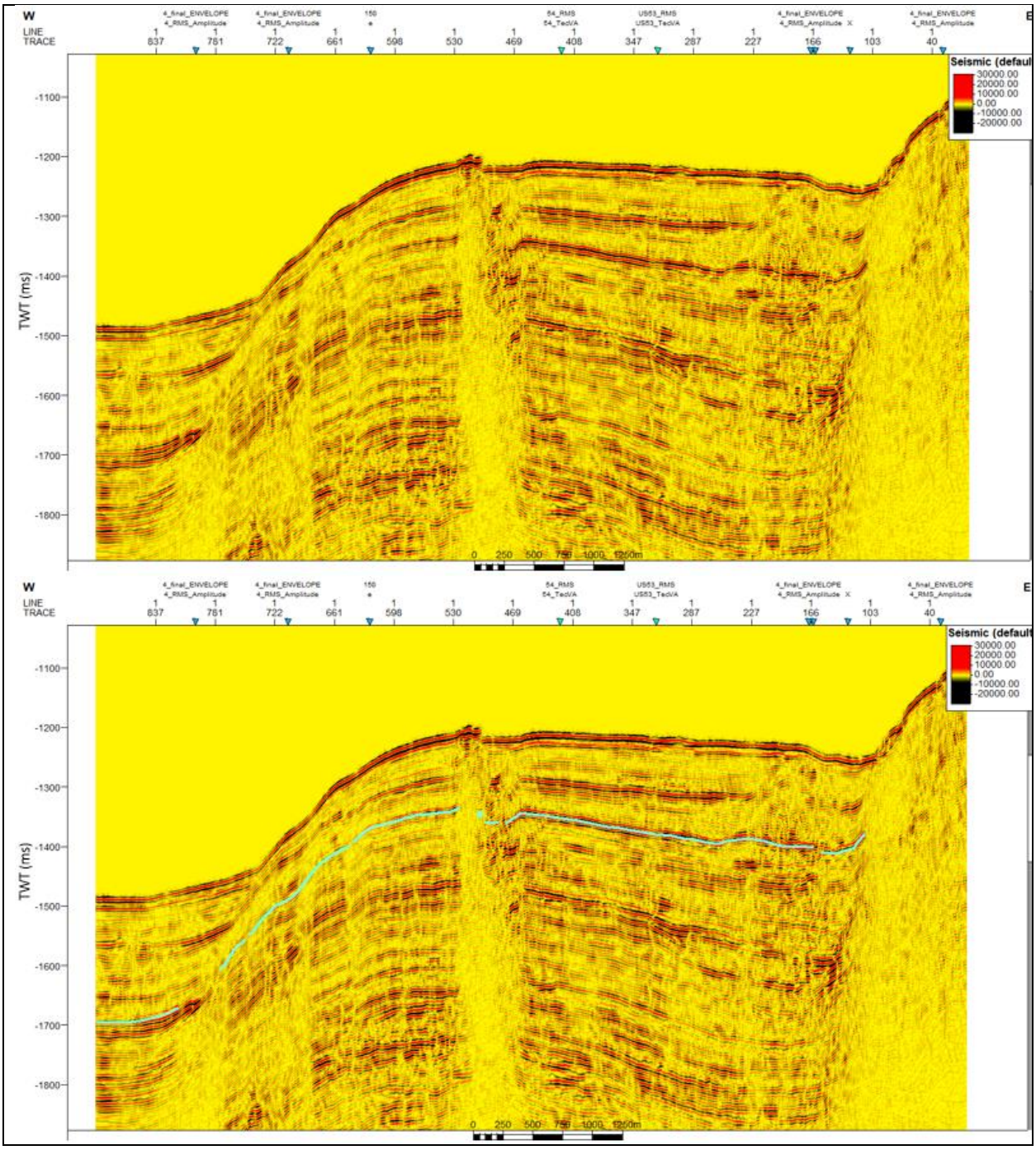

SCS profile US-04 with Spectral Decomposition of 100 Hz. Blue line indicates the BSR.

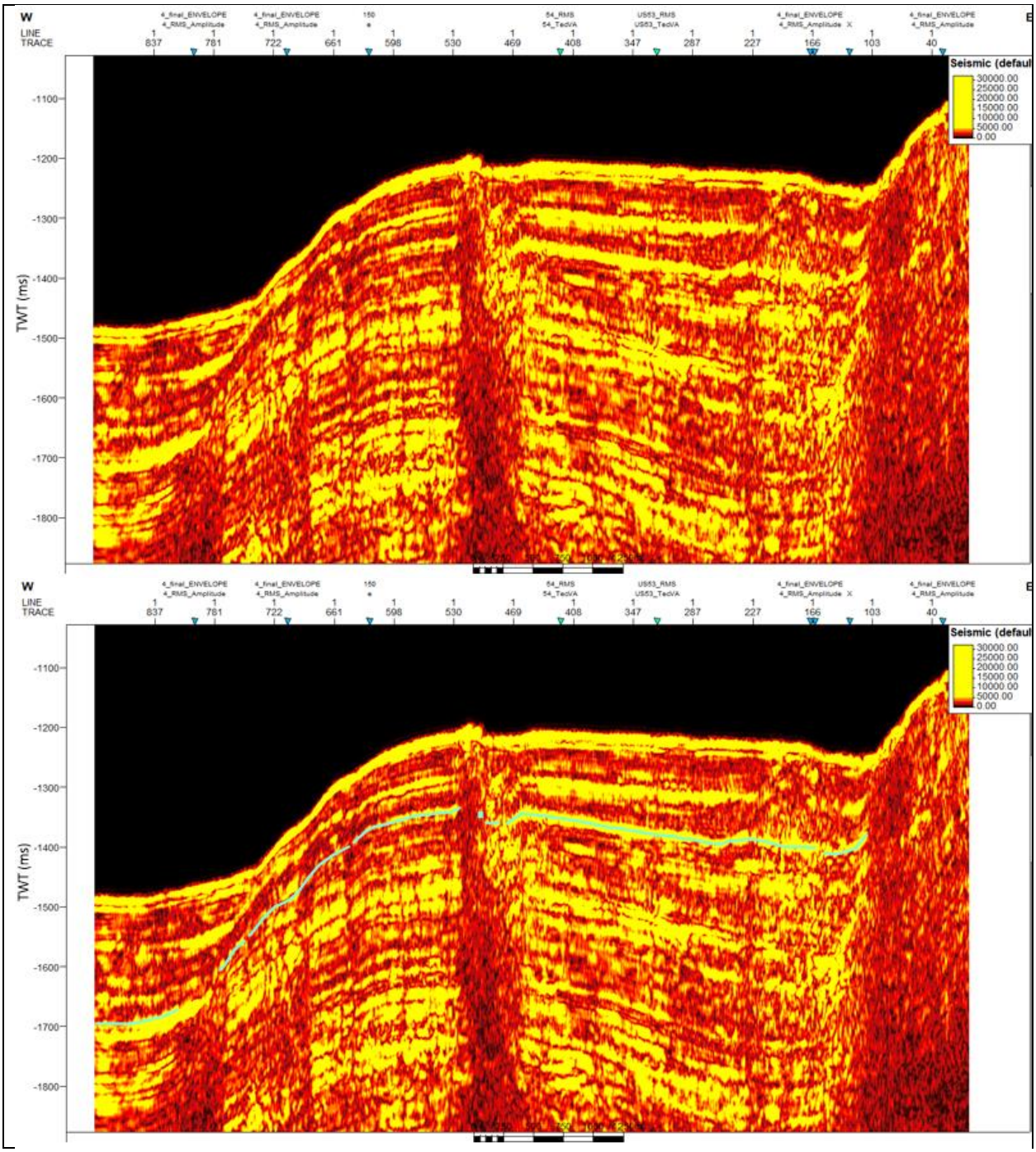

SCS profile US-04 with Spectral Decomposition of 100 Hz plus Envelope. Blue line indicates the BSR.

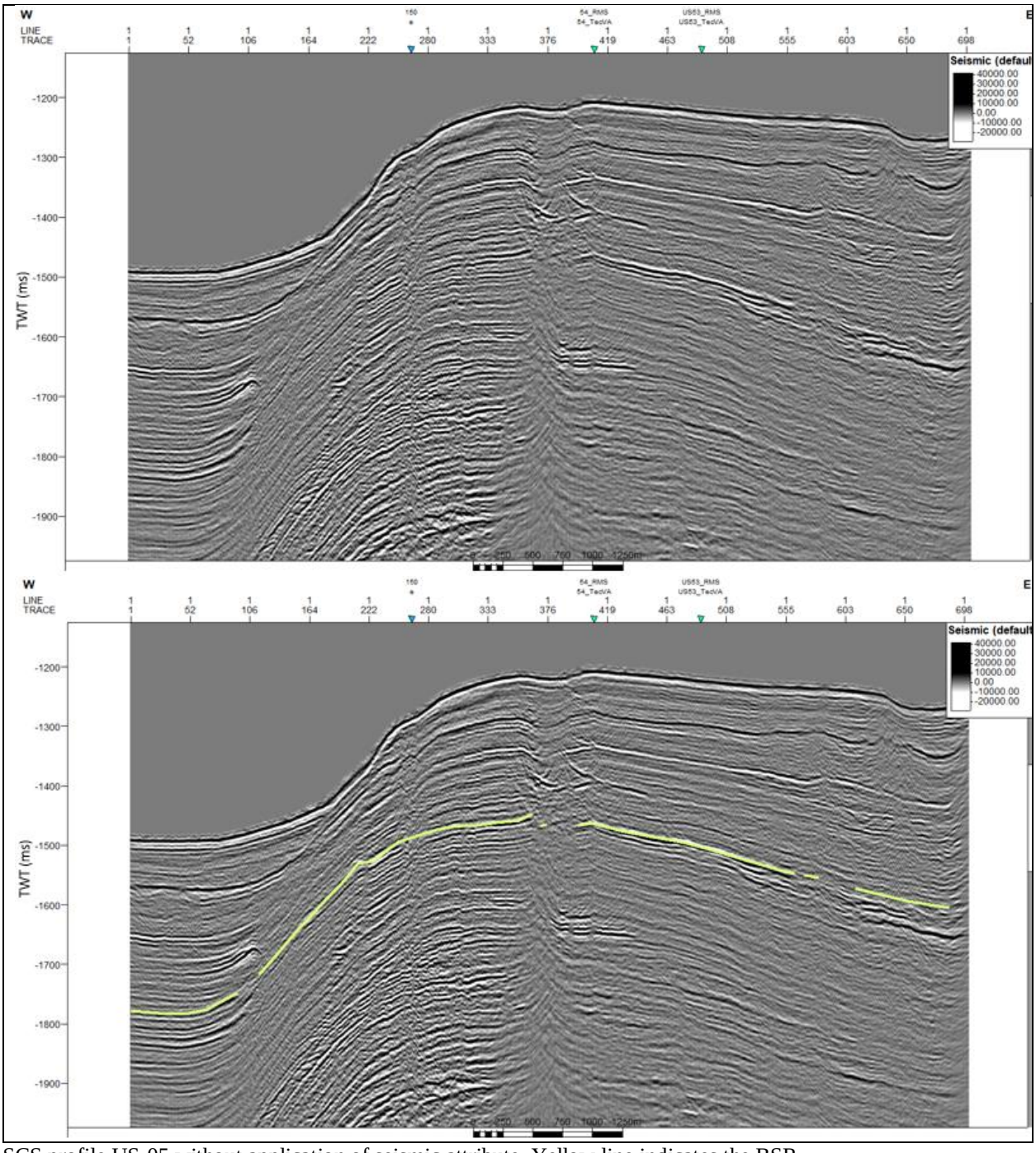

SCS profile US-05 without application of seismic attribute. Yellow line indicates the BSR.

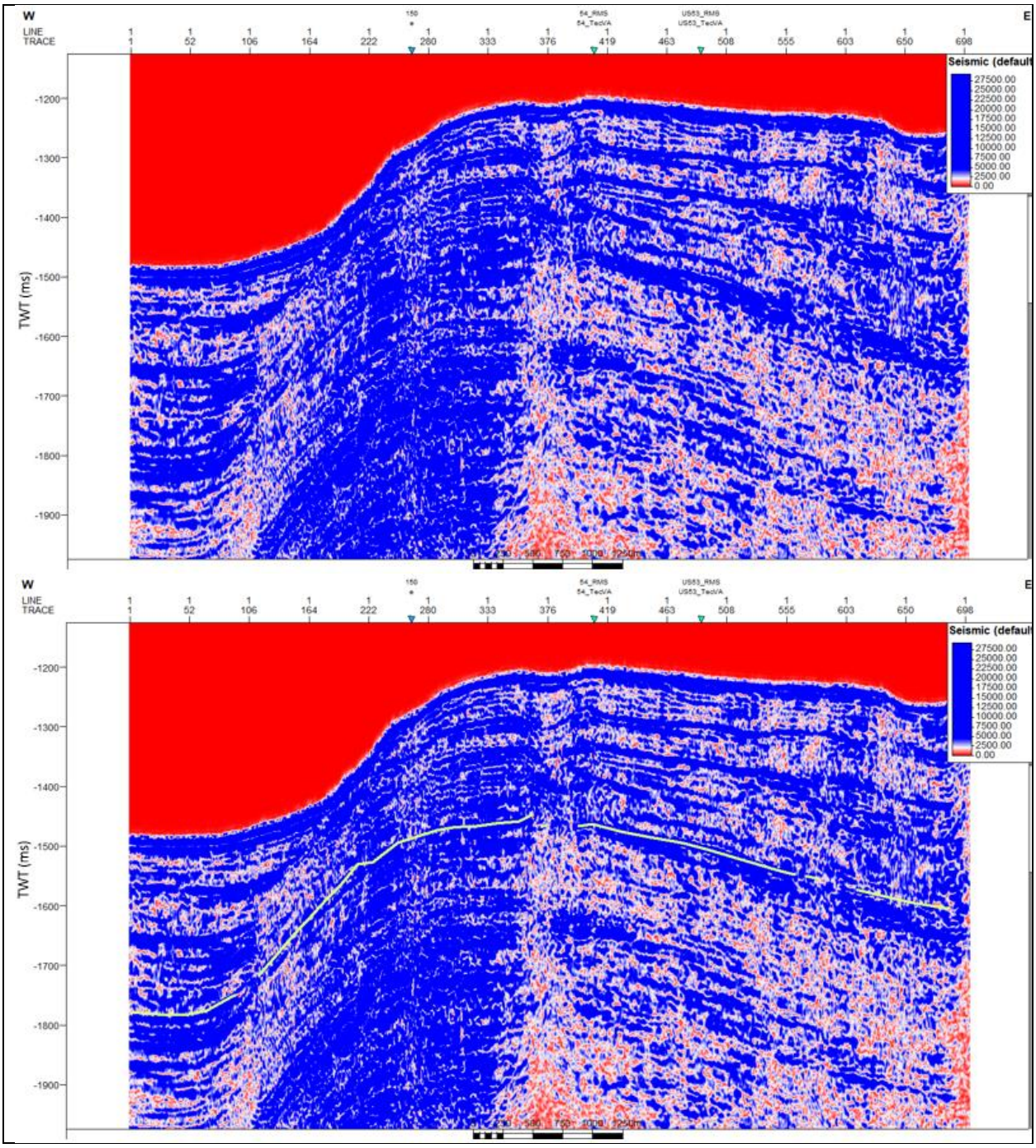

SCS profile US-05 with Envelope. Yellow line indicates the BSR.

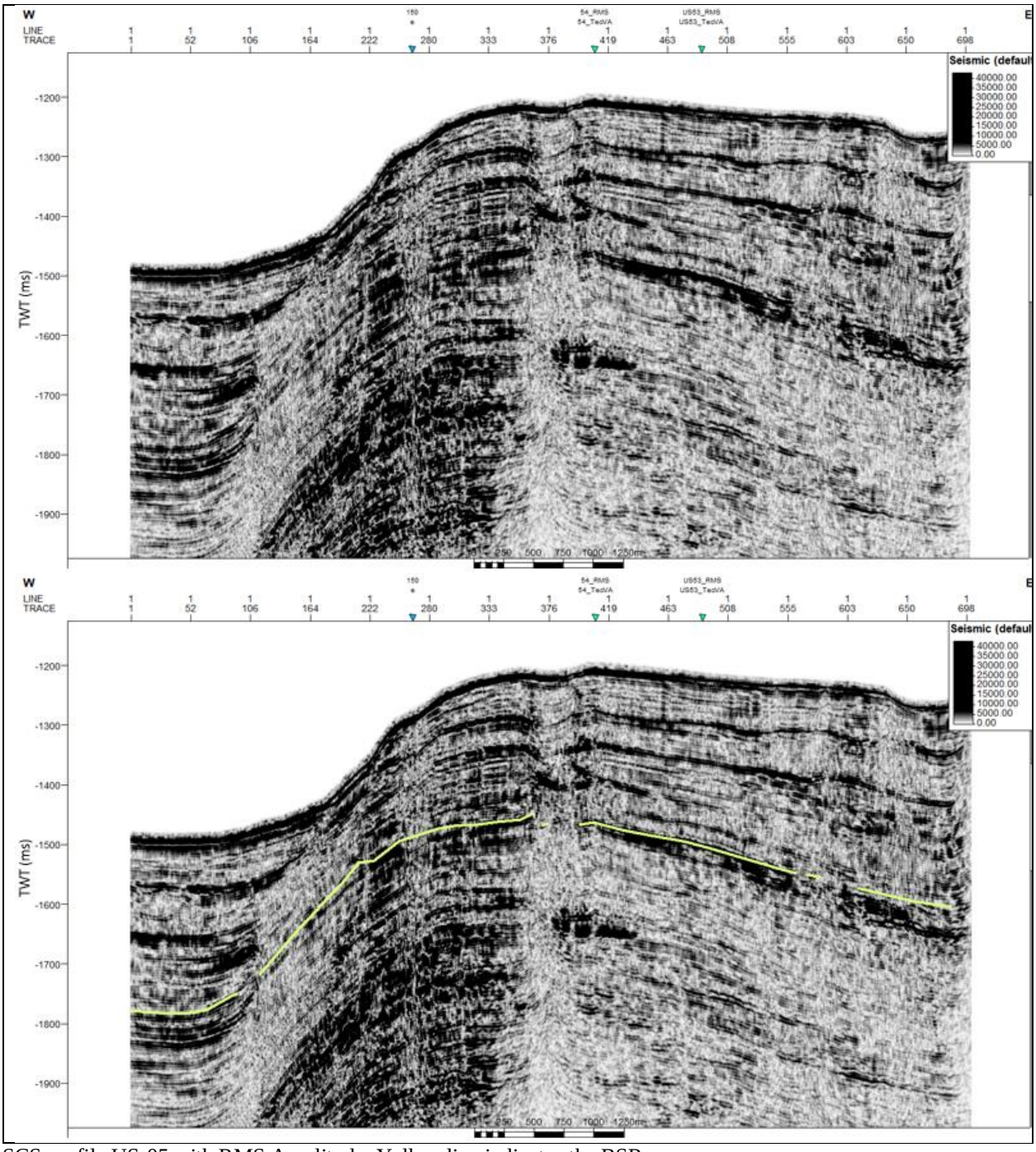

SCS profile US-05 with RMS Amplitude. Yellow line indicates the BSR.

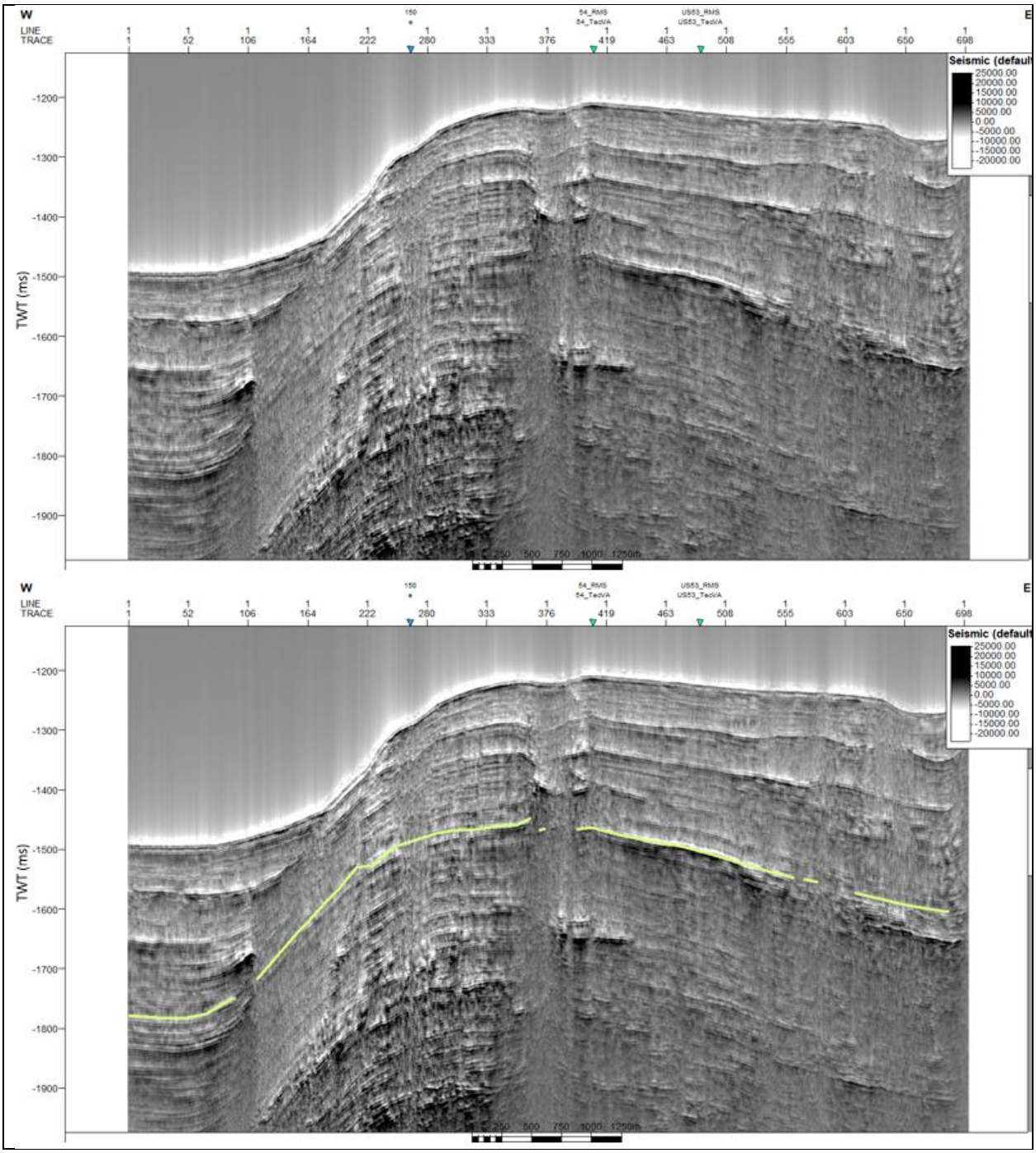

SCS profile US-05 with Amplitude Volume Technique. Yellow line indicates the BSR.

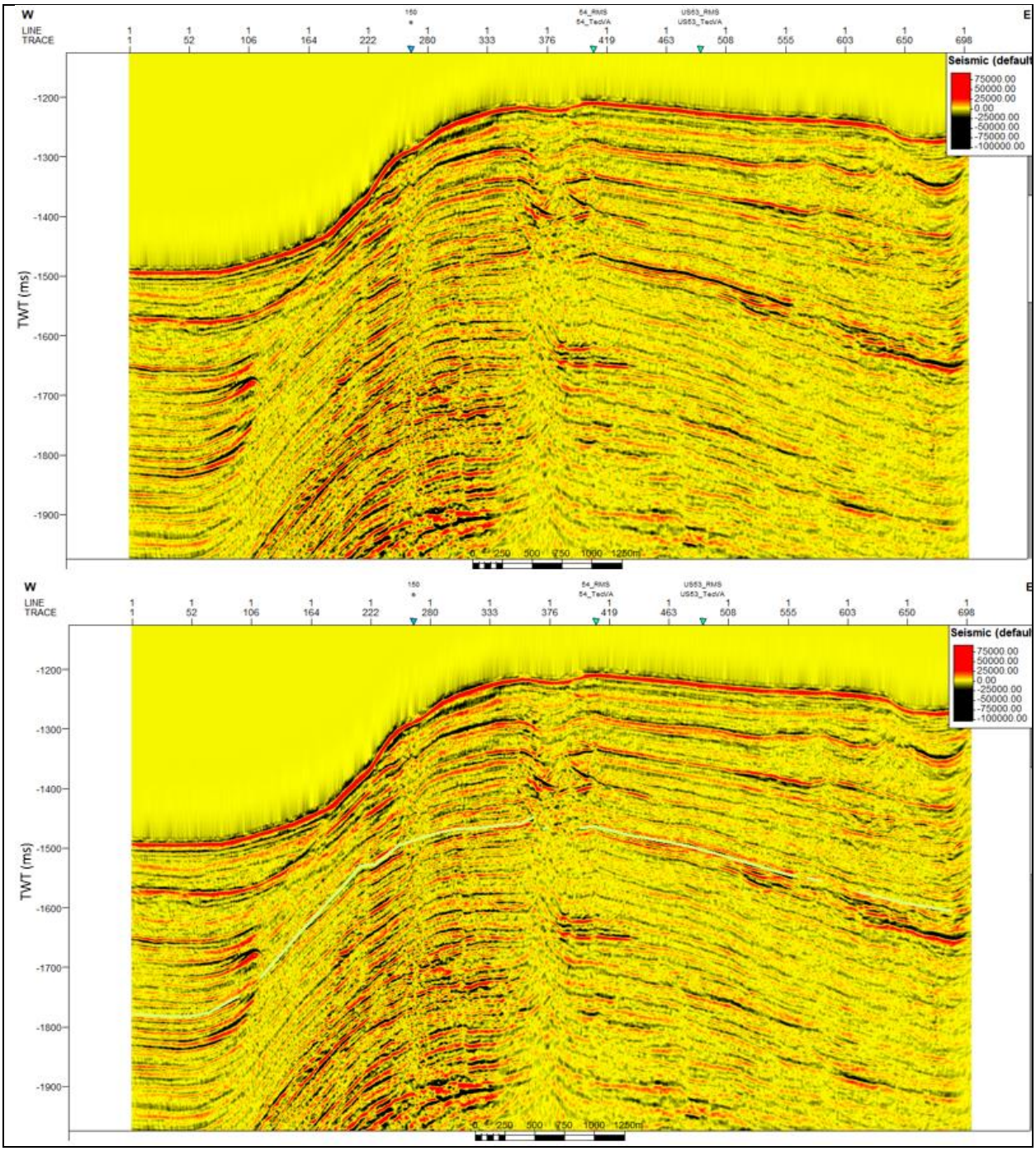

SCS profile US-05 with Relative Acoustic Impedance. Yellow line indicates the BSR.

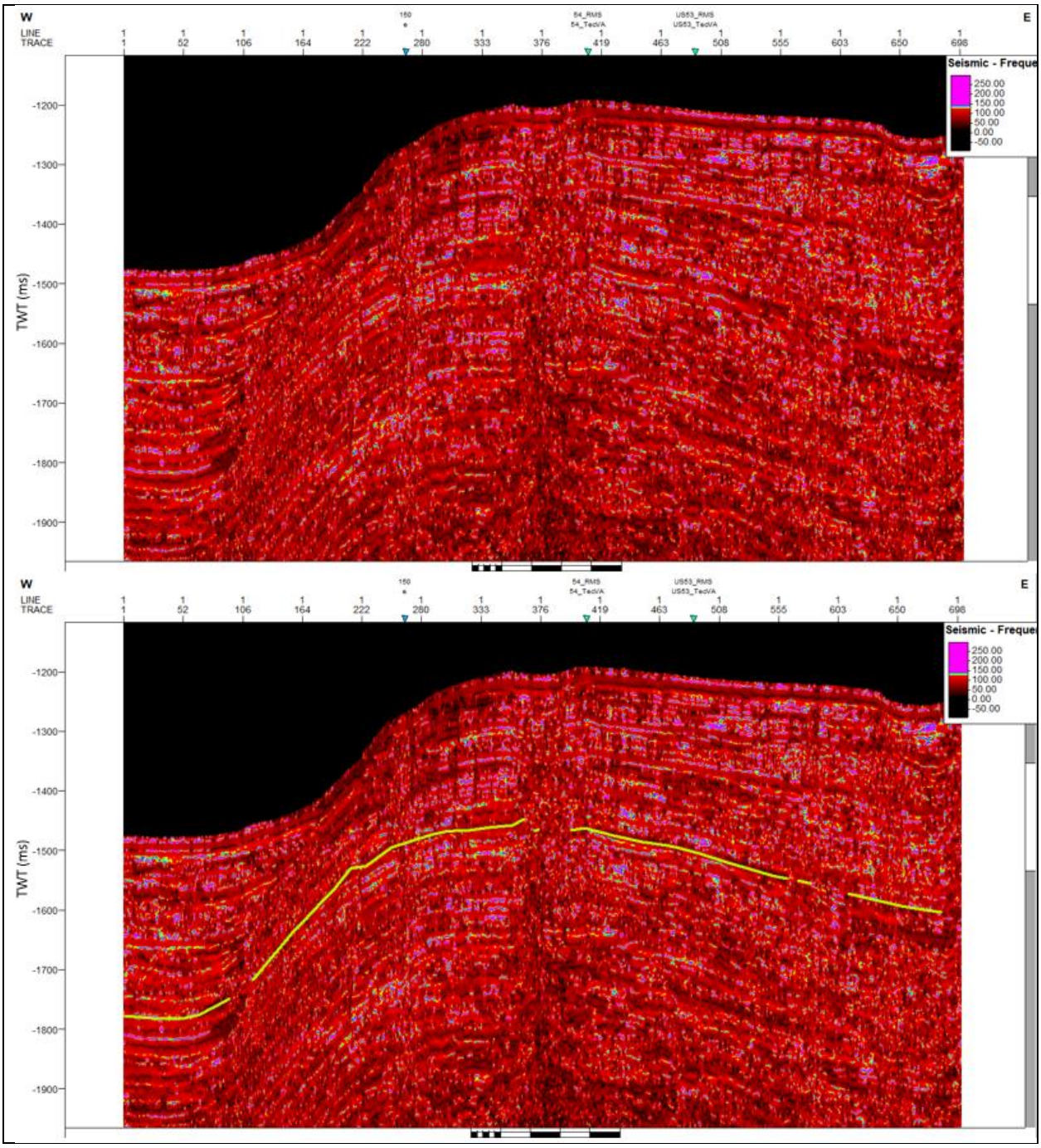

SCS profile US-05 with Instantaneous Frequency. Yellow line indicates the BSR.

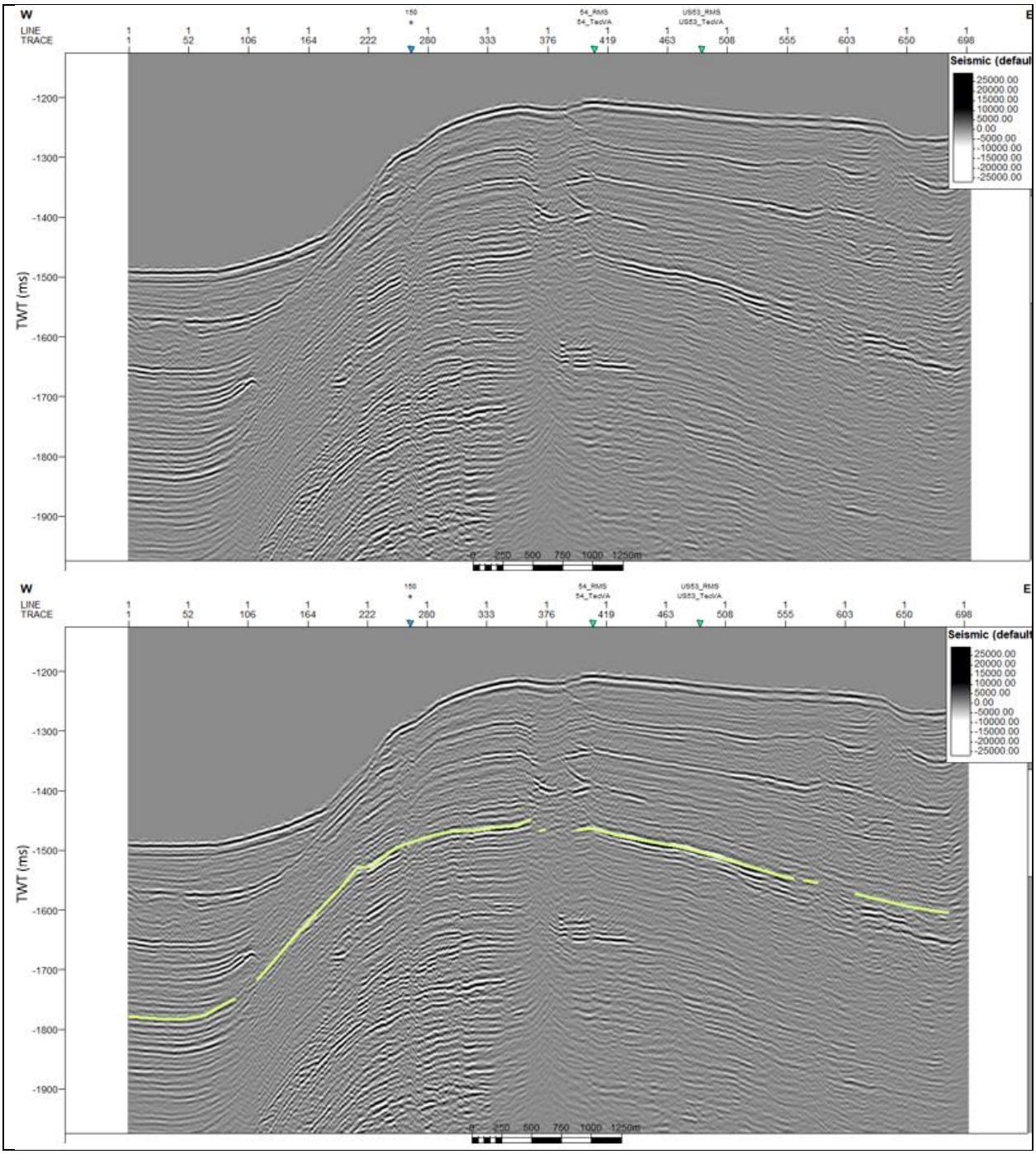

SCS profile US-05 with Spectral Decomposition of 100 Hz. Yellow line indicates the BSR.

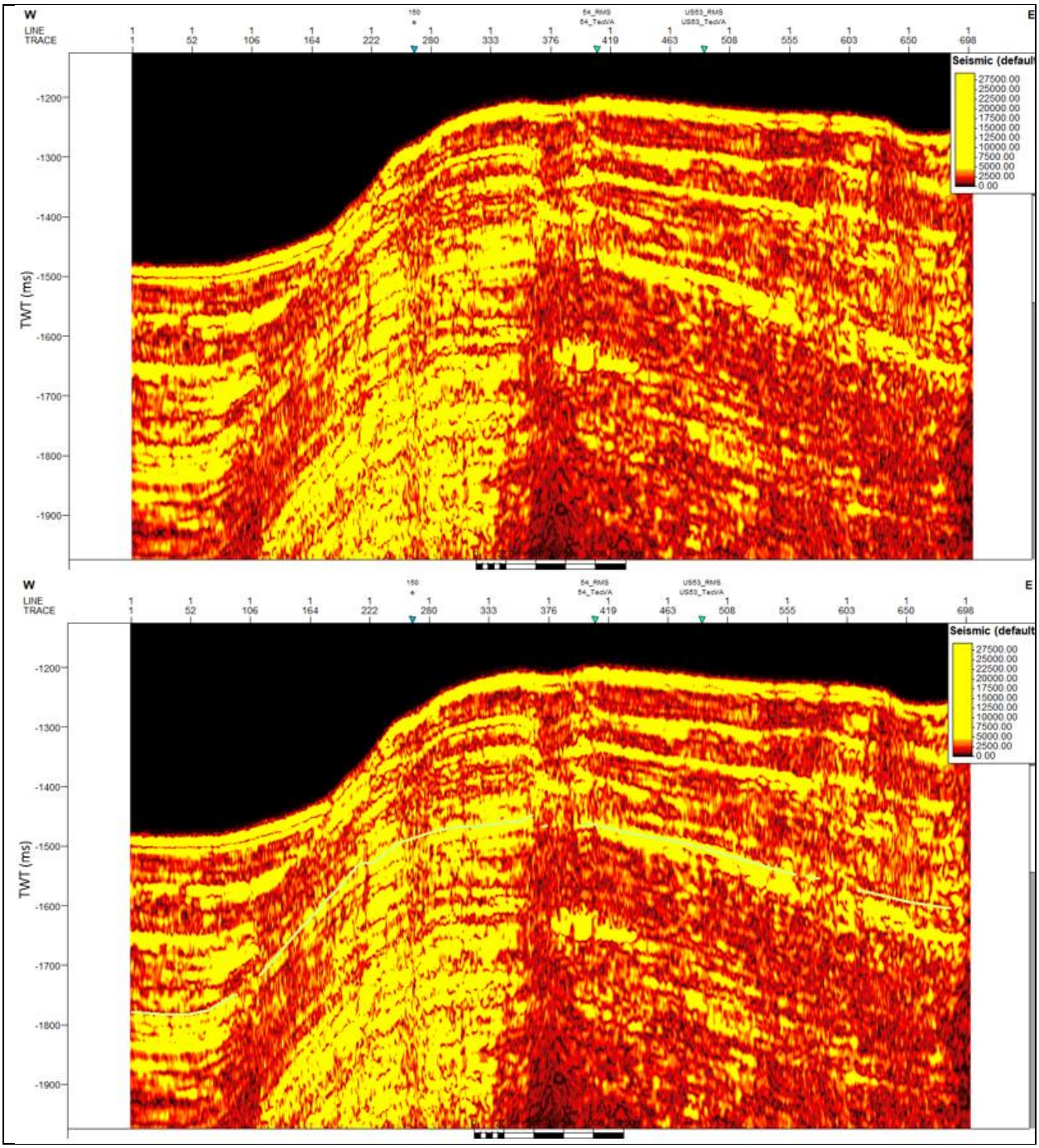

SCS profile US-05 with Spectral Decomposition of 100 Hz plus Envelope. Yellow line indicates the BSR.

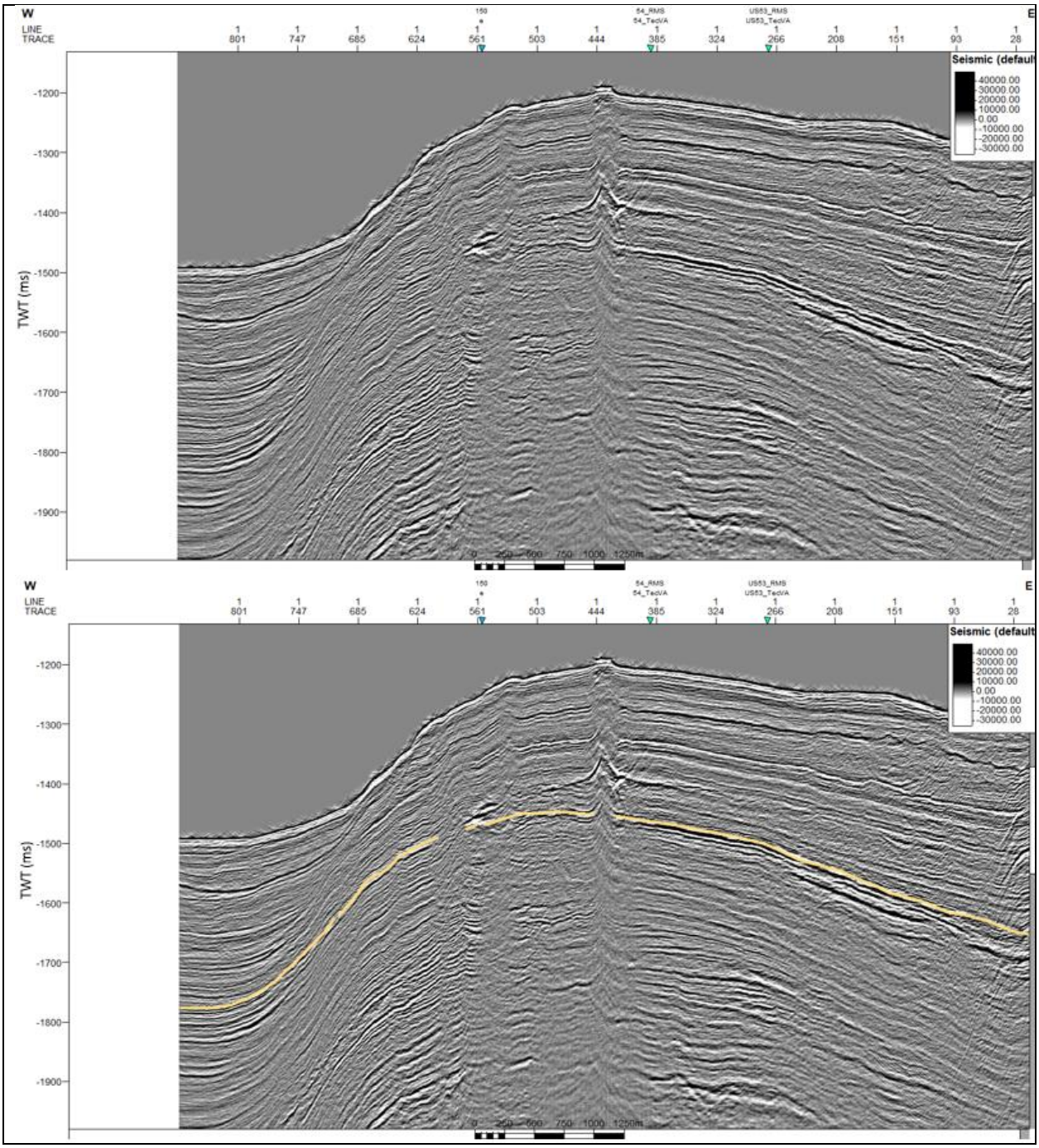

SCS profile US-06 without application of seismic attribute. Yellow line indicates the BSR.

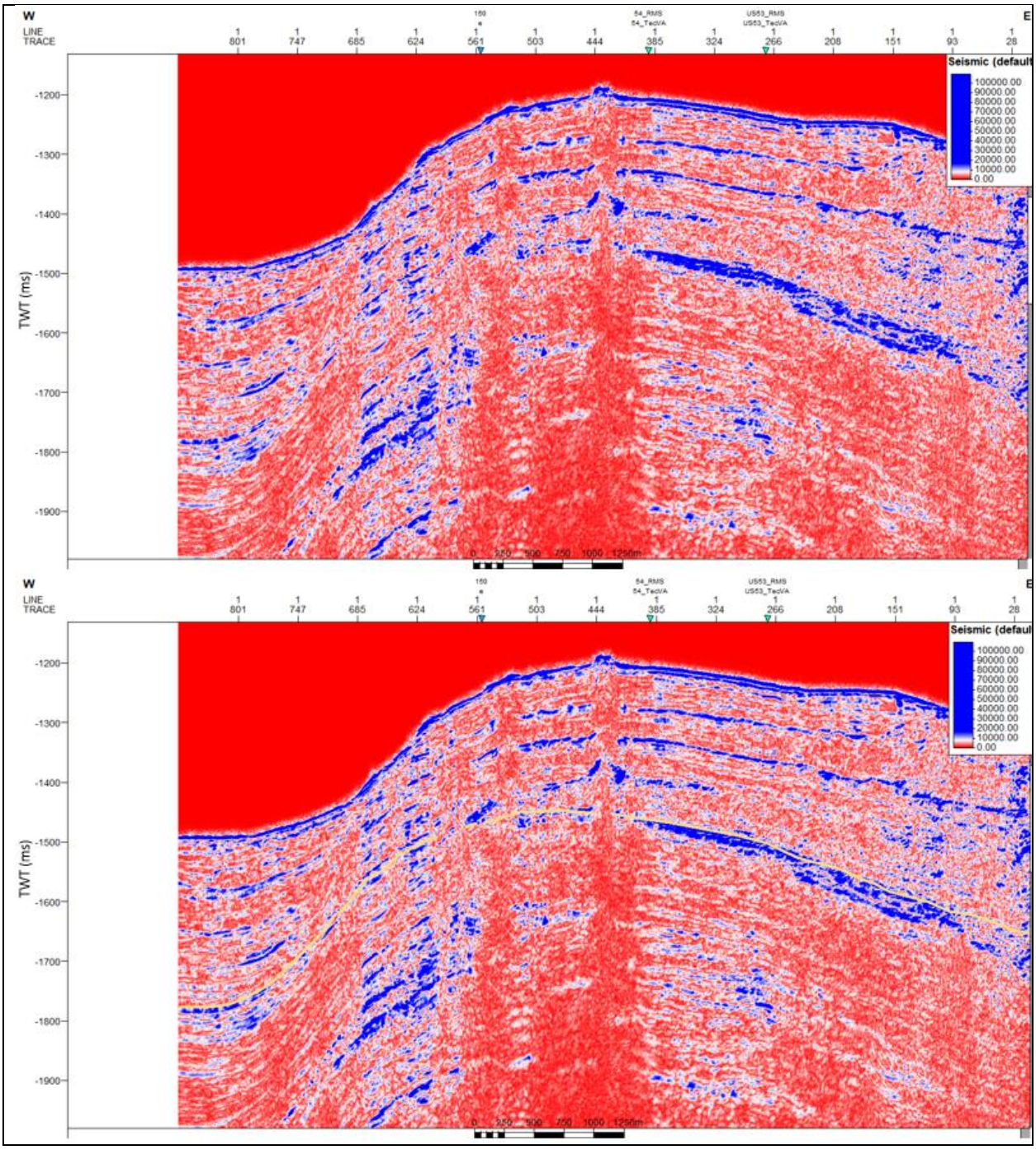

SCS profile US-06 with Envelope. Yellow line indicates the BSR.

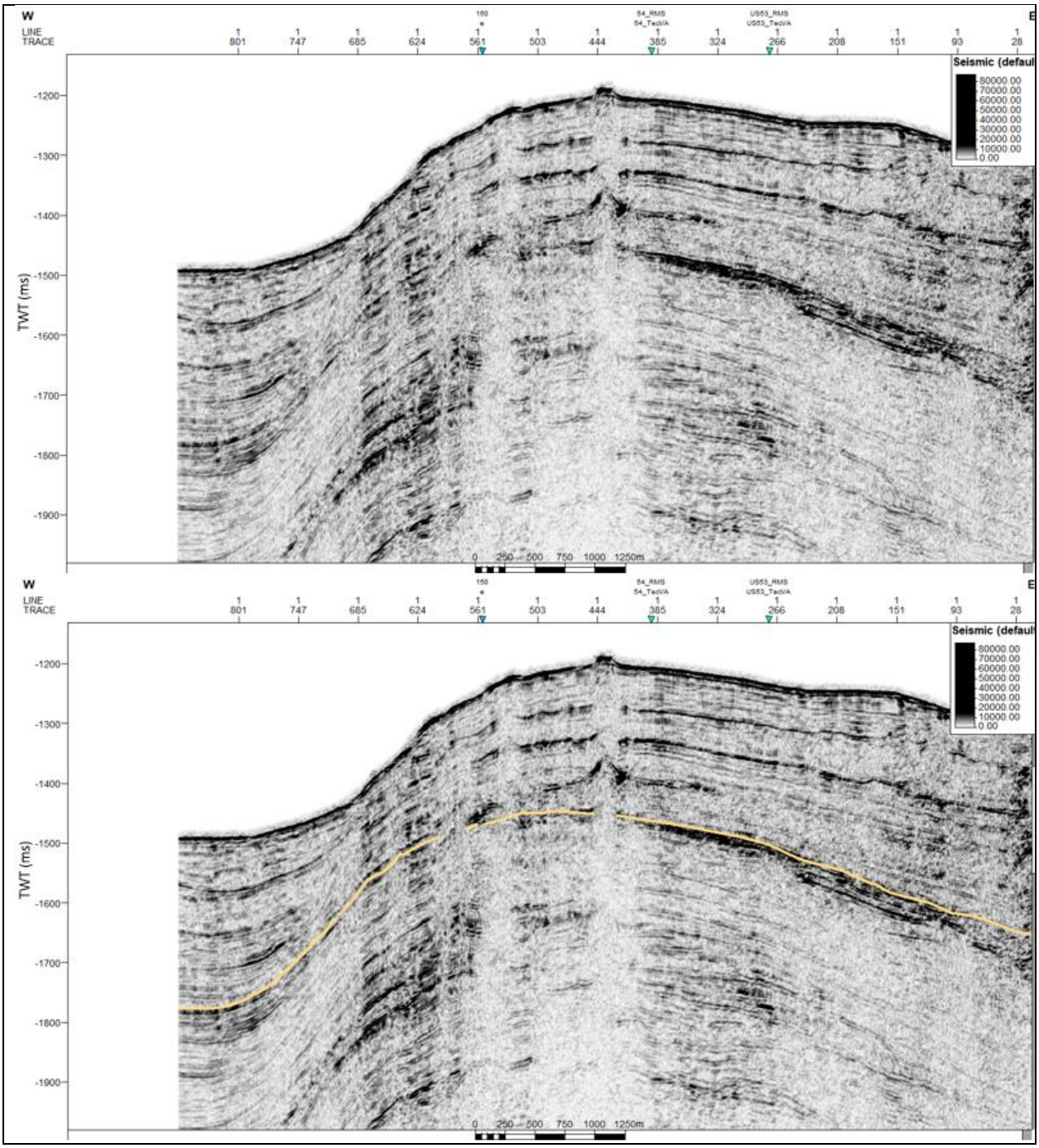

SCS profile US-06 with RMS Amplitude. Yellow line indicates the BSR.

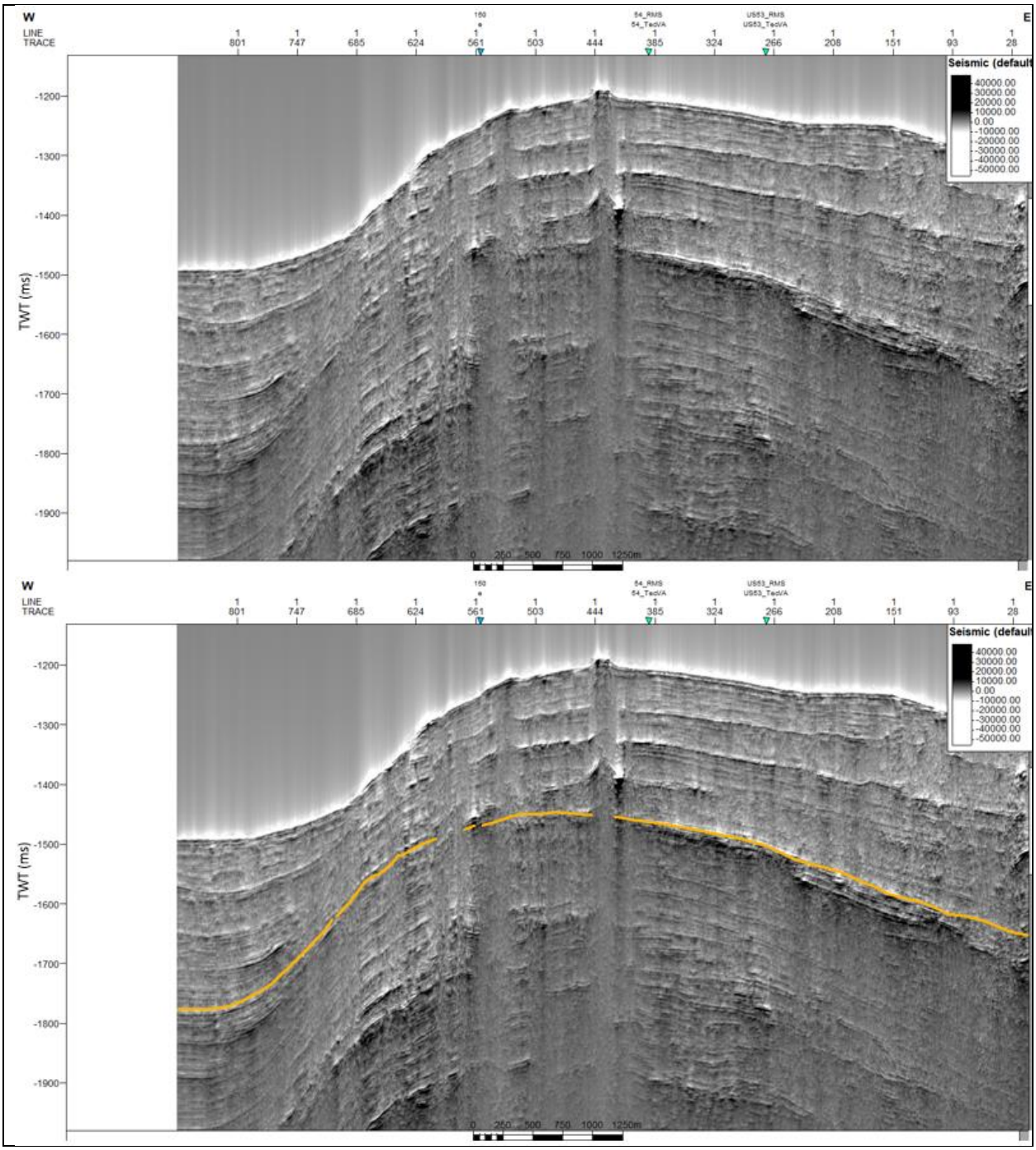

SCS profile US-06 with Amplitude Volume Technique. Orange line indicates the BSR.

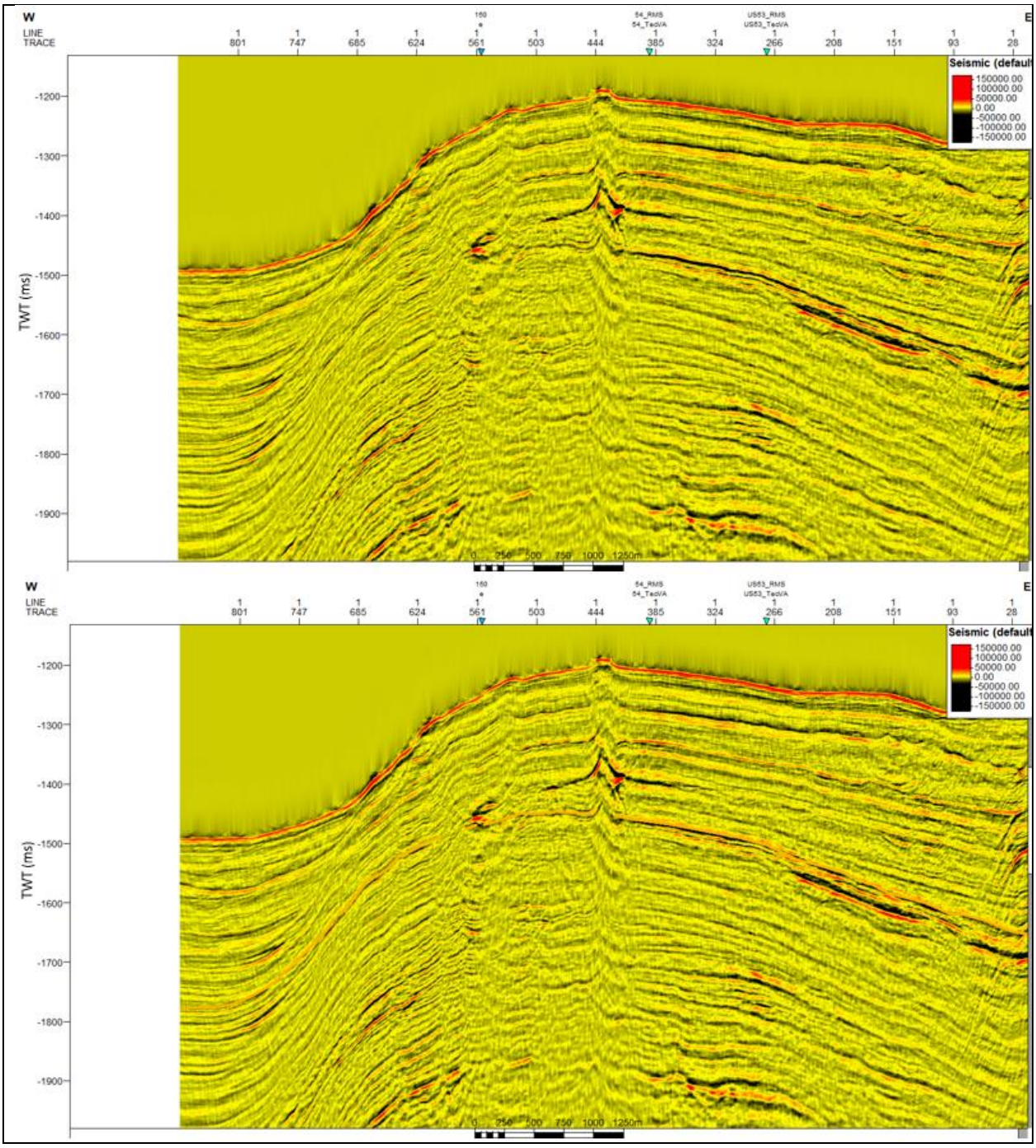

SCS profile US-06 with Relative Acoustic Impedance. Yellow line indicates the BSR.

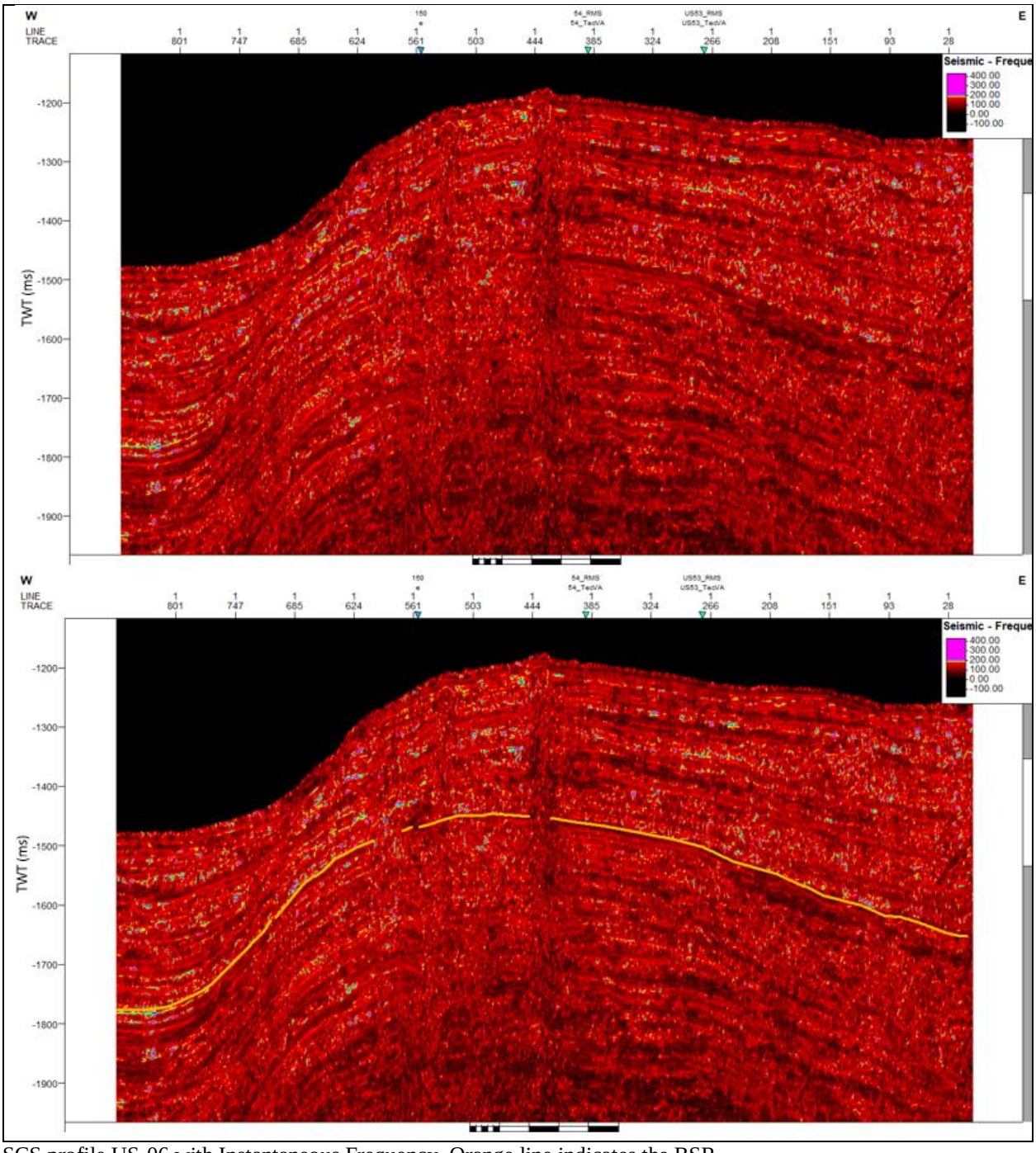

SCS profile US-06 with Instantaneous Frequency. Orange line indicates the BSR.

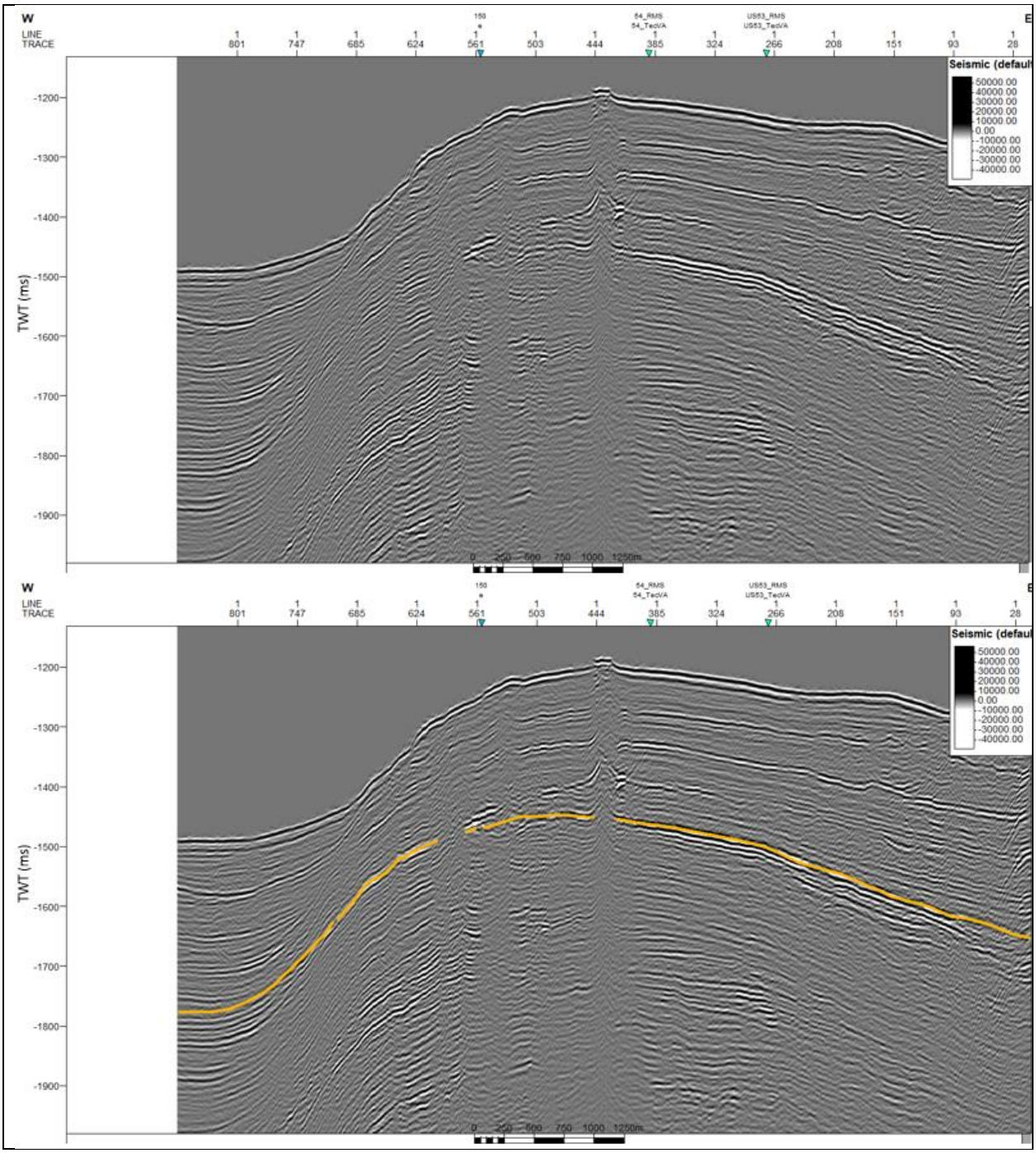

SCS profile US-06 with Spectral Decomposition with 100 Hz. Orange line indicates the BSR.

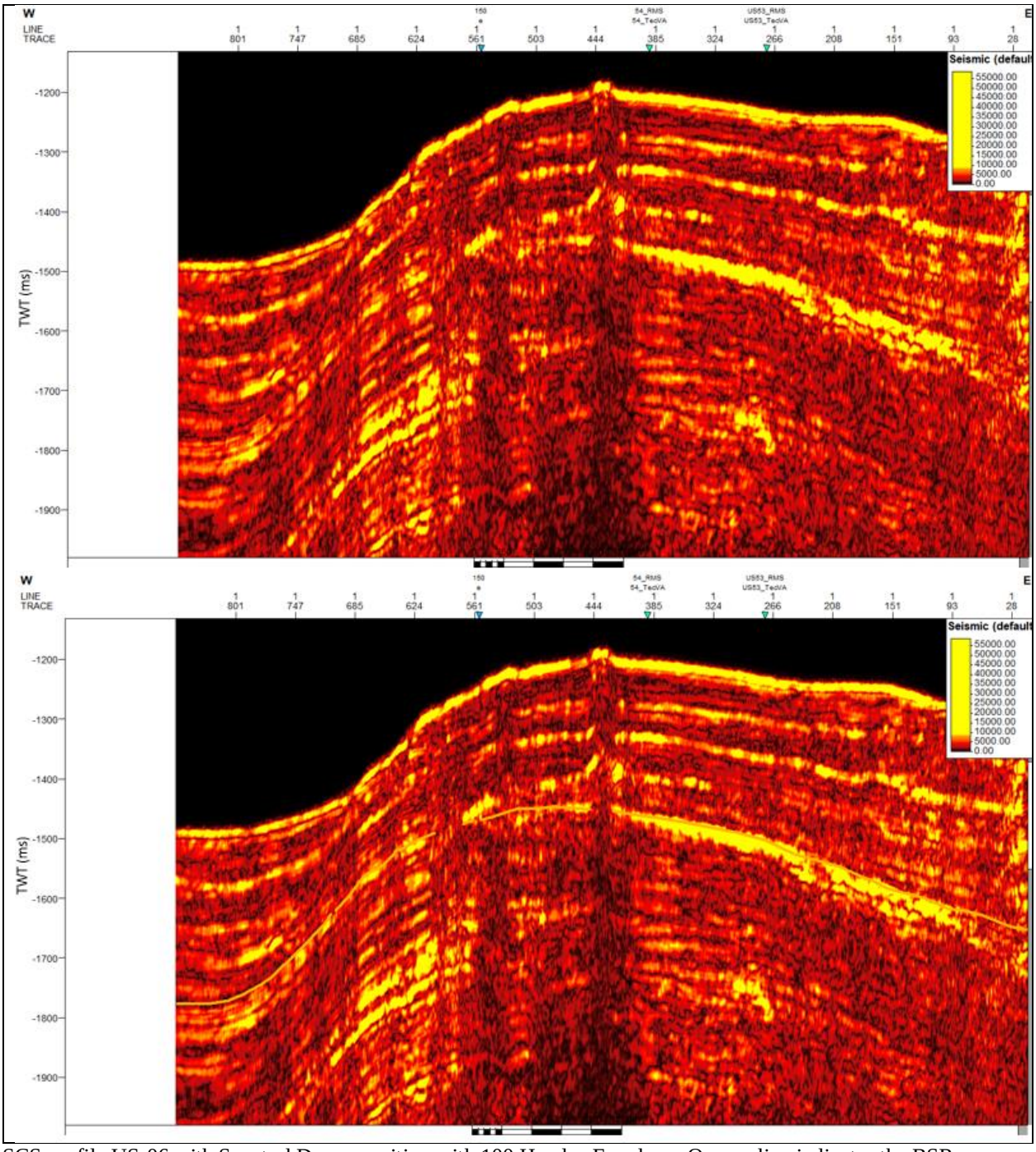

SCS profile US-06 with Spectral Decomposition with 100 Hz plus Envelope. Orange line indicates the BSR.

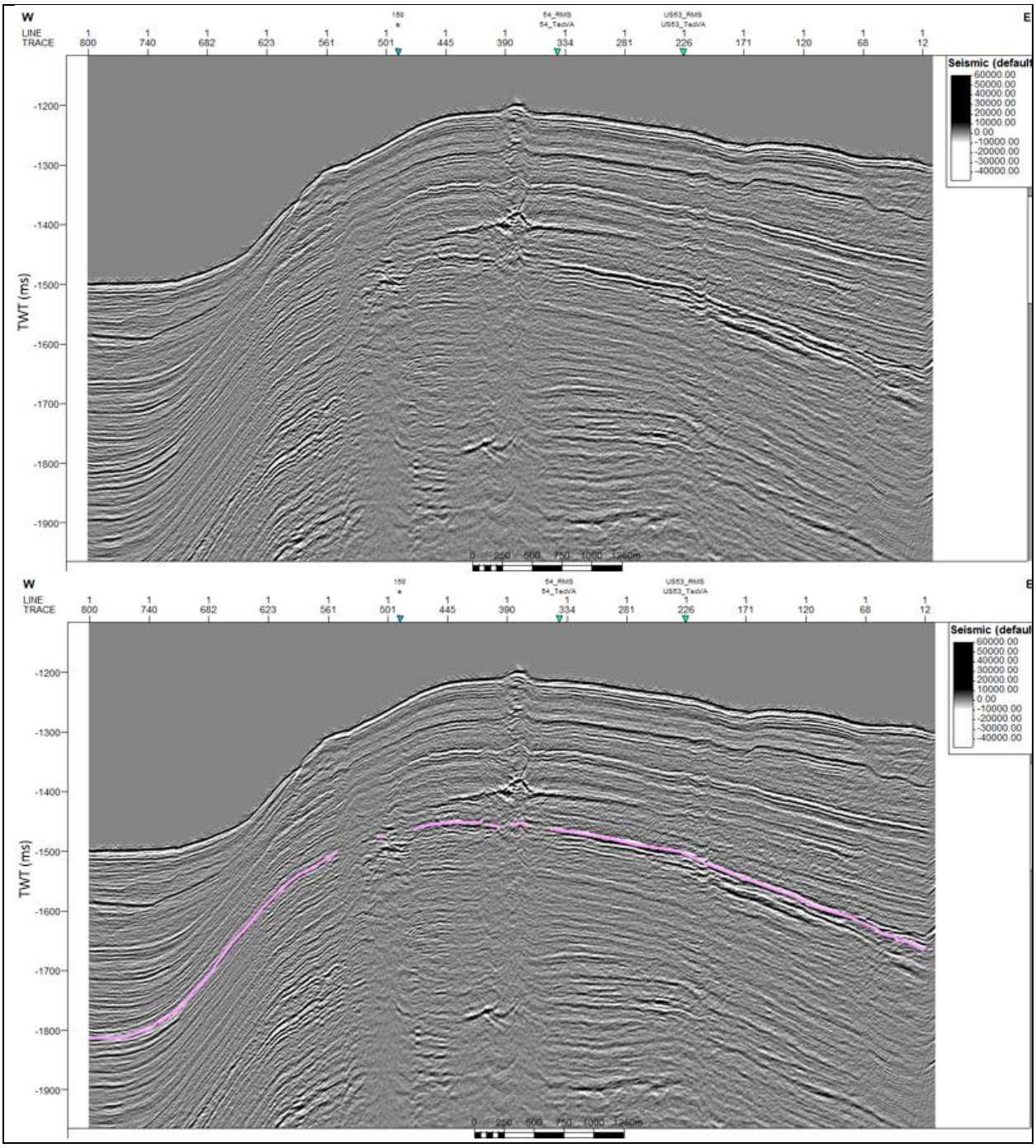

SCS profile US-07 without application of seismic attribute. Lilac line indicates BSR.

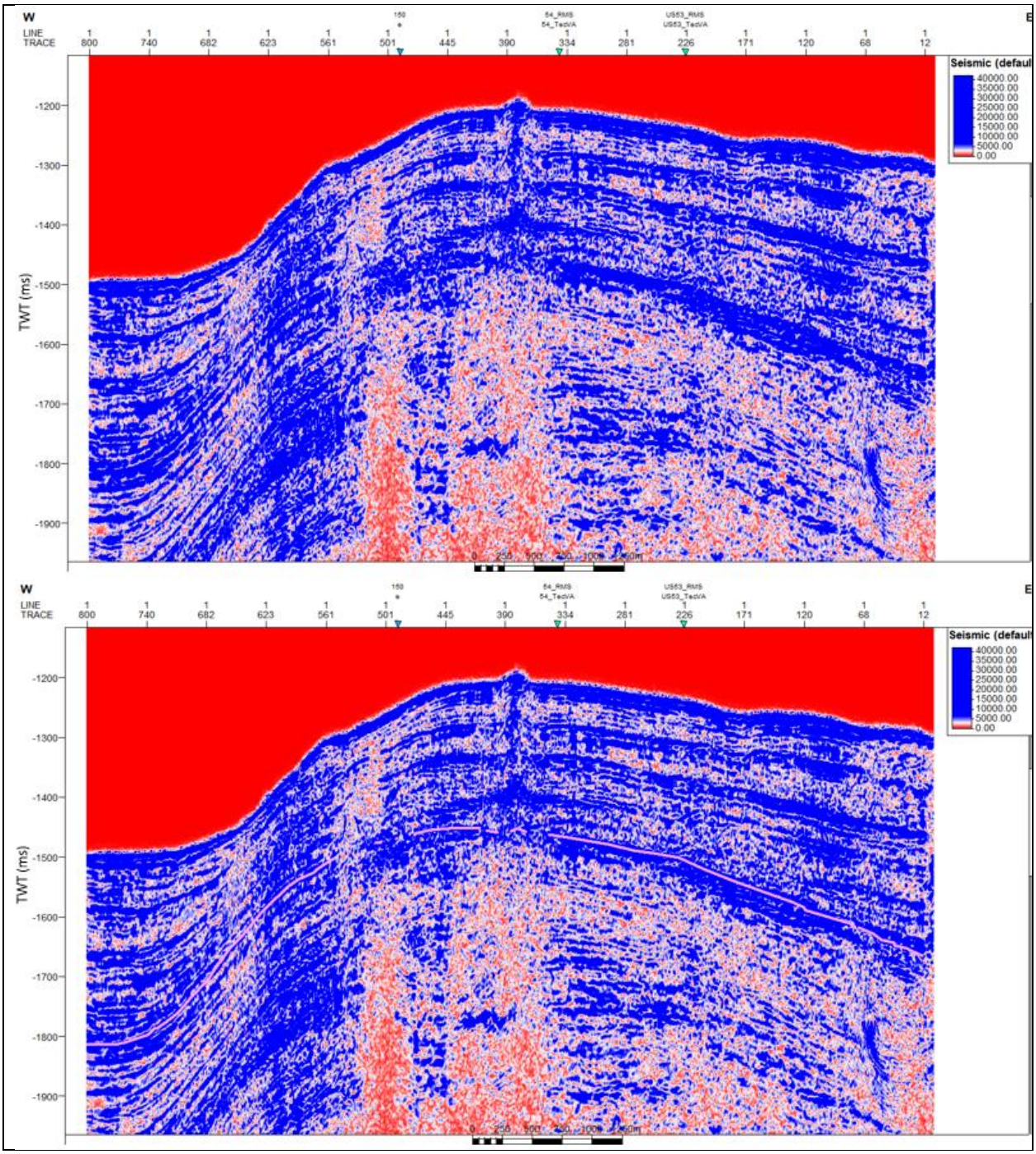

SCS profile US-07 with Envelope. Lilac line indicates BSR.

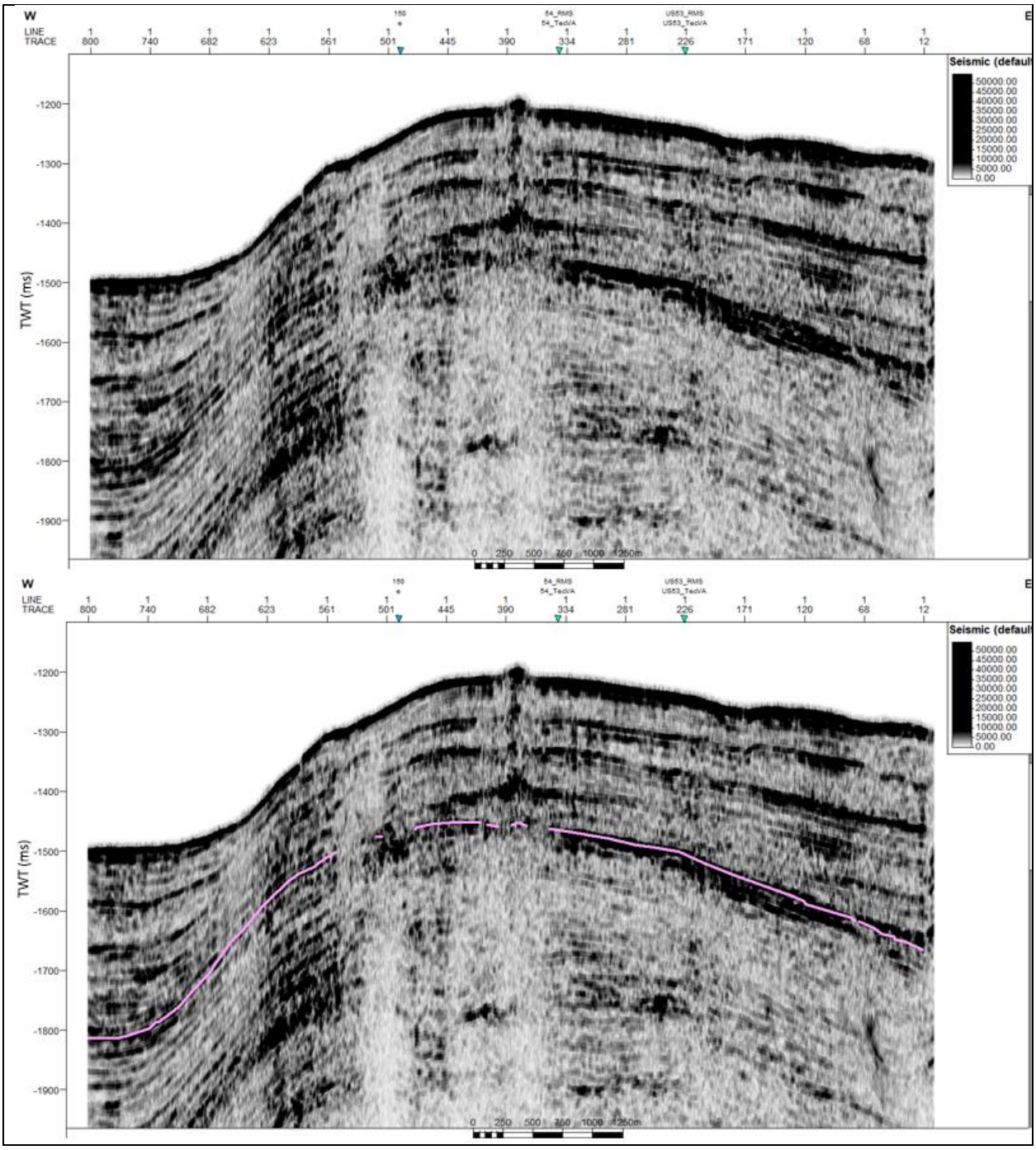

SCS profile US-07 with RMS Amplitude. Lilac line indicates BSR.

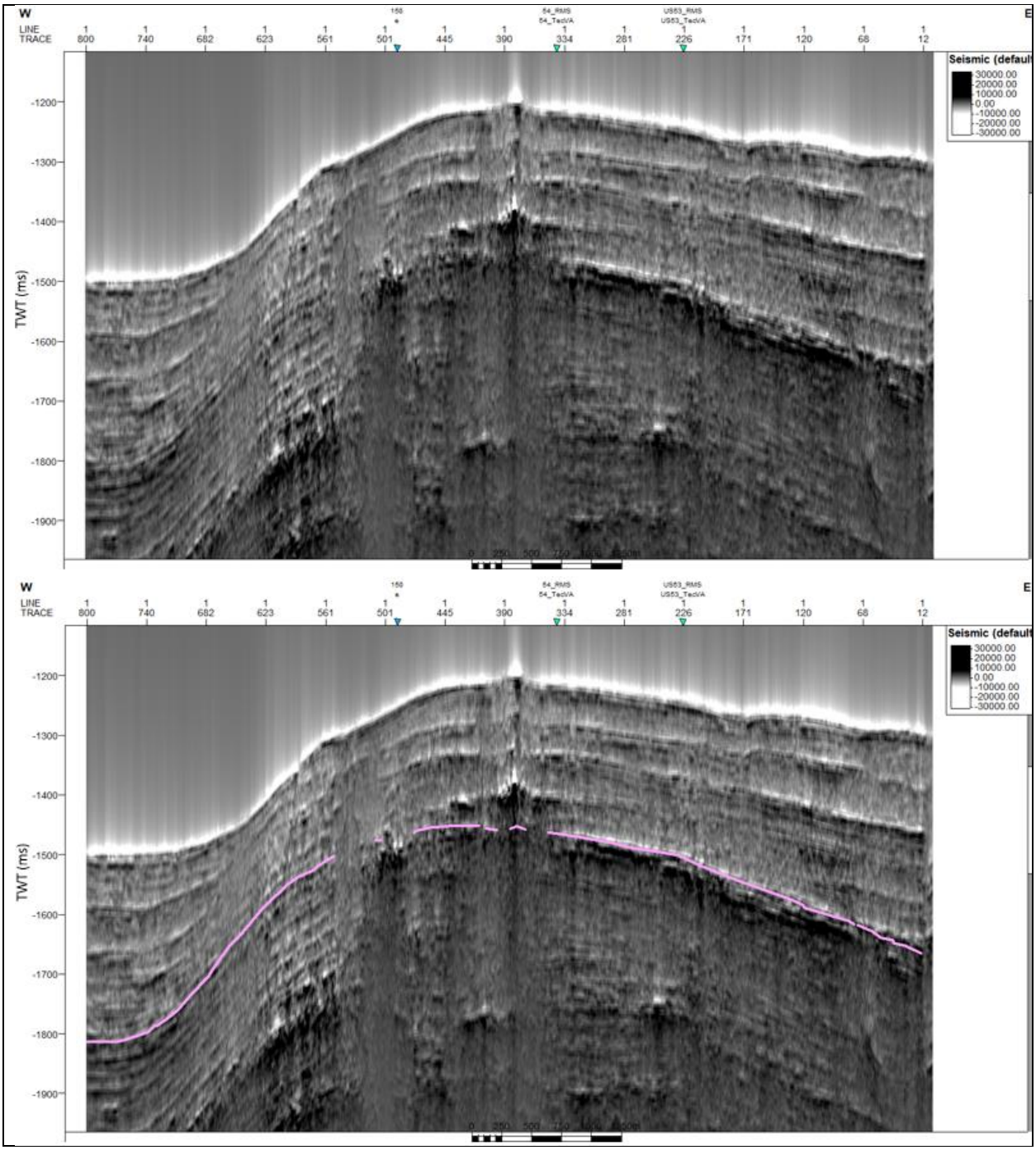

SCS profile US-07 with Amplitude Volume Technique. Lilac line indicates BSR.

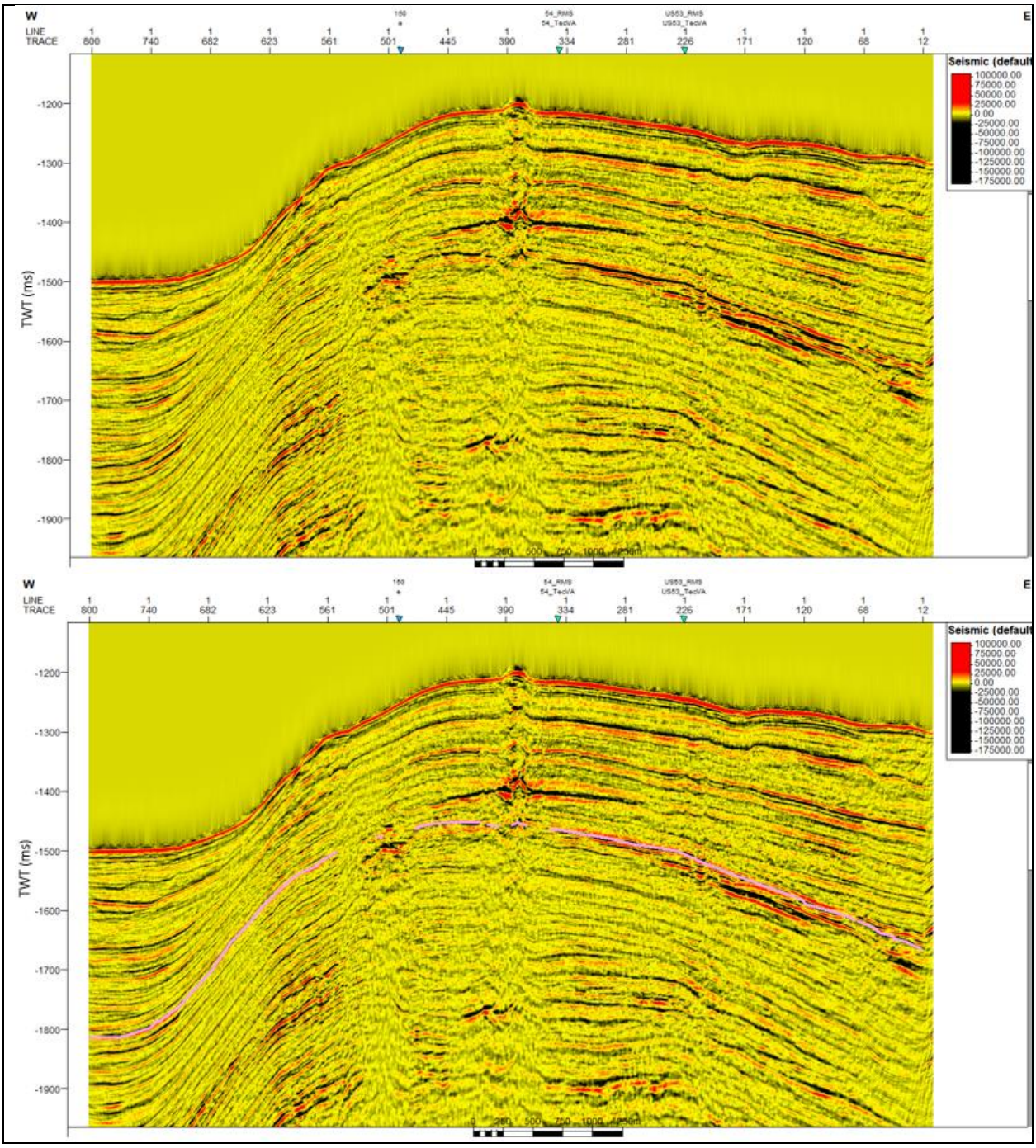

SCS profile US-07 with Relative Acoustic Impedance. Lilac line indicates BSR.

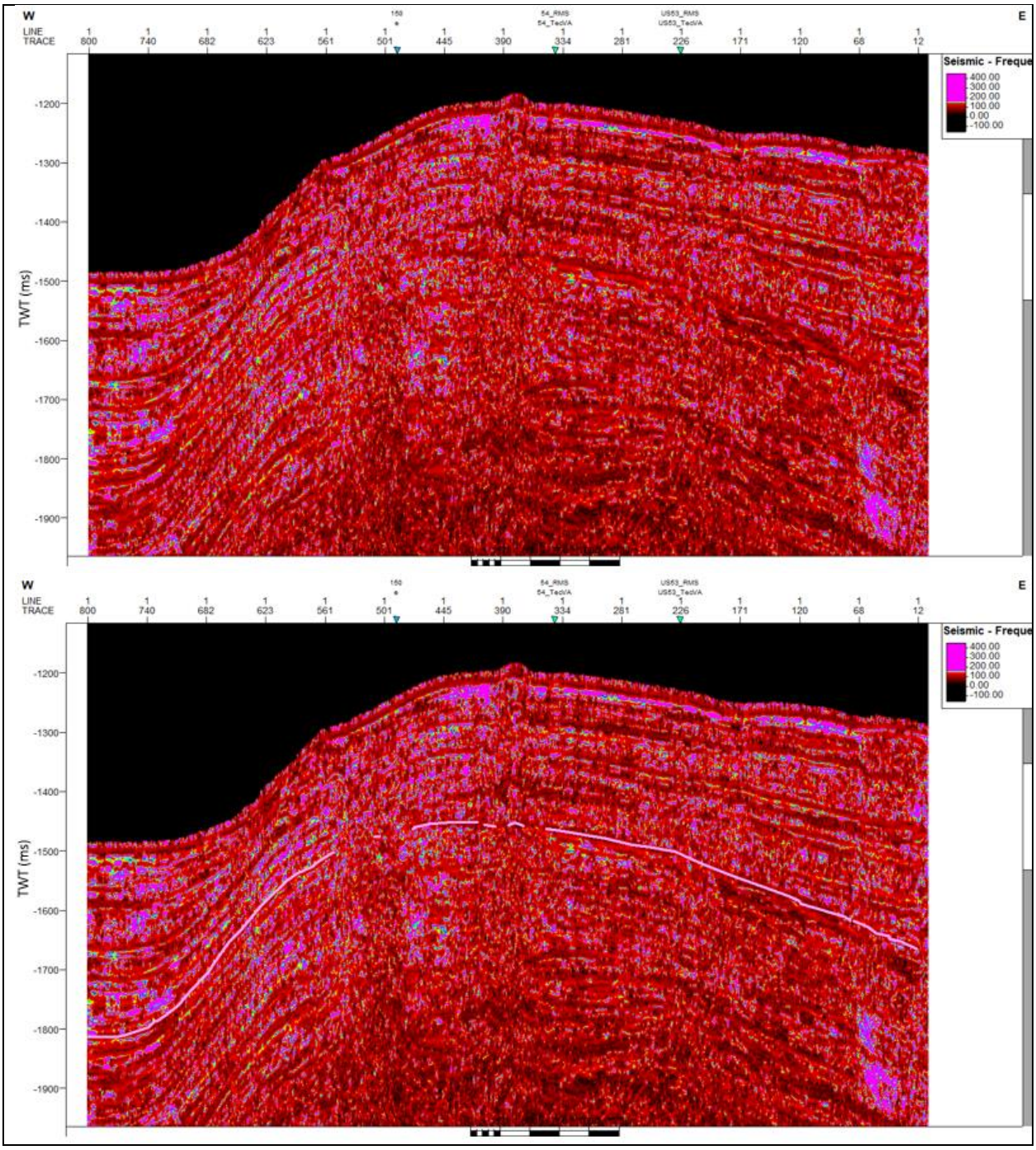

SCS profile US-07 with Instantaneous Frequency. Lilac line indicates BSR.

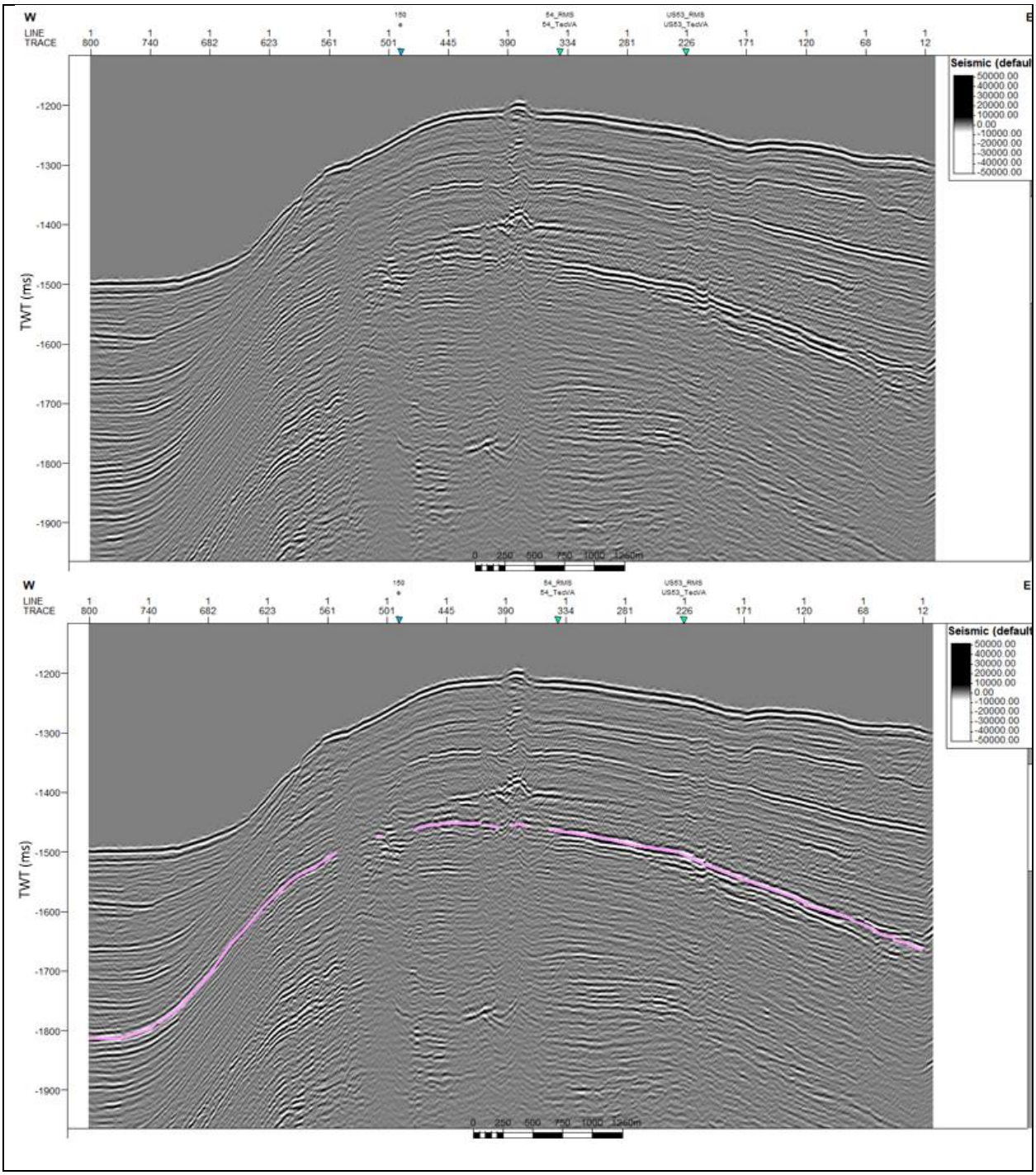

SCS profile US-07 with Spectral Decomposition of 100 Hz. Lilac line indicates BSR.

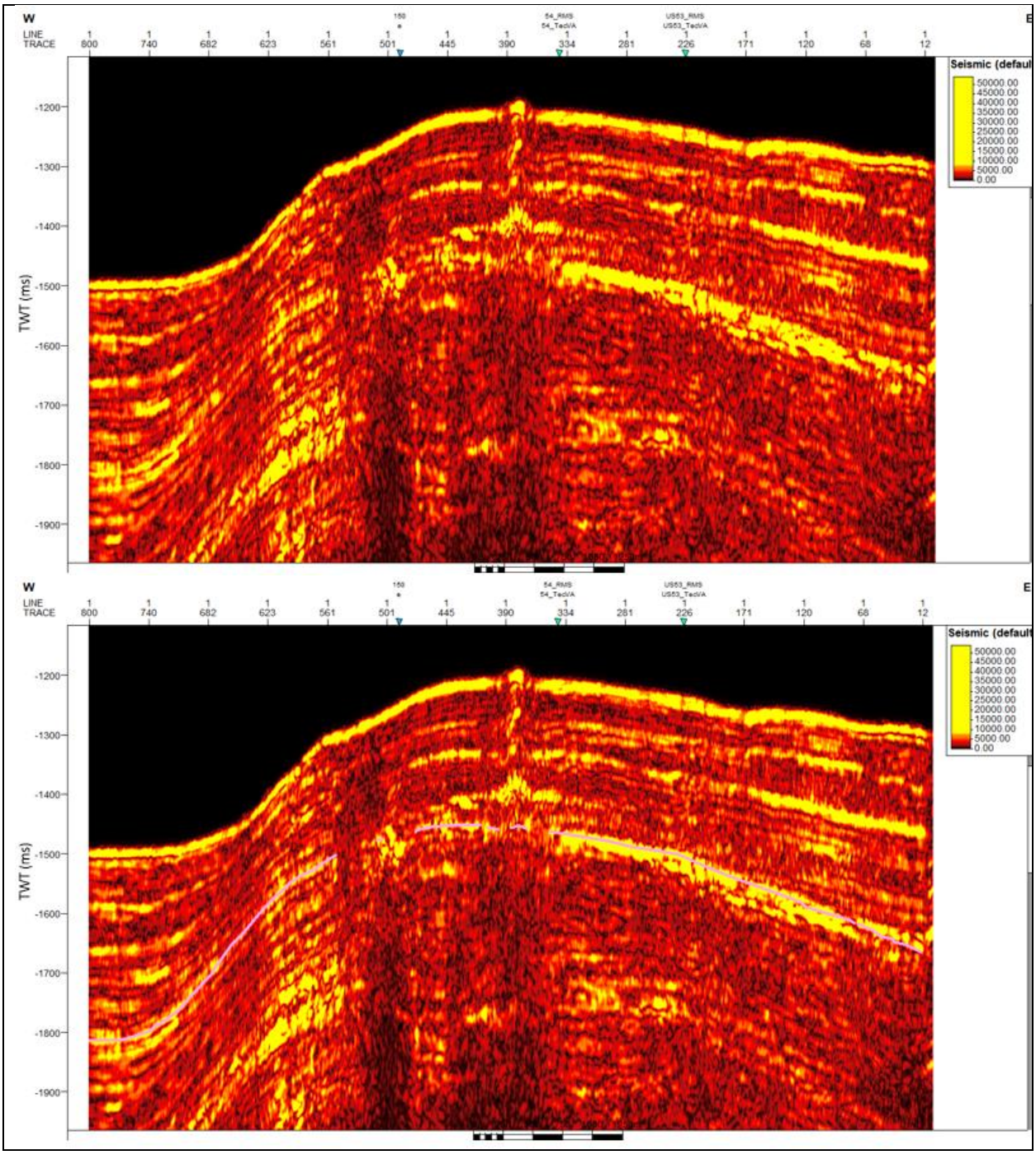

SCS profile US-07 with Spectral Decomposition of 100 Hz plus Envelope. Lilac line indicates BSR.

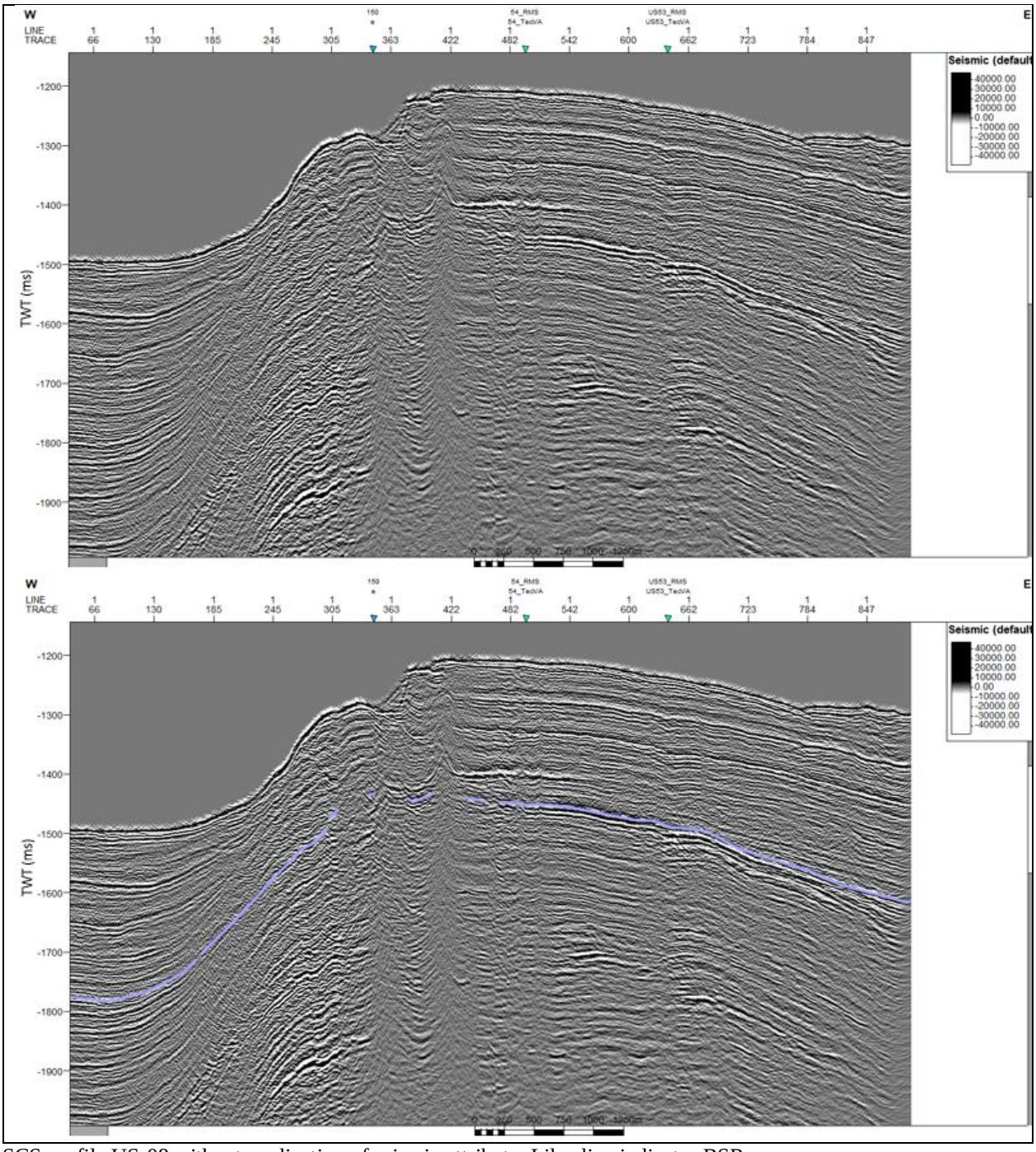

SCS profile US-08 without application of seismic attribute. Lilac line indicates BSR.

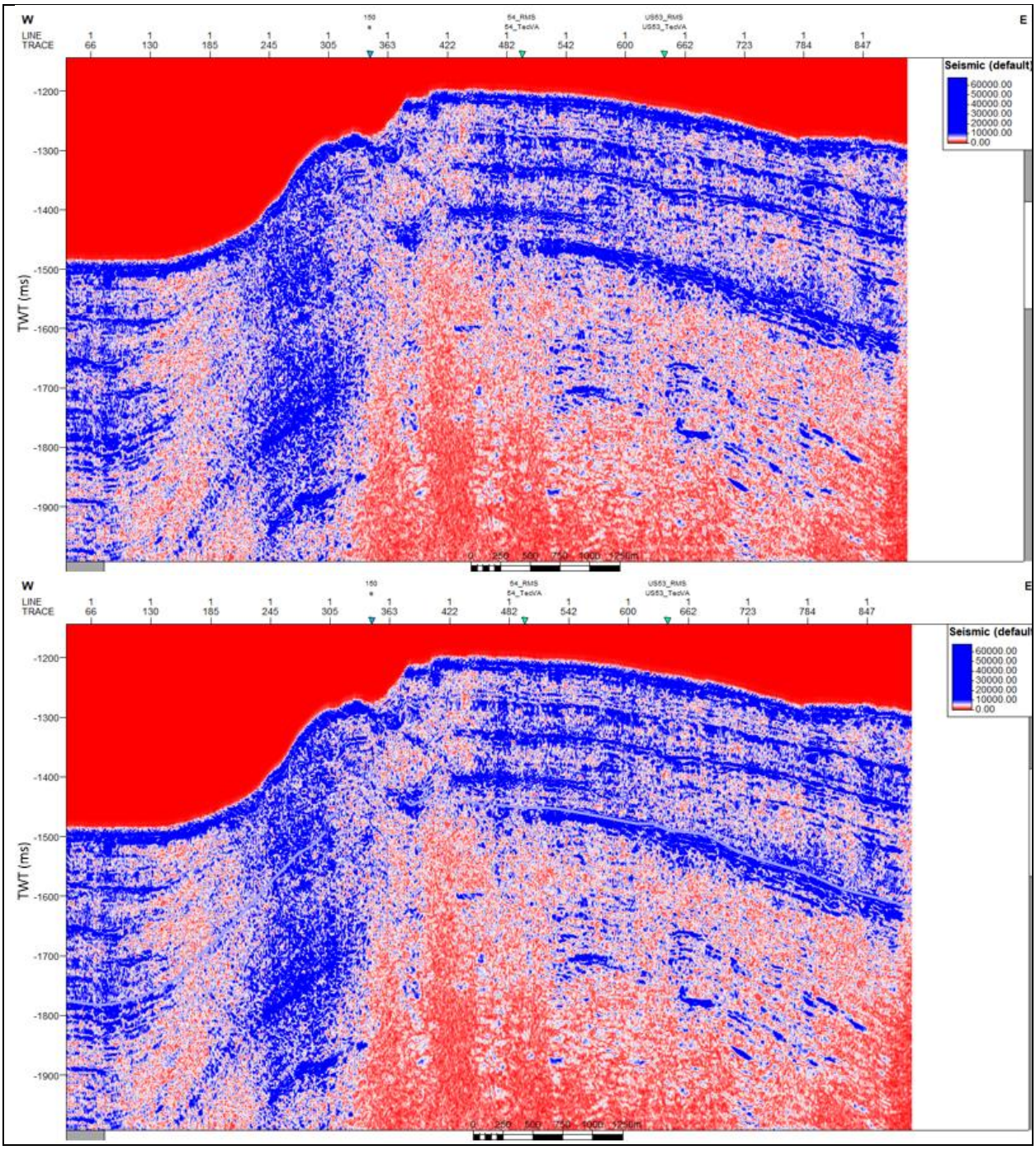

SCS profile US-08 with Envelope. Lilac line indicates BSR.

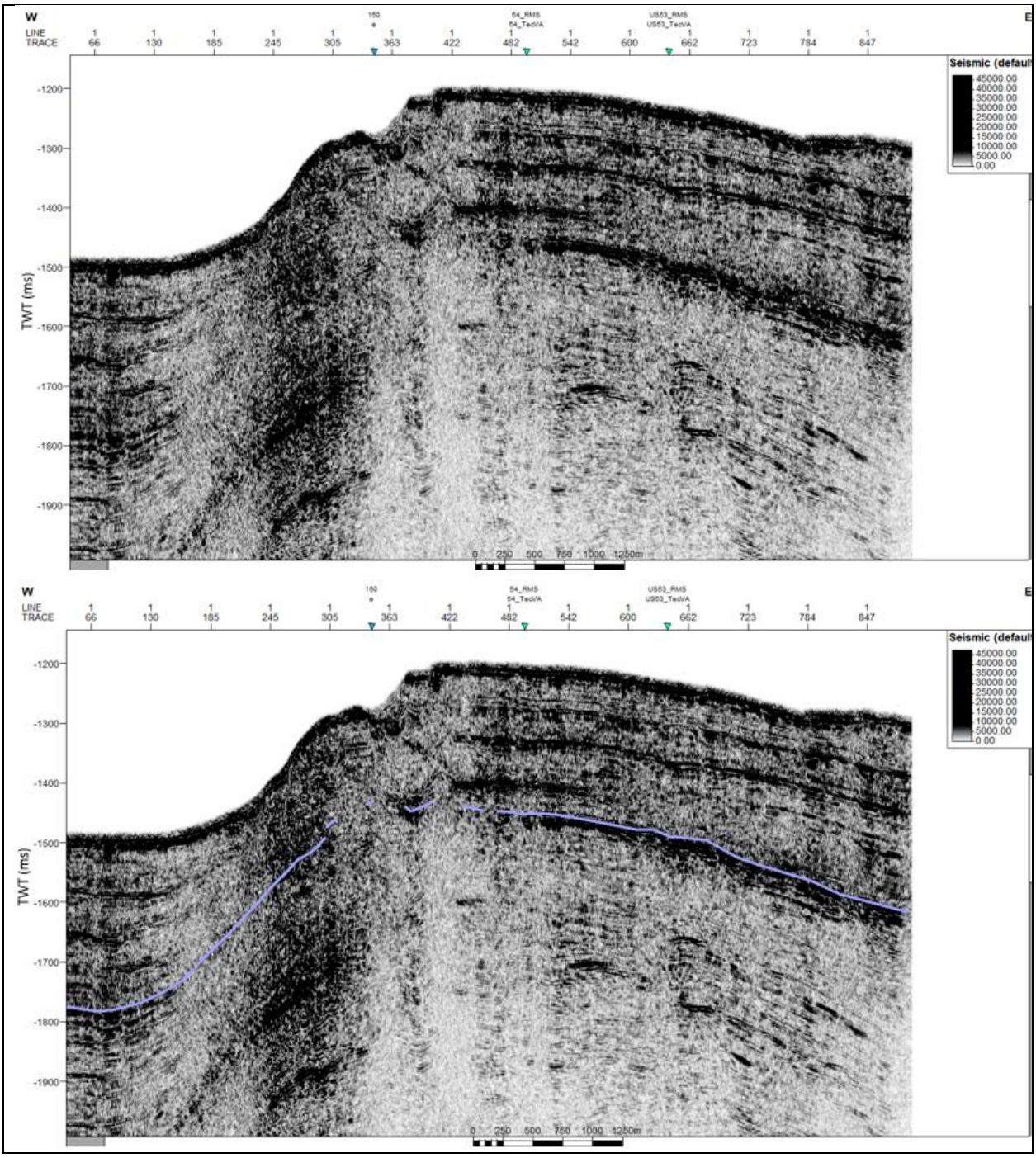

SCS profile US-08 with RMS Amplitude. Lilac line indicates BSR.

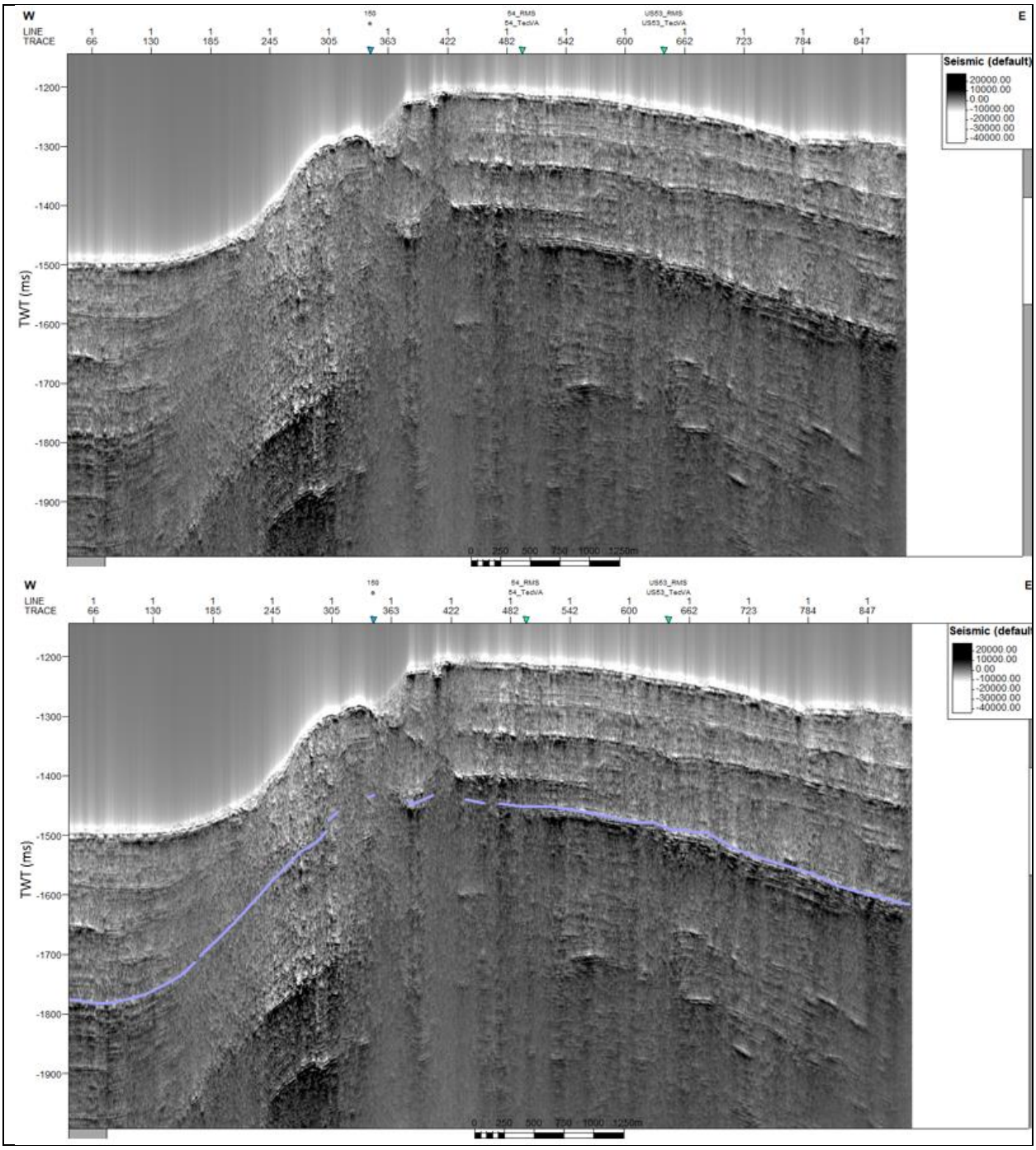

SCS profile US-08 with Amplitude Volume Technique. Lilac line indicates BSR.

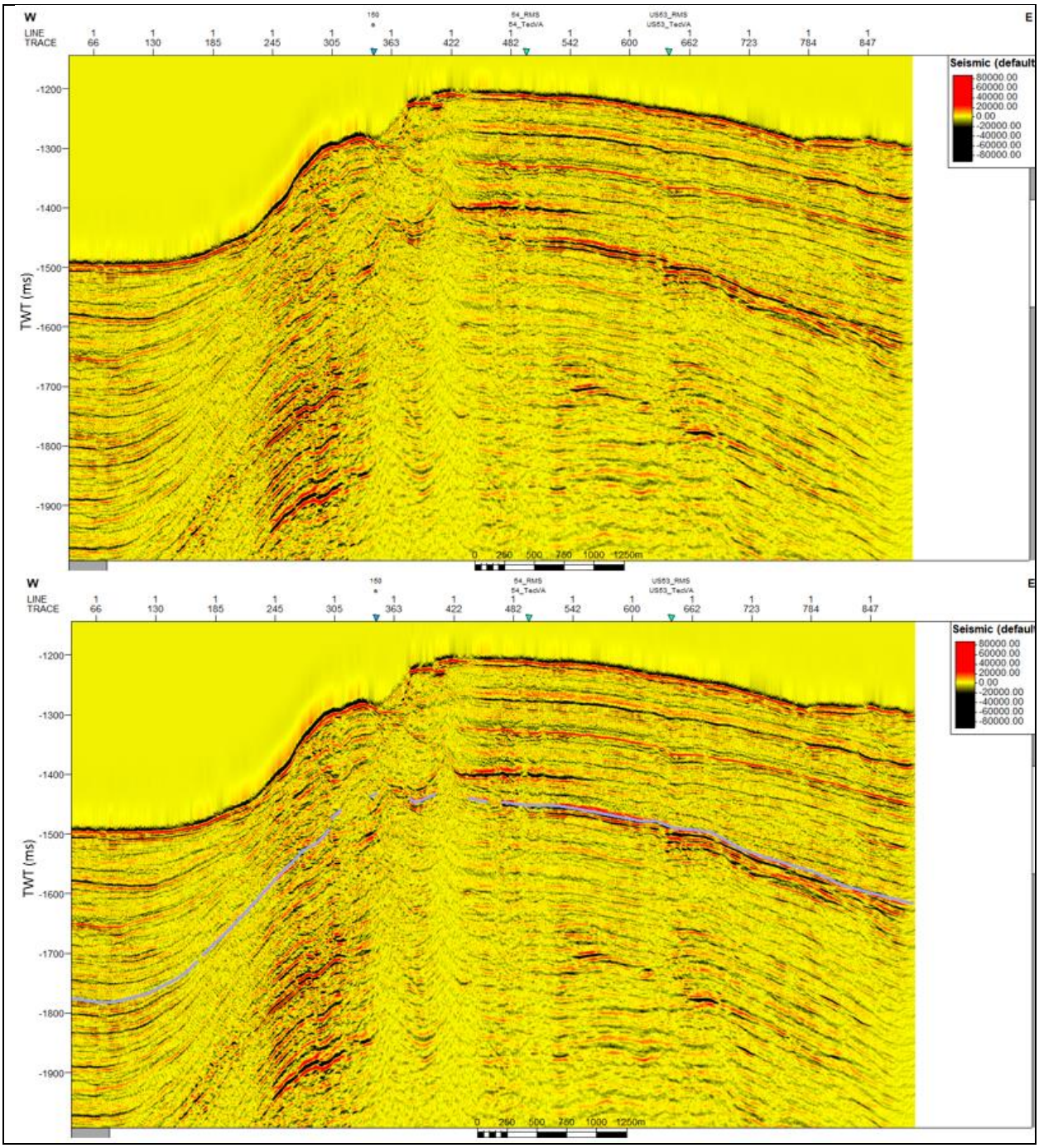

SCS profile US-08 with Relative Acoustic Impedance. Lilac line indicates BSR.

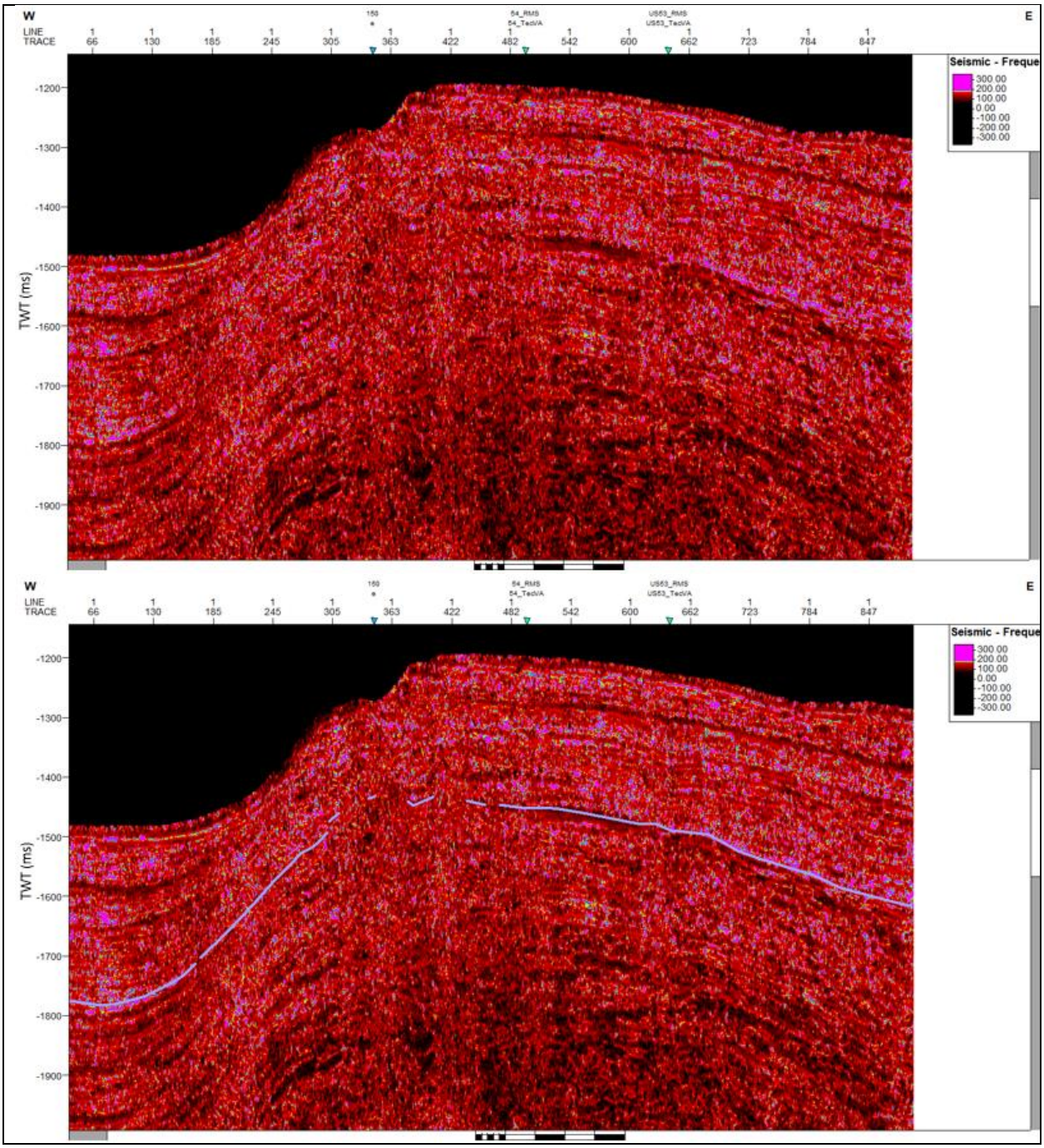

SCS profile US-08 with Instantaneous Frequency. Lilac line indicates BSR.

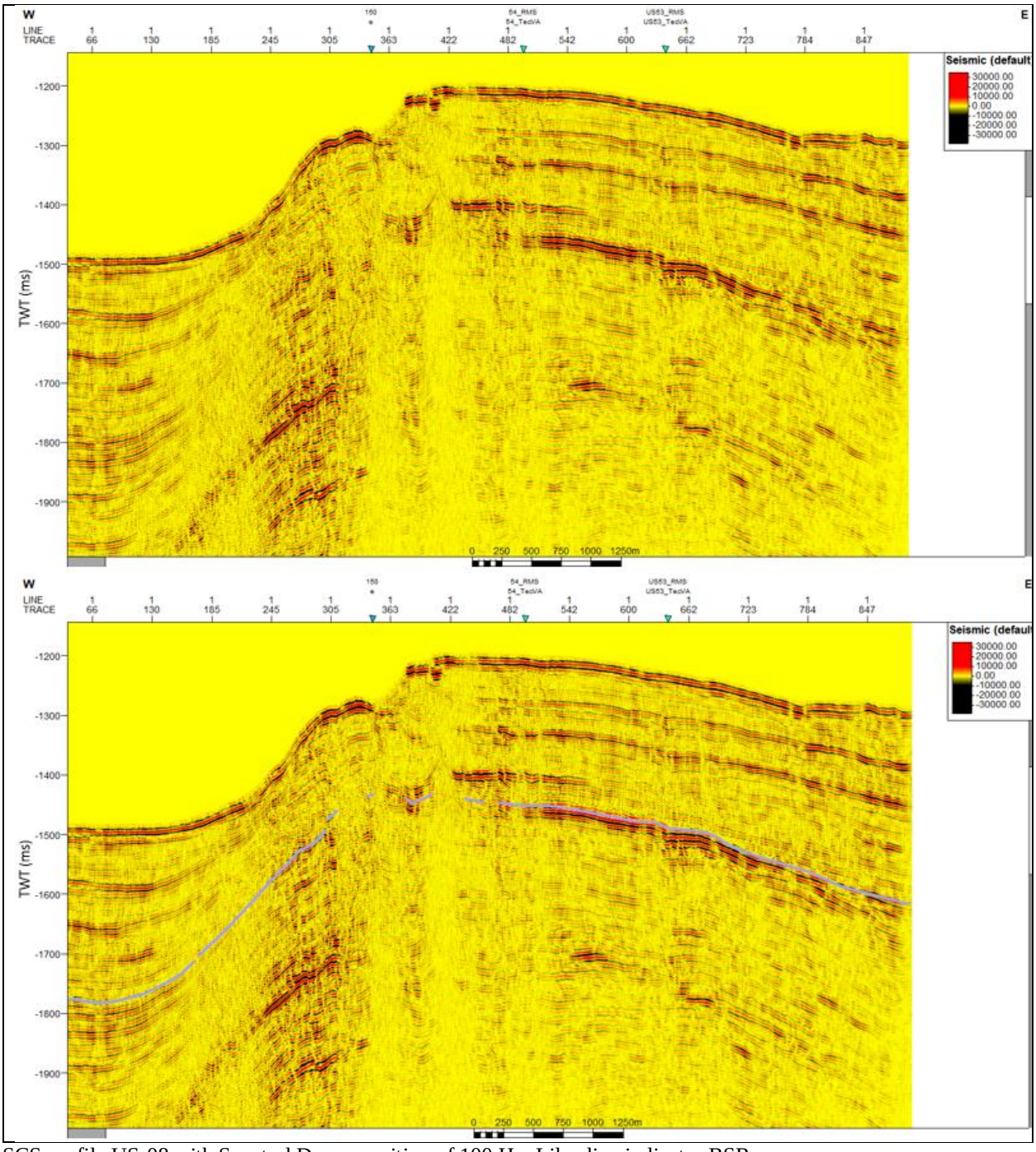

SCS profile US-08 with Spectral Decomposition of 100 Hz. Lilac line indicates BSR.

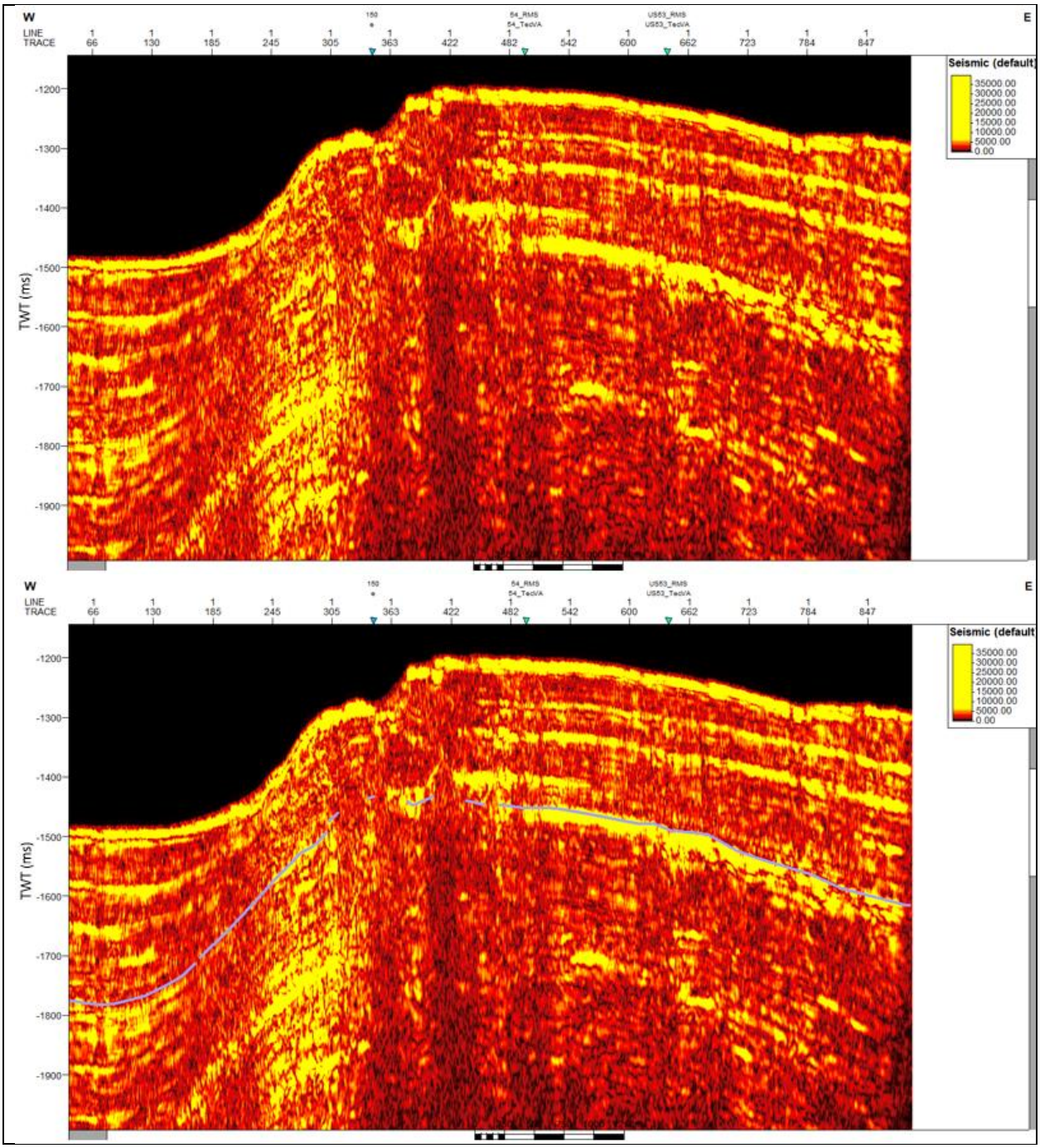

SCS profile US-08 with Spectral Decomposition of 100 Hz plus Envelope. Lilac line indicates BSR.

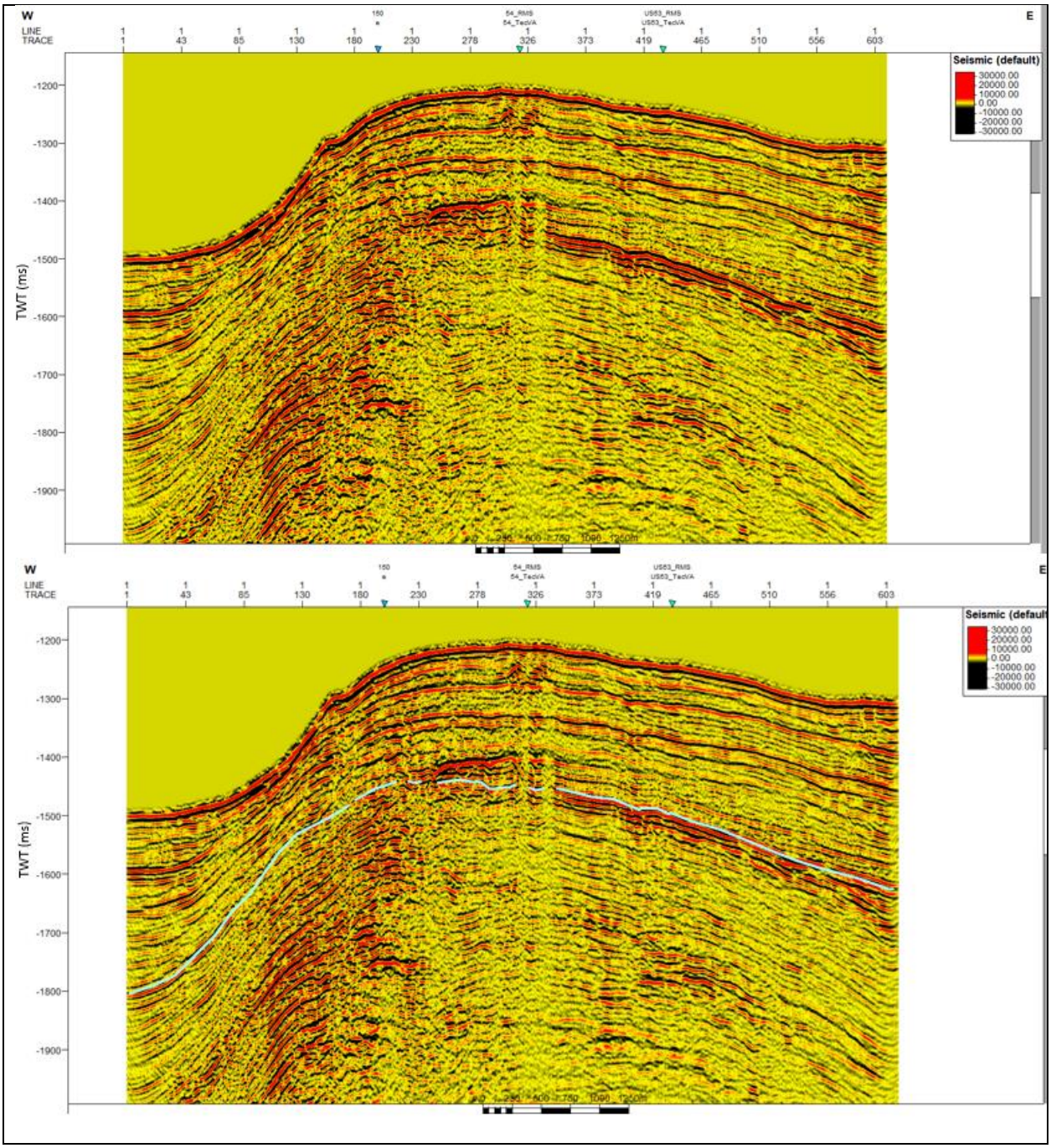

SCS profile US-09 without application of seismic attribute. Blue line indicates BSR.

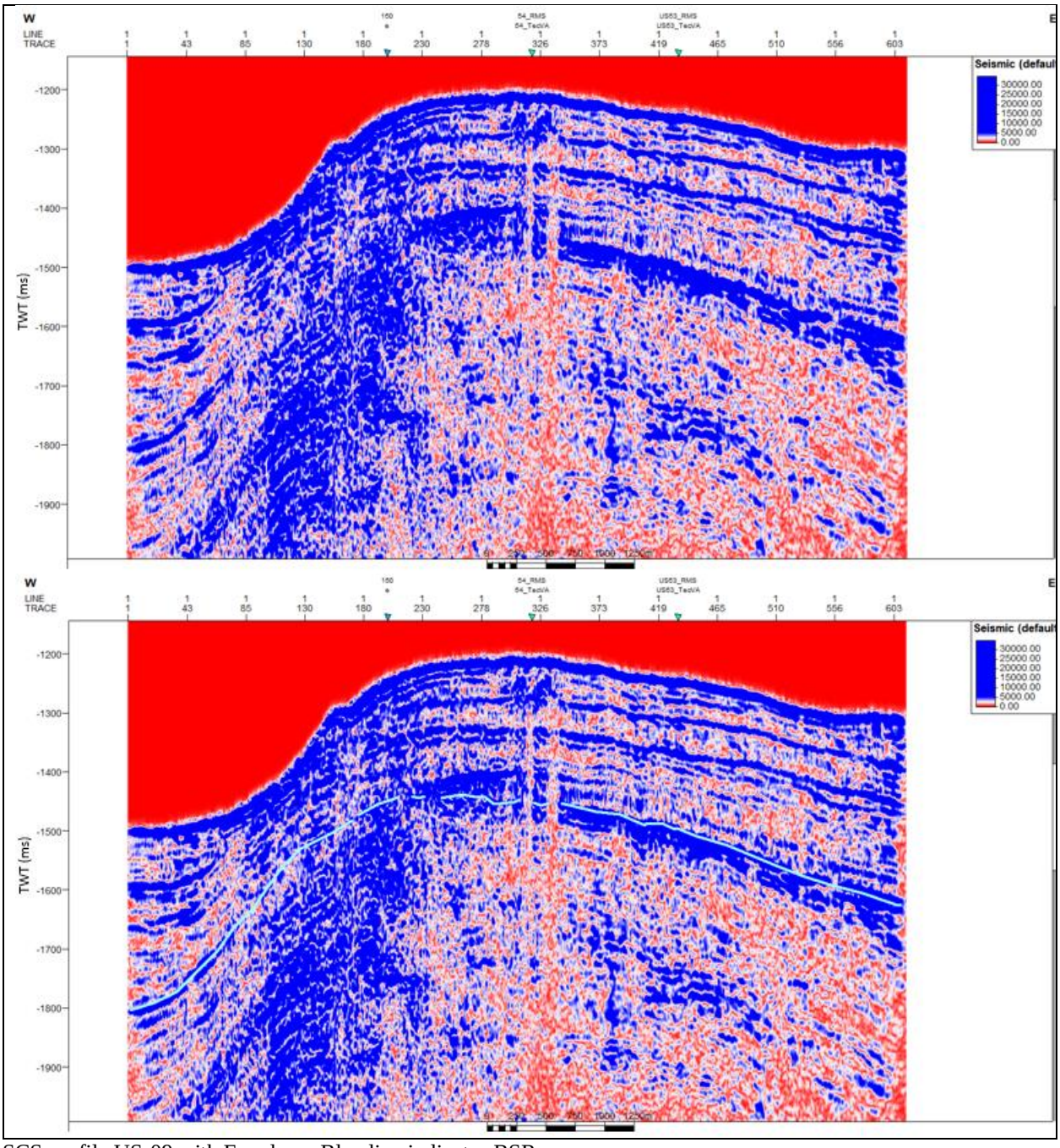

SCS profile US-09 with Envelope. Blue line indicates BSR.

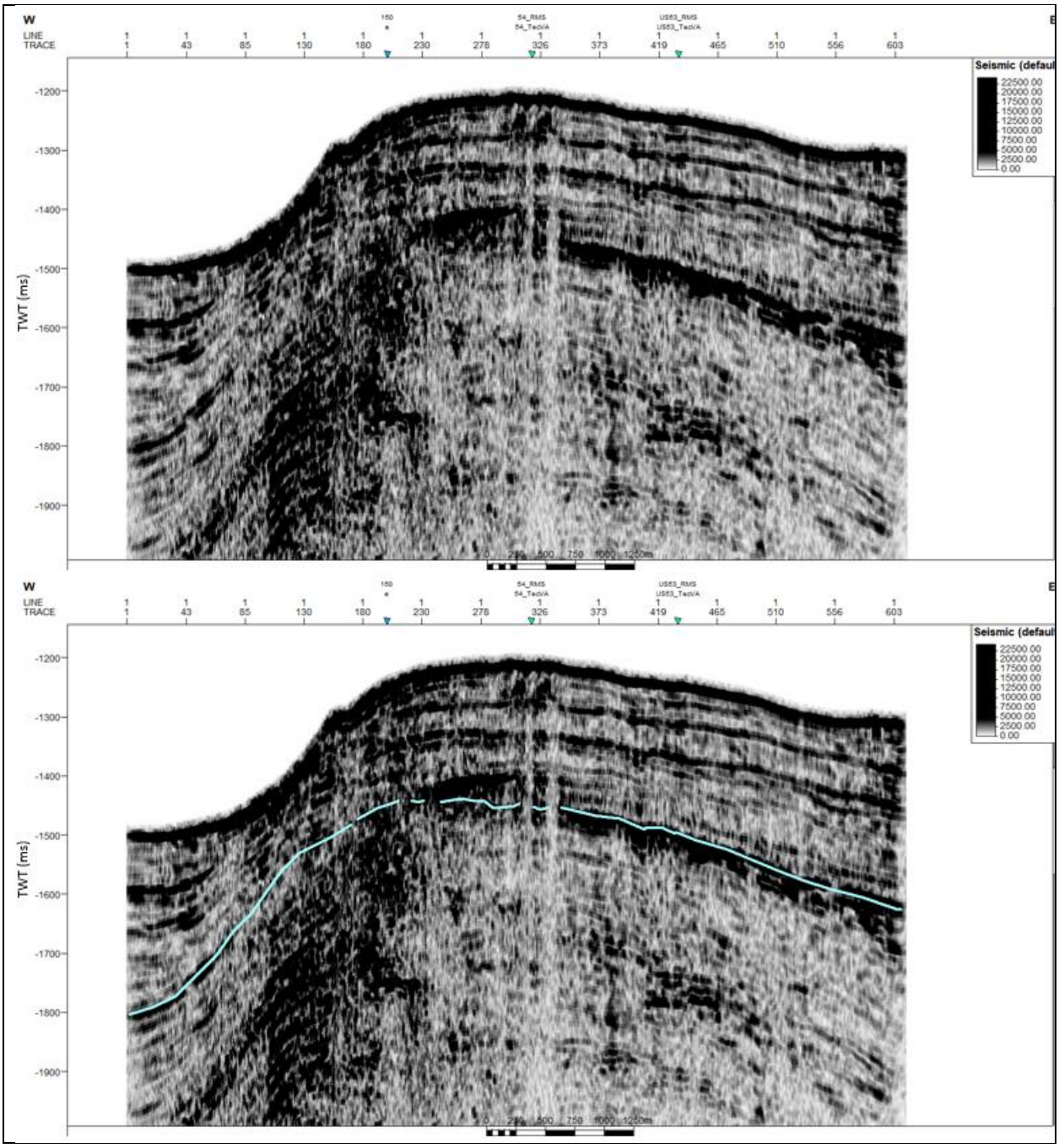

SCS profile US-09 with RMS Amplitude. Blue line indicates BSR.

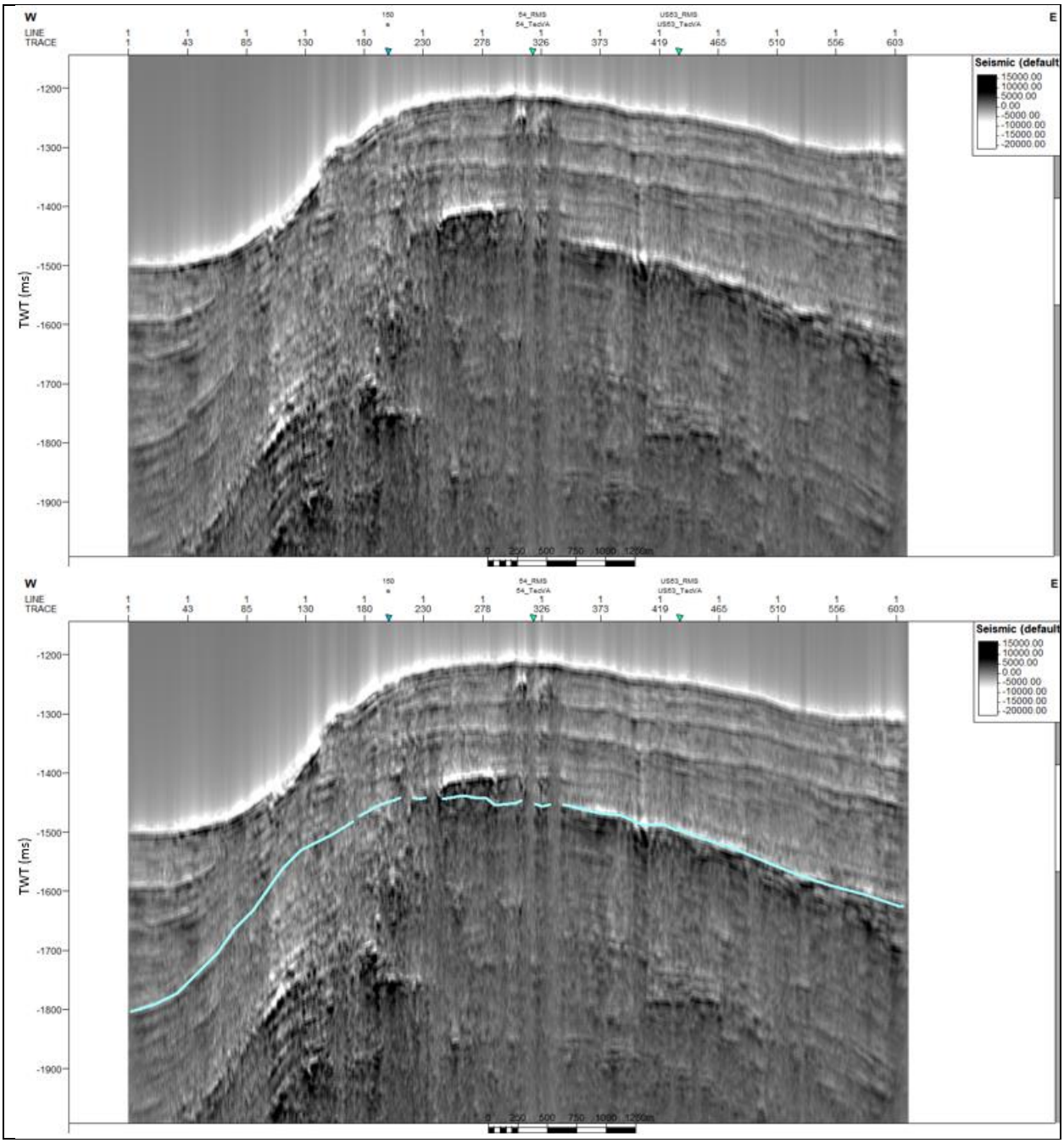

SCS profile US-09 with Amplitude Volume Technique. Blue line indicates BSR.

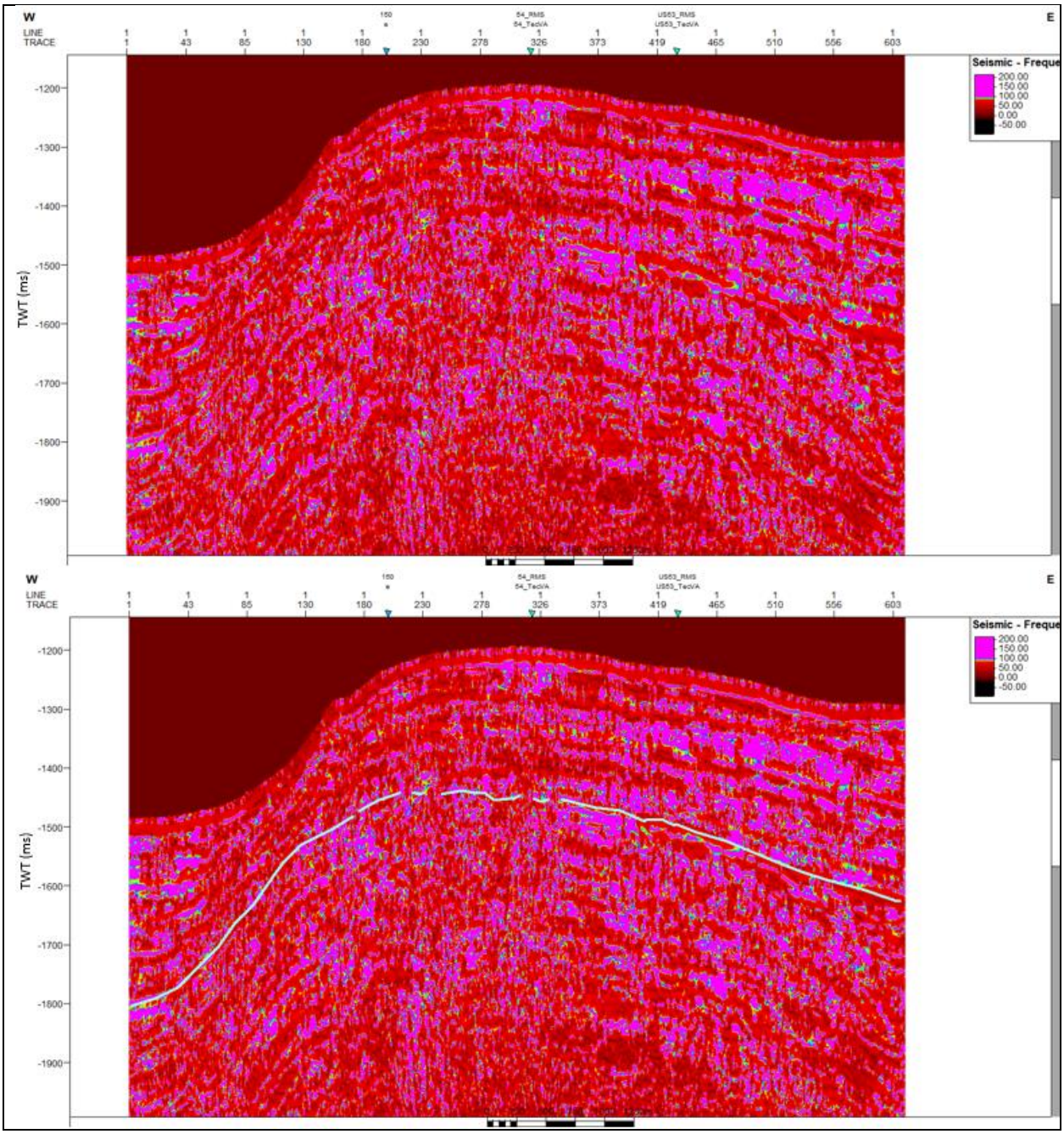

SCS profile US-09 with Instantaneous Frequency. Blue line indicates BSR.

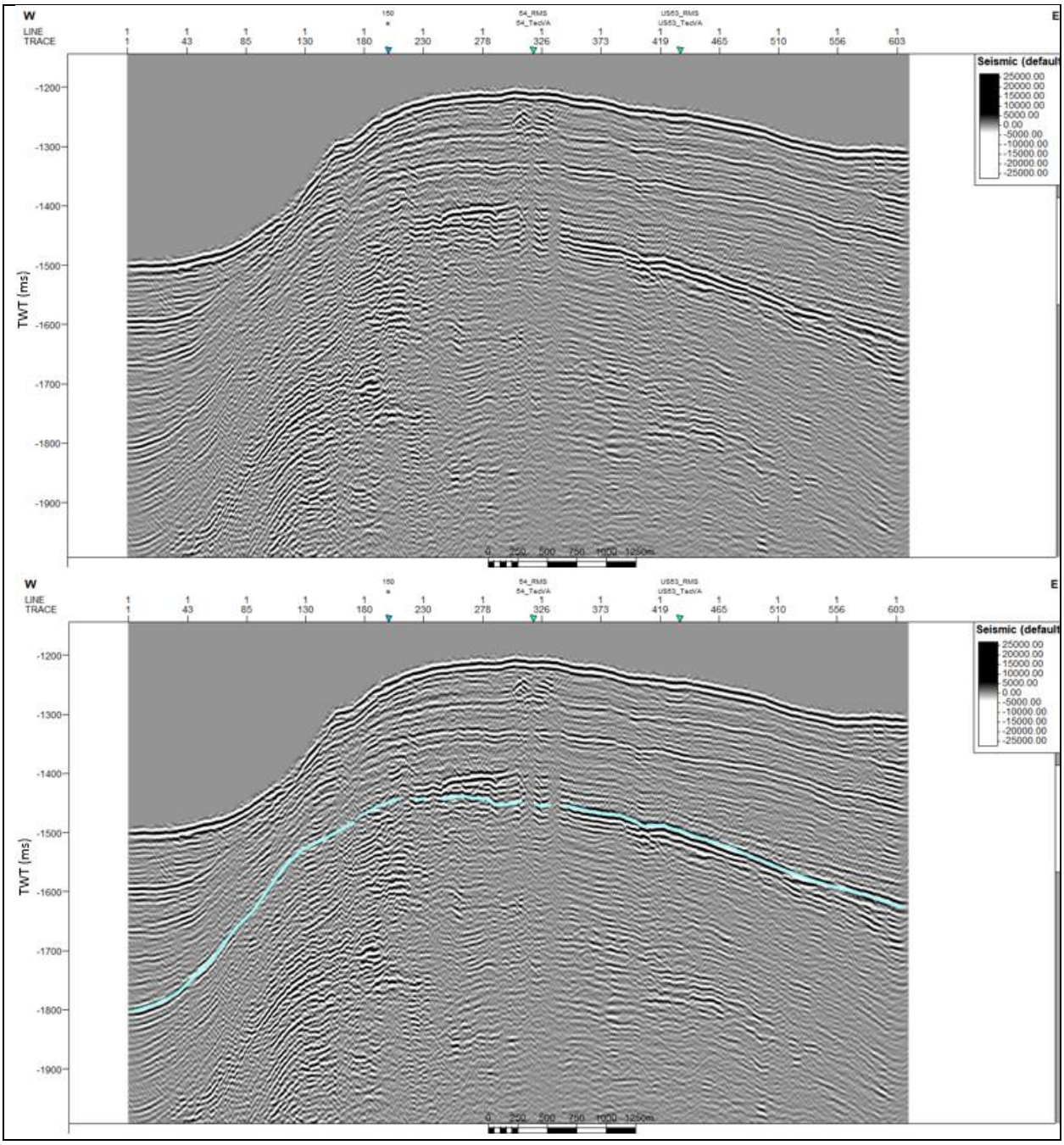

SCS profile US-09 with Spectral Decomposition of 100 Hz. Blue line indicates BSR.

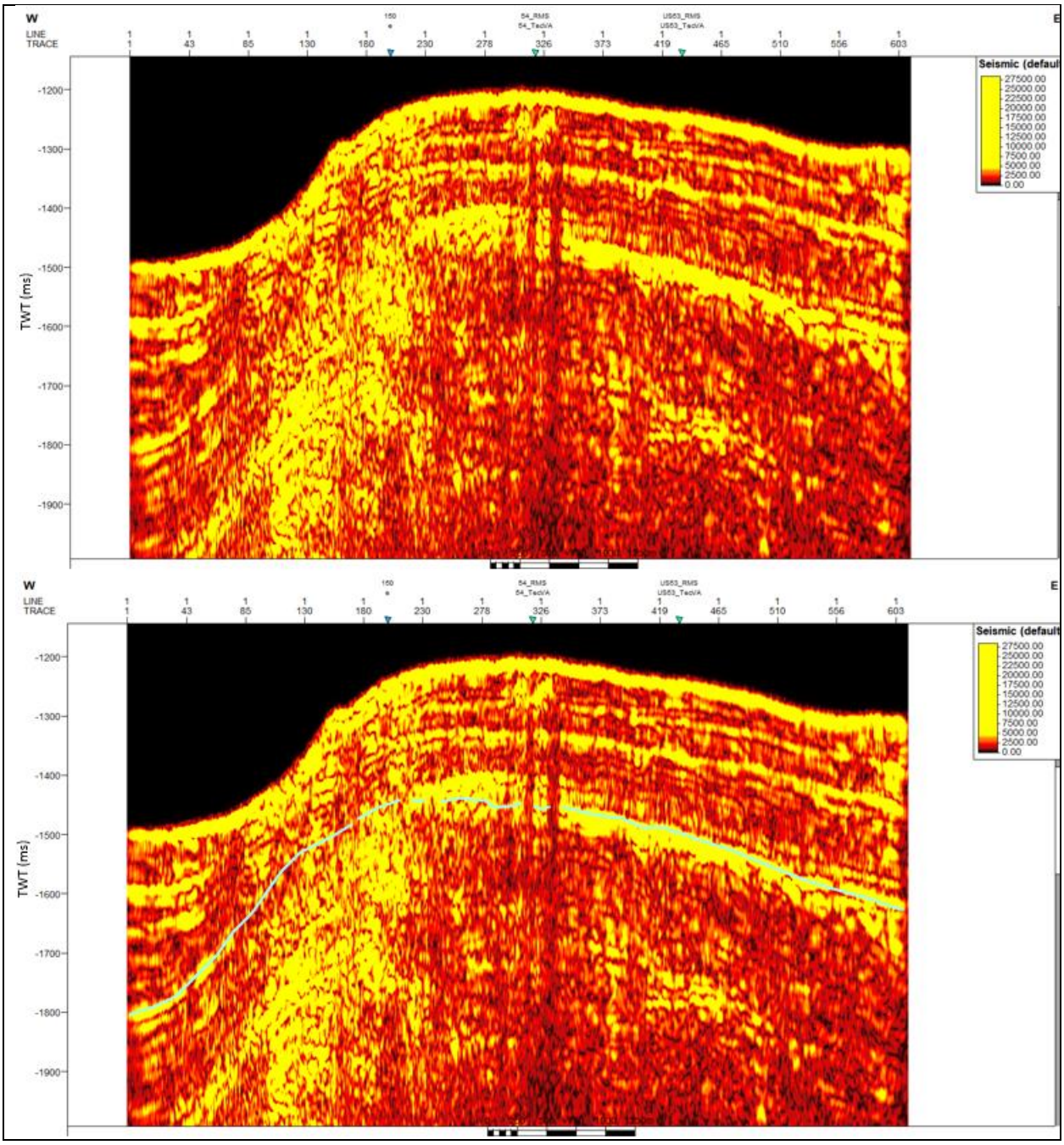

SCS profile US-09 with Spectral Decomposition of 100 Hz plus Envelope. Blue line indicates BSR.

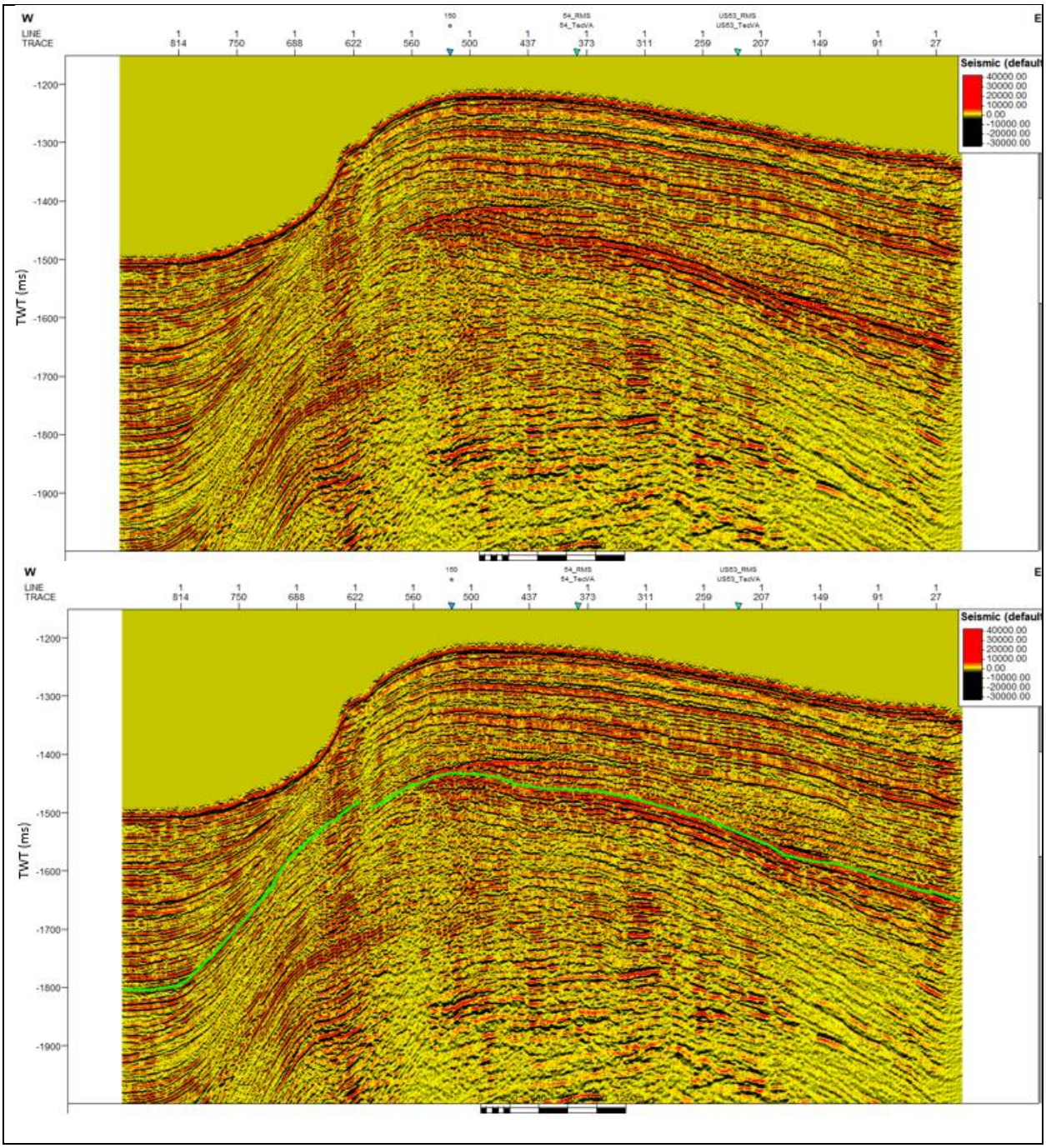

SCS profile US-10 without application of seismic attribute. Green line indicates BSR.

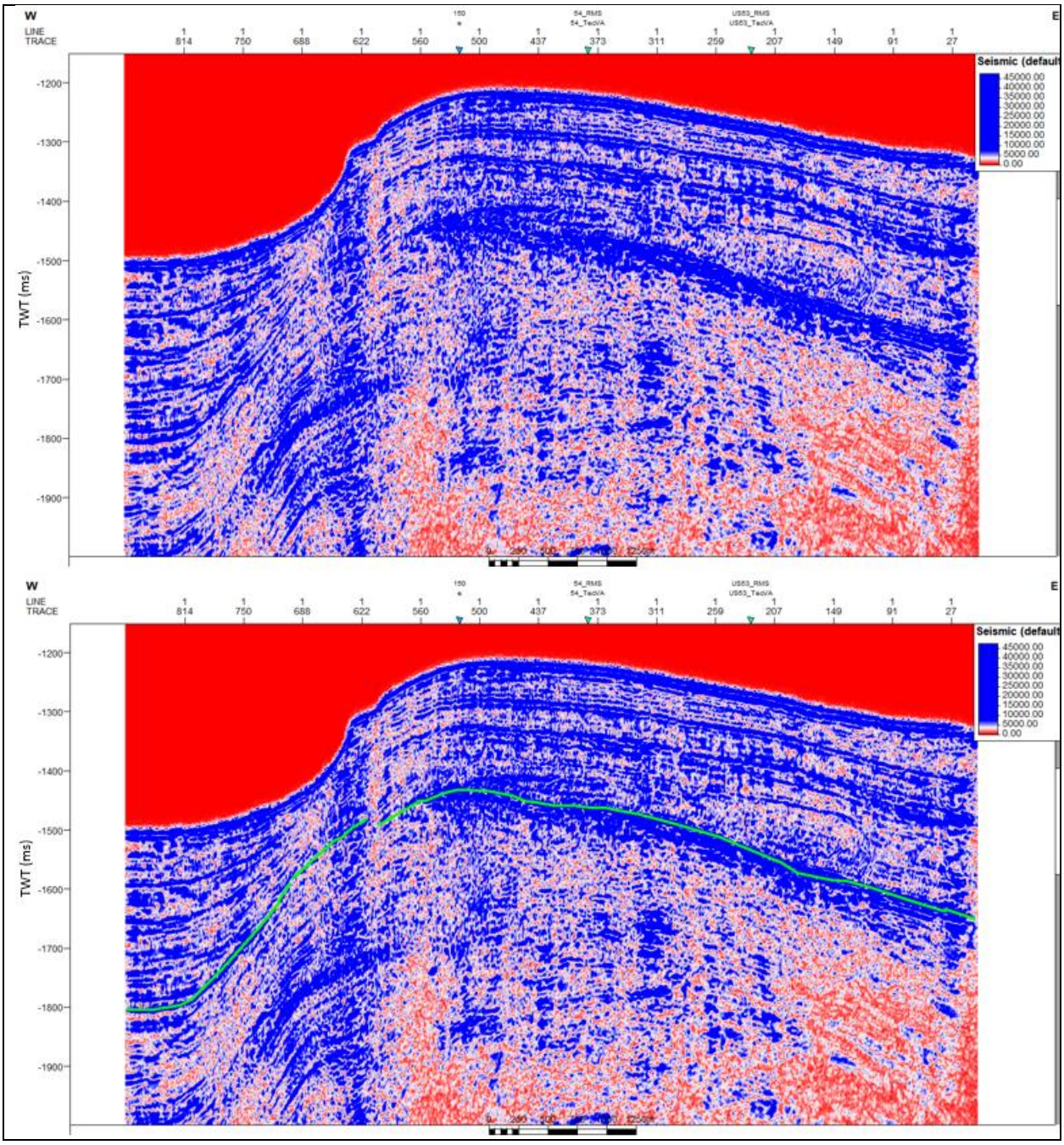

SCS profile US-10 with Envelope. Green line indicates BSR.

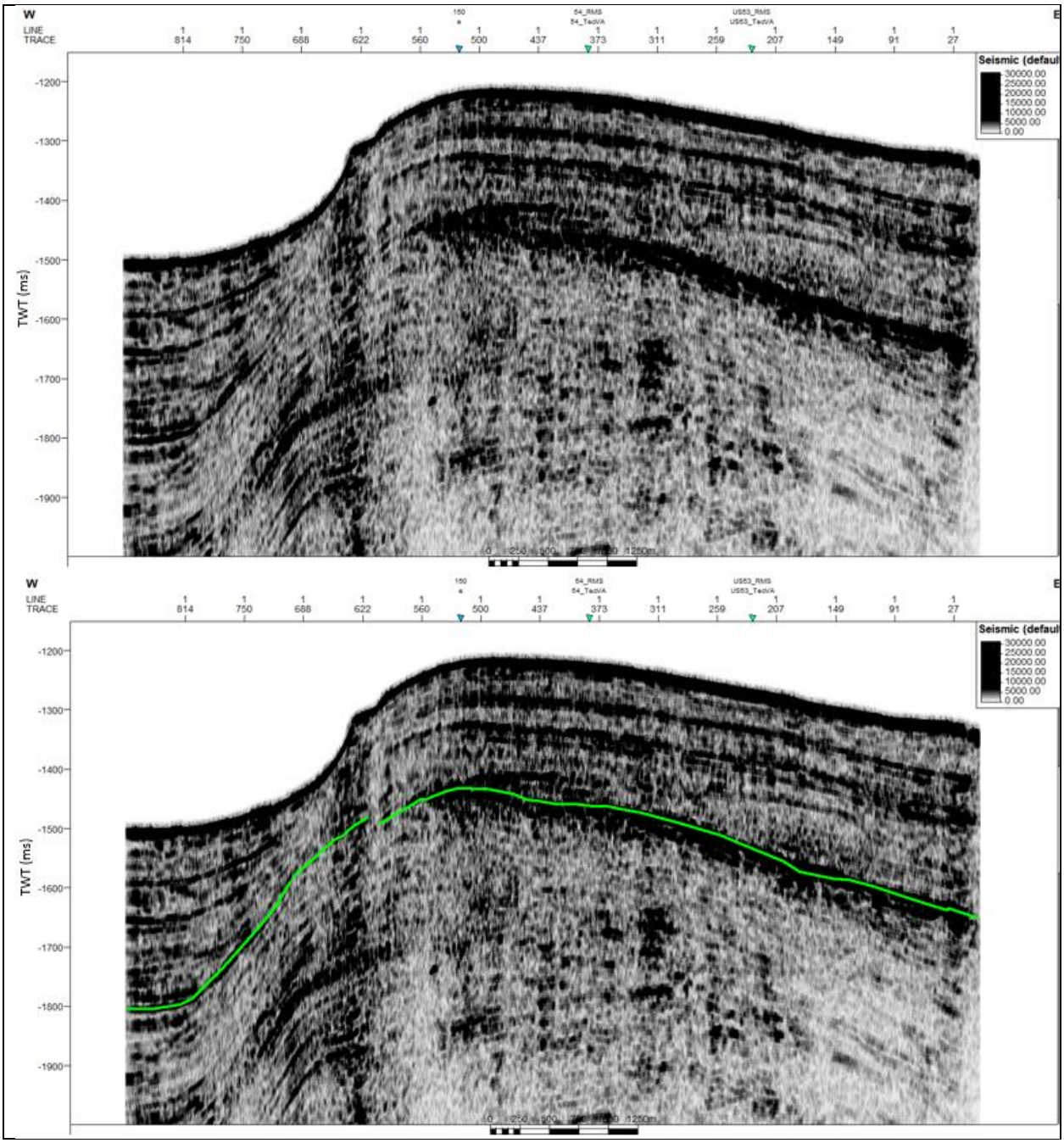

SCS profile US-10 with RMS Amplitude. Green line indicates BSR.

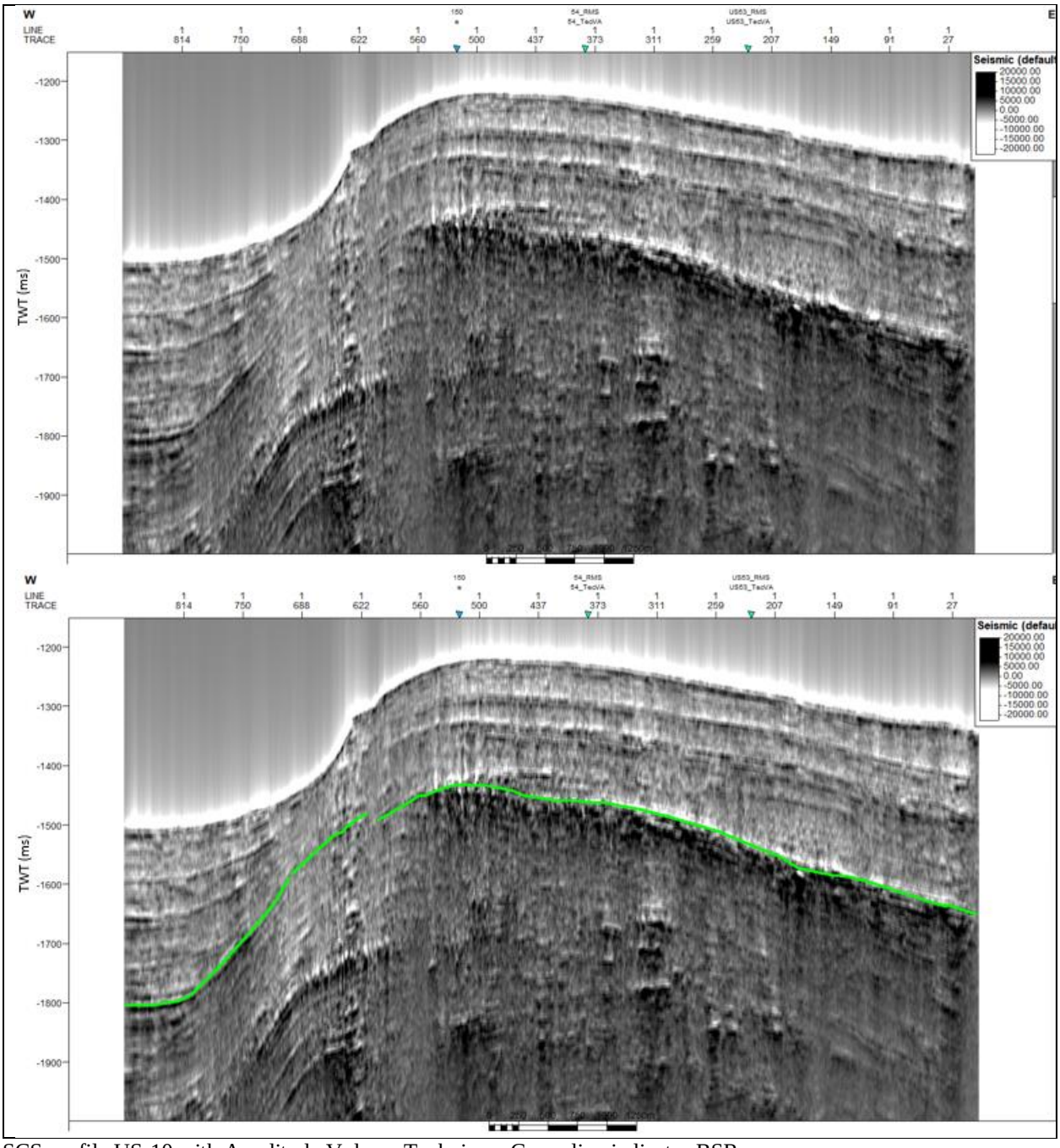

SCS profile US-10 with Amplitude Volume Technique. Green line indicates BSR.

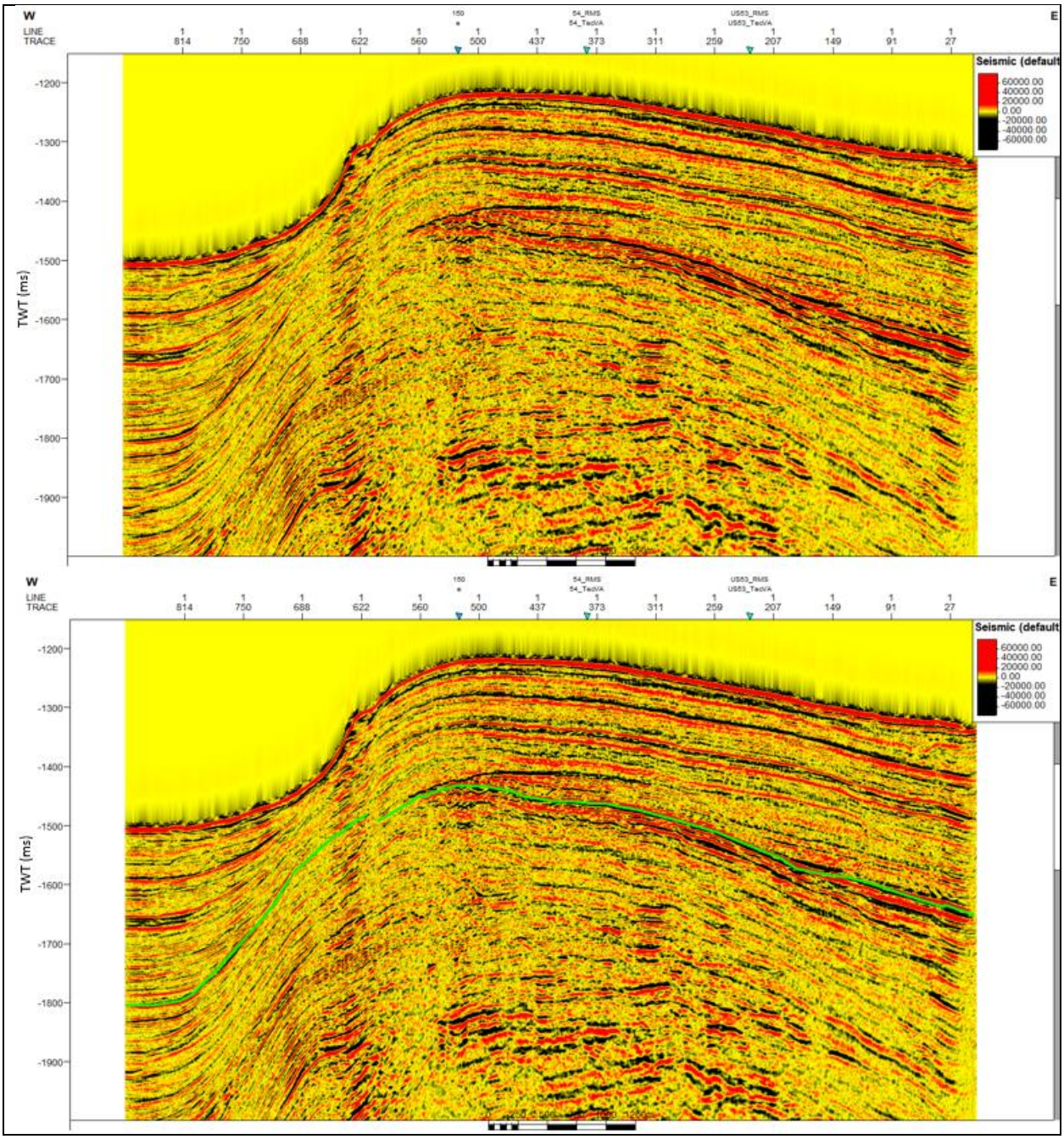

SCS profile US-10 with Relative Acoustic Impedance. Green line indicates BSR.

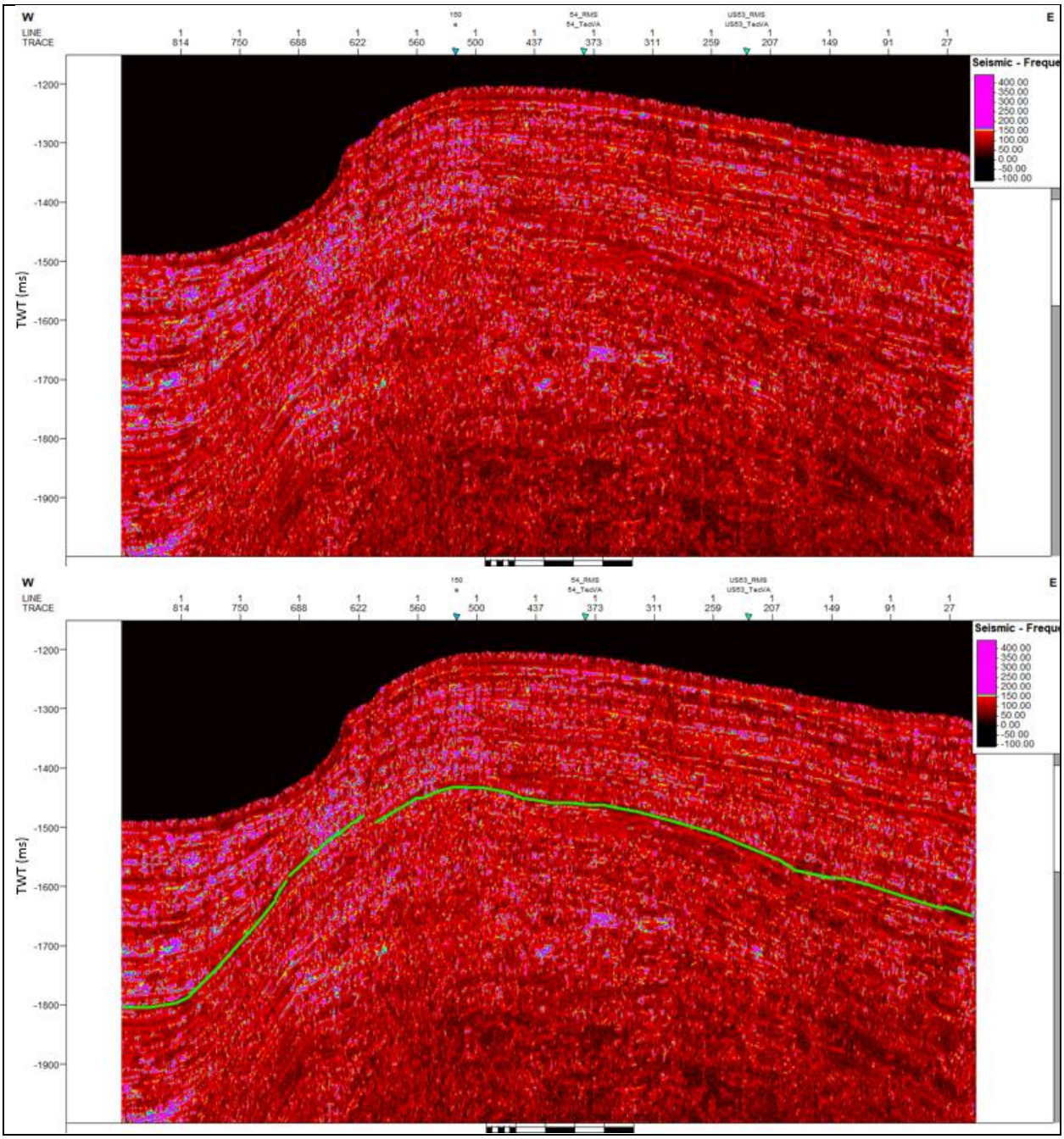

SCS profile US-10 with Instantaneous Frequency. Green line indicates BSR.

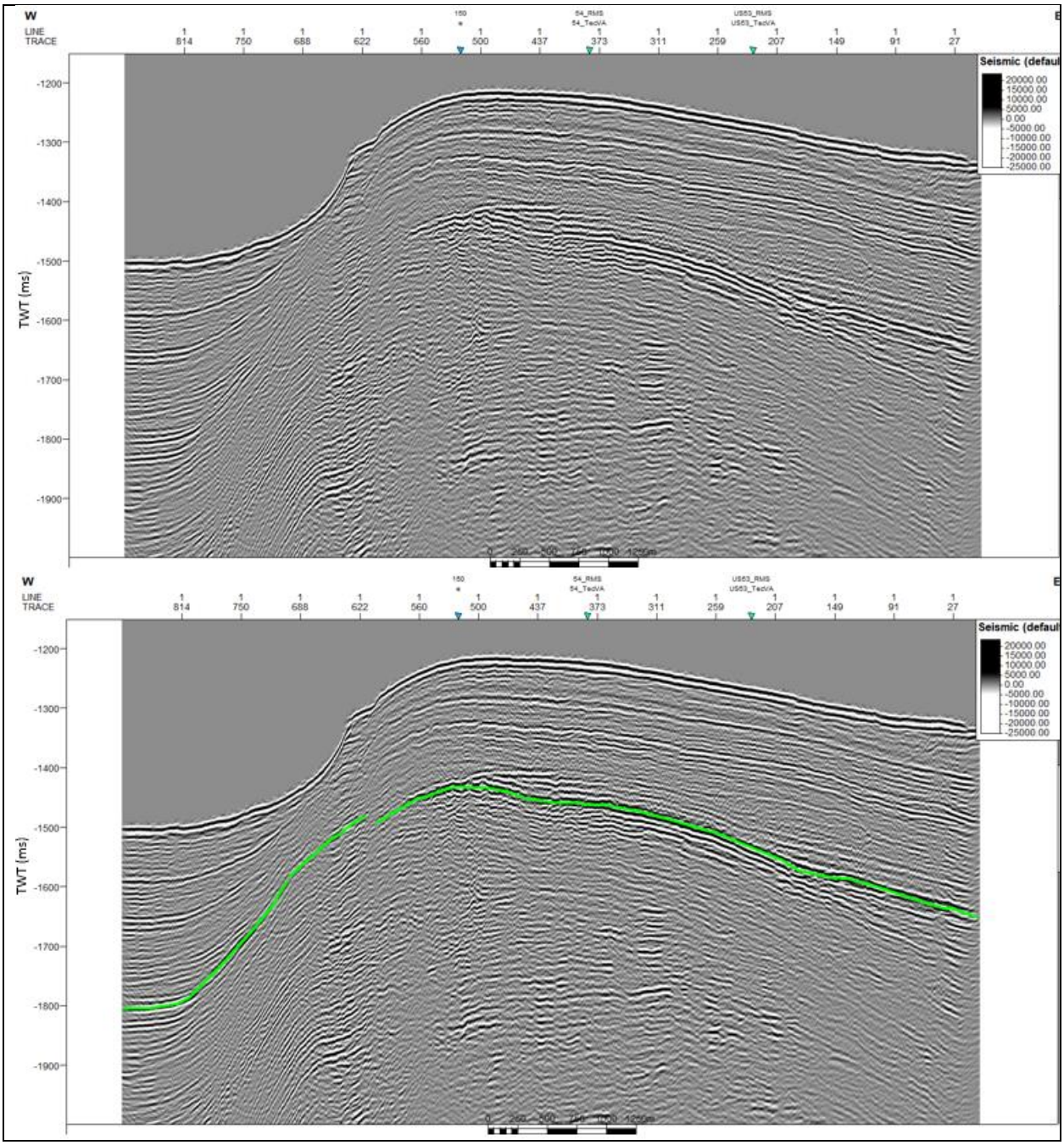

SCS profile US-10 with Spectral Decomposition of 100 Hz. Green line indicates BSR.

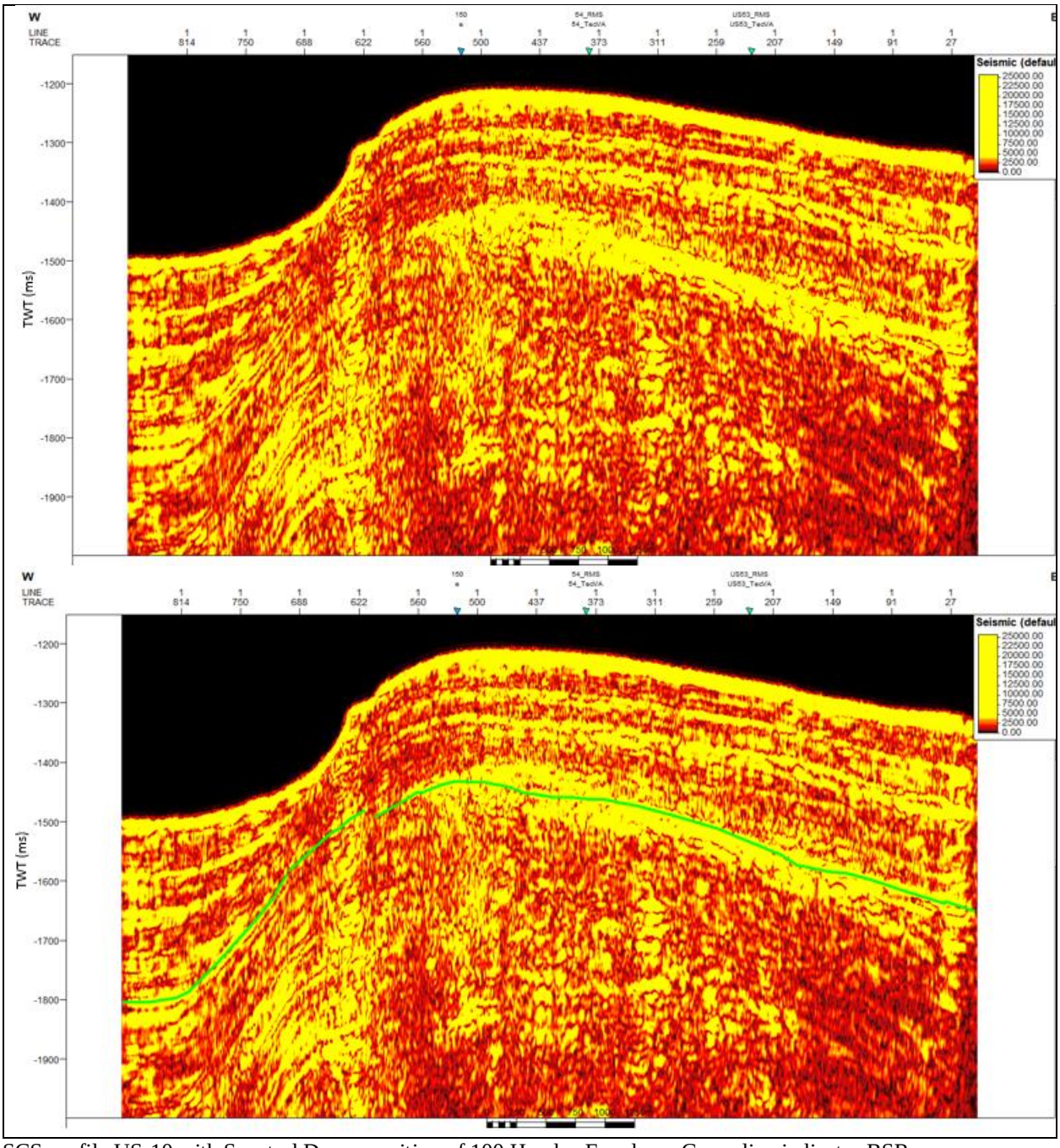

SCS profile US-10 with Spectral Decomposition of 100 Hz plus Envelope. Green line indicates BSR.

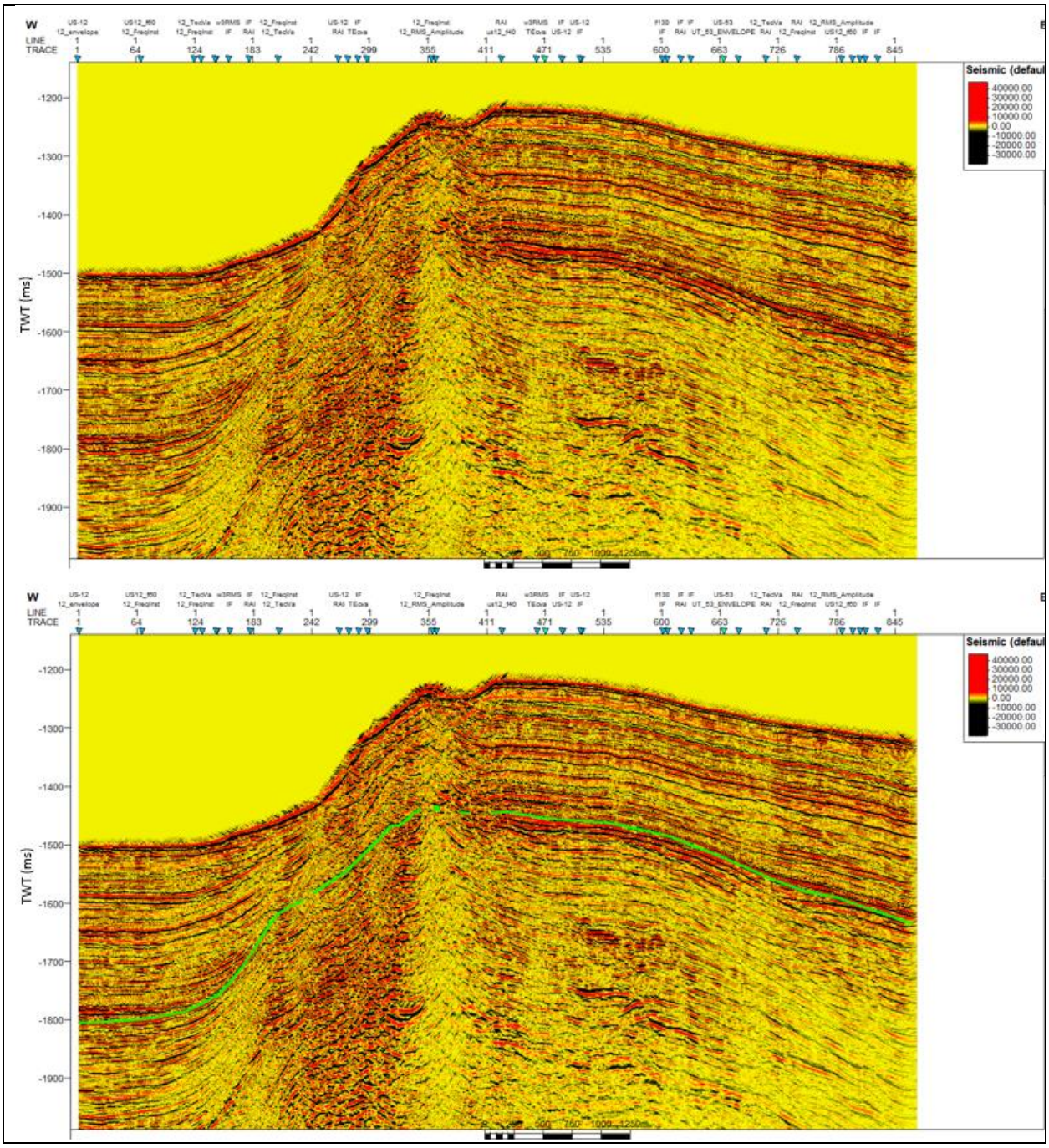

SCS profile US-11 without application of seismic attribute. Green line indicates BSR.

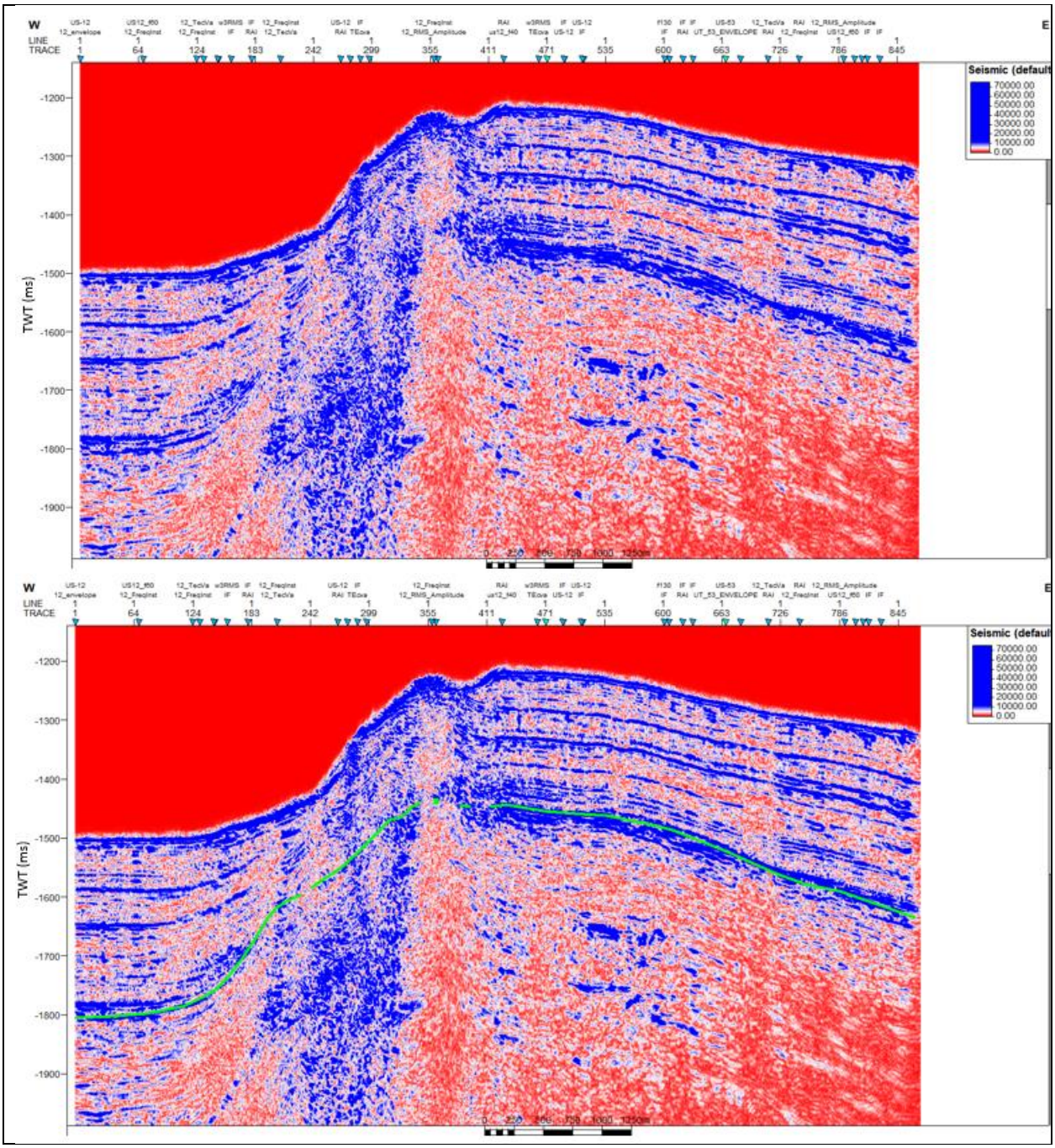

SCS profile US-11 with Envelope. Green line indicates BSR.

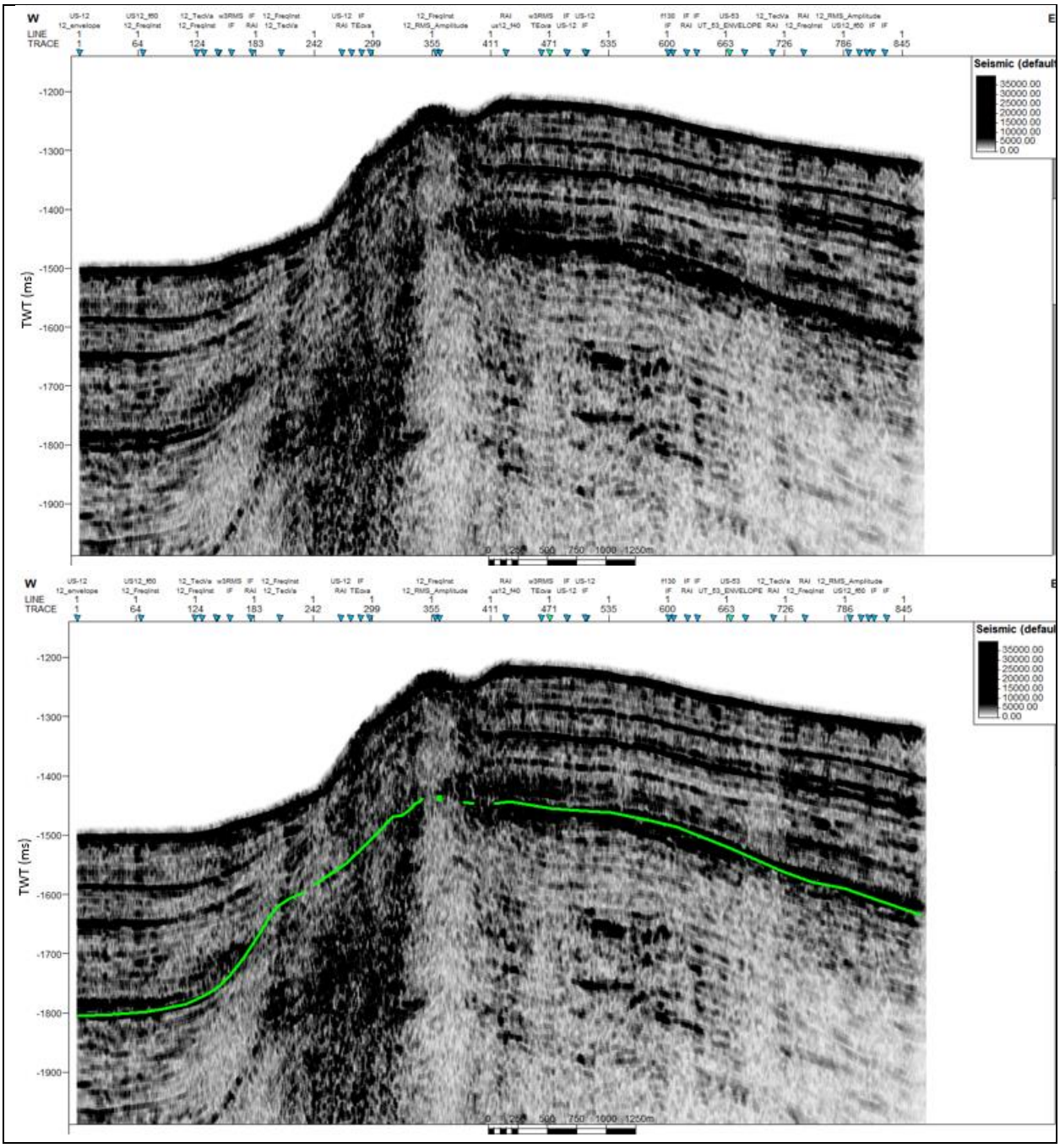

SCS profile US-11 with RMS Amplitude. Green line indicates BSR.

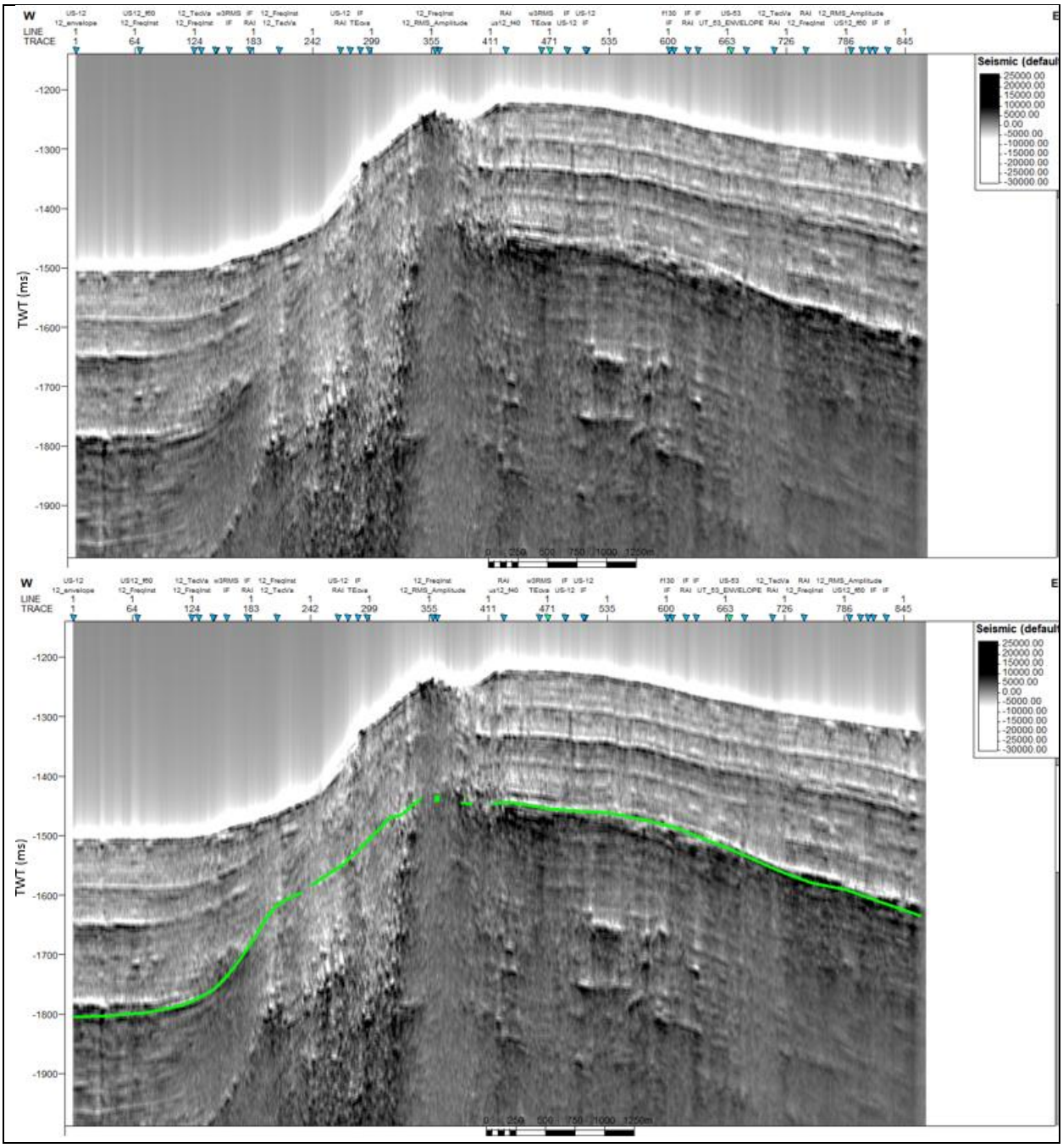

SCS profile US-11 with Amplitude Volume Technique. Green line indicates BSR.

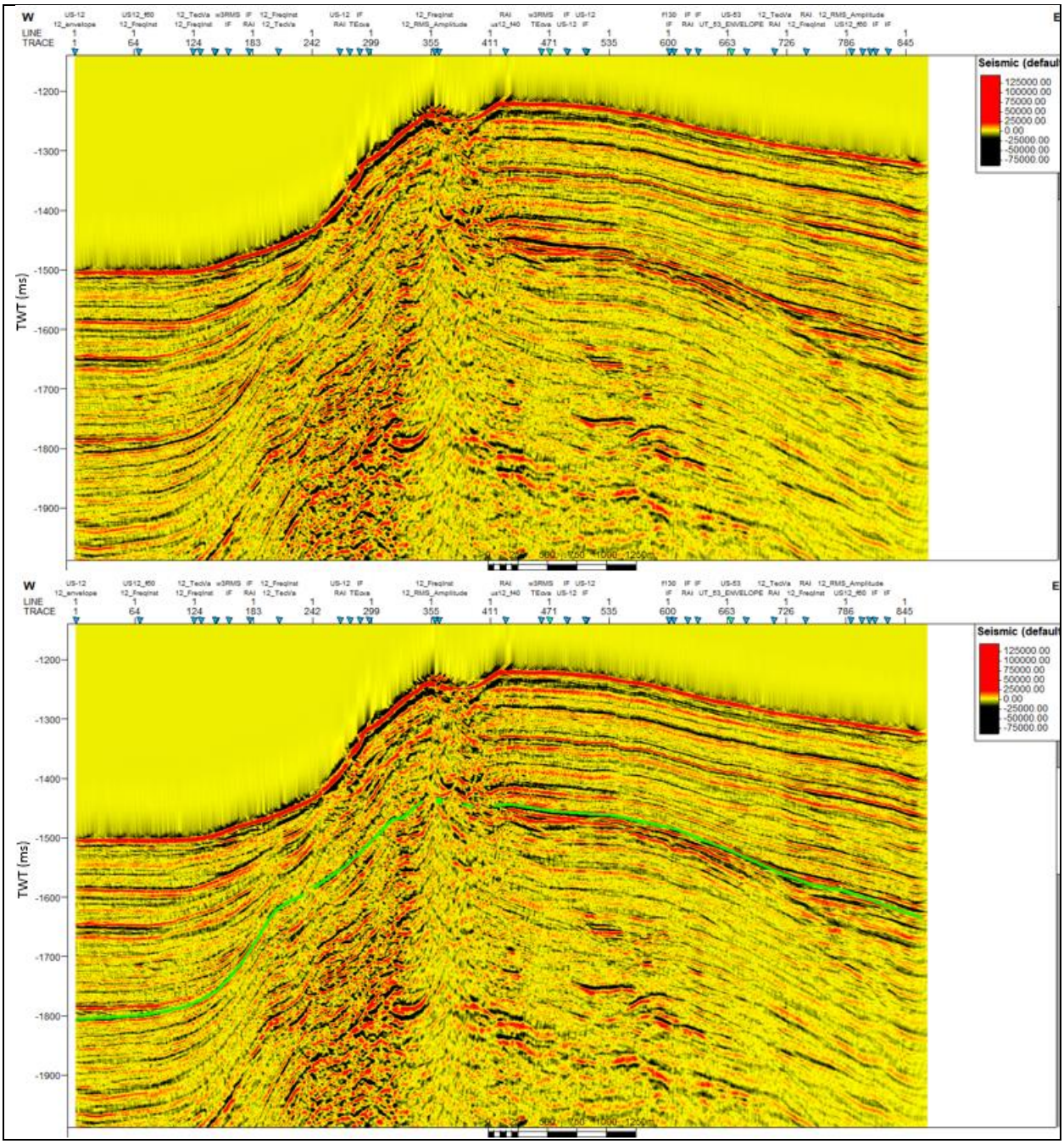

SCS profile US-11 with Relative Acoustic Impedance. Green line indicates BSR.

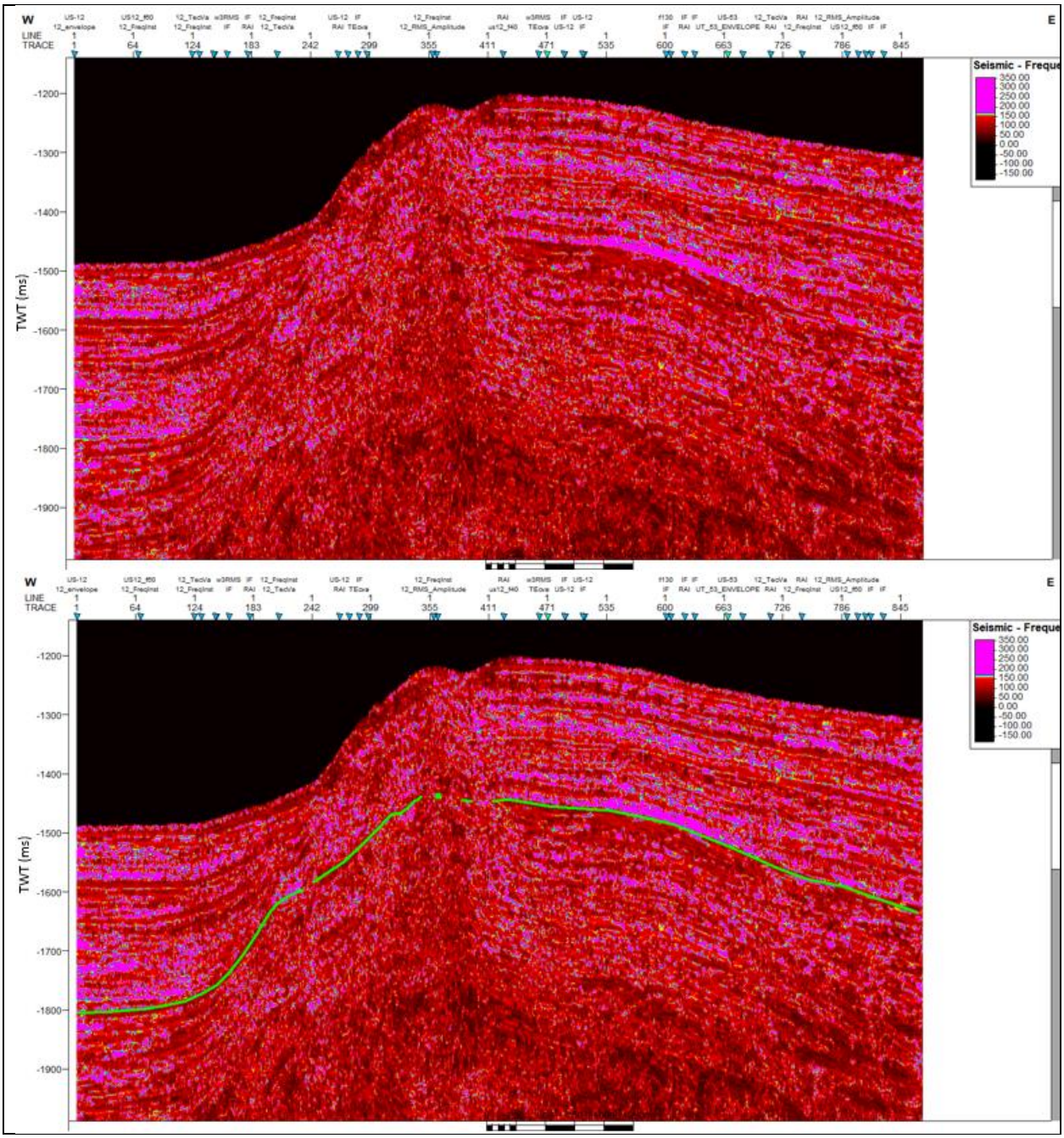

SCS profile US-11 with Instantaneous Frequency. Green line indicates BSR.

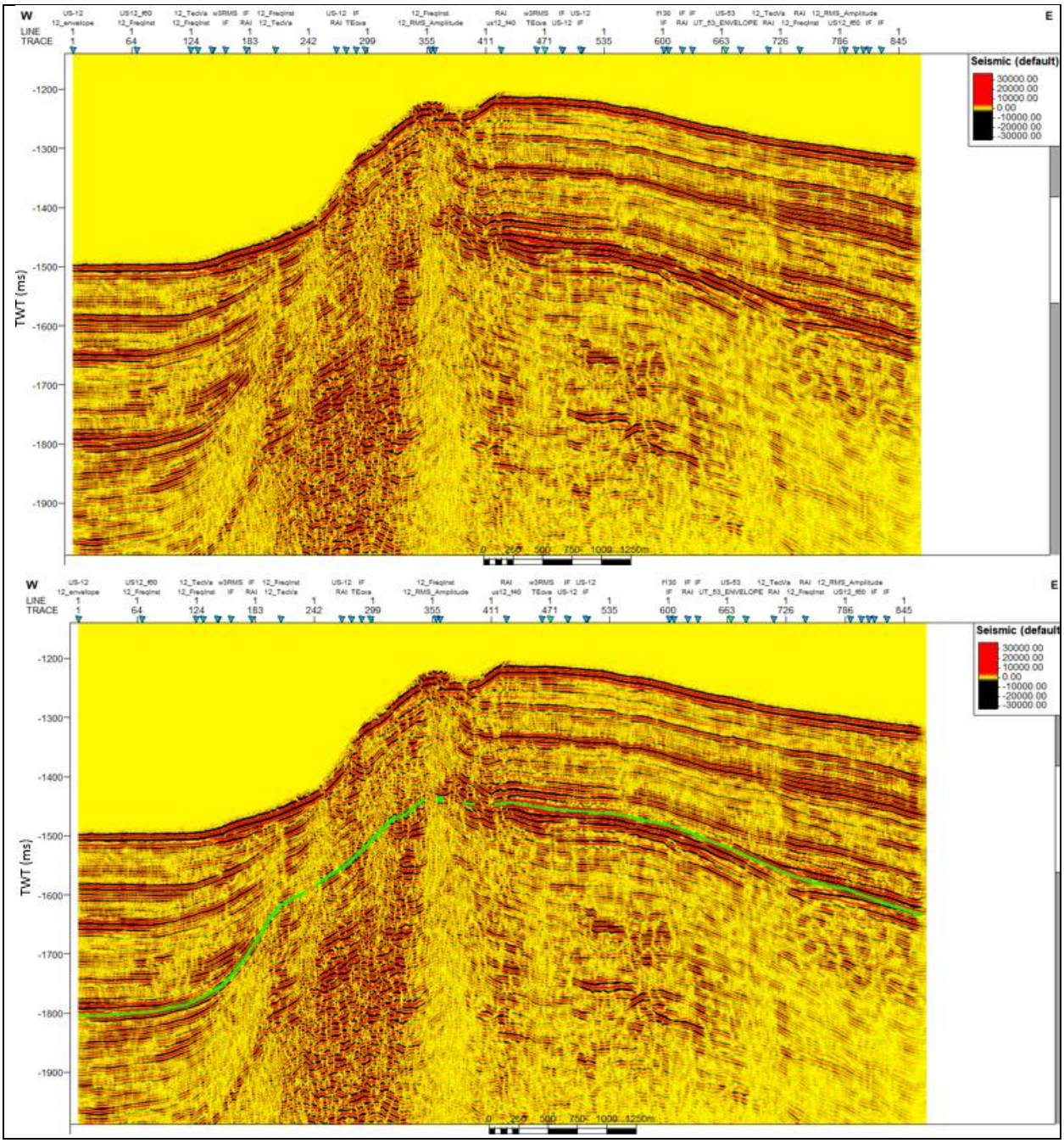

SCS profile US-11 with Spectral Decomposition of 100 Hz. Green line indicates BSR.

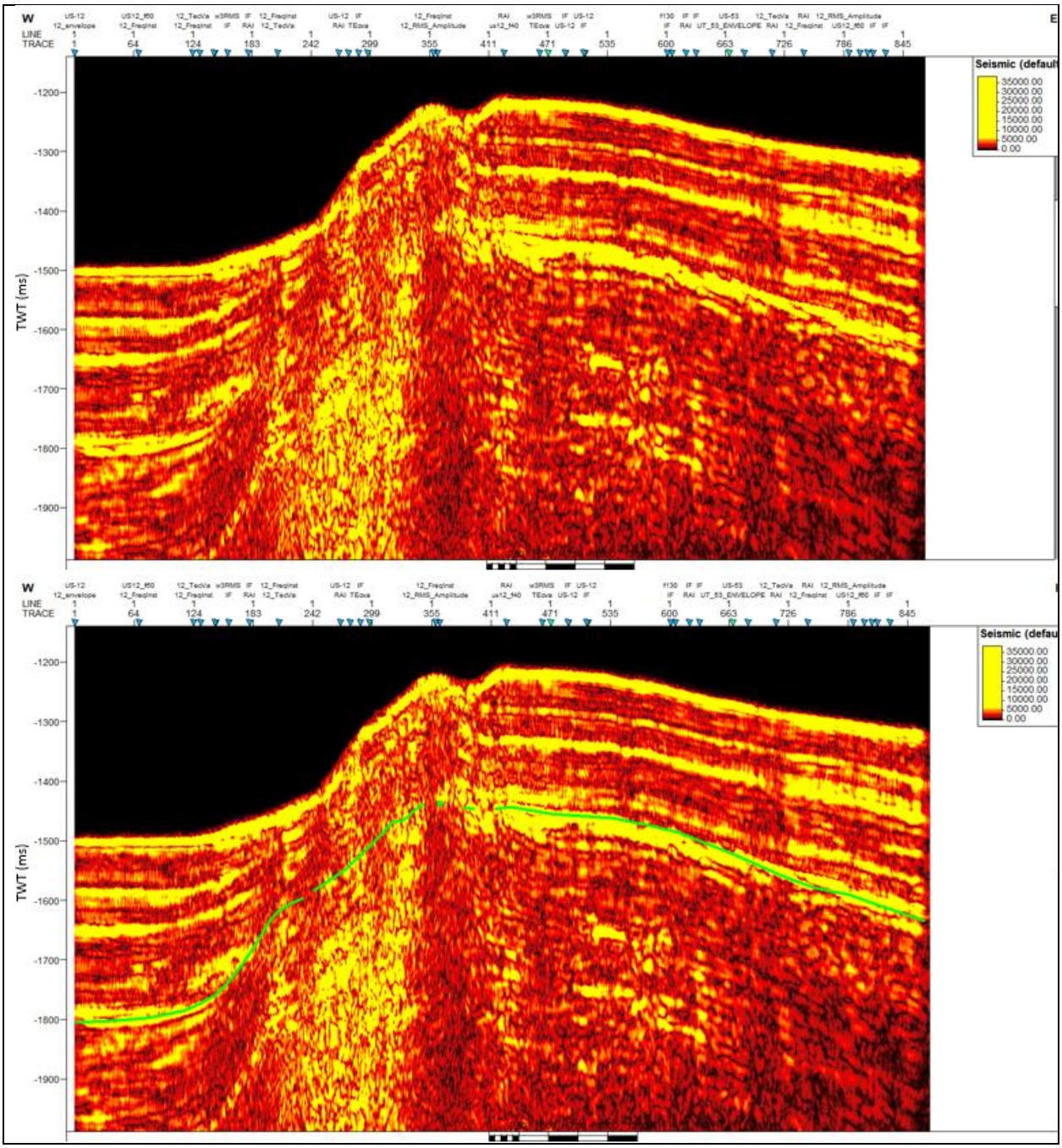

SCS profile US-11 with Spectral Decomposition of 100 Hz plus Envelope. Green line indicates BSR.

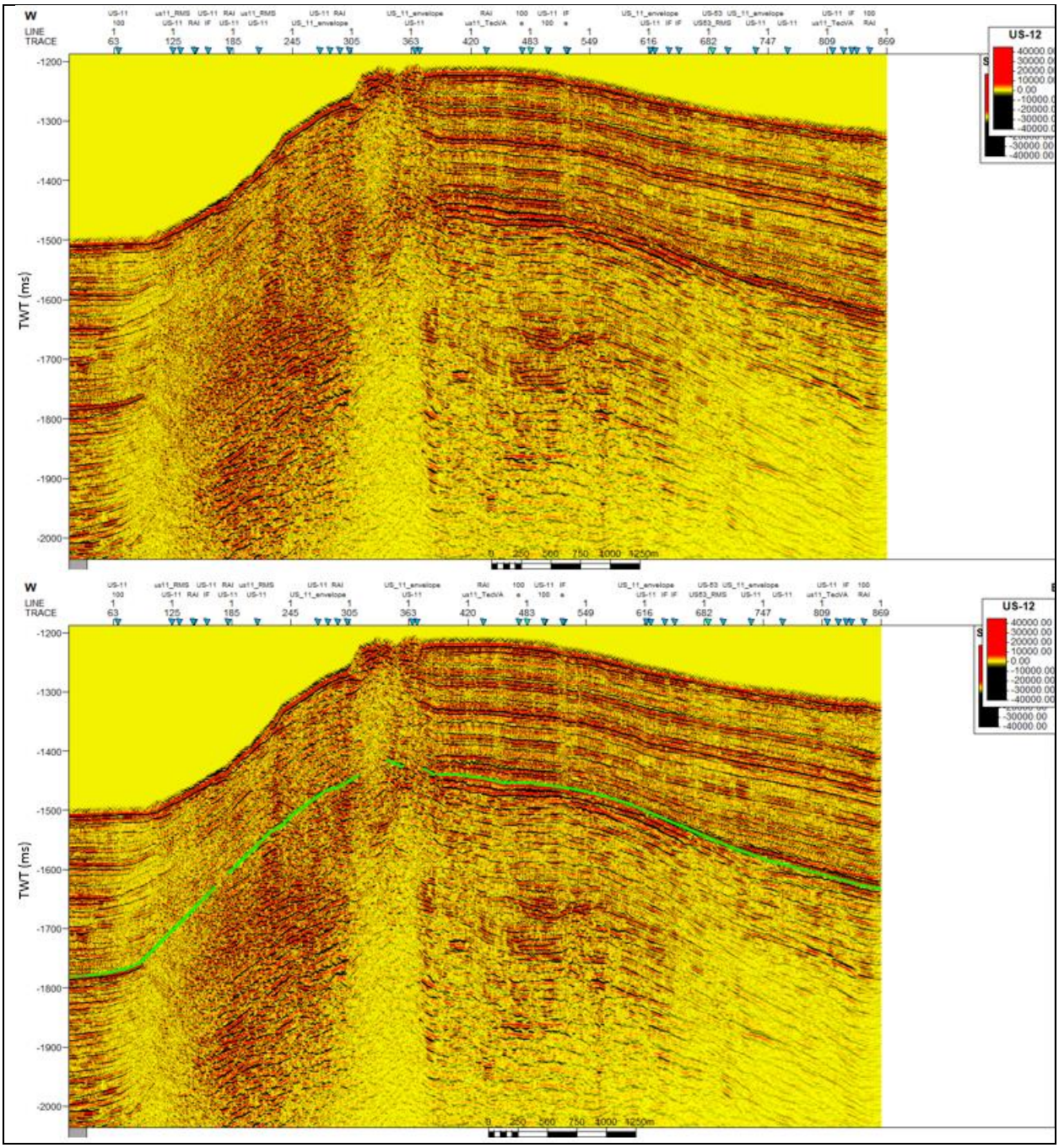

SCS profile US-12 without seismic attribute application. Green line indicates BSR.

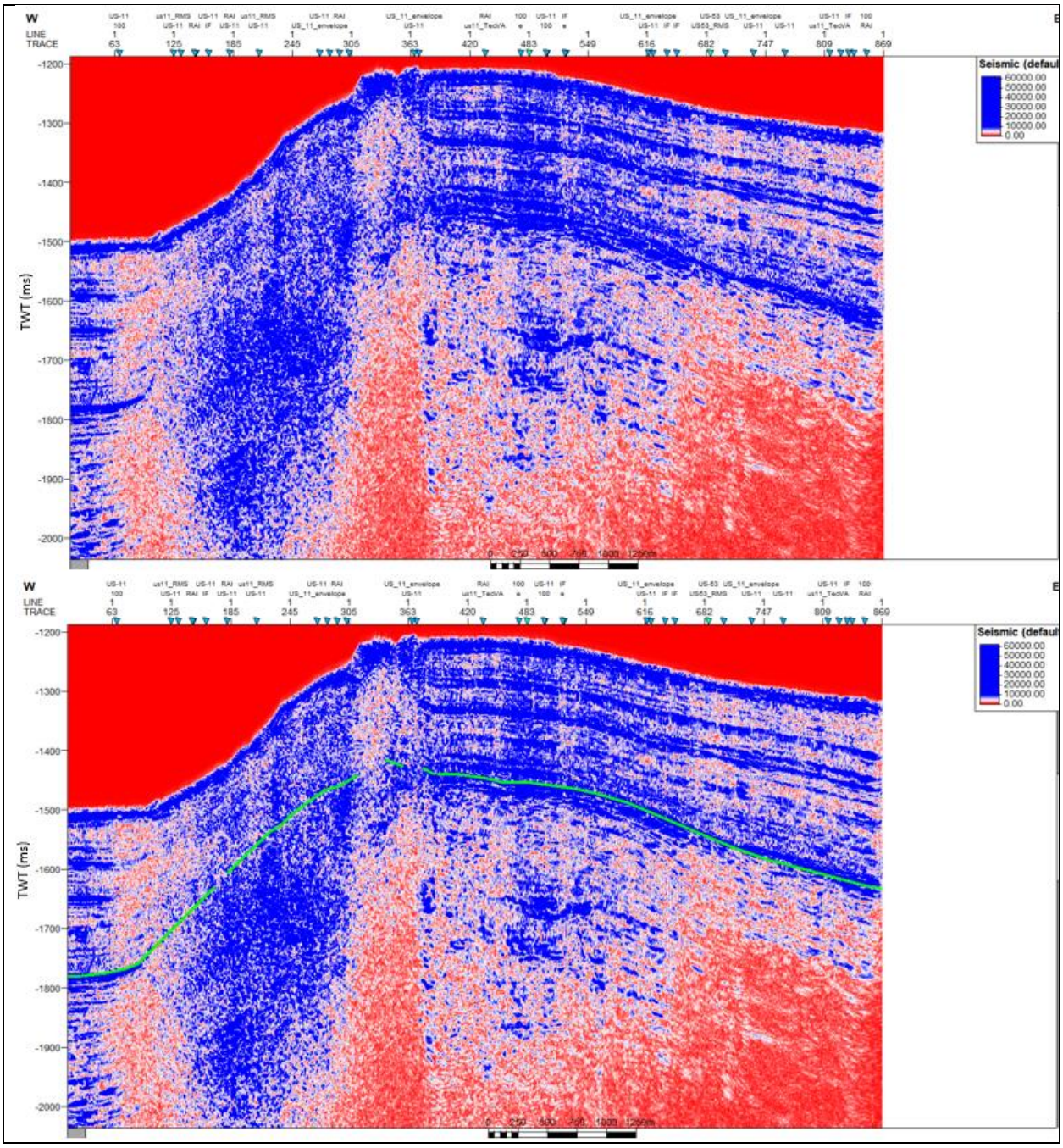

SCS profile US-12 with Envelope. Green line indicates BSR.

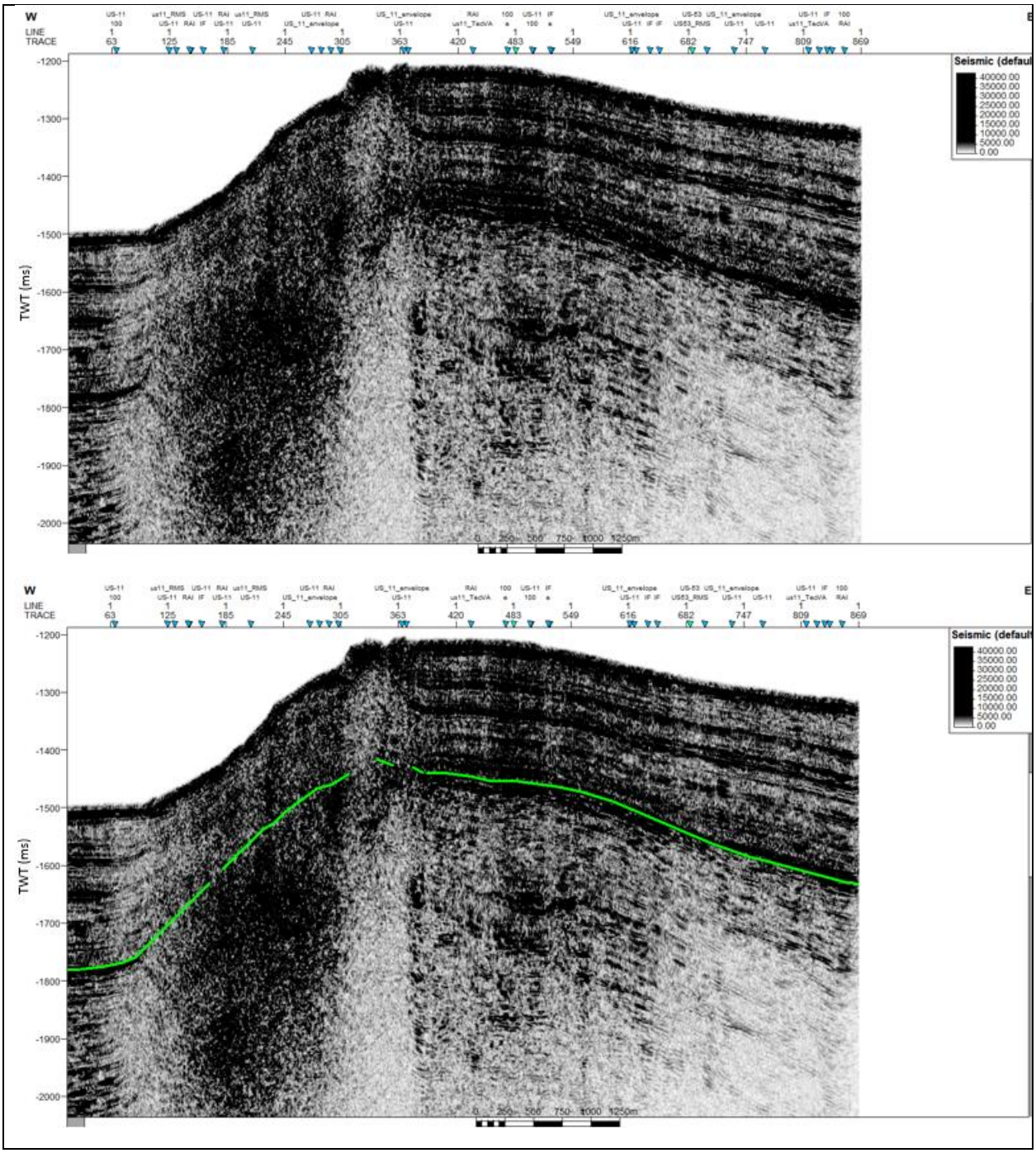

SCS profile US-12 with RMS Amplitude. Green line indicates BSR.

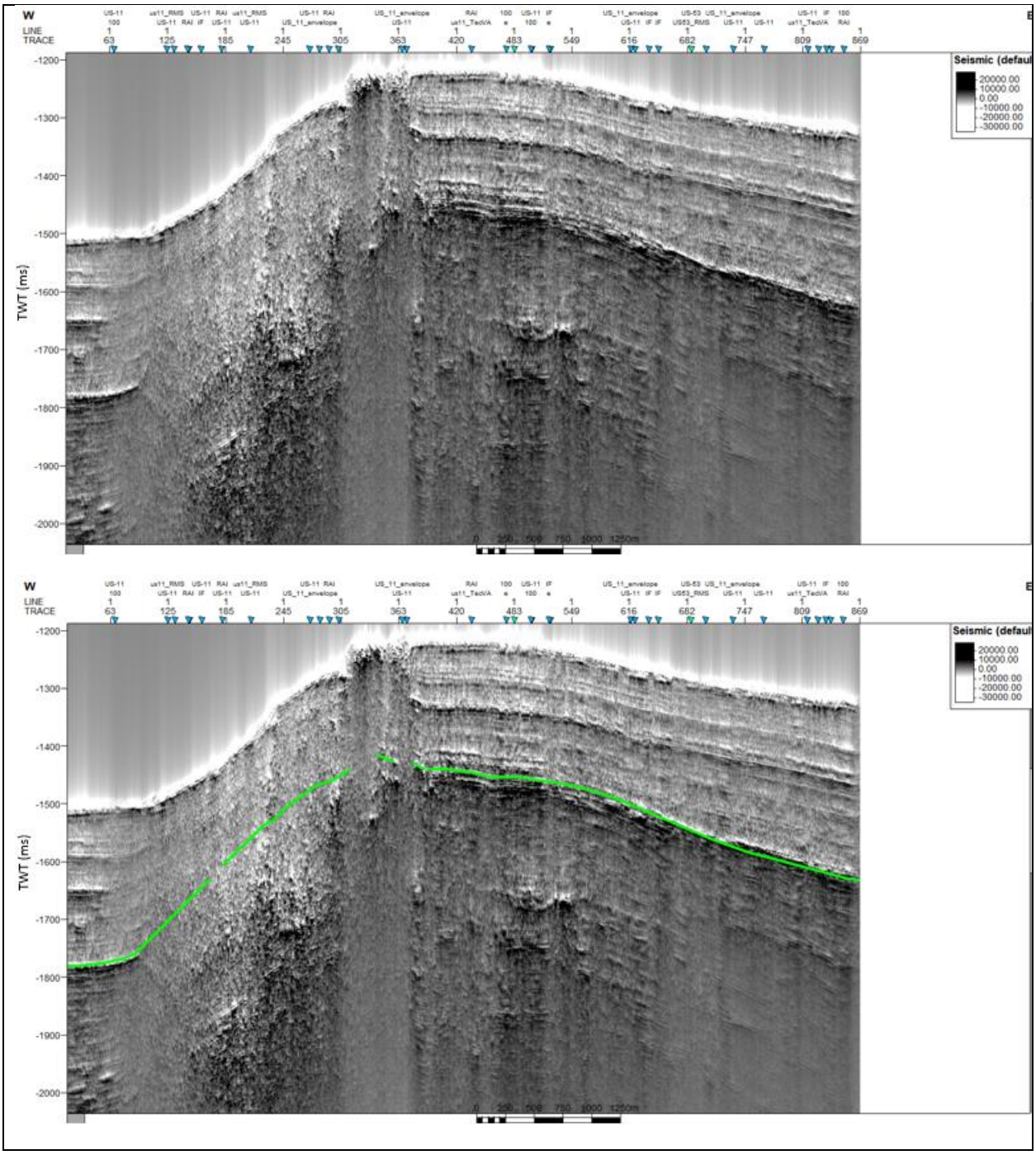

SCS profile US-12 with Amplitude Volume Technique. Green line indicates BSR.

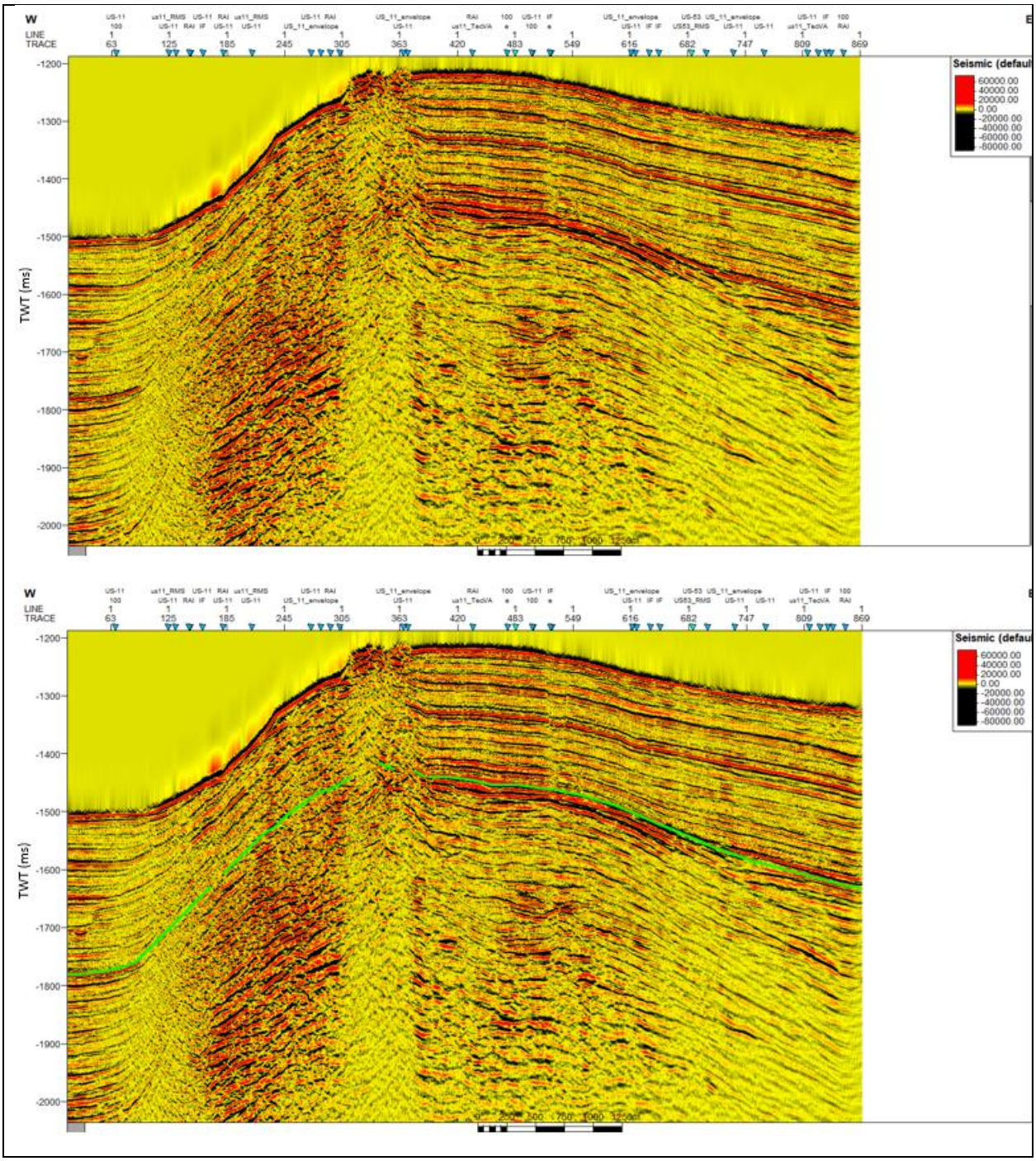

SCS profile US-12 with Relative Acoustic Impedance. Green line indicates BSR.

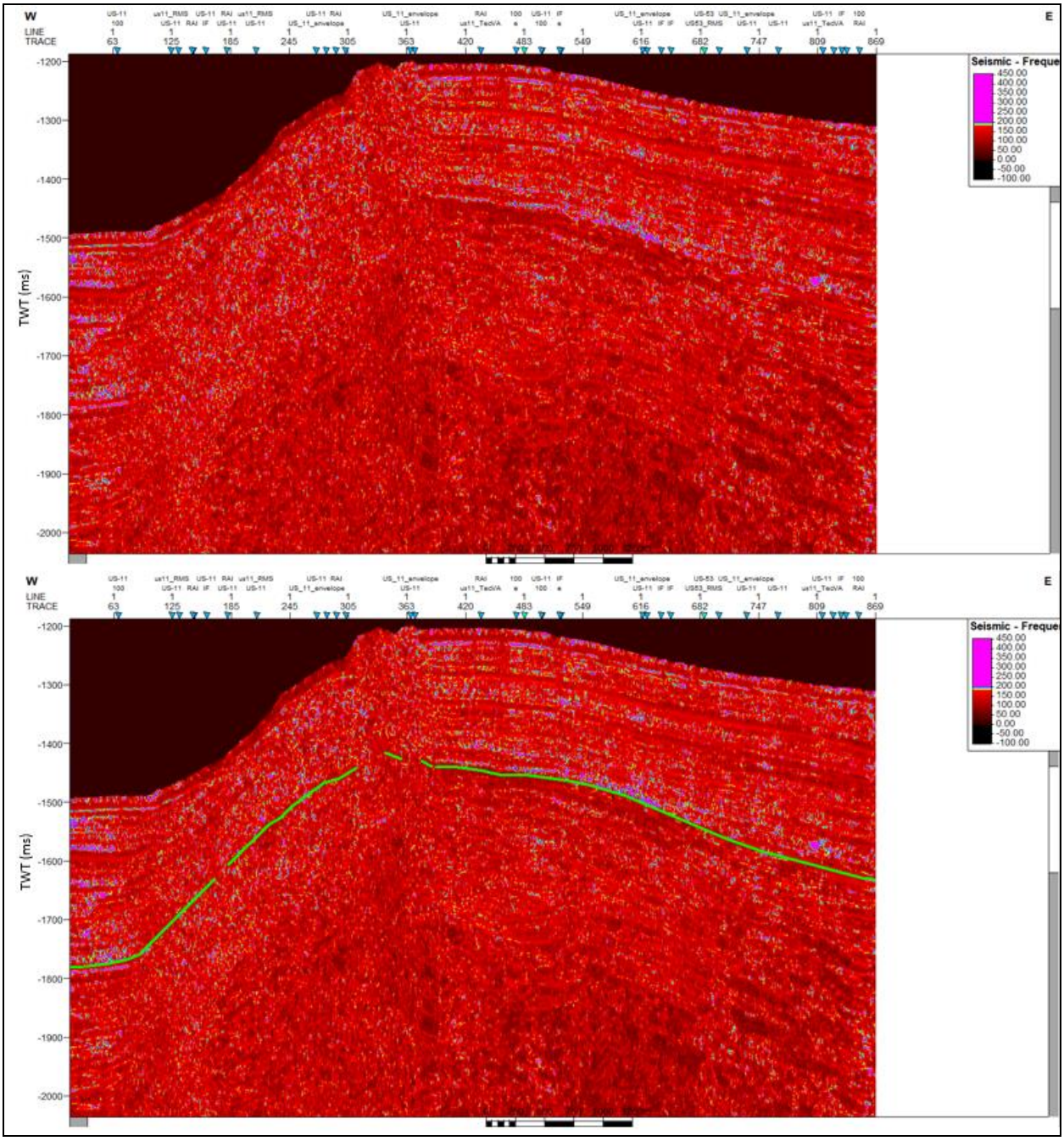

SCS profile US-12 with Instantaneous Frequency. Green line indicates BSR.

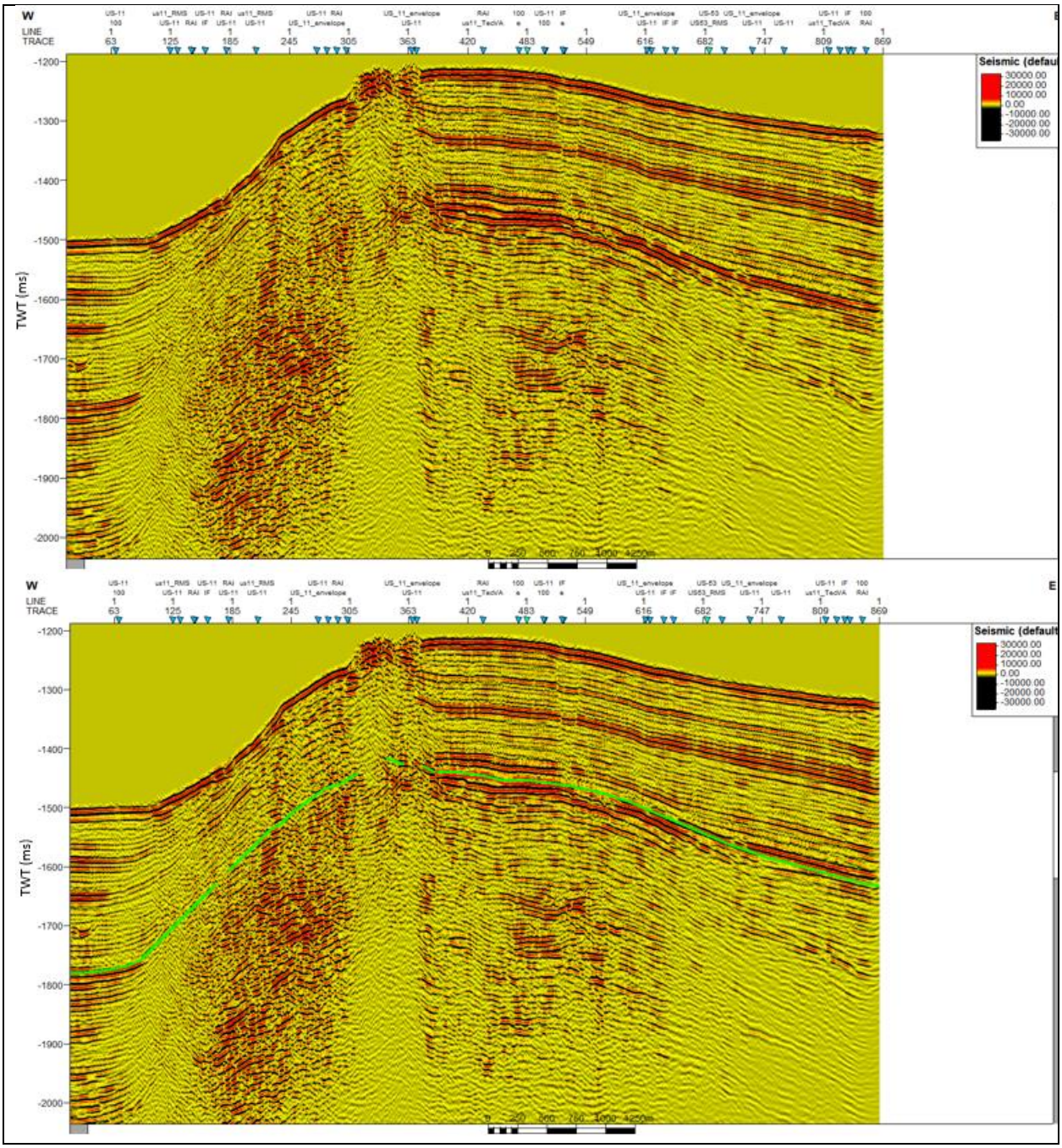

SCS profile US-12 with Spectral Decomposition of 100 Hz. Green line indicates BSR.

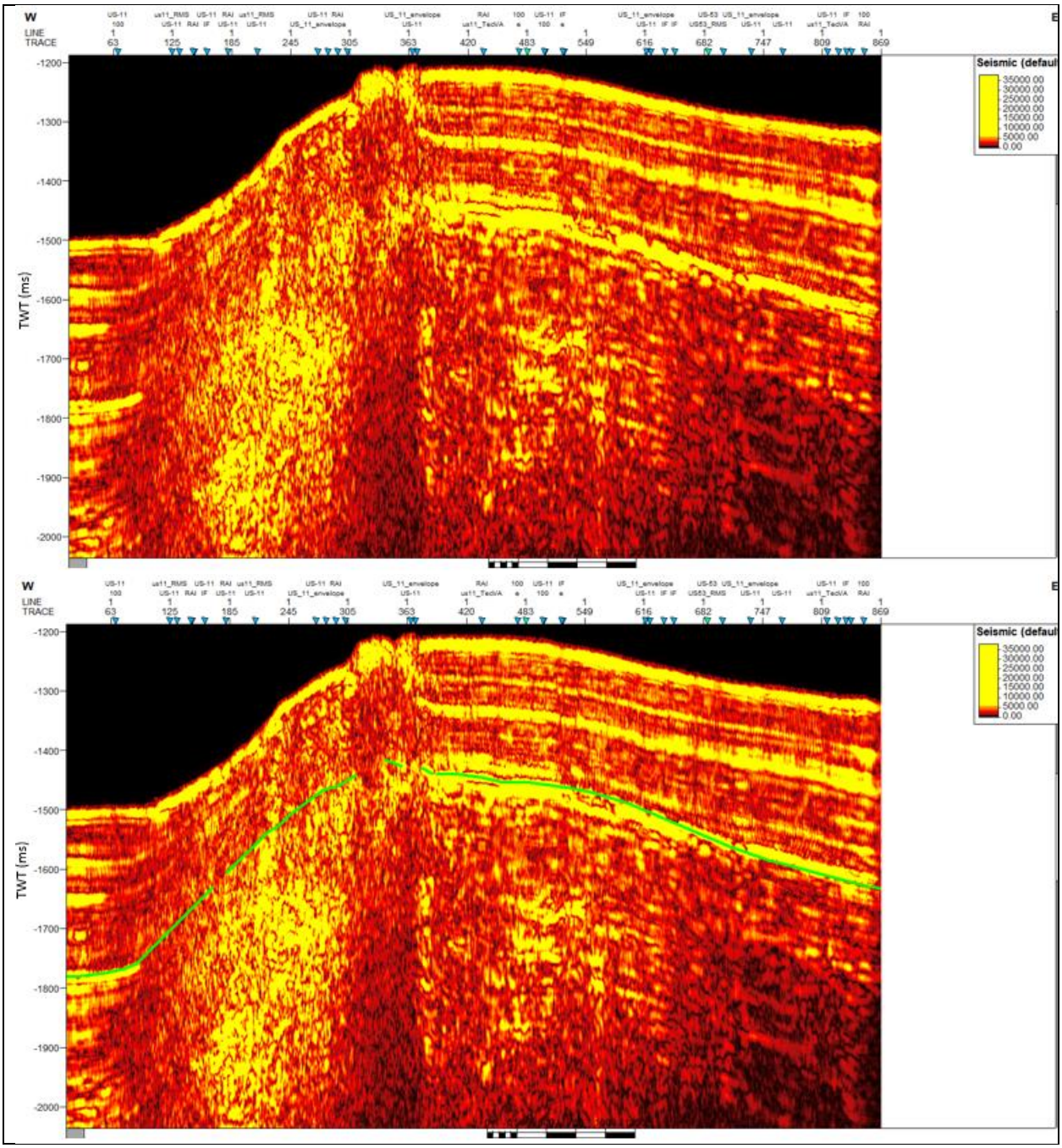

SCS profile US-12 with Spectral Decomposition of 100 Hz plus Envelope. Green line indicates BSR.

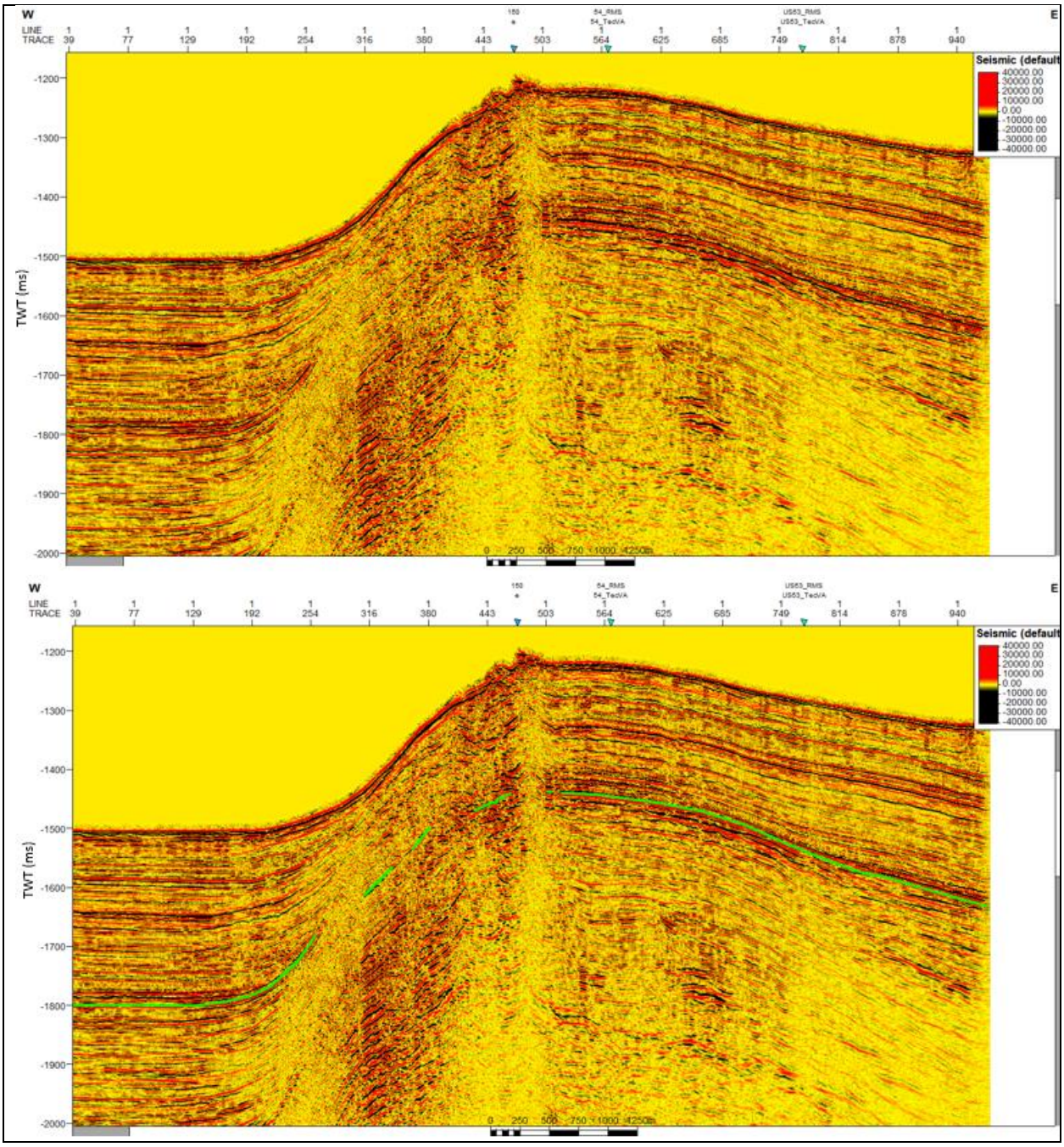

SCS profile US-13 without application of seismic attribute. Green line indicates BSR.

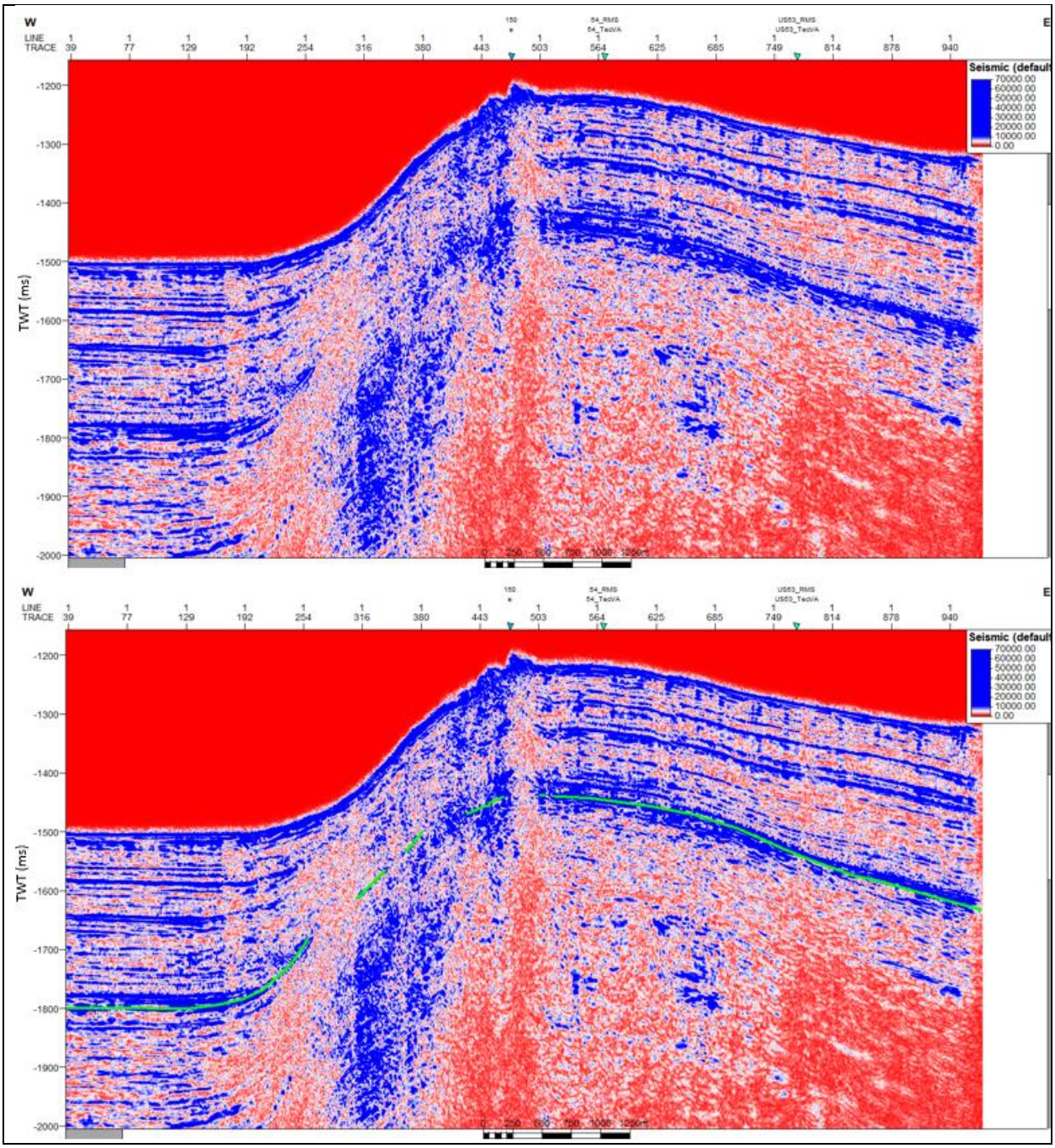

SCS profile US-13 with Envelope. Green line indicates BSR.

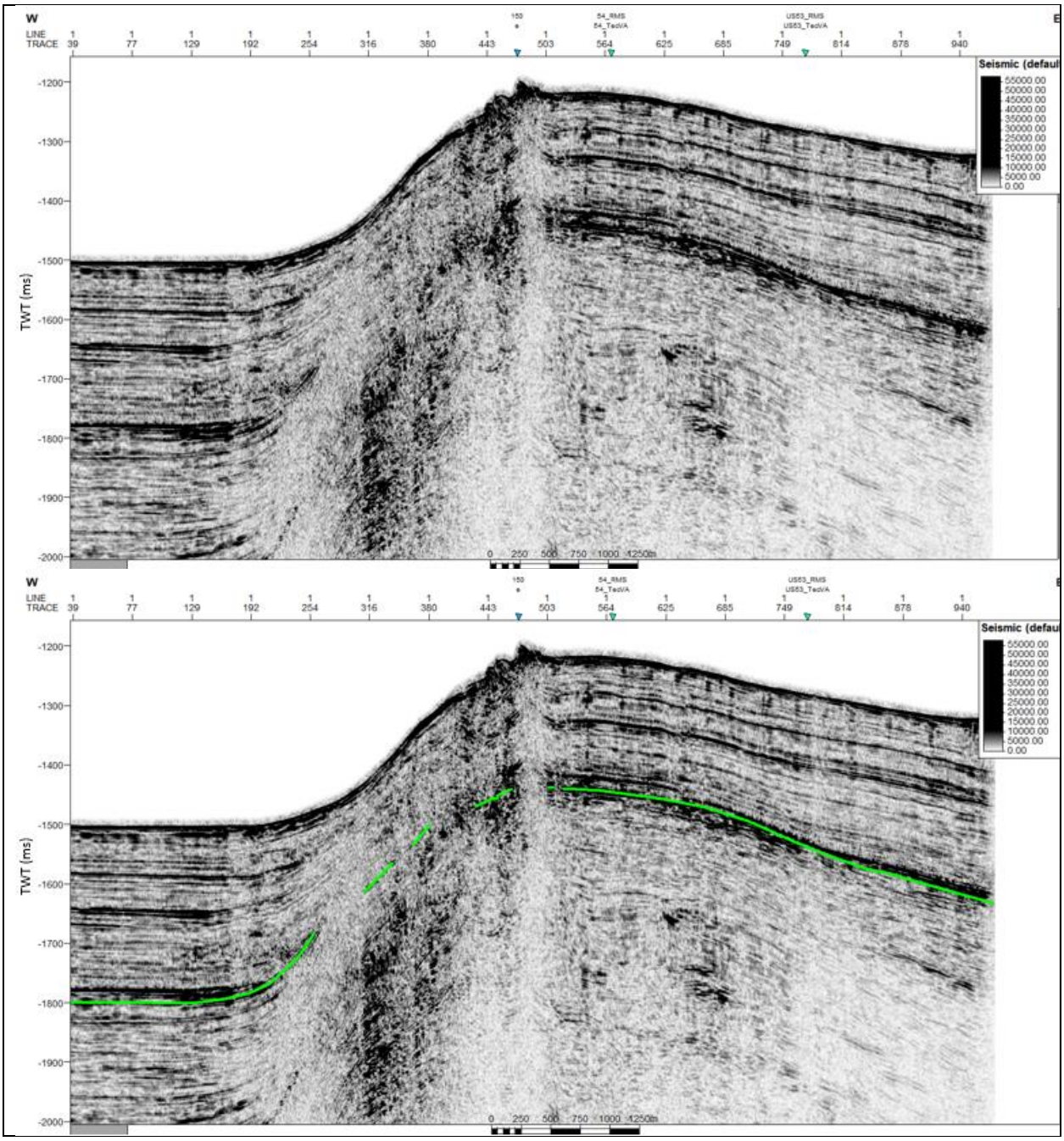

SCS profile US-13 with Amplitude RMS. Green line indicates BSR.

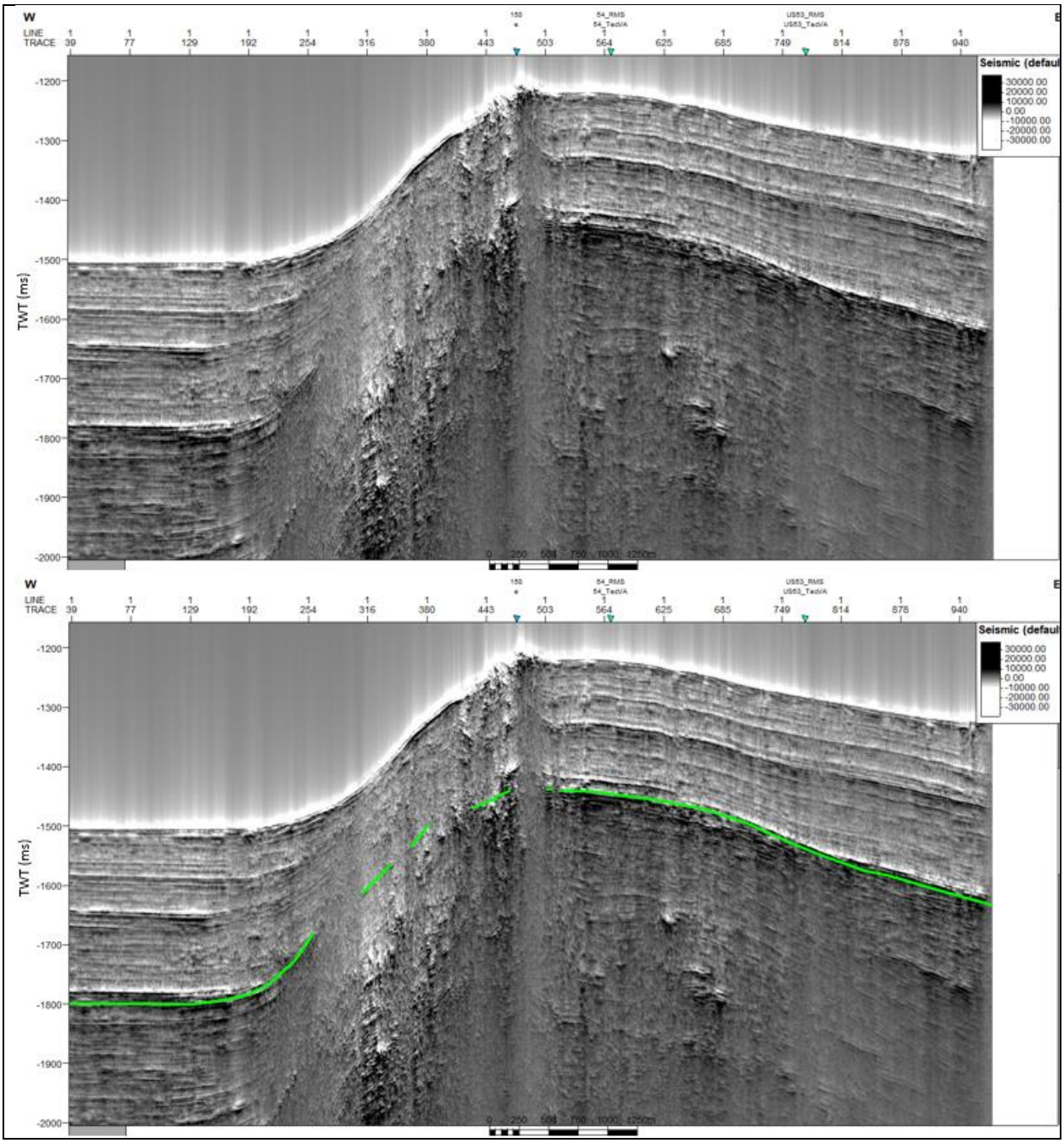

SCS profile US-13 with Amplitude Volume Technique. Green line indicates BSR.

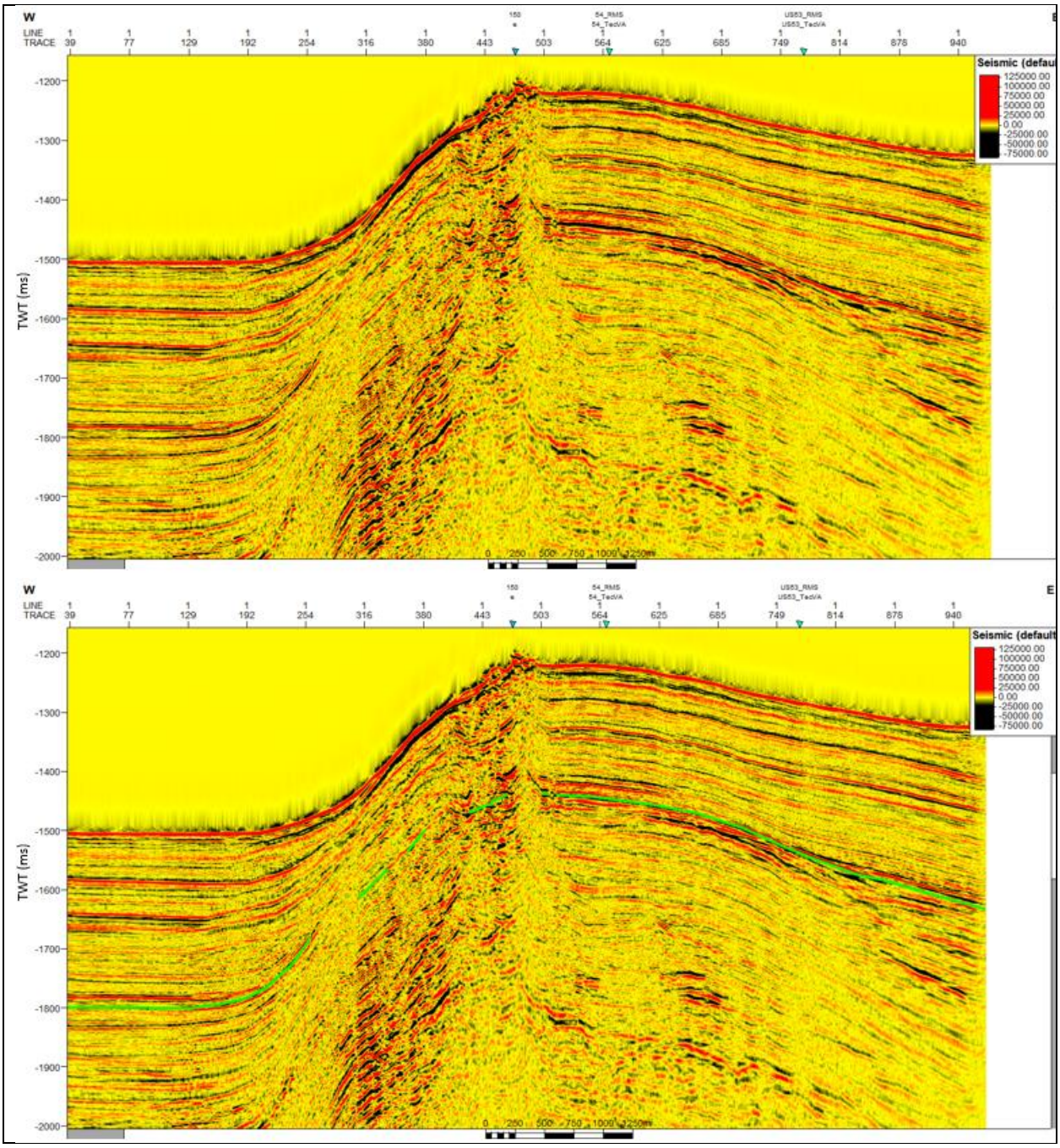

SCS profile US-13 with Relative Acoustic Impedance. Green line indicates BSR.

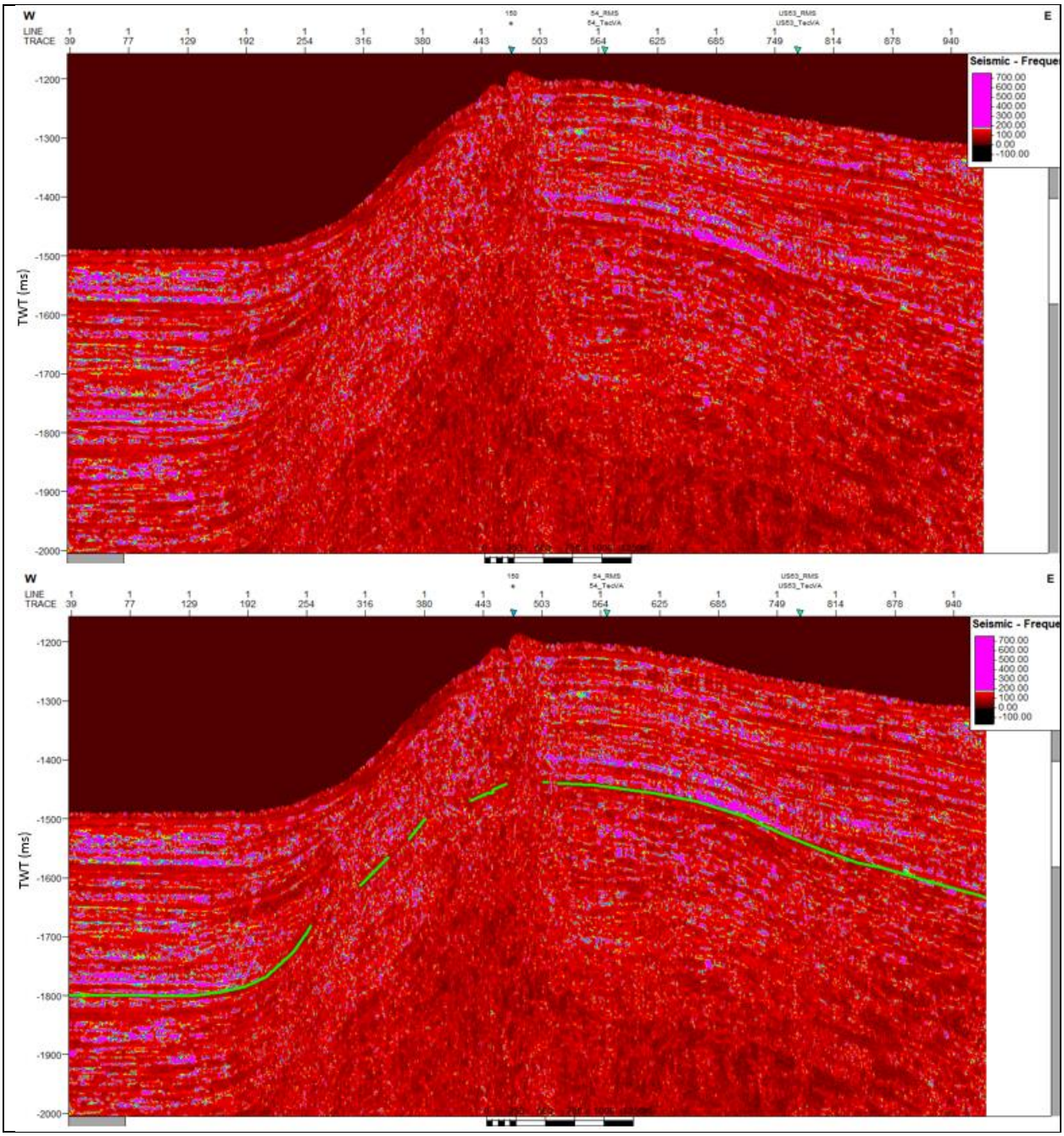

SCS profile US-13 with Instantaneous Frequency. Green line indicates BSR.

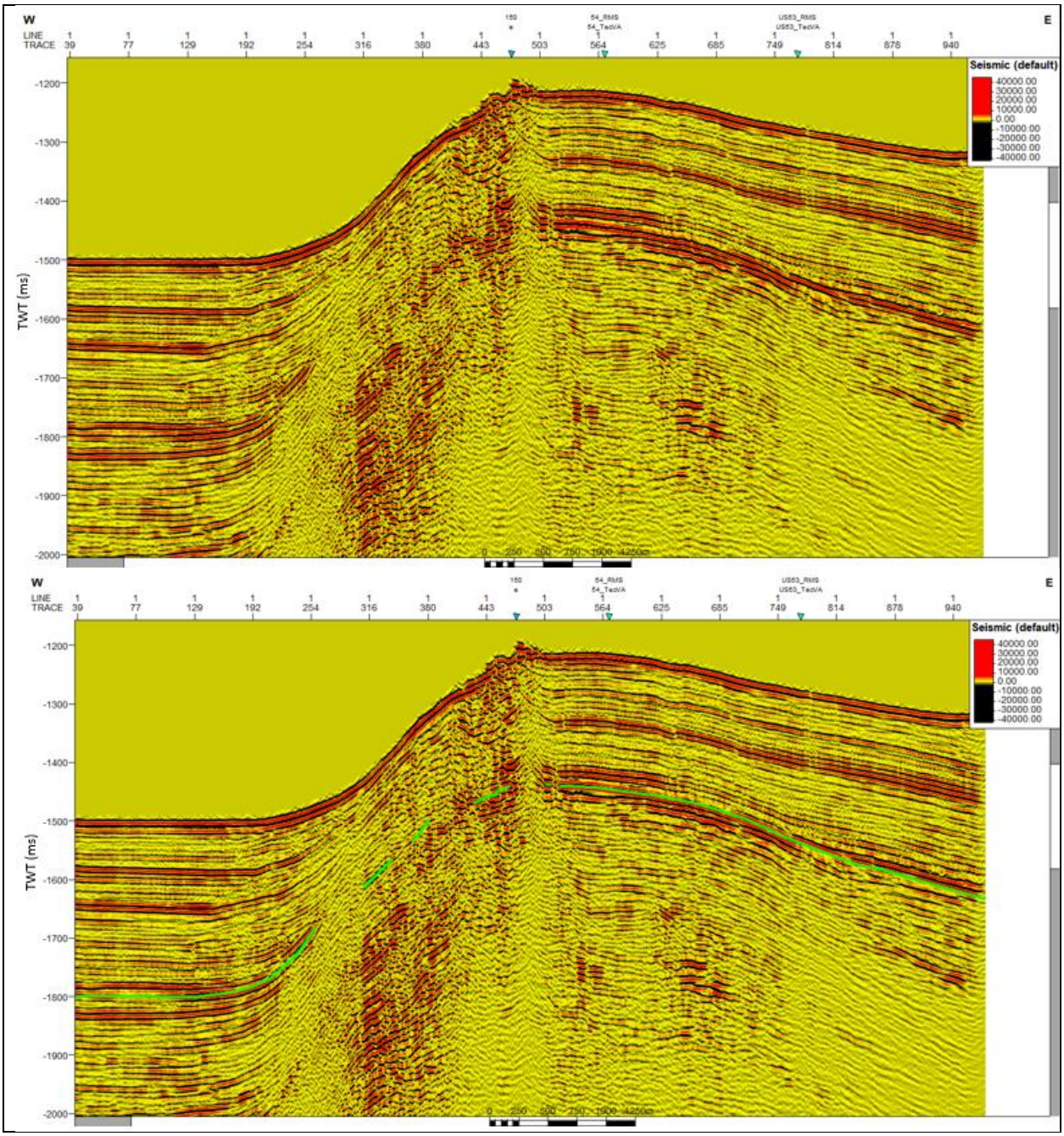

SCS profile US-13 with Spectral Decomposition of 100 Hz. Green line indicates BSR.

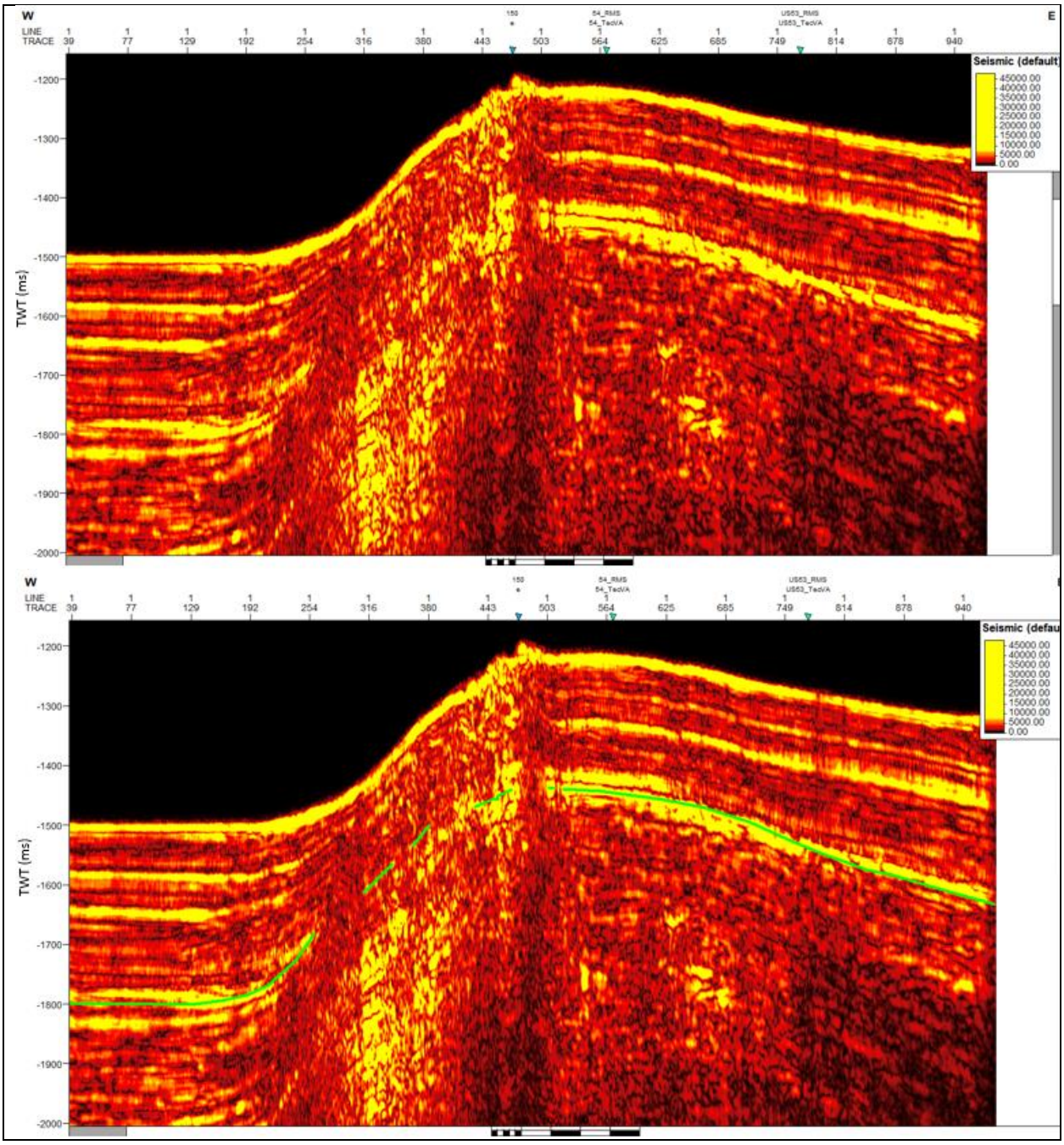

SCS profile US-13 with Spectral Decomposition of 100 Hz plus Envelope. Green line indicates BSR.

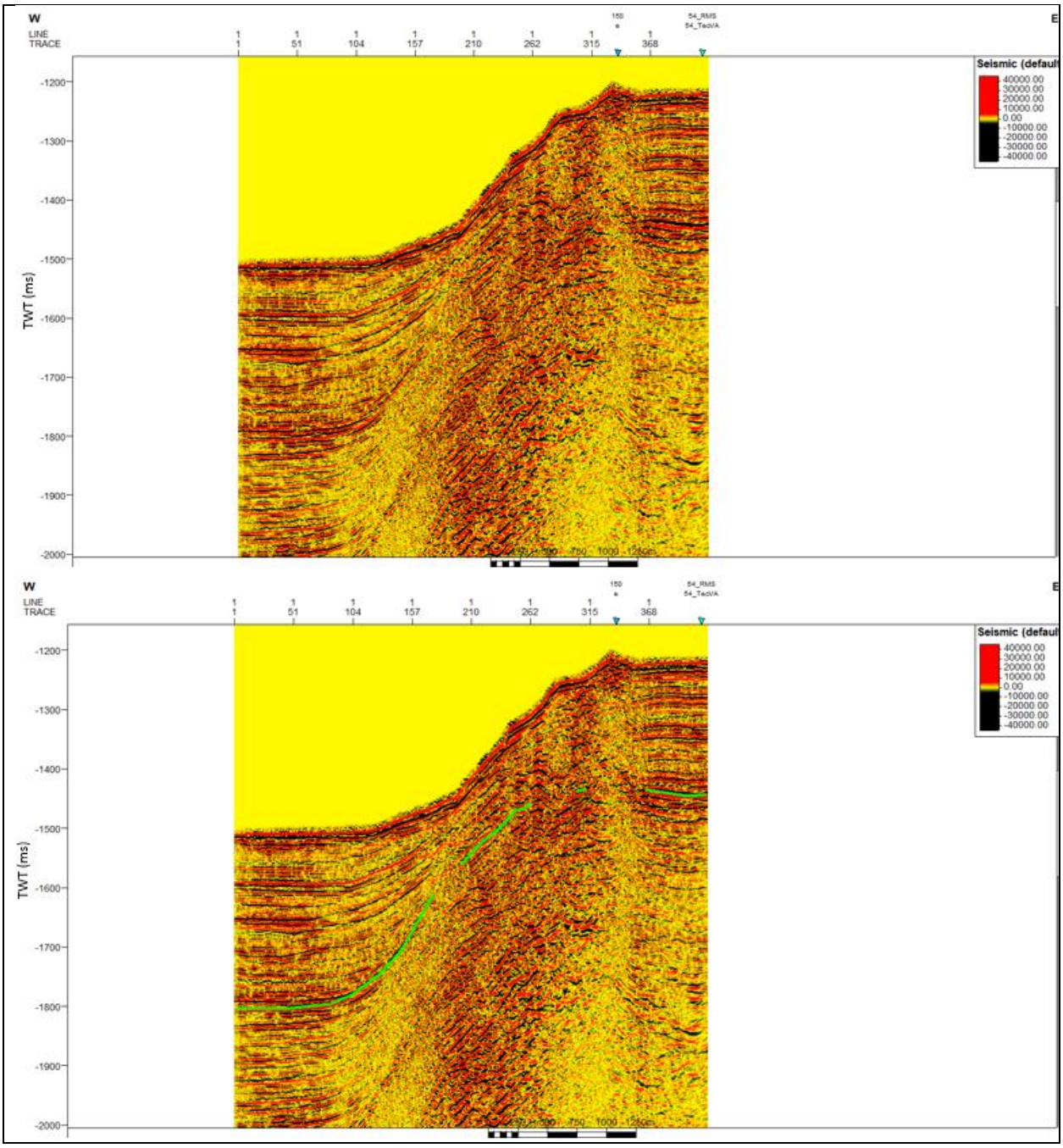

SCS profile US-14 without application of seismic attribute. Green line indicates BSR.

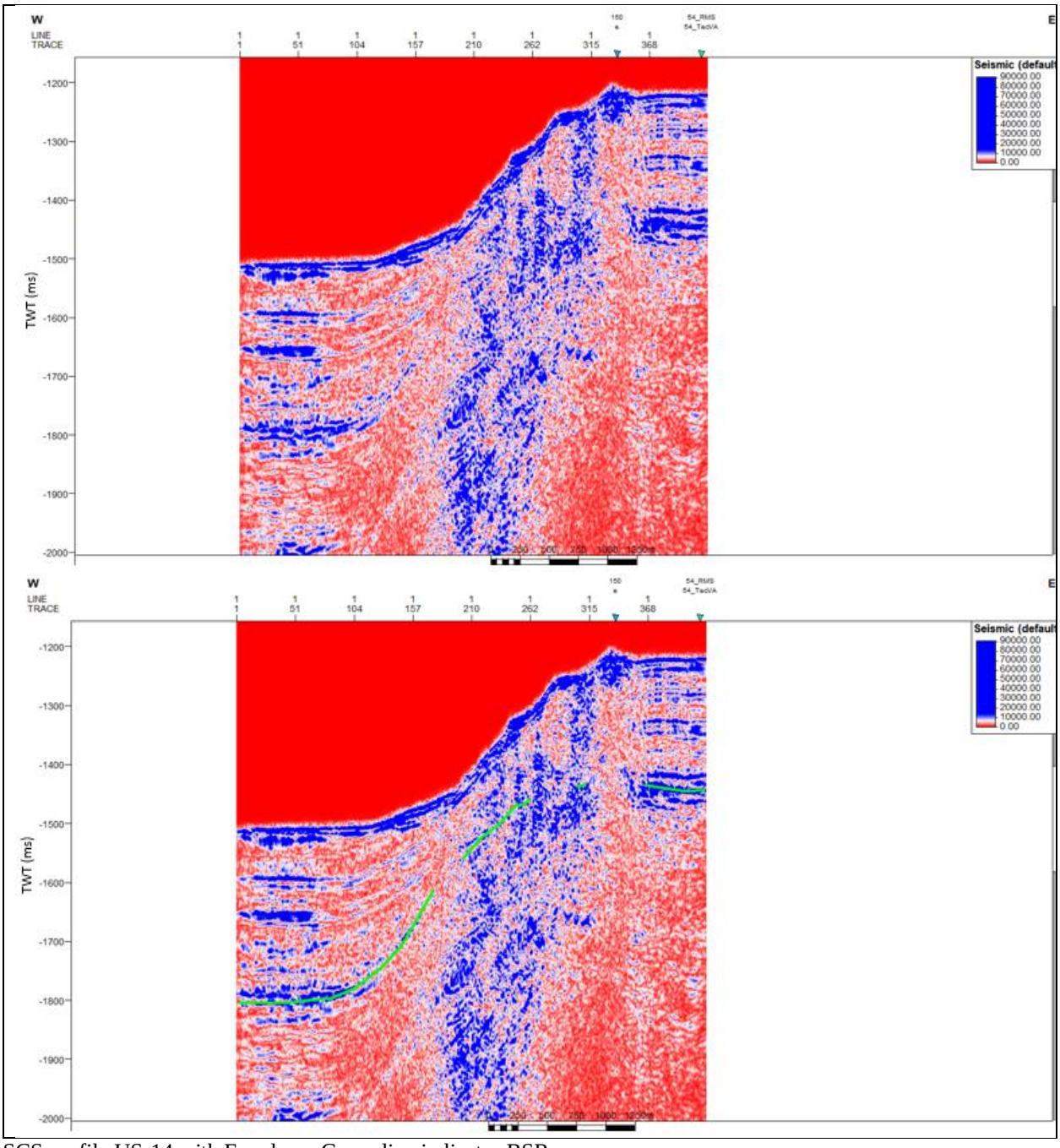

SCS profile US-14 with Envelope. Green line indicates BSR.

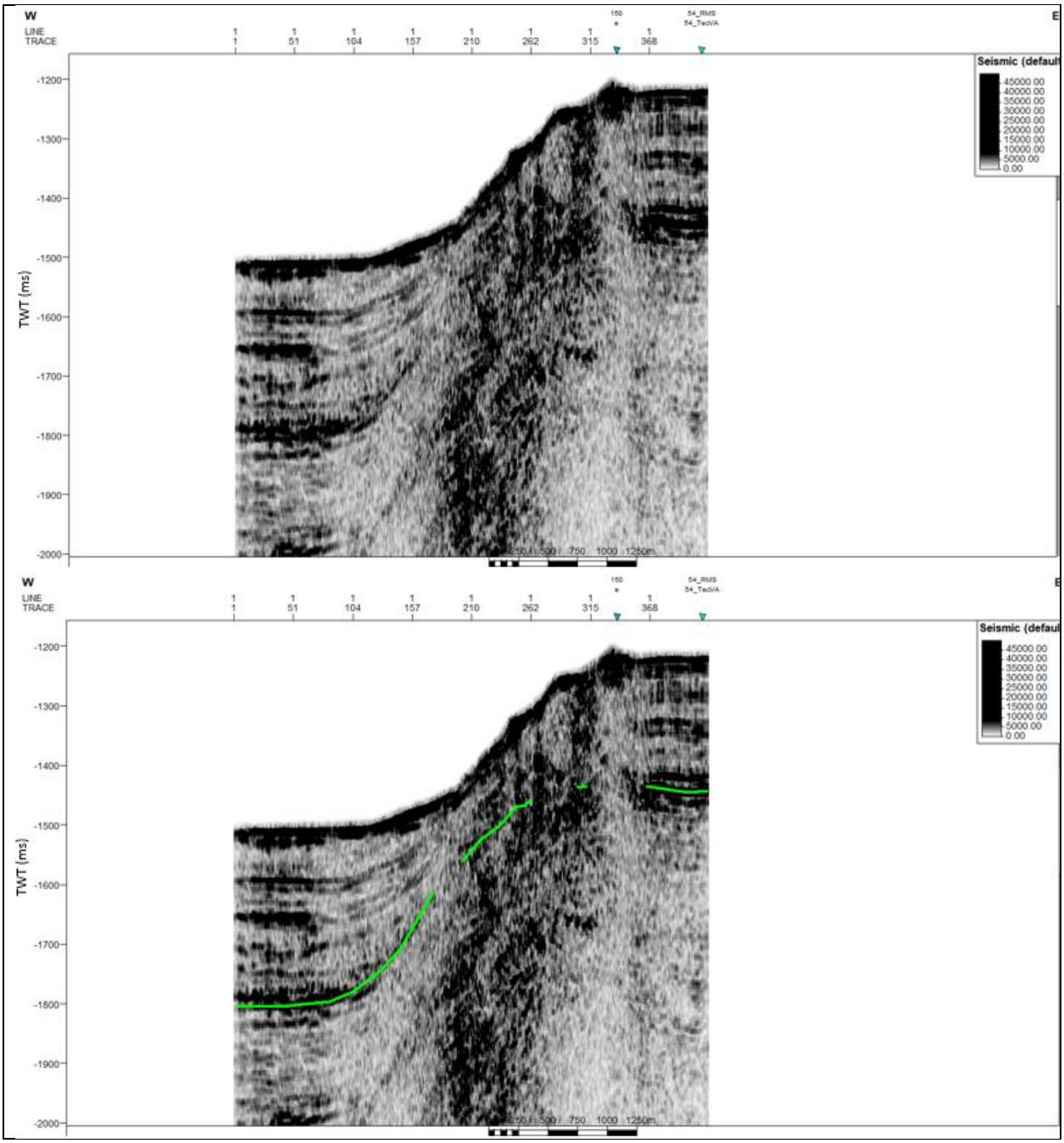

SCS profile US-14 with RMS Amplitude. Green line indicates BSR.

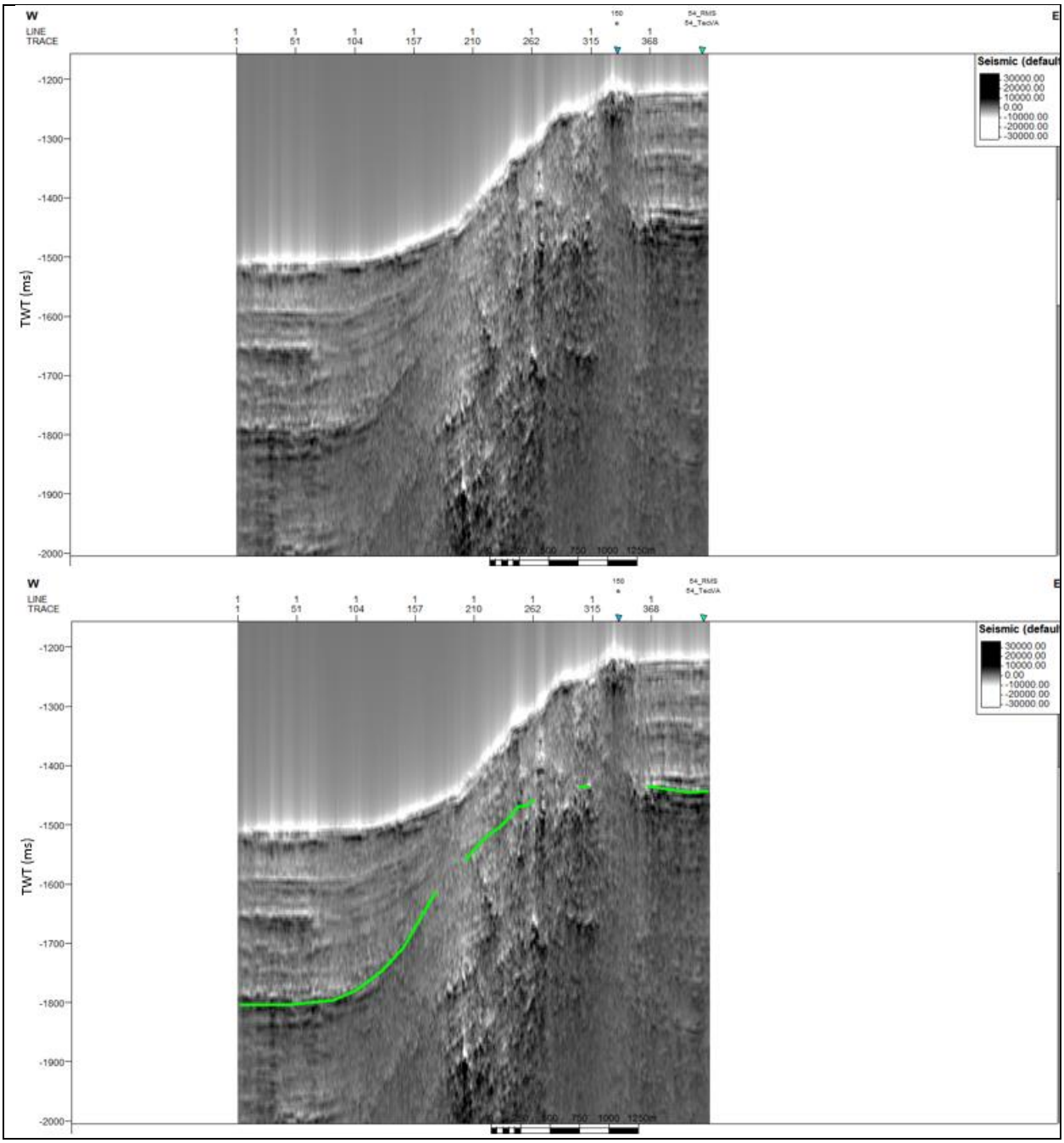

SCS profile US-14 with Amplitude Volume Technique. Green line indicates BSR.

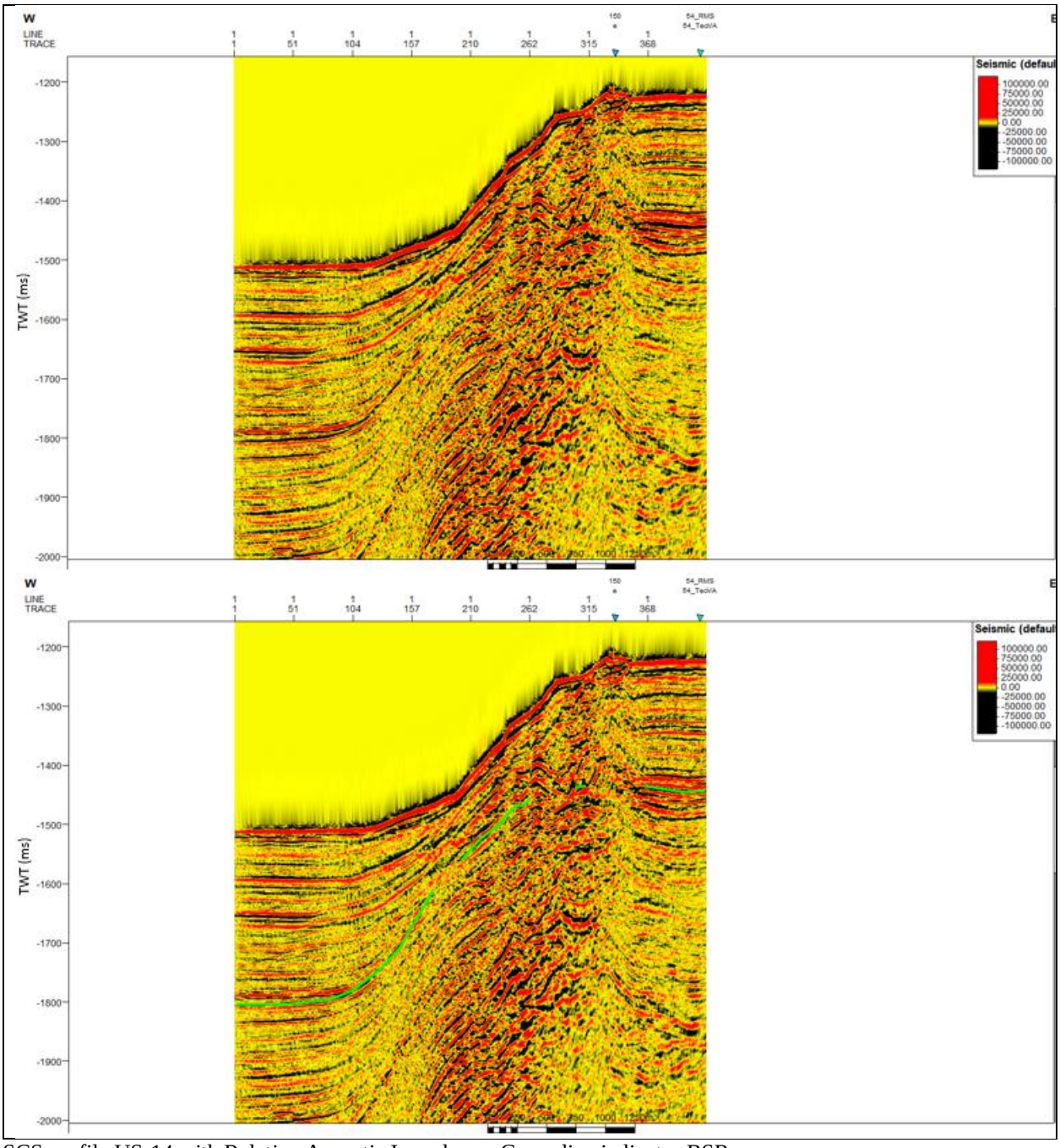

SCS profile US-14 with Relative Acoustic Impedance. Green line indicates BSR.

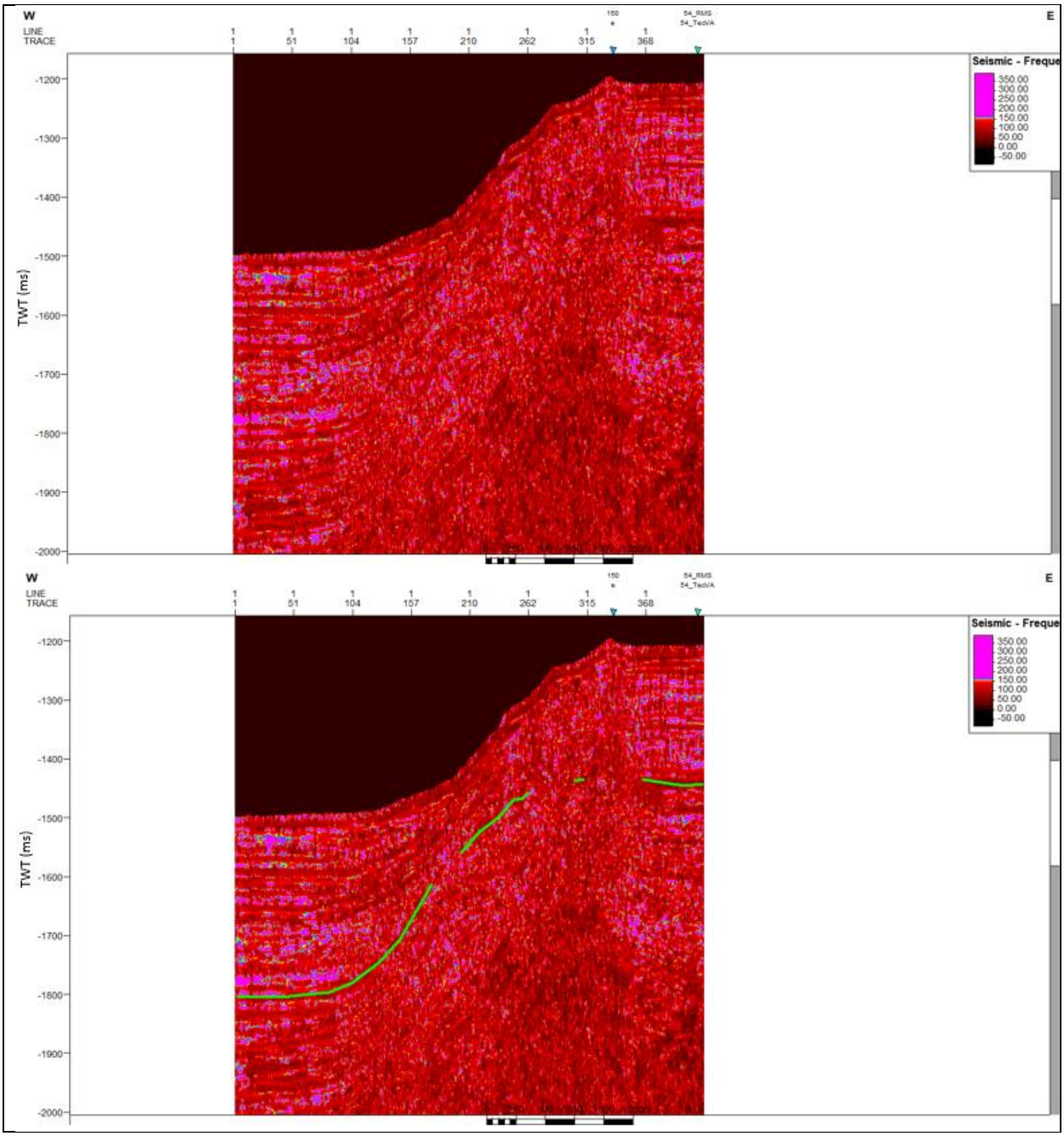

SCS profile US-14 with Instantaneous Frequency. Green line indicates BSR.

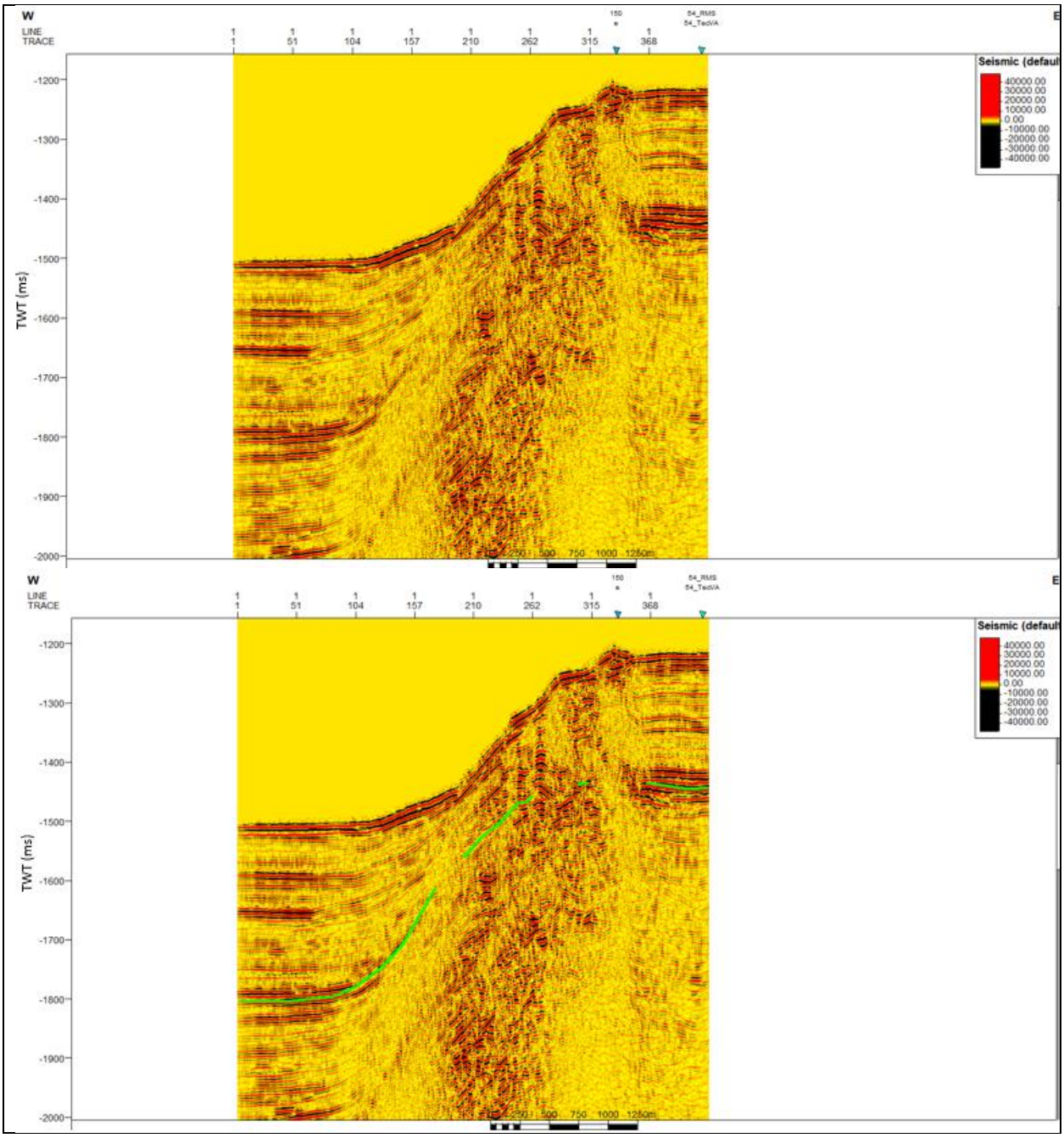

SCS profile US-14 with Spectral Decomposition of 100 Hz. Green line indicates BSR.

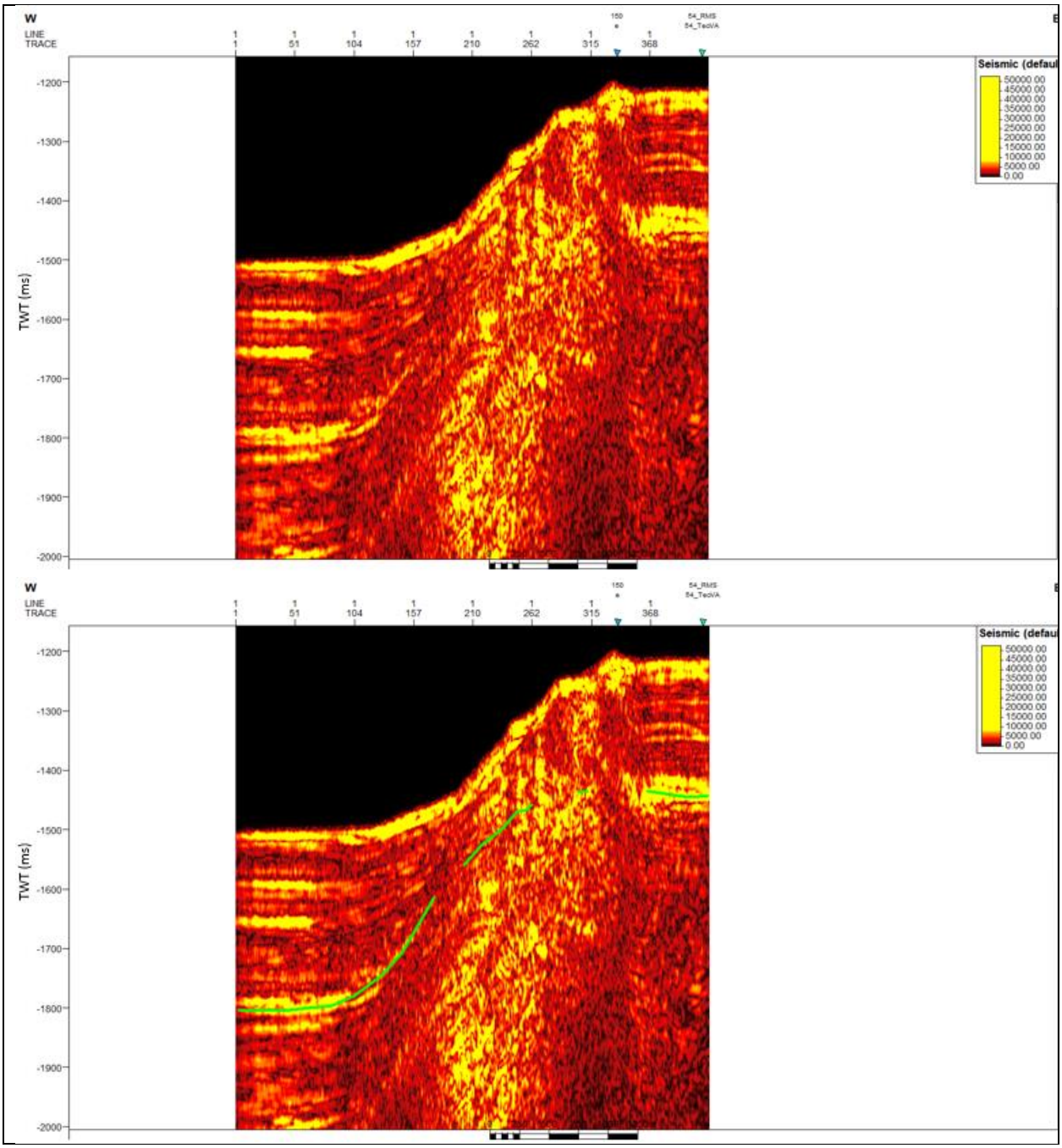

SCS profile US-14 with Spectral Decomposition of 100 Hz plus Envelope. Green line indicates BSR.

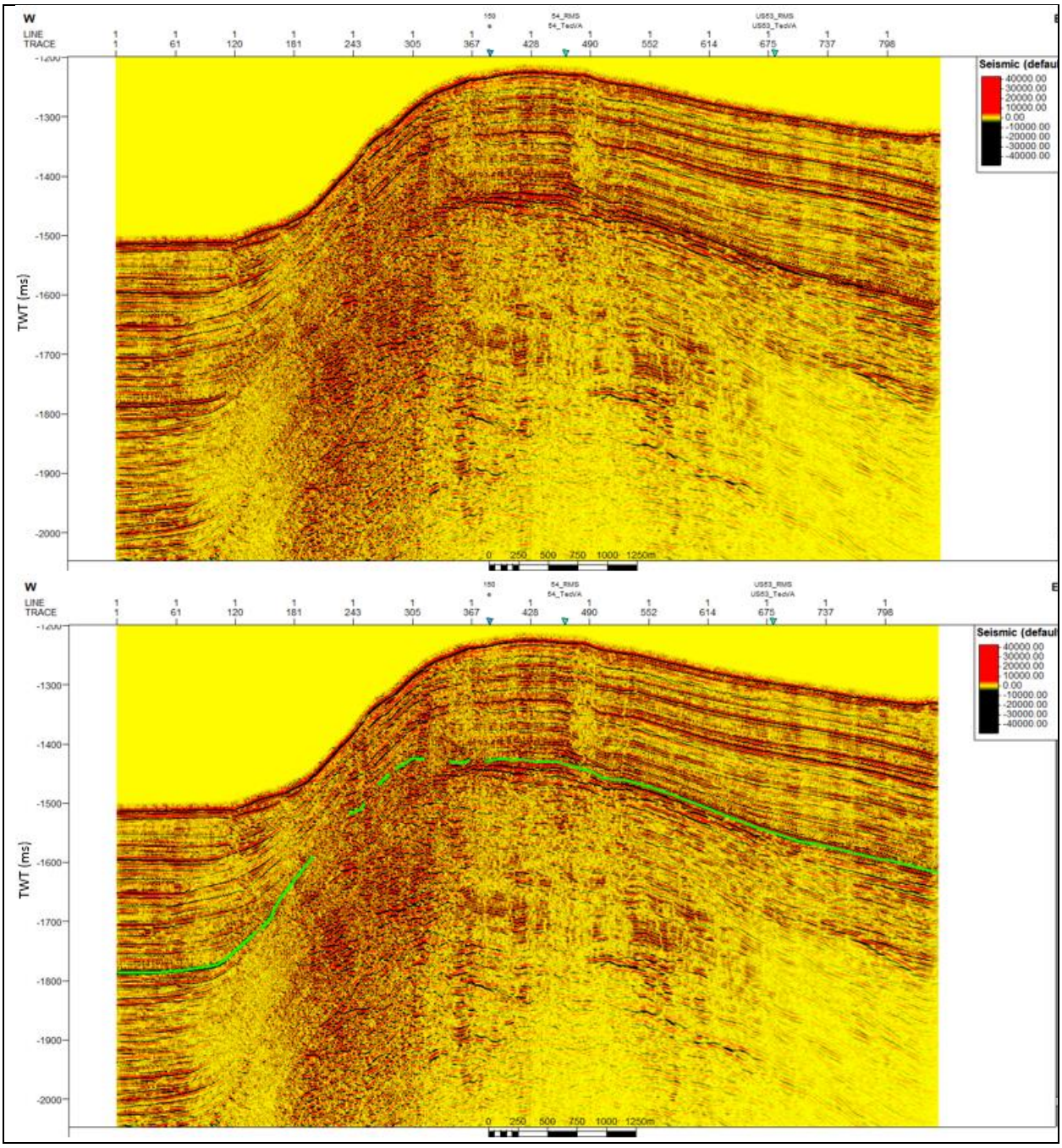

SCS profile US-15 without application of seismic attribute. Green line indicates BSR.

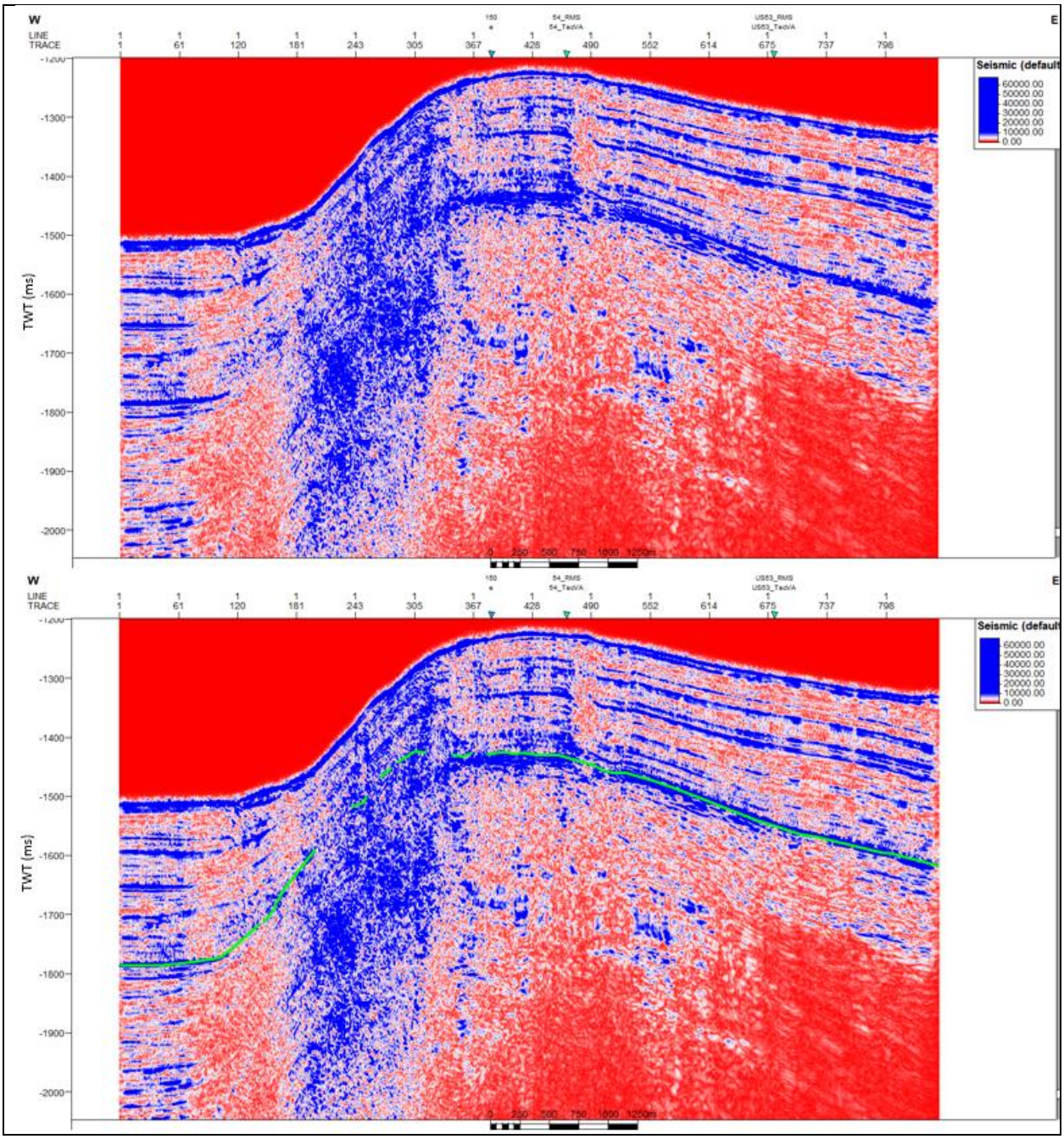

SCS profile US-15 with Envelope. Green line indicates BSR.

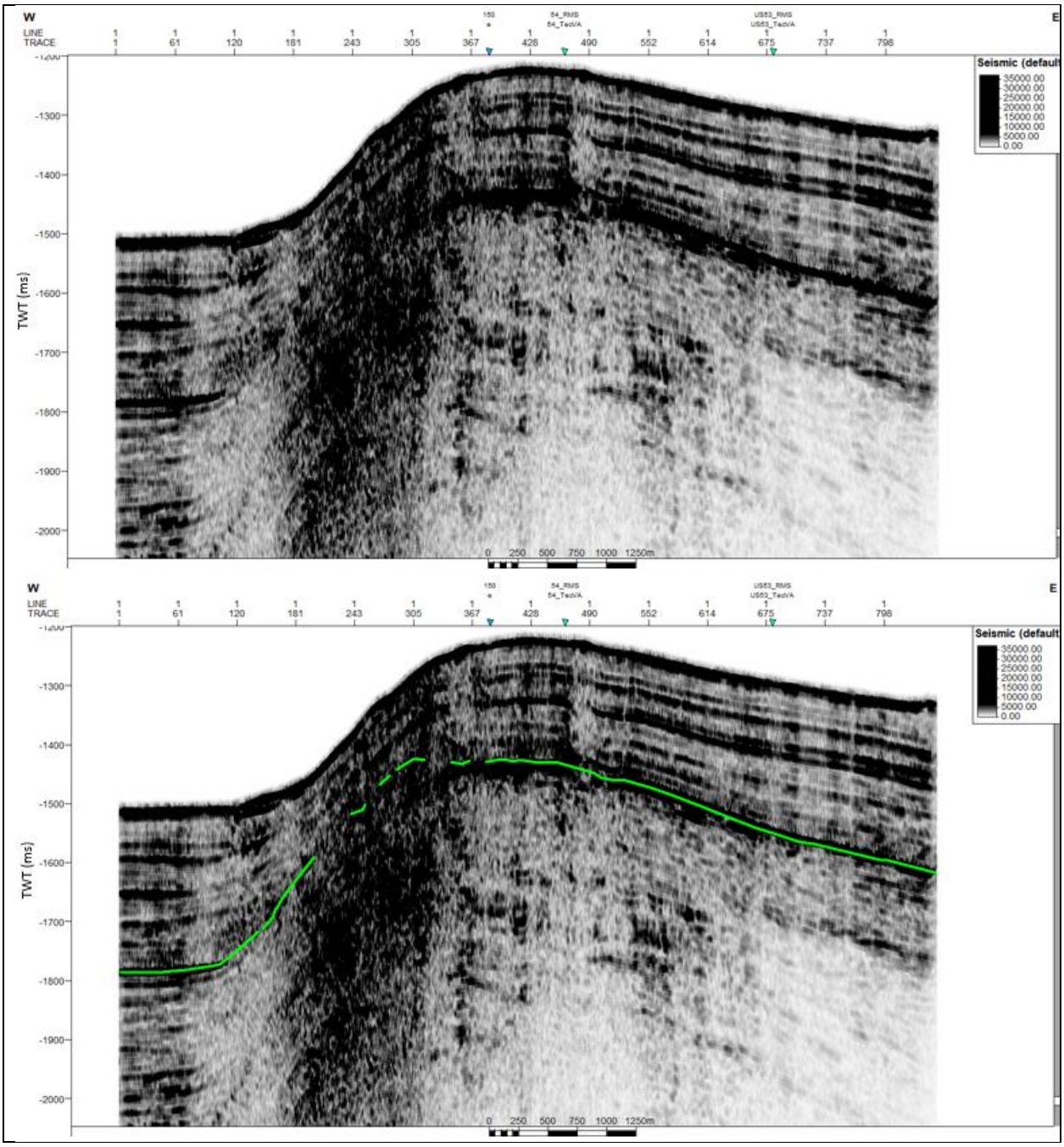

SCS profile US-15 with RMS Amplitude. Green line indicates BSR.

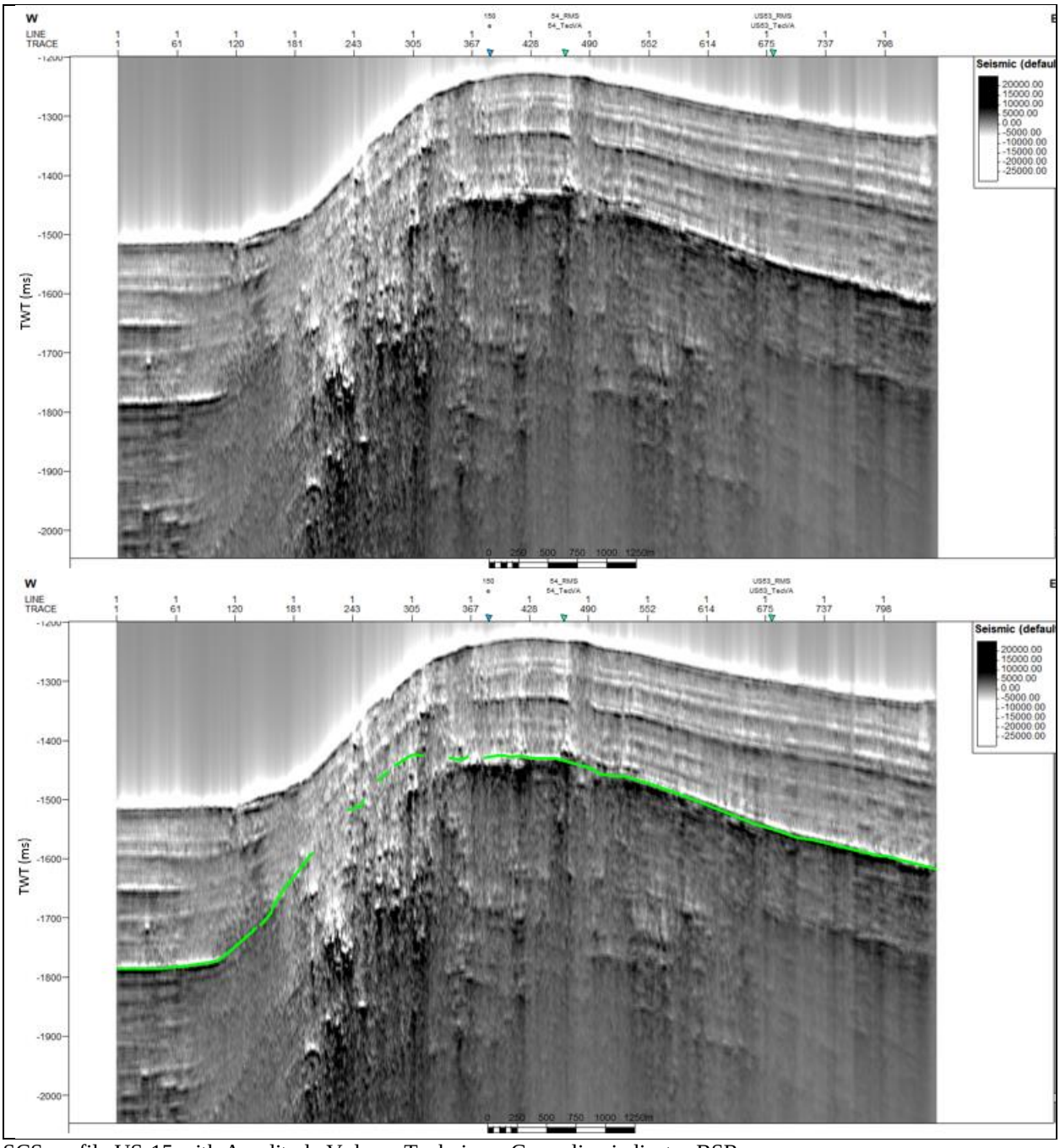

SCS profile US-15 with Amplitude Volume Technique. Green line indicates BSR.

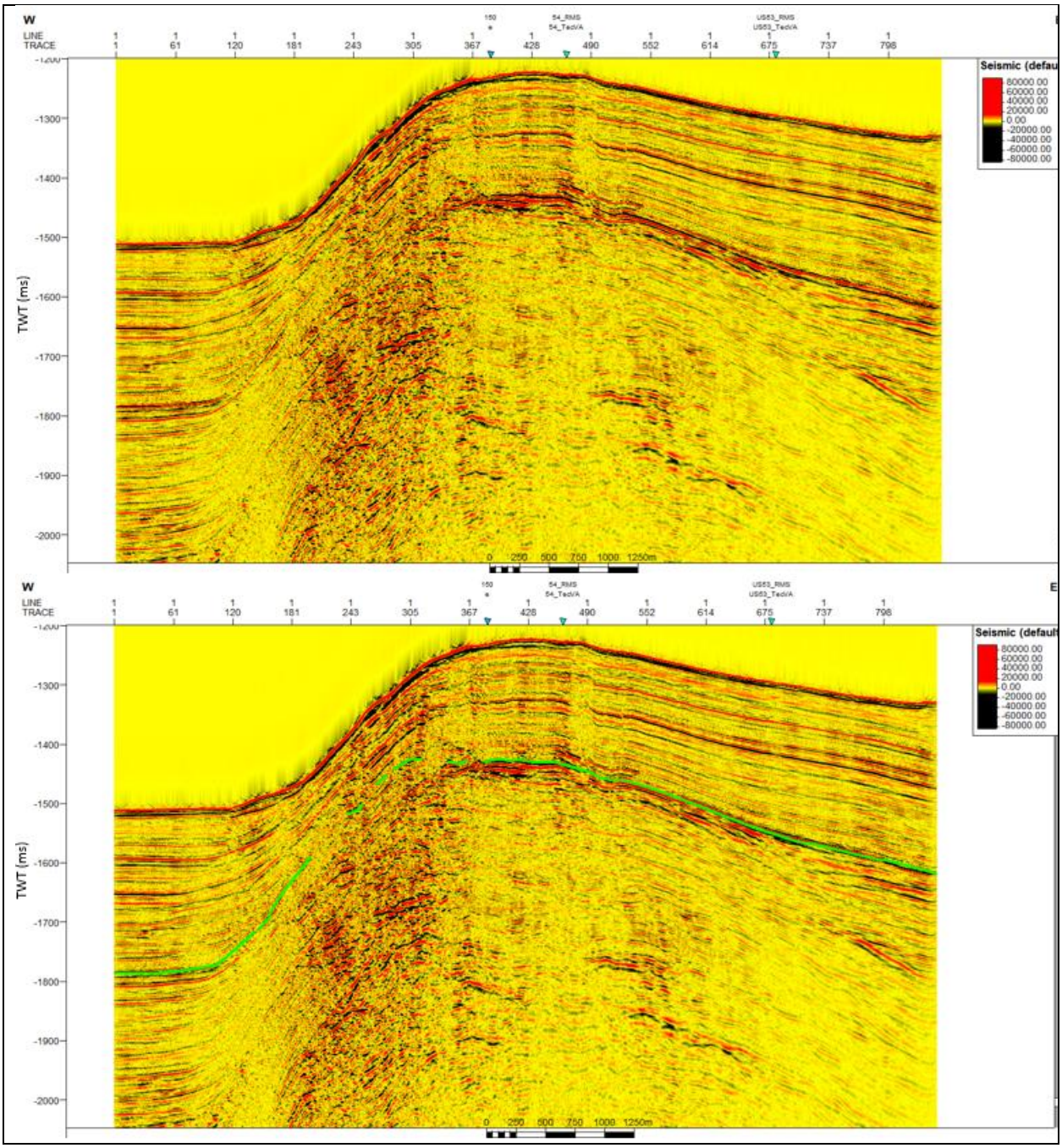

SCS profile US-15 with Relative Acoustic Impedance. Green line indicates BSR.

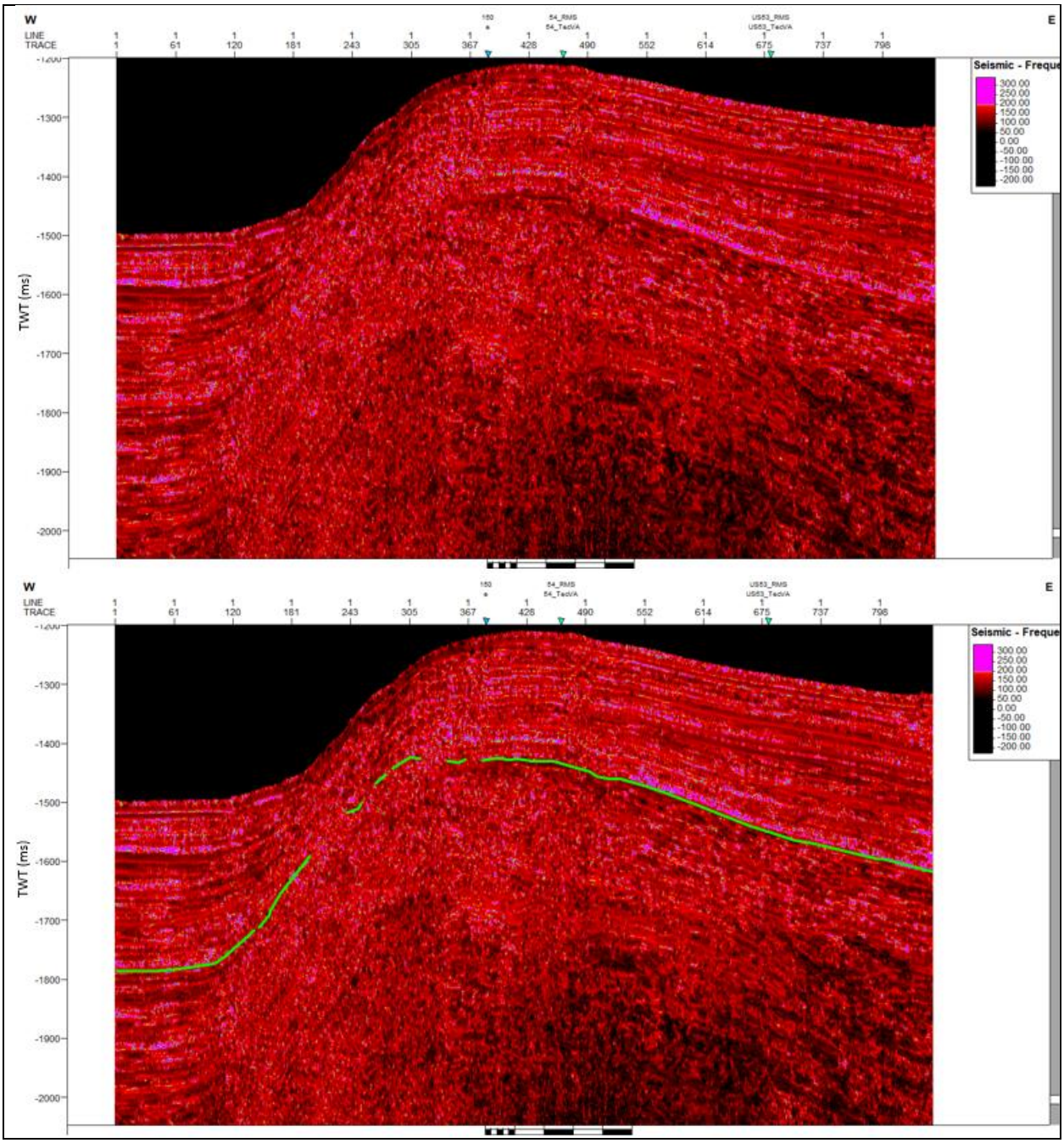

SCS profile US-15 with Instantaneous Frequency. Green line indicates BSR.

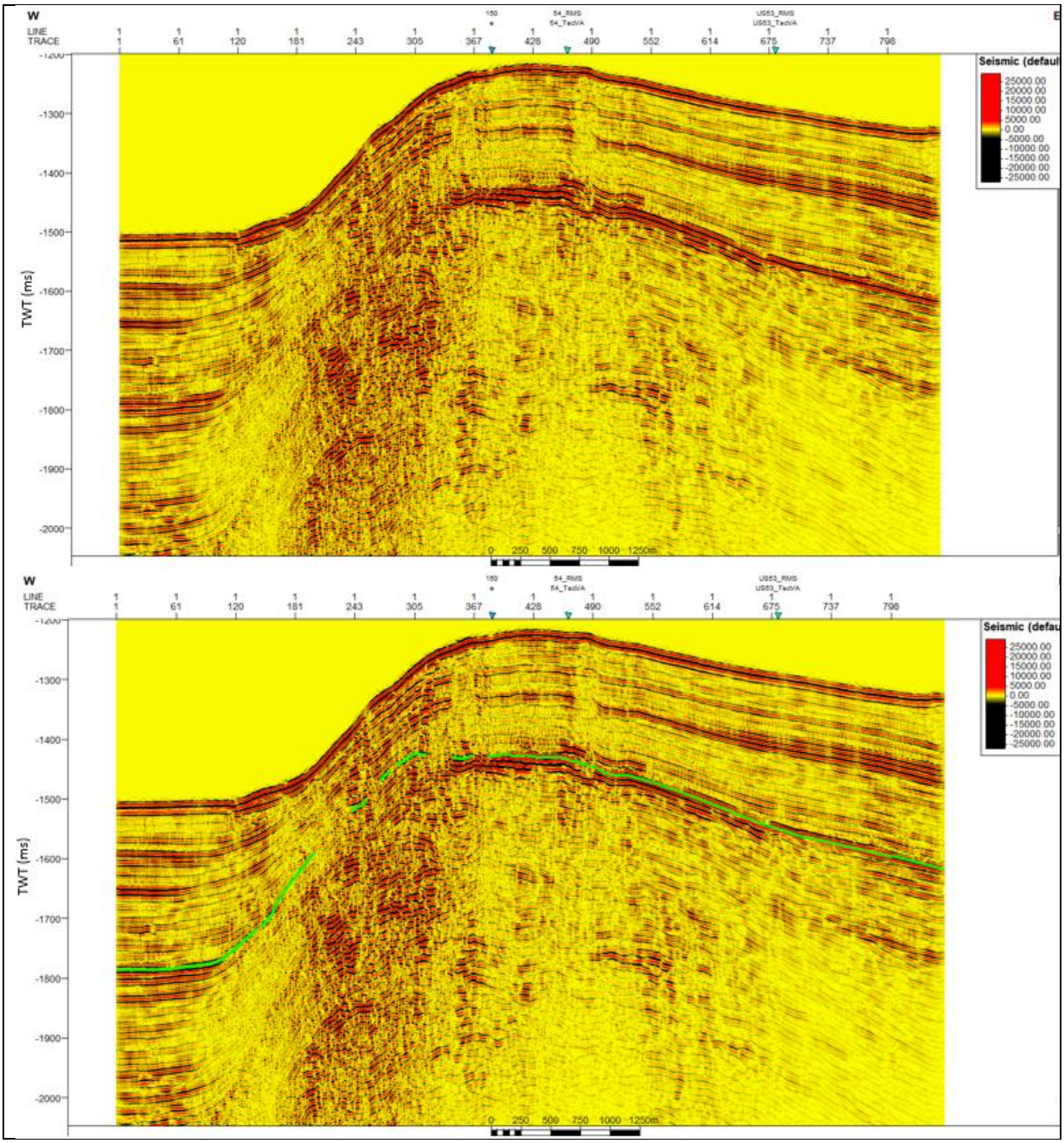

SCS profile US-15 with Spectral Decomposition of 100 Hz. Green line indicates BSR.

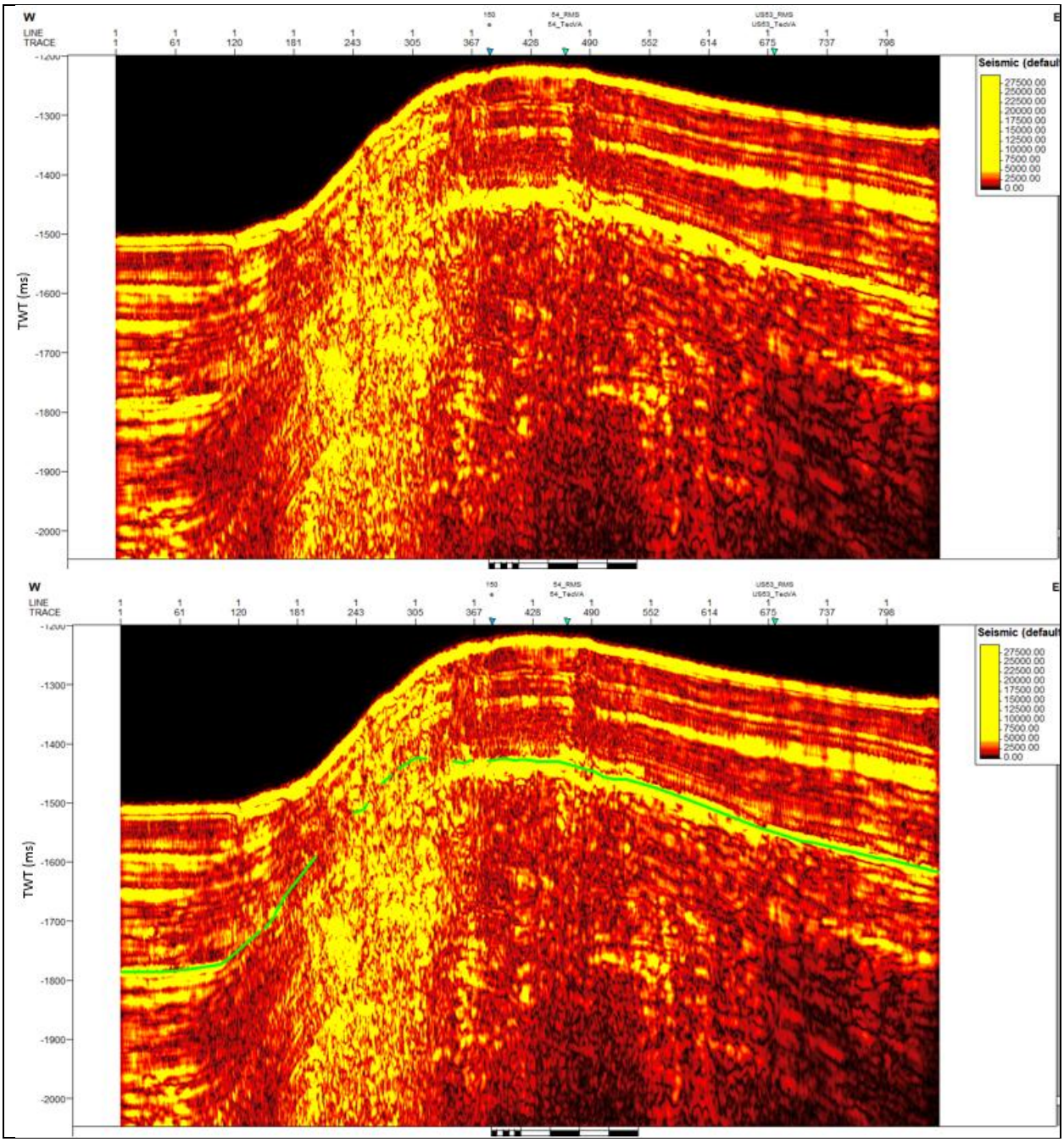

SCS profile US-15 with Spectral Decomposition of 100 Hz plus Envelope. Green line indicates BSR.

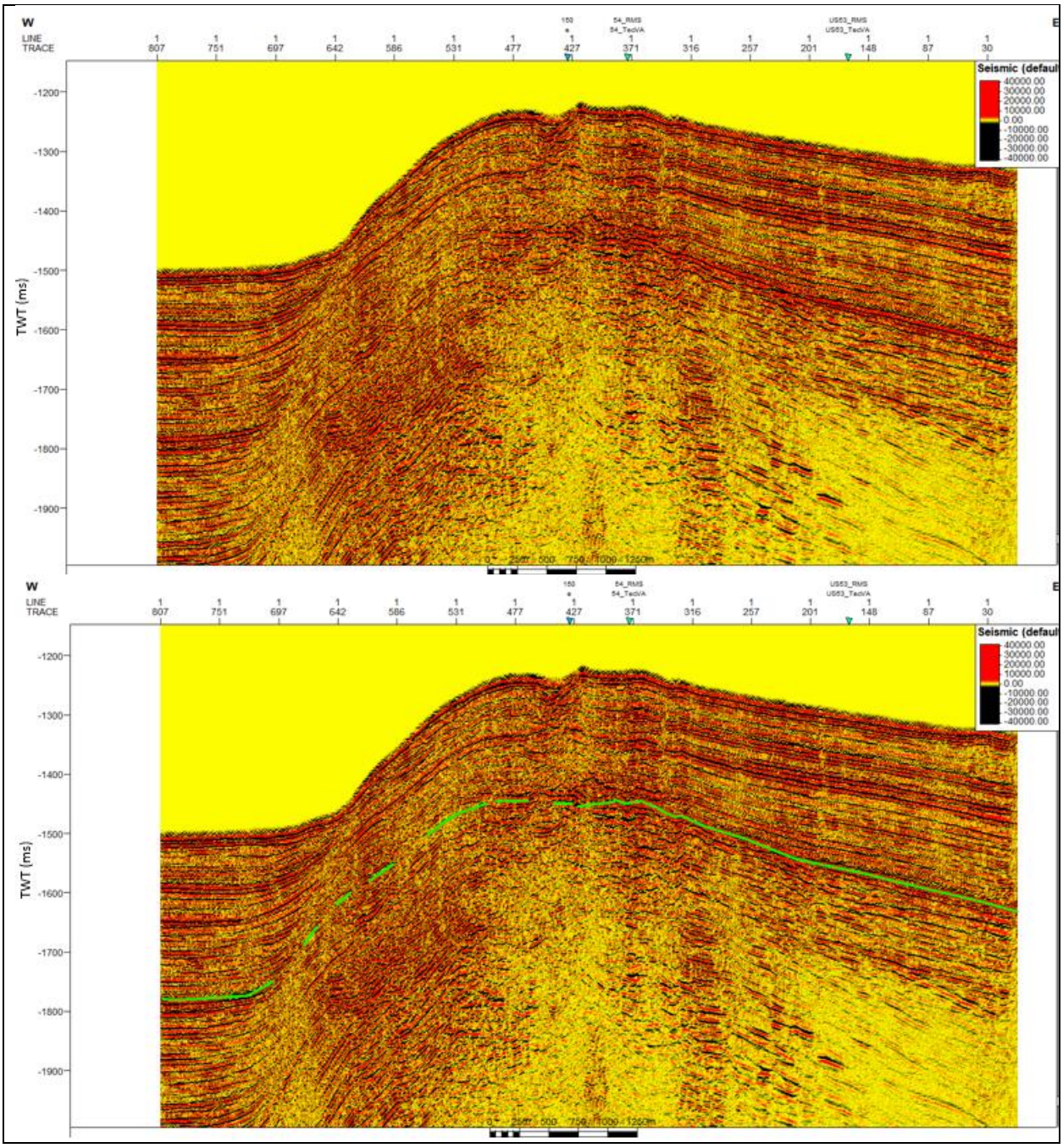

SCS profile US-17 without application of seismic attribute. Green line indicates BSR.

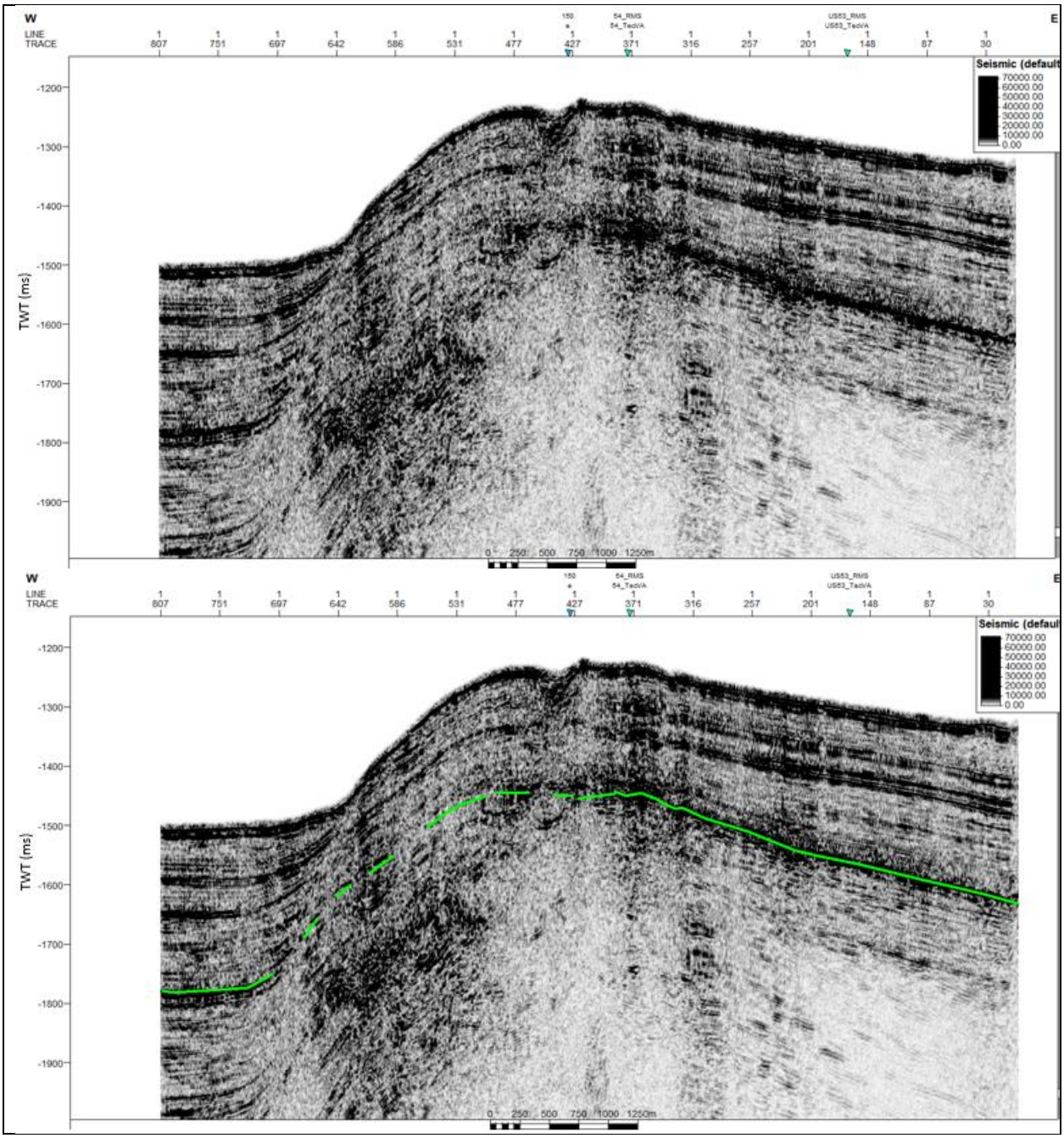

SCS profile US-17 with RMS Amplitude. Green line indicates BSR.

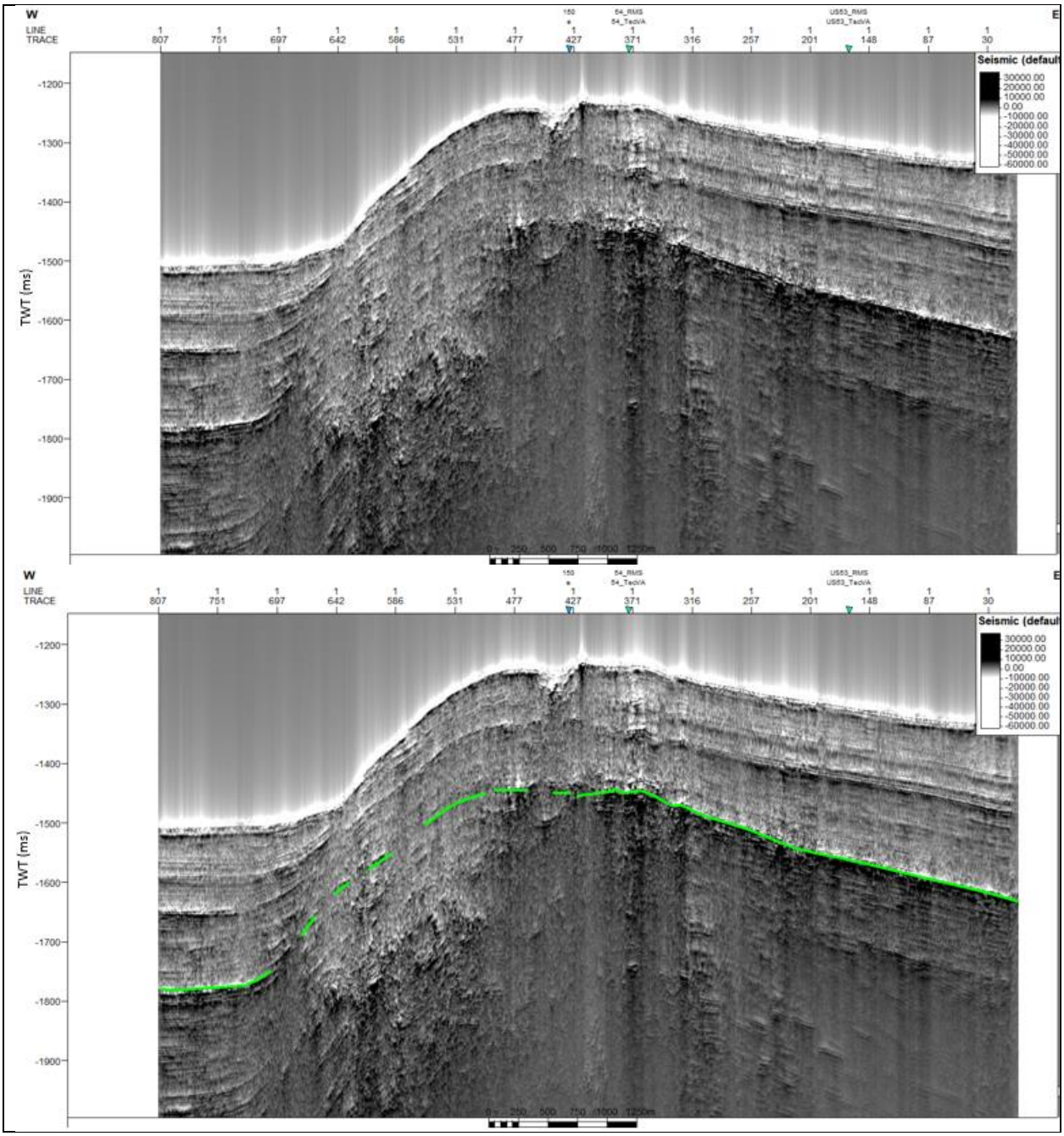

SCS profile US-17 with Amplitude Volume Technique. Green line indicates BSR.

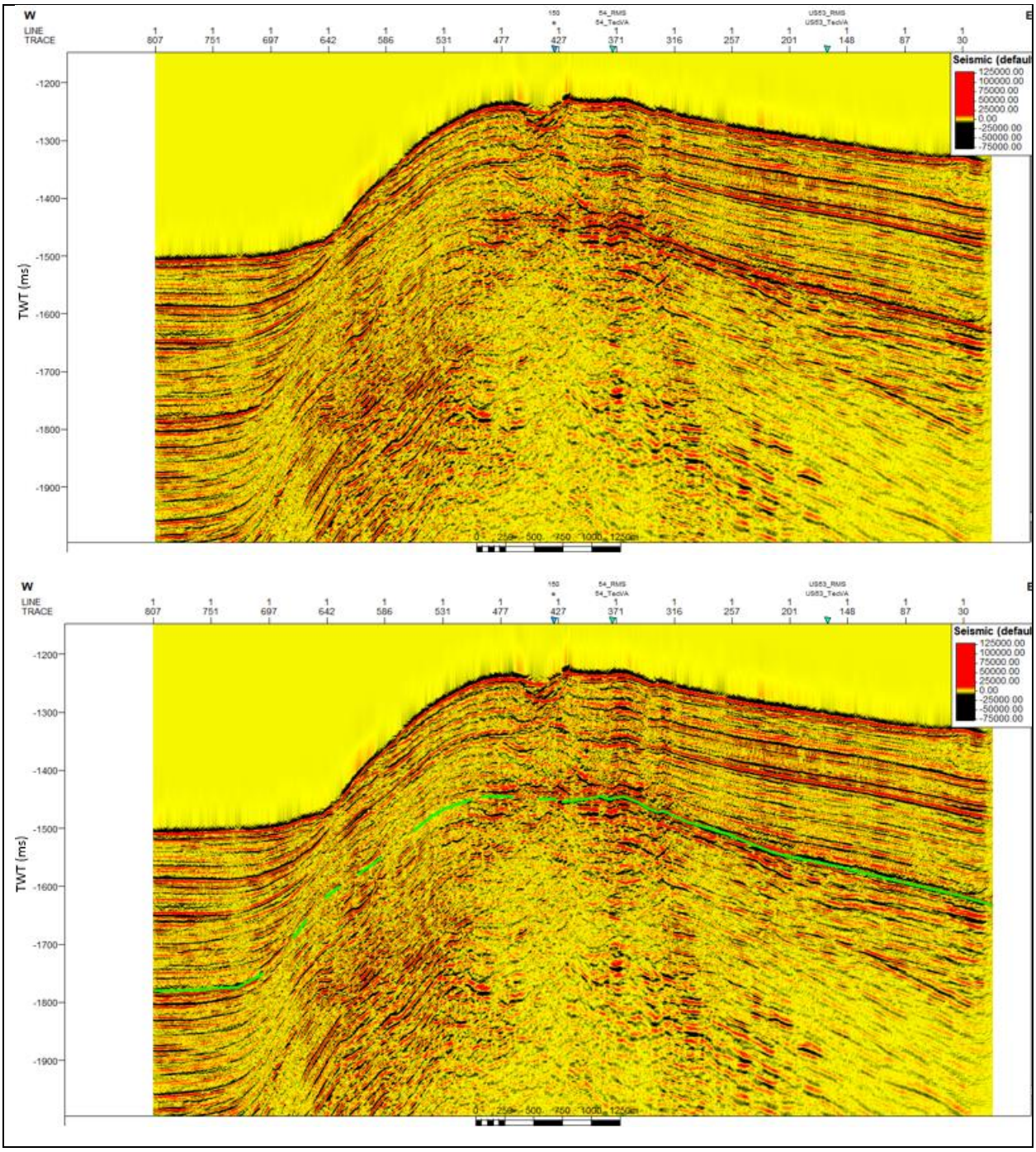

SCS profile US-17 with Relative Acoustic Impedance. Green line indicates BSR.

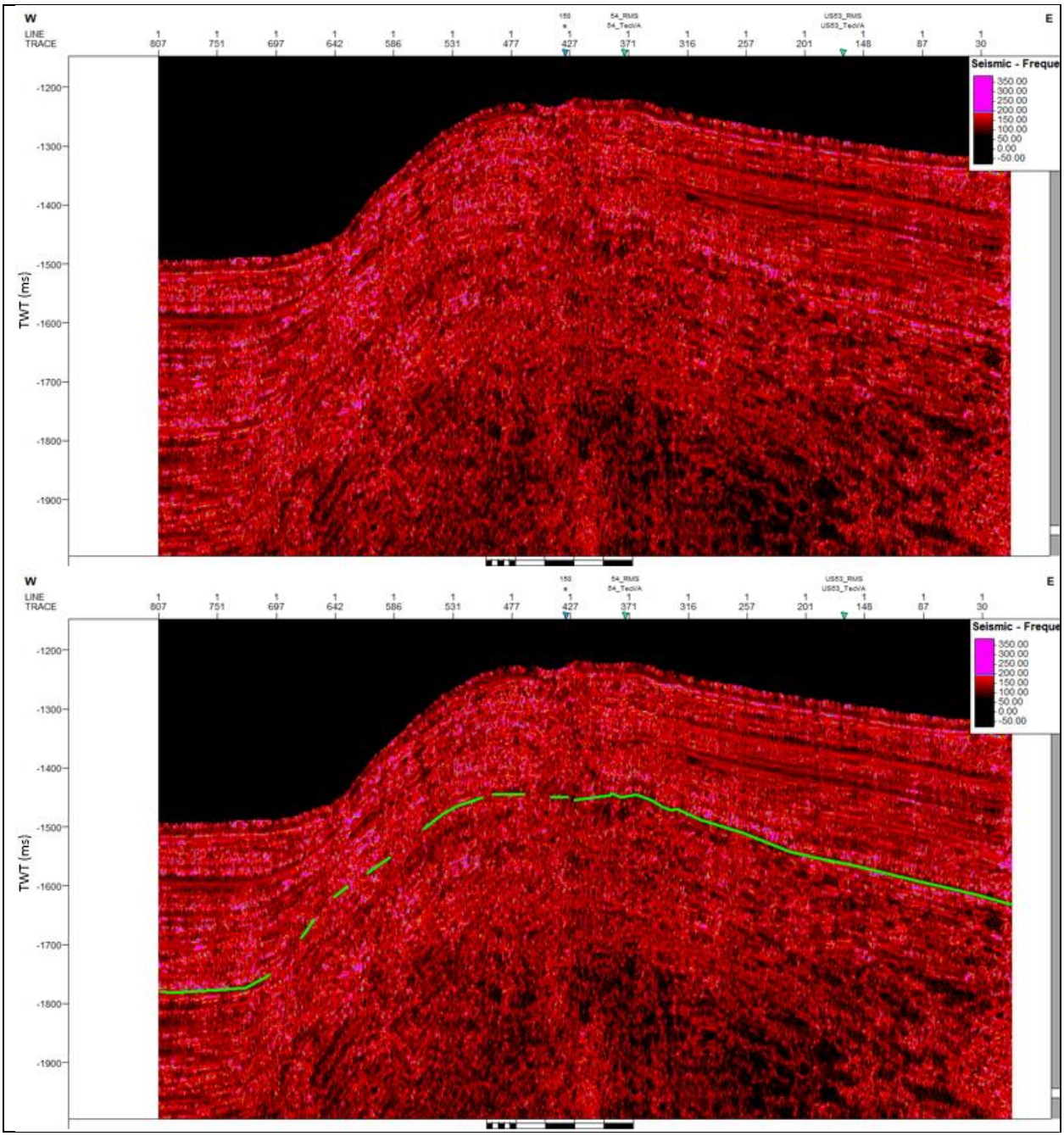

SCS profile US-17 with Instantaneous Frequency. Green line indicates BSR.

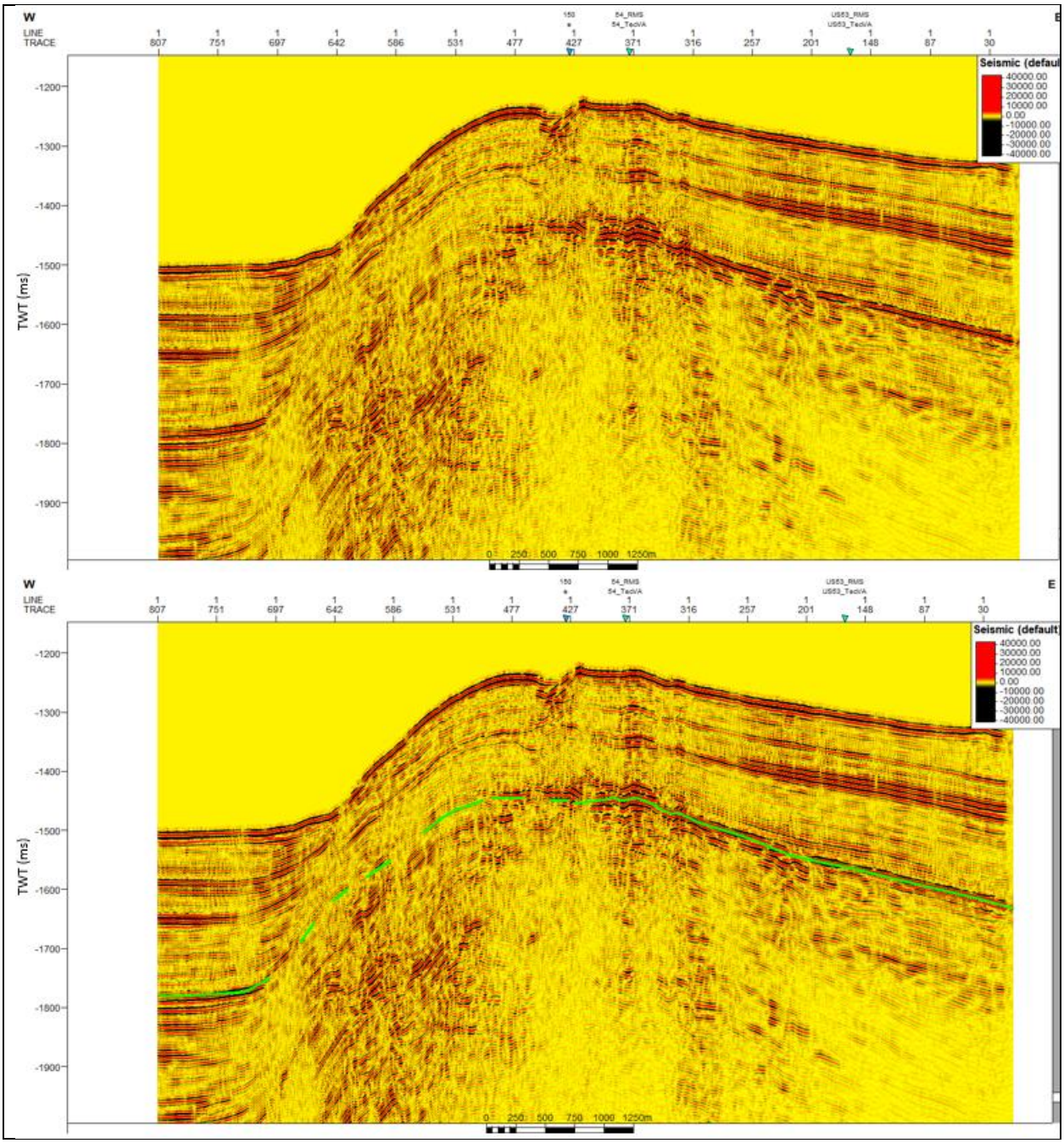

SCS profile US-17 with Spectral Decomposition of 100 Hz. Green line indicates BSR.

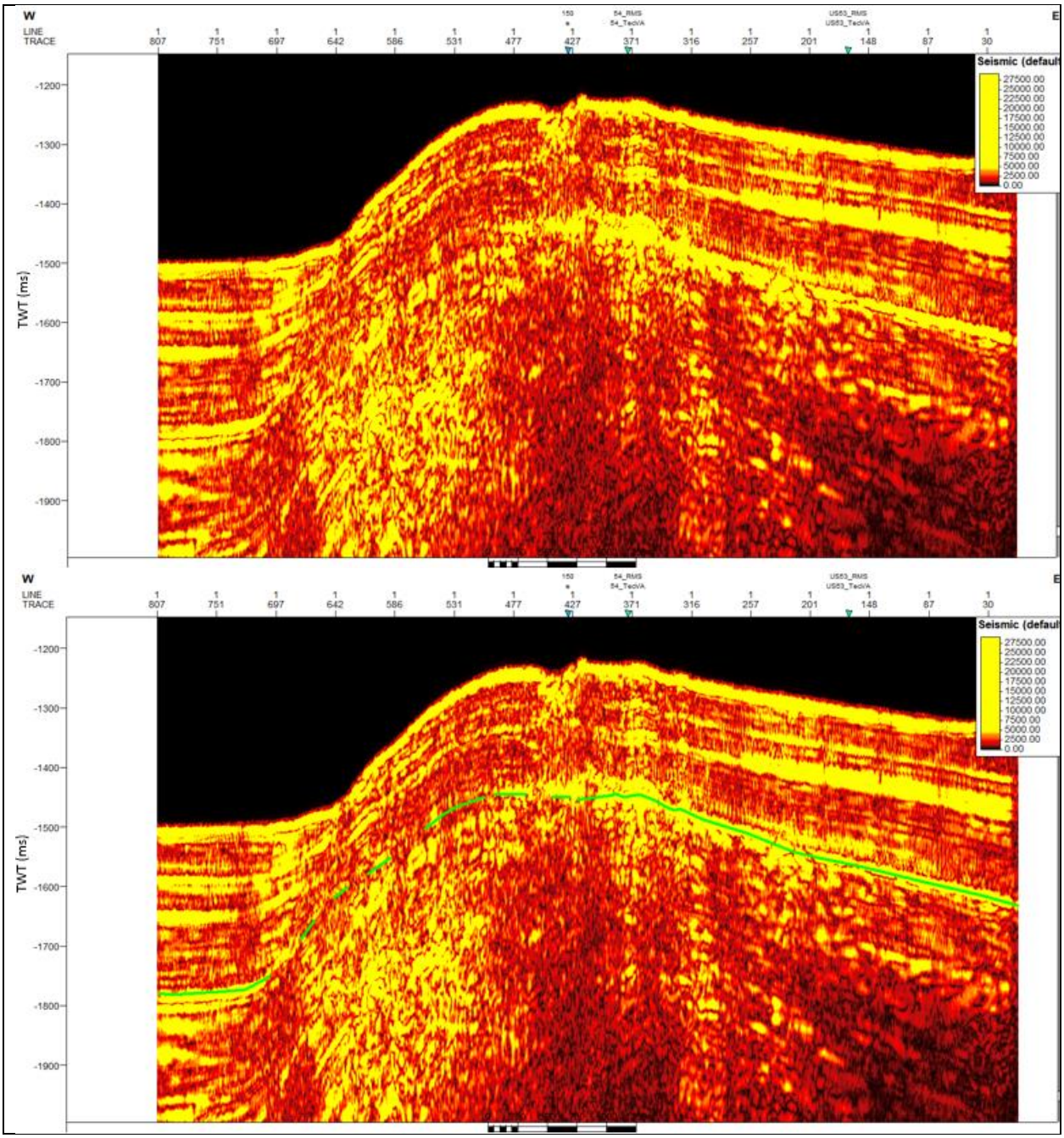

SCS profile US-17 with Spectral Decomposition of 100 Hz plus Envelope. Green line indicates BSR.

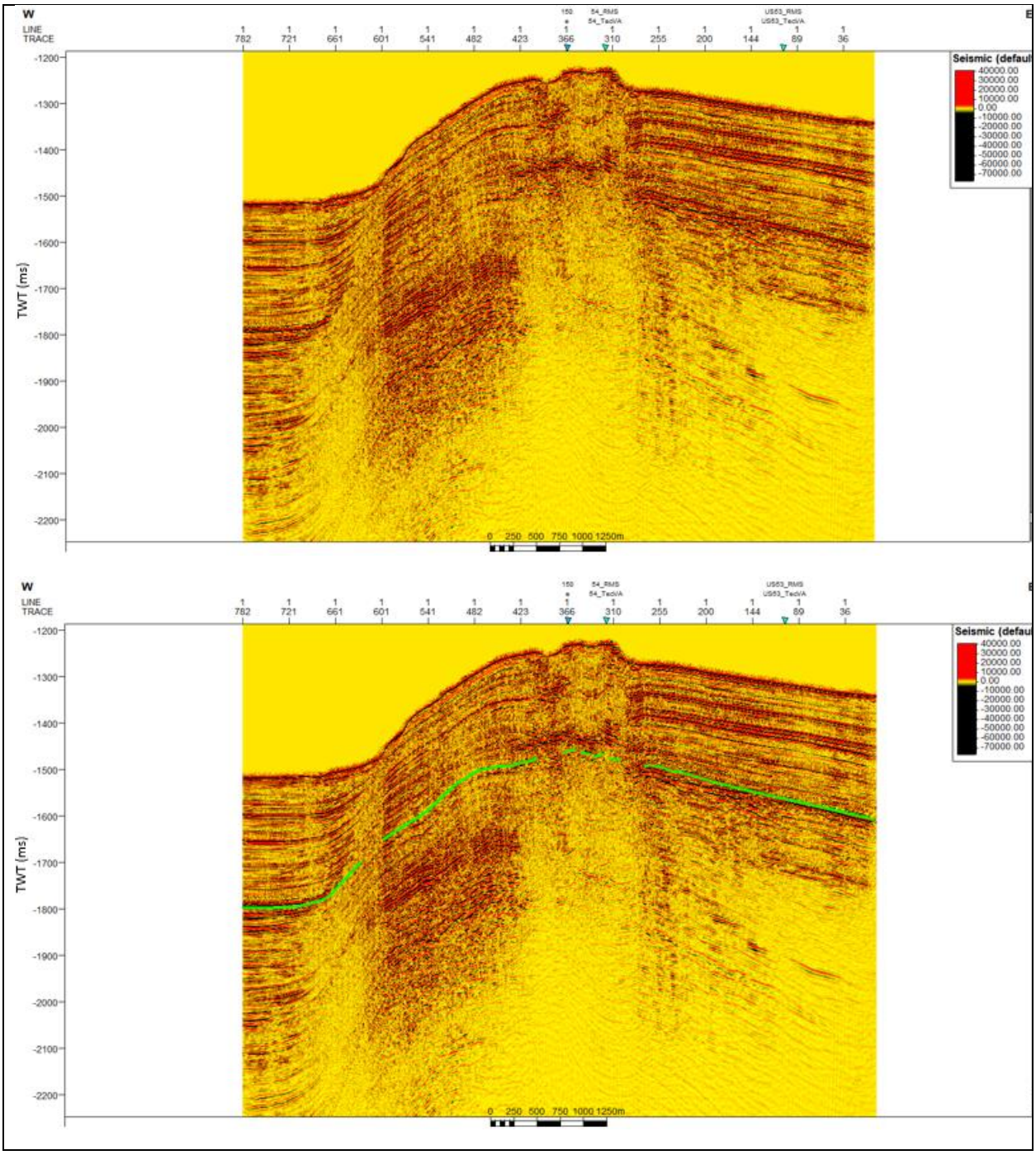

SCS profile US-18 without application of seismic attribute. Green line indicates BSR.

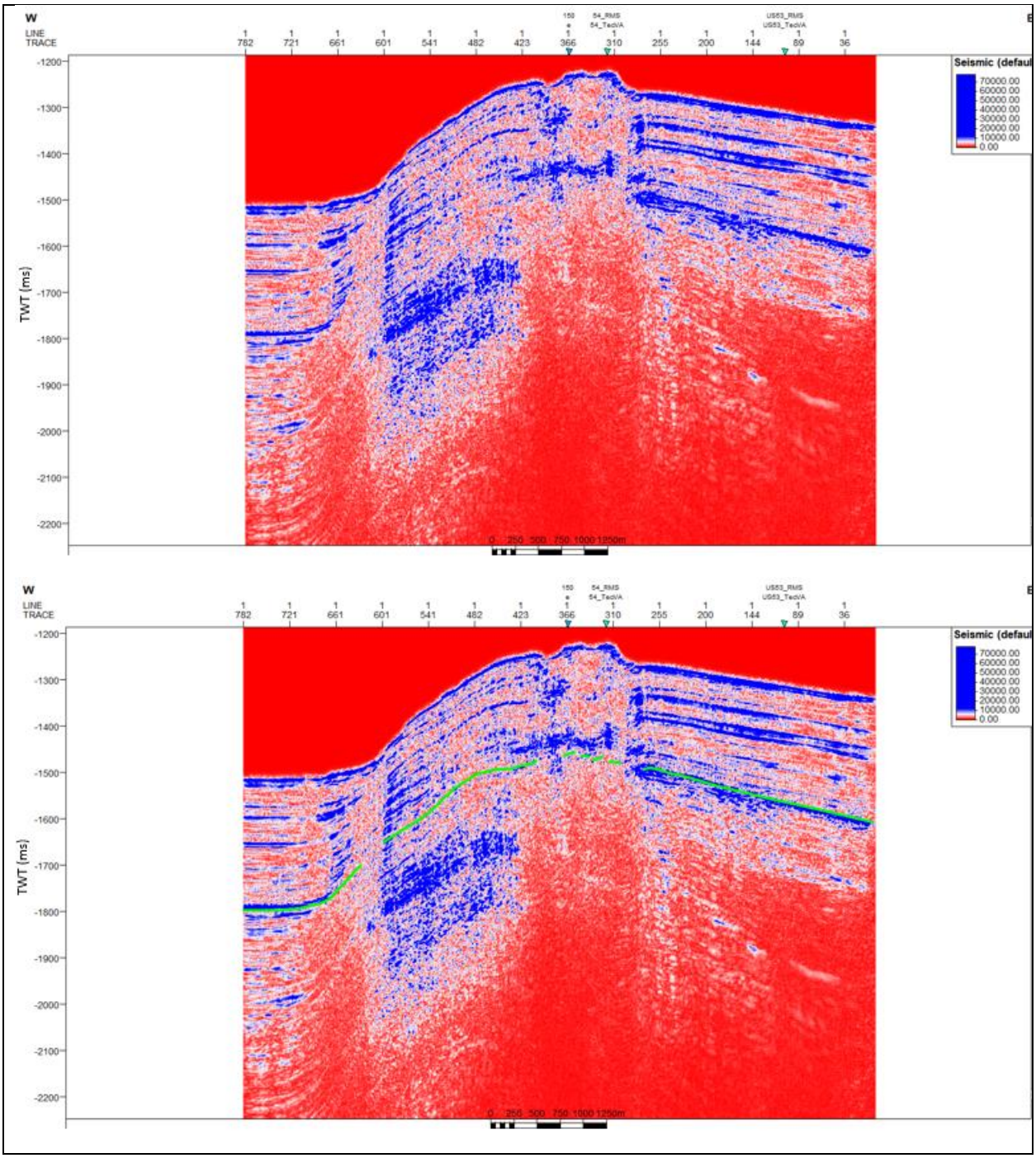

SCS profile US-18 with Envelope. Green line indicates BSR.

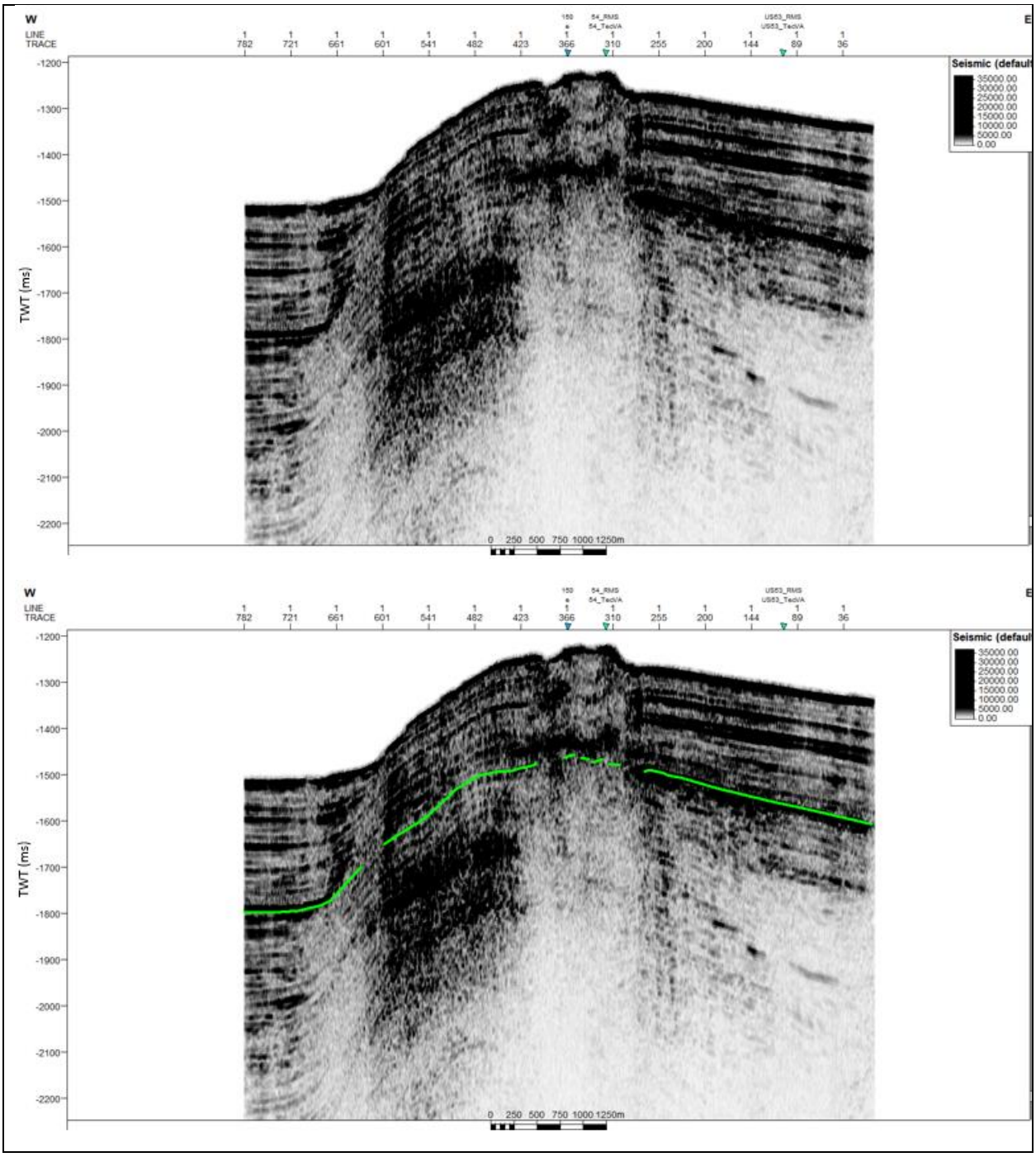

SCS profile US-18 with RMS Amplitude. Green line indicates BSR.

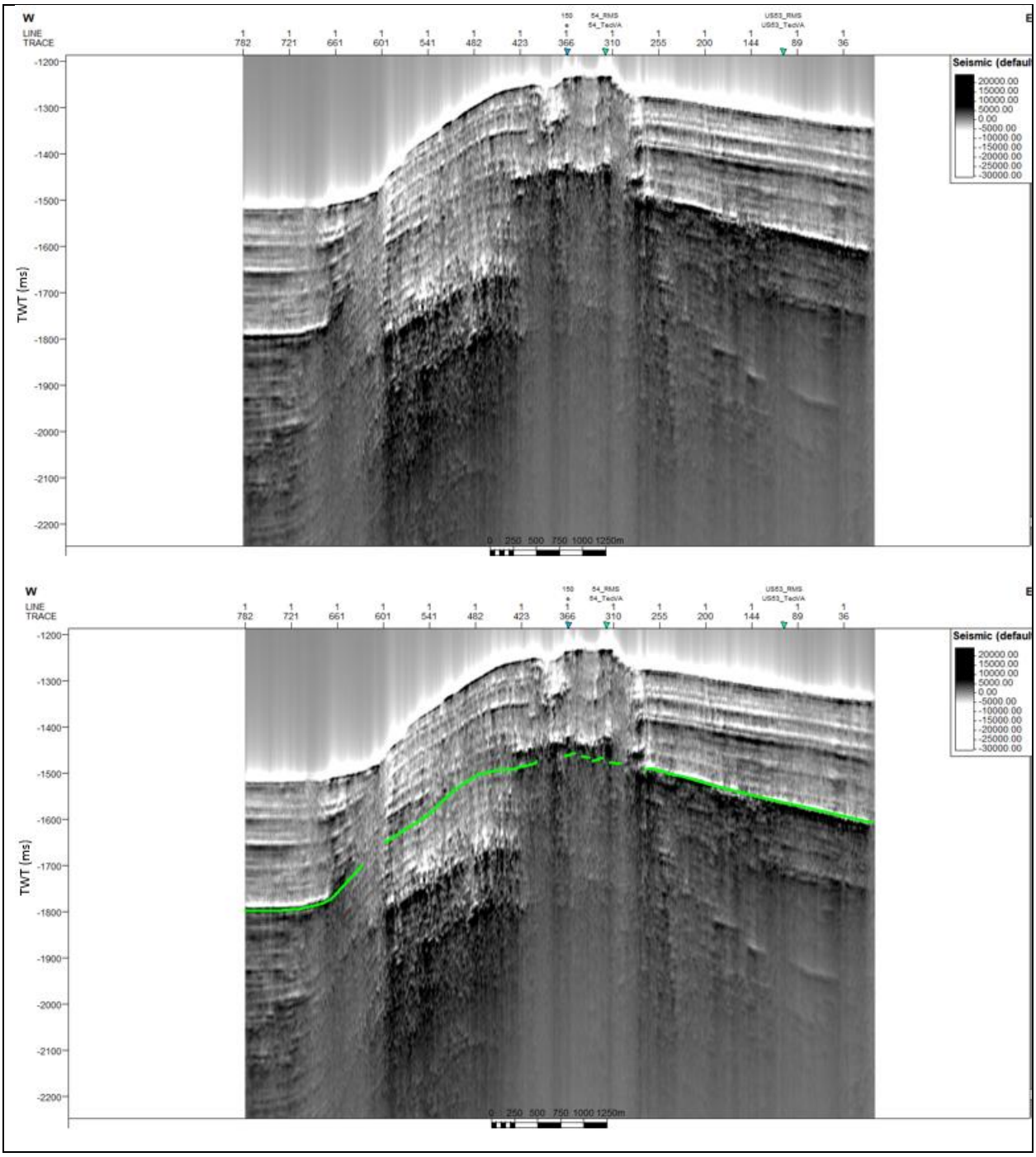

SCS profile US-18 with Amplitude Volume Technique. Green line indicates BSR.

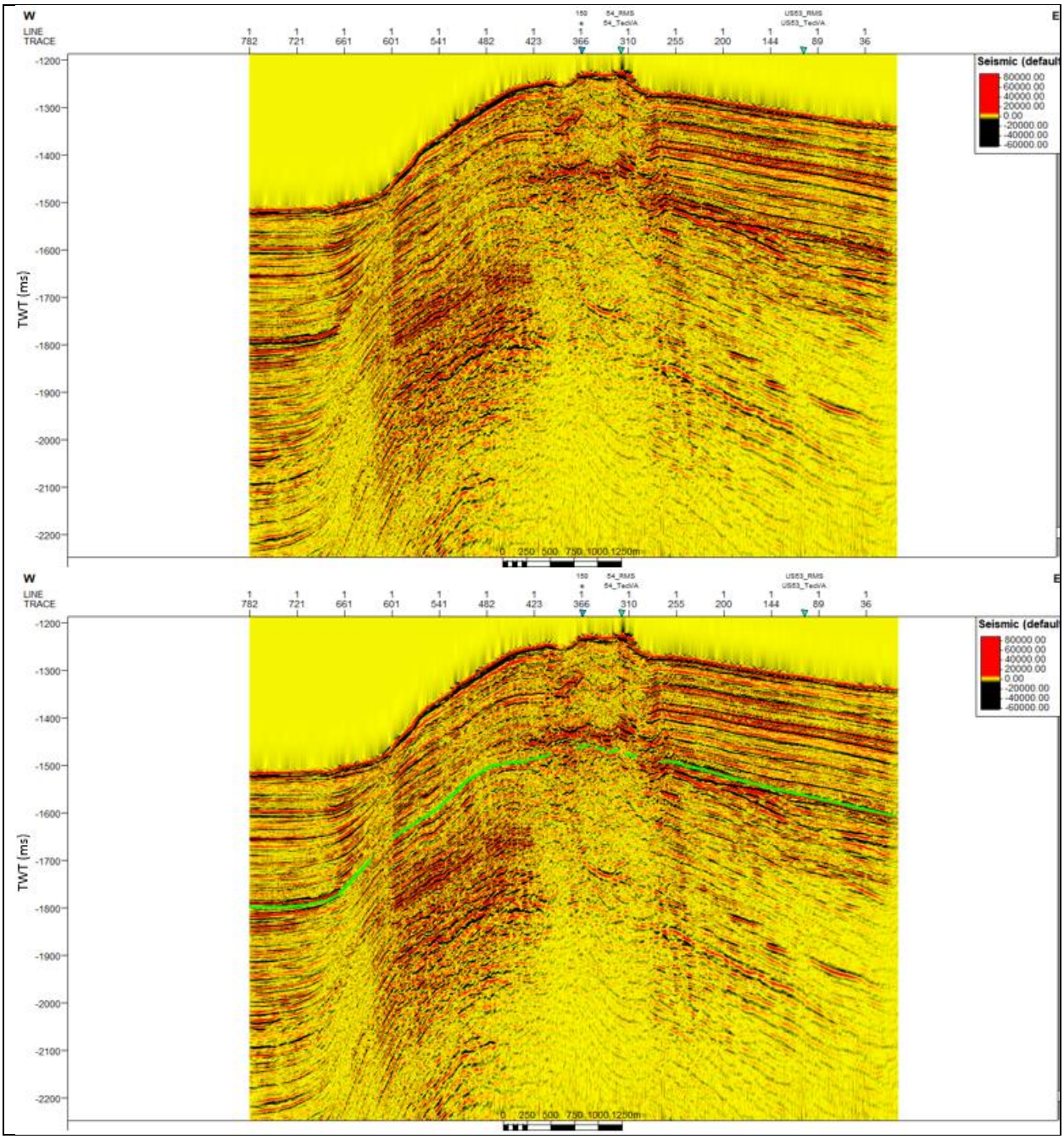

SCS profile US-18 with Relative Acoustic Impedance. Green line indicates BSR.

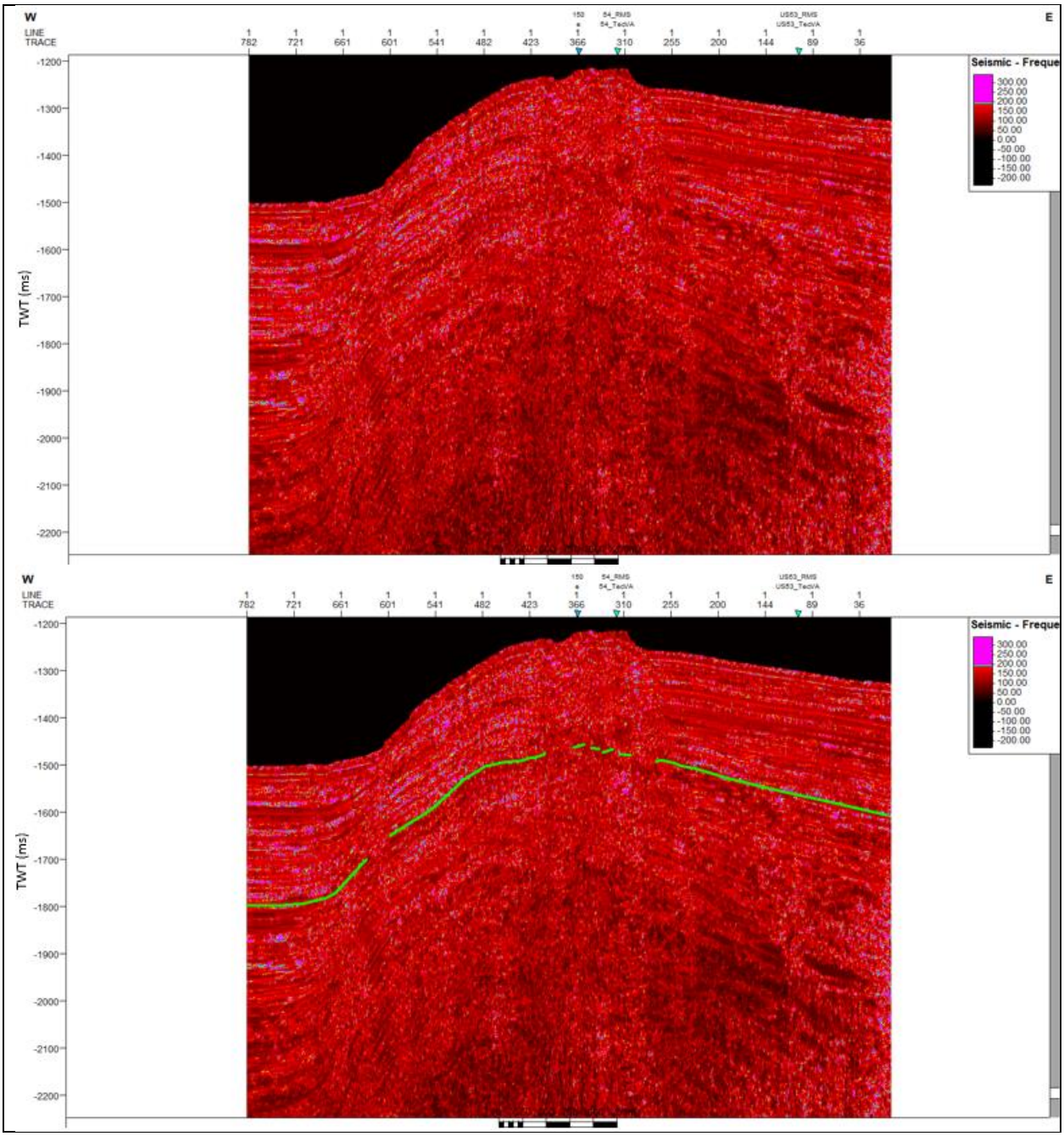

SCS profile US-18 with Instantaneous Frequency. Green line indicates BSR.

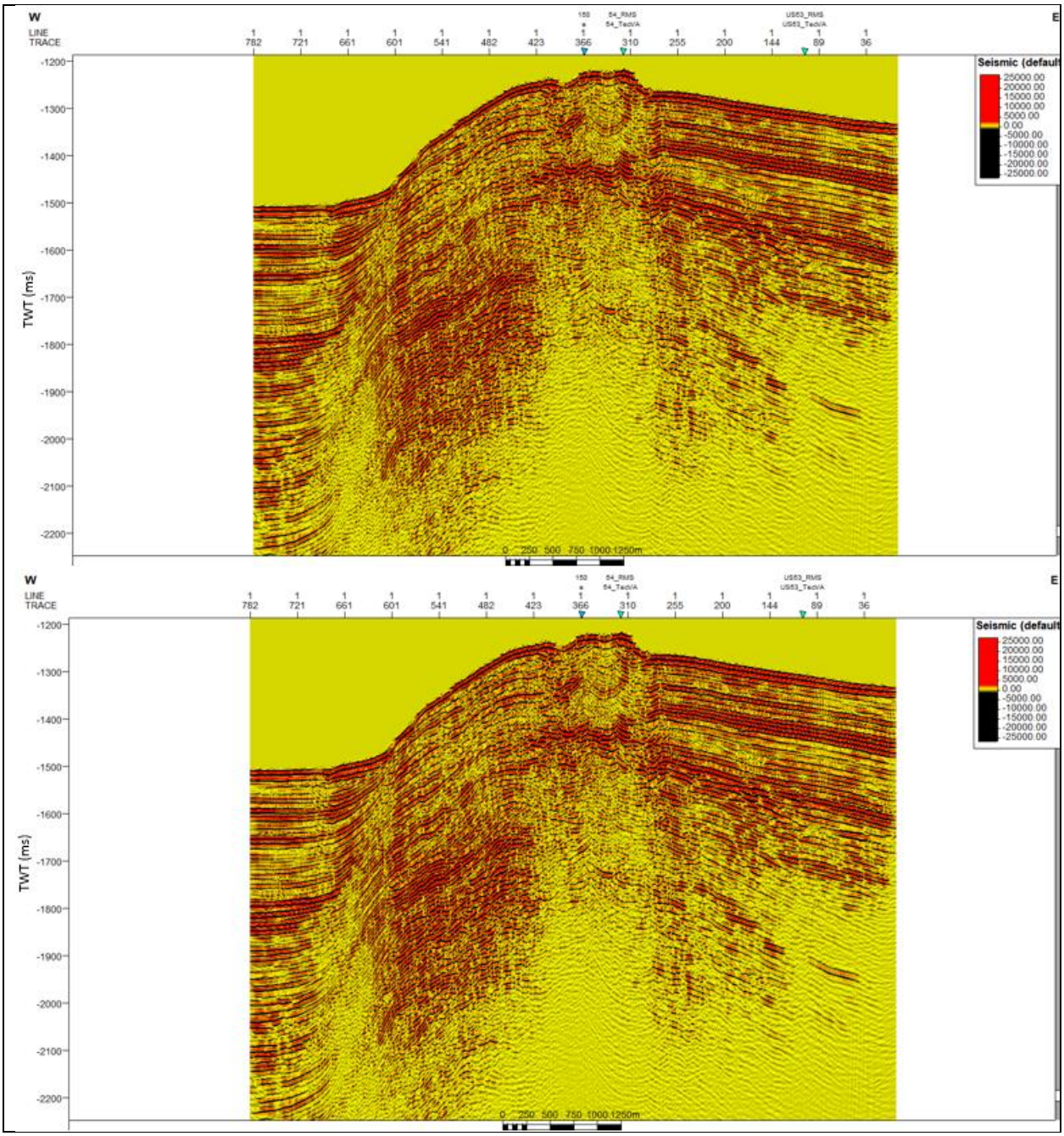

SCS profile US-18 with Spectral Decomposition of 100 Hz. Green line indicates BSR.

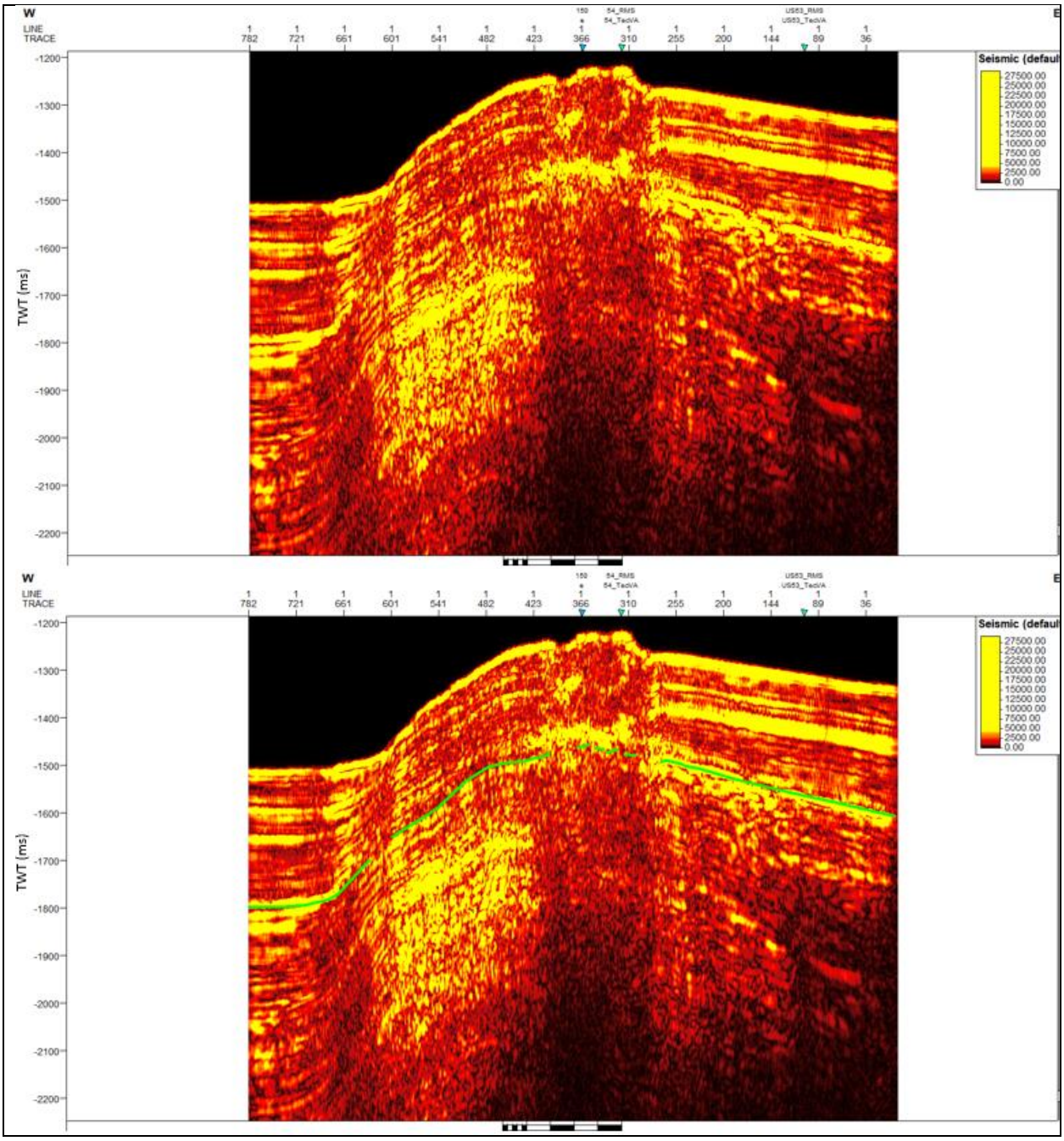

SCS profile US-18 with Spectral Decomposition of 100 Hz plus Envelope. Green line indicates BSR.

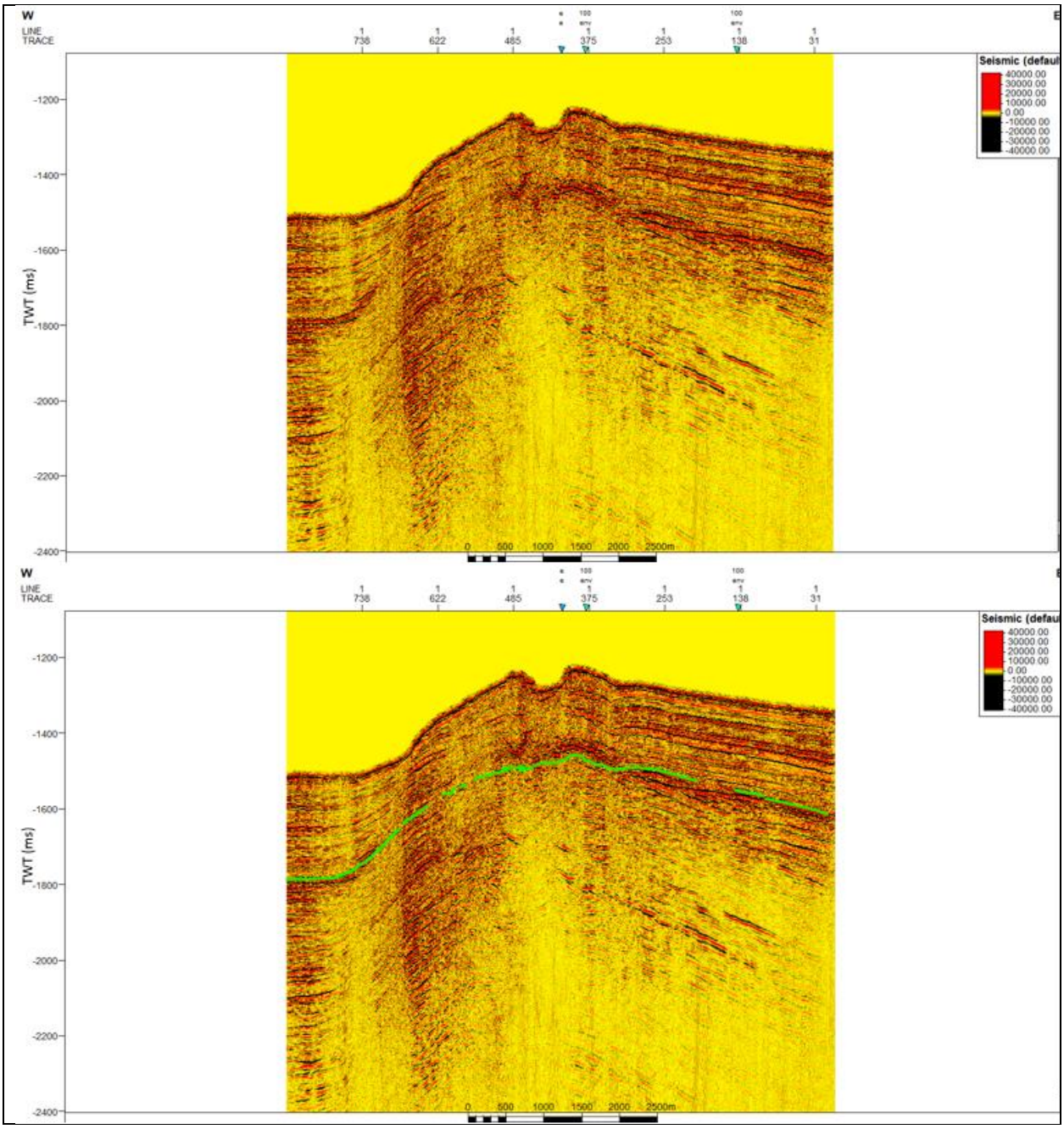

SCS profile US-19 without application of seismic attribute. Green line indicates BSR.

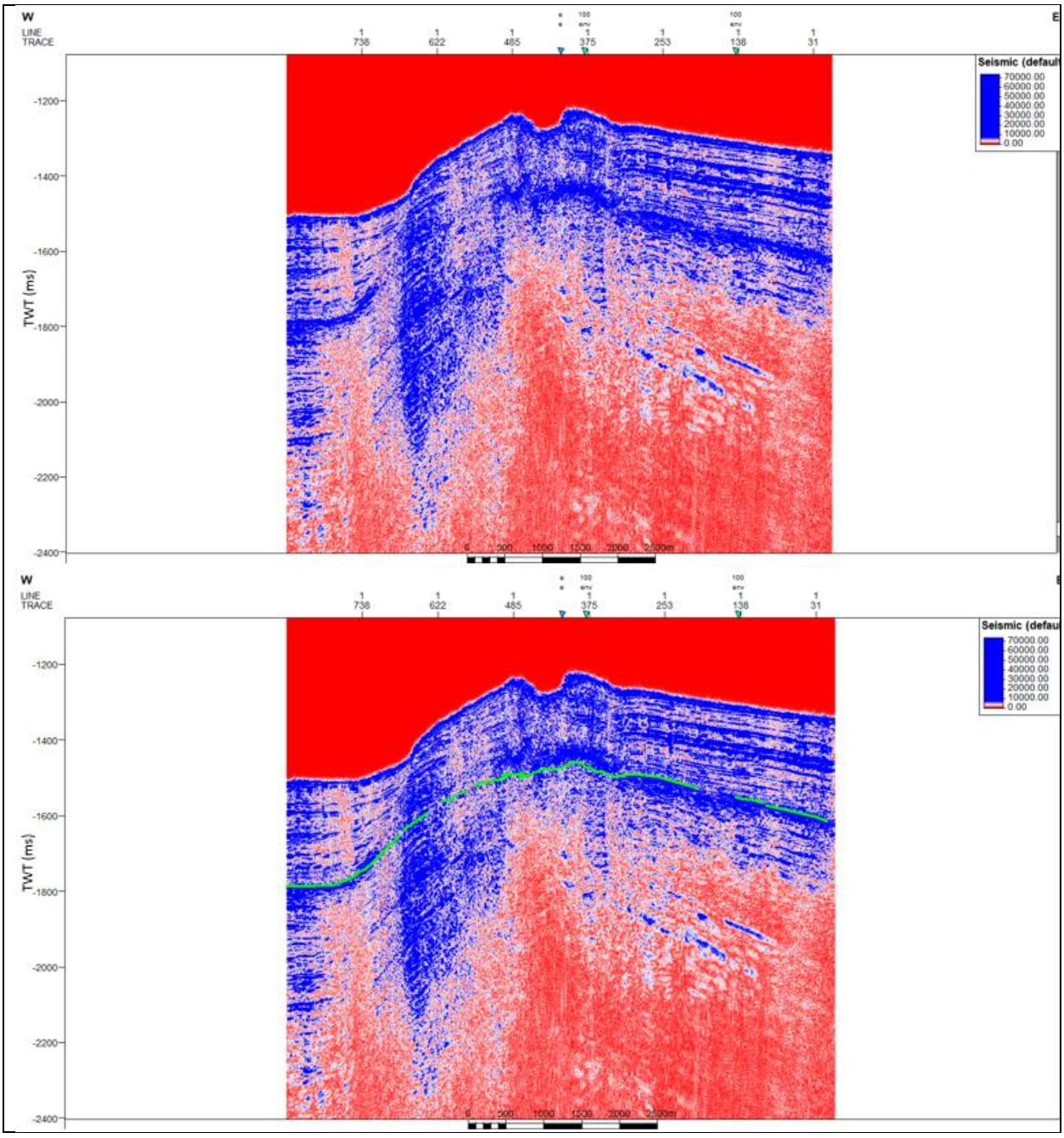

SCS profile US-19 with Envelope. Green line indicates BSR.

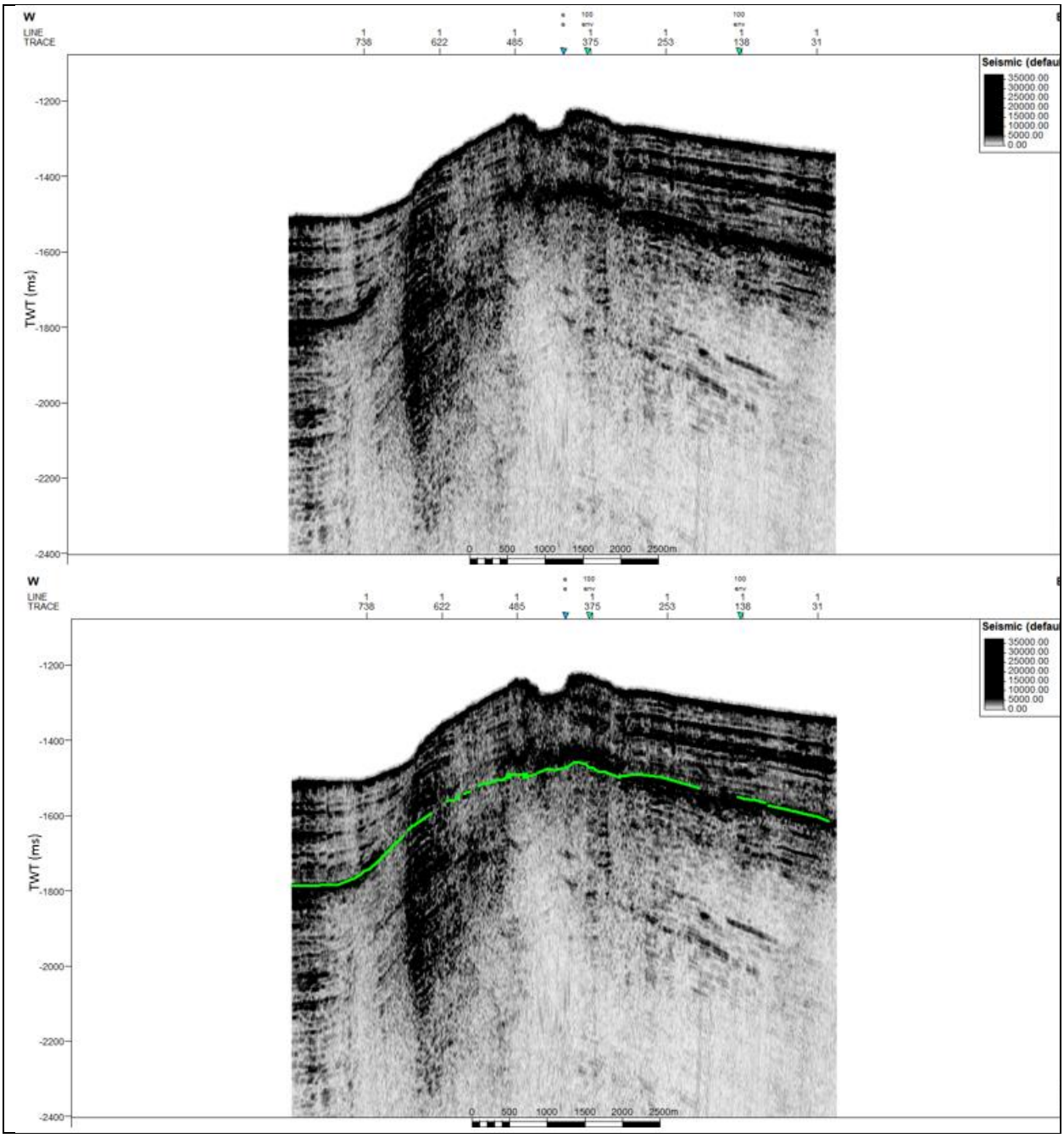

SCS profile US-19 with RMS Amplitude. Green line indicates BSR.

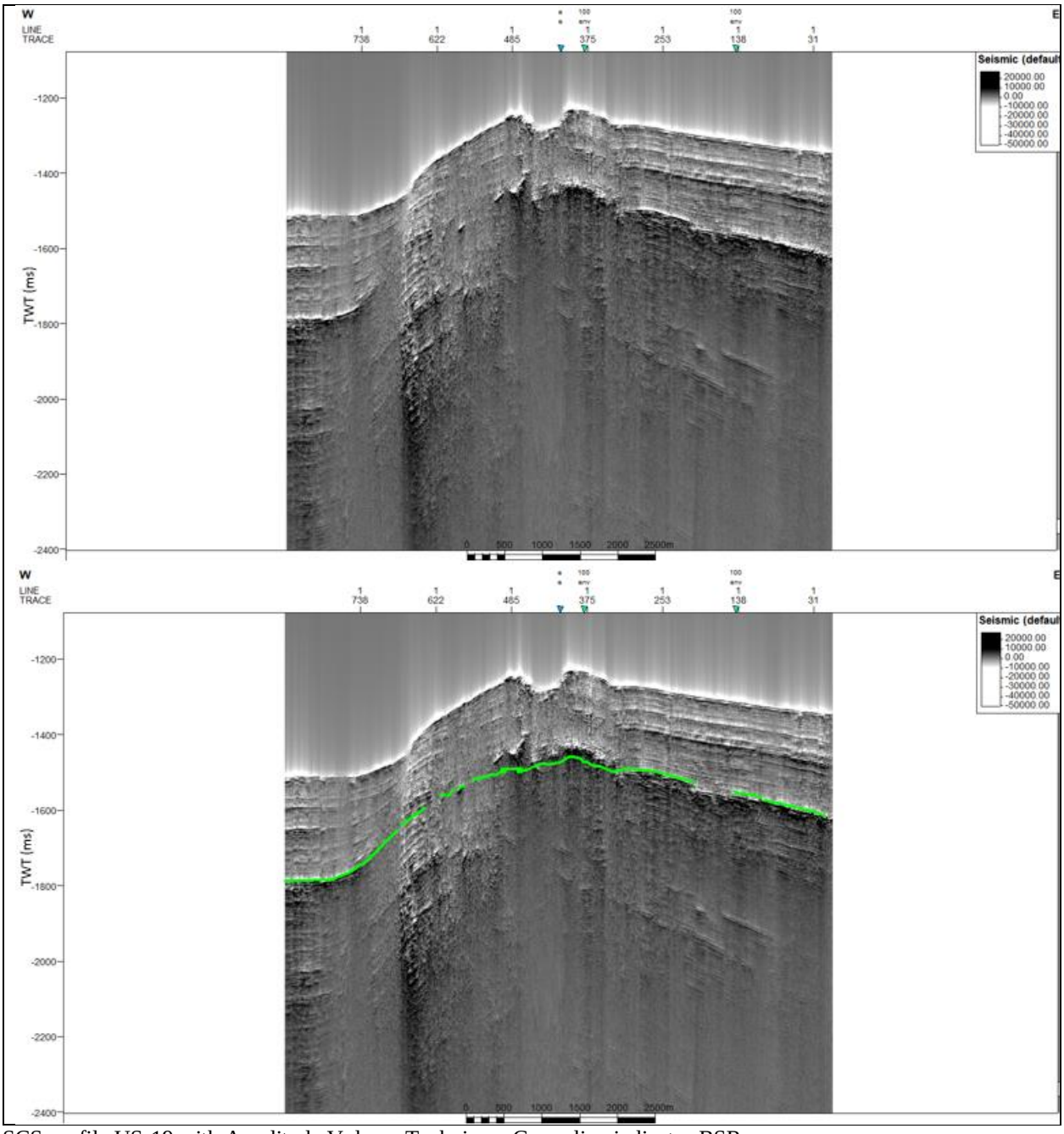

SCS profile US-19 with Amplitude Volume Technique. Green line indicates BSR.

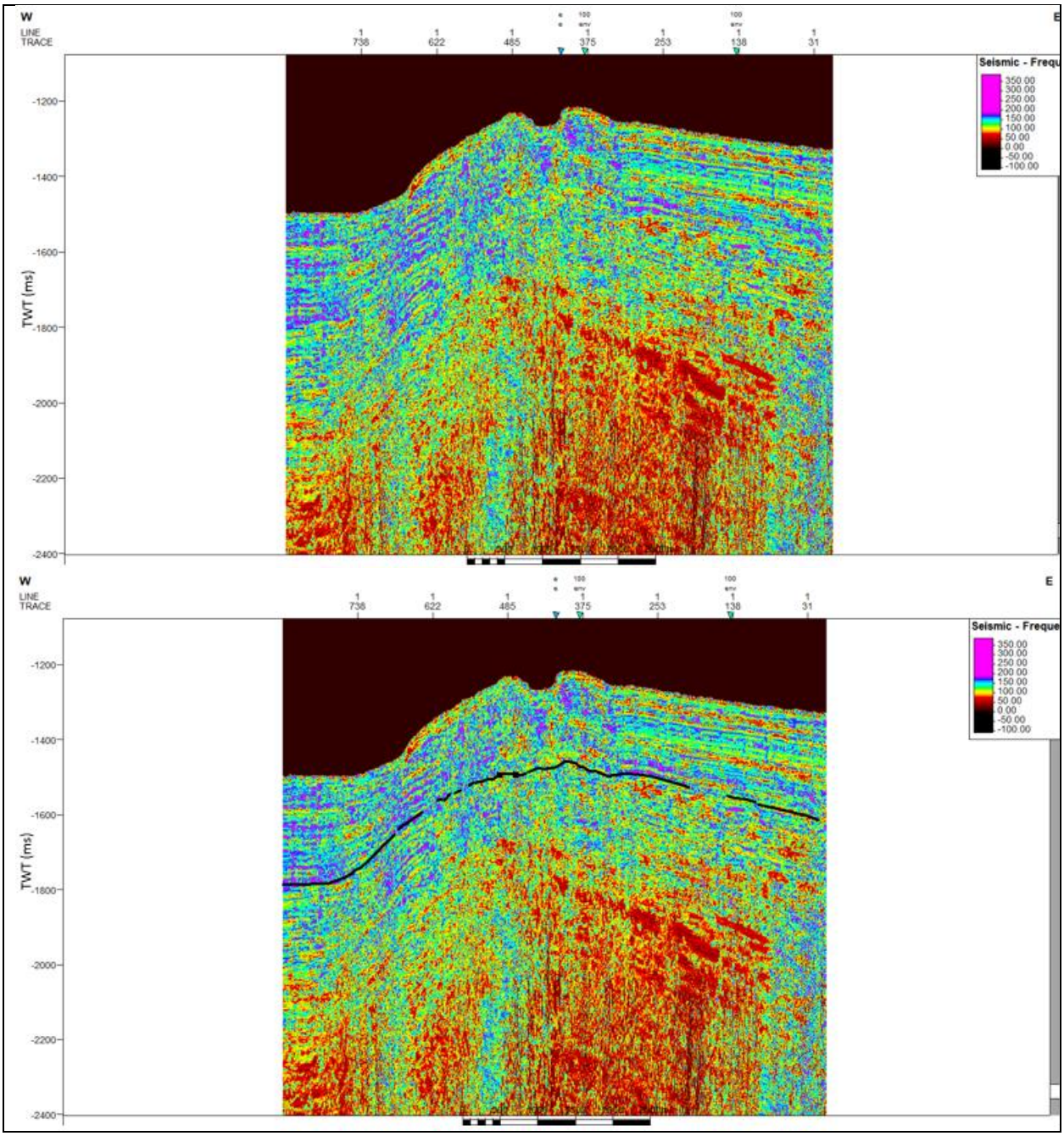

SCS profile US-19 with Instantaneous Frequency. Green line indicates BSR.

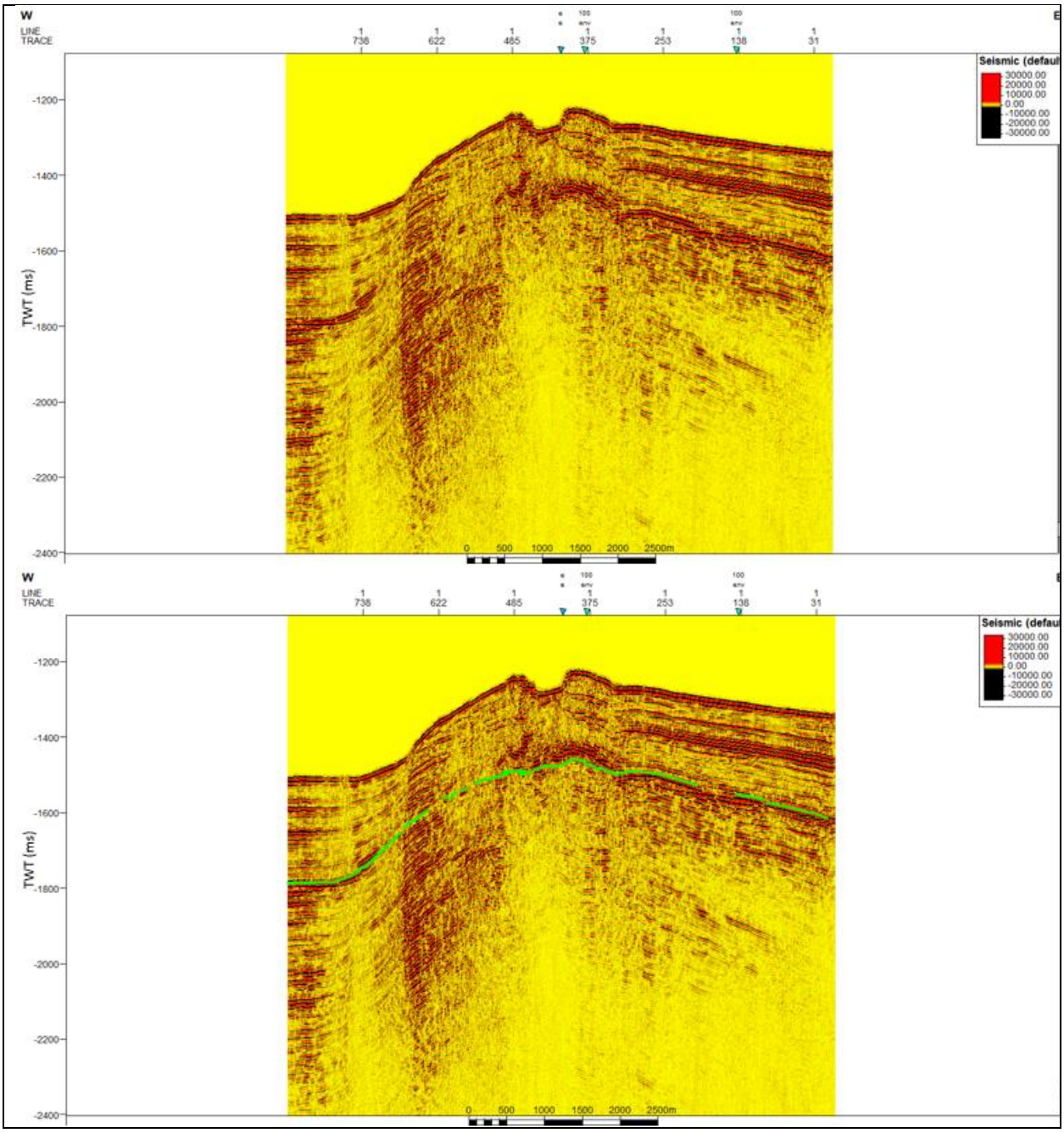

SCS profile US-19 with Spectral Decomposition of 100 Hz. Green line indicates BSR.

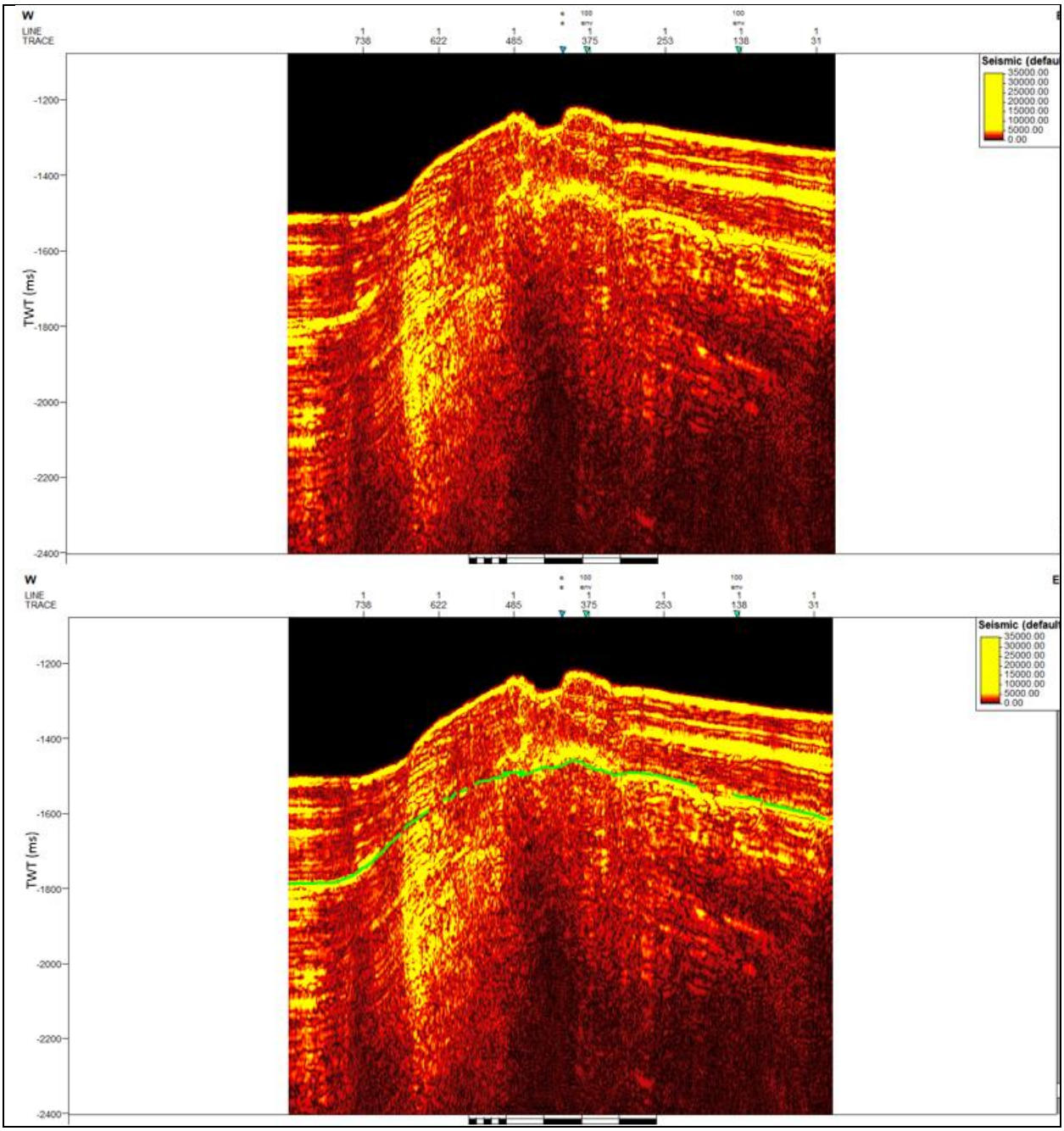

SCS profile US-19 with Spectral Decomposition of 100 Hz plus Envelope. Green line indicates BSR.

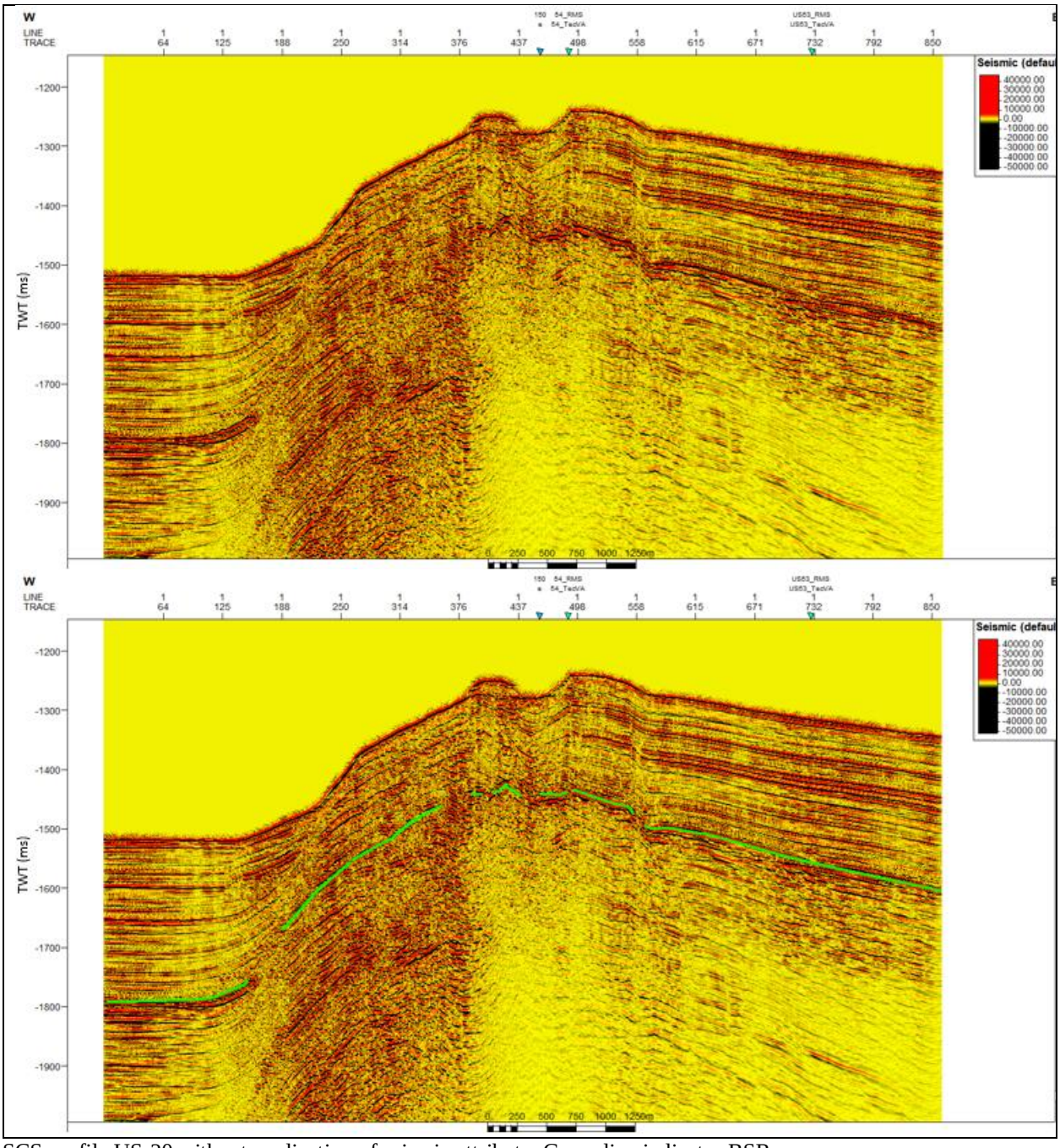

SCS profile US-20 without application of seismic attribute. Green line indicates BSR.

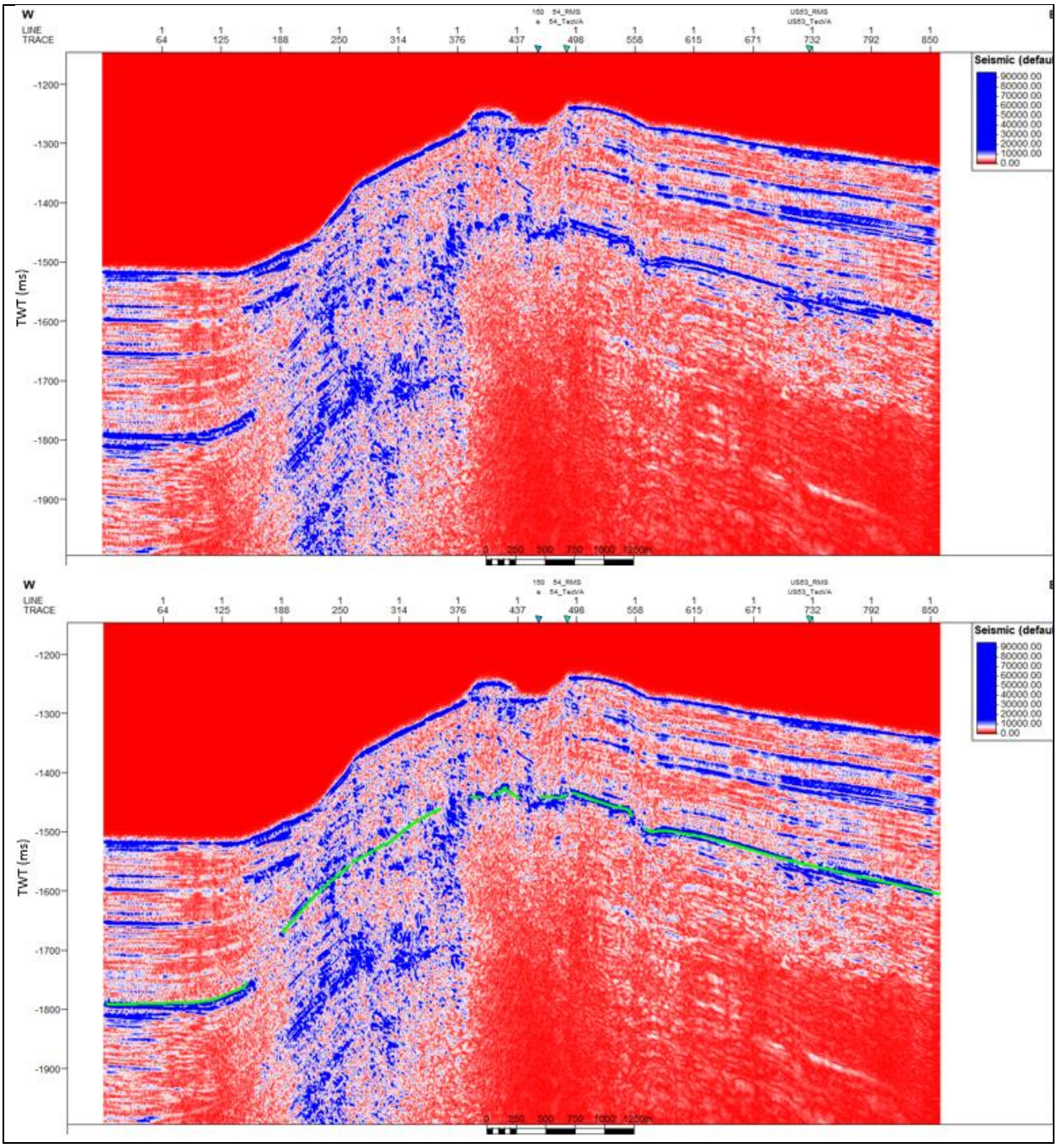

SCS profile US-20 with Envelope. Green line indicates BSR.

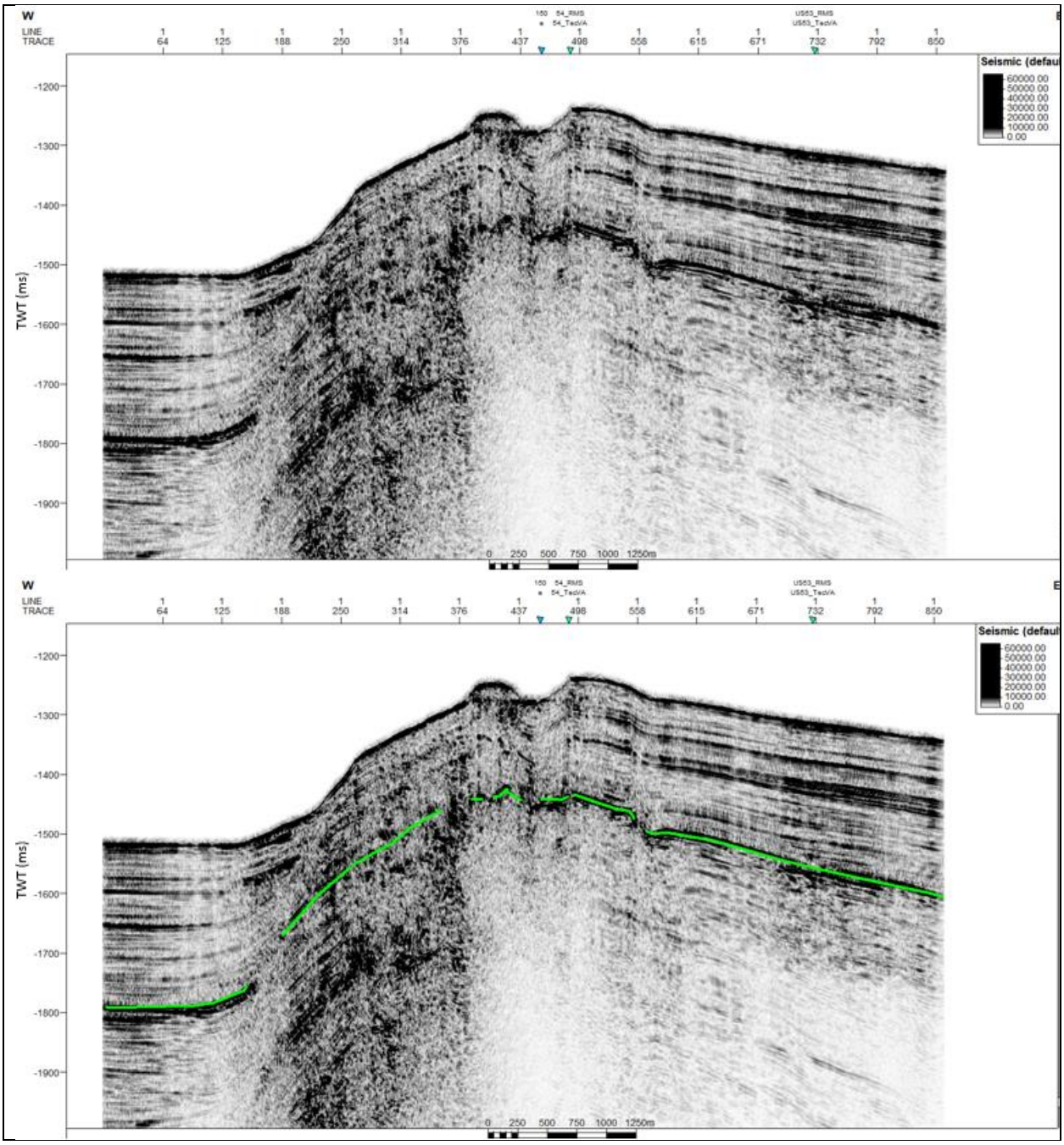

SCS profile US-20 with RMS Amplitude. Green line indicates BSR.

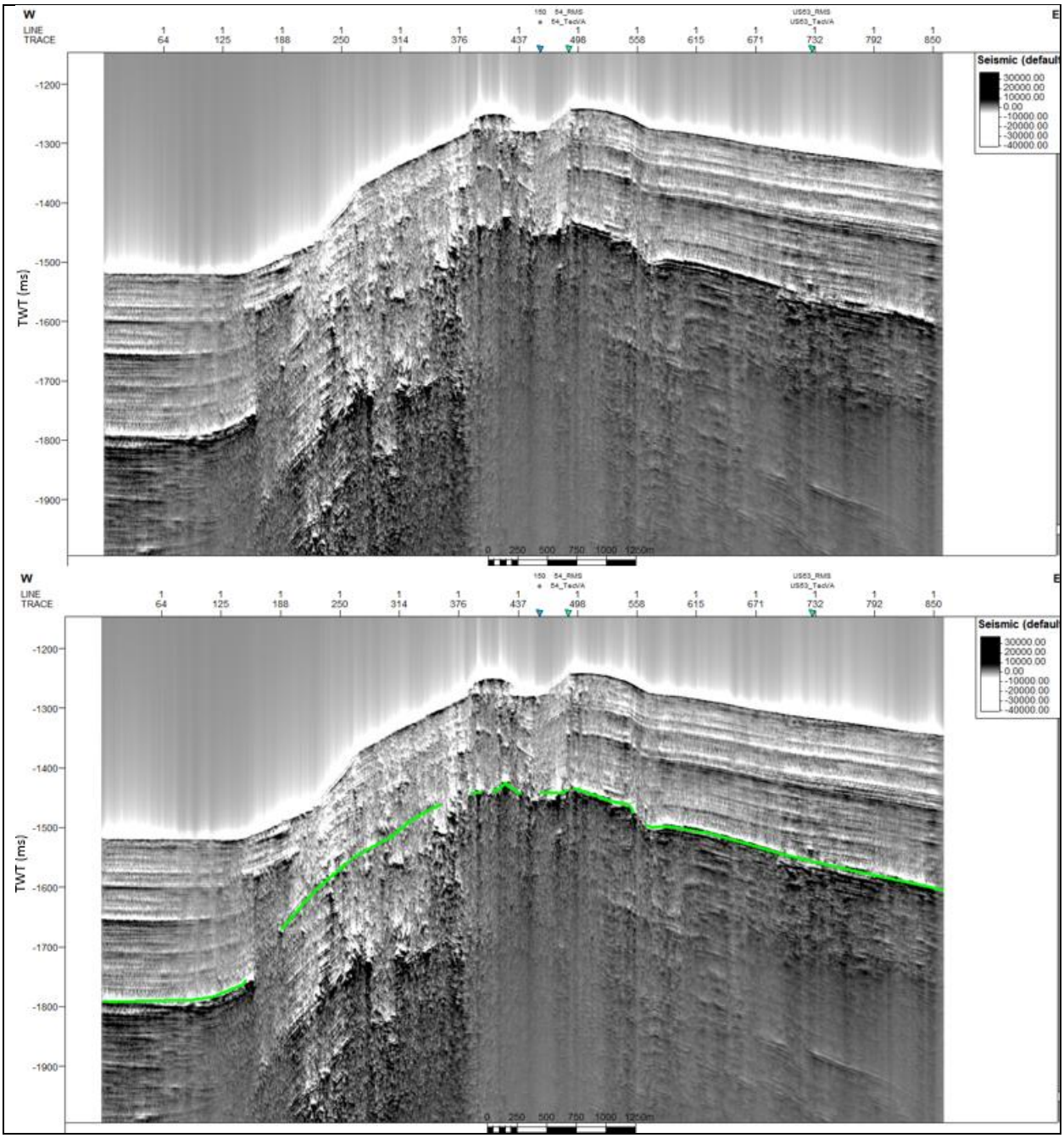

SCS profile US-20 with Amplitude Volume Technique. Green line indicates BSR.

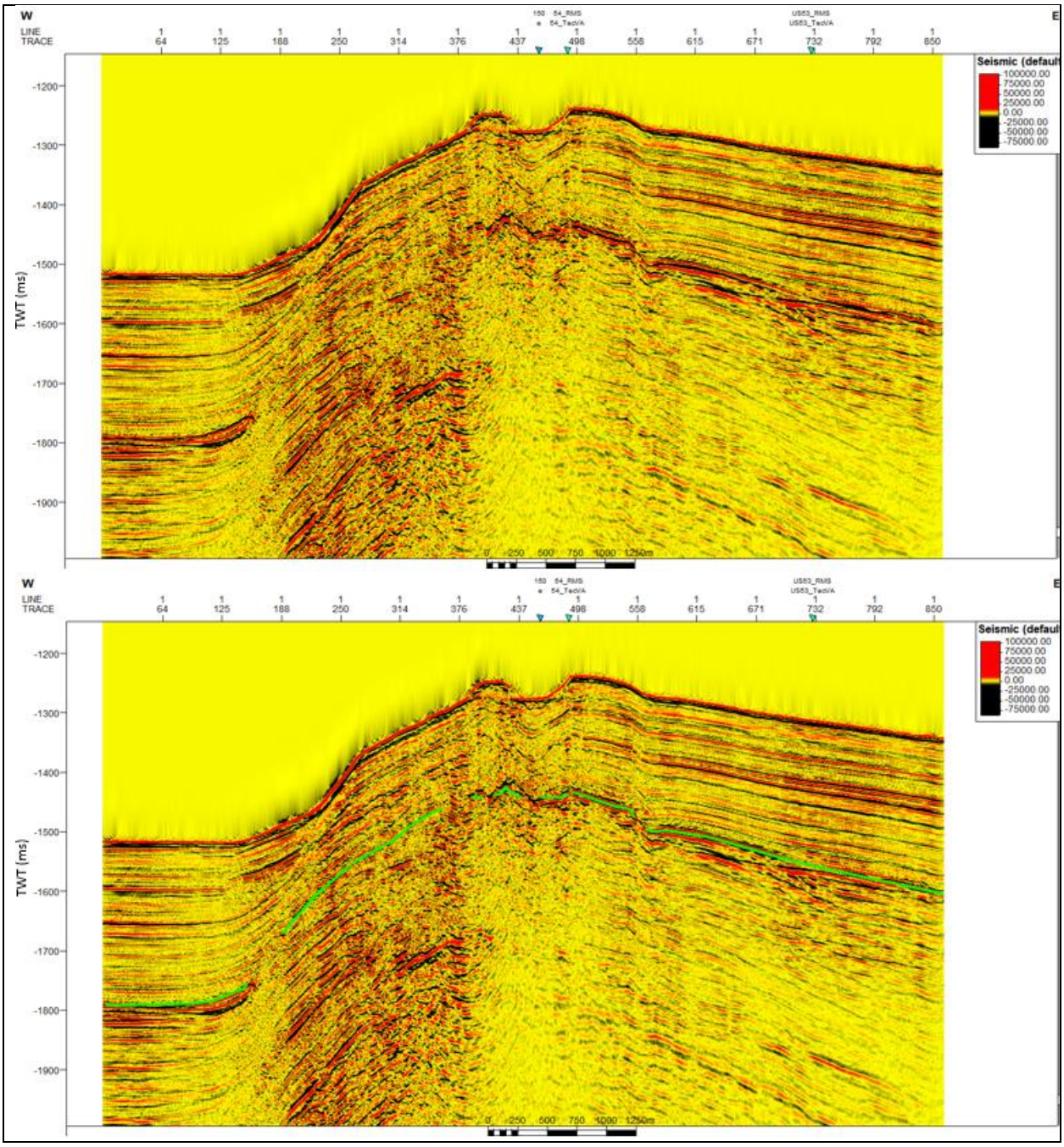

SCS profile US-20 with Relative Acoustic Impedance. Green line indicates BSR.

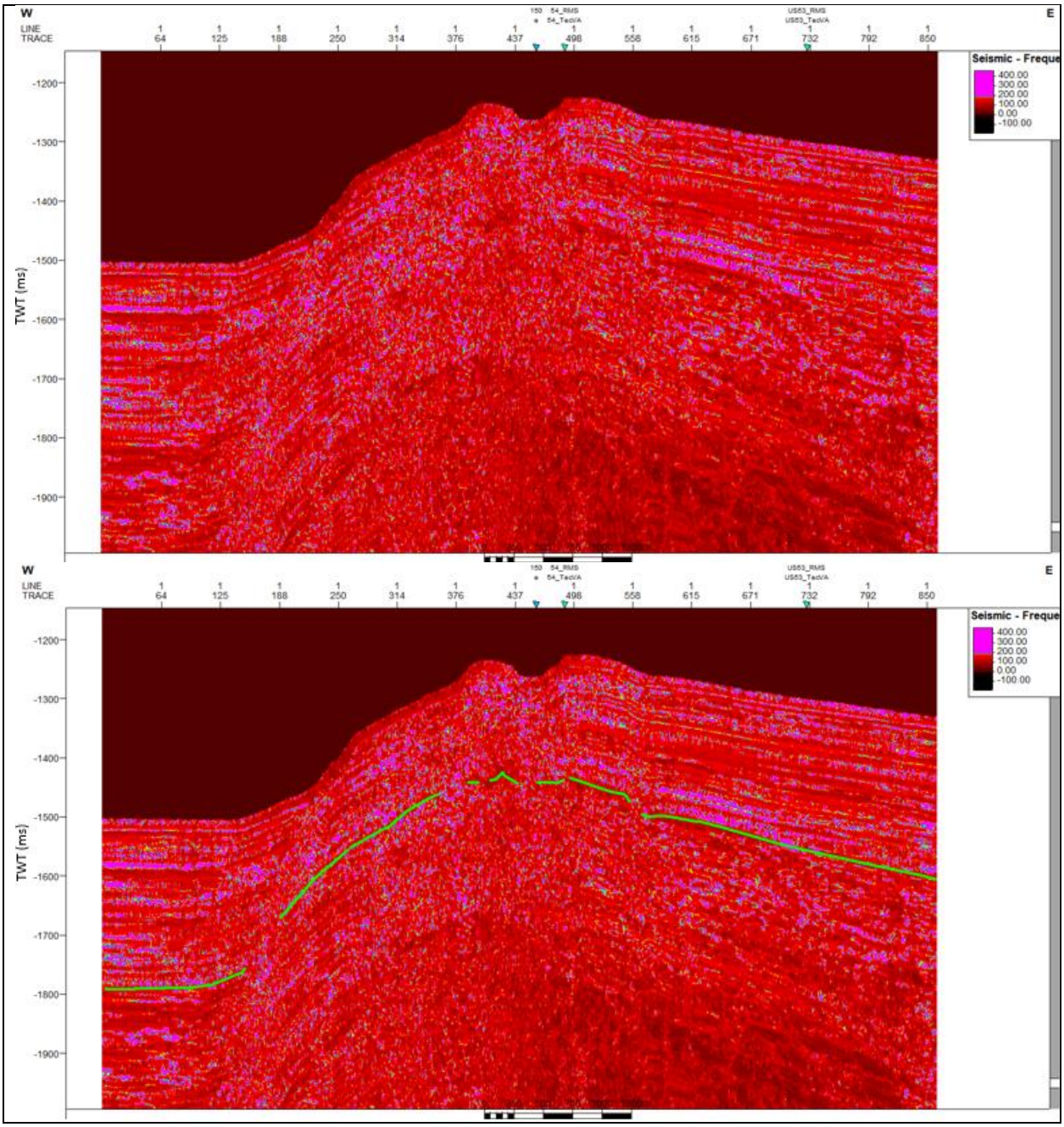

SCS profile US-20 with Instantaneous Frequency. Green line indicates BSR.

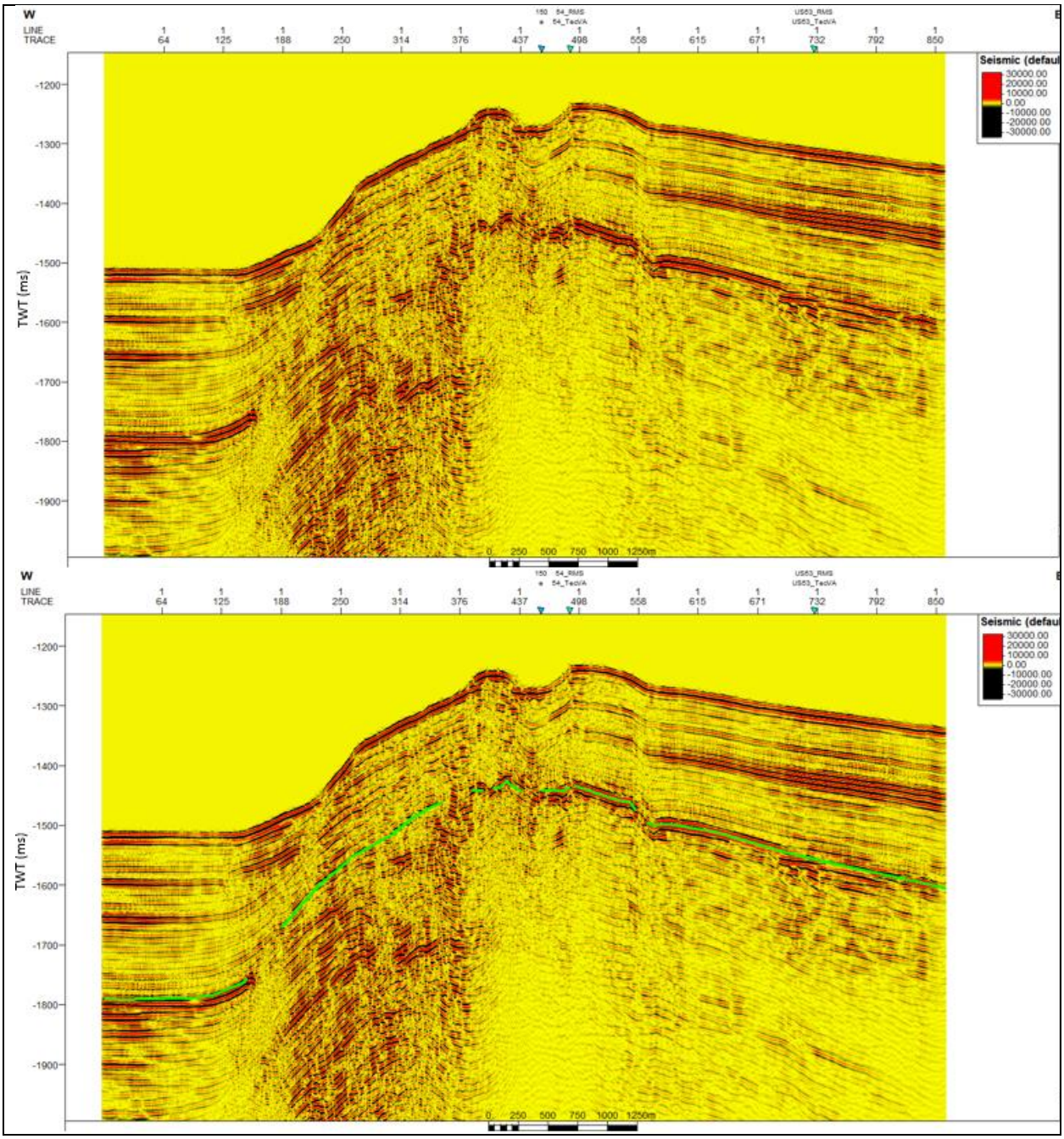

SCS profile US-20 with Spectral Decomposition of 100 Hz. Green line indicates BSR.

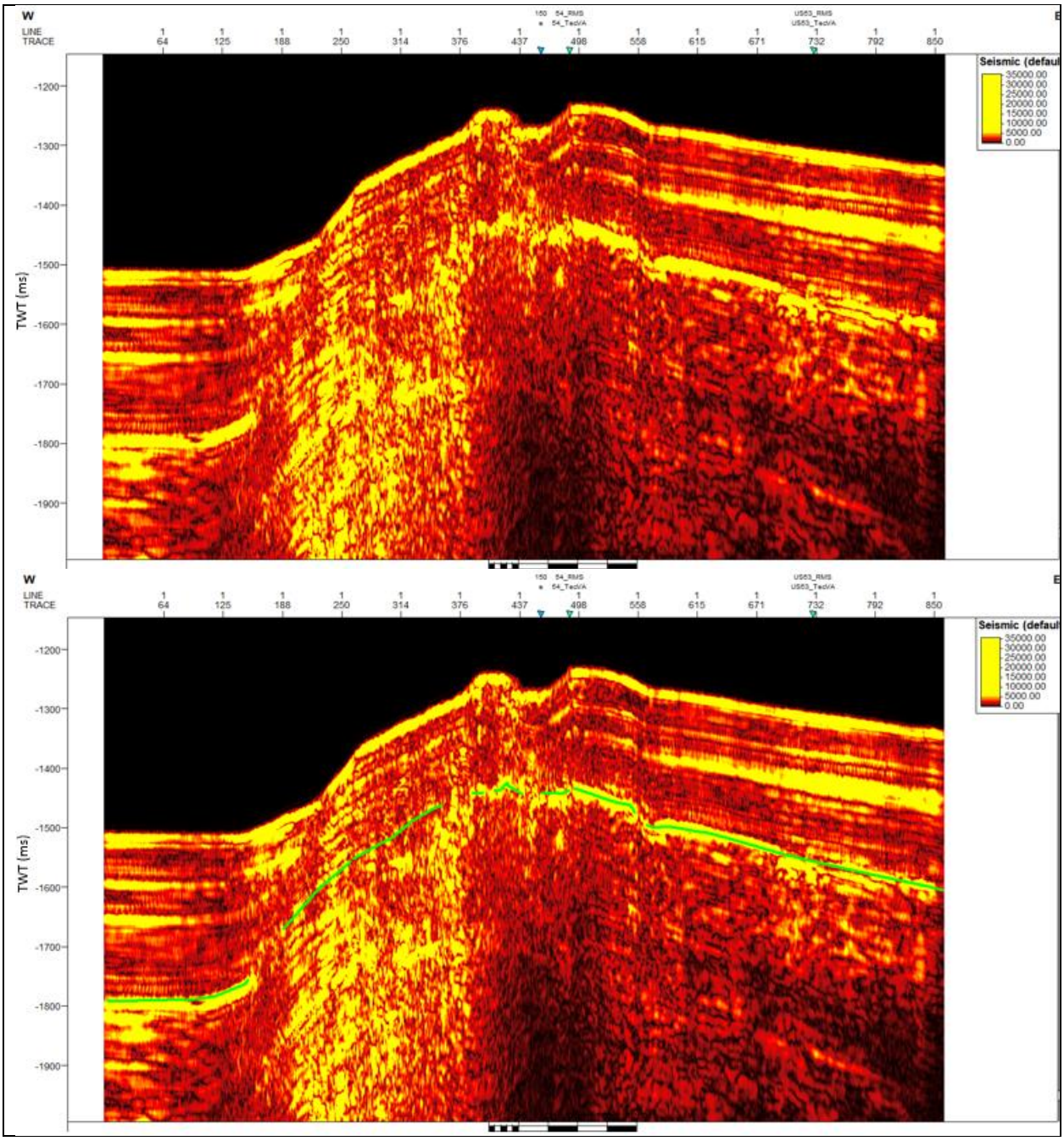

SCS profile US-20 with Spectral Decomposition of 100 Hz plus Envelope. Green line indicates BSR.

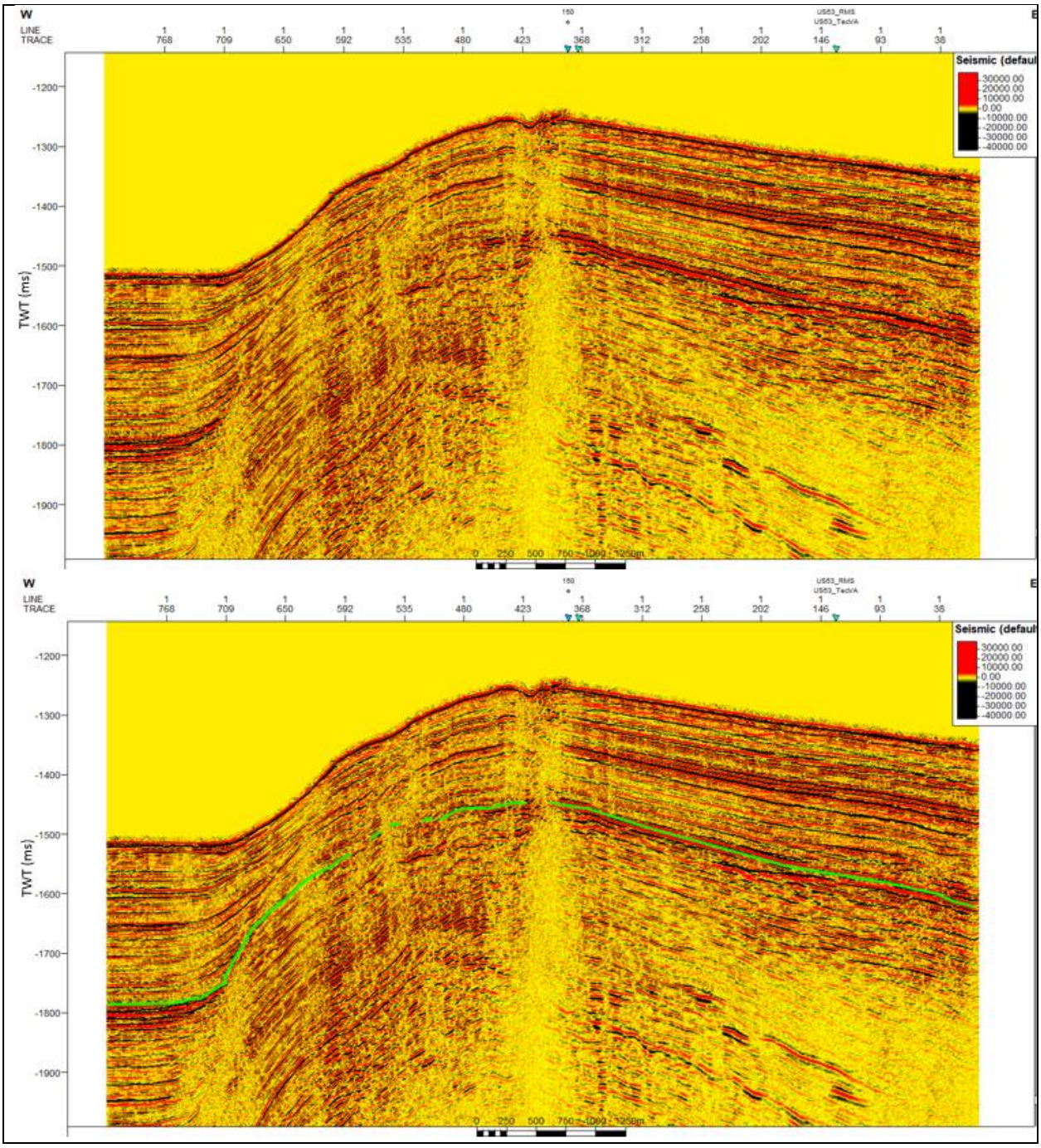

SCS profile US-22 without application of seismic attribute. Green line indicates BSR.

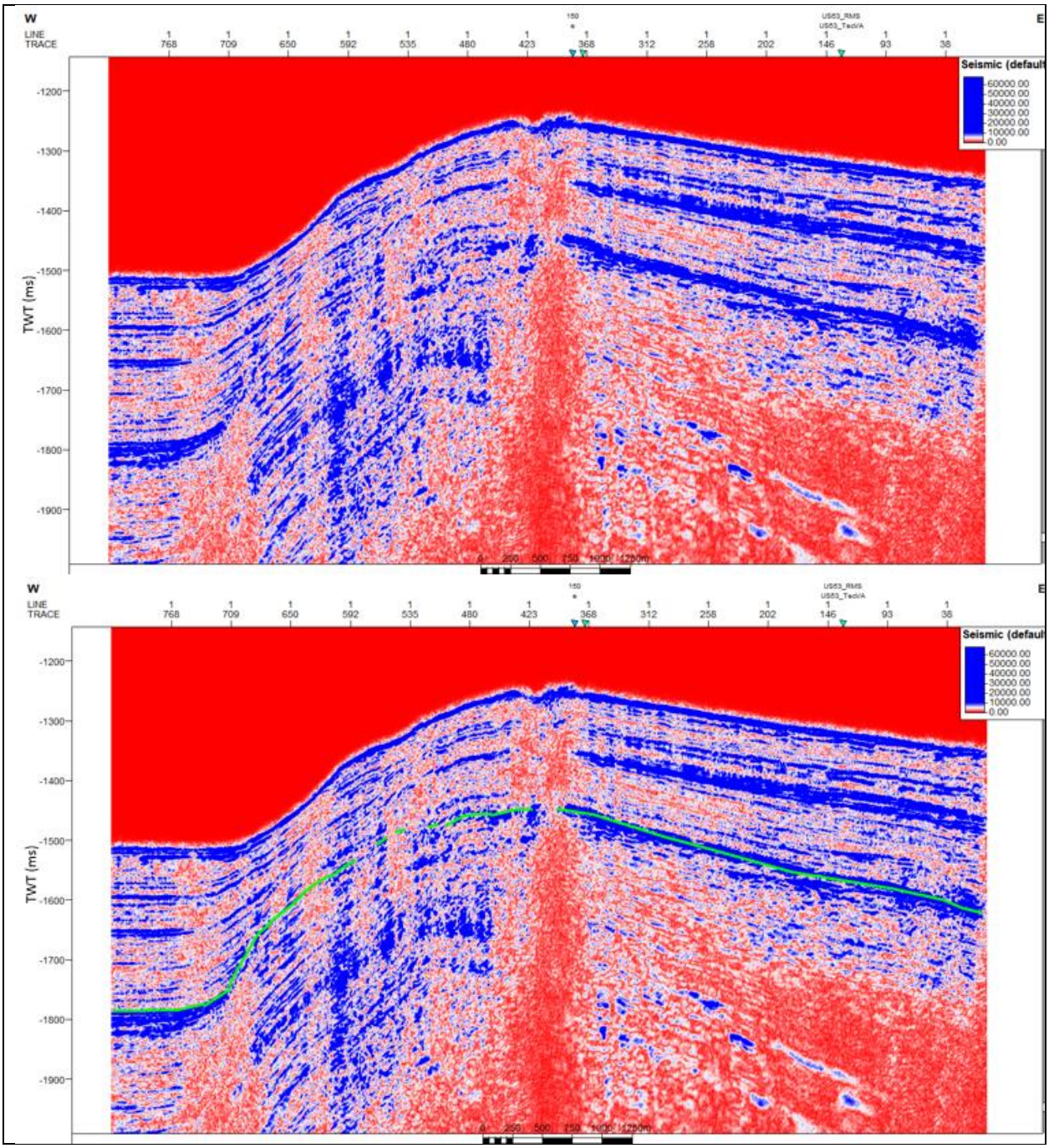

SCS profile US-22 with Envelope. Green line indicates BSR.

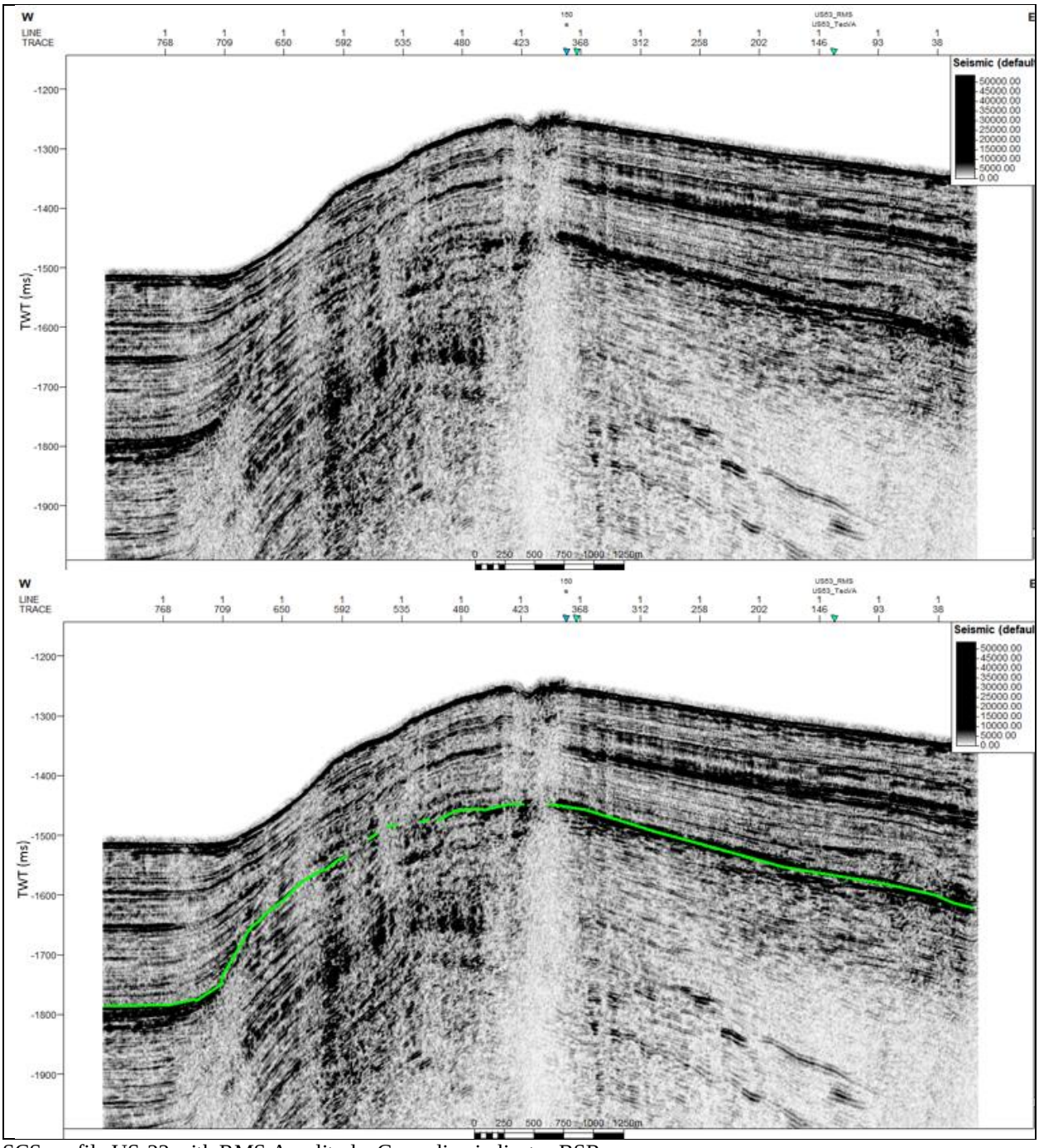

SCS profile US-22 with RMS Amplitude. Green line indicates BSR.

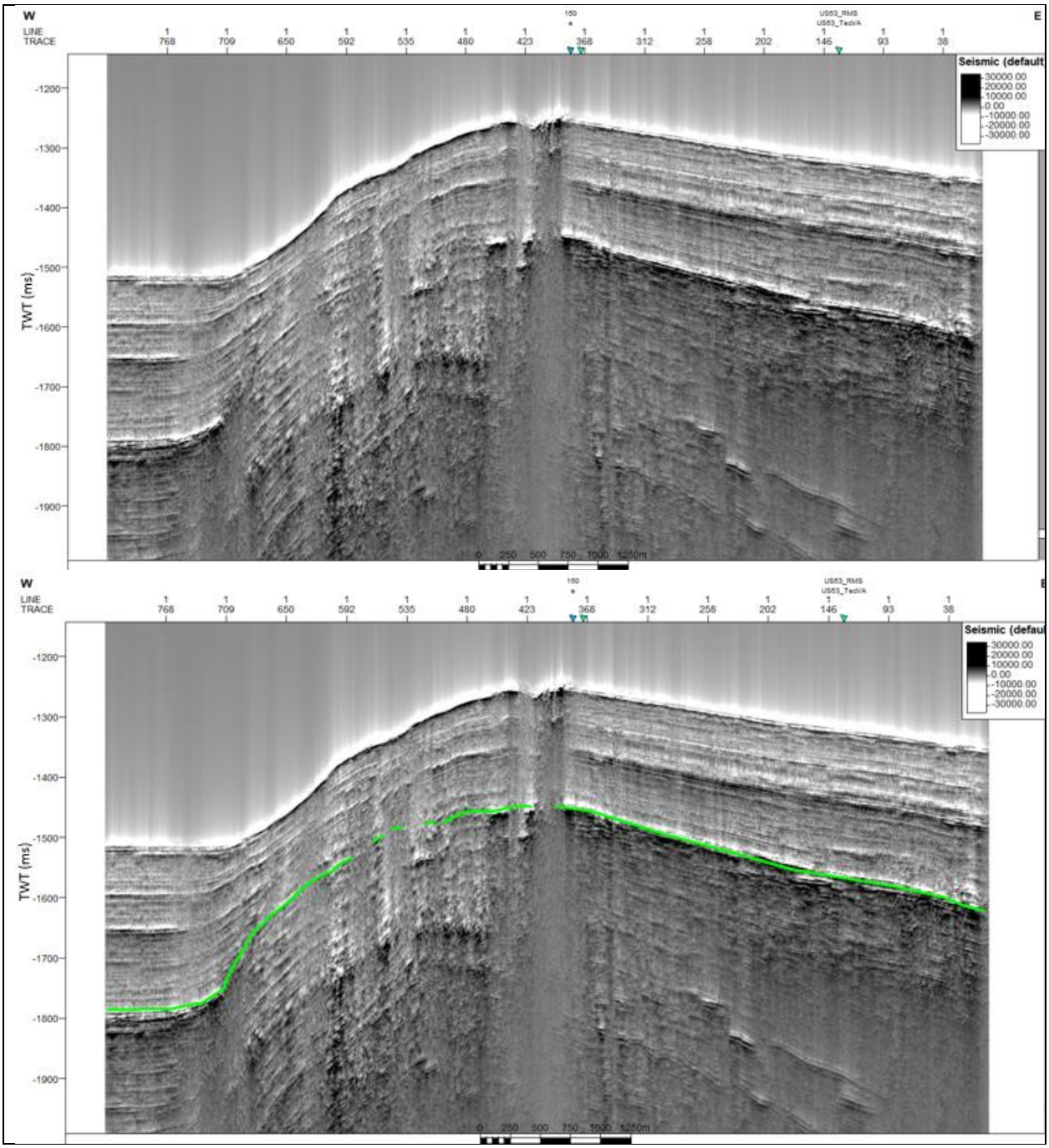

SCS profile US-22 with Amplitude Volume Technique. Green line indicates BSR.

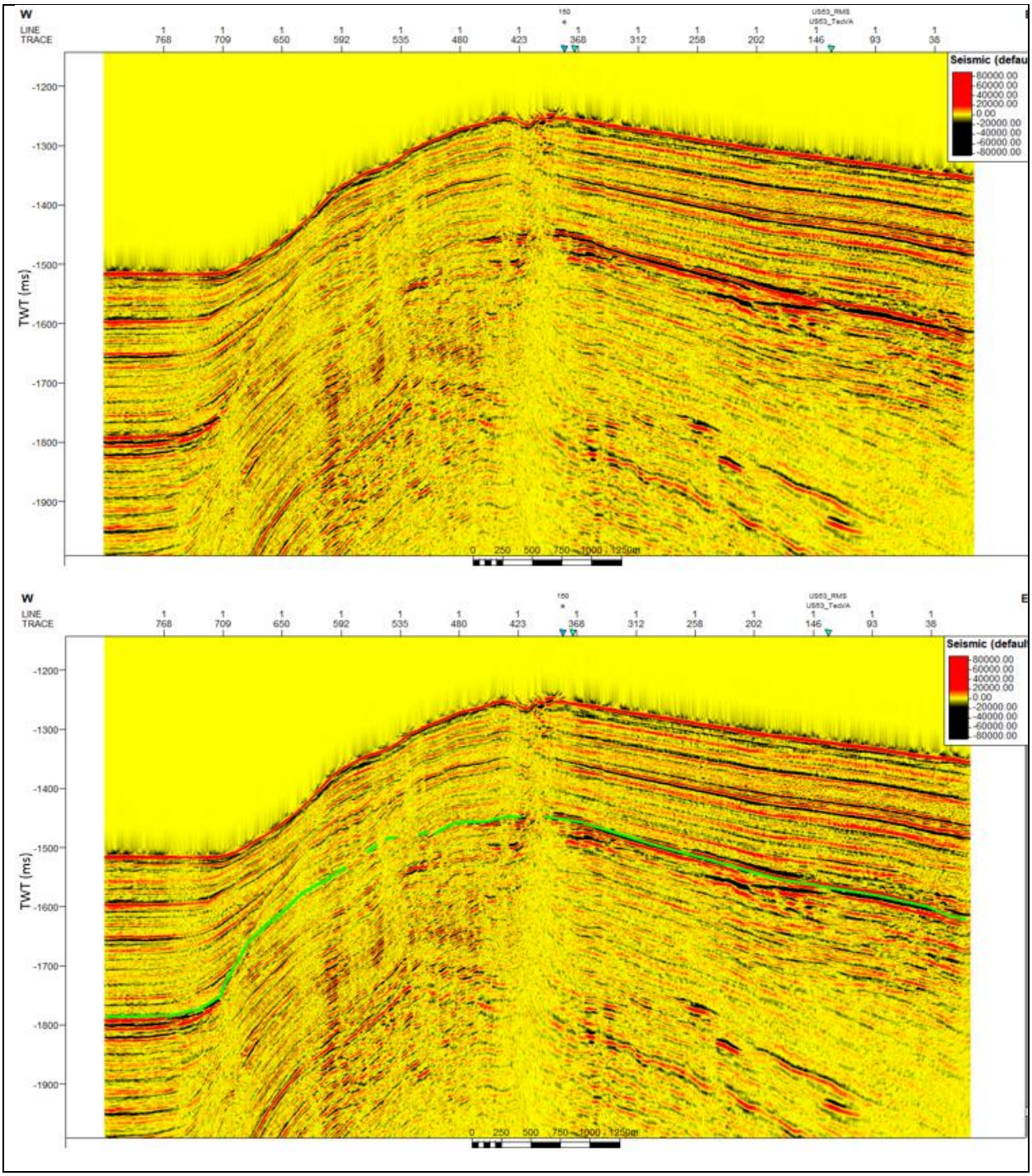

SCS profile US-22 with Relative Acoustic Impedance. Green line indicates BSR.

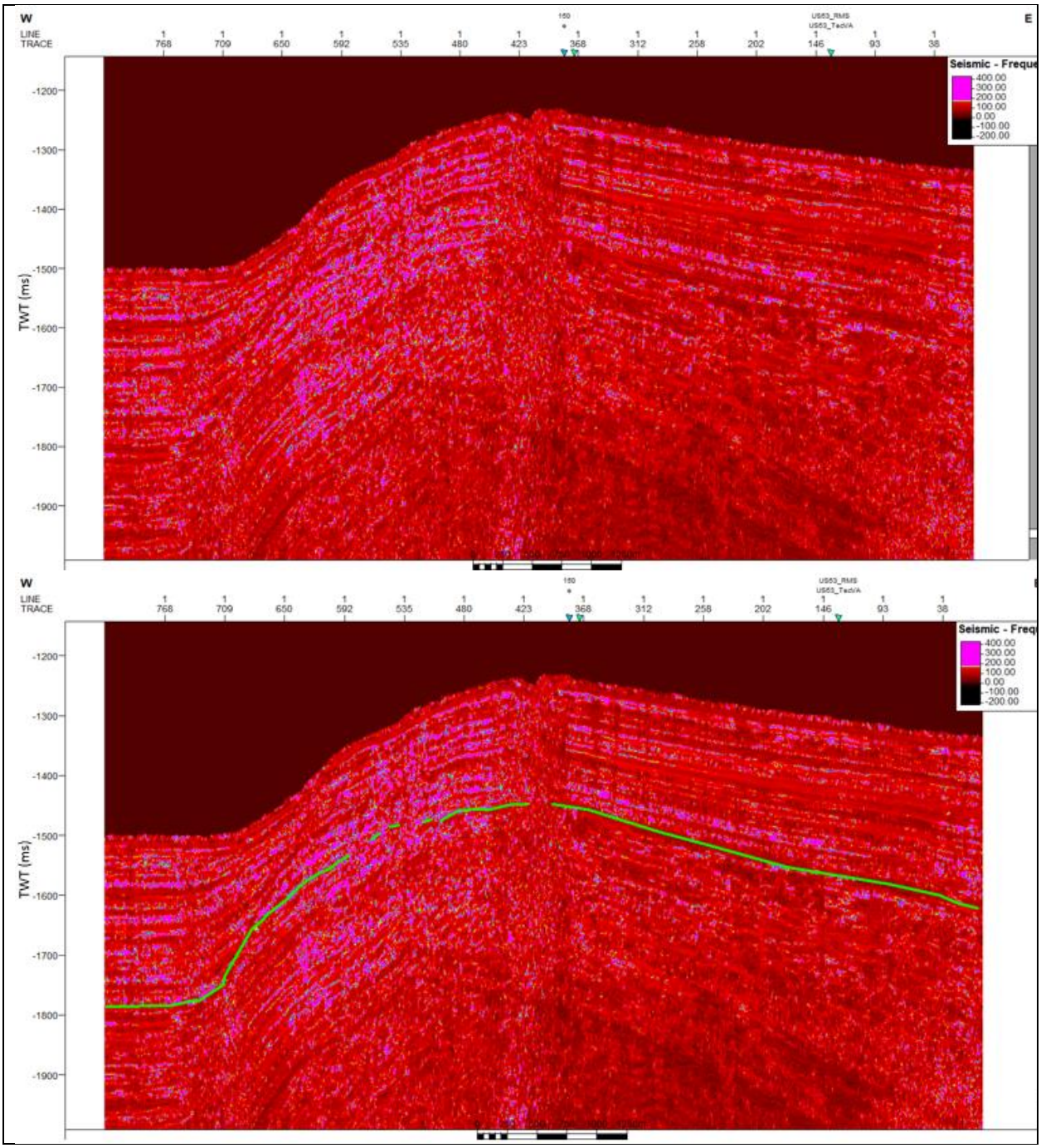

SCS profile US-22 with Instantaneous Frequency. Green line indicates BSR.

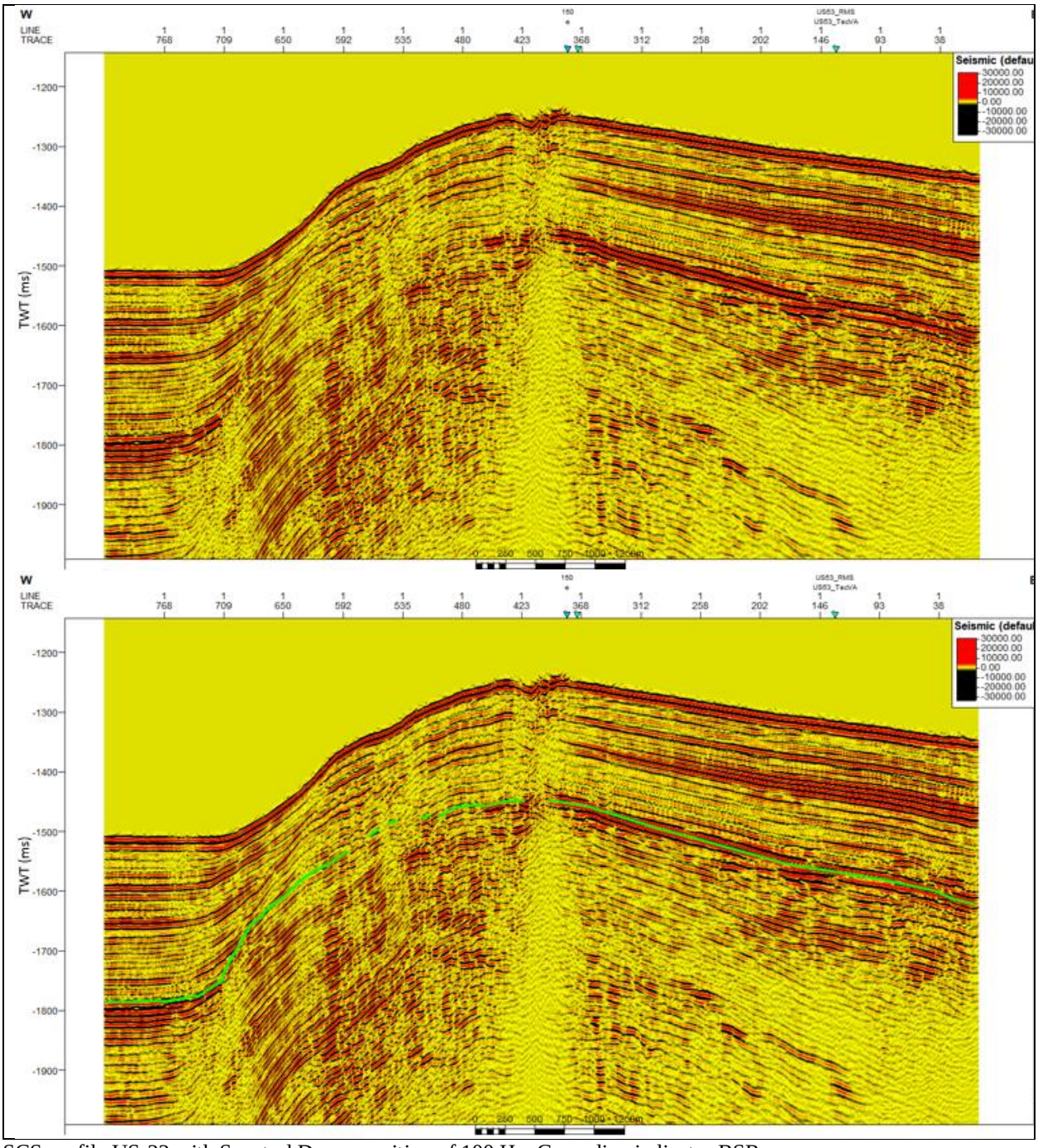

SCS profile US-22 with Spectral Decomposition of 100 Hz. Green line indicates BSR.

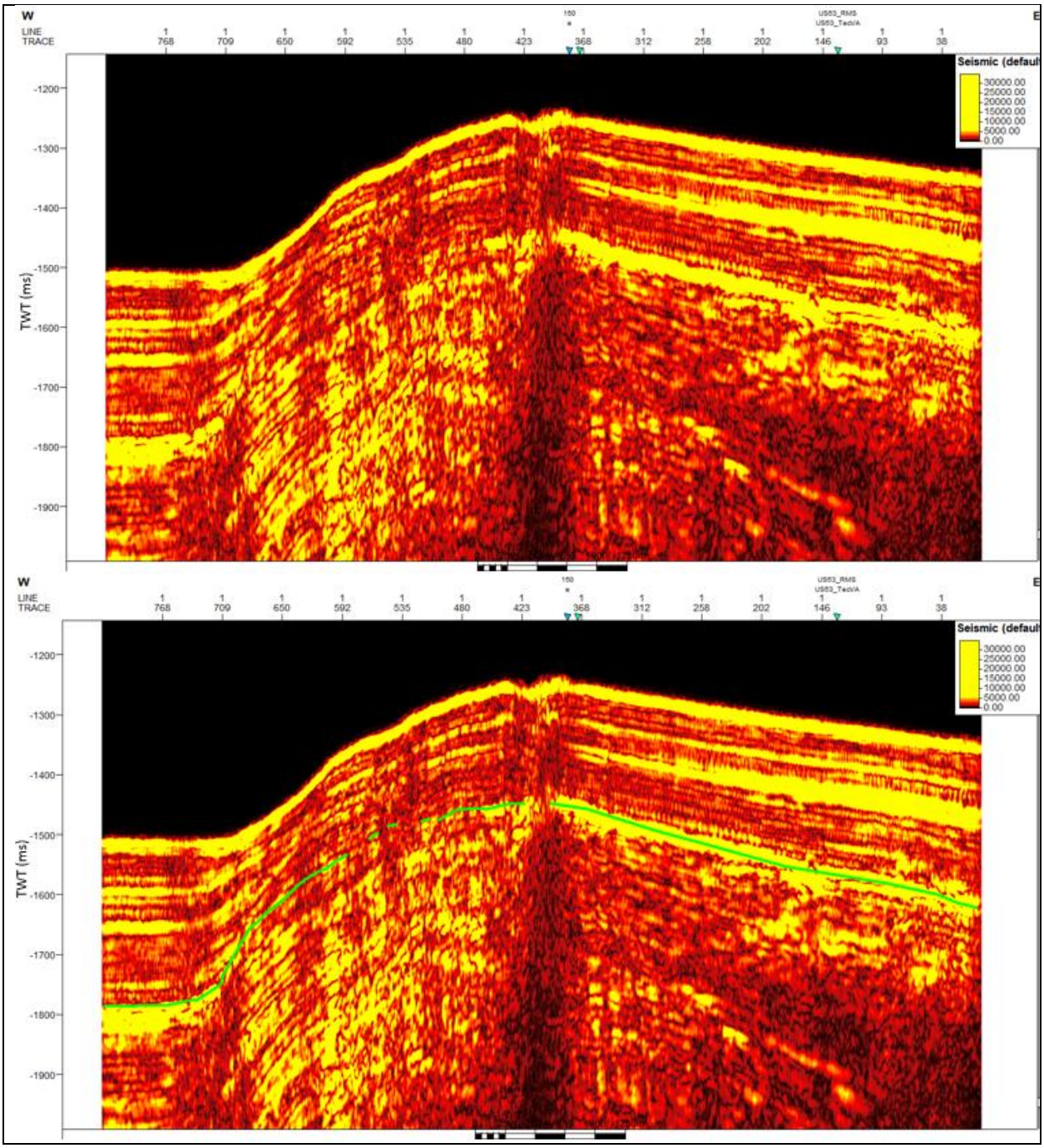

SCS profile US-22 with Spectral Decomposition of 100 Hz plus Envelope. Green line indicates BSR.

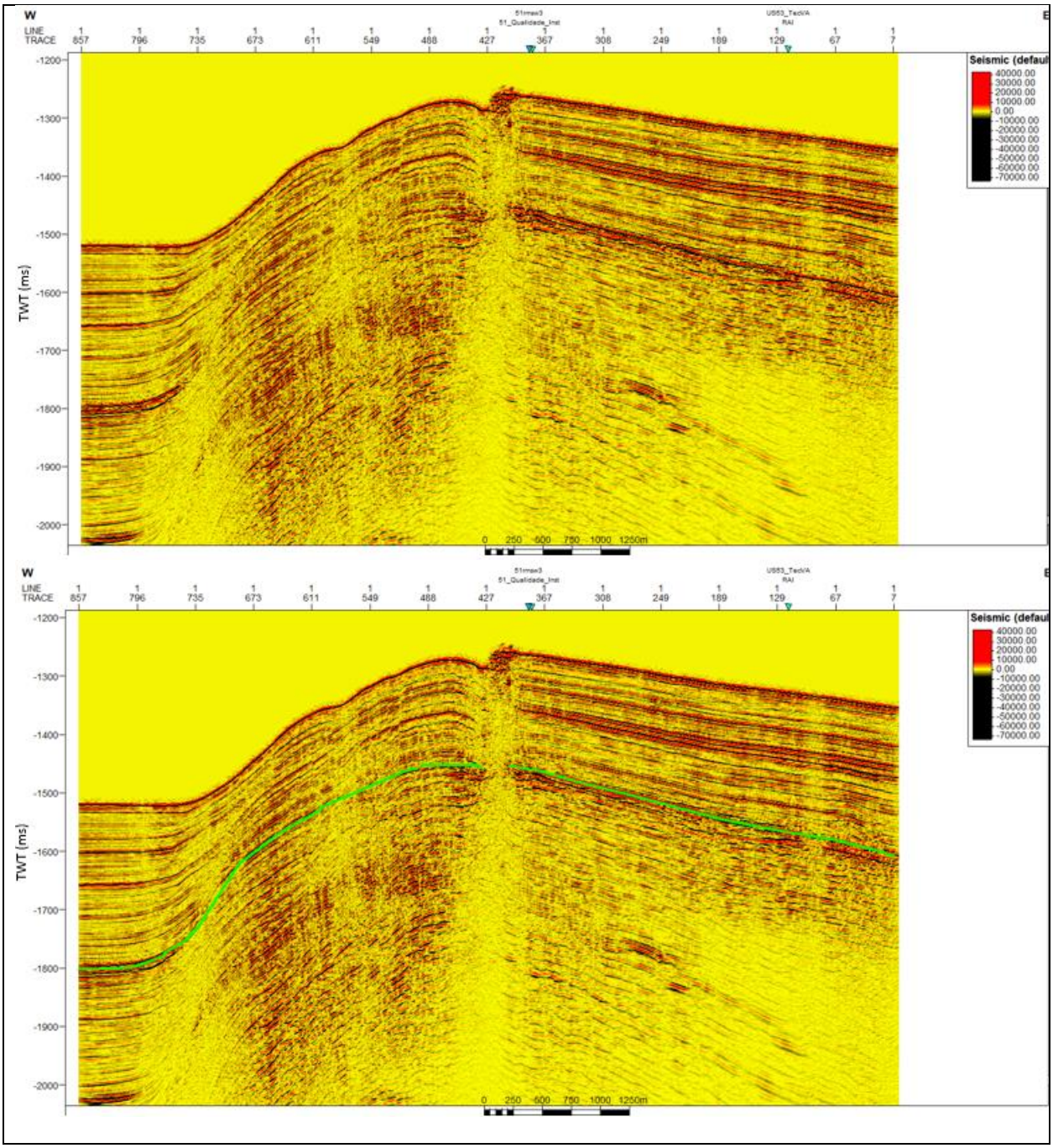

SCS profile US-23 without application of seismic attribute. Green line indicates BSR.

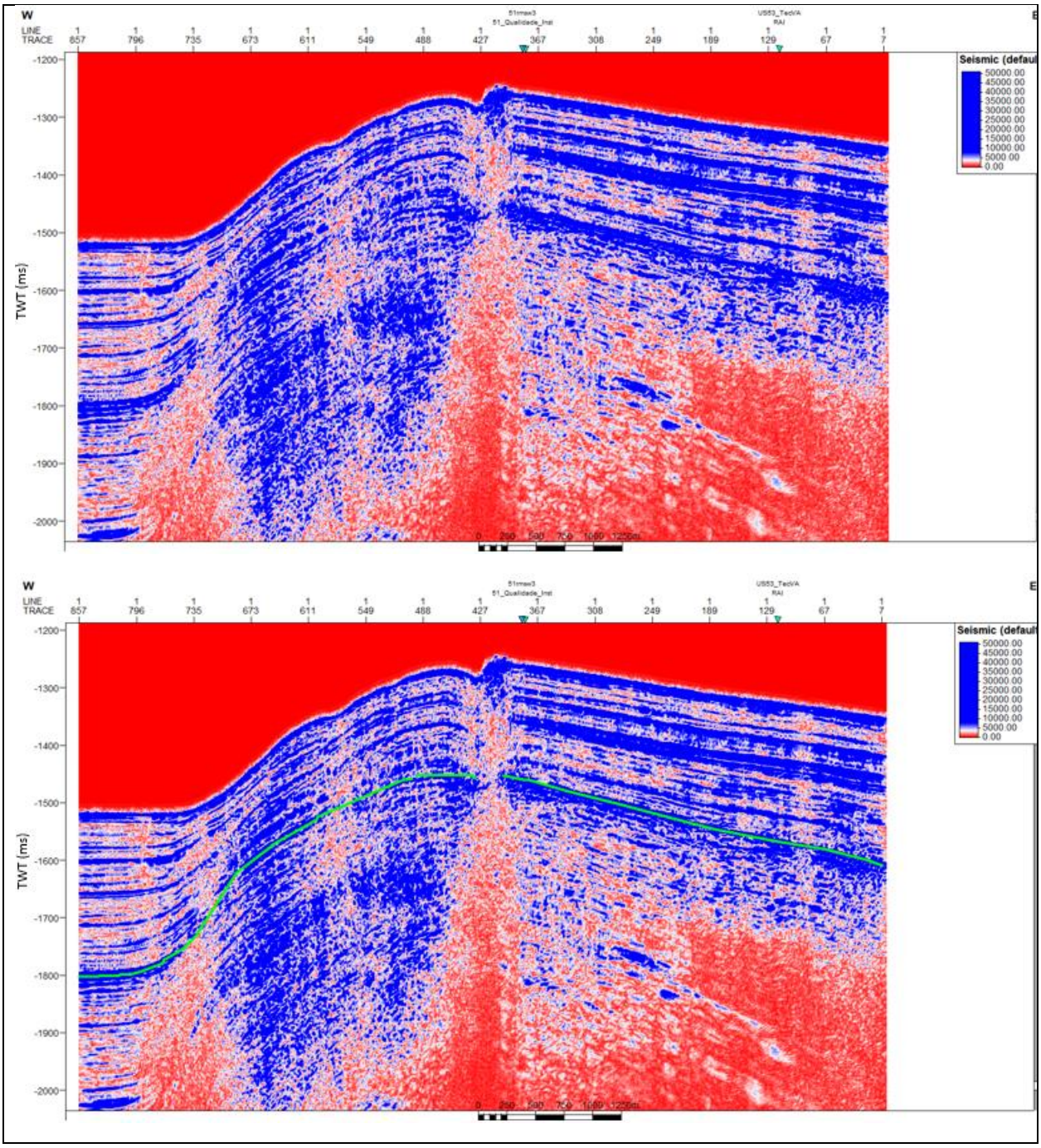

SCS profile US-23 with Envelope. Green line indicates BSR.

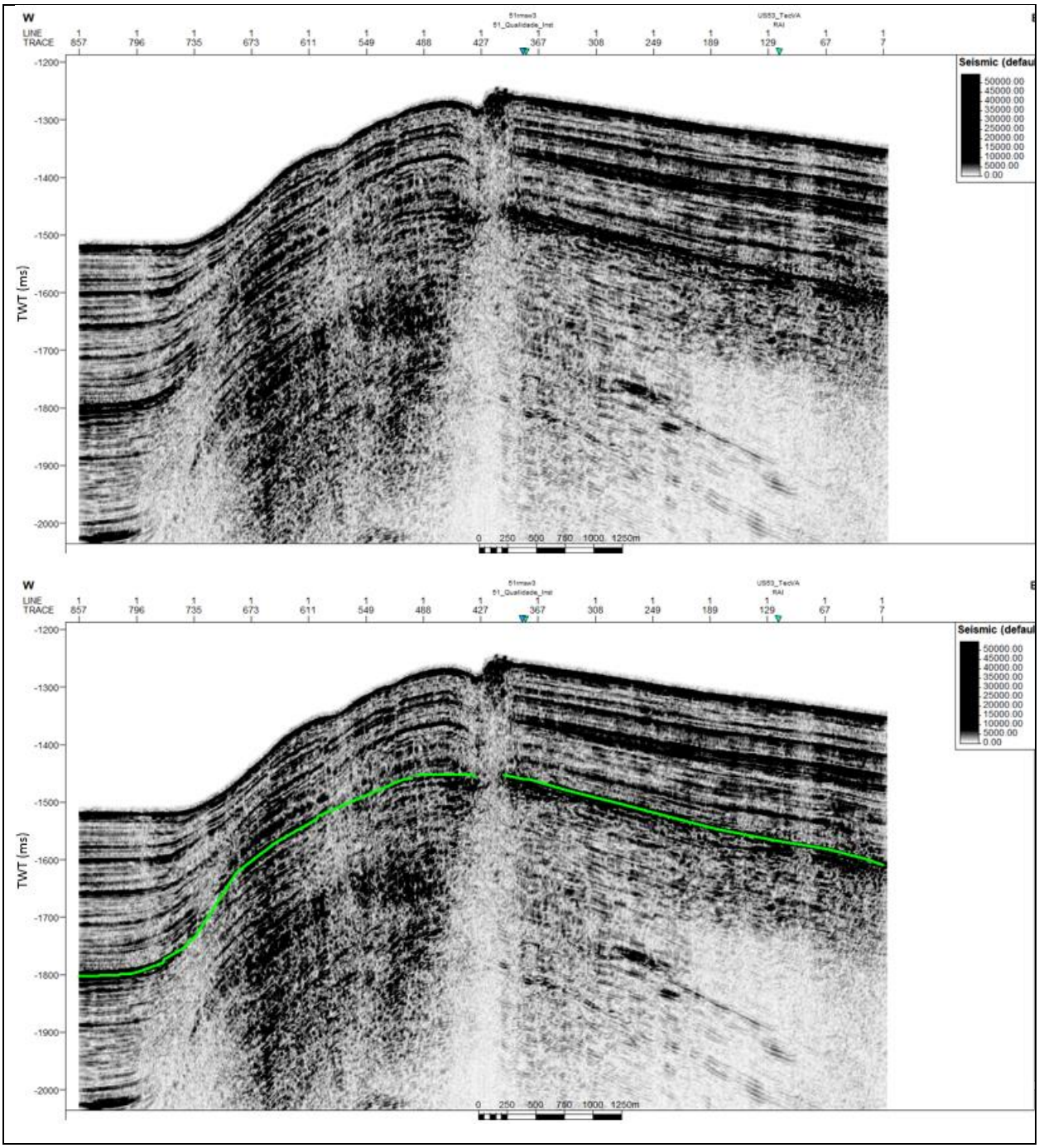

SCS profile US-23 with RMS Amplitude. Green line indicates BSR.

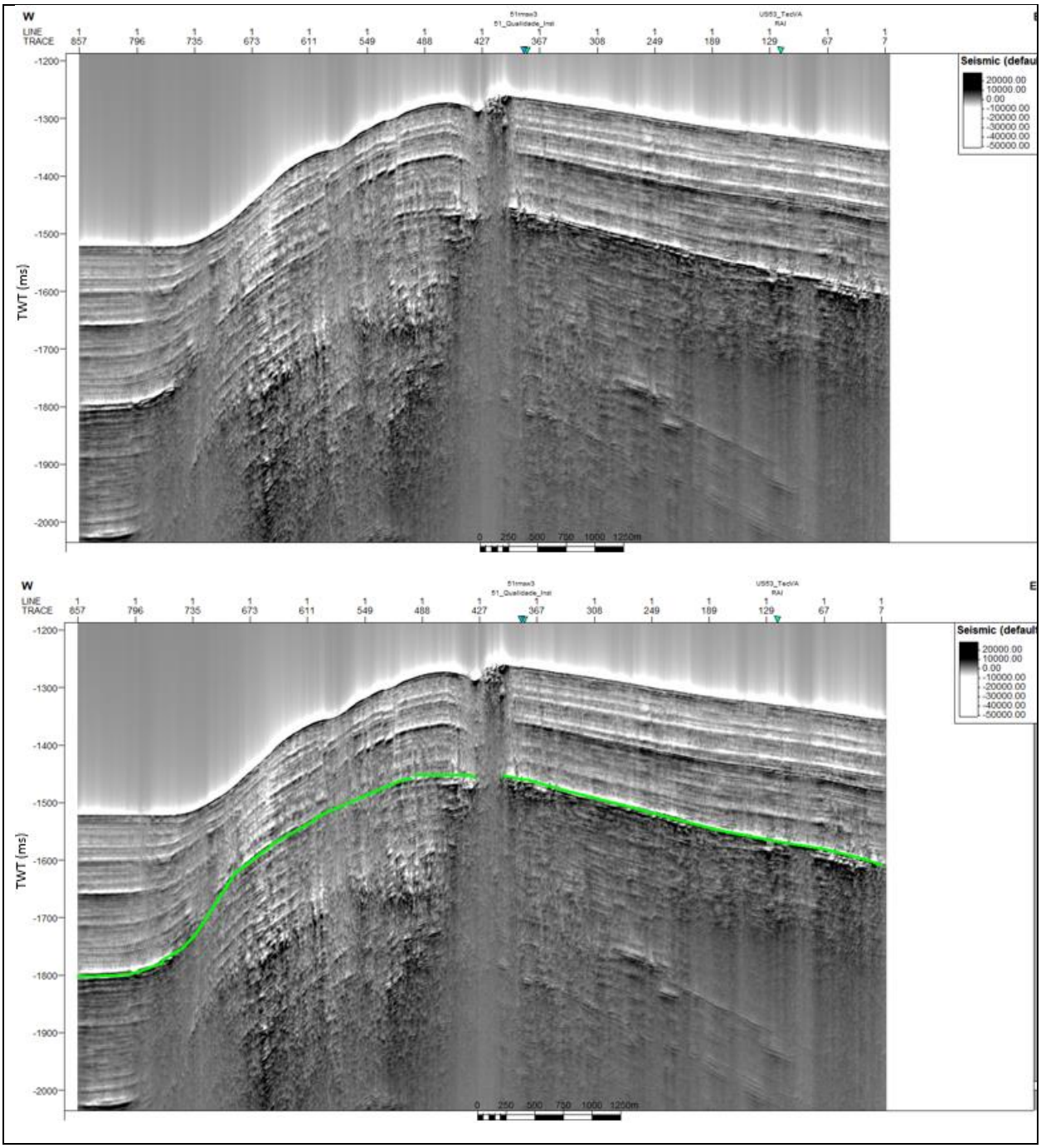

SCS profile US-23 with Amplitude Volume Technique. Green line indicates BSR.

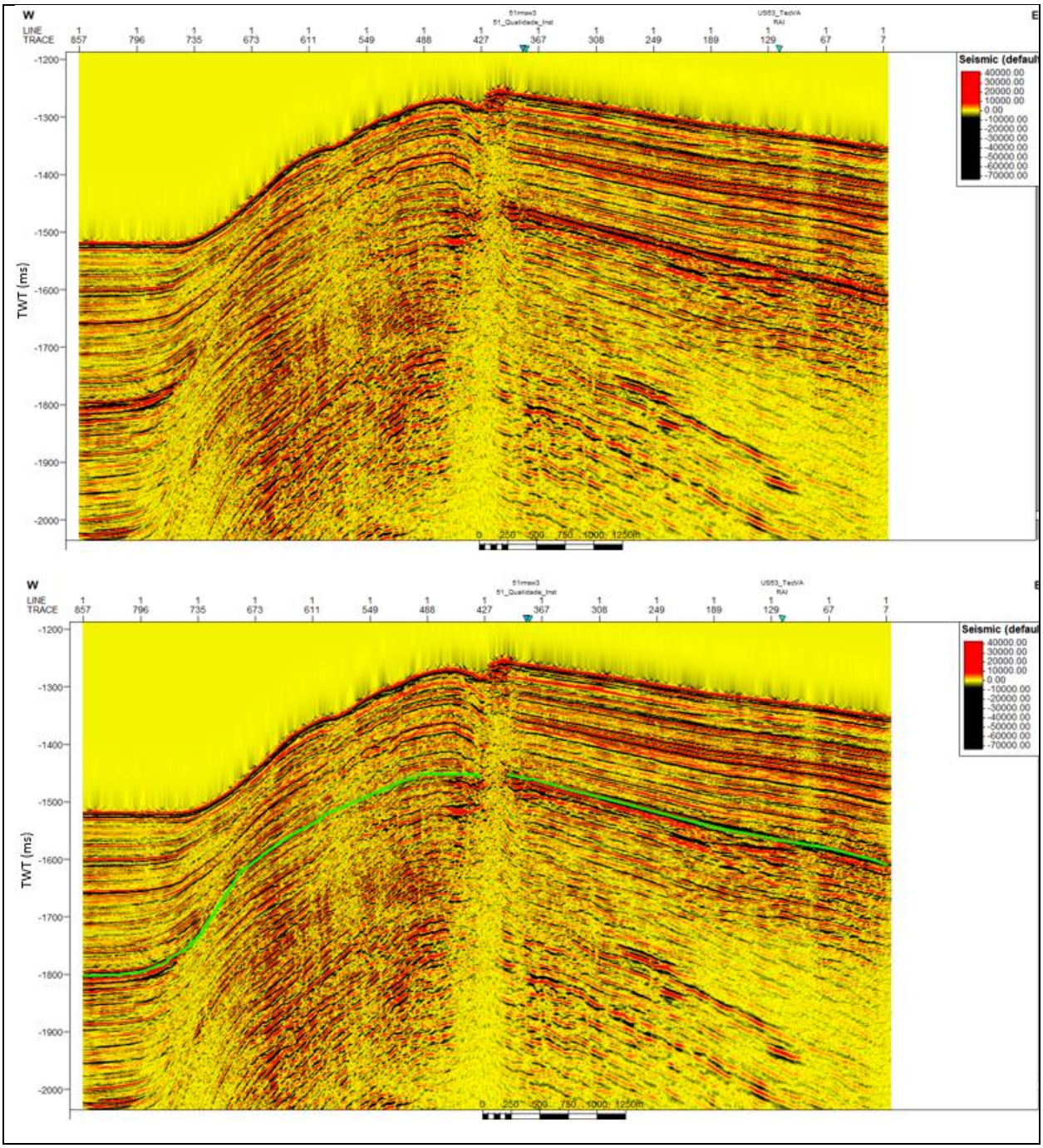

SCS profile US-23 with Relative Acoustic Impedance. Green line indicates BSR.

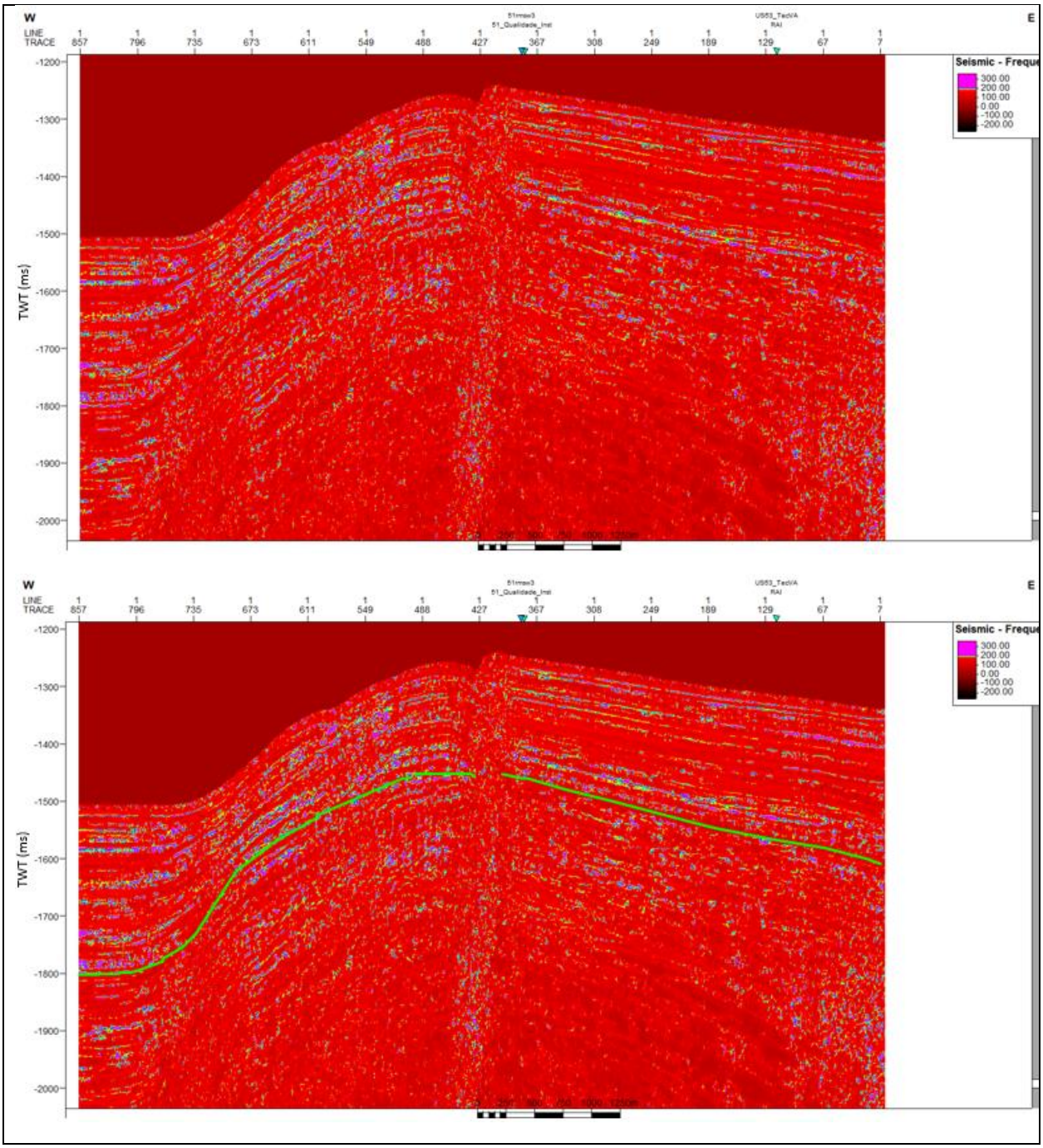

SCS profile US-23 with Instantaneous Frequency. Green line indicates BSR.

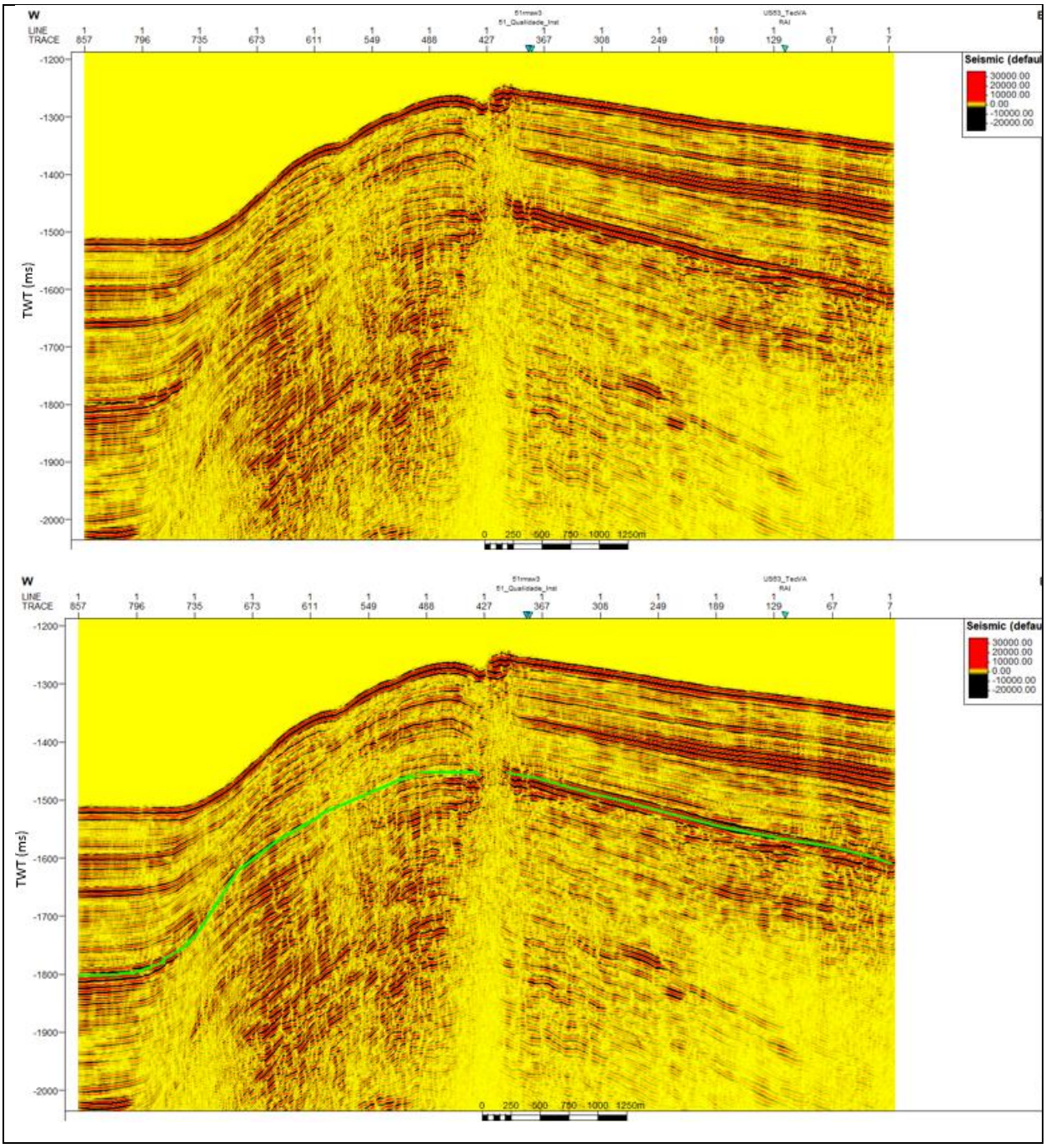

SCS profile US-23 with Spectral Decomposition of 100 Hz. Green line indicates BSR.

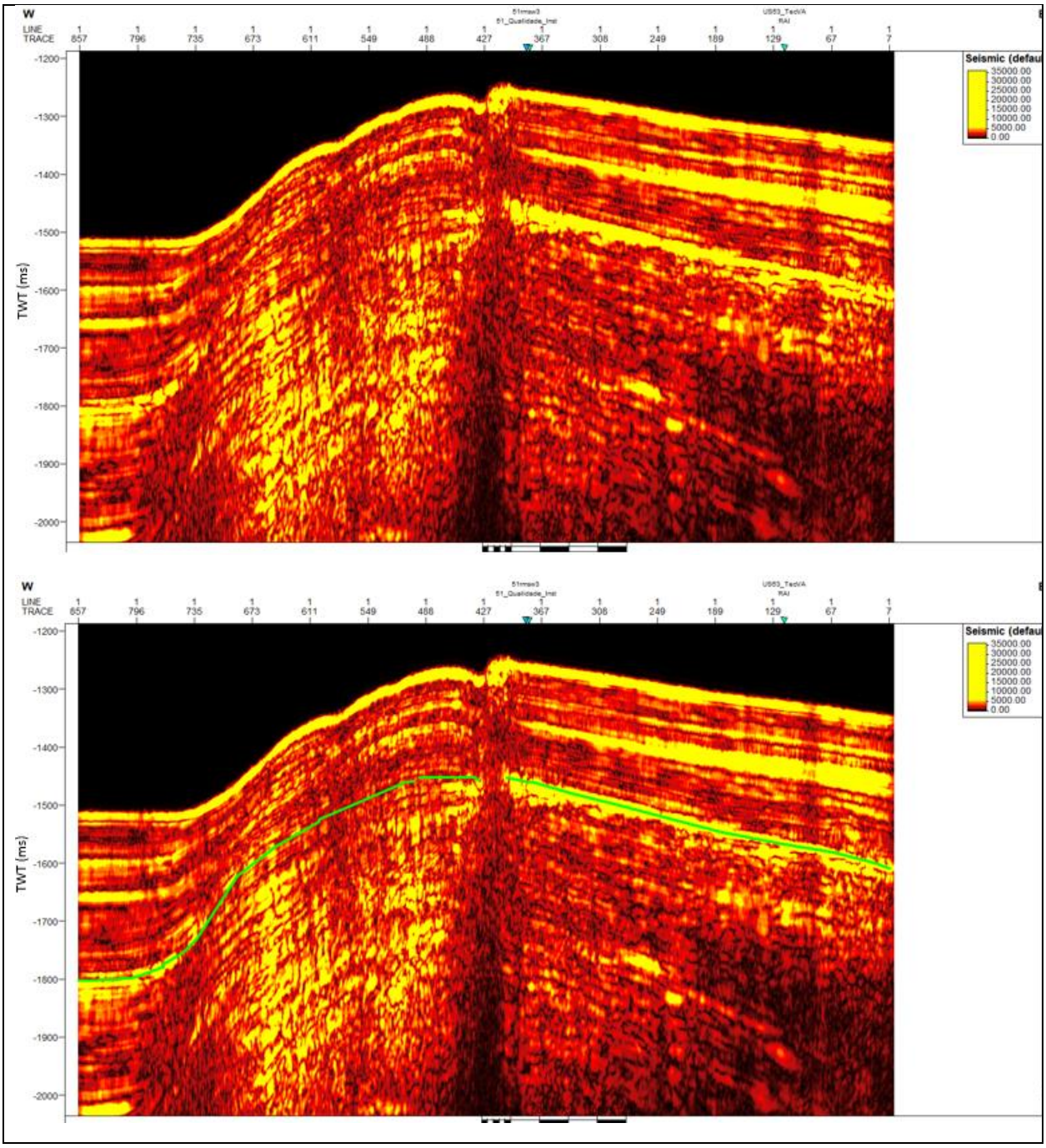

SCS profile US-23 with Spectral Decomposition of 100 Hz plus Envelope. Green line indicates BSR.

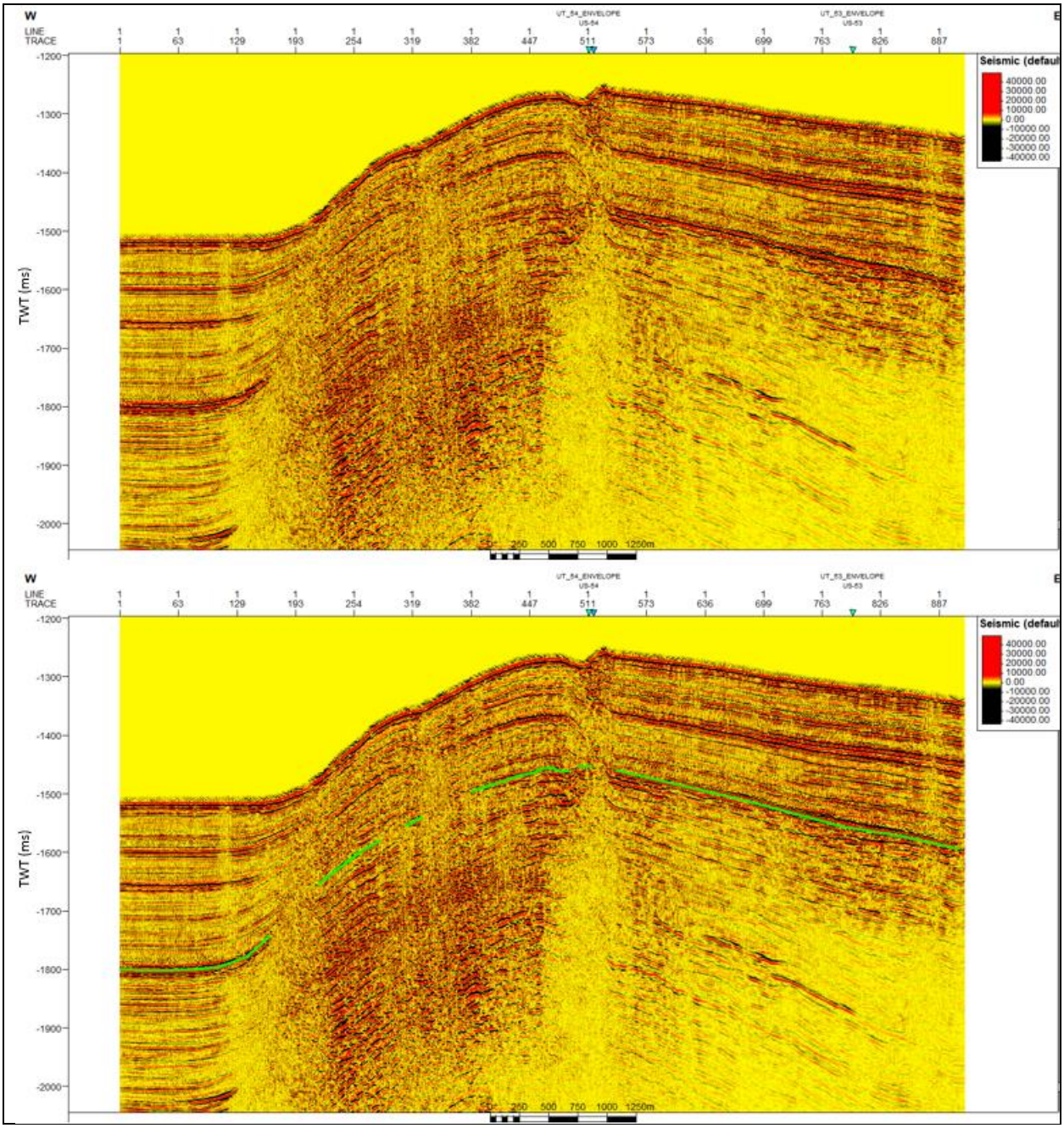

SCS profile US-24 without application of seismic attribute. Green line indicates BSR.

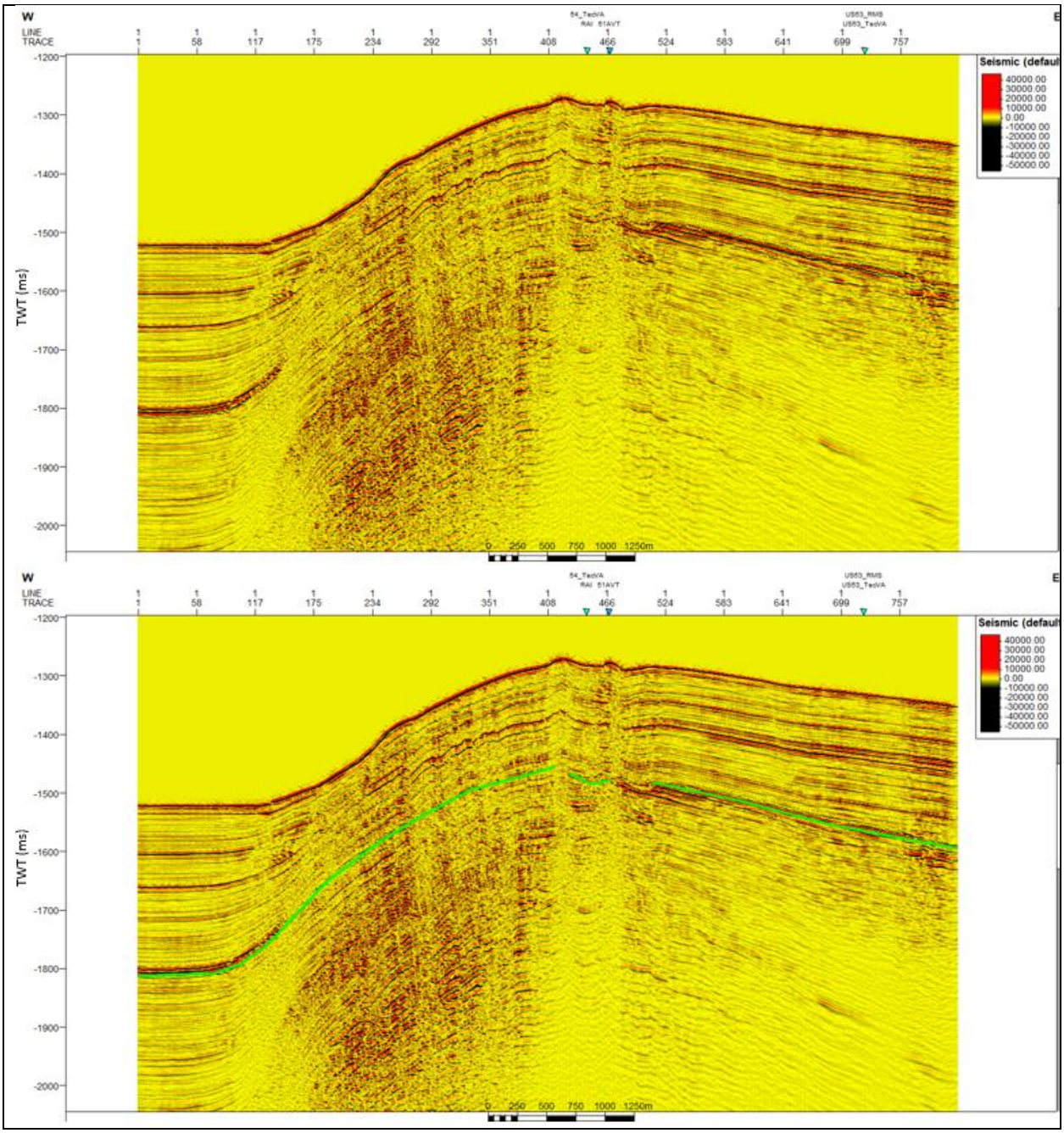

SCS profile US-26 without application of seismic attribute. Green line indicates BSR.

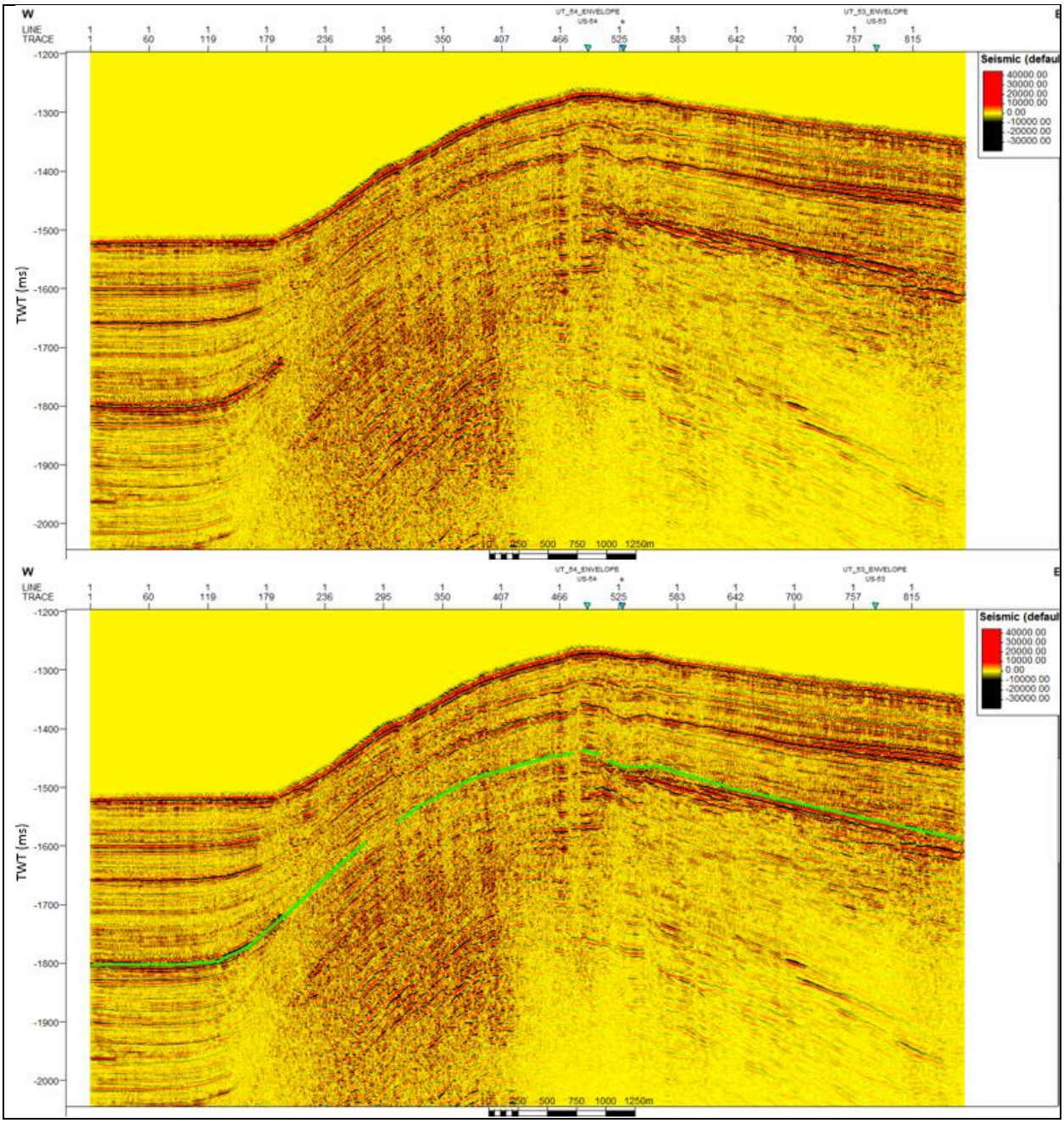

SCS profile US-27 without application of seismic attribute. Green line indicates BSR.

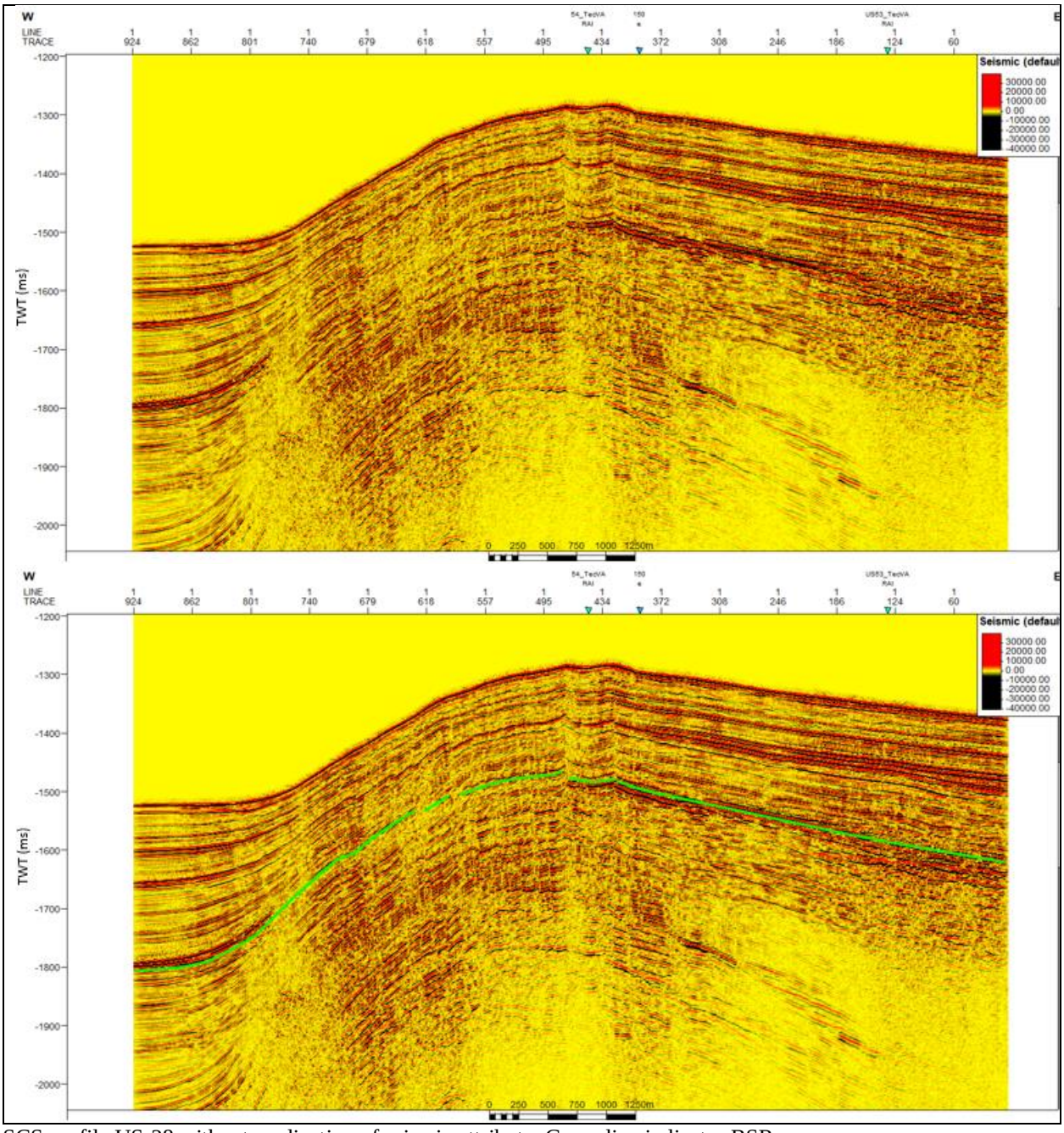

SCS profile US-28 without application of seismic attribute. Green line indicates BSR.

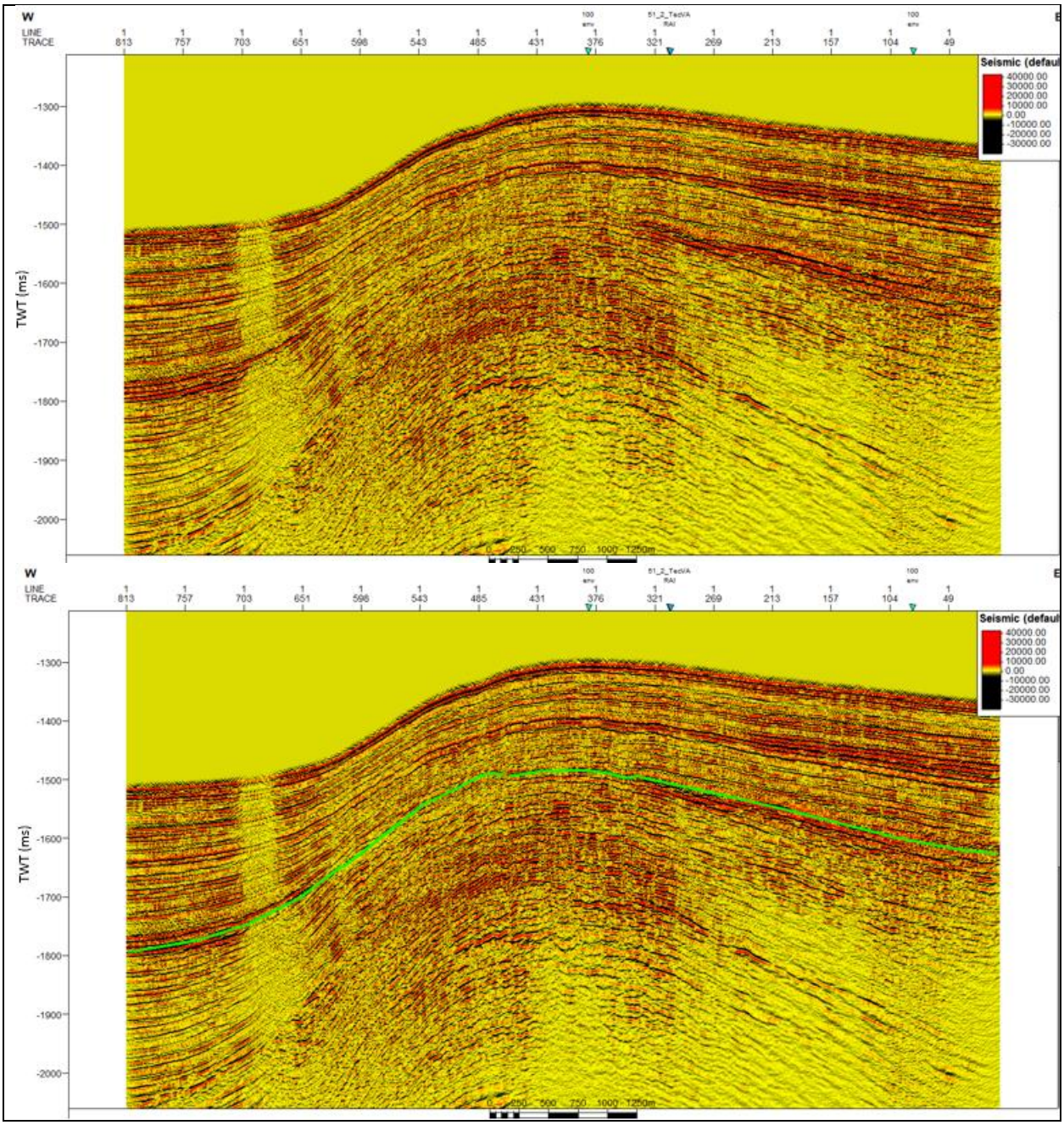

SCS profile US-29 without application of seismic attribute. Green line indicates BSR.

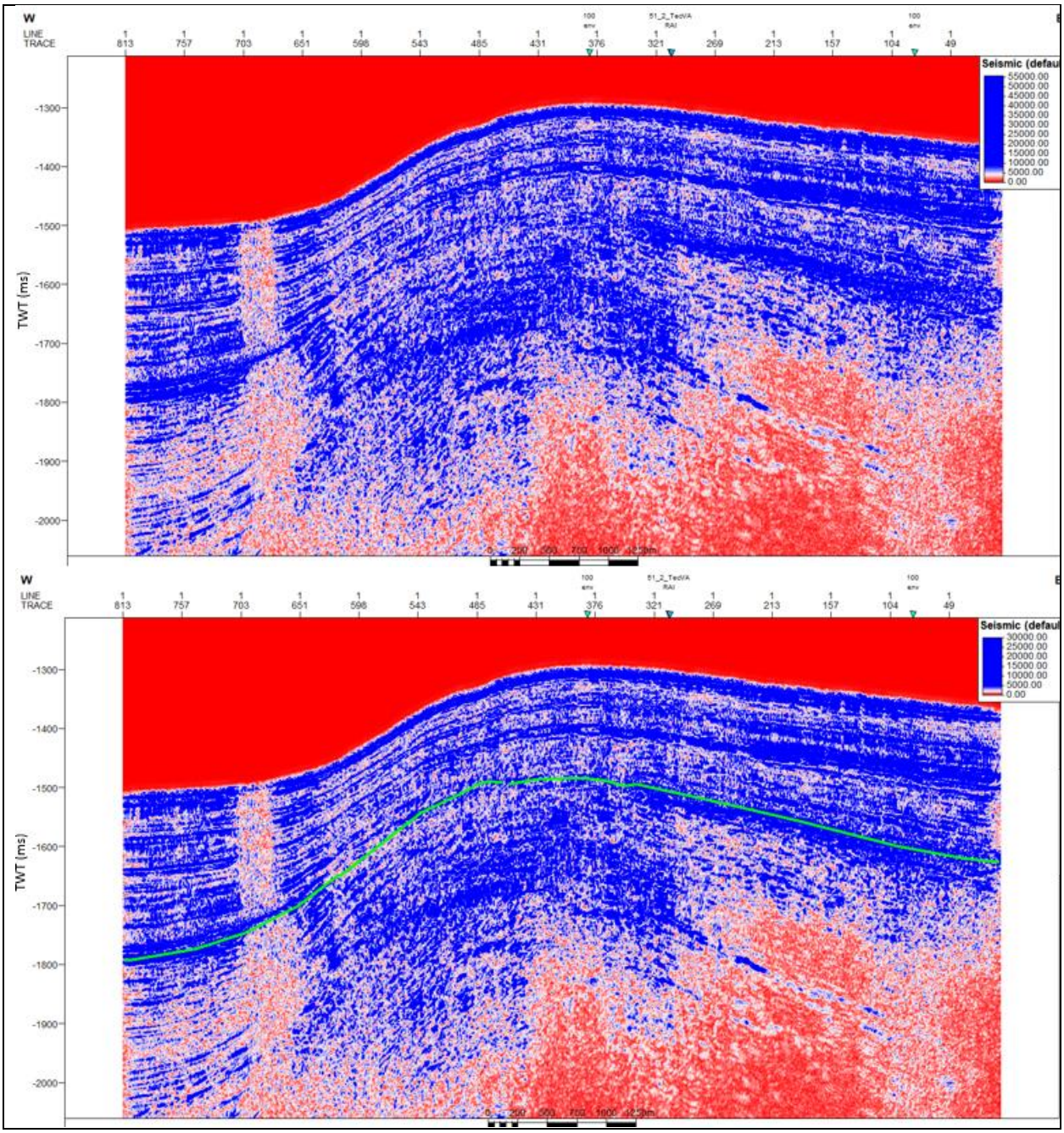

SCS profile US-29 with Envelope. Green line indicates BSR.

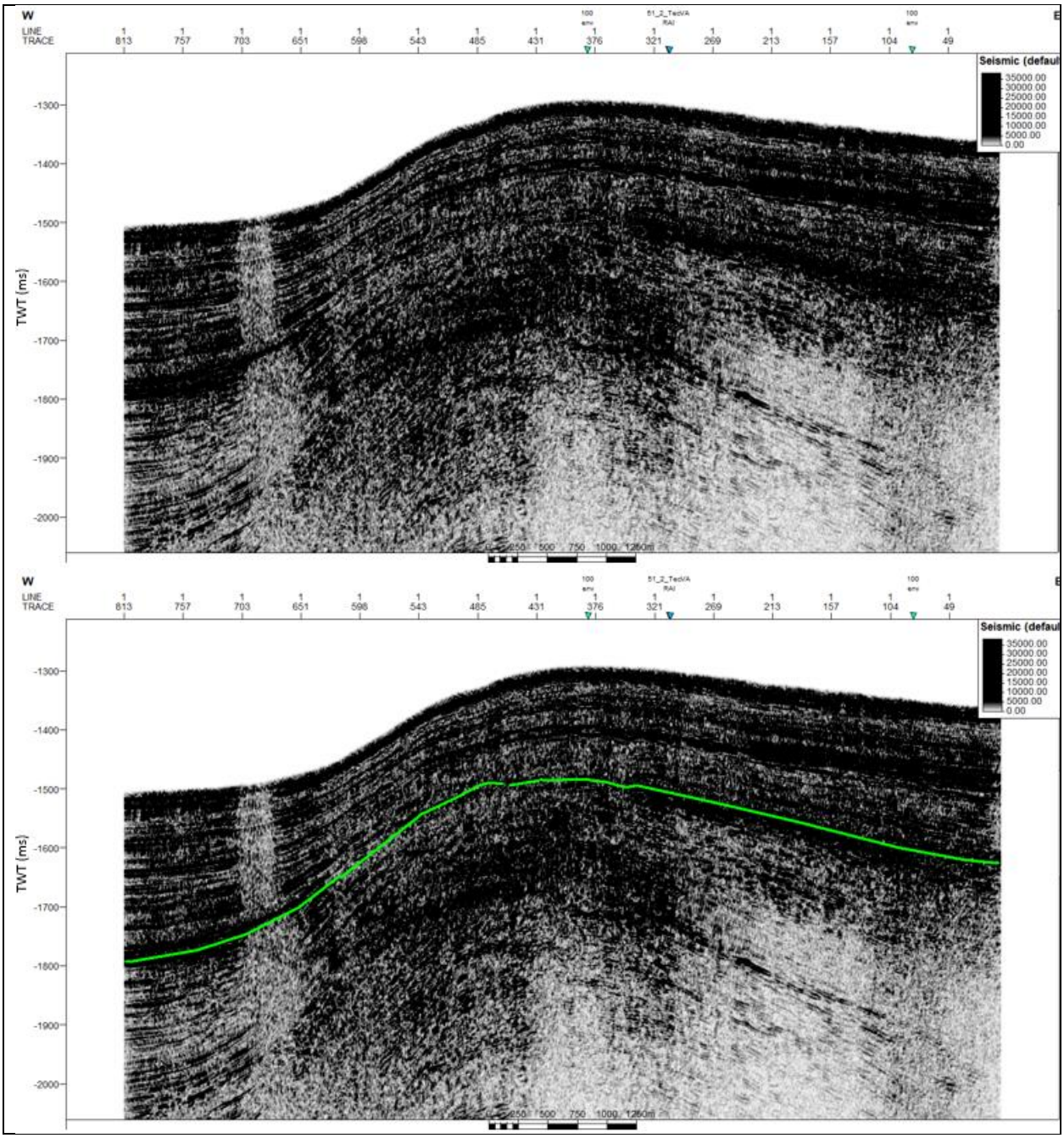

SCS profile US-29 with RMS Amplitude. Green line indicates BSR.

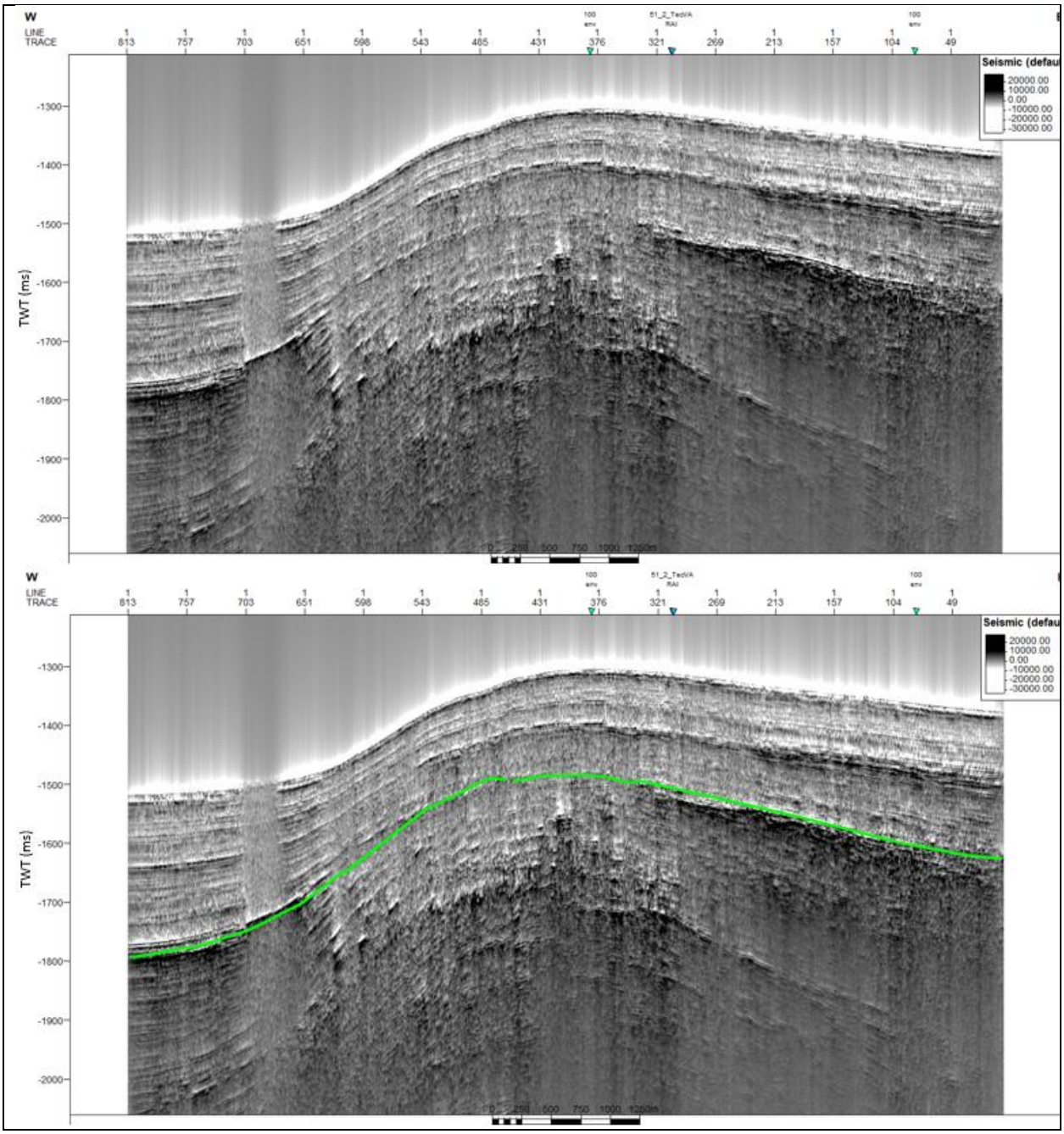

SCS profile US-29 with Amplitude Volume Technique. Green line indicates BSR.

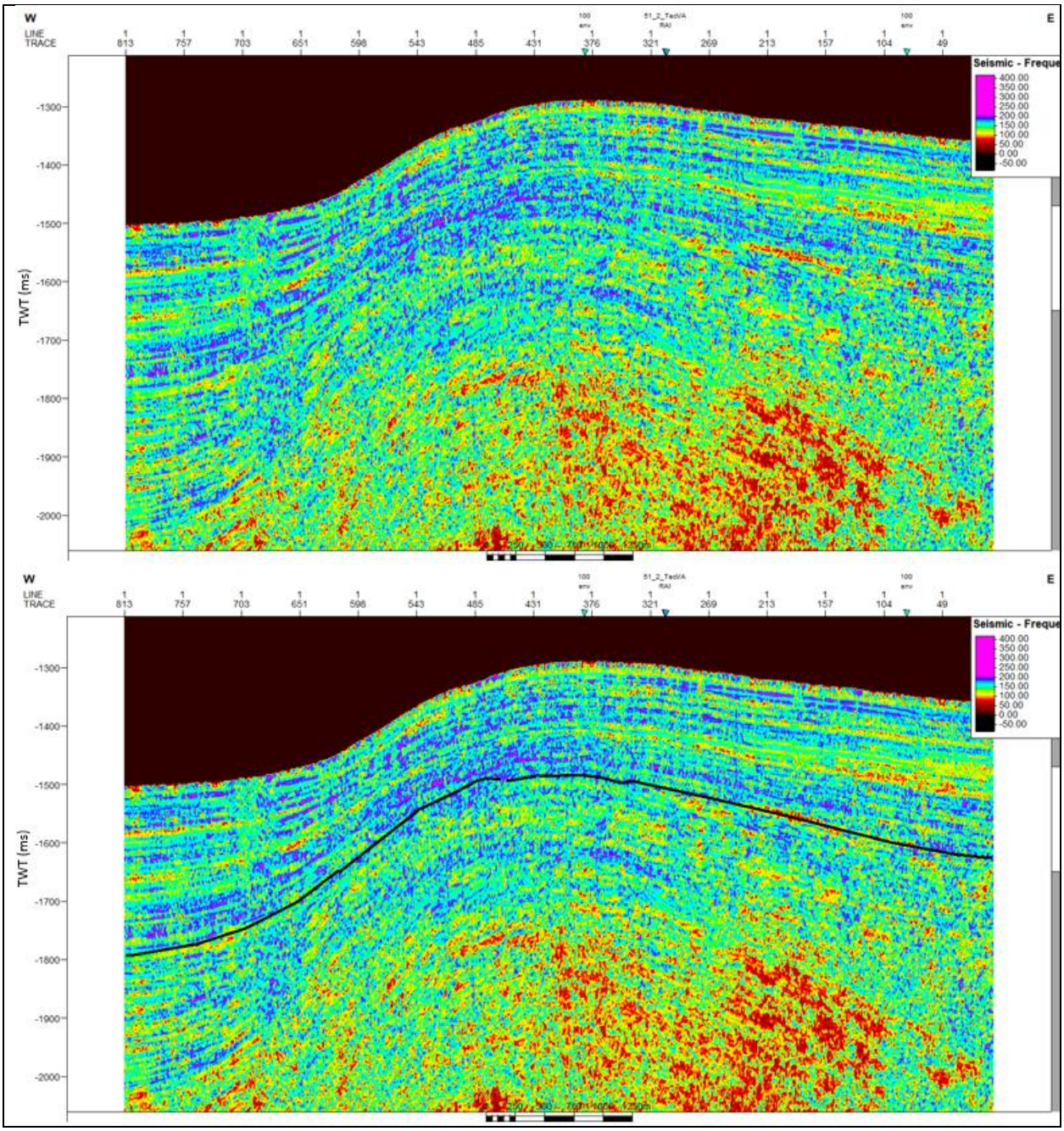

SCS profile US-29 with Instantaneous Frequency. Black line indicates BSR.

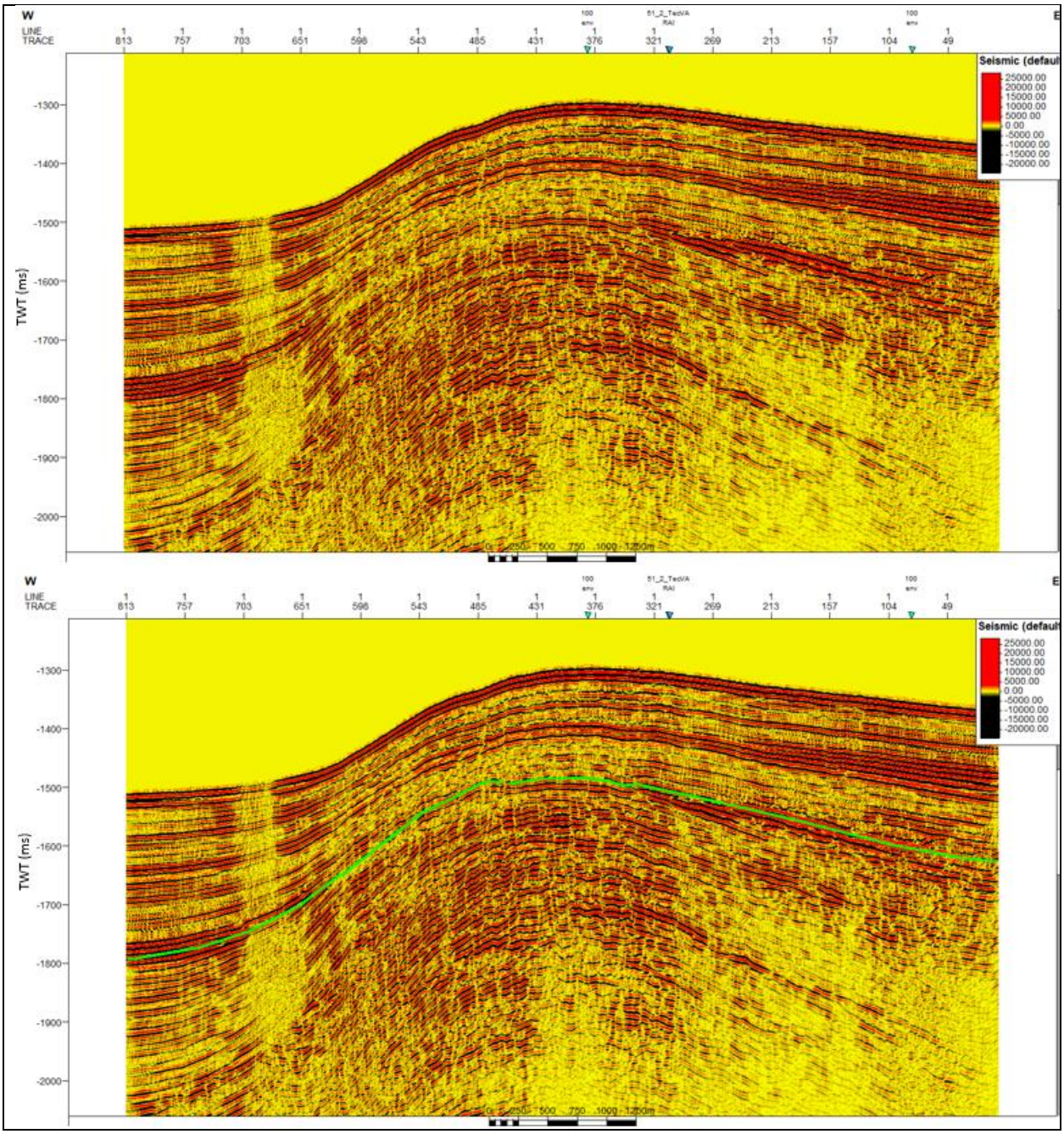

SCS profile US-29 with Spectral Decomposition of 100 Hz. Green line indicates BSR.

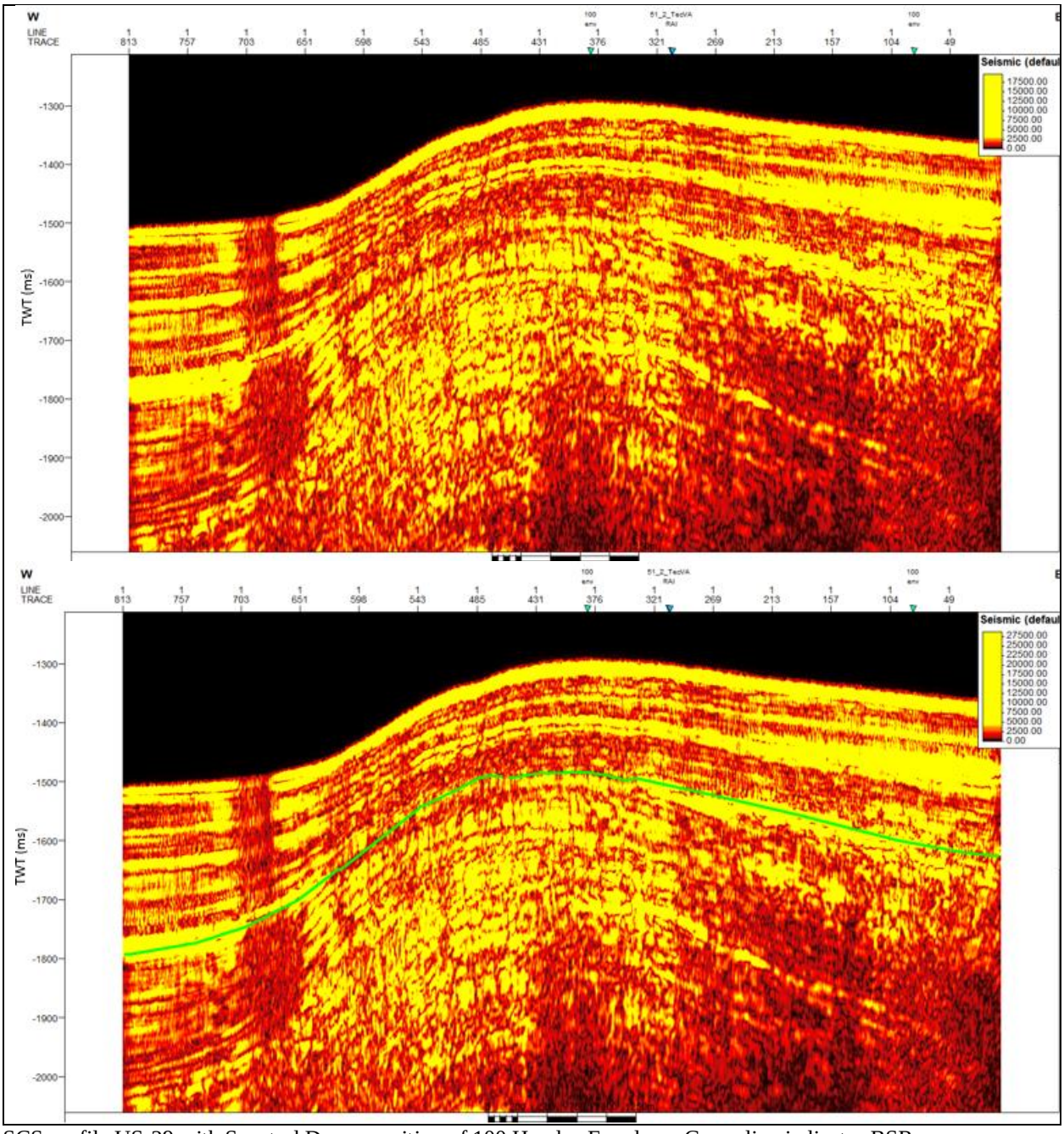

SCS profile US-29 with Spectral Decomposition of 100 Hz plus Envelope. Green line indicates BSR.

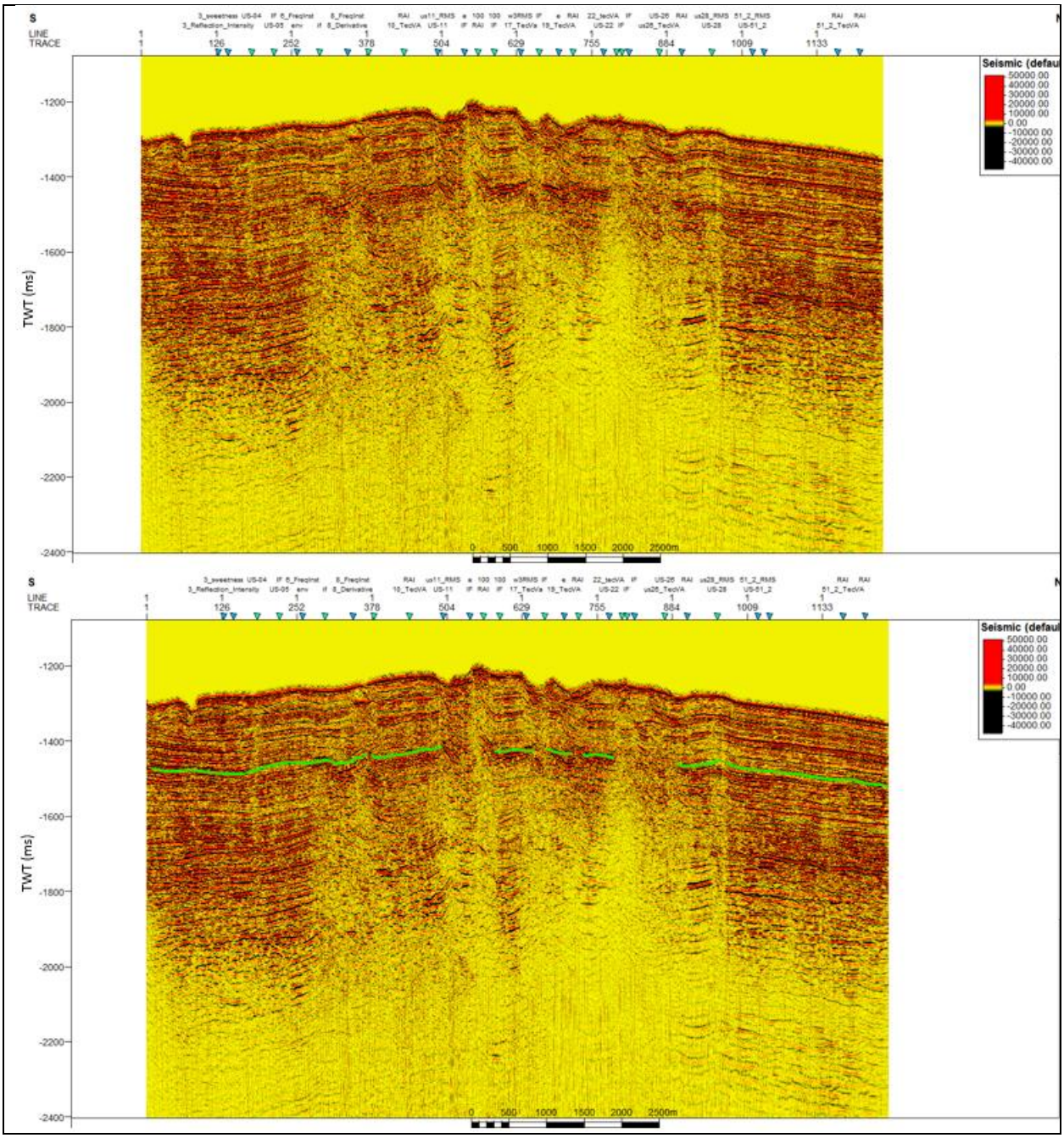

SCS profile US-51_1 without application of seismic attribute. Green line indicates BSR.

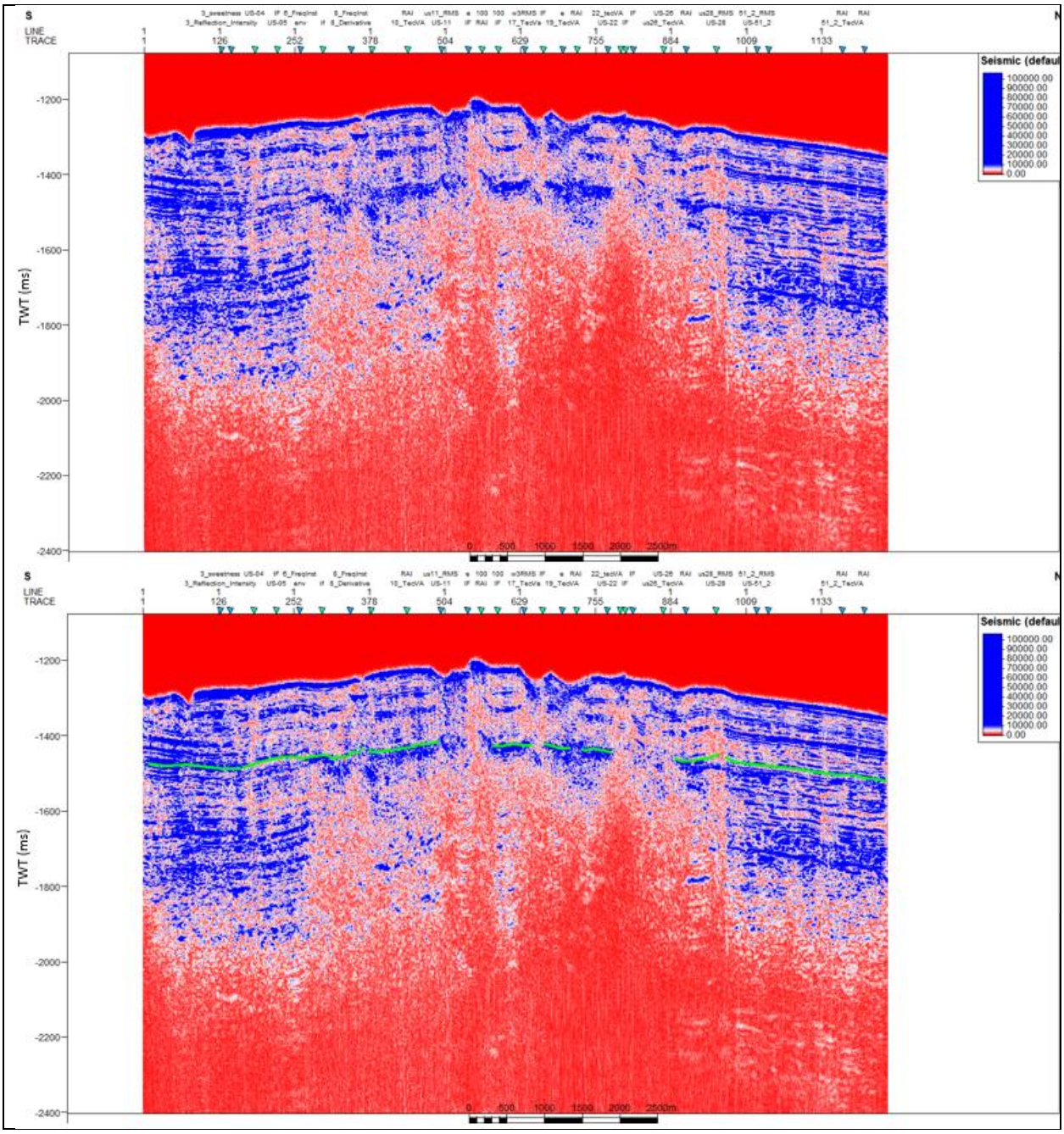

SCS profile US-51_1 with Envelope. Green line indicates BSR.

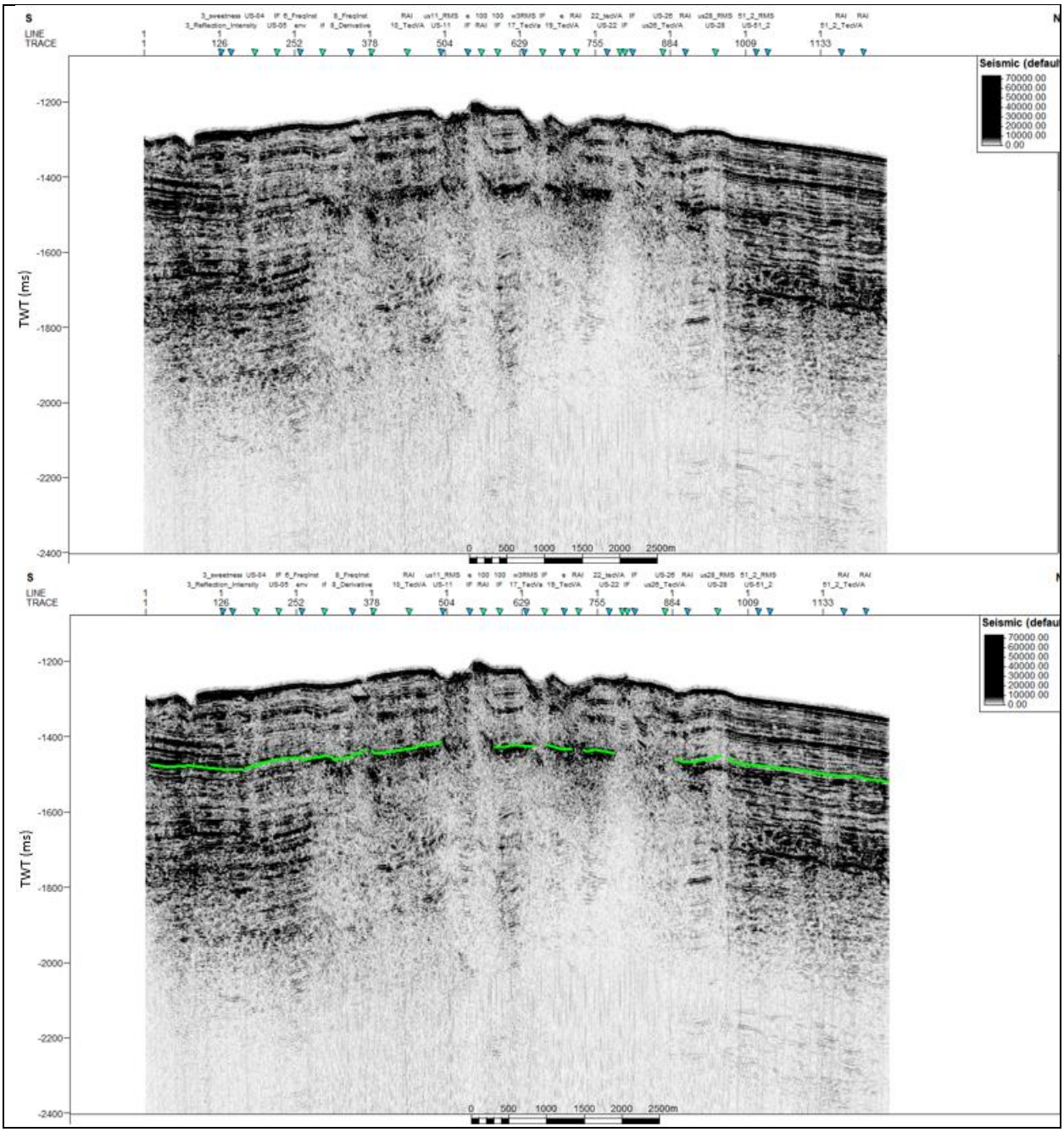

SCS profile US-51_1 with RMS Amplitude. Green line indicates BSR.

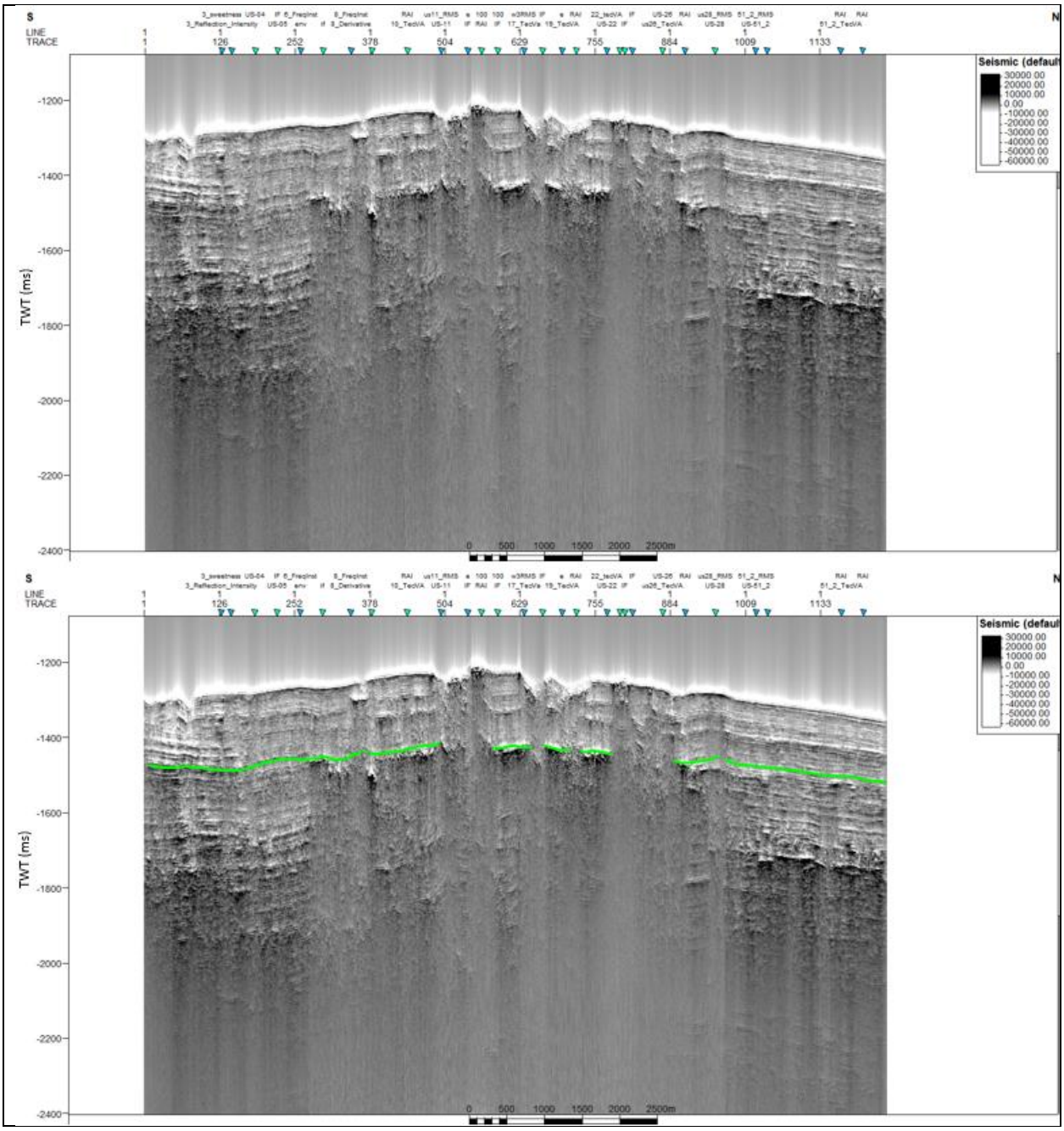

SCS profile US-51_1 with Amplitude Volume Technique. Green line indicates BSR.

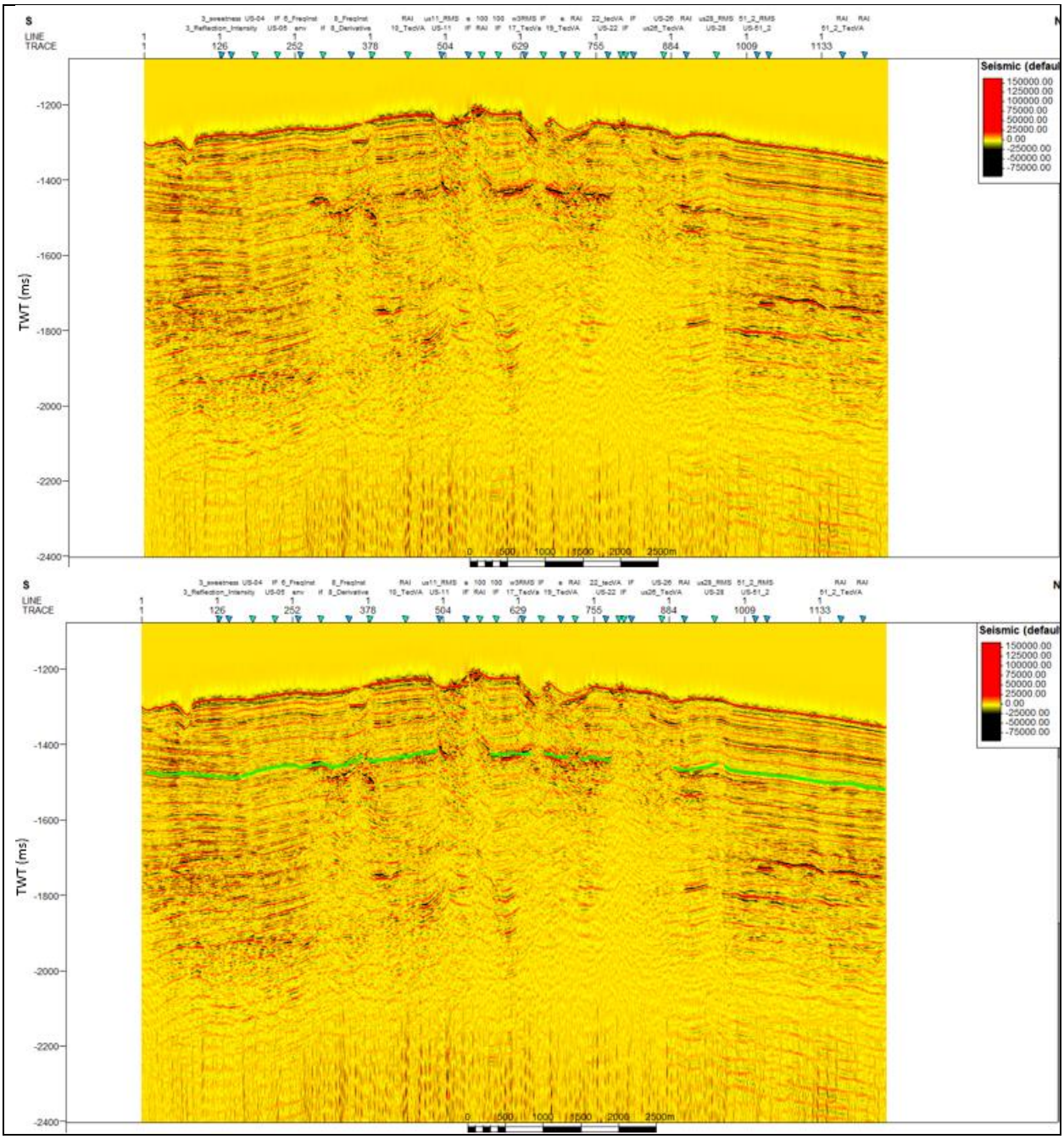

SCS profile US-51_1 with Relative Acoustic Impedance. Green line indicates BSR.

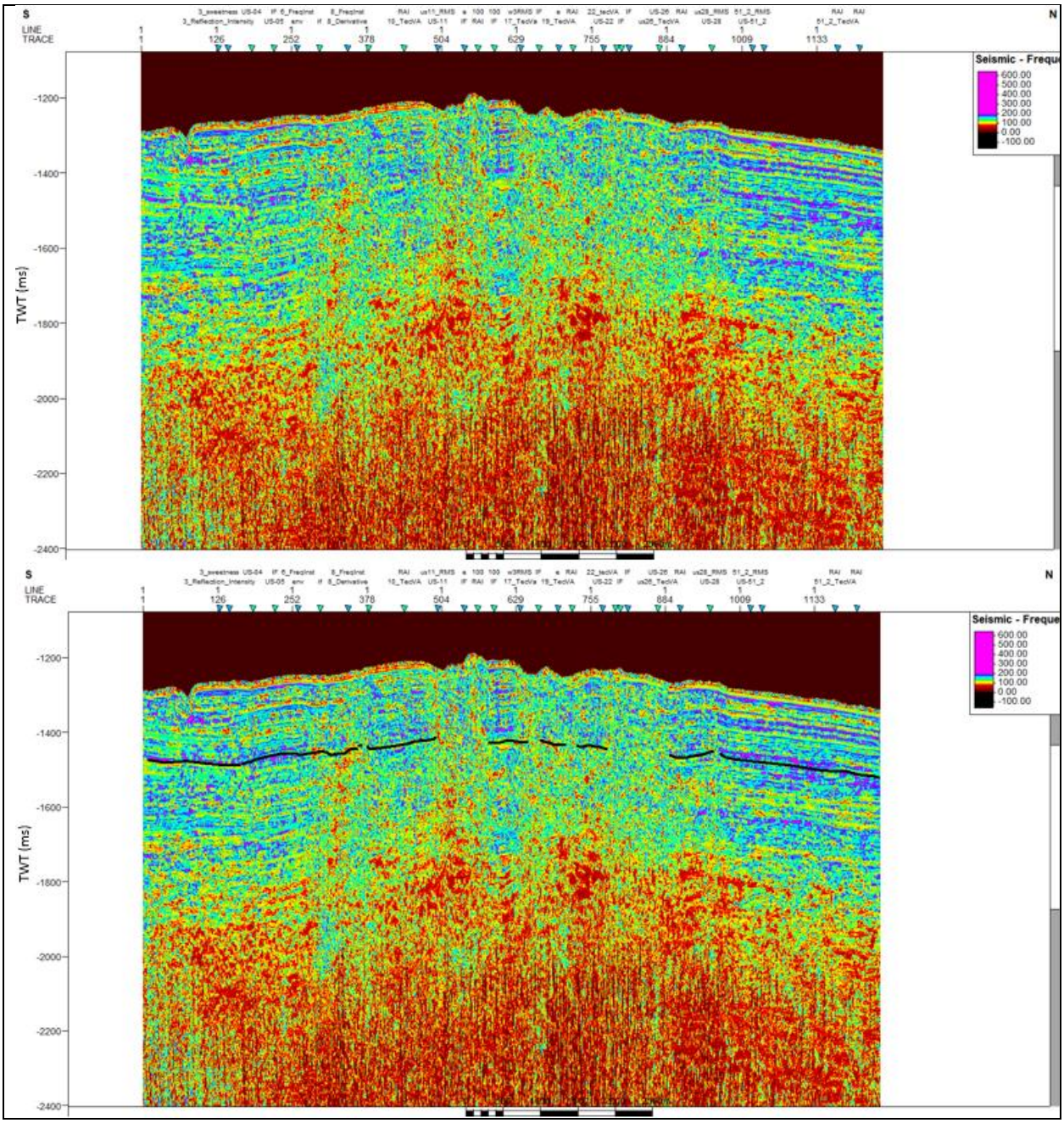

SCS profile US-51_1 with Instantaneous Frequency. Green line indicates BSR.

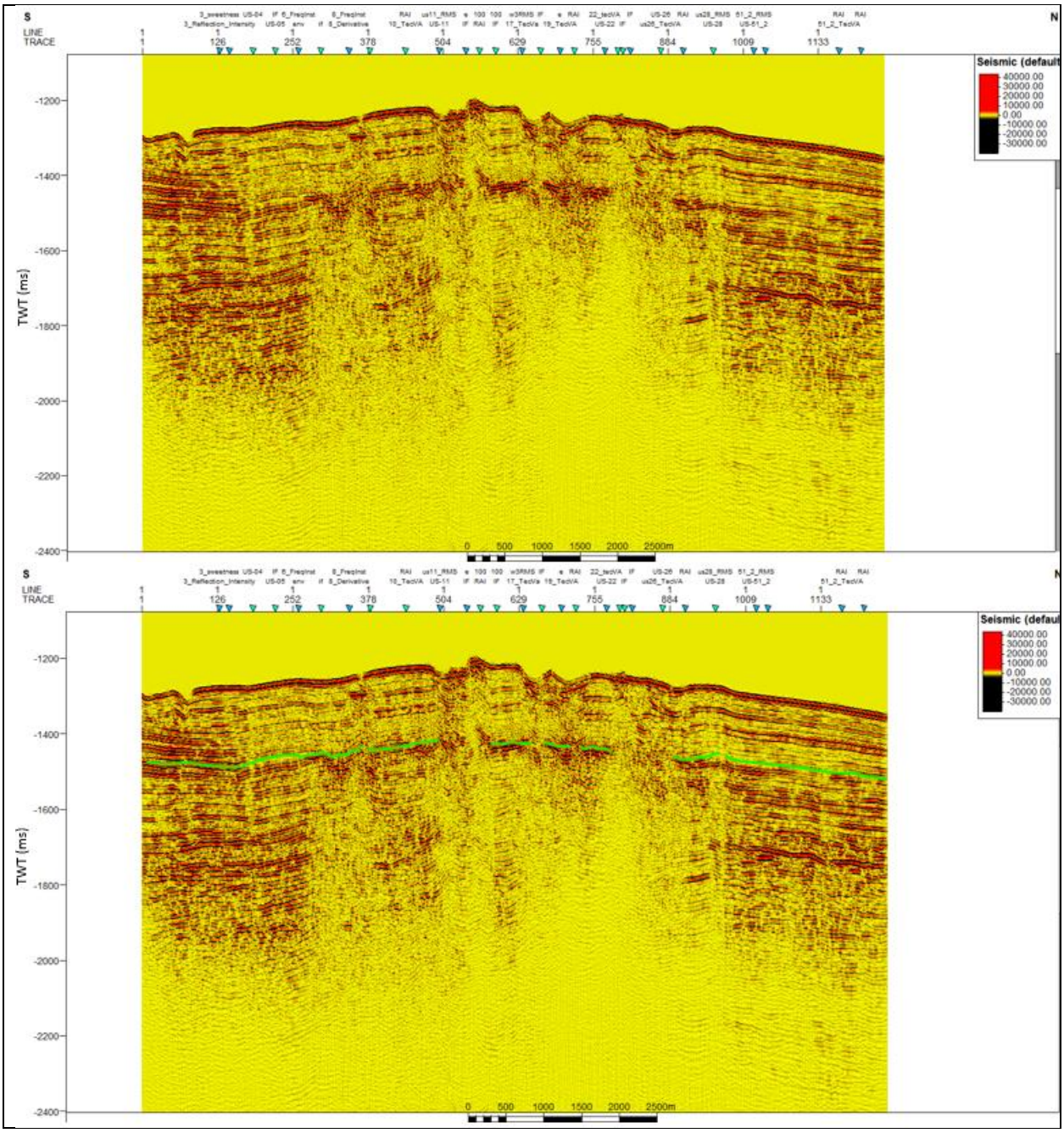

SCS profile US-51_1 with Spectral Decomposition of 100 Hz. Green line indicates BSR.

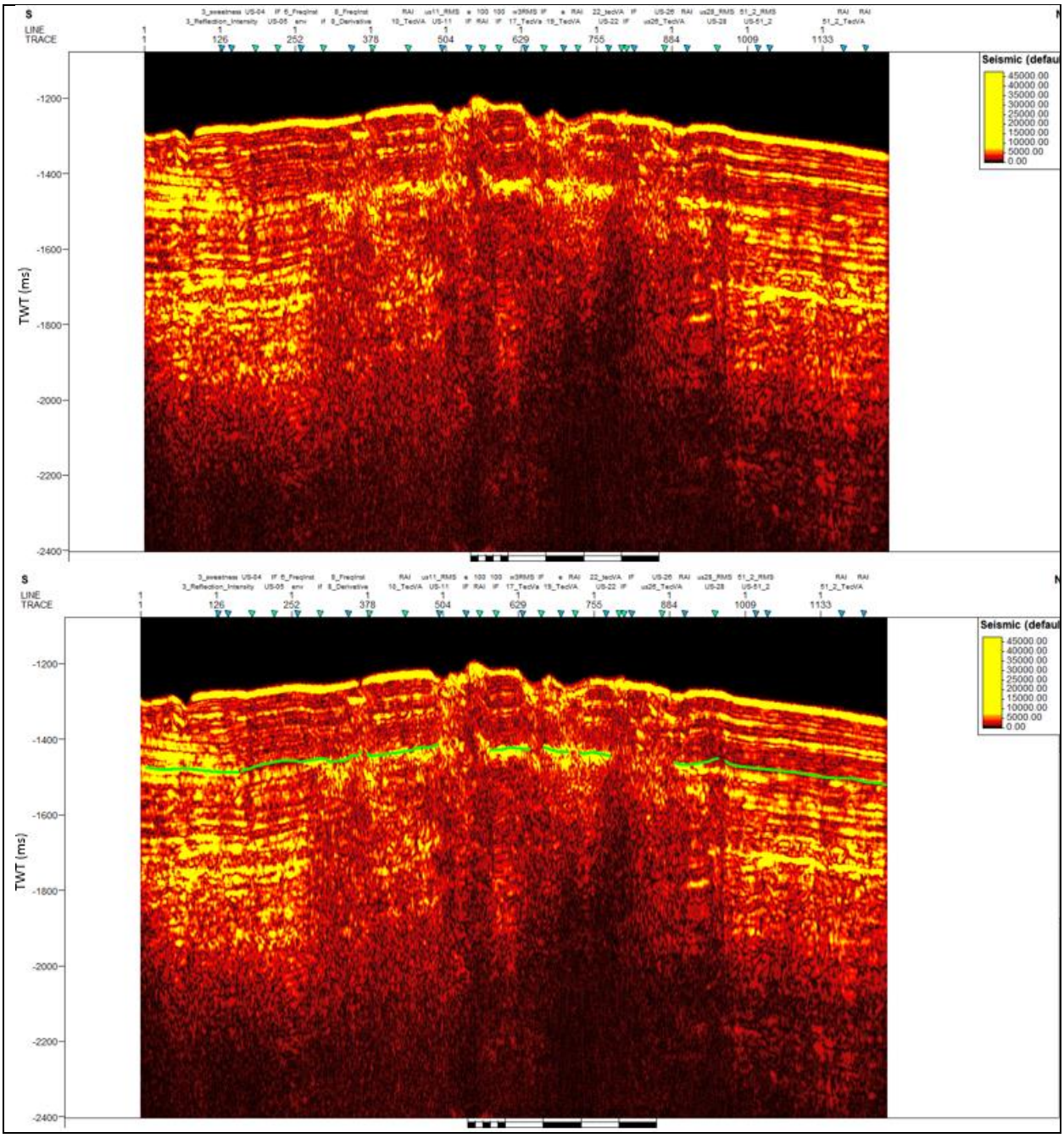

SCS profile US-51_1 with Spectral Decomposition of 100 Hz plus Envelope. Green line indicates BSR.

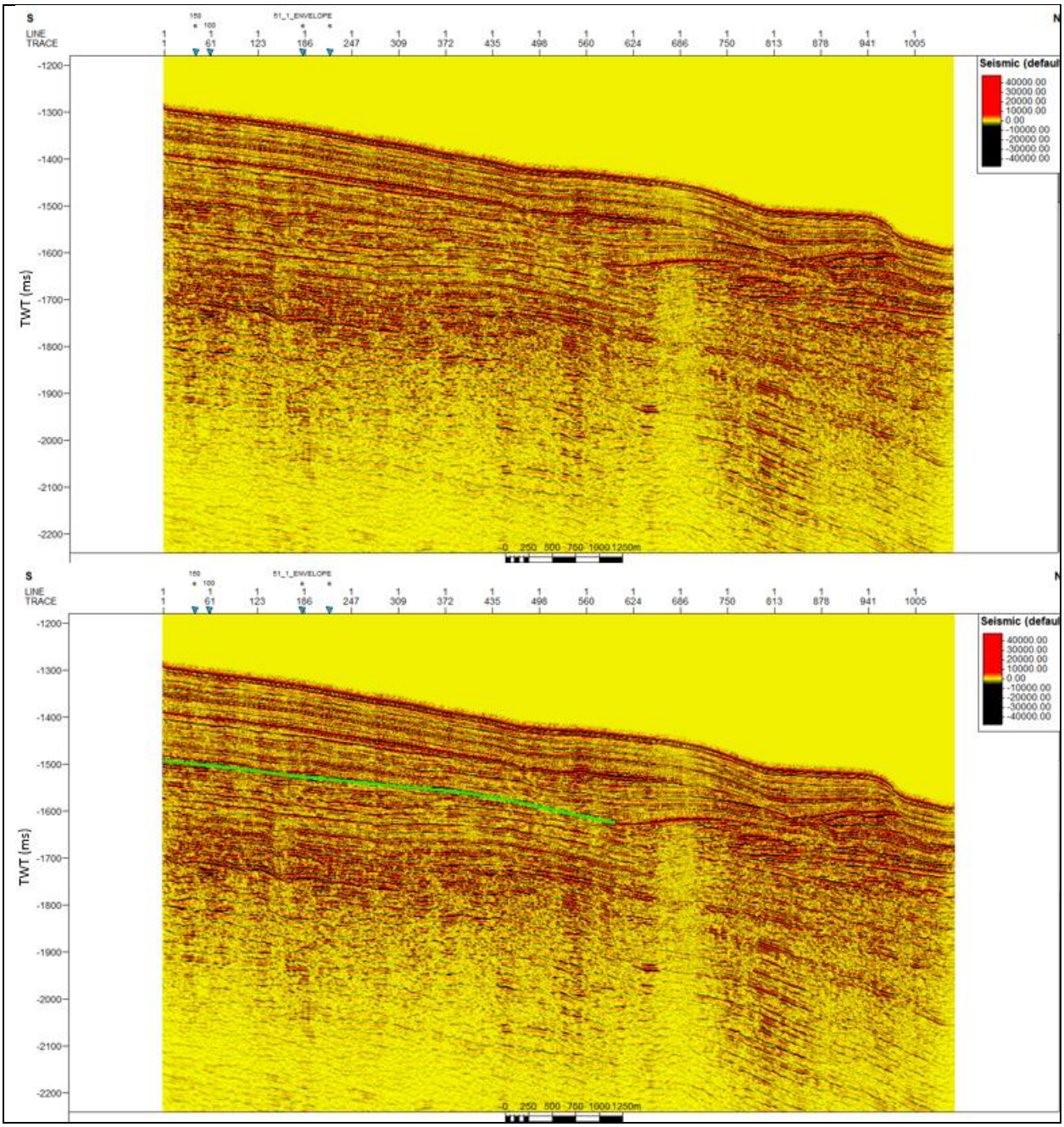

SCS profile US-51-2 without application of seismic attribute. Green line indicates BSR.

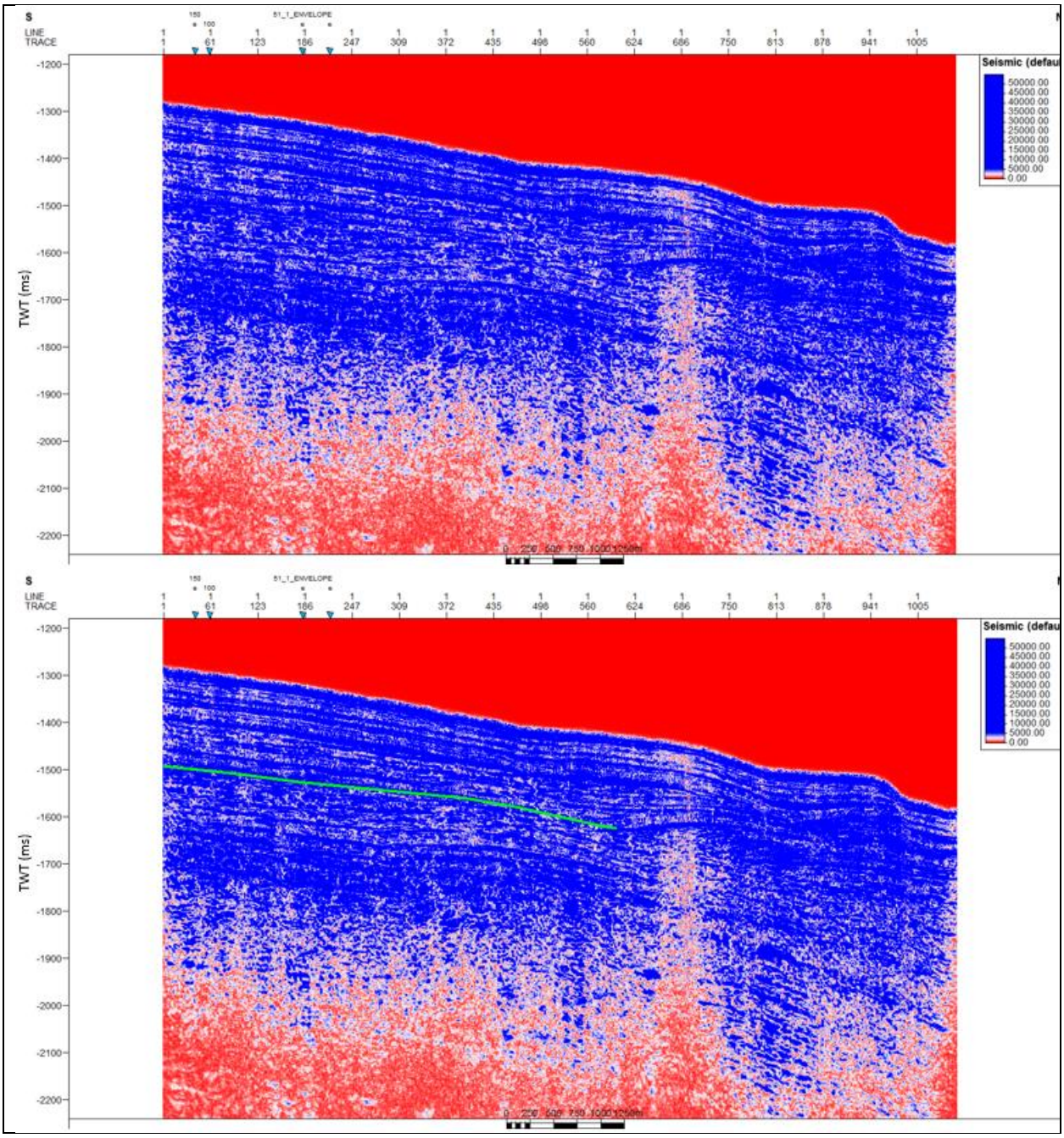

SCS profile US-51-2 with Envelope. Green line indicates BSR.

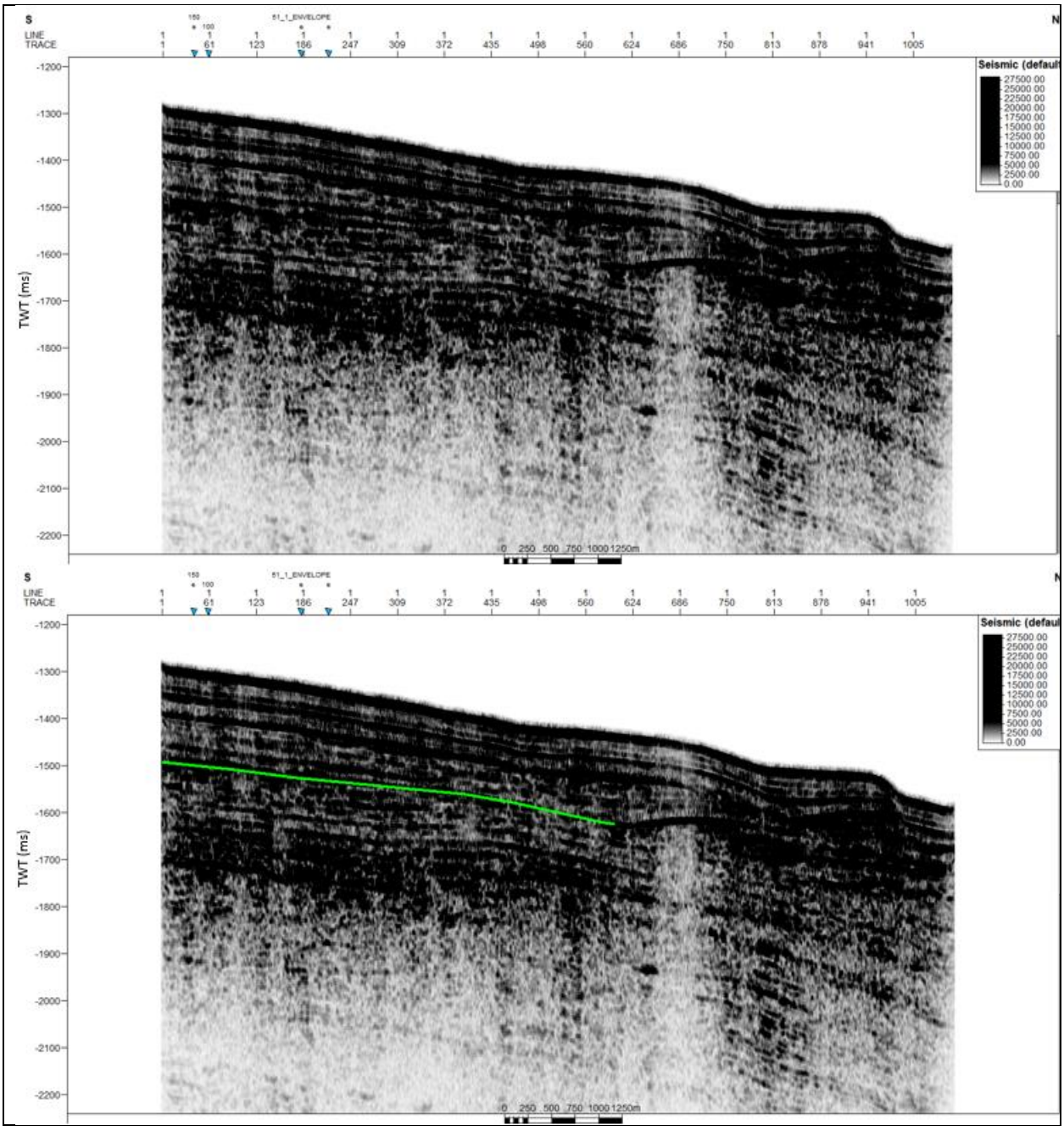

SCS profile US-51-2 with RMS Amplitude. Green line indicates BSR.

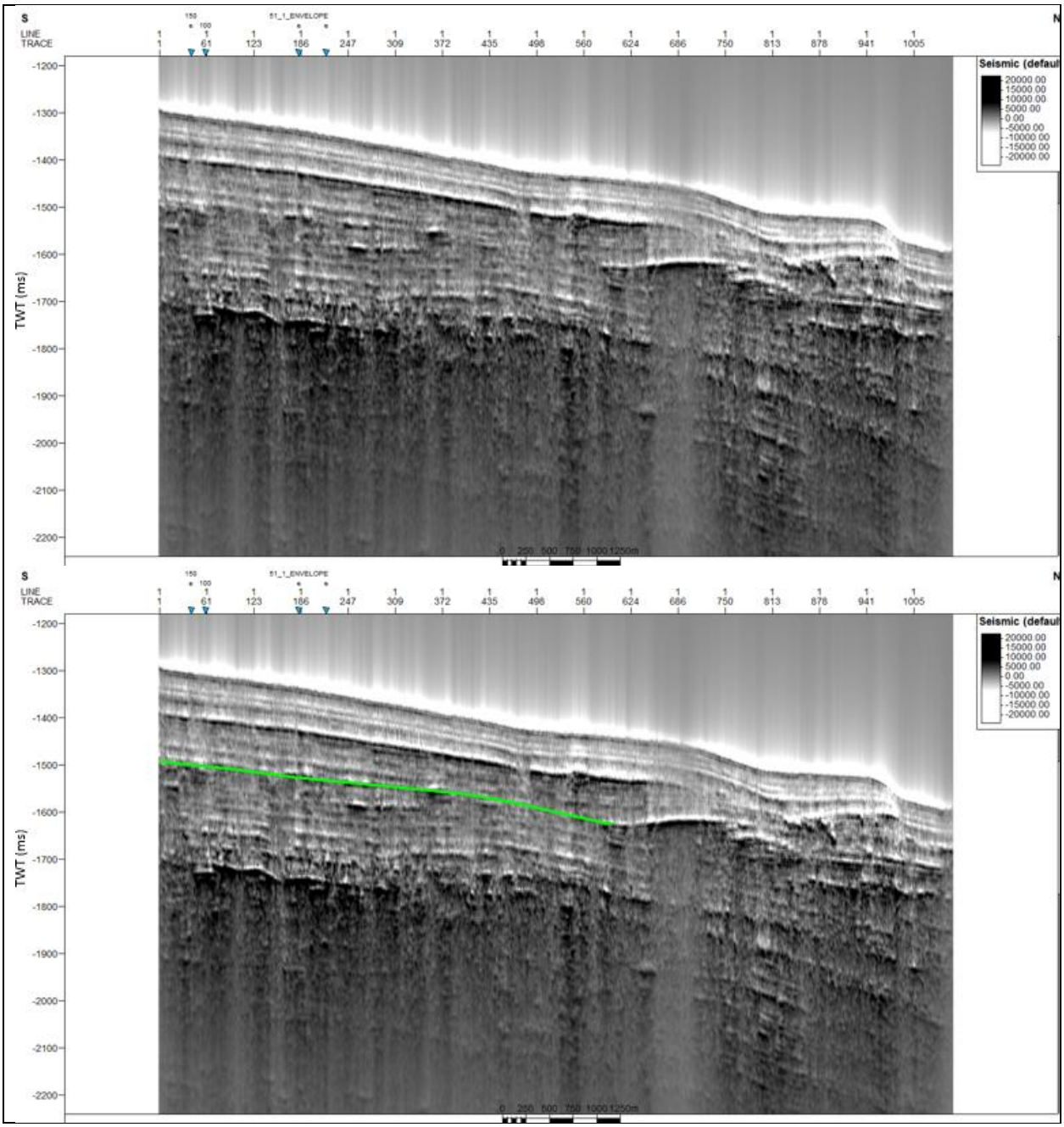

SCS profile US-51-2 with Amplitude Volume Technique. Green line indicates BSR.

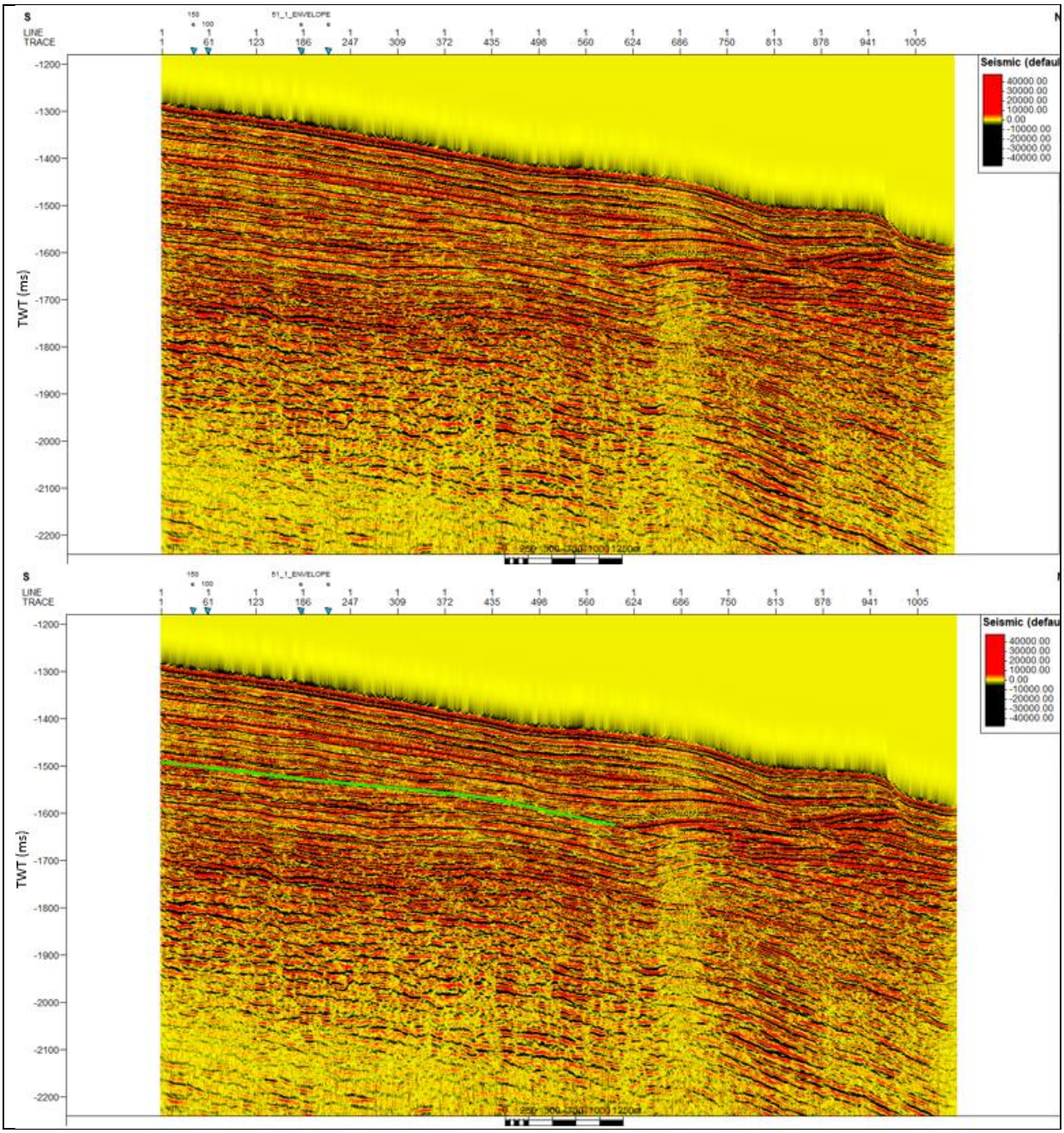

SCS profile US-51-2 with Relative Acoustic Impedance. Green line indicates BSR.

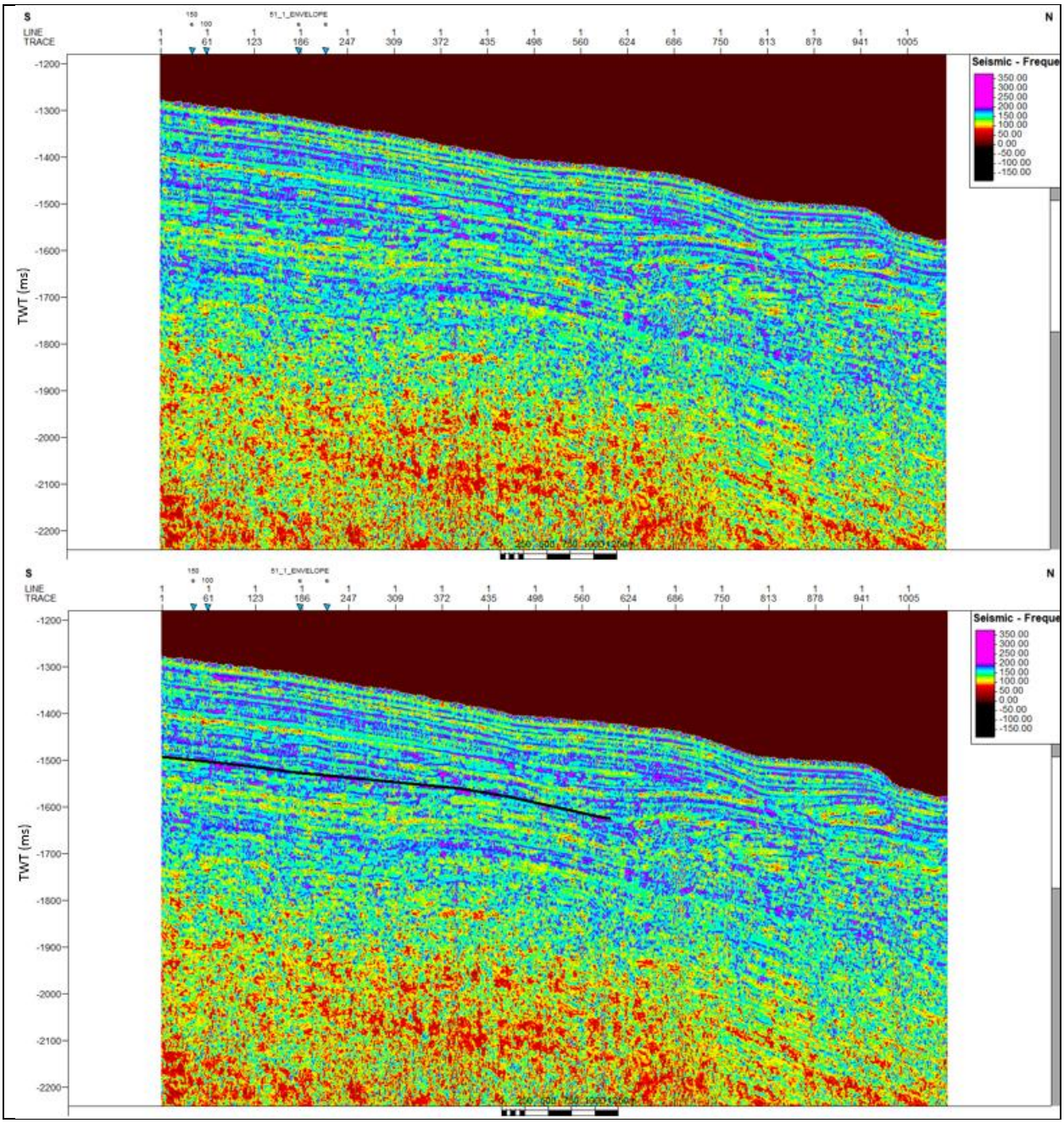

SCS profile US-51-2 with Instantaneous Frequency. Black line indicates BSR.

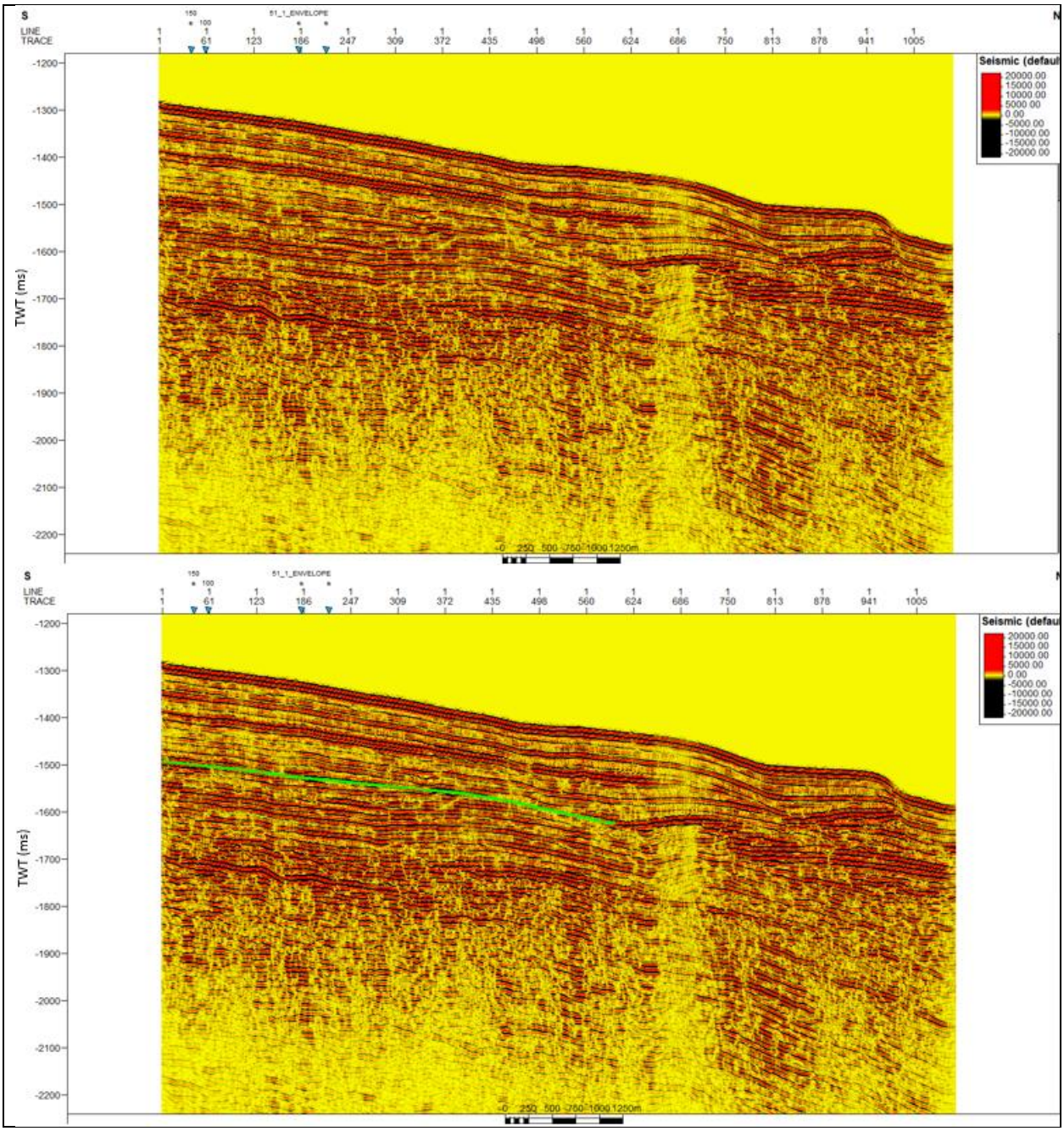

SCS profile US-51-2 with Spectral Decomposition of 100 Hz. Green line indicates BSR.

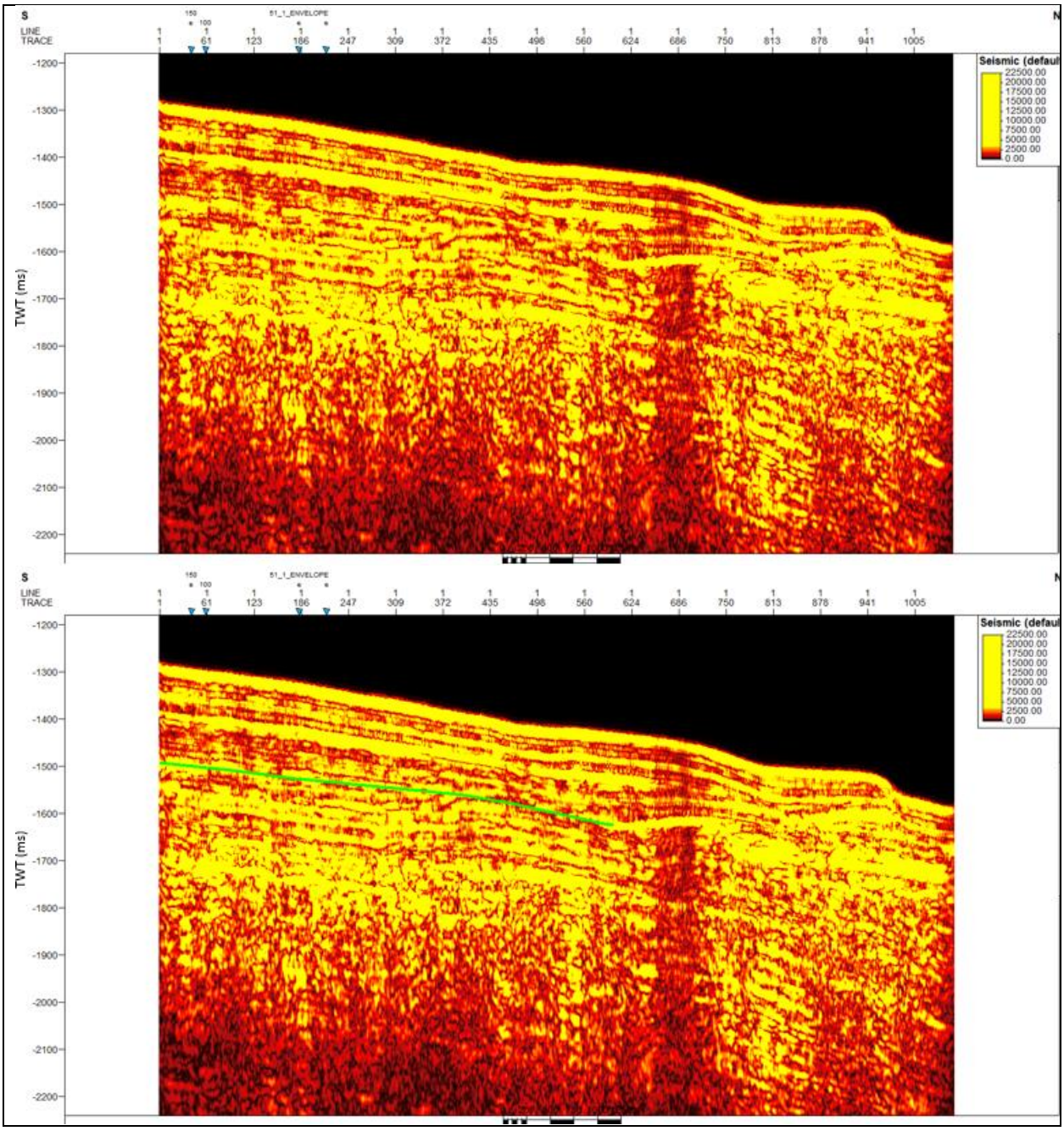

SCS profile US-51-2 with Spectral Decomposition of 100 Hz plus Envelope. Green line indicates BSR.

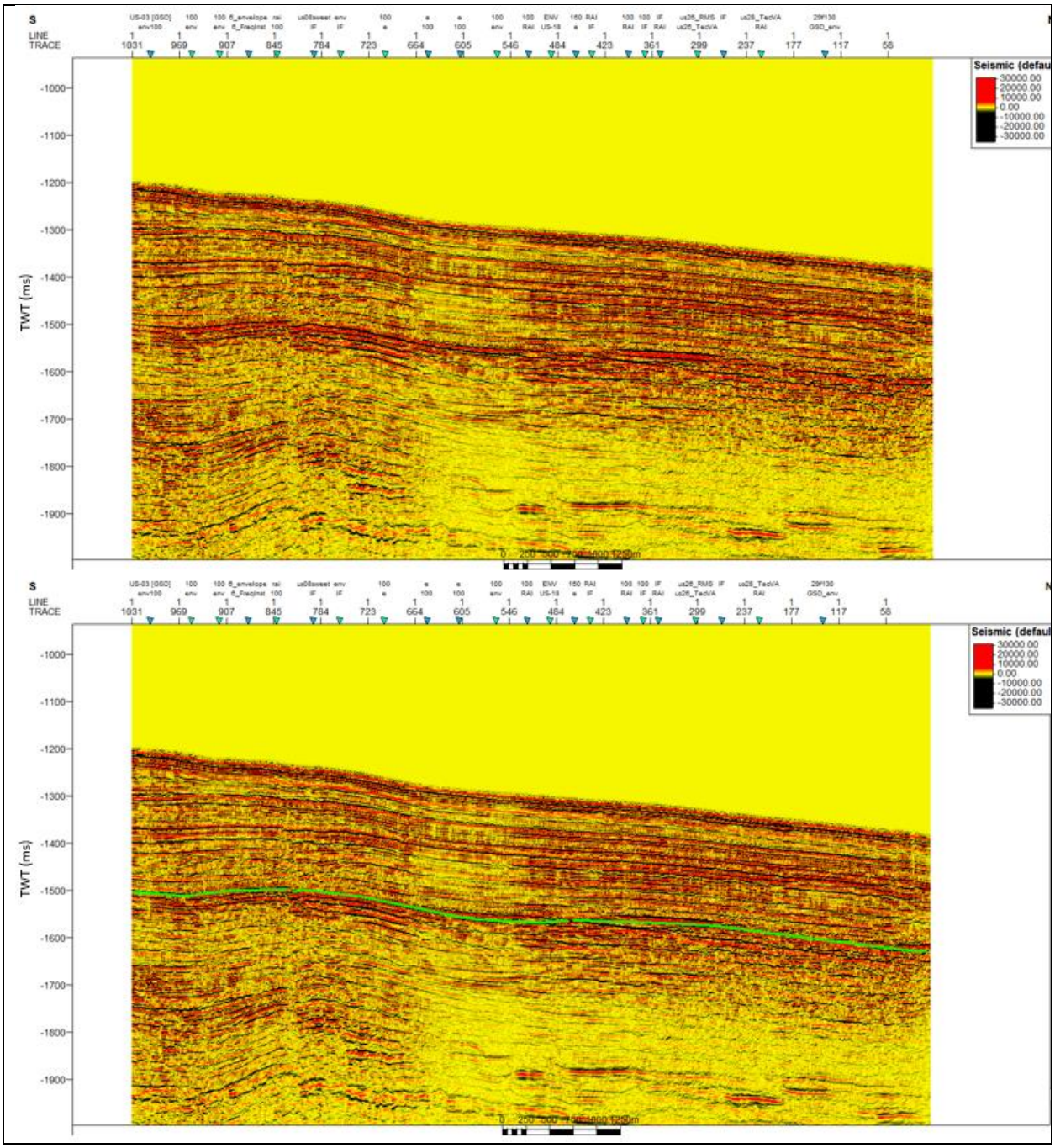

SCS profile US-53 without application of seismic attribute. Green line indicates BSR.

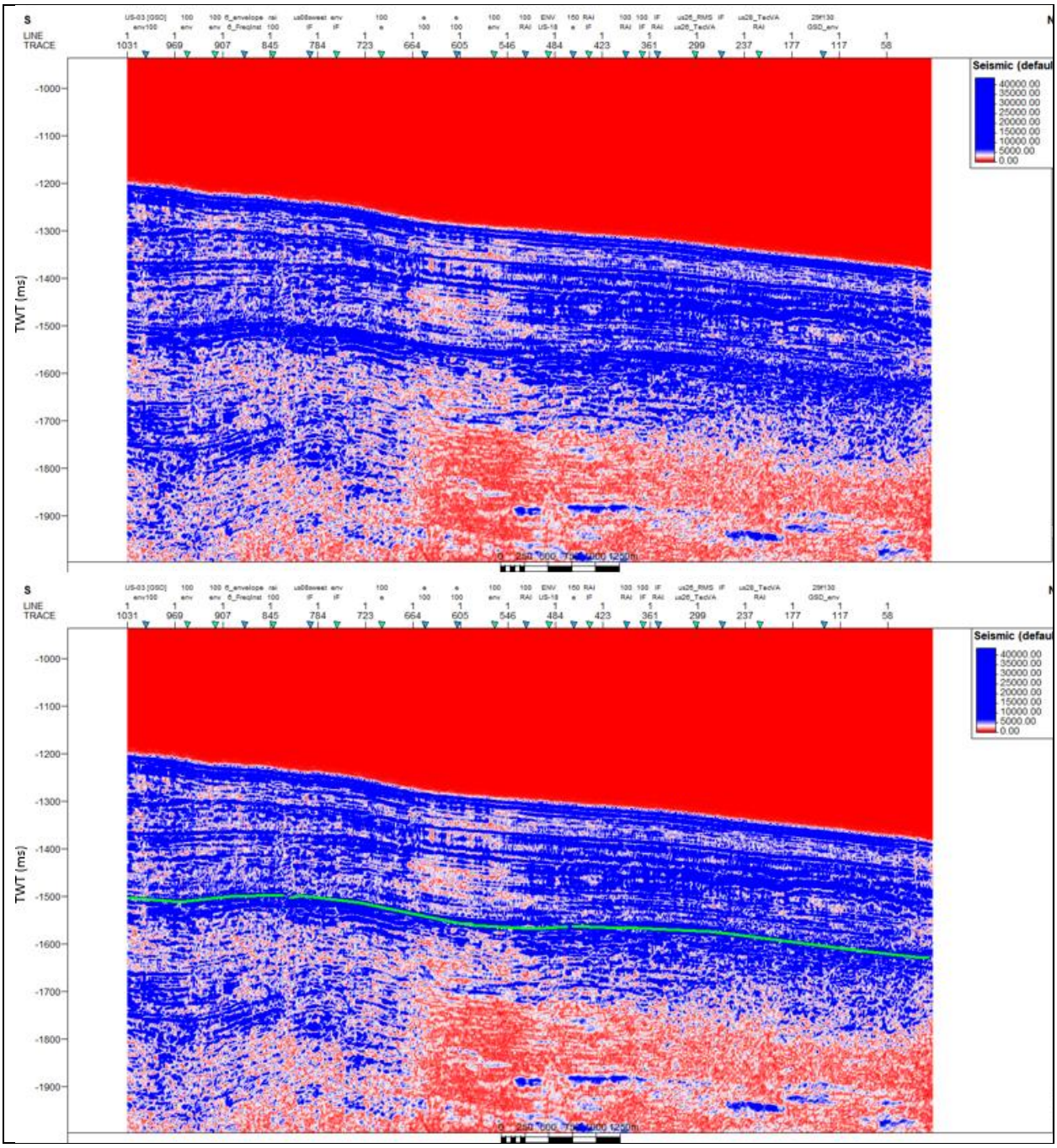

SCS profile US-53 with Envelope. Green line indicates BSR.

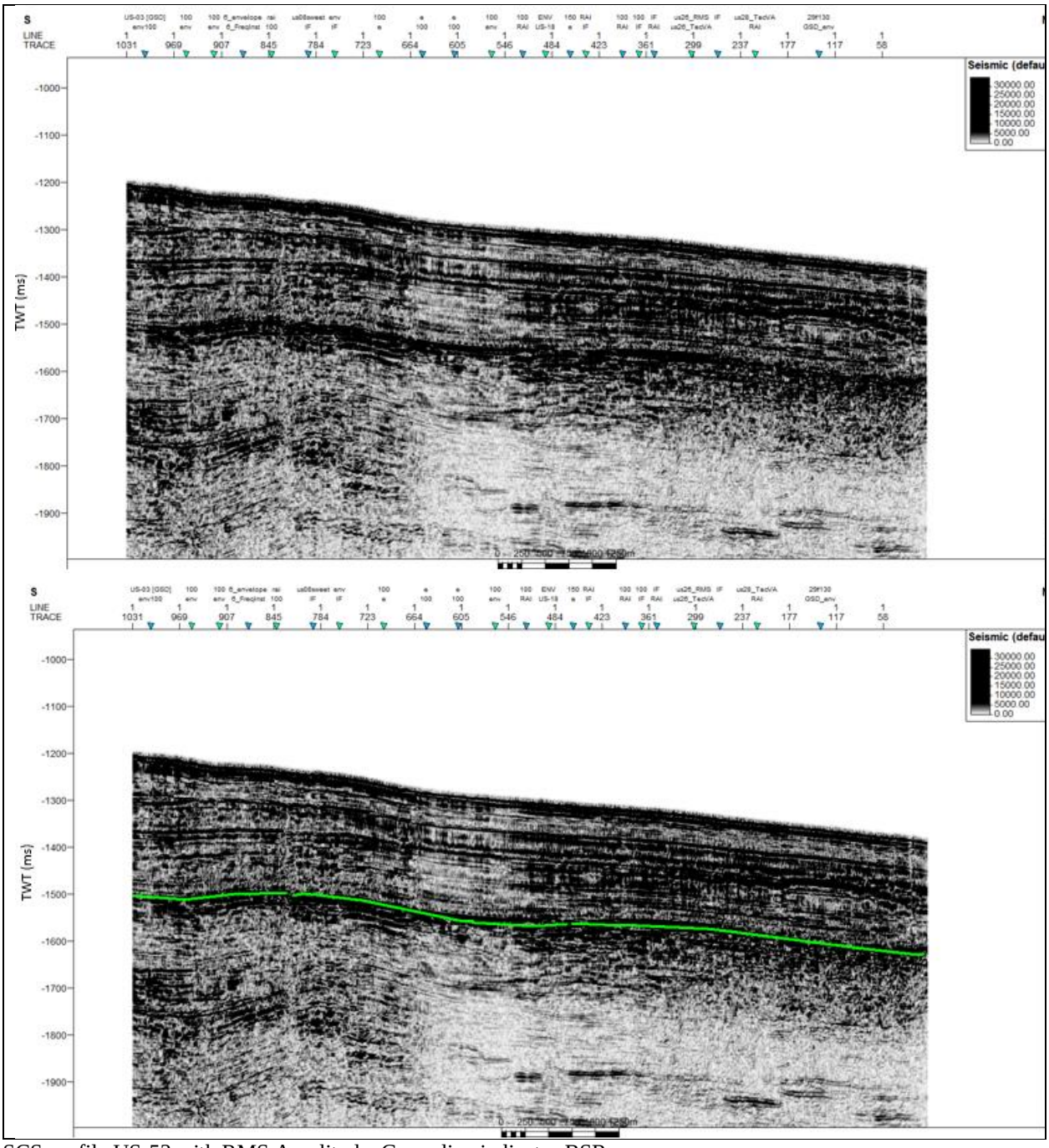

SCS profile US-53 with RMS Amplitude. Green line indicates BSR.

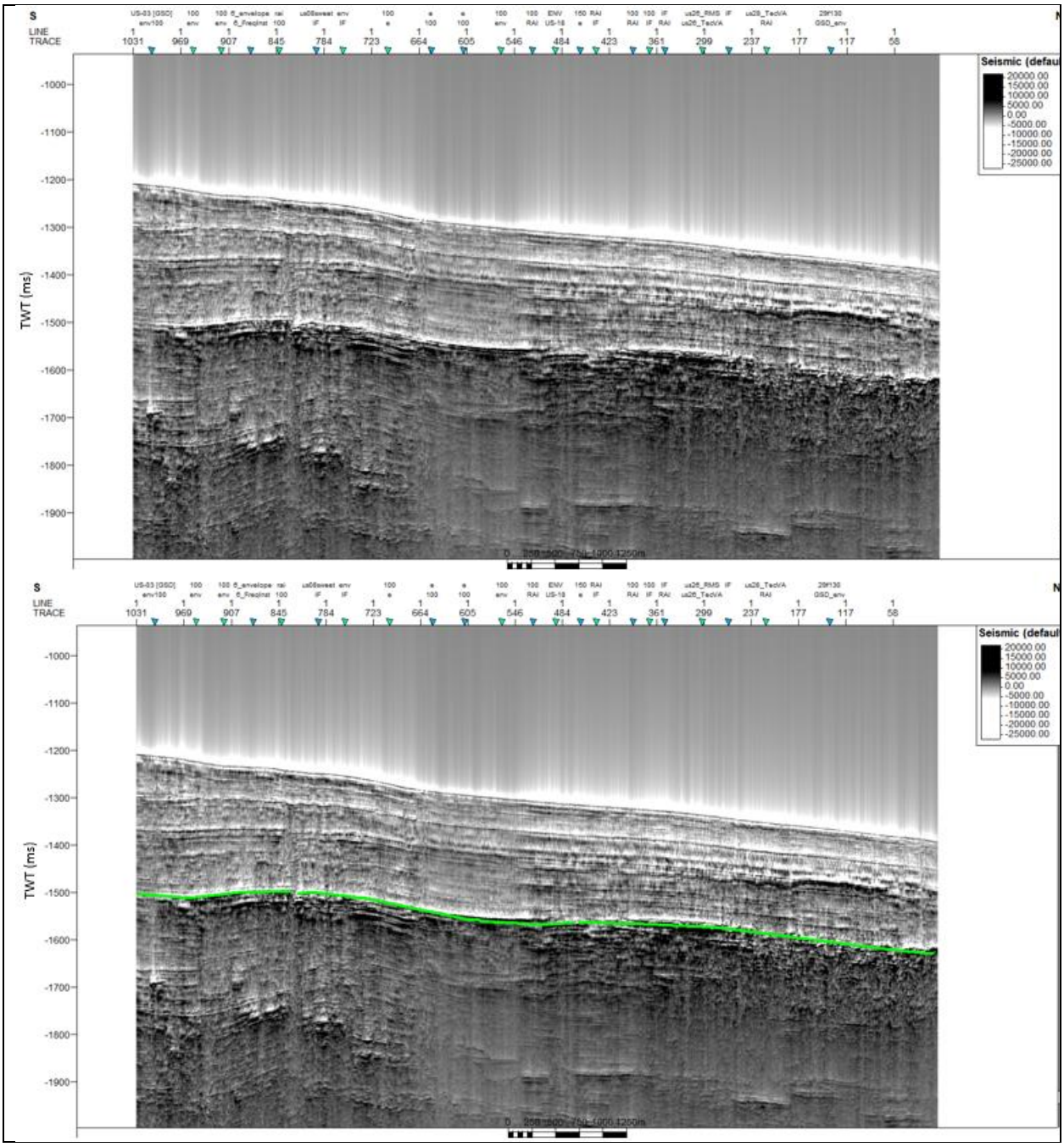

SCS profile US-53 with Amplitude Volume Technique. Green line indicates BSR.

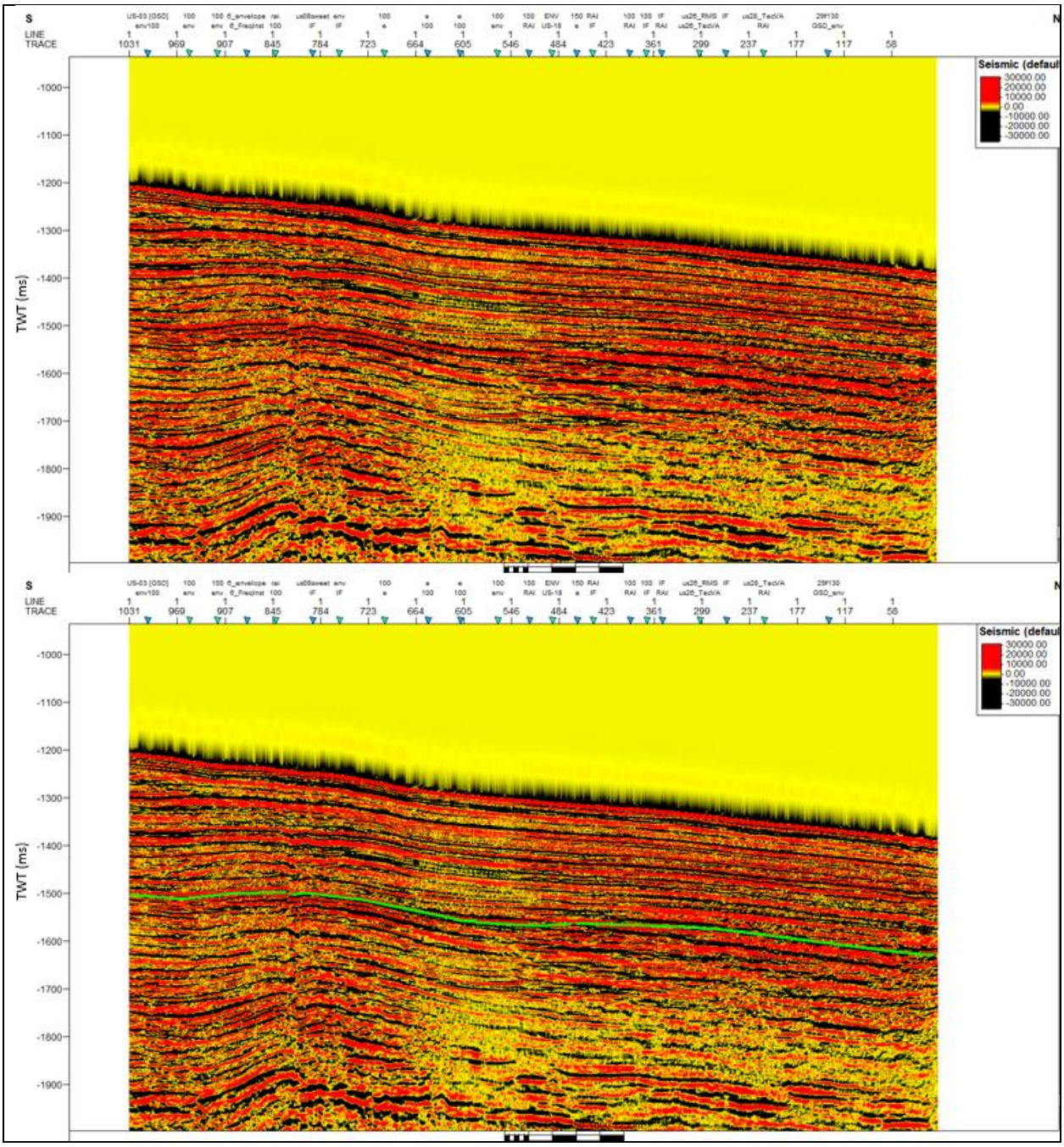

SCS profile US-53 with Relative Acoustic Impedance. Green line indicates BSR.

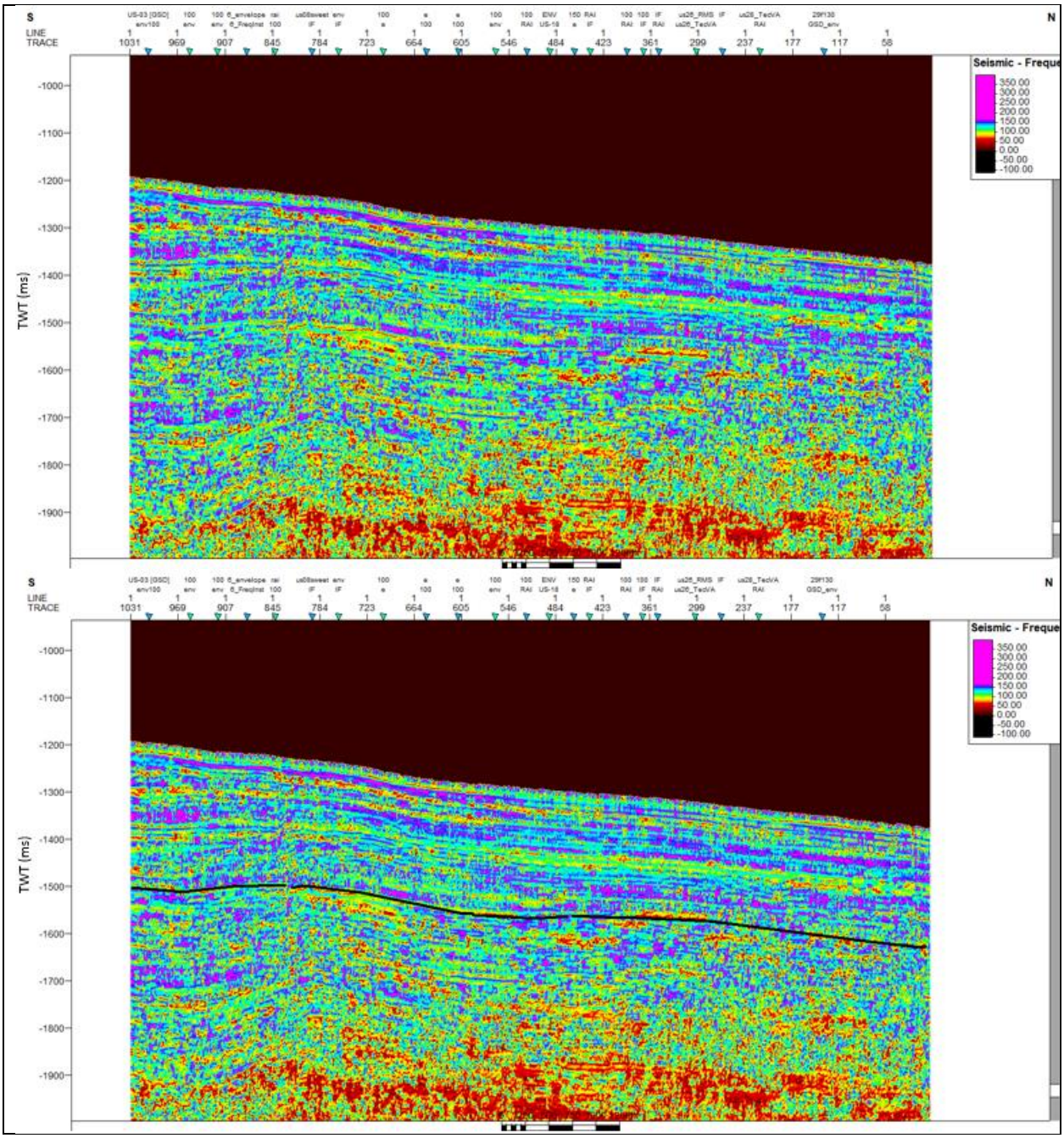

SCS profile US-53 with Instantaneous Frequency. Black line indicates BSR.

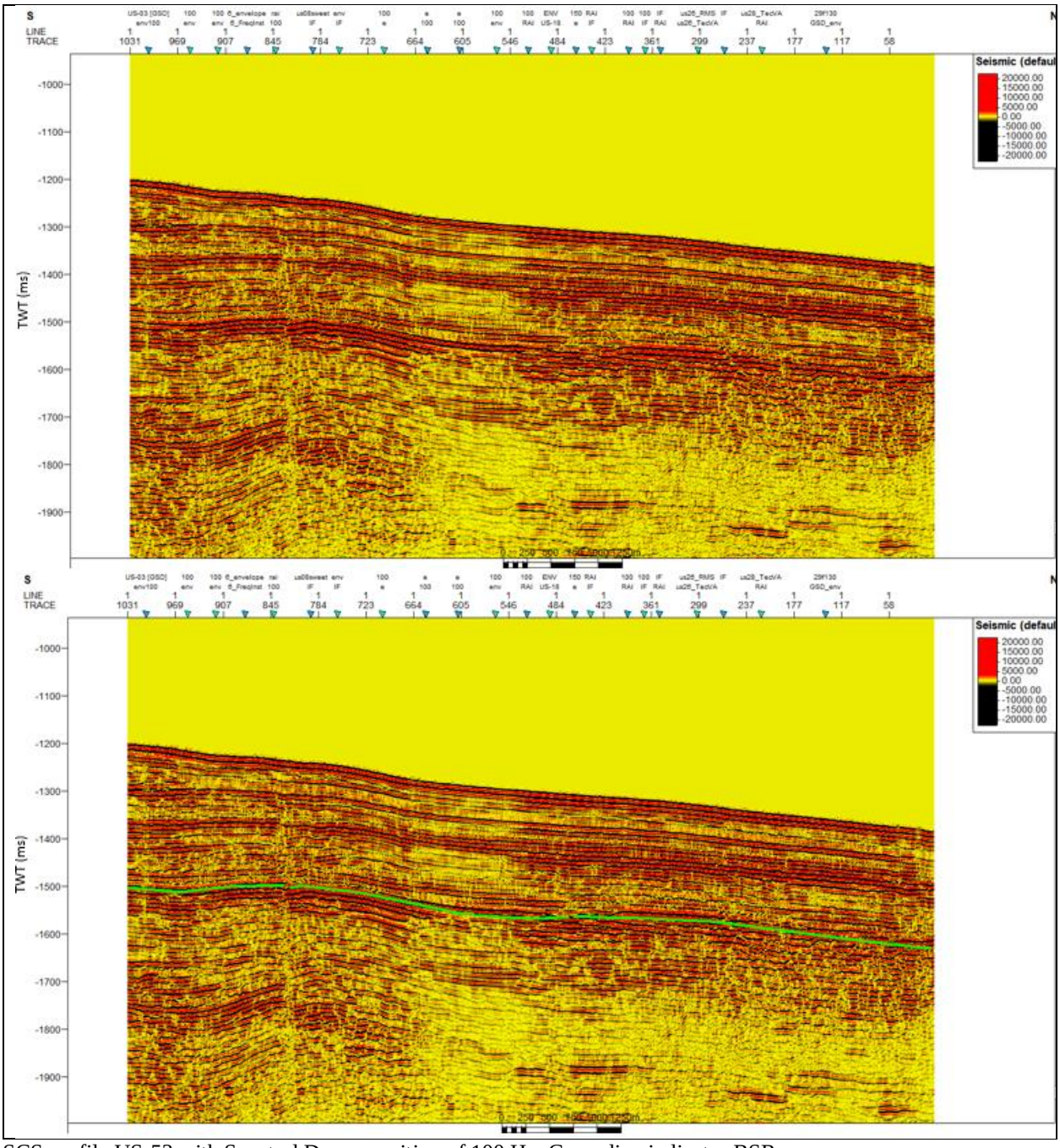

SCS profile US-53 with Spectral Decomposition of 100 Hz. Green line indicates BSR.

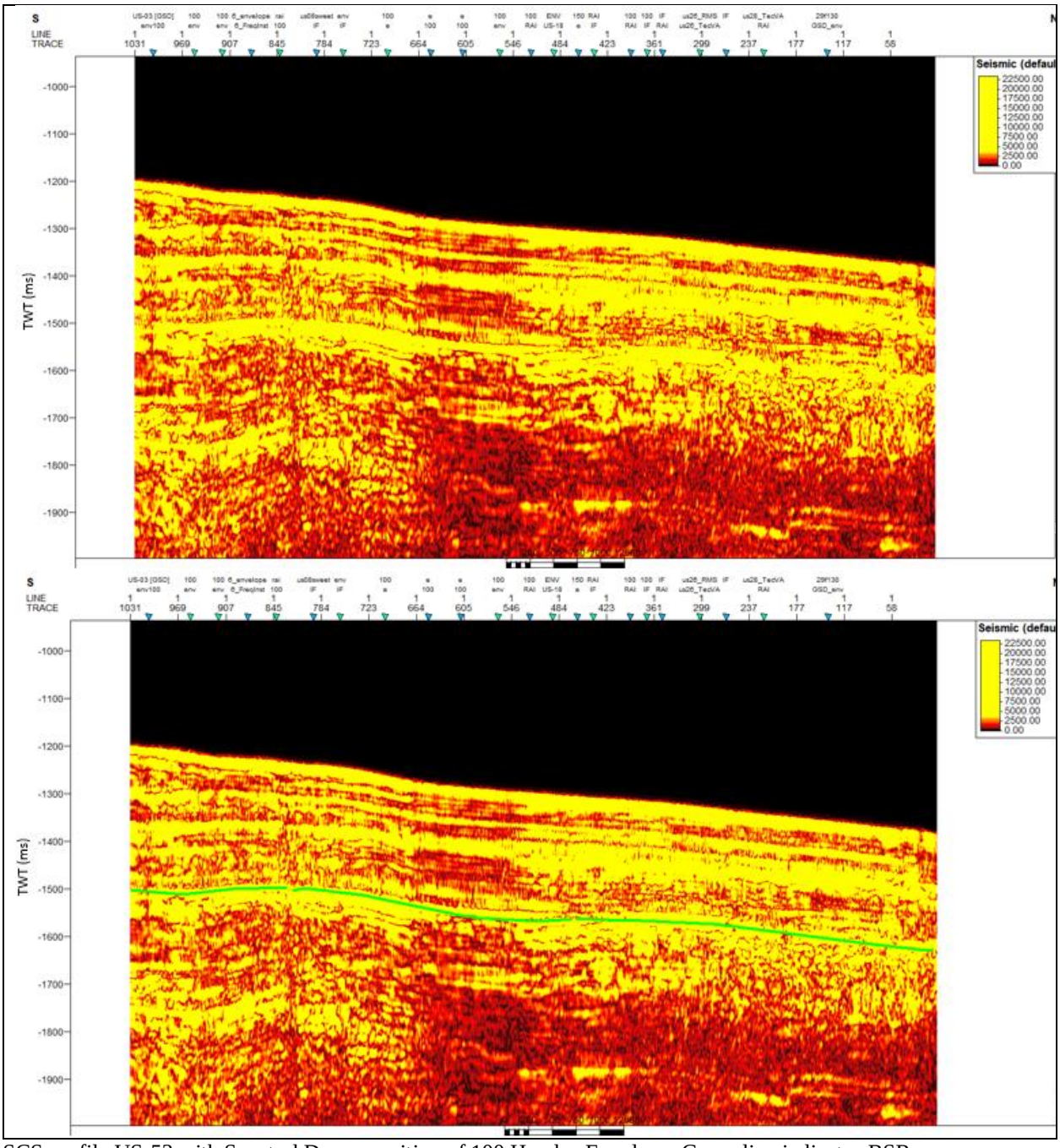

SCS profile US-53 with Spectral Decomposition of 100 Hz plus Envelope. Green line indicates BSR.

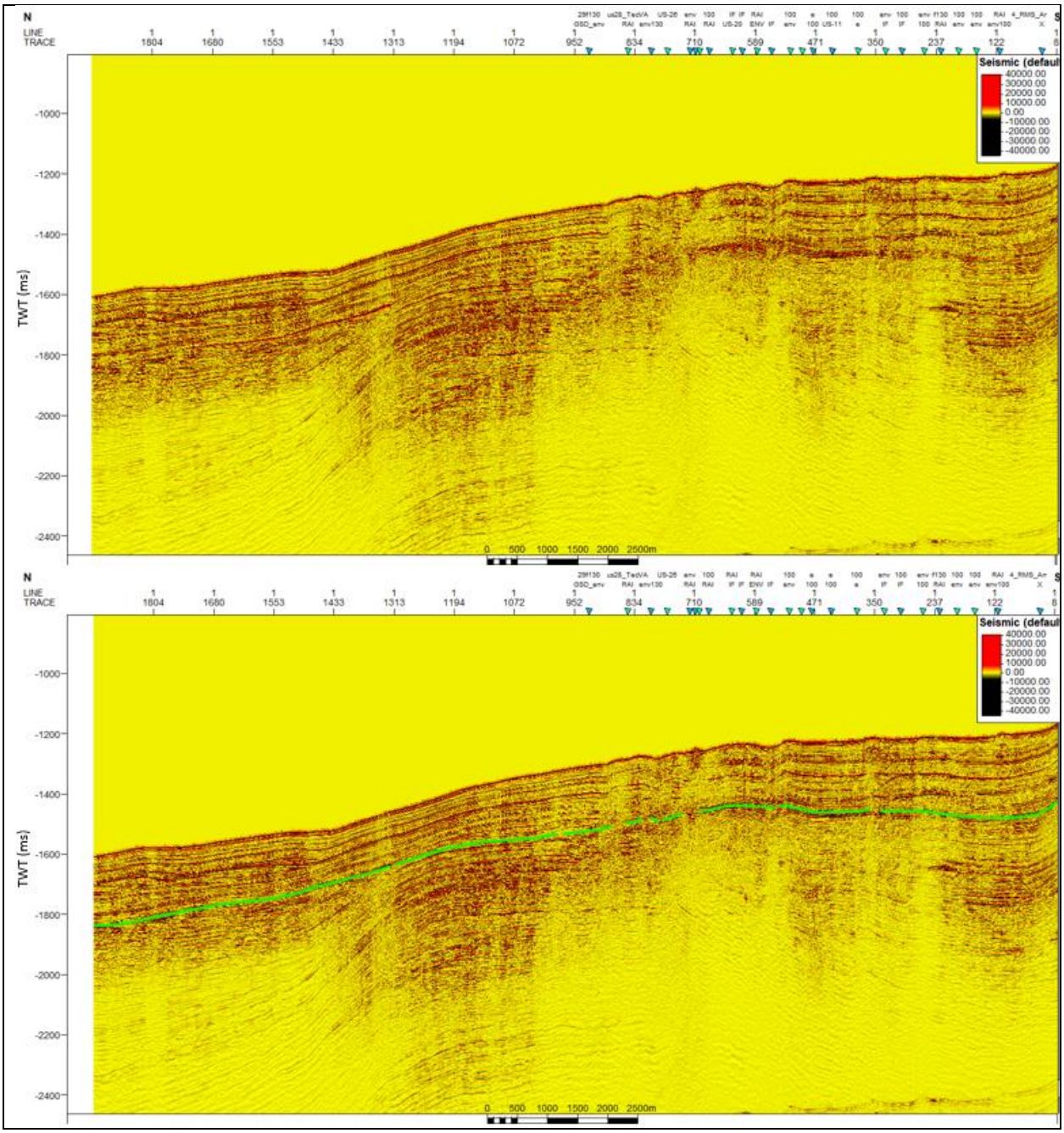

SCS profile US-54 without application of seismic attributes. Green line indicates BSR.

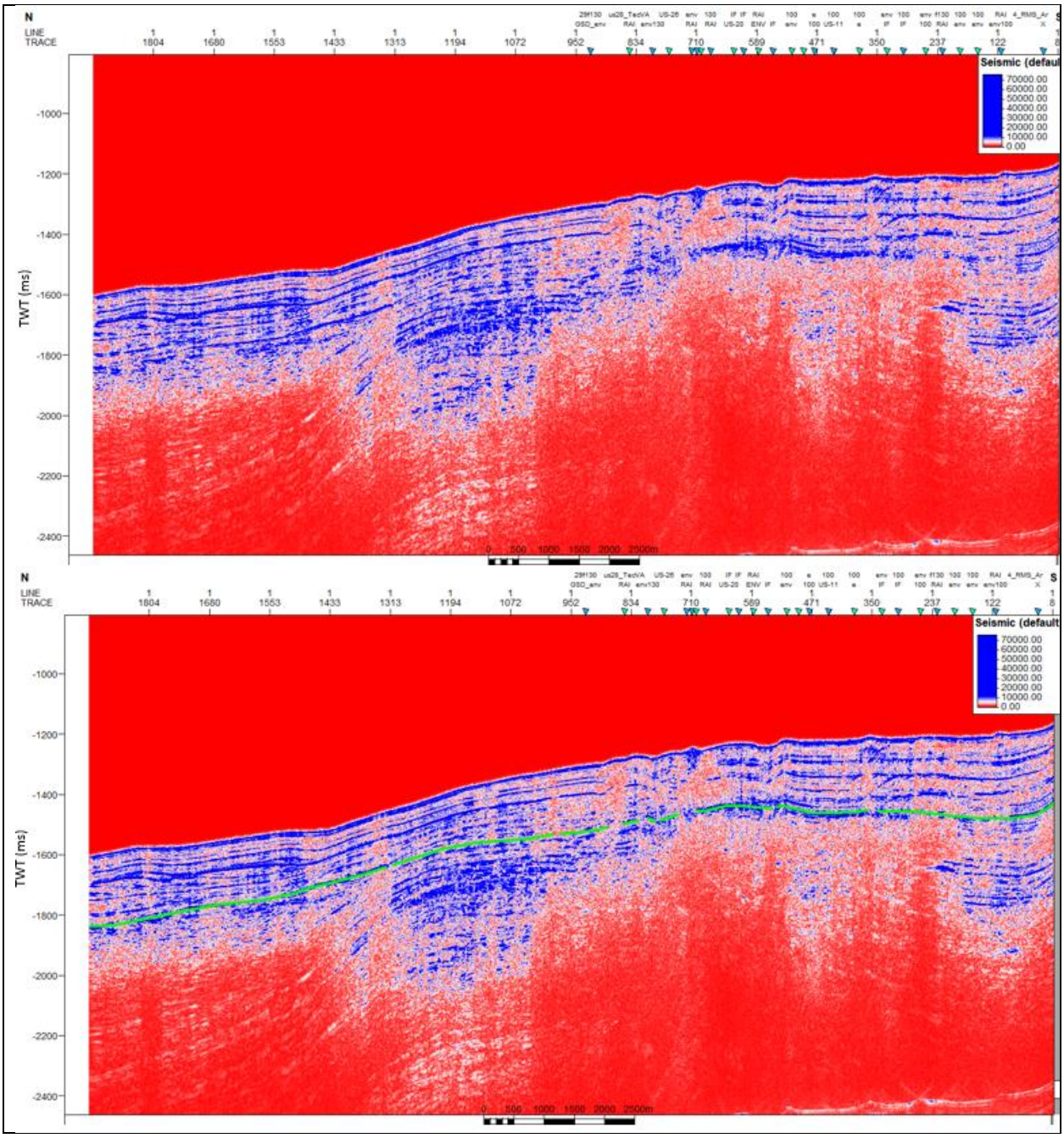

SCS profile US-54 with Envelope. Green line indicates BSR.

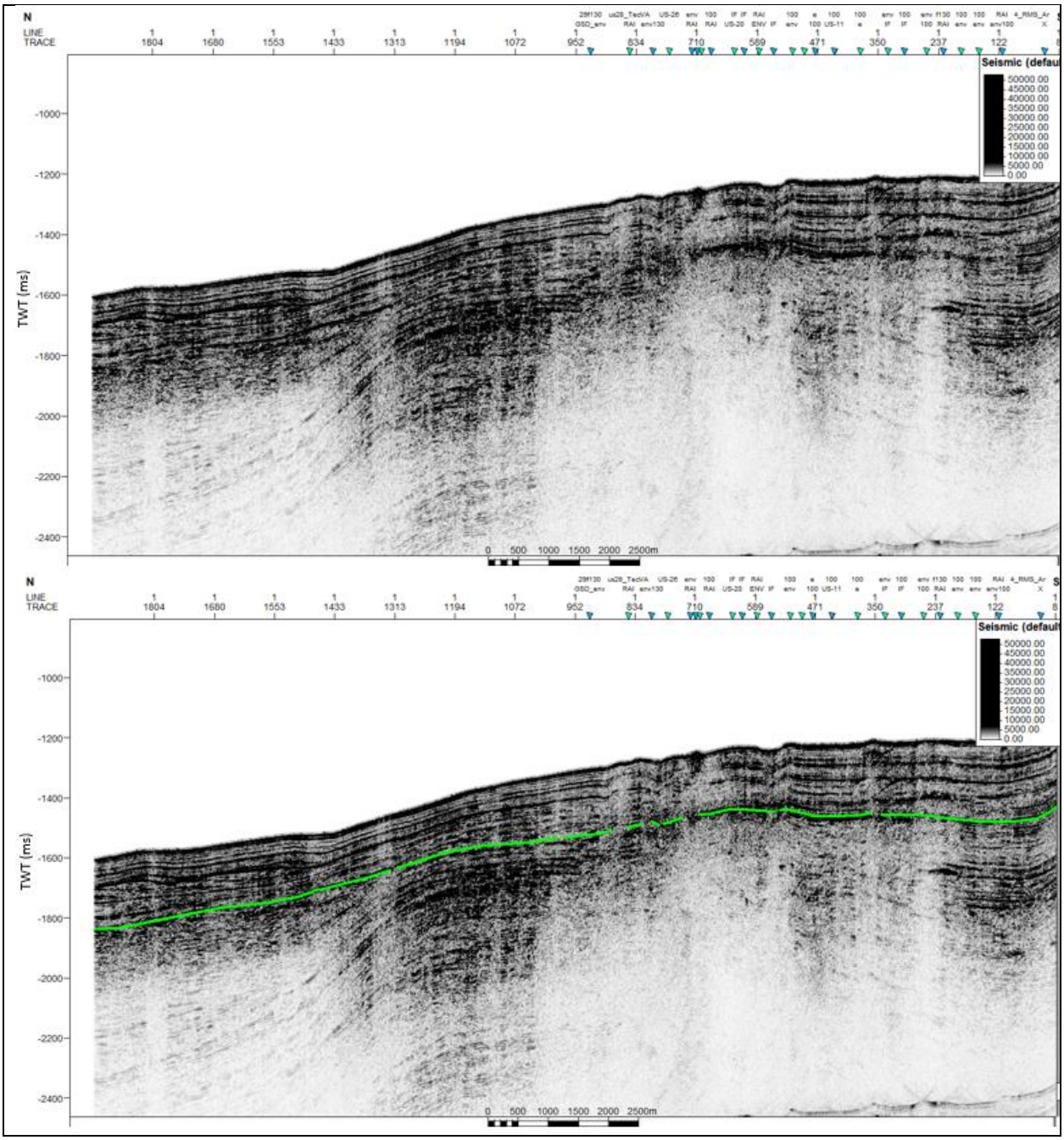

SCS profile US-54 with RMS Amplitude. Green line indicates BSR.

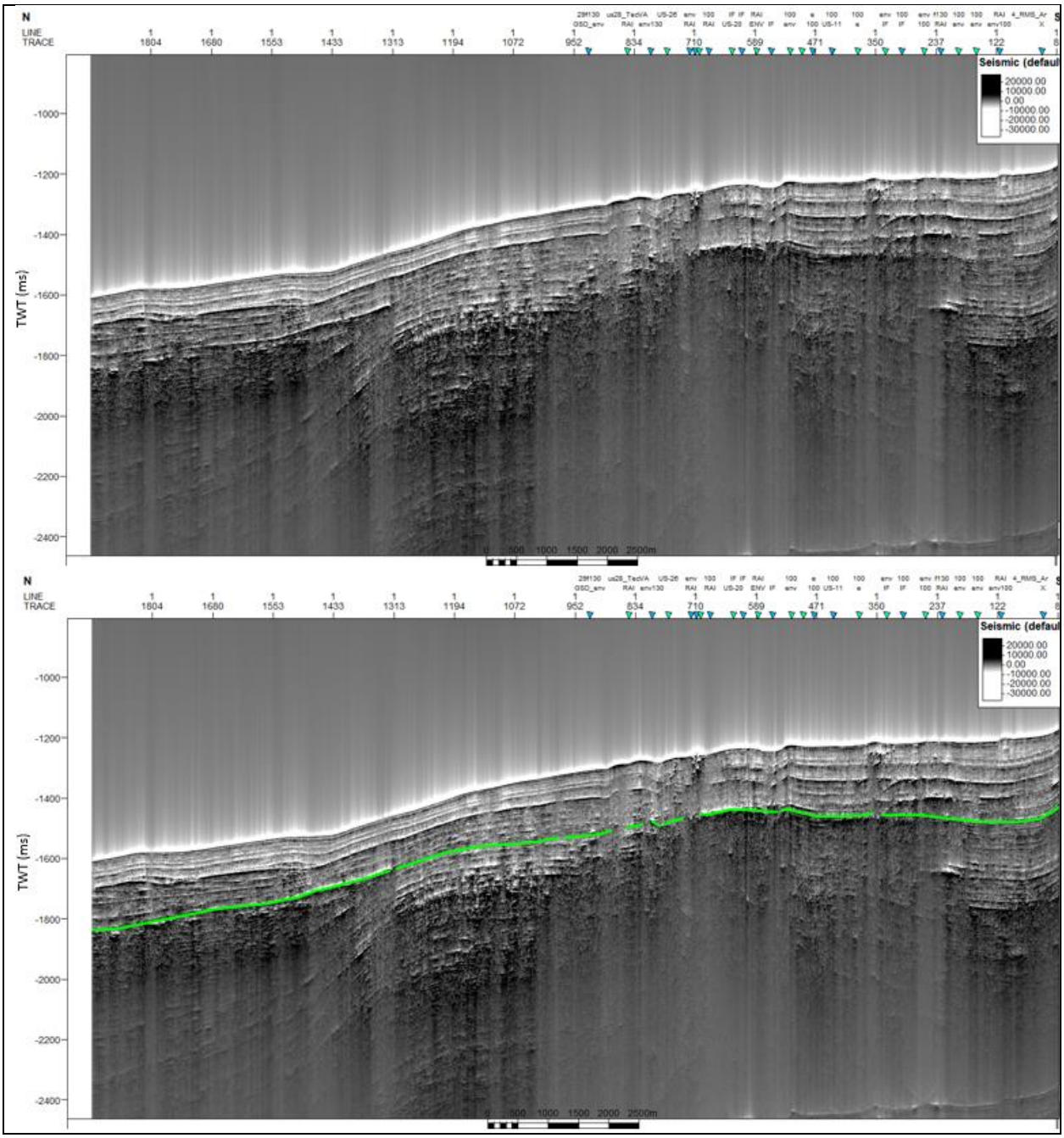

SCS profile US-54 with Amplitude Volume Technique. Green line indicates BSR.

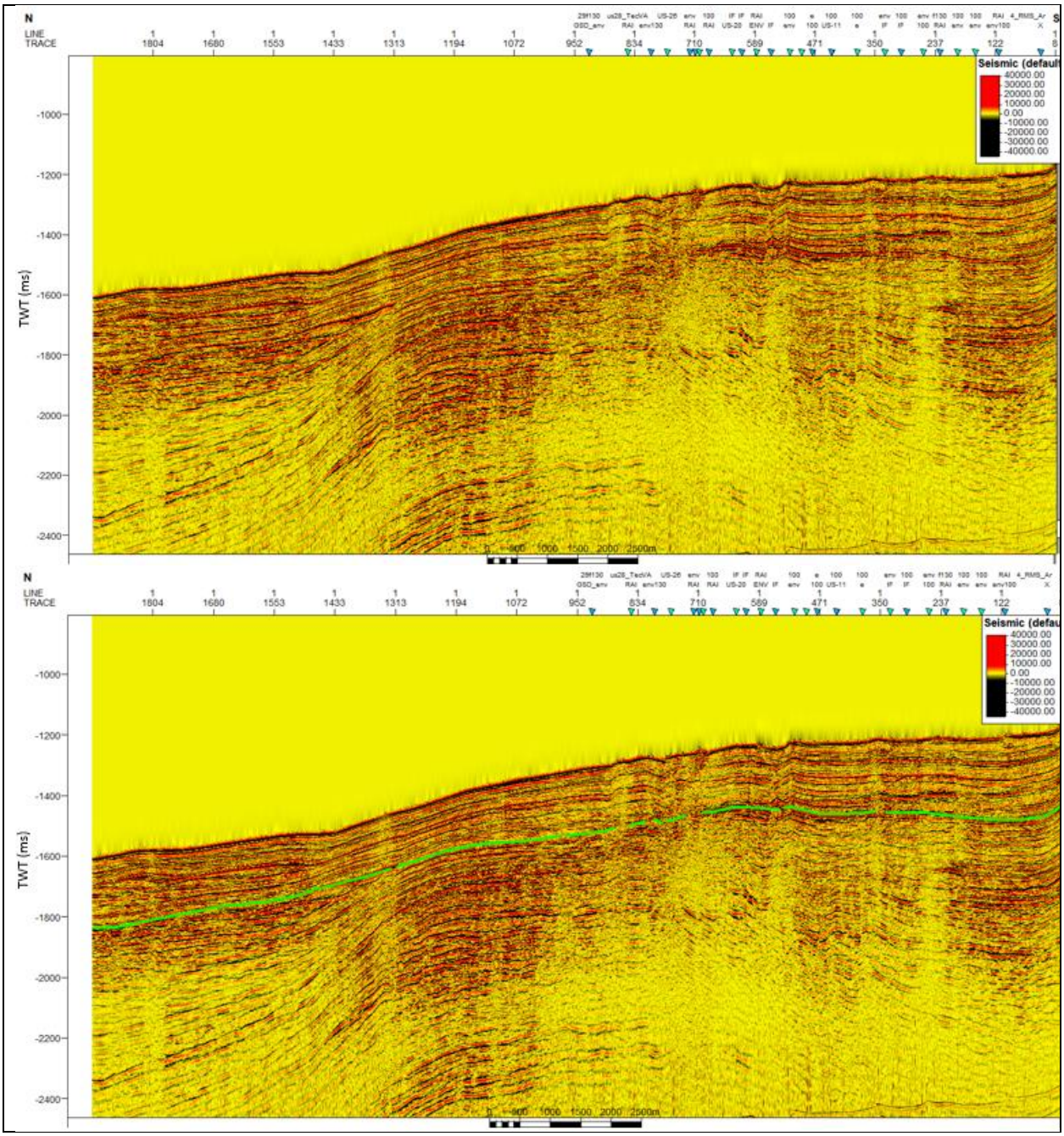

SCS profile US-54 with Relative Acoustic Impedance. Green line indicates BSR.

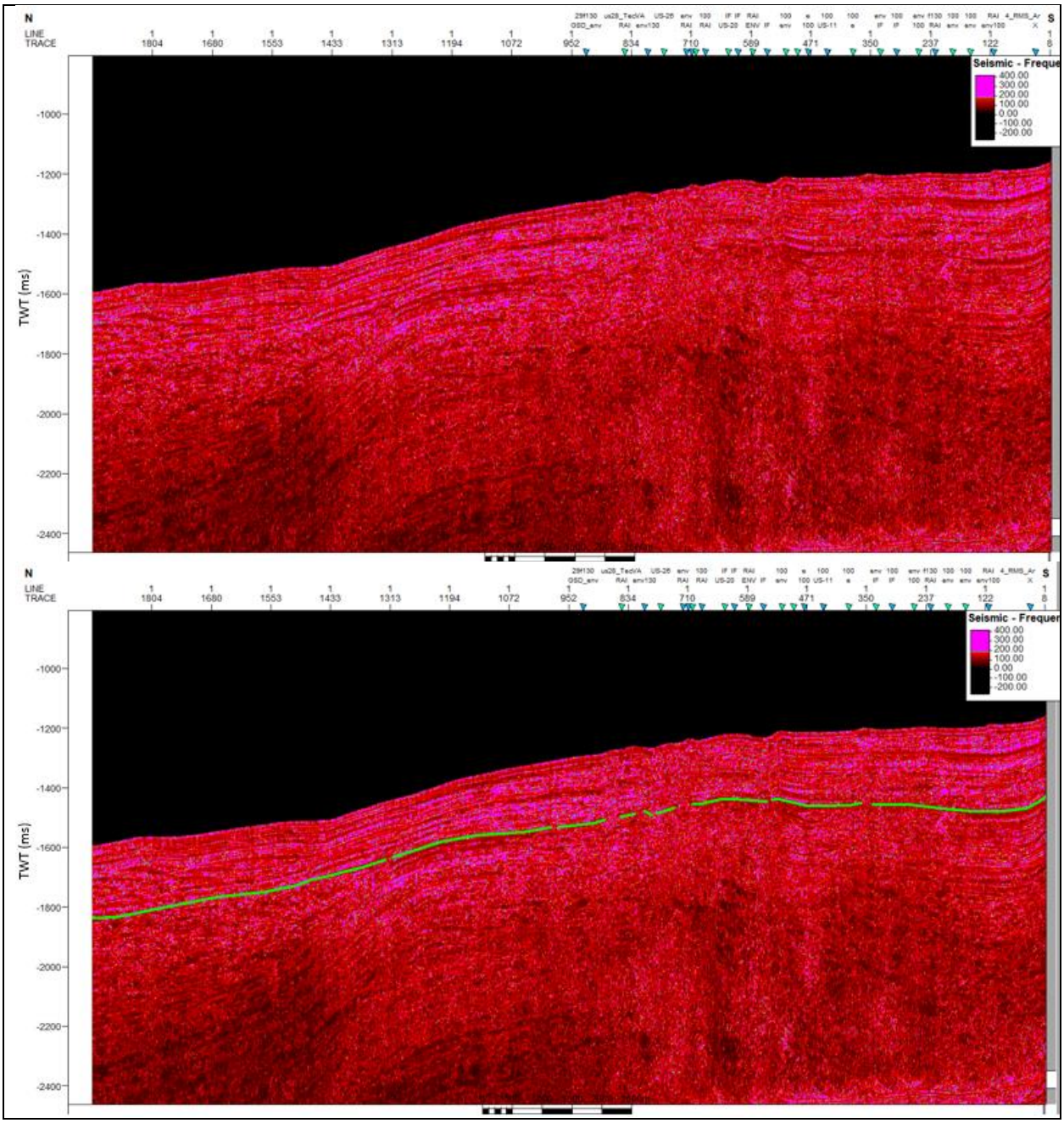

SCS profile US-54 with Instantaneous Frequency. Green line indicates BSR.

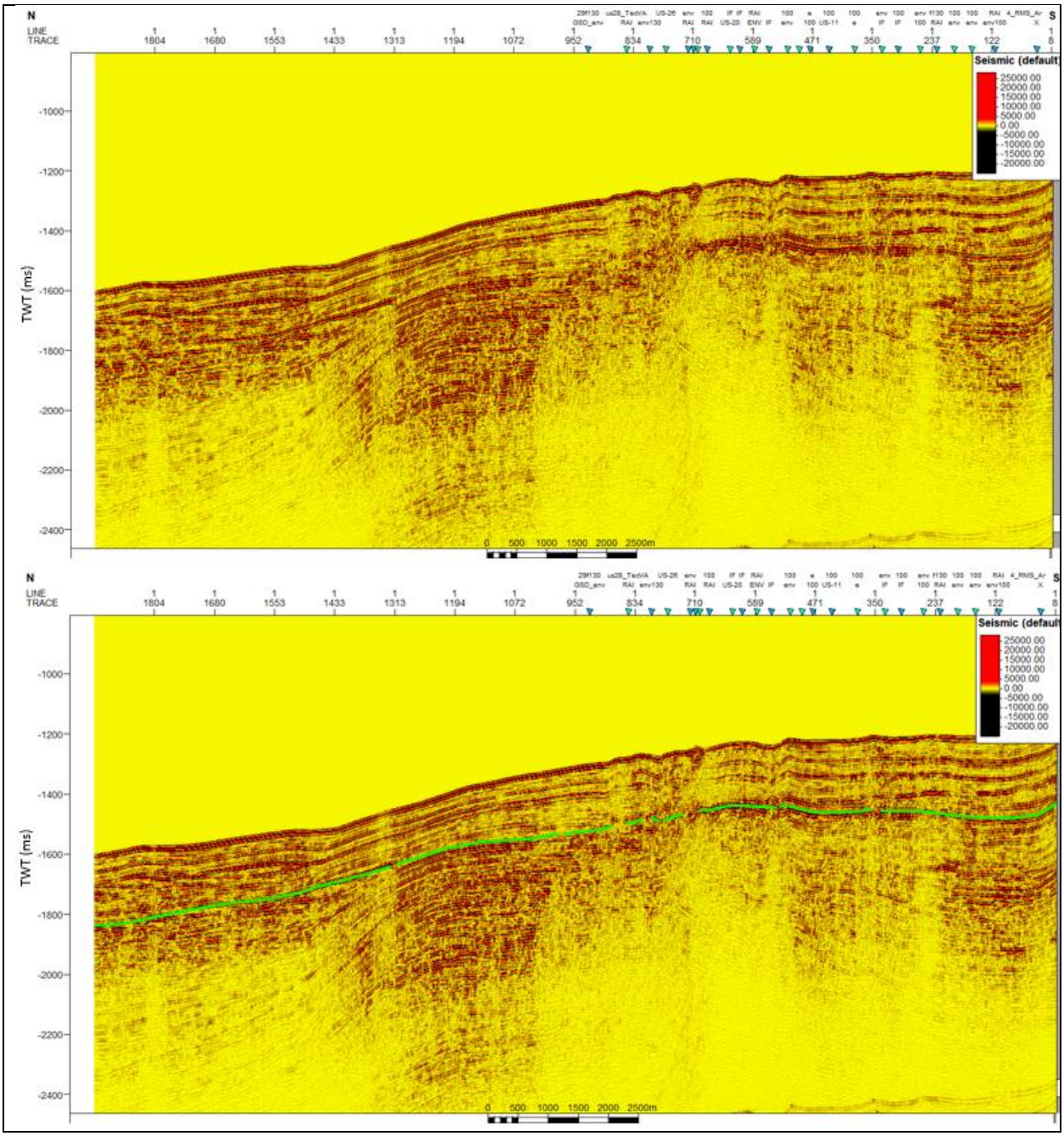

SCS profile US-54 with Spectral Decomposition of 100 Hz. Green line indicates BSR.

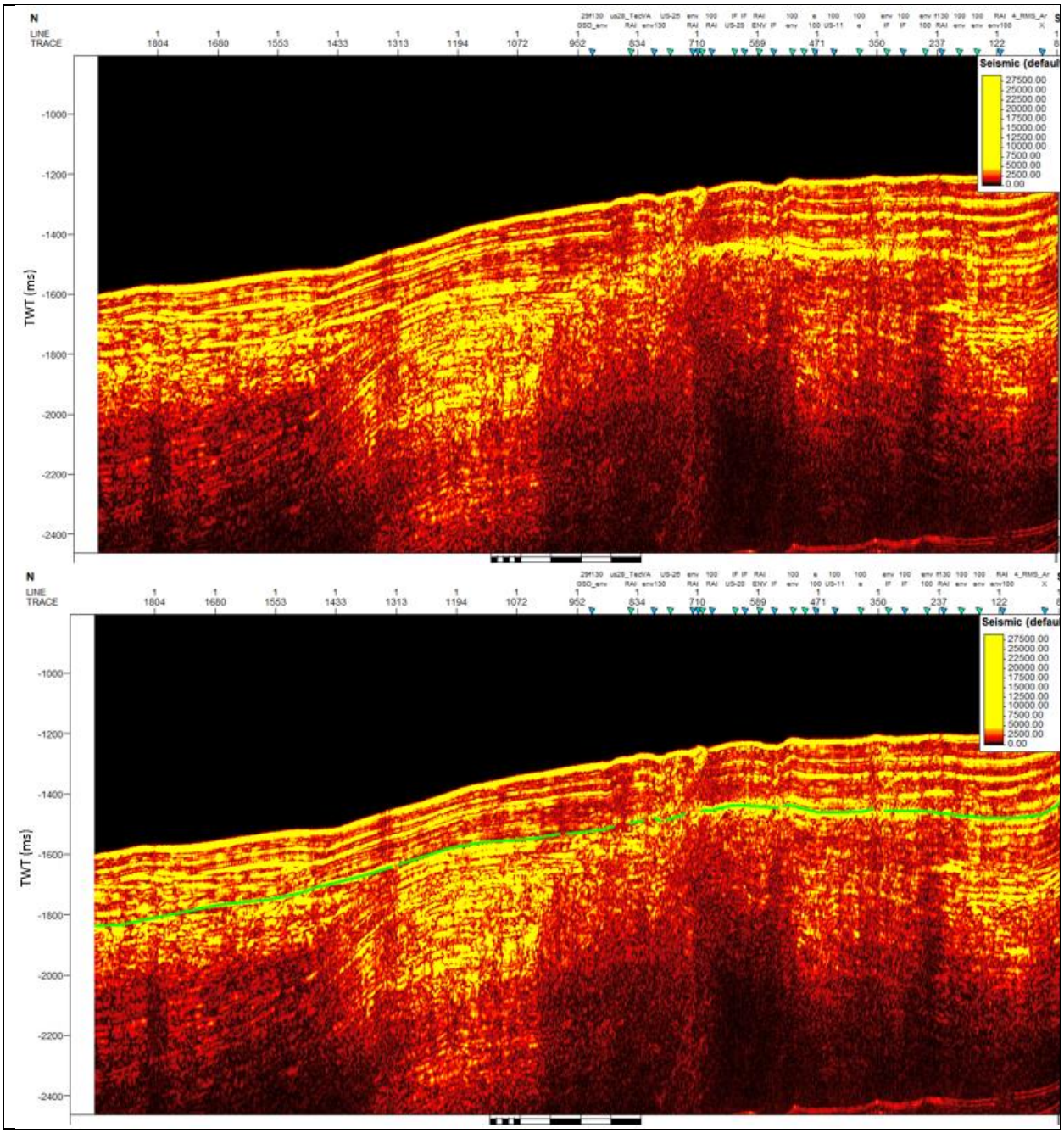

SCS profile US-54 with Spectral Decomposition of 100 Hz plus Envelope. Green line indicates BSR.